REPORT NO.
UCB/EERC-87/16
OCTOBER 1987

EARTHQUAKE ENGINEERING RESEARCH CENTER

EXPERIMENTAL STUDY OF SEISMIC RESPONSE OF R.C. SETBACK BUILDINGS

by

BAHRAM M. SHAHROOZ
JACK P. MOEHLE

Report to the National Science Foundation

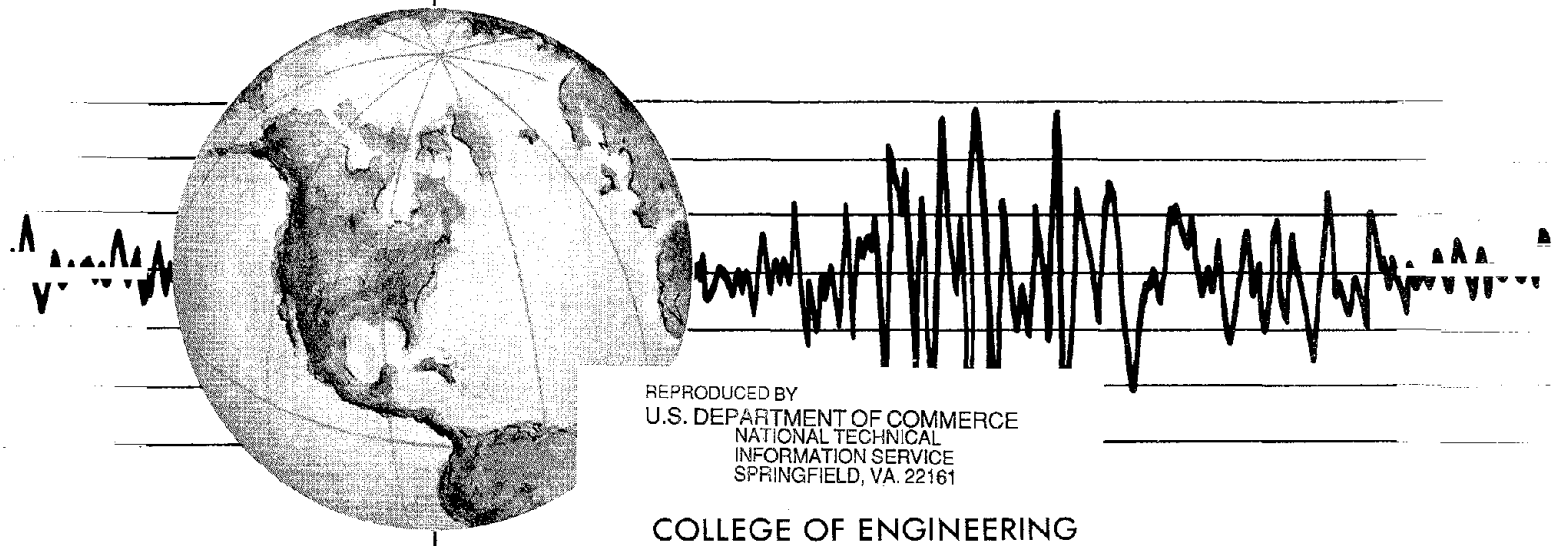

COLLEGE OF ENGINEERING

UNIVERSITY OF CALIFORNIA AT BERKELEY

For sale by the National Technical information Service, U.S. Department of Commerce, Springfield, Virginia 22161.

See back of report for up to date listing of EERC reports.

EXPERIMENTAL STUDY OF SEISMIC RESPONSE OF R.C. SETBACK BUILDINGS

by

Bahram M. Shahrooz

and

Jack P. Moehle

A Report to Sponsor:
National Science Foundation

Report No. UCB/EERC-87/16
Earthquake Engineering Research Center
College of Engineering
University of California at Berkeley

October 1987

1 2

ABSTRACT

A one-quarter scale model of a two-bay by two-bay, six-story reinforced concrete ductile moment resisting frame having 50 percent setback at the mid-height was designed, constructed, and tested. The prototype structure was designed for combined gravity and seismic effects determined according to the requirements of the 1982 Uniform Building Code. Proportion and details were provided to satisfy the seismic provisions of Appendix A of the ACI Building Code (ACI 318-83) and the ACI-ASCE Committee 352 recommendations for design of beam-column connections.

The test structure was subjected to a number of tests including static pull-back tests, free-vibration tests, and undirectional and bidirectional earthquake simulations on the earthquake simulator at the Earthquake Engineering Research Center of the University of California, Berkeley. The base motions modeled records obtained from the 1940 El Centro, 1978 Miyagi-Ken-Oki, or 1985 Mexico City earthquakes. The experimental findings from the response of the test structure were extended to a broad spectrum of response of setback frames.

This report documents design, construction, testing, and observed behavior of the test structure. Interpretations of the measured response are presented. Correlations obtained from three-dimensional elastic analysis and two-dimensional inelastic static and dynamic analyses are presented. Current provisions for seismic design of ductile reinforced concrete structures are evaluated. A method is presented by which potential concentration of damage in tower members of a setback building can be identified. A static analysis technique is proposed for design of setback structures.

ACKNOWLEDGEMENTS

The work described in this report was sponsored by the National Science Foundation under Grant No. CEE-8316662. Opinions, findings, conclusions, and recommendations in this report are those of the authors and do not necessarily represent those of the sponsor.

The research in this report was carried by the first author in partial fulfillment of the requirements for the degree of Doctor of Philosophy in Engineering under the supervision of the second. Professor Joseph Penzien is thanked for advice on response of setback buildings. Professor Graham H. Powell is acknowledged for offering assistance to modify the computer program DRAIN-2D.

The first author would like to express his sincere appreciation to his wife, Irene, for her love, encouragement, and support.

P. Quin is thanked for supervision of personnel at the Earthquake simulator Laboratory. R. Parson, W. Neighbor, and I. Van Asten were invaluable for their assistance in construction of the model. D. Clyde is acknowledged for his careful testing and calibration of all instrumentation.

S. J. Pantazapoulou is thanked for her constructive criticisms. C. M. Uang, a former graduate student at the University of California at Berkeley and now a faculty at the Northeastern University, willingly provided some of the computer programs used in this study. Construction of the model was not possible without the help of many students from the University of California at Berkeley. Their help is appreciated.

TABLE OF CONTENTS

LIST OF TABLES

LIST OF FIGURES

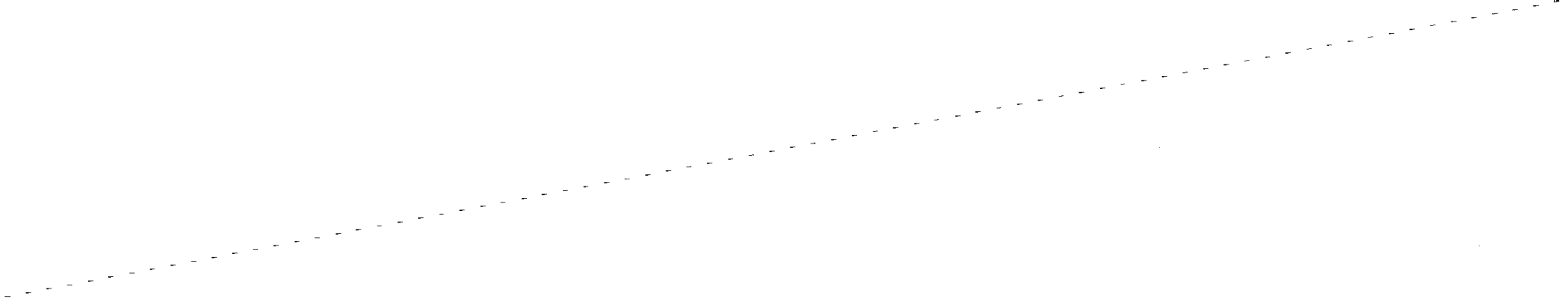

1. INTRODUCTION

Behavior of a multi-story building during strong earthquake motions depends on distribution of mass, stiffness, and strength in both horizontal and vertical planes of the building. Structural engineers have developed confidence in the design of buildings in which those distributions are more or less uniform. There appears to be less confidence about the design of structures having irregular distribution. A type of irregular structure that has repeatedly shown poor performance during past earthquakes is the setback building. For example, collapse of penthouses was reported after the 1981 central Greece earthquake [69], and whipping phenomenon caused failure in many buildings with penthouse towers during Tokachi-Oki earthquake of 1968 [21]. In most cases, the poor performance has been attributed to torsional effects and to concentration of inelastic action at the setback level or in the tower[6,7].

Many investigations have been performed to understand the behavior of setback structures, and to ascertain methods of improving their performance. Most of previous studies have been analytical often studying elastic response of simple structural systems that do not satisfy current code requirements. Experimental results are scarce.

The unsatisfactory performance of several setback buildings and the paucity of relevant research data on structures meeting current code requirements warrant a focused research to ascertain methods of improving performance of setback structures. Among the issues to be addressed are (1) the influence of setbacks on dynamic response, (2) the adequacy of current design requirements for setback buildings, and (3) design methods to improve the response of setback buildings. In an effort to investigate these issues, an experimental and analytical study was undertaken in which a complete moment-resisting reinforced concrete frame with floor slab was designed, constructed,

References are given in brackets [ ], and are listed alphabetically at the end of this report.

and subjected to simulated earthquake motions on a shaking table. Performance of this structure is studied to gain insight into behavior of setback structures. The study is extended to a broad spectrum of setback frames, from which an understanding of behavior and design requirements is ascertained.

The objectives and scope of the research reported herein are outlined in this chapter. The chapter also summarizes existing studies on the response of the setback buildings, building code methods for design of the setback structures, and the available experimental research on the performance of reinforced concrete frames.

1.1 Review of Previous Research

Aside from the forced-vibration test performed on the Hills Brothers Building in San Francisco in 1939, as presented in Appendix C of the 1980 Structural Engineers Association of California (SEAOC) [58], and the stepped structure in Merchant and Hudson's investigation [34], the dynamic behavior of irregular structures received little attention until the mid-1960's. In the past two decades, some analytical and experimental studies have been performed on the dynamic response of structures having setbacks or appendages. A review of these is presented next.

(a) Penzien and Chopra (1965)

Seismic forces in appendages located on top of a multi-story building were determined [53] using three different schemes. The structures were assumed to respond elastically. The study examined multi-degree of freedom, two-degree of freedom, and single-degree of freedom systems. In the two-degree-of-freedom analysis, each normal mode of the building (without appendage) was modeled by a separate two-degree-of-freedom system. The defining parameters were the generalized properties of the building without the appendage and the corresponding values for the appendage. The appendage seismic coefficient in the nth mode was then calculated as $C_{an}=\left|(X_a-X_n)\frac{k_a}{gm_a}\right|_{max}$; where

X_a and X_n are the generalized displacements of the appendage and building without the appendage, respectively, k_a is the appendage generalized spring constant, m_a is the appendage generalized mass, and g is the acceleration of gravity. The SRSS (square root of the sums of the squares) technique was used to obtain the "true" seismic coefficient. For the single-degree-of-freedom analysis, the two-degree-of-freedom system is reduced to two generalized single-degree-of-freedom systems representing its first and second modes of vibration. The maximum response in each of these two modes is obtained. The SRSS of the two maximum appendage spring forces is obtained to compute the maximum spring force produced by the nth building mode.

A comparison of the results indicated that the appendage maximum dynamic response could be predicted accurately using the two-degree-of-freedom method. This conclusion was true even when the appendage fundamental period coincided with the building period. Nevertheless, the single-degree-of-freedom system resulted in error when the appendage period was close to the period of one of the lower building modes.

(b) Skinner, Skilton, and Laws (1965)

A single-story building with a single-story tower was analyzed elastically under the El Centro earthquake [65]. It was found that if the tower and base periods (computed by specified equations) were not close, the tower shear force can be determined using the square-root-sum-of-squares of the two modal shear forces. When the period difference was under 5 percent, typical tower shears were determined to be about 4 and 1.5 times the tower weight for 5 percent and 10 percent building damping, respectively.

(c) Jhaveri (1967)

Linear elastic dynamic analysis of symmetric and asymmetric setback structures was performed [26]. The asymmetry was due to offset between the tower and base centroids. The parameters used were level of setback, p (defined as the ratio of the base

height to the tower height) and degree of setback, c (defined as the ratio of the tower area to the base plan area). A uniform frame with similar properties was also studied.

Computations indicated that the floor displacements in the tower portion were larger than those at similar levels in the uniform frame. The smaller the tower, the greater was the difference in the displacements. Defining the seismic coefficient as the ratio between story shear and weight above that story, it was found that the maximum seismic coefficient at the base of the tower was greater than the corresponding seismic coefficient in the uniform frame. This seismic coefficient was especially large when the tower was slender ($c<0.05$), and the lower mode periods of the base and tower (considered separately) were close or equal.

In buildings with asymmetric setbacks, the torque distribution was similar in profile to the shear distribution, except the kink of shear distribution at the setback level was absent from the torque distribution. The shear distribution was almost identical for buildings having symmetric and asymmetric setbacks.

(d) Blume and Jhaveri (1969)

Several linear elastic dynamic analyses were performed [10] on shear buildings with symmetric setbacks. Fifteen-story buildings with various degrees and locations of setback were subjected to the N-S 1940 El Centro and N69W 1952 Taft ground motions. For all setback locations, the responses under the El Centro record indicated an increase in the building base-shear coefficient as the tower size decreased relative to the base. Nevertheless, when the buildings were subjected to the Taft record, the base-shear coefficient did not change significantly as the tower size decreased. Analyses under both records showed an increase in the seismic coefficient at the base of the tower as the tower size decreased relative to the size of the base portion.

(e) Penzien (1969)

The research conducted in [53] was extended in this study [52]. The investigation concluded that conventional response spectrum analysis procedures underestimate the magnitude of the appendage base shear for closely spaced frequencies. The concentration of the forces in the appendage could not be identified by using a single oscillator to represent the entire structure. A two-degree-of-freedom modal analysis procedure was reported which yielded approximately the same force amplification as the response history calculations.

(f) Pekau and Green (1974)

Dynamic response of ten-story setback buildings was investigated [51]. Calculated inelastic response was compared with the elastic response of setback and uniform structures. A story stiffness ratio can be defined as the ratio between the tower story stiffness and that of a corresponding uniform structure. It was found that if the story stiffness ratio was greater than 0.60, the setback frame responded effectively as a uniform structure. However, elastic analysis of setback structures underestimated the story drift and ductility in structures with story stiffness ratio less than 0.60 and level of setback (the ratio of the base height to the total height) greater than 0.80. For setback structures in the latter range of parameters, excessive whipping of the tower was thought to lead to the discrepancy between elastic and inelastic response.

(g) Humar and Wright (1977)

Inelastic dynamic behavior of a class of setback structures was examined under the N-S component of 1940 El Centro earthquake [25]. A uniform frame and a setback frame were derived from a single-bay fifteen story frame termed the "basic frame". The uniform frame was a three-bay fifteen story frame made by joining three basic frames. Thus, the member properties were similar to those in the basic frame, except that the

interior columns were twice as strong as the columns of the basic frame, as these columns comprised of two basic frame columns. The base portion of the setback frame had three equal bays, and the single-bay tower was located centrally.

Two parameters were used to define the different frames. The level of setback, l_s, was defined as the ratio of the base portion height to the overall building height. The tower-base-plan area ratio, R_s, was defined as the ratio of the tower plan area to the base plan area.

For the inelastic analyses, the members were assumed to have a stable bilinear hysteresis behavior. A similar mass was used for each floor of the uniform frame. For the setback frame, floor mass in the base portion was assumed to be equal to a typical floor mass of the uniform frame. Floor mass in the tower was taken as the base floor mass multiplied by R_s. The combined column and beam lateral stiffness at any level of the tower was taken as the corresponding stiffness of the uniform frame multiplied by R_s. The base portion had same properties as the uniform frame.

It was observed that a decrease in value of R_s decreases the fundamental period of vibration (with a less pronounced change for the second and third modes), increases the contribution of higher modes to the base shear, decreases inter-story drifts in the base portion (with a more pronounced reduction when the setback is near the mid-height), and increases the seismic coefficients throughout the building height. The inter-story drifts in the base portion were found to be smaller than those in the uniform frame. In the tower portion, the maximum inter-story drifts, maximum shear coefficients, and maximum girder ductility ratios were substantially greater than the corresponding responses of the uniform frame.

Story shear envelopes were computed for the different test models when subjected to the El Centro record, and compared with the profiles obtained using the 1973 SEAOC code provisions. It was found that the code method underestimates the story shears in the upper one third of the building even when it is uniform. The discrepancy was larger

for the setback models.

(h) Aranda (1984)

Ductility demands for reinforced concrete frames with setbacks were investigated using analytical models [4]. The ten-story test models had three equal bays, and the tower was centrally located at the mid-height. The structures were designed in accordance with the 1977 Mexico City Building Code.

Inelastic behavior was observed even for the cases where ductility factor of one had been used in design. The maximum computed ductility demand was found to be twice the design ductility factor for setback frames, while it was 1.5 times the design value for an equivalent regular frame. The ductility demand was larger near the setback level.

(i) Korkut (1984)

The elastic response of two structures with irregular profiles was investigated [30]. The test structures were eight-story frames with 50 and approximately 80 percent setbacks located at the mid-height. The computed shear distribution (from the elastic dynamic analysis) and the corresponding value obtained by assuming a linear acceleration over the height were found to be different by 40-50 percent. Large discrepancies were also found between the computed shear distribution and that from the first mode. Elastic dynamic analysis was recommended as an indispensable method for seismic design of setback structures.

(j) Wood (1986)

Two planar small-scale reinforced concrete frames with setbacks were constructed and tested on an earthquake simulator [77]. The structures were approximately 1/15

scale models of nine-story, three-bay frames. Symmetrical and asymmetrical arrangements of setbacks were selected, and the story weights and floor areas varied by as much as 66 percent in the adjacent stories. It was concluded by Wood that the observed dynamic behavior of both the frames did not indicate any unusual behavior, and no evidence was found that the design analysis for such frames should be different from that for regular frames.

1.2 Review of Recommended Building Code Methods

The Uniform Building Code (UBC) [72], Structural Engineers Association of California (SEAOC) [58], and Applied Technology Council (ATC) [68] permit the use of equivalent lateral force analysis for buildings with setbacks when the tower plan dimension is at least 75 percent of the corresponding base plan dimension. For buildings with smaller tower-plan dimension, the equivalent lateral force analysis is no longer applicable and alternative approaches are recommended as follows.

(a) SEAOC Setback Sub-Committee Report (1958)

In Appendix C of the 1980 SEAOC, some special provisions are presented for design of setback structures. These requirements are similar to the "standard" lateral force analysis technique for uniform buildings, but the lateral force distribution might not be continuous over the building height. Depending on the range of two parameters, four procedures are recommended. (This report does not clarify whether there is a scientific basis for the methods.) These parameters are the ratio of the tower width parallel to the direction under consideration to the corresponding dimension of the base, and the ratio of the tower height to the building height. The three-dimensional behavior is ignored, and the two orthogonal lateral forces are treated separately. The different methods are :

(1) The entire building system is considered. The period and base shear are then obtained using some weighted average width of the tower and base; no specific

guideline is given as how to determine the average width. The base shear is distributed along the building height using the "standard" methods.

(2) The base is treated as a separate building. Considering the tower weight and the tower base shear applied at the base top story, the standard procedures are followed to obtain the lateral force distribution over the base height. The tower base shear is calculated as if the tower is a separate building situated on ground. This force, increased by 40 percent, is then distributed over the tower height following the usual techniques.

(3) A fictitious building is obtained by extending the tower through the base to the foundation level. Lateral forces are distributed over the fictitious building height, which is equal to the entire building height. Portions of the base not included in the extended tower are used to determine additional lateral forces over the base height.

(4) Two methods are recommended; the one which produces larger design forces is to be used. One approach is to treat the base and tower as separate structures and to follow method (2), as discussed previously. The other method is to consider the tower and base as one building with the full height and some weighted width. The base shear is obtained for this structure, but it must be increased by 20 percent.

(b) ATC (1978)

A simple procedure may be used if (1) the base and tower, when considered separately, can be classified as regular structures and (2) the base top story is at least five times stiffer than the first story of the tower. If these conditions are satisfied, then the base and tower can be analyzed separately. Lateral forces are distributed over the tower and base using standard techniques. The tower base shear and its weight must be considered to determine lateral forces acting on the base. A modal analysis technique is recommended if the abovementioned procedure is not applicable.

(c) UBC(1982) and SEAOC(1980)

Both the UBC and SEAOC require a complete analysis of the structure when the plan dimension of the tower in any direction is smaller than 75 percent of the building plan dimension. The analysis should account for the stiffness properties and mass distribution. A modal analysis method is recommended in the SEAOC commentary; the acceleration spectrum can either be constructed using the UBC or SEAOC base shear formula or can be a more appropriate spectrum suitable to the site conditions. The two horizontal ground motion components are incorporated separately, i.e., the structure is analyzed separately in each principal direction. Modal analysis must account for the possible lateral-torsional coupling. One approach is to idealize each floor with three degrees of freedom (two translational and one torsional).

1.3 Abbreviated Review of Previous Experimental Research on Response of R/C Structures

There have been numerous research studies aimed at improving seismic performance of reinforced concrete structures. Many of these are experimental studies of components of a building [e.g., 18,19,31,33,55,56,78]. Even though it is necessary to understand behavior of different components composing a structure, it is essential to investigate the interrelation of beams, columns, and joints in a complete building system. Such study is not possible unless a complete structural system is tested.

A number of such experiments on nearly complete structural systems has been performed. Two-story reinforced concrete frames with a single bay in each direction were tested by Clough and Oliva [15,44]. The 0.707-scale models were intended to represent a portion of a typical low-rise building designed to meet most of the ductile requirements of the 1970 Uniform Building Code (UBC) and the ACI Building Code (ACI 318-71). A series of shaking table tests was performed by Bertero [9] on a 1/5-scale model of a seven-story, two by three bay reinforced concrete frame-wall structure. The

model did not entirely satisfy the UBC requirements. Several small-scale planar models have been tested at the University of Illinois at Urbana-Champaign[1,5,22,23,32,39,40,60,76,77]. Many of the test structures had been designed using principles of the substitute structure design method [62]. Behavior of flat-plate structures was studied by Moehle [38]. The test structure was a 1/3-scale model of a two-story reinforced flat-plate structure having three bays in one direction and multiple bays in the transverse direction. Proportions of the structure were determined according to conventional design practice satisfying ductile requirements of ACI 318-83 for structures located in a region of moderate seismic risk, and design seismic lateral forces as specified for Zone 2 of the 1982 UBC. With the exception of the structure reported in Reference [38], none of the test frames satisfies current design and detailing practice.

1.4 Objectives and Scope

(a) Objectives

As noted in the preceding paragraphs, there are limited experimental data on the seismic response of structures with setbacks, and current seismic design and detailing requirements for reinforced concrete frames have not been investigated experimentally for a complete structural system. The majority of previous analytical studies have concentrated on the elastic response of setback structures with little emphasis on damage distribution. Considering the need for experimental results, and the limitations of the available information, the analytical and experimental study reported herein was undertaken. Specific objectives of this research are (1) to study the effects of setbacks on the dynamic response of structures during low, moderate, and high intensity seismic loading, (2) to observe the adequacy of current code requirements for design and detailing of reinforced concrete structures in regions of high seismic risks, (3) to investigate the reliability of existing modeling techniques to correctly compute global

response of a complete reinforced concrete frame, and (4) to construct a simple method for design of setback structures.

(b) Scope

In an effort to achieve the abovementioned objectives, an experimental and analytical study was undertaken. A 1/4-scale model of a two-bay by two-bay, six-story reinforced concrete ductile moment resisting frame with floor slabs having 50 percent setback at the mid-height was designed and constructed. The structure was assumed to be located in a seismically active region classified as Zone 4 by the 1982 Uniform Building Code. Members were proportioned and detailed to satisfy the seismic provisions of Appendix A of the ACI Building Code (ACI 318-83). Connection design was based on the ACI-ASCE Committee 352 recommendations. The test structure design is described in Chapter 2. A summary of the actual material properties is provided in Appendix A.

The experimental model was subjected to a number of tests including static pull-back tests, free-vibration tests, and unidirectional and bidirectional earthquake simulations using base motions modeling records obtained from the 1940 El Centro NS record, the 1978 Miyagi-Ken-Oki S00E record, and the 1985 SCT Mexico City S60E record. Continuous response measurements monitored behavior of the specimen. The test structure construction, testing procedures, and instrumentation are presented in Chapter 3 and Appendix B.

Data reduction and sign convention are presented in Chapter 4 and Appendix C. In Chapter 4, the linear elastic response spectra, Housner spectrum intensity, and a Fourier amplitude spectrum are presented for each input motion. Measured responses and the damage patterns are also presented from an objective point of view.

In Chapter 5, the base motions are interpreted using the information presented in Chapter 4. The methods by which the mode shapes and vibration frequencies were

obtained are summarized, and the dynamic characteristics of the test structure are tabulated. General characteristics of measured responses, and their variations throughout the experimental program are discussed.

Using available three-dimensional elastic and two-dimensional inelastic mathematical models, the response of the test structure is studied in Chapter 6. The mathematical models and different assumptions used to calculate the responses are presented. Measured and calculated stiffness and strength characteristics are compared to assess the reliability of the analytical models in correlating with the measured responses. Results of a sensitivity study are also presented to establish the dependency of the computed responses on various parameters such as beam effective flange width and load-deflection characteristics of individual members. Conclusions are drawn relative to the success of the existing analytical methods in correctly computing responses.

The design method is evaluated in terms of the expected and observed damage, drift, and strength. The findings are discussed in Chapter 7. Various design and detailing provisions are carefully examined to determine the sources of the differences between the "design" and observed behavior. Simple methods are presented by which to estimate the drift expected during high-intensity ground shaking, and by which to obtain a reasonable approximation of the strength.

In Chapter 8, the experimental findings from the response of the test structure are supplemented with a series of parametric studies that was performed to establish rational guidelines to detect and to avoid potential concentration of damage in setback buildings. Inelastic dynamic response of six generic frames (with various setback configurations) is examined. Based on elastic response of a two-degree-of-freedom system, a chart is constructed by which potential concentration of damage in the tower members could be identified. Using the same chart, a method utilizing static analysis is proposed for design of setback structures. Conclusions are made relative to the success

of the proposed techniques in detecting and preventing damage concentration in the tower members.

2. TEST STRUCTURE

This chapter describes design of the test structure. Overall configuration of the test structure is described first, followed by a description of different aspects of the design methods and resulting details.

2.1 Test Structure

The test structure modeled an imaginary prototype structure. The prototype is a six-story, two-bay by two-bay reinforced concrete ductile moment resisting frame having 50 percent setback at the mid-height. The prototype is represented by the 1/4 scale model depicted in Fig. 2.1.

The overall configuration, i.e., number of bays and floors was chosen based on the construction feasibility and testing facility limitations on the weight of the model. The fifty percent setback was selected to simulate a case for which the static lateral force analysis for seismic design is no longer applicable according to the current codes [58,68,72]. The layout of columns and beam spans (Fig. 2.1) was chosen so that fundamental frequencies in the two orthogonal directions would be substantially different.

2.2 Design

Prototype seismic design forces were determined according to the requirements of the Uniform Building Code (UBC) [72]. Proportions and details satisfy the seismic provisions of Appendix A of the ACI Building Code (ACI 318-83) [11]. The design of connections, including minimum column flexural strengths, was based on the ACI-ASCE Committee 352 recommendations (Comm. 352) [2]. All the UBC serviceability requirements were checked and found to be satisfied.

The prototype dimensions were scaled using the length factor of 0.25 to obtain the corresponding dimensions and details for the test structure. Design concrete strength was 4000 psi and all reinforcement was Grade 60 (minimum yield stress of 60 ksi). Provided material properties for the test structure are described in Appendix A. Different aspects of design are described in greater detail in the following sections.

2.2.1 Analytical Modeling

Current codes and recommended practice (ATC and UBC) do not allow use of the equivalent lateral force static analysis for seismic design of structures having a 25 percent setback because of concerns over irregular dynamic behaviors. Rather, a dynamic modal spectral analysis is recommended for such structures. For the test structure, a modal analysis was performed using a microcomputer version of the program TABS [73]. The three-dimensional structure was idealized as six plane frames (three in the long direction and three in the short direction) interconnected by the rigid floor slab having two translational and one rotational degrees of freedom. The modal contributions from six modes were combined using the CQC (Complete Quadratic Combination) method [74]. Interaction between the long-direction and short-direction frames is not considered in this program. Thus, the column axial forces from each plane frame had to be combined to obtain the total axial forces for a column common in the long-direction and short-direction frames.

Each plane frame was modeled using two-dimensional frame elements. Column flexural stiffnesses were based on gross uncracked sections; cracking and the slab contribution were approximately taken into account by using half of the gross uncracked flexural stiffness computed for a "T" cross section representing beam and slab (the effective flange width is given in Section 2.2.3). Effects of shear deformation, although computed to be small, were included in member stiffnesses. Youngs modulus for concrete was assumed to be 3600 ksi, and shear modulus was taken as 1200 psi.

Computed periods and mode shapes are in Table 2.1. It is noted that the first-mode translational period of 0.57 sec. and 0.45 sec. in the long and short directions, respectively, correspond to N/10.5 and N/13.3, where N is the number of floors.

2.2.2 Design Loads

The prototype structure was designed for the combined effects of factored gravity and earthquake loads according to U=0.75(1.4D+1.7L+1.87E), U=0.90D+1.43E, and U=1.4D+1.7L, in which U, D, L, and E are the ultimate design load, service dead load, service live load, and code design earthquake load, respectively. These ultimate design load combinations are in accordance with ACI 318-83 [11].

The gravity loads consisted of the self weight and live load equal to 40 psf. The lateral loads were accounted for by an acceleration spectrum constructed using S_a=gZICKS, which is a different form of the UBC base shear equation (V=ZICKSW), in which g is the acceleration of gravity, Z is a numerical coefficient dependent upon the zone specified by the UBC, C in a numerical value as defined by the UBC, I is the occupancy importance factor as set by the UBC, K is a numerical coefficient as given by the UBC, S is a numerical coefficient for site-structure resonance, W is the total dead load as defined by the UBC, and S_g is the acceleration spectrum. The resulting spectral acceleration was multiplied by the ratio of the total weight to the effective modal weight in order to make the resulting base shear force comparable with its code counterpart[15]. Assuming a linear mode shape, the spectral acceleration becomes

$$S_a=\Sigma W_i\frac{\Sigma W_i X_i^2}{\left\{\Sigma W_i X_i\right\}^2}gZICKS$$

where W_i is the ith floor weight and X_i is the height of the ith level above the building base. The UBC values for Z,I,C,K, and S were used so that the first mode base shear would be equal to the UBC design base shear for a building in seismic Zone 4. In this equation, S was assumed equal to 1.5, and I was taken as 1.0. The resulting base shear

in the first mode is equal to 129 kips and 113 kips in the long and short directions, respectively. Total design base shears equal to 150 kips and 141 kips in the two orthogonal directions result following modal combination.

2.2.3 Beam Design

The beams were proportioned and detailed in accordance with the seismic provisions in Appendix A of ACI 318-83. Eight different beams , labeled B1 through B8, were selected (Fig. 2.2). Flexural strengths were computed according to ACI 318-83, ignoring contributions of slab reinforcement. Occasionally, for some beams the provided ultimate flexural strength was smaller than the required capacity (Fig. 2.3). Nevertheless, the strengths were considered to be adequate since the "understrengths " were not more than 5%.

For the test structure, long-direction beams are 5" wide and 7" deep, and those in the short direction are 4" wide and 7.5" deep. Beam longitudinal reinforcement is deformed nominal #2 (Type 1) and #1 bars (Appendix A). The longitudinal reinforcement ratio varies between 0.41% and 0.66% for beams spanning in the long direction, and between 0.36% and 0.72% for those in the short direction. Different beam cross sections, for the test structure, are depicted in Fig. 2.4. In this figure, "end cross section" refers to sections within 27" and 16" from column face for the long-direction and short-direction beams, respectively.

The transverse reinforcement was selected following the provisions in section A.3.3 of ACI 318-83. The probable beam flexural strength was calculated differently by considering the slab contribution within an effective flange width equal to b+h (for the exterior beams) and b+2h (for the interior beams), where b is beam web width and h is beam depth minus slab thickness. The shear strength of concrete was ignored and the transverse reinforcement spacing was based on only the shear capacity of stirrups. For the model, the transverse reinforcement is galvanized plain wire gauge # 11 (Appendix

A), and the spacing is illustrated in Fig. 2.5.

2.2.4 Column Design

The report of ACI-ASCE Committee 352 (Comm. 352) recommends that the sum of nominal column strengths should be at least 1.4 times the sum of nominal beam strengths at a connection. Nominal beam strength is based on a rectangular cross section, and the slab contribution is ignored. For the prototype structure, column flexural overstrength ratios computed from the provided properties are generally in excess of 1.4. The ratios typically exceed the value of 1.4 because of limitations in available model materials. The higher ratios are likely to be beneficial to structural performance because of anticipated effects of the slab which could enhance beam flexural strengths [9,18,45,56], and higher modes which could affect plastic hinge patterns [47,49,50]. The final "amplifying factors" in each principal direction for the test structure are shown in Fig. 2.6, the smaller amplification factor is more critical and controls flexural design of columns. In the first four floors, the ratios range between 1.6 and 2.2, and it is much larger than the target ratio of 1.4 for the upper two floors. At the third-floor corner joints, the overstrength ratios are below 1.4. The columns were not changed since the potential plastic hinges at these locations would not be critical.

Columns for the test structure consisted of two types, labeled C1 and C2 (Fig. 2.2). Column cross sections are depicted in Fig. 2.7. Details of the footing are shown in Fig. 2.8. Longitudinal reinforcement ratios are 1.5% and 2.3% for the column type C1 and C2, respectively, and column longitudinal reinforcing bars are deformed nominal #3 and #2(Types 1, 2, and 3) (Appendix A). With the exception of the central column, the column longitudinal reinforcing bars are continuous throughout the height. For the central column, the reinforcing bars were spliced between the first and second floors, and between the third and fourth levels. The lap splice length was determined using recommendations of Sivakumar, Gergely, and White [64]; a lap splice length equal to 13

in. was used for all the longitudinal bars (Fig. 2.5(b)).

The transverse reinforcement spacing within the potential plastic hinge region was based on the ACI 318-83 provisions in section A.4.4. The length of plastic hinge was governed by the larger column dimension (6.5"); this length was increased to 7" for the column type C2. Inelastic action can be more extensive at the foundation level [49]; thus, the closely spaced hoops at this level were extended for a larger distance (8" and 9" from the foundation face for columns C1 and C2, respectively). In checking shear resistance, the effective shear cross section was taken equal to the confined core dimensions, and the shear resistance of concrete was considered as per ACI 318-83, which specifies that shear resistance of concrete can be considered if $P > \frac{A_g f_c'}{20}$ (P is axial load, A_g is the gross cross-sectional area, and f_c' is the compressive strength of concrete). This provision of ACI 318-83 was violated in the 5th and 6th floors for which $P = \frac{A_g f_c'}{24}$ and $P = \frac{A_g f_c'}{40}$, respectively. This was not considered significant, as anticipated shears in these floors were well below available strengths. Due to construction constraints, the first column hoop was placed at the footing face, violating the ACI 318-83 provision 7.10.5.4 that ties shall be located vertically not more than 1/2 tie spacing above the top of footing or slab in any story. No unusual behavior was apparently attributable to this procedure, but the positive results in this experiment are not intended to encourage this practice in general. Transverse reinforcement is gauge #9 galvanized plain wire (Appendix A). Spacing of the transverse reinforcement is depicted in Fig. 2.5.

2.2.5 Slab Design

The slab thickness of the test structure was selected to be 1.75" to satisfy the ACI 318-83 minimum thickness requirement in section 9.5.3. Using the strip design method [46], flexural reinforcement was designed to carry the factored gravity loads. Adequate

strength could be provided by placing the reinforcement at the maximum allowable spacing, i.e., two times the slab thickness. Nevertheless, the reinforcement was occasionally placed at a smaller spacing to coincide with the locations of the beam shear stirrups since the slab reinforcement had to be tied to the beam transverse reinforcement. The slab reinforcement for the test structure is gauge #9 plain wire which was lightly deformed to improve its bond strength. The arrangement is depicted in Fig. 2.9.

2.2.6 Joint Design

The Comm. 352 recommendations [2] were closely followed. The recommendations had the intended effect of boosting member dimensions above those that would have been required to satisfy element flexural and shear strength requirements, as follows. The smaller column cross-sectional dimension and depth of the deeper beam were selected to satisfy the recommended development length (20 times the reinforcing bar diameter). The larger column dimension and beam widths were selected such that the resulting joint would have adequate area to resist the anticipated shear force. The beam depth and cover for the top reinforcement in the long direction were chosen to avoid bending of beam longitudinal bars within the joint. Finally, the number of column longitudinal bars was decided by the maximum allowable bar separation permitted in the recommendations.

Selecting the gross dimensions as above, the joint design required a check of the joint shear strengths. Required spacing of the column transverse steel within the joint became identical to the spacing within the plastic hinge region. Design joint shear stresses ranged between $11.0\sqrt{f_c'}$ and $13.1\sqrt{f_c'}$ for interior joints, $3.5\sqrt{f_c'}$ and $13.1\sqrt{f_c'}$ for exterior joints, and $2.5\sqrt{f_c'}$ and $6.6\sqrt{f_c'}$ for corner joints. These values compare with recommended maximum design strengths (nominal strength reduced by strength reduction factor) of $17\sqrt{f_c'}$, $12.8\sqrt{f_c'}$, and $10.2\sqrt{f_c'}$, respectively, with the exception of

joint shear stress for the exterior joints in the first two levels of Frame 4 (Fig. 2.1) which exceeds the recommended maximum design value of $12.8\sqrt{f'_c}$ by 2.0 percent. This was not considered significant, as the "understrength" is small.

3. EXPERIMENTAL PROGRAM

This chapter describes fabrication of the test structure, testing procedure, and instrumentation.

3.1 Fabrication

To avoid difficulty in casting the quarter-scale columns, the test structure was constructed in an unconventional manner. Reinforcement for the long-direction beams and slabs at the joints was tied in position before the short-direction frames were cast (Fig. 3.1). The three short-direction frames (Frames 4-4, 5-5, and 6-6 in Fig. 2.1) were cast separately in a horizontal position atop a pivoting platform (Fig. 3.2). The short-direction frames were subsequently pivoted to an upright position and fixed above a steel foundation frame (Fig. 3.3). After forms and reinforcing cage for the long-direction beams and slabs were completed (Fig. 3.4), the first two floors were cast. After an appropriate curing period for these floors, the remainder of the model was cast. No unusual behavior was apparently attributable to this construction procedure. An overall view of the test structure is shown in Fig. 3.5.

Gross cross-sectional dimensions of the beams and columns, and the slab thickness were measured following construction. Average dimensions of the long-direction beams, short-direction beams, columns, and floor slabs are 7.1" x 5.0", 7.6" x 4.1", 5.1" x 6.6", and 2.0", respectively, and variation of the measured dimensions is summarized in Table 3.1. With the exception of the slab thickness, the actual dimensions are within the selected construction tolerance of 1/8", corresponding to 1/2" for the prototype structure.

Following the construction, the model was moved (on rollers) from the construction site to the shaking table at the Earthquake Engineering Research Center at the University of California at Berkeley. Then, the steel foundation was hydrostoned in

place on the shaking table, and subsequently prestressed to the shaking platform. Absence of cracking in the hyrdostone during the experiments verified that the foundation was adequately fixed to the test platform. For the biaxial earthquake simulations (as explained in section 3.2.3), the model with steel foundation was jacked onto rollers, rotated, and then secured in a similar manner on the testing platform.

In order to simulate effects of the service dead load expected for the prototype, subsidiary lead pigs were fastened to the top surface of slabs. Live load was not simulated. 112 lead pigs (each approximately 97 lbs) (stacked in two layers at locations adjacent to the beams, and in one layer in the middle (Fig. 3.6(b)) were attached to the top surface of each floor in the first three floors. 62 lead pigs (stacked in two layers) were placed on each floor for the upper three stories. The lead pigs were held in place with a connection system (Fig. 3.6(a)) designed to ensure that the weights moved with the slab, but that the weights did not change stiffness and strength of the slab. A complete discussion of the connection system is given elsewhere [38]. The lead pigs were distributed to produce approximately the correct magnitude of beam dead load shear and moment in both the long and short directions. The location of the lead pigs is illustrated in Fig. 3.6(b). Total weight of the test structure, including lead pigs, was 72.2 kips.

3.2 Testing Procedure

Tests included static pull-back tests, low-amplitude free-vibration tests, and earthquake simulation of varying intensity. The test sequence is summarized in Table 3.2. Each type of test is explained in the following sections.

3.2.1 Static Tests

Static tests were conducted before subjecting the test structure to any earthquake simulation. The tests were performed by pulling the structure with a cable attached at

the roof (Fig. 3.7). After each loading increment (measured by a load cell) the roof displacements relative to a reference frame (measured by Direct Current Differential Transformers (DCDTs)) were recorded digitally by a data acquisition system. The structure was pulled at three different points, labeled pull types 1, 2, and 3 in Fig. 3.7. The lateral load-displacement relations enable determination of initial lateral and rotational stiffnesses of the test model.

These tests were performed when the model was at the construction site, and when it (with and without lead pigs) was on the shaking table platform. Thus, any possible change in the lateral stiffness due to the lead pigs could be detected. Foundation fixity was ensured by blocking the shaking table platform (wooden blocks wedged against the test platform to ensure base fixity) when the model was on the test site (shake table), and by stacking lead pigs on the steel platform when the model was at the construction site. The sequence of the tests is summarized in Table 3.2.

3.2.2 Free-Vibration Tests

For tests at the construction site, the free-vibration test setup was identical to that used for the static tests. For tests on the shaking table, the shaking table platform was blocked for each test, as described in Section 3.2.1. A test was performed by first pulling the model with a cable attached at the roof. When the cable applied a force having a horizontal component of 1000 lbs, the structure was suddenly released by cutting the cable. For consistency throughout the testing program, the force in the cable was kept the same for all the tests. Response was monitored by three accelerometers per floor that were attached to the top surface of floor slab (Fig. 3.9); only three accelerometers (attached to the sixth floor) were used during the tests conducted while the test structure was at the construction site.

Six free-vibration tests were conducted while the model was at the construction site. When the test structure (with and without lead pigs) was on the shaking table

platform, twelve more tests were completed before subjecting to any earthquake simulation. These tests were intended to measure the free-vibration frequencies, vibration mode shapes, and damping properties of the "uncracked" test structure. Variation of the low-amplitude vibration frequencies and damping values were monitored throughout the testing program by performing free-vibration tests before and after each earthquake simulation. A total of nine such free-vibration tests was performed. It was, then, possible to assess the increase in vibration periods and damping properties associated with different damages occurred during earthquake simulations. These tests are summarized in Table 3.2.

For the "uncracked" model on the shaking table, the free-vibration tests were performed in both long and short directions (using pull types 1, 2, and 3 in Fig. 3.7) in order to excite translational and torsional modes of vibration. The model was pulled only in the long direction during the free-vibration tests conducted after each earthquake simulation. In order to keep the foundation fixity consistent, the shaking table platform was blocked (Section 3.2.1) during all the free-vibration tests.

A series of forced-vibration tests was also performed. The test structure was excited by a shaker placed on the top surface of the sixth floor. Different signals in the long and short directions were input to the test structure using the shaker. The results of the "shaker tests" are not discussed in this report.

3.2.3 Earthquake Simulation Tests

The test structure was subjected to ten base motions of varying intensity. The simulations are summarized in Table 3.2. Earthquake simulations were conducted in two stages. In the first stage of testing (Fig. 3.8), a series of horizontal base motions of successively increasing intensity was applied parallel to the long-direction frames to simulate uniaxial response. In the second phase (Fig. 3.8), unidirectional horizontal motions were input at an angle of 45 degrees relative to the principal axes of the frames

to impart biaxial lateral-torsional response. Vertical and rotational base motions were not input intentionally during these tests, although secondary motions of this type occurred.

The input signals to the shaking table modeled acceleration and displacement histories of the 1940 El Centro NS record, the 1978 Miyagi-Ken-Oki S00E record, or the 1985 SCT Mexico City S60E record as indicated in Table 3.2. Durations of the prototype El Centro , Miyagi-Ken-Oki , and Mexico City (for tests MX10.3B and MX19.7B) records were compressed by a factor of 2 so that frequency content of the base motion and that of the scaled model would be approximately in accord. For the final test, the Mexico City record (during test MX34.6B) was compressed by a factor of 3 in order to "resonate" the test structure and achieve a desirable damage state.

Following each earthquake simulation, visible damage was observed and recorded. This information was helpful to identify actions occurring at locations where there was no instrumentation, and also to correlate with damage indicated by strains in the reinforcing bars.

3.3 Instrumentation

A total of 126 data channels of electronic instrumentation monitored motion of the shaking table, horizontal accelerations and relative displacements of floors, and strains on selected beam and column reinforcing bars. The data channels were organized as indicated in Appendix B. Detailed information is presented in the following paragraphs.

(i) Table instrumentation measured base accelerations (including average horizontal, vertical, roll, pitch, and twist accelerations), vertical and horizontal displacements, and horizontal velocity.

(ii) Accelerometers (acc1-acc18) measured absolute accelerations of floor slabs along principal axes of the test structure (Fig. 3.9).

(iii) Direct Current Differential Transformers (DCDTs D1-D7) and linear potentiometers (POTs P1-P9) monitored absolute horizontal displacements at mid-depth of the short-direction beams at each floor parallel to the input motions during the uniaxial tests (Fig. 3.10a). DCDTs D1-D7 and POTs P1-P7 were fixed on a reference frame and targeted to the test structure, and POTs P8 and P9 were targeted to an interior balcony in the test laboratory at a distance of approximately 15 ft. from the target point on the test structure. The horizontal displacements were also derived by DCDTs mounted diagonally to measure inter-story drifts (Fig. 3.10b). DCDTs DG1-DG18 provided a check on readings from D1-D7 and P1-P9 during uniaxial series of tests. For the biaxial tests, nevertheless, the diagonal DCDTs were essential to obtain floor lateral displacements, because readings from D1-D7 and P1-P9 would be "polluted" by additional displacements due to twist of the model, and pure displacements could not be obtained using these instruments. Thus, inter-story drifts measured by DCDTs DG1-DG18 were utilized to calculate the lateral displacements for the biaxial tests.

(v) Slab "growth" due to cracking in the floor members was monitored by DCDTs S1-S4 (Fig. 3.11a).

(vi) Rotation and translation of the footings were monitored using DCDTs F1-F4 (Fig. 3.11b), negligible footing movements were observed.

(vii) During tests EC6.6L, EC7.7L, and EC16.6L, the shaking table pitch was measured by DCDTs R1-R2, as illustrated in Fig. 3.11b. These channels were changed for other tests, and the measured vertical shaking table displacements were used instead to determine the shaking table roll and pitch (roll= (v1disp-v2disp)/2 and pitch=(v1disp-v3disp)/2, where v1disp, v2disp, and v3disp are the vertical displacements of the shaking table platform at different locations [57]).

(viii) Weldable strain gauges on selected beam and column longitudinal bars near beam-column joints measured reinforcement strains (Fig. 3.12).

4. RESPONSE TO SIMULATED EARTHQUAKES

This chapter presents data on response of the test structure to the earthquake simulations EC7.7L, EC16.6L, EC49.3L, EC47.7B, MO63.4B, and MX34.6B. The response amplitudes measured during tests MX10.3B and MX19.B were smaller than those measured when the test structure was subjected to the Miyagi-Ken-Oki record (MO63.4B), and they are not discussed here. Details of the data reduction and sign convention are discussed briefly. For each of these input motions, linear elastic response spectra, Housner spectrum intensity, and a Fourier amplitude spectrum are presented. Selected global and local response histories are illustrated. Relations between roof displacement and base shear are also presented for these simulations. Extreme values of the responses are tabulated. Typical observed damage is depicted. The data presentation in this chapter is intended to be objective; interpretations are reserved for subsequent chapters.

4.1 Sign Convention

Principal axes XYZ are defined relative to the principal directions of the test structure, as illustrated in Fig. 4.1. Positive senses of global displacements, accelerations, inertial forces, story shears, story moments, and story torques are defined in that figure. Reinforcement tensile strain is defined to be positive.

4.2 Data Accumulation

Initial and final readings "at rest" were determined by averaging data readings for a one second interval before and after each test. For all but accelerometers, offsets that trailed the responses were accumulated in subsequent response histories (accelerometers were assumed to be equal to zero at the beginning and end of each test). Thus, the

permanent offset in displacement and strains could be monitored.

Lateral displacement, inter-story drift, story rotation, story shearing force, story overturning moment, and story torque responses were derived from the basic measurements as described in Chapter 3 and Appendix B. The statistical package S [8] was used to reduce the raw data. A summary of the procedures and the responses is presented in the following paragraphs.

4.3 Linear Elastic Response Spectra, Housner Spectrum Intensities, and Fourier Amplitude Spectra

For each earthquake simulation, the input acceleration history and linear elastic response spectra (for 2%, 5%, and 10% viscous damping ratios) [43] are plotted in Fig. 4.2. The response spectra include absolute pseudo acceleration and relative displacement spectra plotted on linear scales.

Housner spectrum intensity [24] was calculated for each input motion. The spectrum intensity was defined by Housner as the area under the 20% damping (viscous damping ratio) pseudo velocity between periods of 0.1 and 2.5 sec. To accommodate for the time scale of the base motions used in these experiments, the period range was compressed by a factor of two (to 0.05 to 1.3 sec.), except for the Mexico City input motion used during test MX34.6B. As discussed in Chapter 3, the time scale for this test was 3; hence, the period range to calculate Housner spectrum intensity was 0.04 to 0.8 sec. Spectrum intensities are presented in Table 4.1. The calculated intensities are also presented as a fraction of the 20% damped intensity of the scaled El Centro NS 1940 [24,38].

Fourier amplitude spectra of the base acceleration records were obtained using a discrete Fast Fourier Transform. Peaks on the Fourier amplitude spectrum correspond to frequencies at which relatively large amounts of energy were input into the test structure. Fourier amplitude spectra, normalized with respect to the maximum value,

are shown in Fig. 4.3 for the six input motions discussed in this chapter.

4.4 Global Responses

The histories of maximum lateral floor displacement, maximum lateral floor acceleration, maximum inter-story drift, base shear force, and base overturning moment are illustrated in Fig. 4.4 ("base" refers to the base of the first-floor columns). The peak values of lateral displacements, inter-story drifts, base shear force, overturning moment at the base of the first-floor columns, and base torque (calculated with respect to the central column) are tabulated in Table 4.2. A description of the data reduction is given in the following paragraphs.

4.4.1 Displacement

Displacements were measured by two different procedures. Instrumentation for these procedures is documented in Chapter 3 and Appendix B. In the first procedure, DCDTs and POTs (Fig. 3.10(a)) directly measured displacement at mid-depth of the short-direction beams in each floor relative to a reference frame situated off the test platform of the shake table. Lateral displacements at mid-depth of the short-direction beams, as reported in this chapter, were obtained by subtracting rigid-body movements due to shake table translation and pitch. Thus, displacements obtained by this procedure are ideally floor displacements relative to a rigid reference frame attached to the shake table. In the second procedure, inter-story lateral drifts were derived from diagonal DCDT measurements (Fig. 3.10(b)) using simple trigonometry (assuming floor beams and columns did not elongate or compress). Individual inter-story drift measurements were added to obtain the total floor relative displacements. Detailed information is given in Appendix C. Additional displacements due to "slab growth" (Fig. 3.11(a)) caused by cracking in the floor slab were added to the 1st, 2nd, 3rd, and 4th floor displacements.

4.4.2 Acceleration

Long-direction floor accelerations were taken directly from the measured values. The translational acceleration in the short direction, and the floor rotational acceleration, were computed from locations of and measurements by the accelerometers placed in the short direction. For each floor, the readings from the two short-direction accelerometers were averaged to obtain the translational acceleration. Knowing accelerometer readings and given the distance between the two accelerometers, the rotational acceleration was calculated by the difference of the two measurements divided by the distance between the accelerometers.

4.4.3 Story Shear, Overturning Moment, and Torque

Lateral inertia forces, in both the long and short directions, were derived from the products of calculated tributary floor masses (lumped at each floor, Table 4.3) and measured floor translational accelerations. Rotational inertias were calculated similarly using derived rotational accelerations and calculated mass moments of inertia about the "Z" axis (Fig. 4.1). The story shear, story overturning moment, and story torque (about the central column) were computed using simple equilibrium relations.

In the calculations, it was assumed that the lumped masses are located at mid-depth of the long-direction beams, and not at the center of mass. Because of the height of the lead pigs (Fig. 3.6(a)), the center of mass does not coincide with the center of floor slab; thus, the moment arms used to compute the overturning moment are not precise. Nevertheless, the computed moments are reasonably accurate since the difference between the center of mass and the center of floor slab is small relative to the moment arms, particularly for the upper floors which contribute more significantly to the overturning moment.

4.5 Base Shear - Top Displacement Relations

Degradation of the structural lateral stiffness due to cracking and spalling of concrete and yielding of reinforcing bars could be monitored by plotting relations between base shear and roof lateral displacement. The measured relations are plotted in Fig. 4.5. In each plot, the response for selected time intervals is broken into several short intervals such that only a few response cycles are plotted on each graph.

4.6 Reinforcement Strains

Strains in selected reinforcing bars were monitored, as discussed in Chapter 3. Strains due to auxiliary lead weights and self weight are summarized in Table 4.4. The peak strains that were measured during each test are presented in Table 4.5. Typical strain histories normalized with respect to yield strain are illustrated in Fig. 4.6.

4.7 Observed Damage

After each test, the test structure was examined to detect any sign of concrete spalling and cracking. The observed damage is explained in the following paragraphs.

Immediately before the first earthquake simulation, limited hairline shrinkage cracks were found on the structure. Crack width was 0.002 in. or smaller. Most of the cracks were concentrated near the floor slab corners at the second and fourth floors. The damage after tests EC7.7L and EC16.6L comprised limited extensions of the existing shrinkage cracks and a few additional hairline cracks. During the last unidirectional test (EC49.3L), concrete spalled off a first-floor beam near the beam-column joint, and a portion (approximately 2 in. high, 0.75 in. wide, and 0.5 in. deep) of the beam shell concrete fell off. Cracks as wide as 0.016 in. and 0.025 in. were opened in the long and short direction beams, respectively near the beam-column joints. Typical crack patterns (for the exterior face of frames 3 and 4 (Fig. 2.1)) are sketched in Fig. 4.7. The predominant damage was flexural cracking concentrated at the ends of the long-direction

beams. No significant cracking could be found in the columns except at a few locations, mainly at the footing level. Extensive cracking was observed in slabs, more significantly at the first and fourth floors (Fig. 4.7). The maximum crack width was about 0.013 in.

With the exception of a few minor cracks, no additional damage was found after the first biaxial earthquake simulation (EC47.7B). However, after subjecting the test model to the Miyagi-Ken-Oki input motion, the beams and columns experienced major additional cracking and spalling at several locations in the first, second, and third levels. Cracks as wide as 0.05 in. were opened in a first-floor beam near the beam-column joint. Spalling of the column shell concrete was more significant at the footing level, and part of the column reinforcement became visible. Minor diagonal shear cracking formed at some exterior joints in both principal directions (Fig. 4.7). Following the Mexico City input motion (MX34.6B), extensive spalling and cracking were apparent in beam ends and columns at the footing level. At the fourth and second levels, the longitudinal reinforcement of the long-direction beams became visible where shell concrete had spalled off at the joints (Fig. 4.8). Shell concrete over an exterior joint spalled subsequent to formation of significant diagonal shear cracking. Despite clear indication of inelastic behavior, nonductile failure modes such as extensive shear cracking, bar buckling, or anchorage failure, were not observed.

5. DISCUSSION OF OBSERVED BEHAVIOR

This chapter describes behavior of the test structure during the earthquake simulations and free-vibration tests. Base motions are studied in the first portion to interpret base motion intensities. General characteristics of the measured responses, and their variation throughout the experimental program are also discussed.

5.1 Terminology

Various terms commonly used in classical structural dynamics do not apply to inelastic systems, and require definition. In this report, the term "mode" refers to an apparent phase relationship of the response at various floors. The "first" or "fundamental" mode represents the "appearance" of motion at all levels being in phase, i.e., the response of all levels is in the same direction. "Higher modes" refer to motion being generally out of phase at different levels, i.e., the condition of one or more changes in the direction of response over the height. "Node" or "nodal point" refers to a point over height where motion is negligible relative to motions at other levels, and where the direction of response changes (for a given mode and in the same frequency range). The second mode has one node, the third mode has two nodes, and so on. "Apparent frequency" refers to observed frequency of a particular mode.

5.2 Base Motions

Base accelerations recorded during the earthquake simulations are plotted in Fig. 4.2. The base motions are studied so that responses of the test structure to different intensity motions could be evaluated. The base motions are studied using Fourier amplitude spectra, linear elastic response spectra, and Housner spectrum intensities.

As explained in Chapter 3, durations of the prototype El Centro and Miyagi-Ken-Oki records were compressed by a factor of two so that frequency content of the base motion and of the scaled model would be in accord. However, the Mexico City record was scaled down by a factor of three during test MX34.6B for reasons explained subsequently through Fourier amplitude spectra and linear elastic response spectra.

5.2.1 Fourier Amplitude Spectra

Fourier amplitude spectra of the base acceleration records were obtained using a discrete Fast Fourier Transform. The spectrum is a measure of the final energy in zero-damped, single-degree-of-freedom oscillators subjected to a base excitation. Peaks on the Fourier amplitude spectrum represent frequencies at which relatively large amounts of energy are input to a system.

Fourier amplitude spectra for the six earthquake simulations discussed in this report are shown in Fig. 4.3. The ordinates of the spectra were normalized with respect to the maximum value. An absence of large peaks above 12 Hz may be observed in all the excitations. Spectra for the acceleration inputs modeling the El Centro NS 1940 record (EC) had a similar frequency content up to 5 Hz. However, the spectra for tests EC49.9L and EC47.7B indicate a slightly larger input energy between 4 and 5 Hz. Concentration of large spectral amplitudes in a small frequency band can be observed for both tests MO63.4B and MX34.6B, modeling the Miyagi-Ken-Oki S00E 1978 (MO) and SCT Mexico City S60E 1985 (MX) input motions, respectively. For the scaled MO record, there is a sharp increase in the Fourier spectrum amplitude in a range between 1.5 and 3 Hz, particularly at 2 Hz. Similarly, the scaled MX input motion has a concentration of spectral amplitude between 1 and 1.5 Hz, and it peaks at 1.5 Hz.

If the dominant vibration frequencies of a structure are within the range of large spectral amplitudes, base motion can be expected to excite those frequencies. With the exception of the Mexico City record, the predominant frequency content of the base

motions (compressed in duration by a factor of two) corresponded approximately with the fundamental frequency of the test structure. Thus, desirable levels of excitation were possible during simulations with acceleration inputs modeling the EC and MO records. Had the duration of the Mexico City record also been scaled down by a factor of two, the significant frequency content of the resulting record would not have been close to the vibration frequencies of the test model, as measured prior to the simulations with the Mexico City record. Thus, the desired damage state would not have been achieved. Duration of the Mexico City record (for test MX34.6B) was consequently compressed by a factor of three in order to ensure that the important vibration frequencies of the test structure would be in a range of large spectral amplitude. It was, then, possible to impart large amounts of energy into the model.

5.2.2 Linear Elastic Response Spectra

Measured horizontal base motion records are plotted in Fig. 4.2. Relative displacement and absolute acceleration response spectra [13] are also plotted in linear format in this figure for various damping ratios.

The similarity in frequency content of all the base motions modeling the El Centro NS 1940 record is apparent by examining the displacement and acceleration response spectra. The acceleration spectra increase in a period range of 0.0 to about 3.0 sec. The displacement spectra increase in a period range between 0.0 and 1.5 sec., and decrease afterwards. Peaks in the pseudo acceleration spectra for simulations modeling the Miyagi-Ken-Oki and Mexico City acceleration records occur at longer periods than for the simulations modeling the El Centro record. The relative displacement spectra also have large peaks in the longer period range, which corresponded with the fundamental period of the test structure during the later stage of testing.

As noted earlier, duration of the Mexico City record (for test MX34.6B) was compressed by a factor of three instead of two. This was intended to resonate the

model. At the beginning of the test, the fundamental period (left vertical line in Fig. 5.1), was slightly less than that corresponding to the peak of the acceleration spectrum. During the test, the period elongated into the range of increased spectral acceleration (Fig. 5.1) with consequent amplification of response and damage.

To facilitate comparison among relative intensities of different input accelerations, the relative displacement and absolute acceleration response spectra for 5% damping ratio are plotted in Fig. 5.2. Shapes of acceleration spectra for tests EC49.3L and EC47.7B are generally the same. They reach a peak value at a period of approximately 0.3 sec. These two records have effectively identical characteristics (the test structure was oriented parallel the base motion for test EC49.3L and skewed for test EC47.7B). The scaled Miyagi-Ken-Oki (MO) input motion differs significantly. The peak pseudo acceleration is approximately 15% more than that for the El Centro (EC) record. The characteristics of the scaled MO and EC signals are similar for the period range below 0.2 sec. Beyond 0.2 sec. the two records are different, the pseudo acceleration for the MO record reaching its peak value at a longer period. For periods smaller than 0.5 sec., the Mexico City record input motion has a smaller spectral acceleration than records with comparable "intensities". The peak pseudo acceleration occurs at an even longer period than that for the MO signal, but its magnitude is almost the same as for the simulation modeling the Miyagi-Ken-Oki acceleration record. For periods smaller than 0.5 sec., the scaled Mexico City record has relatively small spectral displacement, but beyond this limit its spectral displacement peaks to much larger values than the other records. All of the acceleration records result in an increase in spectral displacement with an increase in the vibration period.

5.2.3 Spectrum Intensities

The intensity of a base motion is conveniently represented by the Housner spectrum intensity [24]. It is a single number by which different motions can be

compared. However, the adequacy of the spectrum intensity in representing the severity of an earthquake is questionable and warrants consideration. The spectrum intensity was defined by Housner as the area under the 20-percent damping linear elastic velocity spectrum; thus, it is not a complete measure of intensity for structures responding in the inelastic range. In addition, the spectrum intensity does not reflect the duration of strong shaking, and it may not be a precise measure of effects on inelastic response unless the motions have similar frequency content. Considering that different base motions with different frequency characteristics were used, care must be exercised in interpreting the spectrum intensities. For the tests modeling the El Centro acceleration record, the calculated intensities (Table 4.1) are an acceptable measure of intensity because they all have similar duration and frequency content. For the earthquake simulations using the Miyagi-Ken-Oki and Mexico City records, however, the calculated intensities are not comparable, as their frequency characteristics are different from that for the El Centro record.

Spectrum intensities are tabulated for different simulations in Table 4.1, and are plotted versus peak base acceleration in Fig. 5.3. Spectrum intensities gradually increase with an increase in the peak base acceleration. The intensities for simulations EC49.3L and EC47.7B are nearly equal. This supports the previous observations that these two input motions are practically identical. Despite a lower spectrum intensity for test MX34.6B, this simulation produced a significant level of excitation due to resonance conditions, as explained in Section 5.2.2.

The spectrum intensities have also been presented as a ratio of the scaled spectrum intensity of the El Centro NS 1940 acceleration record (Table 4.1). As reported by Housner [24], the-twenty-percent-damped spectrum intensity for the prototype motion is 32.5 inches. Considering the length scale equal to four, this scales to a spectrum intensity of 8.13 inches. If a low intensity motion is arbitrarily assumed to have an intensity of approximately one-quarter of the scaled El Centro intensity, test EC7.7L will

be classified as a "low-intensity" simulation. Defining a moderate base motion as having approximately half the intensity of the scaled El Centro record, test EC16.6L may be classified as "moderate". The remaining tests would then be considered to be "strong" motions if the El Centro record is defined to be "strong".

5.3 Global Response Trends of the Test Structure

Variation of lateral displacements, floor accelerations, and base shear followed logical patterns with increasing spectrum intensities and peak acceleration. The patterns are discussed in the following paragraphs.

5.3.1 Displacements

For a given type of base motion, the lateral displacements tend to generally increase with increasing spectrum intensity and peak input acceleration. The variation of the sixth-floor maximum lateral displacement, both in the short and long directions, with the peak input acceleration is plotted in Fig. 5.4. In order to obtain a meaningful trend, the peak base acceleration for the biaxial simulations had to be modified. During the biaxial tests (EC47.7B, MO63.4B, and MX34.6B), the test structure was at a 45 degree angle relative to the single horizontal input motion. The single input acceleration should, then, be resolved into its components along the two principal directions of the test structure. The peak acceleration was multiplied by $\text{Cos}(45^{\circ})=0.707$ in order to obtain the peak value in each direction; thus, the maximum roof displacements would be comparable with the peak input acceleration. This "effective" peak acceleration was used to plot Fig. 5.4 (in that figure the symbol "+" refers to response parallel the long direction and "x" refers to the short-direction response).

As discussed in Section 5.2.3, during test MX34.6B the vibration period of the test structure elongated into the range of increased spectral acceleration with consequent amplification of response. Thus, the peak roof displacements for that test are larger

than those during tests with larger peak accelerations. If this point is taken into account, the overall trend could be represented approximately by a linear variation of peak roof displacement with maximum base acceleration. Similar trends have been observed in other experiments [38,40]. However, the anomalous data obtained for test MX34.6B confute the general conclusion that base acceleration alone is an adequate measure of intensity.

A prominent feature observed in the roof displacement history (Fig. 4.4) is a smooth waveform. The feature indicates the predominance of the fundamental mode. Profiles of the recorded displacements are discussed in Section 5.4. Profiles of displacement over height did not vary significantly during testing, which further supports the conclusion that displacement response was predominantly in the fundamental mode.

There is no clear relation between the long-direction lateral displacements relative to those in the short direction. Nevertheless, the short-direction roof displacement is larger than the corresponding value in the long direction.

5.3.2 Accelerations

In contrast with the displacement response history, the rugged appearance of acceleration waveforms (Fig. 4.4) reveals considerable participation of higher modes. Fourier amplitude spectra of all the floor accelerations, normalized to a peak value of one, are plotted in Fig. 5.5. The first apparent frequency is predicted similarly from every floor acceleration spectrum, this implies that the tower did not respond differently from the base in either the uniaxial or biaxial tests. The test structure appears to have behaved as a single unit, and the Fourier amplitude spectra do not indicate that the tower was excited independently from the base.

Variation of peak roof acceleration with peak input acceleration is plotted in Fig. 5.6. As described in Section 5.3.1, the component of peak acceleration in the two

principal directions is presented for the biaxial earthquake simulations. There seems to be less anomaly associated with test MX34.6B than was observed for displacements (Fig. 5.4). The peak roof acceleration varies reasonably well as a linear function of the maximum input acceleration. The roof acceleration in the long direction tends to be slightly larger than its counterpart in the short direction.

For each direction, an acceleration amplification factor, defined as the ratio between peak roof acceleration and peak base acceleration, was calculated (Table 5.1). For the biaxial earthquake simulations, the peak acceleration was multiplied by $\mathrm{Cos}(45^{\circ})$, as noted previously, before calculating the amplification factor. The mean amplification factor was 3.3 with a standard deviation of 0.76 in the long direction, and 2.6 with a standard deviation of 0.12 in the short direction. The largest amplification was observed during test MX34.6B; the long-direction roof acceleration was as much as five times the peak base acceleration.

5.3.3 Base Shear

Higher-mode participation could be identified in the base shear waveforms (Fig. 4.4); however, the contribution appears to be less than in the acceleration waveforms. The reason that higher modes are less apparent is that the higher mode contributions to the floor accelerations (floor inertia forces) tend to cancel as they are summed over the height to obtain the base shear.

Variation of peak base shear with peak base acceleration is depicted in Fig. 5.7. The peak base shear tends to increase with increase in peak base acceleration; however, the relation between the two is irregular.

5.3.4 Torsion

Torsional response was visually clear during the biaxial earthquake simulations. The roof twisted as much as 0.048 rad. during test MO63.4B. The maximum torque,

computed at the base of the first-floor columns with respect to the central column, reached peak values of 687, 776, and 587 kips-in. when the test structure was subjected to the El Centro, Miyagi-Ken-Oki, and Mexico City records, respectively. If the torque is taken as the product of the base shear by an eccentricity perpendicular to the direction of base shear, the maximum torque will correspond to eccentricities equal to 21.6, 21.5, and 20.7 in. for tests EC47.7B, MO63.4B, and MX34.6B, respectively. Hence, the eccentricities relative to the central column correspond to approximately 14 percent of the long-direction dimension.

An interesting observation is made by computing the torsional force, obtained with respect to the central column, if the lateral forces are assumed to be distributed according to the Uniform Building Code (UBC) [72] requirements (but ignoring the specified accidental torsion) (Fig. 5.8). From this figure, the torsion is calculated as $(f_6+f_5+f_4)e$, where e is the eccentricity between the center of mass and central column. Substituting the values of f_6, f_5, and f_4 (Fig. 5.8), torque is equal to $(0.56V_{base})37.5=21V_{base}$. This relation indicates an eccentricity equal to 21 in., which is approximately equal to the measured values. Although detailed discussions of lateral-torsional response are beyond the scope of this report, this observation implies that the torsional response induced by presence of the setback was minimal and could be predicted by static relations. Further research is necessary to verify this finding, and to study the effect of setback on lateral-torsional response.

5.4 Response Profiles

In this section, variation over height of the lateral displacement, inter-story drift, lateral forces, and reinforcement strain are presented. The response profiles are evaluated to investigate the influence of the setback on the dynamic response of the test structure.

(a) Displacement and Inertia Force

Variation over height of the lateral displacement, inter-story drift, and lateral inertia forces in the long direction at selected times are plotted in Fig. 5.9. The times correspond to the instances at which the base shear, inter-story drifts, and lateral displacements reach their extreme values. The displacement profiles do not display any kink at the setback level; they are very much similar to those expected for a structure with uniform configuration. As observed for more regular structures [12,38], the variation of the lateral forces is less consistent for different tests and times. A sudden reduction in the lateral forces is observed at the fourth level. This is not unexpected as the tower floor mass is almost one-half of the corresponding value in the base; hence, there is less inertia force associated with these floors. More interestingly is that at some instances (e.g., at 4.8 sec. during MO63.4B and at 16.29 sec. during MX34.6B) the distribution of lateral forces is nearly identical to the distribution of lateral forces as specified by the Uniform Building Code (UBC). The predominance of the fundamental mode is clear from the smooth sixth-floor displacement waveforms (Fig. 4.4), and from the lateral displacement and inertia force profiles over height (Fig. 5.9) as there is no change in the direction of response over the height. The inter-story drift profiles indicate more drift in the second and fourth floors. The observation of large drift at the base of the tower conforms with past research findings but should not be suggestive of dynamic characteristics of setback structures, as some studies imply [e.g., 25]. This point is made clear by examining the internal actions, as discussed in the following.

(b) Reinforcement Strain

Beam and column strain profiles (Fig. 5.10) indicate a relatively smooth distribution of internal actions at the time of maximum beam and column strains, except for the fourth-level beam, which sustained larger strains than adjacent beams. This discontinuity is not unexpected, as there is only one beam to resist column moments,

whereas below this level there are two beams framing into the column. The level of damage is higher at the fourth level, but there is no apparent indication that this behavior is due to dynamic response phenomena.

5.5 Lateral Load-Displacement Characteristics

In order to assess the lateral stiffness of the test structure, its lateral load-displacement characteristics were studied. An overall stiffness was either measured by the static pull-back tests or inferred from the base shear-roof displacement hysteresis loops. Variation of the lateral stiffness is discussed in this section.

5.5.1 Static Lateral-Displacement Response

Before subjecting the test structure to any earthquake simulation, its lateral stiffness was measured by pull-back tests (Chapter 3). The slope of the best linear fit to the load-displacement relation measured during the pull-back test is defined as the lateral stiffness of the test structure. Variation of this value at different stages is given in Table 5.2. The lateral stiffness increased after prestressing the model on the shaking table platform. This is believed to be due to a more rigid foundation when the structure was on the shaking table platform. There is a further increase in the lateral stiffness when the test structure was loaded with auxiliary lead pigs. The lateral stiffness in the long and short directions was increased by seven and fourteen percent, respectively. It is possible that the increased stiffness is due to stiffness of the lead pig connection system. It is also possible that the shrinkage cracks, particularly in the columns, were closed by the additional weight, and hence the structure exhibits a larger stiffness. The precise source has not been identified, and will not be further studied because the stiffness change is not significant.

5.5.2 Overall Stiffness Characteristics

The dynamic characteristics of a structure are largely dependent on the effective stiffness and mass characteristics. An overall lateral load stiffness of a structure is reflected through study of its hysteretic behavior; for example, a plot of base shear versus roof displacement would gauge variation of lateral stiffness. Such hysteretic response would show progressive softening of the structure, and would also give a qualitative indication of the energy dissipation capacity.

Measured relations between base shear and roof displacement are plotted in Fig. 4.5. They are discussed in the following two subsections.

(a) Long Direction

The measured hysteretic curves (Fig. 4.5) are reasonably smooth, especially at high displacement amplitudes where the first mode dominated. However, during response at low amplitudes, where higher modes can dominate the overall response, the curves are no longer smooth. Contribution of higher modes result in loops oriented approximately perpendicular to the "first-mode" loops. As indicated by the hysteretic response, the overall stiffness tended to decrease with increasing displacement amplitude. Progressive "softening" of the structure is indicative of concrete cracking and reinforcement yielding.

An interesting feature of the hysteretic response is that, while the structure became softer as displacement exceeded a previous maximum value, response below the previous maximum was that of a stiffening system. This "pinching" phenomenon is clearly apparent in the small-amplitude displacement in the interval of 3.5 and 5 sec. during test EC16.6L, 8 and 9.5 sec. during test EC49.3L, and 10 and 18 sec. for the long-direction response during test MX34.6B. The softening and stiffening behavior results in "pinching" of the base shear-roof displacement hysteresis loops, i.e., there is a low incremental stiffness (base shear-roof displacement slope) at low shears followed by increasing stiffness. Pinching became more pronounced as the displacement amplitudes

were increased. Such behavior is attributed to reinforcement slip, and has been observed during other small-scale reinforced concrete models and full-scale reinforced concrete elements[e.g., 38,40,77]. Pinching results in a reduction of the energy dissipation capacities, and also in a lower effective lateral stiffness for low displacement amplitude than for high amplitudes.

"Primary" load-displacement curves were estimated by superimposing hysteretic loops and interpolating between measured peaks to obtain smooth curves. The envelope relation between base shear and roof displacement (Fig. 5.11) indicates the stiffness and strength of the test structure. The relations show an initially "stiff" response, followed by a gradual reduction in stiffness. The "primary" curves constructed for biaxial simulations indicate a significant reduction of lateral stiffness due (at least in part) to damage accumulated previously during the unidirectional tests. Yield was first detected in the longitudinal reinforcement at the footing level of the central column during test EC49.3L. The corresponding lateral roof drift at the instance of this column yielding was 0.3 percent of the test structure height.

The model was designed for a service level base shear equal to 6.67 kips (9.2 percent of the total weight), but it sustained base shears as high as 49 kips (68 percent of the total weight). In addition, the roof displaced as large as 4.35 inches (2 percent of the height measured above footings). The maximum roof displacement exceeds the upper limit of 1.5 percent of structure height that was indicated by Algan [3] as corresponding to severe damage in a building. Despite the severity of the excitation, there was no sign of imminent collapse of the test structure. An in-depth discussion of the lateral-load strength and stiffness of the test structure is given in Chapter 7.

(b) Short Direction

In contrast with the long direction, the short-direction hysteretic curves (Fig. 4.5) are not smooth. The shape of the loops could indicate a significant amount of energy

dissipation, and the trend might imply a large reduction in lateral stiffness. Nevertheless, these potential observations do not conform with the observed damage, and the measured beam strains in the short-direction frames. Test results did not reveal major damage in the short-direction frames.

There is no clear explanation for this behavior. It is concluded that the short-direction loops are not representative of the damage and yield in the short direction. A possible reason can be that the transverse response was driven by the response in the long direction. The test structure had previously been damaged during the uniaxial simulations, and the "strong" excitation continued to be in the long direction. In other words, the structure was mainly excited and damaged in the long direction, and the short-direction frames were simply "trailing" the response due to torsional behavior. Further analytical studies are necessary in order to better understand this behavior.

5.6 Effect of the Floor Slab

Observed behavior of the test structure leads to a conclusion that the floor slab contributed significantly to behavior of the structure. For example, cracks at the top of beams near the joints generally extended well into the slab (Fig. 4.7), suggesting that the slab acted as a tensile element in conjunction with beam when the beam was bent by negative moment. This hypothesis is supported by crack patterns in the short-direction beams. As illustrated in Fig. 4.7, the short-direction spandrel beams experienced inclined cracks indicative of torsion near the joint. The torsion could arise due to eccentric loads induced by membrane forces in the slab. The orientation of the majority of these torsional cracks indicates that the slab membrane forces were large in tension than compression at the exterior joints.

It is apparent that the test structure had strength significantly exceeding the design strength (Section 5.5.2). The enhanced strength could be partially attributable to enhanced beam negative moment strengths resulting from the slab contribution. This

conclusion is supported by measured strains in the beam reinforcement. As shown in Table 4.5, strains in top beam longitudinal bars generally were several times less than the bottom bars. The implication is that the beams were flexurally much stronger in negative bending than in positive bending. A significant source of the high strength in negative bending could be the contribution of the slab.

Slab contribution to flexural strength of supporting beams has been discussed in many research studies [e.g., 9,18,45,56]. Enhanced negative moment strengths could result in formation of plastic hinges in columns if design column/beam strength ratios are based on beam flexural strength which ignores contribution of floor slab. In addition, the overall strength and stiffness characteristics of a structure will be changed if the additional beam strength and stiffness are taken into account.

The available experimental data were insufficient to precisely deduce an effective flange width, which quantifies slab contribution to strength and stiffness of supporting beams. Nevertheless, it was possible to estimate an approximate effective flange width for the long-direction beams. Slab contribution to the short-direction beams could not be determined with the available data. The approximate procedure used for the long-direction beams is discussed in the following.

A free-body diagram of the first-story interior joint is depicted in Fig. 5.12. Tensile strains in the beam and column reinforcement at the joint could be obtained from the strain gauge measurements. Knowing the tensile strains and assuming a fixed column axial load equal to the tributary gravity axial load, flexural moments in the columns above and below the joint (Mc_2 and Mc_3) and in the beam having bottom reinforcement stressed in tension (Mb_2) were estimated by comparison with the monotonic behavior of these elements computed by the computer program UNCOLA [27]. For this purpose, flexural moment-strain curves were constructed analytically for a range of reinforcement tensile strain levels. Effects of actual material properties and concrete confinement were considered. Flexural moment at each steel tensile strain was then estimated by

interpolating from the calculated moment-strain relations. Bending moment in the beams with the top reinforcement in tension (Mb_1) could not be computed directly because the slab contribution was unknown. Rather, the moment Mb_1 was deduced using equations of statics applied to the joint, as follows:

$$\Sigma M_o=0;$$

$$Mb_1=Mc_2+Mc_3-Mb_2-0.5c(Vb_1+Vb_2)+0.5h(Vc_1+Vc_2) \tag{5.1}$$

$$Vb_1=(Mb_1)/(0.667L) \tag{5.2a}$$

$$Vb_2=(Mb_2)/(0.333L) \tag{5.2b}$$

$$Vc_1=(Mc_1+Mc_2)/H \tag{5.2c}$$

$$Vc_2=(Mc_3+Mc_4)/H \tag{5.2d}$$

Substituting Eqs (5.2a-5.2d) into Eq. (5.1):

$$Mb_1=\frac{1}{(1+3c/4L)}\left[\frac{hMc_1+(2H+h)(Mc_2+Mc_3)+hMc_4}{2H}-(1+3c/2L)Mb_2\right] \tag{5.3}$$

The computer program UNCOLA was modified in order to estimate the effective flange width. Assuming that the slab reinforcing bars are distributed uniformly in the slab over the short-direction span, a "T" cross section was considered with tensile reinforcement equal to the beam web reinforcement plus the slab reinforcement within the effective flange width. The effective flange width was increased at small increments until, for a given tensile strain in the beam longitudinal reinforcement, the computed moment was within 2 kips-in. (approximately two percent of the computed strength) of the desired flexural moment (Eq. 5.3). The effective flange width corresponding to each strain level was then equal to the flange width at which this condition was satisfied. This procedure was repeated for all the interior joints and calculated bending moments. A histogram of the estimated effective flange width (including web), based on 108 data points, is illustrated in Fig. 5.13. The mean value is 28 in., which corresponds to one-

third of the short-direction span, or alternatively, an overhanging slab width equal to 1.5 long-direction beam depths on each side of the beam. The strain level at the mean effective flange width corresponds approximately to the yield strain. Variation of the estimated effective flange width with the measured beam longitudinal steel strain is plotted in Fig. 5.14 for 108 data points. The scattered data indicate a reduction of effective flange width with an increase in strain. This trend does not conform with that observed during other experiments [e.g., 18]. It is believed that the discrepancy is a result of the method and simplifying assumptions used herein to estimate effective flange width. There were insufficient measurements to assess a reliable mean effective flange width for the corner joints, because the reinforcing bar strains were monitored only at the first-floor corner joint (Fig. 3.12).

A number of underlying assumptions were made in the abovementioned method of estimating the effective flange width. These are as follows: (1) In each response cycle, only tensile strains exceeding the peak values in the previous cycle were considered. Thus, monotonic steel stress-strain relations (Appendix A) could be applied to approximate the envelope curves of steel stress-strain curves [54], and the computed flexural moments would replicate a close estimate of those under cyclic loading condition. (2) Column axial load was assumed not to change significantly during the earthquake simulations. (3) Inflection points for the beams were assumed to be located at one-third of the span length from the positive moment end. This implies that the negative moments are two times the positive-direction flexural moments. Other studies [45] have indicated that the negative bending moments can be two to three times the flexural moments in the opposite direction. Results of a companion analytical study [45] are consistent with the effective flange width reported here, suggesting that the assumptions made herein are reasonable.

Having estimated shears and moments at all elements framing into a joint, the joint shear for a typical interior joint may be estimated (Fig. 5.12). Equilibrium of the

horizontal forces results in:

$$V_j = T_1 + T_2 - Vc_2 \tag{5.4}$$

which can be simplified as follows:

$$V_j = Mb_1/jd_1 + Mb_2/jd_2 - (Mc_3 + Mc_4)/H \tag{5.5}$$

Assuming $jd_1 = jd_2 \doteq 0.95d$,

$$V_j \doteq \frac{Mb_1 + Mb_2}{0.95d} - \frac{Mc_3 + Mc_4}{H} \tag{5.6}$$

in which, d is beam effective depth.

Using the bending moments computed previously, the joint shear could easily be obtained from Eq. 5.6. For corner joints, this equation is still applicable with the exception that there is only one beam framing into column (e.g., Mb_2 in Eq. 5.6 is zero). For corner joints, the slab overhang is assumed equal to that for interior joints. Using Eq. 5.6, the joint shear was calculated for all the interior joints and for the second-floor corner joint (Fig. 3.12) where reinforcement strain was measured. The joint dimensions were defined according to the ACI-ASCE Committee 352 recommendations [2], and the joint cross-sectional area was accordingly computed to be 23 in.^{2}. Knowing the joint area and shear force, the joint shear stress was easily obtained. During test EC49.3L, the maximum shear stress in the first-floor interior joint reached approximately to $21\sqrt{f'_c}$. The peak computed shear stress at the first-floor corner connection (Fig. 3.12) was $7\sqrt{f'_c}$. Implications of these values are postponed until Chapter 7.

5.7 Variation of Dynamic Properties

Vibration periods, viscous damping ratios, and vibration mode shapes of the test structure were determined using different methods. Steps to obtain these dynamic properties and their variation are explained in this section.

(a) Vibration Periods

Data from two sources were used to obtain the vibration periods of the test structure. The methods are discussed in the following paragraphs.

In the first method, an average period was obtained from the peaks of the Fourier amplitude spectrum of the roof acceleration measured during the free-vibration tests. As noted in Chapter 3, the free-vibration tests at the "uncracked" stage were performed by pulling the model in the long and short directions and releasing it suddenly. Long-direction vibration periods can be estimated from the Fourier amplitude spectra obtained from the roof acceleration in the long direction. A typical spectrum is presented in Fig. 5.15; the dominant frequencies could be read from the peaks. When the free-vibration tests were performed in the short direction, both the torsional and translational modes would be excited, such that the torsional and translational frequencies could not be distinguished if the spectra from the short-direction accelerometers, e.g., acc16 and acc18 were considered separately. In order to obtain translational vibration periods, the two short-direction accelerations at the roof (measured by acc16 and acc18 (Fig. 3.9)) were summed before calculating the Fourier amplitude spectrum (Fig. 5.16c). This was intended to reduce contributions of the torsional mode. The torsional vibration periods were obtained after decreasing effects of the translational mode of vibration (by subtracting the two short-direction accelerations) before calculating the Fourier amplitude spectrum. This method did not completely eliminate contributions of the translational mode, but the peaks on the spectrum at torsional frequencies were enhanced (Fig. 5.16d).

In the second method, an effective vibration period was estimated from the roof displacement histories measured during earthquake simulations. Because the displacement response was mainly governed by the first mode, the displacement histories could be used to measure the fundamental vibration period. The displacement records were scanned at two-second intervals. For each two-second interval, the time between

complete response cycles was divided by the number of cycles to obtain the vibration period. Response cycles which contained higher mode effects were not considered. The mean value obtained during different cycles is reported here (Table 5.3).

As noted in Chapter 3, some of the free-vibration tests were performed before the earthquake simulations. Some of the tests were conducted at the construction site, and some were performed while the test structure, with and without auxiliary lead pigs, was prestressed onto the shaking table platform. The vibration periods are summarized in Table 5.3. There was a slight decrease in period when the structure was moved to the shaking table platform. This is consistent with the measured lateral stiffness, as explained in Section 5.5.1. However, the measured vibration periods increased substantially following addition of the auxiliary lead pigs. The change in period can be attributed in part to change in structure mass before and after placement of the lead pigs, and in part to a change in stiffness. Analysis of the lateral stiffness (Section 5.5.1) indicates an increase in stiffness. Longer periods are, thus, due to an increase in structure mass and not to decrease in stiffness.

Vibration periods also changed as testing proceeded and the structure was damaged. The variation of the vibration periods (obtained from the two methods) is tabulated in Table 5.3. The first-mode translational vibration periods are plotted as a function of the previous peak roof displacement during the earthquake simulation in Fig. 5.17. A general trend of increasing period with increasing displacement may be observed. Data points corresponding to test EC47.7B do not follow the trend; the vibration period elongated even though the roof displacement was smaller than the previous test (EC49.3L). The longer period indicates a smaller lateral stiffness as a result of damage accumulated during each earthquake simulation.

A smaller period was obtained from the Fourier amplitude spectrum than from the large-amplitude earthquake simulation responses. The same trend has been observed in other experiments [38,77] as well. It is probable that force levels during free-vibration

tests were insufficient to induce bar slip; thus, the somewhat stiffer response was observed at small amplitudes.

Variation of the apparent vibration period (as measured from the roof displacement history) with time is plotted in Fig. 5.18. The test structure seemed to have an alternating softening-stiffening behavior which resulted in shortening and elongating of the fundamental vibration period. This softening-stiffening behavior was also observed in the base shear-roof displacement hysteretic curves, and it is the result of many factors including the pinching phenomenon (Section 5.5.2) and ground motion characteristics.

(b) Equivalent Viscous Damping

A measure of equivalent viscous damping was obtained using the logarithmic decrement of measured roof acceleration during free-vibration tests. Because the acceleration records contained a number of vibration modes, a direct application of logarithmic decrement to measured acceleration was not meaningful. The following steps were taken to estimate the damping ratio in the first translational mode. Damping in other modes was not investigated.

(1) The recorded acceleration history was band-pass filtered using cut-off frequencies in the range of the first-mode vibration period.

(2) The viscous damping ratio was estimated using the logarithmic decrement of the "filtered" acceleration history.

(3) The above steps were repeated with a number of different cut-off frequencies in order to minimize calculation errors in the damping ratio.

The initial equivalent viscous damping (immediately before the first earthquake simulation) was estimated to be 2.3 percent. This value is in the range of damping ratios reported previously [22,40] for "uncracked" reinforced concrete structures.

Variation of damping ratio throughout the testing program is summarized in Table 5.4, and it is also plotted as a function of the maximum previous roof displacement

during the earthquake simulations in Fig. 5.19. This plot indicates that damping increased gradually with increasing displacement. The damping ratio after test EC47.7B was larger due to additional damage, even though the maximum roof displacement did not exceed the value during test EC49.3L. Hence, the point corresponding to test EC47.7B is not in line with the other test results.

It should be noted that these values of damping were obtained during low-amplitude free-vibration responses. Effective damping would probably be larger at the higher displacement amplitudes observed during the simulations [22]. Because of the questionable value of damping at these low amplitudes, no attempt was made to determine transverse and torsional mode damping.

(c) Vibration Mode Shapes

Different vibration mode shapes of the "uncracked" test structure were estimated from floor accelerations measured during free-vibration tests. For this purpose, the floor accelerations over the height were transformed into the frequency domain, and the amplitude and phase angle spectra were obtained. The Fourier amplitudes from the short-direction accelerations were averaged to obtain the short-direction translational modes. When the torsional mode shapes were sought, difference between the Fourier amplitudes in the short direction was divided by the distance between the two short-direction accelerometers (Fig. 3.9). The Fourier amplitudes, with the positive or negative ordinates depending on whether phase angle spectra indicated the motions were in phase or not, were utilized to plot the displaced position of each floor, i.e., to plot the mode shapes.

The mode shapes obtained immediately before the first earthquake simulation are plotted in large scales in Fig. 5.20. In this figure, the translational mode shapes indicate the relative lateral displacement of each level when the test structure vibrates in each mode, and the torsional mode represents the rotation of each floor when the model is

excited in each mode. The node for the second translational mode in the long direction is approximately at the setback level.

5.8 Summary of Response

The test structure was subjected to a series of earthquake simulations with increasing intensity. The acceleration records were selected to ensure high excitation in the period range of the structure at each phase of the testing program. The peak input acceleration was scaled to produce elastic as well as inelastic response. Thus, the model was subjected to excitations ranging from "low" to "high" intensity. This section provides a qualitative overview of the condition of the test structure before testing, and examines the effects of different earthquake simulations.

(a) Initial Condition

Before the earthquake simulations, the apparent shrinkage cracks comprised limited hairline cracks as described in Section 4.7. The equivalent viscous damping ratio was approximately 2 percent of critical, which is within the range of values expected for "uncracked" reinforced concrete structures. The fundamental translational period was 0.27 sec. This is equivalent to 0.54 sec. for the full-scale prototype, which corresponds reasonably with the value of N/10 suggested by seismic codes [72], where N is number of floors.

(b) Response During EC7.7L

This simulation was arbitrarily classified as a "low-intensity" motion on the basis that the Housner spectrum intensity was approximately one-quarter of the scaled intensity of the prototype El Centro N-S 1940 record (Table 4.1). The observed damage after this test comprised limited extensions of the existing shrinkage cracks and a few additional hairline cracks. The measured vibration period increased by approximately 10

percent, and damping ratio increased by approximately 20 percent of values measured before the test (Tables 5.3 and 5.4).

Hysteretic curves (base shear-roof displacement) were narrow and revealed essentially linear elastic response (Fig. 4.5(a)). Maximum roof displacement was 0.13 percent of the structure height (measured above the footing), and peak base shear reached 18 percent of the total weight (72.2 kips). No yielding was detected in the beam and column longitudinal reinforcements.

(c) Response During EC16.6L

This test was classified to be of "moderate" intensity (spectrum intensity 0.60 times the intensity of the prototype El Centro, Table 4.1). The peak base shear and roof displacement were 35 and 0.29 percent of the total weight and the total height, respectively.

Some limited inelastic response occurred during this test. Hysteretic loops of base shear versus roof displacement indicate a reduction of effective lateral stiffness compared with test EC7.7L (Fig. 4.5(b)). The loops are wider than in the preceding test, with a slight amount of pinching.

Although the strains in the reinforcing bars were considerably larger than those during the previous test, maximum reinforcement strain did not reach yield (Table 4.5). The visual damage found after this test consisted of more hairline cracks. However, the observed damage was of limited nature that would probably not require repair.

(d) Response During EC49.3L

This test was arbitrarily classified as a "high-intensity" test because its spectrum intensity was approximately 1.7 times that of the scaled intensity of the prototype El Centro base motion (Table 4.1). The maximum base shear was 68 percent of the total

weight. Peak roof displacement and inter-story drift were 1.2 and 1.6 percent of the structure height and the inter-story height, respectively. The maximum base shear exceeds the design base shear, and the drifts are in the range of the maximum drift commonly accepted for a well-designed reinforced concrete structure.

The hysteretic relation between base shear and roof displacement appears more erratic, with reduced effective lateral stiffness and increased pinching (Fig. 4.5(c)). The first-mode vibration period, as measured during free-vibration tests, reached 0.48 sec. which is 1.8 times the value measured in the "uncracked" stage, suggesting that stiffness had been reduced to approximately one-third of the "uncracked" structure (Table 5.3). The equivalent viscous damping ratio measured during free-vibration response increased to 5 percent of critical damping after this test (Table 5.4).

Reinforcement in the central column at the footing was strained 3.5 times yield strain, and the first-floor longitudinal beam strain reached a peak equal to 4.5 times yield strain (Table 4.5). Slight concrete spalling on a beam near a first-floor corner joint was observed, and cracks as wide as 0.016 in. opened in a first-floor beam near the beam-column joint. Extensive cracking was also observed in slabs, the most extensive apparent on the both top and bottom slab surfaces of the first and fourth floors (Figs. 4.7(c) and 4.7(d)).

(e) Response During EC47.7B

This earthquake simulation had essentially the same intensity as the preceding test, but was oriented skewed to the principal axes of the structure. The long-direction hysteretic curves (Fig. 4.5(d)) are more erratic than the previous tests. The loops in the short direction (Fig. 4.5(e)) are wide, suggesting substantial inelastic action. Nevertheless, strains in the reinforcing bars (Table 4.5) in this direction did not exceed the yield strains, and no major cracking was detected for frames along the short direction.

The maximum base shear was 40 and 44 percent of the total weight along the long and short axes, respectively. Roof peak displacement was as high as 0.9 and 1.0 percent of the structure height in the long and short direction, respectively. With the exception of a few minor cracks, no additional damage was found after this test. Strain levels were lower than those during the previous test (Table 4.5). The vibration period elongated, and the damping ratio in the long direction increased to 6.4 percent of critical damping (Table 5.4). Overall, the response during this test was similar to that observed in the previous test (EC49.3L).

(f) Response During MO63.4B

This test was classified as a "strong-intensity" earthquake simulation (spectrum intensity ratio is equal to 2.22, Table 4.1). The peak inter-story drift was nearly 3 percent of the inetr-story height. The maximum roof displacement was 1.2 and 2.2 percent of the structure height in the long and short directions, respectively. Torsional response was visually clear during the test, the roof twisting as much as 0.045 rad. The peak base shear reached 60 and 50 percent of the total weight in the long and short axes of the structure, respectively.

Major cracking and spalling were observed at several locations in the first, second, and third levels (Fig. 4.7). Column reinforcing bars were strained to a maximum of six times the yield strain (Table 4.5). Spalling of column shell concrete was detected at the second and third floors. Minor torsional cracking was found in the short-direction beams (Fig. 4.7(f)), suggesting that they had contributed in resistance to loads in the long direction. Diagonal shear cracking formed at some exterior joints in both principal directions.

The hysteretic loops (Fig. 4.5(f)) appear more erratic with reduced effective lateral stiffness than the previous tests. The relation between the base shear and roof displacement in the short direction (Fig. 4.5(g)) is similar to that during EC47.7B, i.e.,

wide loops but no sign of major damage and yield in this direction. The first-mode vibration period elongated to 0.67 sec., and the damping ratio was 9.6 percent of the critical damping (Tables 5.3 and 5.4).

(g) Response During MX34.6B

Even though the spectrum intensity (Table 4.1) was smaller than those for previous tests, significant response was observed during this test as a result of apparent resonance. Peak base shear reached 65 percent of the total weight in the long direction, and 39 percent of the structure weight in the short direction. Inter-story drift was as high as 3.3 percent of the inter-story height. The roof displaced to a maximum of 2 percent of the structure height in both principal directions. Torsional response was also apparent, the roof twisting as much as 0.038 rad.

Substantial inelastic response could be observed from the base shear-roof displacement hysteretic loops in the long direction (Fig. 4.5(h)). The hysteretic curves indicate reduction of effective lateral stiffness and an increase of pinching. Previous observations regarding base shear-roof displacement relation in the short direction could be seen for this test as well (Fig. 4.5(i)). The first-mode vibration period elongated (Table 5.3) to 2.9 times over the "uncracked" period, confirming loss of stiffness due to inelastic response. This implies reduction of stiffness to approximately one-tenth of the "uncracked" structure. The measured damping ratio was 11 percent of critical damping (Table 5.4).

Extensive cracking and spalling were apparent in beam ends and columns at the footing level (Fig. 4.8). At the fourth and second levels, the longitudinal reinforcement of the long-direction beam became visible where cover had spalled at the joint. Reinforcement in the long-direction beam at the fourth-level interior joint was strained as much as 11 times yield (Table 4.5). Column reinforcing bars at the footing level reached strains corresponding to 7 times yield.

5.9 Performance of the Test Structure

From the preceding discussion, it is concluded that the test structure experienced significant inelastic response during the "strong" earthquake simulations. Roof displacement was in excess of 2 percent of the structure height, and inter-story drift reached 3 percent of the floor height. Nevertheless, there was no sign of imminent collapse.

The observed response was significantly different from that expected by the seismic code provisions for which the test structure had been designed. For example, the test structure sustained simulations which resulted in base shear as much as seven times the service level design shear force. The overstrength and related issues are discussed in Chapter 7.

6. RESPONSE CORRELATION

Response of the test structure was studied using available analytical methods. The long-direction lateral strength and stiffness were studied using step-by-step inelastic static analysis, limit analysis, and inelastic dynamic response history analysis. Lateral stiffness and dynamic characteristics (mode shapes and vibration periods) of the test structure prior to the first earthquake simulation were evaluated using a three-dimensional elastic model. This chapter presents the mathematical model and different assumptions used to calculate the response. Measured and calculated stiffness and strength characteristics are compared to assess the reliability of the analytical models in correlating with the response. Results of a sensitivity study are also discussed to establish the dependency of the calculated response on various parameters such as effective flange width and load-deformation characteristics of individual members.

6.1 Analytical Model

Stiffness and strength of the test structure were computed. The analyses included calculation of the gross-section, three-dimensional vibration period and mode shapes, inelastic step-by-step static analysis, limit analysis, and inelastic dynamic response history analysis. A microcomputer version of the computer program TABS [73] was used to obtain the elastic dynamic characteristics. Inelastic static and dynamic analyses were carried out by the computer programs ANSR [41] and a modified version of DRAIN-2D [29], respectively. Geometry, member modeling, loading, and solution procedure are presented in this section.

(a) Geometry

The elastic dynamic characteristics were computed using a three-dimensional elastic model. For this purpose, the test structure was idealized as six plane frames (three in the

long direction and three in the short direction (Fig. 2.1)) interconnected by a floor slab (rigid in the plane of slab) having two translational and one rotational degrees of freedom. In each plane frame, rigid end zones equal to the column width and beam depth were assumed for the beams and columns, respectively. The floor mass (Table 4.3) was assumed to possess lateral inertia only, and was lumped at the plan centroid of the floor, at an elevation corresponding to mid-depth of the long-direction beams.

Limit analysis, step-by-step nonlinear static analyses, and nonlinear dynamic response history analyses were conducted using the mathematical model depicted in Fig. 6.1. The model comprised plane frames constrained to have the same lateral deflection at each floor. Frames 1 and 3 (Fig. 2.1) were represented by one frame having the properties equal to the sum of those in each frame. The beams and columns were assumed to have rigid end zones equal to the column width and beam depth, respectively. The floor mass (Table 4.3) was treated as described for the elastic analysis.

(b) Element Modeling

Two-dimensional frame elements were used to construct the plane frames which comprised the three-dimensional elastic model of the test structure. Column flexural stiffnesses were computed using gross uncracked cross sections. Beam stiffnesses were obtained by two methods. First, the slab contribution was not accounted for, and beam stiffnesses were based on gross uncracked cross sections (web only). In the second analysis, beam stiffnesses were computed for "T" uncracked cross sections. Effective flange was computed from elastic theory using a solution [45] similar to that presented by Timoshenko [70]. Overhanging slab width was equal to 11.4 in. and 7 in. on each side of the long-direction and short-direction beams, respectively. Axial deformation was considered for the columns, and the effects of shear deformation were included in beam and column stiffnesses. Youngs modulus for concrete was assumed to be the average of the measured values, i.e., 3086 ksi (Appendix A). Shear modulus was taken as 1400 ksi.

The computer programs ANSR and DRAIN-2D (used to carry out the inelastic static and dynamic analyses) represent beams and columns by elastic line segments connected to nodes by bilinear springs at the member ends. For inelastic static analyses, the nonlinear rotational springs at each end follow a set of bilinear rules. Dynamic response history analyses were conducted using nonlinear rotational springs which follow degrading stiffness rules similar to those known as Takeda's model. Moment-axial load interaction was ignored for the columns, and both the columns and beams were modeled by a yield interaction surface which neglects axial load. Flexural deformation only was included to compute member stiffnesses. Effects of gravity loads on element strength were considered by initializing the member end forces equal to those under gravity loads. Procedures to obtain properties of the nonlinear springs are described in the following paragraphs

Yield moments and stiffnesses (initial and strain hardening) of bilinear springs at the two ends of beams and columns were based on moment-rotation relations which were obtained from moment-curvature curves. Using the computer program MOMCUR[36], moment-curvature responses were computed accounting for actual material strengths, concrete confinement, strain-hardening effects, and floor slab contribution. Column axial load was assumed to be equal to the tributary gravity axial load, and its variation during the earthquake simulations was ignored. The modified Kent and Park [48] concrete model was used, and the steel model incorporated elastic, plastic, and strain-hardening that closely follows the actual stress-strain behavior [28]. The slab reinforcing bars within 28 or 16.5 in.(for interior or corner joints, respectively) were considered to contribute to the beam flexural resistance. A fixed effective flange width is strictly not correct because slab contribution increases with an increase in tensile strain of beam longitudinal reinforcement after initial cracking [18,45]. The proposed method would then overestimate beam flexural resistance at low strain levels, but it should result in a close estimate of the "actual" behavior near the ultimate limit state.

The moment-curvature relationship was idealized as a trilinear curve (Fig. 6.2) with two breakpoints at cracking and yielding. "Cracking" occurs when tensile stress at the extreme fiber of concrete under tension is exceeded. "Yielding" corresponds to the first yielding of tensile reinforcement. Beyond yield, the moment-curvature relation is taken as linear, passing through a point defined as "ultimate". The ultimate moment and curvature were taken arbitrarily as the computed values for a compressive strain of 0.003 at the extreme concrete fiber. Strictly speaking, this definition is not unique. Approximate trilinear moment-rotation relations were derived by integrating trilinear moment-curvature responses over length of members assumed to be flexed in double curvature with equal end moments [59]. The breakpoints in the trilinear relation are defined by onset of cracking and yielding (Fig. 6.3).

As noted previously, joints were assumed to be rigid. For some of the analyses, additional rotational flexibilities due to reinforcement slip from beam-column joints were considered. An approximate procedure similar to one suggested by Takeda [67] was used to account for reinforcement slip. According to the model (Fig. 6.4), the increase in member rotation at each end (Θ) can be expressed as

$$\Theta = \frac{f_s^2 d_b}{8\bar{u} j d E_s}$$

in which jd is the distance between tension-compression couple, f_s is steel stress at joint face, $\bar{u}$ is average bond stress, E_s is steel modulus of elasticity, and d_b is diameter of reinforcing bar.

At each "breakpoint" (cracking, yield, and ultimate), the corresponding values for jd and f_s were used to calculate rotation due to reinforcement slip. An average bond stress equal to 450 psi , corresponding to approximately 10 percent of the average concrete compressive strength (Appendix A), was used. The additional rotations were added to the corresponding values at yield and cracking (Θ_y and Θ_u (Fig. 6.3)). Although slip could occur at cracking level, the magnitude was significantly small that

the effect was ignored.

As required by the computer programs ANSR and DRAIN-2D, properties of the concentrated nonlinear springs at each end of a member are based on bilinear moment-rotation relations. Because the calculated moment-rotation curves were idealized as trilinear, they need to be converted to an equivalent bilinear relation. This may be achieved using a number of possible methods, three are: (1) Use the initial "uncracked" stiffness or a fraction of it (to account for reduced stiffness due to cracking). (2) Assume a completely cracked cross section, and use the "cracked" stiffness. (3) Use the average of the "uncracked" and "cracked" stiffnesses.

A limitation of the available computer programs (ANSR and DRAIN-2D) is that only a single initial stiffness and single strain-hardening stiffness can be specified to represent the nonlinear springs at the member ends. Thus, these programs ignore the difference in stiffness under opposite directions of bending. This limitation is a severe drawback for reinforced concrete members which exhibit substantially different responses under different directions of bending. The calculated stiffnesses for the two bending directions were averaged to obtain a single set of stiffness values (initial and strain-hardening stiffnesses).

The limiting strengths of the structure were computed using the computer program ANSR. Rigid-plastic flexural hinges were assumed to form at beam-column faces. Elastic line elements representing beams and columns framed between the hinges. The ultimate flexural strength was used for the limit analysis calculations. As noted previously, the ultimate state was assumed to correspond to a maximum concrete compressive strain of 0.003 in./in. at the extreme fiber. Trilinear moment-curvature relations for the beams and columns were converted to equivalent elastic-perfectly plastic relations (Fig. 6.5) by setting the areas under the two curves equal. Then, the equivalent yield curvature is determined from

$$\Phi_y^* = \frac{1}{M_u}(-M_c\Phi_y + M_y\Phi_c + M_u\Phi_u + M_u\Phi_y - M_y\Phi_u)$$

All the parameters are defined in Fig. 6.5 and Appendix D.

(c) Loading and Solution

As noted in Chapters 3 and 5, the lateral stiffness of the test structure prior to the first earthquake simulation was measured by applying a lateral load at the roof (Fig. 3.7) and by monitoring the lateral displacement. The slope of the resulting force-deflection relation was defined as the lateral stiffness. To model this loading, the three-dimensional elastic analytical model was subjected to a lateral load equal to one kip applied at the centroid (as defined for masses in Section 6.1a) of the sixth floor. The lateral load was applied once parallel the long direction and once along the other principal axis, and the corresponding roof displacement at the floor centroid was obtained using the program TABS. The lateral stiffness is, then, the inverse of the computed lateral displacement.

Nonlinear static and limit analyses were performed using the computer program ANSR. The step-by-step integration solution was based on the Newton-Raphson scheme. The response was calculated under two types of lateral load distribution (Fig. 6.6), corresponding to a uniform or triangular acceleration profile. These distributions are referred to as the "rectangular" and "UBC" types. The former distribution was not observed among the measured lateral force profiles (Fig. 5.9). It is noted that the measured distributions were apparently somewhere between the UBC and rectangular distributions. The base shear (sum of the lateral forces) was increased at one-kip increments, and the test structure was analyzed for the resulting lateral loads. Roof displacement and base shear were monitored during each load increment to construct the lateral load-displacement relation. The ultimate base shear strength of the test structure was assumed to have reached when a collapse mechanism formed.

The standard computer program DRAIN-2D allows only a vertical and horizontal input ground acceleration. Nevertheless, the interaction between the shaking table platform and test structure resulted in an additional pitching acceleration. As a result,

the test structure was subjected to both a horizontal acceleration and a pitching acceleration. Considering the limitation of the program DRAIN-2D, two options have been used in past studies. In the first method, the complete table-structure system is modeled and subjected to the measured horizontal acceleration. The shaking-table platform is modeled as a rigid beam supported on two vertical springs simulating the vertical hydraulic actuators [57]. Generally, the springs are assumed to be linear elastic, and a trial-and-error procedure is necessary to select the stiffness. The stiffness is "tuned" such that the vibration period of the complete table-structure system coincides with the value obtained from the response histories measured during the earthquake simulation. This method has previously been used in a number of studies [12,44]. In the second method, a single equivalent horizontal base acceleration is estimated [71], which accounts for both the horizontal and pitching accelerations. The equivalent input motion is then applied to the structure, fixed at the base. In the present study, a third option was utilized. The computer program DRAIN-2D was modified to include a rotational input acceleration in addition to the two independent horizontal and vertical ground accelerations. Thus, it was possible to analyze the test structure, fixed at the base, under the measured horizontal and pitching accelerations. The formulation to include the third independent input motion is summarized in the following paragraphs.

Consider a structure subjected to a horizontal, vertical, and rotational ground acceleration (Fig. 6.7). The equations of motion can be written as

$$\ddot{M}r+\dot{C}r+Kr=-MB\ddot{U}_g$$

where M, C, and K are the mass, damping, and stiffness matrices, respectively, r is the relative displacement (translational and rotational) vector, and $\ddot{r}$ and $\dot{r}$ are the acceleration and velocity vectors, respectively. $\ddot{U}_g$ is the input acceleration vector, i.e.,

$$\begin{Bmatrix} \ddot{X}_g \\ \ddot{Y}_g \\ \ddot{\Theta}_g \end{Bmatrix}$$

B is an Nx3 (N= number of degrees of freedom) matrix which specifies the dynamic load vector. It can be written as

$$\begin{bmatrix} r1 & 0 & r4 \\ 0 & r2 & r5 \\ 0 & 0 & r3 \end{bmatrix}$$

where r1, r2, and r3 are the influence coefficient vectors [15]. For the structure shown in Fig. 6.7, the coefficient vectors are determined from the following relations:

$$r1^T = r2^T = r3^T = [111111]$$

$$r4^T = y - \bar{y}$$

$$r5^T = x - \bar{x}$$

where y and x are the coordinate vectors specifying the coordinates of the joints, and $\bar{x}$ and $\bar{y}$ are the center of rotation coordinates, usually taken at the footing centroid. The original version of the computer program DRAIN-2D ignores the terms associated with $\ddot{\Theta}_g$, i.e., r3, r4, and r5. The program was modified by including these terms in the dynamic load vector. Thus, the additional inertia forces due to the base rotational acceleration are accounted for.

Nonlinear dynamic response history analysis was carried out by the modified version of the computer program DRAIN-2D. The Newmark constant average acceleration integration scheme was used, with an integration time step set at 0.01 sec. Viscous damping was assumed to be proportional to the mass and original stiffness. Damping values were based on the values measured during the free-vibration tests conducted after each earthquake simulation. The measured horizontal and pitching accelerations were used as input records.

6.2 Correlation of Stiffness and Dynamic Characteristics

A close correlation of the lateral stiffness, vibration periods, and mode shapes for a "virgin" structure should serve as a check on the mathematical modeling of the actual

structural system. At this stage, the response is approximately linear elastic, with cracking limited to shrinkage cracks. Prediction of such initial properties, then, appears to be a simple task if floor mass and member stiffnesses are computed accurately.

In the following sections, the computed mode shapes and vibration periods from the three-dimensional elastic model are presented. The computed responses are compared with the measured quantities to assess the accuracy of the analytical model.

(a) Lateral Stiffness

As mentioned previously, gross uncracked column and beam (with and without flange) stiffnesses were used to compute lateral stiffnesses of the test structure. Computed lateral stiffnesses (1/roof displacement, as defined in Section 6.1(c)) are compared with the measured values in Table 6.1. The lateral stiffnesses in the long and short directions are 11 and 20 percent larger than the measured values when beam stiffnesses are based on web only. The computed values are significantly boosted when the slab contribution is taken into account. Including the slab contribution, the computed stiffnesses are 44 and 55 percent larger than the measured values in the long and short directions, respectively.

As noted previously in Chapters 4 and 5, the test structure was not entirely uncracked prior to the first earthquake simulation. Consistent with this observation, the measured stiffnesses are smaller than the computed values. As noted above, a closer correlation was achieved when beam stiffnesses do not account for the slab contribution. A possible explanation for this observation is that effects of shrinkage cracks on beam stiffnesses are approximately modeled by using a smaller beam stiffness based on web only. Beam stiffnesses for sections without flange are approximately one-half of those computed for sections with flange. The relative stiffness is in accord with a common ad hoc practice [16] that one-half of gross section stiffness is recommended to account for cracking. Because a better correlation was possible by using beam stiffnesses computed

for web cross section only, this procedure was followed to obtain vibration periods and mode shapes in all the discussion that follows.

(b) Vibration Periods and Mode Shapes

The three-dimensional elastic model (using beam web cross section) was used to correlate dynamic characteristics of the test structure as measured by the low-amplitude free-vibration tests before the first earthquake simulation. The computed vibration periods (Table 6.2) are close to the measured values. Smaller computed periods are in accord with larger calculated stiffnesses (Section 6.2a). This difference is mostly attributable to the assumed uncracked stiffnesses which ignore the presence of shrinkage cracks found on the test structure. With the exception of the first "torsional" mode shape (Fig. 6.8c), the mode shapes were computed closely using the elastic three-dimensional analytical model. (The mode shapes are shown in large scales.)

(c) Summary

It can be concluded that the initial global stiffness of the test structure was modeled reasonably well by a simple elastic model. The computed translational vibration periods and mode shapes were almost identical to the measured quantities. The "torsional" dynamic properties did not correlate as well. Overall, the degree of correlation suggests that the test structure was slightly cracked, and the effects of cracking on stiffness were approximately taken into account by using beam web cross sections to model beam stiffnesses.

6.3 Lateral-Load Strength

Lateral load-strength of the test structure was evaluated, as explained in Section 6.1c. Slab contribution to the overall strength was studied by varying the effective flange width used to compute beam strengths. Three different analyses were carried out

as follows: (1) no slab contribution was considered, i.e., strength was based on beam web cross section only, (2) effective flange widths gauged from experimental data (Section 5.6) were used, and (3) the floor slab spanning in the short direction on either side of the beam was considered. Lateral loads were assumed to act in a single direction as shown in Fig. 6.6. Because the structure is not symmetric about a vertical plane perpendicular to the direction of loading, slightly different results would be expected for loading in the opposite direction. The result of these studies is outlined in the following sections.

(a) No Slab Contribution

Assuming that the slab does not contribute to beam flexural strength, the computed collapse mechanism is as shown in Fig. 6.9(a), where solid circles indicate plastic hinges involved in the final mechanism. The mode of collapse is indicated to be due to development of plastic hinges in beams. Thus, by assuming that the slab does not contribute, the structure should perform as designed, that is, strength is limited by flexural hinging in beams. Computed base shear strength is 31 and 41 kips for the UBC and rectangular distributions, respectively. The computed roof displacement at formation of the mechanism is approximately 2 percent of the structure height.

(b) Calculated Effective Flange Width

The slab reinforcement within the experimentally obtained effective flange width (28.5 in. for interior joints and 16.5 in. for corner joints, Section 5.6) was taken into account in this analysis. The resulting beam negative moment strengths were on the average twice those ignoring the slab contribution. When the lateral forces had the UBC distribution, some plastic hinges are anticipated in the beams; however, the computed mechanism is a "sway" mechanism formed in the first two levels, Fig. 6.9(b), where open circles indicate locations where yielding is anticipated when the mechanism forms. The base shear is computed to be 48 kips, and the mechanism appears at lateral drift equal

to approximately 4.0 percent of the structure height. Under the rectangular distribution of lateral forces, the mechanism remains to be a "sway" mechanism formed in the first two stories. The estimated base shear strength is increased to 52 kips, and the computed roof drift at formation of the mechanism is approximately 2.6 percent of the structure height.

(c) Entire Span

By taking half the short-direction span on either side of the beams as being effective, beam flexural strengths are on the average 30 percent larger than those obtained assuming that the effective flange width is equal to the experimentally obtained value (Section 5.6). The computed collapse mechanism is a soft-story mechanism formed in the first story for the rectangular distribution, and a "sway" mechanism formed in the first two stories when the UBC distribution was utilized (Fig. 6.9c). The estimated base shear strength is 52 and 53 kips for the UBC and rectangular load distributions, respectively. The computed roof drift at formation of the mechanism is approximately 4 and 2.3 percent of the structure height for the UBC and rectangular load distributions, respectively.

(d) Summary

During test EC49.3L (the most severe of the unidirectional tests), the test structure sustained a maximum base shear equal to 49 kips at lateral drift equal to approximately 1.2 percent of the structure height. By taking the effective flange width equal to the experimentally estimated value (Section 5.6), the computed base shear strengths were 48 kips and 52 kips for the UBC and rectangular distributions. The computed strengths correspond to 98 and 106 percent of the maximum measured. Although the computed base shear strengths are close to that measured, it is noted that the UBC and rectangular distributions were not observed at time of maximum response. In reference

to Fig. 5.9 (time = 3.75 sec.), it is noted that the measured distribution at time of maximum base shear was somewhere between the UBC and rectangular distributions.

By considering the slab contribution, the computations indicate a shift from a more desirable "beam sway" mechanism to an undesirable "column sway" mechanism. It is probably unnecessary to emphasize a well-established observation that formation of plastic hinges in beams is more desirable because it is relatively easier to supply the required ductility in beams than in columns [e.g., 47]. The collapse mechanism found by accounting for slab contribution is a more realistic estimate of the failure mode. A mechanism involving plastic hinges in the columns would not be predicted if the beam flexural strength were based solely on web cross section and reinforcement.

It is noted that the computed column sway mechanisms do not occur until the computed lateral roof drift exceeds approximately 2 percent of the structure height. Apparently, significant deformations are occurring throughout the structure prior to the formation of the computed mechanism. There is no strong experimental evidence to support the computed mechanism. This subject is discussed further in Section 6.5.

6.4 Correlation of Measured Response

The measured responses during the earthquake simulations were computed by the modified version of the computer program DRAIN-2D (described in Section 6.1c). The calculated response quantities are compared with their measured counterparts in order to establish adequacy of the available analytical techniques to predict seismic response of structures. The correlation findings for tests EC7.7L, EC16.6L, EC49.3L, and MO63.4B are summarized in this section. The member model used in the analysis is limited to a single initial stiffness, the value of which cannot be defined uniquely for the test structure. Thus, several different initial stiffness are investigated (as discussed in Section 6.1(b)). Member stiffnesses were obtained using half the uncracked stiffness (to account for cracking as described in Section 6.2a), the average of half the uncracked and fully-

cracked stiffnesses, and fully-cracked stiffness. The effects of reinforcement slip were considered for all the beams and the first-floor columns in all the analyses. Consideration of the bond-slip phenomenon was limited to the first-floor columns in most of the analysis because the reinforcement yielding and concrete spalling were mainly concentrated in these columns. For tests EC49.3L and MO63.4B, slip was considered for all columns in some of the analyses.

(a) Test EC7.7L

Evaluation of the test structure response and visual appearance following this test suggest a low level of damage. The reinforcing bars did not yield, and the concrete cracking comprised a few hairline cracks. Based on these observations, member stiffnesses were computed as either half the uncracked stiffness (referred to as Model A) or the average of half the uncracked and fully-cracked stiffnesses (referred to as Model B). The viscous damping ratio was assumed to be 2.2 percent of critical, which is the measured value prior to this test.

The computed roof displacement and base shear response histories are compared with the measured responses in Fig. 6.10. The measured apparent vibration period, as observed from the roof displacement or base shear histories, is close to the value indicated by Model B. Model A is stiffer, as indicated by a shorter apparent vibration period. The lateral displacement and inter-story drift envelopes (Fig. 6.11) are more closely matched by Model B. The maximum measured base shear is almost identically computed by both models (Table 6.3(a)). A better match of the maximum values is generally obtained by Model B probably because the extreme values occurred during the first three seconds, when the computed responses by Model B almost match the measured waveforms. During response between 3.5 and 7 sec., Model A results in better correlation. The global lateral stiffness, i.e., the trend of the base shear-roof displacement hysteresis loops (Fig. 6.12) does not show any significant difference between

the two analytical models. During this test, reinforcement yielding was not detected either experimentally or analytically.

Considering the maximum values, displacement and inter-story drift profiles, and observed vibration frequencies, Model B has resulted in the more successful correlation of the measured responses. Nevertheless, both the mathematical models have produced reasonably acceptable estimates of maximum responses and periods. It is noted, however, that neither of the analytical models produces the correct waveform even though response is effectively elastic.

(b) Test EC16.6L

Because the degree of damage for this test was not substantially different from that of test EC7.7L, Models A and B were used. Additionally, member stiffnesses were obtained using fully-cracked stiffness (referred to as Model C). The viscous damping ratio was set to 2.7 percent of critical, as measured during the free-vibration test before this earthquake simulation.

Examination of the roof displacement and base shear response histories (Fig. 6.13) indicates that the responses computed using Model B match closely the first three seconds of the response. The computed displacement responses from Model C are significantly larger than the measured displacements. The apparent vibration periods indicated by Models A and B are shorter than the measured value, and the responses computed using Model C show longer apparent vibration period. The lateral displacement and inter-story drift envelopes (Fig. 6.14), and the maximum response values (Table 6.3(b)) also indicate a better overall correlation by Model B. Although Model B results in a closer estimation of maximum responses, both Models A and B are considered to have produced acceptable values, but Model C apparently does not represent the state of the test structure during this test.

The computed base shear-roof displacement hysteresis loops (Fig. 6.15) do not indicate any significant difference between Models A and B. Both of these mathematical models approximately match the trend of the hysteresis loops. Model C is too flexible for this level of response. No reinforcement yielding was detected during this test or from analyses.

Both mathematical models A and B have produced reasonably acceptable estimates of response. Generally, Model B appears to have resulted in the more successful correlation. The use of fully-cracked stiffness (Model C) is apparently not suitable to model the state of the structure during this test. The computed responses from this model are significantly different from the measured responses.

(c) Test EC49.3L

Member stiffnesses were obtained using Models A, B, and C as described in the previous section. Because of the response levels measured during this test (Chapters 4 and 5), it was considered appropriate to model effects of reinforcement slip for all the columns in addition to those in the first story, the resulting model is referred to as Model D. Viscous damping was set equal to the value measured preceding the test (3.6 percent of critical).

Both Models A and B apparently fail to correlate the measured roof response waveforms (Fig. 6.16). The apparent frequency content and more importantly the magnitudes of the computed responses clearly indicate that the member stiffnesses were not appropriately modeled by these two analytical models. The computed responses from Model C match the measured responses better than those obtained previously. A substantial improvement is achieved when the bond-slip phenomenon is considered for all the columns (Model D). Using Model D, the magnitudes and apparent frequency content of the measured responses are reasonably correlated, as observed from Fig. 6.16 and Table 6.3(c). The envelope of the lateral displacements and inter-story drifts (Fig.

6.17) support the conclusion that Model D results in better correlation. However, even for this model the computed responses fail to match the waveform of the measured responses as the test progressed. The poorer correlation in later stages of the test is partially attributed to the inability of the hysteresis mathematical model to represent the stiffness degradation ("pinching") of the members [59]. Because the maximum measured responses occur early in the test, the envelopes tend to be correlated closely.

The computed hysteresis loops indicated (not shown) that Models A and B were significantly stiffer than the measured behavior. Even though there were significant differences between the computed waveforms from Models C and D, the overall trend of the computed base shear-roof displacement hysteretic loops from these two models is similar (Fig. 6.18). Both models correlate the initial global stiffness (the trend of the base shear-roof displacement relation) reasonably well during the early response cycles. During the later stages, the degree of correlation is poorer.

The computed locations at which beams and columns yield are shown in Fig. 6.19. All the mathematical models indicate identical yield patterns, with the majority of the yielding occurring in the beams. The computed distribution of damage corresponds approximately to the apparent damage occurred during this test.

Reasonably acceptable estimates of the responses were possible by using fully cracked stiffness. Better correlations were obtained by accounting for reinforcement bond slip for all the members in contrast with accounting for slip in the beams and only the first-floor columns. The calculated damage distributions were found not to be sensitive to how the member stiffnesses are modeled. The computed locations of the damage pattern approximately match the observed pattern.

(d) Test MO63.4B

An attempt was made to correlate the three-dimensional response measured during test MO63.4B by an equivalent two-dimensional analysis. Only the long-direction

responses were studied and are reported here.

The mathematical model is the same as that used previously for correlation of the long-direction responses (Fig. 6.1). The member stiffnesses were assumed to be identical to those used in Models C and D for correlation of test EC49.3L. To account for the damage that occurred during test EC49.3L, and thus to approximately represent the initial condition of the structure prior to test MO63.4B, the mathematical model was first subjected to the input acceleration used for test EC49.3L. Because the responses during test EC47.7B did not exceed those measured during test EC49.3L, it was considered sufficient to account for the changes in member stiffnesses as occurred during EC49.3L only. Viscous damping was set equal to the value measured preceding test EC49.3L (3.6 percent of critical).

The computed long-direction roof displacement and base-shear response histories are compared with the measured responses in Fig. 6.20. Both of the mathematical models result in poor correlation of the measured waveforms. During the maximum response cycles (between 4 and 7 sec.), the computed responses are considerably smaller than the measured values. An identical observation may be made from the response envelopes (Fig. 6.21), and the extreme values (Table 6.3(d)). The frequency content is also correlated poorly. The degree of correlation is significantly less than that found for test EC49.3L. The overall stiffness characteristics of the test structure are approximately correlated by Model D during 2 and 7 sec. (Fig. 6.22). Nevertheless, during the later stages of the test, both the mathematical models fail to match the trend of the measured roof displacement-base shear relation.

The poor correlation can be attributed in part to the inadequacy of using a two-dimensional mathematical model to represent the biaxial response experienced by the test structure during this test. The poor correlation can also suggest that the selected member properties do not adequately represent the state of the test structure. Considering the poor correlation and the biaxial response, a three-dimensional analysis

seems to be more appropriate. The results of the three-dimensional analyses are presented in a companion study [45].

(e) Summary

The frequency content and magnitude of the computed responses were found to be sensitive to the assumed initial member stiffnesses. If an appropriate initial stiffness is assumed, the magnitudes of the measured uniaxial responses were reasonably correlated. For tests with significant inelastic response, the degree of correlation was deemed good for the first few cycles, but poorer towards the end of the test. The poor correlation was partially attributed to the inability of the mathematical hysteresis model to properly represent stiffness degradation. The computed yield pattern was also found to be reasonably in accord with the measured damage distribution. Acceptable correlation of the long-direction responses for the biaxial test MO63.4B was not obtained using models that had previously correlated well with the uniaxial tests.

6.5 Evaluation of Static Analysis and Dynamic Analysis

As observed in Section 6.4, the measured uniaxial responses were correlated reasonably with dynamic analysis. Nevertheless, it was found that depending on how an idealized trilinear moment-rotation curve for a member is converted to a bilinear relation, the computed responses vary. Conversion of a trilinear moment-rotation into a bilinear curve is perhaps one of the basic obstacles that an analyst faces. There are further complications in modeling a structure, for example, how to account for the slab contribution to beam strength, and how to average flexural stiffnesses for bending in different directions. From a design point of view, a close estimate of drifts and strength is generally the primary objective. Considering the abovementioned uncertainties of modeling a structure, it warrants to search for a simple but reliable method.

In the hierarchy of analytical methods, inelastic dynamic and static analyses are perhaps the most comprehensive methods among others. For both methods, the same assumptions are needed to represent member behavior. Estimation of the damping ratio, and selection of input motion are not required for static analysis, but the distribution of lateral forces for static analysis must be representative of those found during ground shaking. In the following section, static and dynamic analyses are evaluated with reference to the lateral load-displacement characteristics and distribution of inelastic response.

(a) Lateral Load-Displacement

Lateral load-displacement relations were obtained by inelastic static analysis as carried out by the computer program ANSR. The member properties were identical to those in Model D, which was used to correlate the response histories during test EC49.3L. Two types of lateral force distributions were used, the UBC and rectangular types (Fig. 6.6). Strictly, the assumption of fully-cracked member stiffnesses (used in Model D) is not correct for small lateral loads. During tests EC7.7L and EC16.6L, the degree of damage was small, and inelastic dynamic analyses indicated that reasonable correlations were possible by using the average of one-half the uncracked and fully-cracked stiffnesses. Thus, for small lateral loads it is expected that the computed lateral stiffness would be smaller than measured. For large lateral loads (e. g., greater than 25 kips, which is the maximum measured base shear measured during test EC16.6L), the computed lateral load-displacement relations should represent the lateral stiffness of the test structure.

The computed base shear-roof displacement relations are plotted in Fig. 6.23. On the same figure, the data points corresponding to the measured response envelopes (shown by "*") and those obtained from the envelope of dynamic analyses (shown by "+") are presented. Reasonably good correlation of the measured envelope was obtained

with the inelastic dynamic analyses until significant inelastic response becomes apparent (at lateral drift of approximately 0.50 percent of the structure height). For roof displacements exceeding approximately 1 in., the computed data points indicate a smaller lateral stiffness. The base shear-roof displacement curves computed by inelastic static analysis are shown on the same figure. When the lateral forces are according to the UBC, the relation between the base shear and roof displacement indicates a smaller lateral stiffness. The lower computed stiffness is expected because the computer model assumes fully-cracked member stiffnesses (Model D of the dynamic analysis). The degree of correlation improves as lateral drift (and level of cracking) increases. Even though the rectangular distribution of lateral loads results in a better correlation, it should be noted that this type of distribution was not observed experimentally (Fig. 5.9). Considering that the observed distribution of lateral loads lies between the UBC and rectangular types, the average of the two curves is expected to be close to the measured data points at large drifts.

(b) Distribution of Inelastic Response

Inelastic static and dynamic analyses were also compared from a local point of view. The distribution of the computed plastic hinge rotations over the height for the central column and the long-direction beams framing into that column is plotted in Fig. 6.24. The trends of the computed plastic hinge distribution are similar for static and dynamic analyses. Both the analyses demonstrate the distinct observed behaviors, i. e., the increased yielding at the fourth-floor beam, significant column yielding at the footing, and yielding in "Beam 2" (Fig. 5.10). The distribution of plastic hinge rotation in the column is similar to the measured behavior, i. e., above the first-floor column, the column bars do not yield significantly.

The local behavior is, then, predicted reasonably similar from inelastic static and dynamic analyses. The two methods duplicate the measured distribution of

reinforcement yielding with approximately the same level of accuracy.

(c) Summary

Using reasonable member stiffnesses, it was possible to obtain good estimates of the magnitudes of lateral displacements, inter-story drifts, and base shear by using inelastic dynamic analysis. Nevertheless, the computed quantities were found to be sensitive to member stiffnesses, and the degree of correlation became less reliable as significant damage occurred in the test structure. Static analysis was found to be adequate to obtain an insight into the behavior of the structure. The load-displacement characteristics and the distribution of damage were reasonably estimated by inelastic static analysis. This observation does not imply that static analysis can entirely substitute dynamic analysis. Static analysis is incapable of computing the magnitude of drift and base shear unless the level of lateral loads is known. Additionally, the number of response cycles cannot be obtained by static analysis. The expected drifts during a ground shaking can, nevertheless, be obtained from methods simpler than inelastic dynamic analysis, such as discussed in Chapter 7. The strength of a structure can be obtained using limit analysis. Thus, static analysis in conjunction with limit analysis and other simple methods may adequately be applied to assess the expected performance of a structure.

6.6 Summary of Correlation Studies

The measured "uncracked" lateral stiffness, vibration periods, and mode shapes were matched reasonably well by a simple three-dimensional elastic mathematical model. Overall, the degree of correlation suggests that the test structure was slightly cracked. The effects of cracking on stiffness were approximately taken into account by using beam web cross sections to model beam stiffnesses. (This method corresponds approximately to using one-half the gross stiffness of the "T" beam cross sections).

It was possible to reasonably correlate with the response quantities measured during the uniaxial simulations using elastic or inelastic planar analytical models. Computed responses were found to be poorer in later stages of the tests. It was not possible with the simple techniques investigated to obtain acceptable estimates of the long-direction responses measured during the biaxial test MO63.4B.

The uniaxial load-displacement envelopes and distribution of inelastic response were computed similarly by inelastic static and inelastic dynamic analyses. Static analysis alone is incapable of assessing the performance of a structure, because this method cannot uniquely evaluate the magnitudes of drifts and base shear. Nevertheless, static analysis is a valuable tool for gaining insight into how a structure deforms, and develops damage provided that alternate techniques are used to estimate the absolute magnitude of response.

7. EVALUATION OF DESIGN

As noted in Chapter 5, the observed response of the test structure was significantly different from that anticipated by the seismic provisions for which the structure had been designed. During test EC49.3L and subsequent tests, for which intensities are considered to equal or exceed that anticipated to occur in UBC Zone 4, the test structure sustained a maximum base shear many times the design strength. The maximum inter-story drift was in excess of two percent of the inter-story height. Nevertheless, the damage was limited, and there was no sign of imminent collapse. In this chapter, the design method is evaluated in terms of the expected and observed damage, drift, and strength.

7.1 Damage Pattern

The current seismic codes [58,72] implicitly anticipate damage during the "design" (major) earthquake. For ductile frames, the design philosophy is intended to avoid excessive damage in columns by requiring that columns be stronger than beams. Examination of the observed damage and measured reinforcement strain readings (Chapters 4 and 5) suggests that this philosophy was apparently achieved for the test structure.

During the "design" earthquake (EC49.3L), the maximum reinforcement strain in the central column, at the footing level, reached 3.5 times yield. At other levels, the strains in this column were approximately at yield (Table 4.5). The observed crack patterns (Fig. 4.7) indicate an apparently similar response for other columns. Generally, strains in beams were larger (maximum being 4.5 times yield), and cracking was more extensive. The levels of measured strain are not sufficiently large to warrant formation of plastic hinges in either columns or beams. Nevertheless, the relative magnitude of maximum strain in beams and columns indicates that the majority of inelastic action

occurred in beams, with the exception that columns yielded at the footing level. A similar trend was observed during biaxial earthquake simulations. Observed damage and measured strains in beams during tests MO63.4B and MX34.6B (Figs. 4.7 and 4.8) suggest that beams sustained the majority of inelastic action, and that such action was predominated by flexure.

The abovementioned examination of the observed damage pattern and measured reinforcement readings suggests that the intended "strong column-weak girder" design concept was apparently achieved. It is noted that, according to limit analyses reported in Chapter 6, the base shear strength in the long direction corresponds to formation of a sway mechanism in the first two stories (Fig. 6.9b). Thus, it is reasonable to conclude that additional column hinging would have occurred had the structure been subjected to input motions with more damage potential. However, the corresponding drift would have been well beyond the acceptable range when these column hinges formed.

7.2 Drift

Inter-story drift was as large as 1.6 percent of the story height during test EC49.3L, which can be considered to be the "design" major earthquake. For the biaxial simulations, the maximum inter-story drift was in excess of 3 percent of the story height. The maximum inter-story drifts exceed the upper limit of 1.5 or 2.0 percent of inter-story height that is normally considered acceptable [3]. At the level of maximum inter-story drift sustained by the test structure, severe damage to nonstructural elements would be expected in a real building [20].

The inter-story drift computed in the process of the design analysis was 0.0012H, where H is the inter-story height. This value was computed for a set of static forces, and using an elastic analytical model assuming gross uncracked stiffness for columns and half gross moment of inertia for "T" beams (as described in Chapter 2). Maximum inter-story drift measured during the "design" earthquake (EC49.3L) is, then, 13 times

larger than this computed inter-story drift. For test MO63.4B, which could be considered as "rare" event, the inter-story drift was as large as 28 times that expected from the design analysis. Similar trends have been observed in other studies [35].

The large ratio between the measured and the design estimate of inter-story drift is noteworthy. Higher values are apparently anticipated by current codes [58,72], as the codes require that vertical load carrying capacity of elements should be verified for lateral drifts equal to the code computed drift multiplied by 3/K, where K is 0.67 for frames. Accounting for this factor, the design estimate of inter-story drift becomes 0.005H. It is clear that the code analyses do not adequately reflect actual building drifts. A more rational method to estimate expected inter-story drifts is given next.

As noted by Newmark [42], the displacement in a "long-period" yielding structure is approximately equal to the displacement that would occur if the structure remained elastic. At the initial vibration period of the test structure equal to approximately 0.30 sec. (Chapter 5), the pseudo-acceleration for test EC49.3L is 1.32g (Fig. 7.1), whereas the "UBC design spectrum" (indicated by a solid line in Fig. 7.1) indicates pseudo-acceleration equal to 0.12g. Code forces, then, are approximately one-tenth of those expected for an elastic structure. Consequently, lateral drifts are plausibly ten times those computed for the code forces. A second factor that amplifies the response is that actual effective stiffness is less than that assumed for estimates of drifts in the design process. By halving the beam gross-section stiffness, the effect of cracking on beam stiffness was approximately taken into account in computing the inter-story drift (0.0012H) during the design analysis. Additional effects such as reinforcement slip from joints and cracking in columns, which were not considered, could further reduce the stiffness by a factor of one-half. Accounting for the two abovementioned factors, the code estimate of inter-story drift should be increased to 10x2x0.0012H=0.0024H. This value of inter-story drift is within the range of measured drifts for this test (0.016H). Similar procedures have been proposed by others [63,66].

In view of the preceding discussion, it is concluded that actual inter-story drifts could be several times the value computed by the code analysis. If design inter-story drifts are underestimated, severe structure and partition damage could be expected. As demonstrated, simple but rational procedures can be used to more closely estimate drift during strong ground shaking.

7.3 Strength

The test structure reached a maximum base shear equal to 0.68W, where W is the structure total weight, when subjected to test EC49.3L . During the biaxial earthquake simulations, the maximum shear along any of the principal axes of the structure was 0.60W. It is noted that the maximum base shear was about 7.5 times the design base shear of 0.091W, as calculated using the UBC design formula without load factors. Despite the large difference between the measured and design strengths, structural damage was limited. During test EC49.3L, the maximum joint shear stress in the first-floor interior joint reached approximately $21\sqrt{f_c'}$, which is nearly equal to the nominal design limit of $20\sqrt{f_c'}$ recommended by the ACI-ASCE Committee 352 [2]. The maximum recorded shear stress at a first-floor corner connection (Fig. 3.12) reached $7\sqrt{f_c'}$, compared with the corresponding recommended nominal value of $15\sqrt{f_c'}$. Despite the large shear stresses, there were no visible shear cracks or other visible signs of joint shear deterioration during this test. The joint shear stress could not be computed for the biaxial tests, but shear cracking and cover spalling were observed during these tests, suggesting that higher shear stresses occurred.

The above observations indicate that the test structure possessed a large overstrength. A similar observation has been made for other reinforced concrete [12,38] and steel [71] test structures. The overstrength is in some ways advantageous. For example, the increased strength is likely (but not certain) to result in reduced ductility demands during strong earthquakes. However, the overstrength also indicates that

current design and analysis methods are capable of producing a structure that is significantly different from that which was intended. It is conceivable that in some cases, the structure will differ in such a way that undesirable and unexpected failure modes might result using the current methods. For example, for the test structure, design joint shear stresses range between 11 $\sqrt{f_c'}$ and 13.1 $\sqrt{f_c'}$ for interior joints, whereas the maximum joint shear stress in the first-floor interior joint reached approximately 21 $\sqrt{f_c'}$. Had the design values been larger, actual joint shears would conceivably have been larger also, perhaps resulting in joint failure.

Because the test structure was designed according to currently applied design algorithms, and because it comprises and reasonably replicates the essential primary structural elements of a real building, it is possible to trace through the structural design and analysis process to ascertain the sources of overstrength that might influence real buildings. An evaluation of the overstrength follows.

7.4 Evaluation of the Sources of Structure Overstrength

To arrive at an understanding of the sources of overstrength in the test structure, a series of limit analyses was conducted. The analyses are limited to the long-direction behavior, but it is believed that the findings could be applied for the short direction as well. In each analysis, different design and analysis provisions and their effects on strength are considered separately. A beam "sway" mechanism (Fig. 6.9(a)) was assumed for all the limit analyses. The use of a single collapse mechanism is not correct because the mode of failure changes as member strengths change. However, the main objective of this study is to determine the effects of each design step on the overall strength of the structure. If the mechanism was allowed to change from one analysis to another, the shifting mechanism was found to mask the effect of the design step being studied. The lateral-load distributions for the limit analyses were identical to those discussed in Chapter 6, i.e., the UBC and rectangular types (Fig. 6.6). Results of the analyses are

summarized in Table 7.1, and discussed in the following paragraphs.

(a) Analysis A, The Design Base Shear

According to the UBC, if the test structure is designed following the equivalent static lateral force method for seismic Zone 4, the design base shear (without load factors) in the long direction is 6.67 kips. This strength is listed in Table 7.1 as Analysis A1. If the test structure is assumed to possess strengths equal to those required under the code forces, and the rectangular type distribution of lateral loads (Fig. 6.11) is assumed for the limit analysis, the theoretical base-shear strength is 8.70 kips. Thus, it is noted that the lateral-load distribution influences lateral-load strength.

However, as explained in Chapter 3, the structure was designed for forces calculated using a modal analysis technique as opposed to the equivalent static force method. If the test structure possessed the distribution of strengths equal to those calculated with the modal analysis (referred to as Analysis A2 in Table 7.1), the theoretical base-shear strength is 7.77 kips or 10.1, depending on whether the UBC or the rectangular type distribution of lateral loads is assumed for the limit analysis, respectively.

(b) Analysis B, Load Factors

The ACI Building Code strength design procedure requires consideration of simultaneous effects of factored gravity and earthquake loads according to the formula U=0.75(1.4D+1.7L+1.87E), in which U, D, L, and E are the ultimate design load, service dead load, service live load, and code design earthquake load, respectively. The theoretical long-direction lateral-load strength (Table 7.1) increases above that indicated by Analysis A2 by factors of approximately 1.38 and 1.40 for the UBC and rectangular distributions, respectively, if the member strengths are according to the factored loads.

(c) Analysis C, Beam Proportioning and Detailing Requirements

Actual beam proportions resulted in design strengths (computed according to the ACI Building Code with an equivalent stress block and nominal material properties) which significantly exceeded required strengths. Although limitations in available model reinforcement (Appendix A) resulted in some overstrength, the majority of overstrength arose from the detailing requirements for beam depth and for bottom reinforcement at the connections. According to the ACI-ASCE Committee 352 recommendations [2], minimum beam depths were recommended to be at least 20 times the column rebar diameter. This provision is intended to ensure sufficient development length for the column reinforcing bars. More significantly, whereas the required positive moment strengths at connections were generally small, strengths at least equal to half the negative moment strengths were required by the ACI Building Code provision A.3.2.2. The resulting beams strengthen the entire structure to a value of approximately 1.64 times the long-direction strength obtained in Analysis B under both lateral load distributions (Table 7.1).

(d) Analysis D, Minimum Required Column Overstrength and Actual Column Strengths

The report of ACI-ASCE Committee 352 (Comm. 352) recommends that the sum of the nominal column strengths should be at least 1.4 times the sum of nominal beam strengths at a connection. Nevertheless, additional recommendations of Comm. 352 resulted in actual columns having strengths exceeding the minimum flexural overstrength of 1.4 (as discussed in Chapter 2, the columns possessed overstrength ratios ranging between 1.6 and 2.2). Among these detailing provisions are: (1) Column cross-sectional dimension must be at least 20 times the beam reinforcement diameter. This is intended to provide enough development length for the beam reinforcing bars. (2) Column longitudinal reinforcement must be closely spaced around the column perimeter. That

is, the number of column longitudinal bars was decided by the maximum bar separation permitted in the recommendations, i.e., smaller of 8 in. (full scale) or one-third of the column diameter or cross section dimension in the direction spacing is being considered. (3) Joint dimensions must be such that joint shear failures do not occur. This is accomplished by limiting the interior, exterior, and corner joint shear stress to $\phi 20\sqrt{f_c'}$, $\phi 15\sqrt{f_c'}$, $\phi 12\sqrt{f_c'}$, respectively (ϕ =0.85). Using the actual column cross sections, theoretical long-direction strength (Table 7.1) is boosted to a value of approximately 1.12 times the strengths obtained in Analysis C. It should be noted that the increase in structure strength is much less than the increase in individual column strength. This is attributed to the assumed collapse mechanism. In this mechanism, the structure strength is predominantly controlled by beams.

(e) Analysis E, Capacity Reduction Factors

The preceding analyses were based on design member strengths, which are equal to nominal strengths multiplied by capacity reduction factors, as specified by ACI 318-83. Using nominal strengths rather than design strengths, theoretical strength of the test structure in the long direction (Table 7.1) is boosted by another 11 percent under both lateral load distributions. It is noted that, at this stage, where strengths are computed using the ACI Building Code nominal member strengths, the computed structure strength is approximately 45 or 60 percent (for the UBC or the rectangular lateral load distribution, respectively) of the maximum measured base shear during the uniaxial tests.

(f) Analysis F, Actual Material Properties

The nominal strengths of the ACI Building Code were abandoned, and strengths were computed accounting for actual material strengths, concrete confinement, and strain-hardening effects under monotonically increasing loads, as explained in detail in

Chapter 6. If the "actual" strengths are used, theoretical base-shear strength in the long direction (Table 7.1) is increased by 41 percent (for both lateral load distributions) over the strength based on the nominal member strengths (Analysis E).

(g) Analysis G, Slab Contribution to Beam Flexural Strengths

From analysis F, it is obvious that the computed structure strength was still smaller than the measured maximum base shear. All the previous analyses were based on beam strengths computed ignoring the effect of the floor slab on beam flexural strength. As discussed previously in Chapter 6, beam negative moment strengths, including slab contribution, were estimated based on measured strains and statical considerations for elements framing into a beam-column joint. Computed negative moment strengths were typically 2.5 times strengths computed ignoring the floor slab contribution. With the enhanced beam strengths, theoretical base-shear strength in the long direction (Table 7.1) increases by approximately 66 percent for both lateral-force distributions.

7.5 Summary

Locations of damage anticipated by the design methods were generally in agreement with those observed for the test structure. Apparent damage was mainly in the beams. Thus, the intended "strong column-weak girder" design concept was successfully implemented.

It was found that the test structure underwent inter-story drifts far exceeding the code computed values. Clearly, the code analysis did not adequately reflect actual building drift. An improved estimate of drift sustained by the test structure was achieved by a simple but rational procedure. To achieve this estimate, it was necessary to account for reduced stiffness of the test structure, and to realize that code forces are smaller than those for an elastic structure.

The experiments showed clearly the tendency of current design techniques to result lateral-load strengths significantly exceeding the design strength. Several factors were responsible. Taken individually, no single design step could be identified as having caused the large overstrength observed for the test structure. Taken together, and recognizing that the individual factors are multiplicative, the overstrength could be plausibly explained. Among the factors identified, the most important ones were found to be contribution of the floor slab to beam flexural strength, and column and beam overstrength resulting from detailing requirements.

8. A STUDY OF THE EFFECTS OF SETBACKS

Apparent effects of setbacks on dynamic response of structures are evaluated. The measured responses of the test structure are reviewed. The experimental findings are supplemented with a series of analytical studies. Rational guidelines are established by which to detect and avoid potential concentration of damage in tower members. A lateral-load distribution is proposed for static design analysis of setback structures.

8.1 Introductory Remarks

Examination of the measured data (Chapter 5) revealed that, with the exception of modest torsional effects, the dynamics of the test structure response was similar to that expected for a structure having regular configuration. Results from other experimental studies conducted by Wood [77] support the observations made here. Although concentrations of inelastic behavior were observed in some of the tower members of the present study, similar concentrations were indicated by inelastic static analysis. Thus, it is concluded that the observed concentration of inelastic action is a consequence of the structural configuration, but is not especially manifest in the dynamic response.

Several previous studies (see Chapter 1) have indicated that dynamic response of setback structure involves concentration of drift and damage in the tower. Some [e.g., 25,30] have recommended dynamic response analysis to detect these concentrations. Consistent with these studies, current seismic design codes[58,72] require that the design forces be determined from dynamic analysis when the degree of setback (the degree is defined as the ratio between tower and base area) exceeds a certain level. For example, the UBC [72] requires dynamic analysis if the tower plan dimension is less than 75 percent of the base plan dimension. Although the test structure had a greater degree of setback than the UBC limit, no significant peculiarities in dynamic response were detected. To further investigate the behavior of setback structures, a parametric study

was carried out, as described in the following.

8.2 Parametric Study

Six generic setback frames were designed by the UBC static lateral load force analysis procedure and by a modal analysis procedure. The corresponding structures are referred to as the "UBC" and "modal" frames. The inelastic dynamic responses of the structures were evaluated to observe any unusual distribution of damage over the height due to the setback, and to detect any undesirable behavior associated with the use of static analysis for design of setback structures, as implied by current building codes [72]. To further investigate the response of setback structures, the elastic response of a two-degree-of-freedom system (representing tower and base in a setback frame) was studied. Based on the findings, a rational approach was found to successfully anticipate the potential concentration of damage in the tower. Additionally, a simple method was constructed for static design of a special class of setback structures, i.e., those with a single symmetrical or asymmetrical setback. The method was applied to redesign two of the generic frames. The distribution of inelastic response for the structures designed for the new lateral forces was found to be more uniform. The parametric study is summarized in the following sections.

8.2.1 Behavior of Generic Frames Designed by UBC Static and Dynamic Methods

(a) Selection of Generic Structures

Six generic frames were selected for study (Fig. 8.1). The degree and level of setback varied. (The degree is defined as the ratio between tower and base area. The level is defined as the story level where the setback occurs.) It should be noted that all the frames are classified to have irregular configuration according to the current building

codes[58,72], because the setback is expected to result in "unusual" dynamic response. The frames are ten-story, nine-bay by one-bay frames; the story height and bay width are 12 and 25 ft., respectively.

The frames were designed using a modal analysis technique and the standard UBC static lateral force analysis procedure. Gravity loads were not considered. Because the distribution of design forces from the two methods was of concern, rather than the ability to estimate magnitude of base shear, the base shear was kept identical for the two methods. An extended version of the computer program TABS [75] was used to carry out the design calculations. To approximate lightly-cracked stiffnesses, beam and column flexural inertias were taken equal to half the gross-section values. The modal analysis was performed using an acceleration spectrum constructed from the Applied Technology Council (ATC) [68] lateral design force coefficient, i. e.,

$$C_s = \frac{1.2A_vS}{RT^{2/3}} \leq \frac{2.5A_a}{R}$$

In which, T is the fundamental period of the building, A_v is the coefficient representing effective peak velocity-related acceleration, S is the coefficient for the soil profile characteristics of the site, R is the response modification factor, and A_a is the seismic coefficient representing the effective peak acceleration. This relation may also be written as

$$C_s = \frac{2.5A_a}{R} \quad \text{if} \quad T < 0.33$$

$$C_s = \frac{1.2A_vS}{RT^{2/3}} \quad \text{if} \quad T \geq 0.33$$

Using $A_a = A_v = 0.4$, $S = 1$, and $R = 7$, the pseudo acceleration spectrum (gC_s, where g is the acceleration of gravity) was obtained (Fig. 8.2). The modal contributions from the first six modes were combined using the SRSS (square root of the sum of the squares) method.

For the static design, the base shear obtained from the modal analysis was distributed using the UBC approach, i.e.,

$$F_i = \frac{(V-F_t)W_i h_i}{\sum_{i=1}^{i=N} W_i h_i}$$

$$F_t = 0.07TV \leq 0.25V$$

in which, F_i is the lateral force at the ith level, V is base shear, W_i and h_i are weight and height of the ith level, respectively, and F_t is a portion of base shear concentrated at the top of structure in addition to F_i. The resulting lateral forces are summarized in Table 8.1.

The design of the generic frames did not account for detailing provisions such as limits on beam longitudinal reinforcement ratio, the requirement that the sum of nominal column strengths should be at least 1.4 times the sum of the nominal beam strengths at a connection, and code-specified serviceability requirements. The design and serviceability requirements were ignored because the primary objective was to observe how performance of the structures would be affected by different distributions of design forces. The member strengths would have become nearly identical had these provisions been followed, and the difference between the two design methods would have been "masked". Therefore, the required strengths, as obtained from the mode superposition or the UBC static analysis, were generally assumed to be provided exactly. The design forces for the columns adjacent to the tower were, nevertheless, obtained by an alternate approach, as described next.

The results of static and modal analyses indicated that the bending moments for the columns adjacent to the tower (marked by ">" in Fig. 8.3) were significantly smaller than those (along the same column line) in the lower level or in the first floor of the tower. This behavior can be explained in reference to Figure 8.3. The portion of the base that is not continuous alters the deflected shape of the structure. This portion of

the base acts as a restraint on lateral deflection of the remainder of the structure. The columns immediately below the tower, thus, flex in a single curvature, or the inflection point is close to the top end, such that a relatively small design moment is computed. If the column strengths are assumed to be those obtained from the analysis, a concentration of damage will be excpeted in the columns adjacent to the tower that had been designed for the small moments. Alternative methods are, thus, necessary to obtain the design forces in these columns. In this study, (along each column line) the flexural strengths for these columns were set equal to the corresponding values of the first-level columns in the tower.

(b) Method of Dynamic Analysis

Nonlinear dynamic analyses were performed using the computer program DRAIN-2D [29]. The structures were modeled as equivalent plane frames. Moment-axial load interaction was ignored for the columns, and both the beams and columns were modeled using a degrading-stiffness, single-component element similar to that known as a Takeda's model. Initial flexural stiffness was chosen to be one-half of the gross flexural stiffness to approximately account for cracking, and the strain-hardening stiffness was assumed to be 15 percent of the initial stiffness. Yield moments were chosen to be equal to the provided member strengths, and gravity loads were ignored. Viscous damping was assumed to be proportional to the mass and original stiffness, with viscous damping ratio was taken as 5 percent of critical damping. Floor mass was assumed to be proportional to number of bays, with mass per bay was taken as 0.621 ksec.^{2}/in. Step-by-step analysis was carried out using the Newmark constant acceleration scheme.

The performance of the generic frames was studied under four different ground motions typical of firm-ground acceleration records measured in California. The computed responses under each input acceleration were then averaged to make the findings less dependent on the base motion characteristics (the averaging process is

believed not to have influenced the conclusions). The input ground motions involved the 1940 El Centro NS record, the 1952 Taft N21E record, the 1966 Parkfield N65E record, and the 1971 derived Pacoima S16E record. The time variation and 5-percent damped pseudo acceleration spectrum of each of the acceleration records are shown in Fig. 8.4(a) and 8.4(b). To induce a desirable degree of damage, the Taft and Parkfield records were scaled to have a peak acceleration equal to 0.32g (g is the acceleration of gravity) and 0.38g, respectively. The peak accelerations for the El Centro and derived Pacoima records are 0.35g and 0.40g, respectively.

(c) Method of Comparison

Relative performance of the structures designed by the two methods was evaluated by comparison of ductility demands. It is believed that such comparison would point out any unusual inelastic response due to the setback, such that differences between the two design methods (mode superposition method and equivalent lateral force analysis) could be noted. For each "modal" and "UBC" frame, ductility demands from different ground motions were averaged. Calculation of ductility demand is discussed in the following.

The computer program DRAIN-2D calculates plastic hinge rotations as a measure of inelastic behavior of members. The rotation ductility ratio for a member can be obtained using the available information, that is

$$\mu_\theta = \frac{\Theta_u}{\Theta_y} \tag{8.1}$$

in which, Θ_u is the ultimate plastic hinge rotation, Θ_y is rotation at the incipient yield condition, and μ_θ is member rotational ductility. Approximating $\Theta_y = \frac{M_y}{EI}\frac{L}{6}$ (assumes contraflexure at mid-span) and taking $\Theta_u = \Theta_y + \Theta_p$, the rotational ductility demand is rearranged to

$$\mu_\theta = 1 + \frac{6EI\Theta_p}{M_y L} \tag{8.2}$$

in which, EI is member flexural stiffness, M_y is positive or negative flexural capacity, L is length of member, and Θ_p is plastic hinge rotation as computed by the computer program.

From Eq. 8.2, it is noted that μ_θ is related to the ratios between EI and M_y. For a member of a given cross section, that ratio does not vary significantly with variations in quantity of reinforcing steel. Thus, comparing a given location in the UBC and "modal" frames, the following holds approximately.

$$\frac{EI_{UBC}}{M_{yUBC}} = \frac{EI_{Modal}}{M_{yModal}} \tag{8.3}$$

in which, M_{yUBC} and M_{yModal} are member yield strength in the "UBC" and "modal" frames, respectively. From this relation, the flexural stiffness of the UBC frame (EI_{UBC}) can be written in term of that of the modal frame (EI_{Modal}).

$$EI_{UBC} = \frac{M_{yUBC}}{M_{yModal}} EI_{Modal} \tag{8.4}$$

The result of Eq. 8.4 is used to simplify the evaluation of rotational ductilities. For the "modal" frames, EI_{Modal} was taken equal to one-half of the gross section values. For the UBC frames, the value of EI_{UBC} was computed according to Eq. 8.4. M_{yUBC} and M_{yModal} were taken equal to the provided flexural capacities.

The effect of axial load was not considered to estimate column ductility demands (axial load equal to zero). Nonetheless, the relative comparison between the calculated ductilities are valuable and should ascertain the differences between the two design methods.

Two types of ductility demand could be obtained corresponding to the maximum positive and negative hinge rotations at each end. Both of these values are reported here.

(d) Results

The adequacy of the two design methods (static UBC lateral force analysis and modal analysis) was investigated in reference to the distribution of rotational ductility demands over the height. A design method was considered to be successful if the frame corresponding to the method displayed more or less a uniform distribution of rotational ductility. Particular attention was given to observe the differences between the ductility demands in the "modal" and "UBC" frames in the tower. The results are summarized in the following paragraphs.

The distribution of rotational ductility demand over the height is plotted in Fig. 8.5. For all the six types of setback configurations, the "modal" and "UBC" frames indicate a close amount and distribution of ductility demands. In some limited instances, ductility demands for the "UBC" frames exceed those for the "modal" frames. This could be taken to imply that the static design method is not appropriate for setback structures. However, a similar observation is also expected for structures having regular configuration. Additionally, the differences generally are not significant, and in some cases the "modal" frames indicate larger demands than the "UBC" frames. Hence, no major difference was found between the mode superposition technique and the standard building code lateral force analysis even though the degree of setbacks significantly exceeds the threshold separating regular and irregular configuration as specified by the current building codes (Chapter 1).

Another major observation is that only frames "2C", "3C", and "4C" (Fig. 8.1) display a significant increase of rotational ductility demand in the tower columns, whereas the other frames ("5C", "5D", and "4D") indicate less increase. For all the frames, the tower plan dimension (11 or 33 percent of the base plan dimension) exceeds by far the limit imposed by the current building codes (if the tower plan dimension is less than 75 percent of the corresponding base dimension, dynamic characteristics of the structure need to be considered in design to prevent excessive damage in the tower).

Nevertheless, the response of only frames "2C", "3C", and "4C" shows significant damage concentration in the tower. Perhaps, an even more important observation is that frames "2C" and "5C" have identical plan dimensions, but dynamic response of the former shows a pronounced damage to the tower members, whereas the latter does not. Thus, the current building code approach by which regular and setback structures are differentiated appears to be insufficient and could be misleading.

Two questions were raised in this section, and solutions need to be found. First, a rational method is necessary to predict potential unusual responses associated with setbacks. Second, if the mode superposition method and the standard lateral force analysis technique result in structures with similar dynamic responses, and they both fail to prevent concentration of damage in members near the setback level, an alternative design method needs to be found. These issues are addressed in the balance of this chapter.

8.2.2 Proposed Method to Classify Setback Structures

In order to understand response of setback structures, elastic response of a two-degree-of-freedom (2DOF) stick model (Fig. 8.6) was studied. Mass M2 and stiffness K2 were changed as a ratio of M1 and K1, i.e., K2=αK1 and M2=βM1. The values of K1 and M1 were arbitrarily selected to be 1000 k/in. and 25 ksec.^{2}/in., respectively, which would result in a first-mode vibration period of one second if the mass M2 is zero. By varying α (equal to 0.1, 0.2, 0.3, 0.4, 0.5, 0.6, 0.7, 0.8, 0.9, and 1.0) and β (equal to 0.1, 0.2, 0.4, 0.6, 0.8, and 1.0), it was possible to study effects of mass and stiffness ratios on dynamic response. For each combination of α and β, the 2DOF system was subjected to a sine wave with the amplitude equal to 1 g (386.4 in/sec^2) and vibration period equal to 0.1, 0.2, ..., 3.9, 4.0 sec. For each vibration period, the ratio $\delta=\frac{x_2-x_1}{x_1}$, where x_1 and x_2 are lateral displacements of each degree of freedom (Fig. 8.6), was computed using a

step-by-step integration scheme. The resulting values of δ from each ground motion (input sine wave) were then averaged and plotted as a function of α and β (Fig. 8.6). It is observed that as α decreases (i.e., K2 becomes smaller), δ increases. In addition, the most critical cases correspond to those with large values of β, i.e., large M2. This is expected as more inertia force is associated with larger mass, and hence larger displacements. It is noteworthy that the most critical cases occur for small α with large β, a case that is highly unusual in practical systems. Typically, because mass and stiffness tend to be proportional to floor area, a small value of α generally corresponds to a small value of β, and vice versa.

The above observation was made for an elastic system, but the findings and trend of variation of δ with α and β may be expanded qualitatively for buildings experiencing inelastic response. The 2DOF system could be viewed as a two-story building, and the different values of α and β might be interpreted as representing effects of different degrees of setback. In other words, α=1 and β=1 corresponds to a structure with uniform configuration, and as values of α and β decrease, a setback structure is represented with the size of the tower (represented by the second mass-spring system) becoming smaller. Parameter δ could be interpreted as the ratio of the inter-story drifts. A large value of δ implies a large inter-story drift in the second floor relative to that in the first level. More damage could, then, be expected in the second floor as δ increases if it is assumed that the levels of damage and inelastic response are directly reflected by the magnitude of the inter-story drift. Therefore, the trend of variation of δ with α and β should remain similar even for a system with nonlinear behavior.

As discussed previously, the value of δ can be interpreted to be an indicator of the level of damage in two-degree-of-freedom (2DOF) systems. If a multi-story setback structure could be idealized as an equivalent 2DOF system (one degree of freedom representing the tower portion of the multi-story structure, and the other representing the base), the same concepts developed previously for a 2DOF system can also be

implemented. The proposed procedure is to visualize the tower as a single-degree-of-freedom (SDOF) fixed at its base, and to visualize the base without the tower as a separate SDOF system. Knowing the stiffnesses and masses of each system, the "design chart" could be utilized to check whether presence of a setback could result in a concentration of damage in the tower. Details of the method are explained in the following paragraphs.

Generalized coordinates [15] might be applied to convert base and tower into a single-degree-of-freedom system, and to obtain values of equivalent mass and stiffness. That is, K1, K2, M1, and M2 are assumed to be the generalized stiffness and mass properties of an equivalent single-degree-of-freedom system, respectively, as obtained from the following relations

$$K1^* = \phi 1^T [K1] \phi 1$$

$$K2^* = \phi 2^T [K2] \phi 2$$

$$M1^* = \phi 1^T [M1] \phi 1$$

$$M2^* = \phi 2^T [M2] \phi 2$$

in which, $\phi 1$, [K1], and [M1] are the assumed first-mode shape, stiffness matrix, and mass matrix, respectively for base without tower, and $\phi 2$, [K2], and [M2] are the corresponding values for tower fixed at its base. Assuming a lumped mass matrix, a straight line first-mode shape ($\phi_i = \frac{h_i}{H}$, where h_i is the ith floor height above ground and H is the total height of either tower or base), and that base and tower act as shear systems, the generalized mass and stiffness could be obtained from

$$K^* = [\sum_{i=1}^{i=N-1} (K_i + K_{i+1})(\frac{h_i}{H})^2 - 2K_{i+1}\frac{h_i h_{i+1}}{H^2}] + K_N(\frac{h_N}{H})^2 \qquad (8.4a)$$

$$M^* = \sum_{i=1}^{i=N} M_i(\frac{h_i}{H})^2 \qquad (8.4b)$$

in which, K_i, M_i, h_i, H, and N are story stiffness, floor mass, ith-floor height above

ground, total height, and number of floors for either tower or base.

In a typical building, the floor heights are equal. Using an identical floor height, Eqs 8.4a and 8.4b are simplified to

$$K^*=\frac{1}{N^2}\sum_{i=1}^{i=N} K_i \tag{8.5a}$$

$$M^*=\frac{1}{N^2}\sum_{i=1}^{i=N} i^2 M_i \tag{8.5b}$$

Story stiffness may be computed from the following relation, which is based on the portal method and the assumption that base and tower act as a stick model[77].

$$K_i=\frac{24}{h^2}\frac{1}{[\frac{2}{\sum K_c}+\frac{1}{\sum K_{ga}}+\frac{1}{\sum K_{gb}}]} \tag{8.6}$$

in which, K_i=ith story height, K_c=Column stiffness=$\frac{EI_c}{h}$, K_{ga}=Beam stiffness of (i+1)th floor=$\frac{EI_g}{L}$, K_{gb}=Beam stiffness of (i-1)th floor=$\frac{EI_g}{L}$, I=Moment of inertia, h=Story height, L=Bay width, and E=Modulus of elasticity. Alternatively, K_i may be approximated as $\frac{12EI_c}{h^3}$, where h= story height, I_c= column moment of inertia, and E= modulus of elasticity. If all column cross sections are assumed to be identical, and the floor heights are equal, then α ($=\frac{K2^*}{K1^*}$) is then obtained as

$$\alpha=\frac{(\text{No. of column lines/No. of stories})_{\text{tower}}}{(\text{No. of column lines/No. of stories})_{\text{base}}} \tag{8.7}$$

It is emphasized that in the above discussion the rotational and vertical degrees of freedom at a joint were ignored and floor slabs were assumed to be rigid in the plane. Thus, a single degree of freedom per floor would be sufficient to model each floor. It is believed that this simplifying assumption does not limit the findings discussed here because lateral displacements tend to dominate the response of most structures subjected

to earthquakes.

To test the ideas presented in the preceding paragraphs, the generalized mass (Eq. 8.5(b)) and the generalized stiffness (Eq. 8.5(a)) were computed for the six generic frames, the test structure (denoted as UCB on Fig. 8.6), and the setback frame tested at the University of Illinois [77] (denoted by U of I on Fig. 8.6). The corresponding mass ratio ($\beta = \frac{M2^*}{M1^*}$) and stiffness ratio ($\alpha = \frac{K2^*}{K1^*}$) (from Eq. 8.7 or the computed generalized stiffnesses) were then computed for all the structures. The computed values are indicated in Fig. 8.6. Dynamic response of all the structures could plausibly be justified from this chart. Structures having larger values of δ in Fig. 8.6 generally exhibited relatively large computed ductility demands in the stories above the setback (see Fig. 8.5 for the response of the generic structures). Computed demands were particularly high for structures "2C" and "3C", the structures having the largest values of δ. From this chart, the difference between response of the generic frames having identical tower plan dimension, e.g., "2C" and "5C", could also be explained.

The test structure (which is the subject of this report) has relatively low value of δ in Fig. 8.6, and it did not exhibit significant concentration of damage in the tower, as discussed in Chapters 5 and 6. No analytical information on the distribution of damage is available from the experiments conducted at the University of Illinois [77]. However, it was apparent that the tower members experienced relatively significant degree of damage; the crack widths in the tower were as large as those at the footing, and the story hysteresis loops (inter-story drift versus story shear) indicated a concentration of inelastic response in the tower floors immediately above the setback. To verify the apparent damage in the tower, an inelastic static analysis (under the UBC distribution of lateral loads) was conducted, reaching lateral drift at the roof equal to 2.7 percent of the structure height (the maximum measured roof displacement during the experiments was 2.6 percent of the structure height). The distribution of the computed rotational ductility demand, normalized to a peak value of one, (Fig. 8.7) indicates a sharp increase

in the ductility demands in the tower. This observation matches the response anticipated by the "design chart" (Fig. 8.6), as the model tested at the University of Illinois has relatively large value of δ.

Based on the above observation that the generic structures and the experimental structures did not exhibit indication of damage concentration if $\delta \leq 2$, whereas damage was indicated for $\delta > 2$, the following is concluded. If $\delta < 2$, concentrations of significant damage are considered unlikely. If $\delta \geq 2$, a concentration of damage in the tower is deemed more likely, possibly warranting redesign.

This finding was obtained for a special class of setback structures, i.e., a single symmetrical or asymmetrical setback. Similar studies are necessary for other setback configurations.

8.2.3 Proposed Lateral Force Distribution

Computed responses of the "modal" and "UBC" frames were found to be nearly identical. Thus, the mode superposition method apparently did not provide any advantage over the static lateral-force analysis technique to avoid concentration of damage in the tower. An alternate method is desirable by which to design setback structures. A method based on the "design chart" (Fig. 8.6) and utilizing static analysis is proposed in this section. The derivation of the proposed method follows an approach similar to that used to derive formulas in current building codes for distributing base shear over height for structures having regular configuration. However, the assumed first-mode shape in the present study is no longer a straight line over height. Rather, a kink in the mode shape at the setback level is assumed.

Consider a two-story setback frame acting as a shear building (Fig. 8.8), and assume that the first-mode shape corresponds to the deflected shape as shown. Recalling from the previous section that $\delta = \frac{x_2 - x_1}{x_1}$ (x_1 and x_2 are lateral displacements), the angle

which defines the kink in the mode shape at the setback level ($\theta 2$) can be computed from

$$\tan(\theta 2)=\frac{x_2-x_1}{h}=\frac{\delta x_1}{h}=\delta\tan(\theta 1) \tag{8.8}$$

in which, angle $\theta 1$ defines the slope of the mode shape in the base. This relation is used to define a first-mode shape for a multi-story building. (It is assumed that the relation between $\theta 1$ and $\theta 2$ holds for the multi-story frame regardless of the relative heights of base and tower. This method has an implicit bias that is intended to result in relatively large lateral forces at upper stories of a setback structure with a tall tower.) Using Eq. 8.8, the first-mode shape is then obtained from

$$\phi^T=[\alpha 1h_{1b},\alpha 1h_{2b},\ldots,\alpha 1H_b,x1+\alpha 2h_{1t},x1+\alpha 2h_{2t},\ldots,x1+\alpha 2H_t] \tag{8.9}$$

in which, $\alpha 1=\tan(\theta 1)$, $\alpha 2=\tan(\theta 2)$, h_{ib} is the elevation of the ith floor in the base from the ground level, h_{it} is the elevation of the ith floor in the tower from the setback level, H_t and H_b are the total height of the tower and base, respectively, x1 is the value of the mode shape at the setback level, $\tan(\theta 1)=\frac{x1}{H_b}$, and $\tan(\theta 2)=\delta\tan(\theta 1)$. In a typical building, the floor heights are equal. For this case, Eq. 8.9 (normalized with respect to x1) is simplified to

$$\phi^T=[1/N_b,2/N_b,\ldots,1,1+\delta/N_b,1+2\delta/N_b,\ldots,1+N_t\delta/N_b] \tag{8.10}$$

in which, N_b and N_t are the number of floors in the base and tower, respectively, and the value of δ is computed from the "design chart" (Fig. 8.6). Knowing the mode shape, the base shear is then distributed over the height by

$$F_i=\frac{M_i\phi_i}{\sum_{i=1}^{i=N} M_i\phi_i}(V-F_t)$$

in which, F_i is the lateral force at the ith level, M_i is the ith-floor mass, ϕ_i is the ith value in Eq. 8.10, V is base shear, N is the number of stories, and F_t is a portion of the base shear concentrated at the roof in addition to F_i, as defined by the UBC

(F_t=0.07TV$\leq$0.25V). The resulting lateral forces are used to design a setback structure if a significant concentration of damage is anticipated in the tower (if $\delta \geq 2$, as discussed previously in Section 8.2.2).

The above method was applied to redesign frame "2C" (which experienced the worst concentration of damage in the tower (Fig. 8.5)), and frame "4D". For frame "4D", it is not necessary to use the proposed method because $\delta \leq 2$, and the concentration of inelastic response in the tower is not deemed significant. Nevertheless, this frame was redesigned to further examine the proposed technique. Dynamic responses were evaluated under base motions identical to those used in the initial analyses (Section 8.2.1(b)). Rotational ductility demands were computed as discussed previously (Section 8.2.1(c)). The results (Fig. 8.9) indicate a significant reduction in ductility demand above the setback. The ductility demand is distributed almost uniformly for frame "4D", and there is less concentration of damage for frame "2C". The large ductility demand in the base is a peculiarity of the Pacoima record. A similar concentration of inelastic response was observed from the computed inelastic dynamic response of a uniform frame (from which the setback frames were derived) when subjected to the Pacoima record having identical peak acceleration as that utilized for the analysis of the setback frames (Fig. 8.10).

8.3 Summary

The mode superposition technique was found not to necessarily result in a better design of setback structures. Distribution of rotational ductility demand was found to be nearly identical for structures designed by the mode superposition method and the static lateral force analysis technique, and both methods could fail to prevent concentration of damage in members near the setback. The current building code approach of differentiating setback buildings from those having regular configuration is not rational and could be misleading. As implicit in the UBC, an irregular response is

anticipated if the plan dimension of the tower is less than 75 percent of the base. For all the generic structures and test models (the structure, which is the main subject of this report, and the model tested at the University of Illinois), the tower plan dimension is substantially smaller than 75 percent of the corresponding value for the base. Nevertheless, the distribution of rotational ductility demand did not indicate any significant influence of setback on dynamic response except for frames "2C", "3C", "4C", and the model tested at the University of Illinois, which exhibited a concentration of damage in the tower.

The observed behavior and damage distribution were plausibly explained by evaluating the properties of an equivalent two-degree-of-freedom (2DOF) system representing the complete frames, and by using the information obtained from a chart constructed from the elastic response of a 2DOF system. To use this chart, the complete structure was first converted into a 2DOF system, representing tower and base, through the use of the generalized coordinate system. For the "reduced" structure, the tower-to-base stiffness ratio and tower-to-mass ratio were computed. If the mass and stiffness ratios result in a value of δ (from the "design chart") greater than 2, concentration of damage and increased ductility demand in the tower members is likely.

For structures with potential for abrupt increase of ductility demand in the tower, a special method was proposed to distribute inelastic response more uniformly over the height. A bilinear first-mode shape, rather than a linear one, was chosen for distributing the base shear over the height. A kink in the mode shape at the setback level was considered, the degree of the kink being obtained from the "design chart". When designed according to the proposed method, the degree of damage concentration in the tower was substantially reduced.

The abovementioned techniques were developed for setback structures with a single symmetrical or asymmetrical setback. More test cases are required to substantiate the improved behavior when the proposed lateral force distribution is used.

9. SUMMARY AND CONCLUSIONS

A combined experimental and analytical research program was undertaken to study influence of setbacks on dynamic behavior of structures, and to examine the seismic response of reinforced concrete ductile moment-resisting frames designed according to current seismic provisions. In the course of this study, a six-story ductile moment-resisting frame was designed, constructed, and tested on an earthquake simulator. Measured responses were compared with expectations of various analytical methods. The experimental findings were supplemented with the results obtained from inelastic dynamic response of six generic frames with various setback configurations. Conclusions were drawn regarding the overall characteristics, the design procedure, the applicability of analytical methods, and the dynamic response of setback structures. The study and conclusions are summarized in this chapter.

9.1 Summary of the Experimental Study

(a) Prototype Structure

The test structure modeled an imaginary prototype structure which is a six-story, two-bay by two-bay reinforced ductile moment-resisting frame having 50 percent setback at the mid-height. The prototype structure was designed for combined gravity and seismic effects, determined according to the requirements of the 1982 Uniform Building Code (UBC). Proportions and details were provided to satisfy the seismic provisions of Appendix A of the ACI Building Code (ACI 318-83), and the ACI-ASCE Committee 352 recommendations for design of beam-column connections. The design steps are documented in Chapter 2.

(b) Test Structure and Testing Procedure

A test structure was selected to model the prototype structure at one-quarter scale. The test structure was constructed in different stages. The three short-direction frames were cast separately. The remainder of the model was cast in two lifts after these frames were fixed atop a steel foundation frame. All beam and column longitudinal reinforcement was deformed bars with properties typical of Grade 60 reinforcement (minimum yield stress of 60 ksi). Concrete had mean compressive strength of 4200 psi. Nonstructural load weights were affixed to floor slabs to simulate effects of the service dead load expected for the prototype structure.

The test structure was mounted atop a stiff foundation frame that was prestressed to the test platform of the earthquake simulator of the Earthquake Engineering Research Center (Chapter 3). Tests included static pull-back tests, free-vibration tests, and earthquake simulations of varying intensity. Earthquake simulations were conducted in two stages. In the first stages, a series of horizontal base motions was applied parallel to the long-direction frames to induce uniaxial response, In the next stage, unidirectional horizontal motions were input at an angle of 45 degrees relative to the principal axes of the frames to impart biaxial lateral-torsional response. The base motions modeled acceleration and displacement histories of the 1940 El Centro NS, 1978 Miyagi-Ken-Oki S00E, or 1985 SCT Mexico City S60E records.

Several earthquake simulation tests were conducted. The first tests had intensities sufficiently low that no damage was noted. Intensities of later tests were sufficient to induce significant inelastic response. Continuous records of base motions, displacements, accelerations, and reinforcement strains were obtained for each test (Chapter 3 and Appendix B). Visible damage was recorded at the end of each test.

(c) Measured Responses

The experimental results were reduced to obtain the relative floor lateral displacements, the translational and rotational accelerations at each floor, the inter-story drifts, story and base shear force, overturning moment at the base of the first-floor columns, and torque (computed with respect to the central column) at the base of the first-floor columns. The response waveforms, maximum values, linear elastic response spectra, Housner spectrum intensities, Fourier amplitude spectra, and observed damage patterns for each test are documented in Chapter 4.

In Chapter 5, the characteristics of the base motions are studied so that responses of the test structure to different intensity motions could be evaluated. The earthquake simulation tests are classified as "low", "moderate", or "strong" motions. The frequency content of the measured responses, variation of the peak response values with spectrum intensity and peak base acceleration, and variation over height of the lateral displacement, inter-story drift, lateral forces, and reinforcement strain are also discussed in Chapter 5. The effective flange width and joint shear force were approximated from the measured reinforcement strain, known cross-sectional and material properties, and equations of statics applied to joints.

The vibration periods were obtained from (1) the peaks of the Fourier amplitude spectrum of the roof acceleration measured during the free-vibration tests, and (2) the roof displacement histories measured during the earthquake simulations (Section 5.7(a)). The equivalent viscous damping and mode shapes were also derived from the experimental results (Sections 5.7(b) and 5.7(c)). Variation of the dynamic properties is summarized in Table 5.3.

An overall lateral stiffness of the test structure was computed using the results of the static pull-back tests, and was inferred from the base shear-roof displacement hysteresis loops. The variation of overall lateral stiffness is discussed in Section 5.5.

9.2 Summary of Response Correlation

In Chapter 6, response of the test structure is studied using available analytical methods. The long-direction lateral strength and stiffness were studied using step-by-step inelastic static analysis, limit analysis, and inelastic dynamic response history analysis. Lateral stiffness and dynamic characteristics (mode shapes and vibration periods) of the test structure prior to the first earthquake simulation were evaluated using a three-dimensional elastic model. Different mathematical models and assumptions were utilized to calculate the response. In Chapter 6, measured and calculated stiffness and strength characteristics are compared to assess the reliability of the analytical models in correlating with the measured response. Results of a sensitivity study are also discussed to establish the dependency of the calculated response on various parameters such as effective flange width and load-deformation characteristics of individual members.

9.3 Summary of the Parametric Study of the Effects of Setbacks

Six generic setback frames were designed by the UBC static lateral load force analysis procedure and by a modal analysis procedure. In Chapter 8, the inelastic dynamic responses of the structures are evaluated to observe any unusual distribution of damage over the height due to the setback, and to detect any undesirable behavior associated with the use of static analysis for design of setback structures, as implied by current building codes.

To further investigate the response of setback structures, the elastic response of a two-degree-of-freedom system (representing tower and base in a setback frame) was studied. Based on the findings, a rational approach was found to anticipate the potential concentration of damage in the tower. A simple method was constructed for static design of a special class of setback structures, i.e., those with a single symmetrical or asymmetrical setback.

9.4 Conclusions

(a) Performance of the Test Structure

The test structure reached a base shear in excess of seven times the design base shear. Despite the large difference between the measured and design strengths, structural damage was limited. Overstrengths, such as observed for the test structure, can be either an advantage or a disadvantage. As an example of an advantage, the increased strength is likely (but not certain) to result in reduced ductility demands during strong earthquakes. However, the overstrength also indicates that current design and analysis methods are capable of producing a structure that is significantly different from that which was intended. It is conceivable that in some cases, the structure will differ in such a way that undesirable and unexpected failure modes might result by using the current design methods. For example, for the test structure, design joint shear stresses range between 11 $\sqrt{f_c'}$ and 13.1 $\sqrt{f_c'}$ for interior joints, whereas the maximum joint shear stress in the first-floor interior joint reached approximately 21 $\sqrt{f_c'}$. Had the design values been larger, actual joint shears would conceivably have been larger also, perhaps resulting in joint failure.

Several factors were identified to be responsible for the overstrength. Among the factors identified, the most important ones were found to be contribution of the floor slab to beam flexural strength, column and beam overstrength resulting from detailing requirements, and actual material properties. For example, the mean value of the estimated effective flange width is 28 in. for a typical interior joint in the long direction at a strain level corresponding to approximately yield strain in the beam longitudinal reinforcement. (This effective flange width corresponds to an overhanging width equal to 1.5 times the long-direction beam depth on each side of the beam.) As a result, the beam negative strengths were approximately twice those computed ignoring the slab contribution. Design procedures that account for these factors are desirable so as to

reliably assess the expected behavior of structures.

During the design test (EC49.3L), for which intensity is considered to equal or exceed that anticipated to occur in UBC Zone 4, the maximum joint shear stress reached approximately $21\sqrt{f_c'}$, which is nearly equal to the nominal design limit of $20\sqrt{f_c'}$ (recommended by the 1985 ACI-ASCE Committee 352 report). For the design test, the maximum recorded shear stress at a corner connection reached $7\sqrt{f_c'}$, compared with the corresponding recommended nominal value of $15\sqrt{f_c'}$. Despite the large shear stresses, there were no visible shear cracks or other visible signs of joint deterioration. Thus, it is concluded that the detailing provisions for joint design were apparently successful to prevent shear failure in the joints.

Inter-story drift was as large as 1.6 percent of the story height during the design test. At this level of inter-story drift, severe damage to nonstructural elements would be expected in a real building. The maximum inter-story drift was in excess of 3 percent of the story height for the higher-intensity biaxial earthquake simulations. The measured inter-story drifts exceed by far the values computed in the design process according to the UBC requirements. Thus, the code analysis does not adequately reflect actual building drift. An improved estimate of drift experienced by the test structure was achieved by a simple but rational procedure. To achieve this estimate, it was necessary to account for reduced stiffness, and to realize that code forces are smaller than those for an elastic structure.

Locations of damage anticipated by the design methods were generally in agreement with those observed for the test structure. Apparent damage was mainly in the beams. Thus, the intended "strong column-weak girder" design concept was successfully implemented.

(b) Response Correlation

The measured initial lateral stiffness, vibration periods, and mode shapes were closely matched by a simple three-dimensional elastic mathematical model. The effects of shrinkage cracks on stiffness were reasonably taken into account by modeling beam stiffnesses using the beam web cross section only, which corresponds approximately to using one-half the gross stiffness of the "T" beam cross sections.

By considering an effective flange width equal to the experimentally estimated value, and by computing member strengths according to standard techniques, a close correlation between the measured and computed base shear strength was obtained using limit analysis. It was found that the computed collapse mechanism shifts from a "beam sway" mechanism to a "column sway" mechanism when the slab contribution is considered. However, no strong experimental evidence was found to support the computed mechanisms.

By assuming an appropriate initial stiffness and damping, it was possible to obtain good estimates of the magnitudes of the measured uniaxial responses using inelastic dynamic analysis. Nevertheless, the frequency content and magnitude of the computed responses were found to be sensitive to the assumed initial member stiffnesses. For earthquake simulation tests with significant inelastic response, the degree of correlation was deemed good for the first few cycles, but poorer towards the end of the test (partially because of the inability of the mathematical hysteresis model to properly represent stiffness degradation). The computed yield pattern was found to be reasonably in accord with the measured damage distribution. Using planar analytical models that had previously correlated well with the uniaxial tests, acceptable correlation of the long-direction responses for the biaxial test MO63.4B was not obtained.

The uniaxial load-displacement envelopes, and distribution of inelastic response were computed similarly by inelastic static and inelastic dynamic analyses. Static analysis alone is incapable to assess the performance of a structure, because it cannot

uniquely evaluate the magnitudes of drifts and base shear. Nevertheless, static analysis is a valuable tool for gaining insight into how a structure deforms and develops damage, provided that alternate techniques are utilized to estimate the absolute magnitude of response. Several techniques are available.

(c) Effects of the Setback on the Response of the Test Structure

Variation of the lateral displacement, inter-story drift, and lateral forces in the long direction did not indicate any unusual distribution associated with the presence of the setback. The displacement profiles were similar to those expected for a structure having uniform configuration. No unexpected distribution of inertia forces was observed. The predominant distribution of lateral forces was similar to the distribution of static lateral forces as specified by the Uniform Building Code. Overall, the response appeared to be predominated by the fundamental mode. During the biaxial tests, the torsional response induced by presence of the setback was minimal and could have been predicted by static relations. Thus, the behavior of the test structure did not indicate any unusual dynamic behavior associated with the setback.

Although concentrations of inelastic behavior were observed in some of the tower members, similar concentrations were indicated by inelastic static analysis. Thus, it is concluded that the observed concentration of inelastic action is a consequence of the structural configuration, but is not especially manifest in the dynamic response.

(d) Design of Setback Structures

For a class of setback frames studied, the mode superposition method was found not to result in a better design than conventional static methods. The distribution of rotational ductility demand was found to be nearly identical for structures designed by mode superposition and the static lateral force analysis technique. Both methods were found to be inadequate to prevent concentration of damage in members near the setback

for certain configurations.

Some current building codes require that dynamic analysis be used to establish design forces if the plan dimension of the tower is less than 75 percent of the base dimension of a setback building. Comparison between computed responses of frames having various setbacks and designed by both static and dynamic methods indicates that this simple rule by which to differentiate regular and irregular buildings is inappropriate.

The observed behavior and damage distribution for the setback frames studied in this report were plausibly explained by evaluating the properties of an equivalent two-degree-of-freedom (2DOF) system representing the complete frames, and by using the information obtained from a chart constructed from the elastic response of a 2DOF system. If the mass and stiffness ratios of the equivalent 2DOF system are in a certain range, concentration of damage in the tower is indicated. A design chart is presented to simplify the evaluation.

For structures identified as having the potential for abrupt increase of ductility demand in the tower, a special method is proposed by which to distribute inelastic response more uniformly over height. According to the model, a bilinear first-mode shape, rather than a linear one, is used to distribute the base shear over height. The kink in the mode shape occurs at the setback level. The degree of the kink is obtained from a "design chart". When designed according to the proposed method, the degree of damage concentration in the tower was substantially reduced.

REFERENCES

[1] Abrams, D. P. and Sozen, M. A., "Experimental Study of Frame-Wall Interaction in Reinforced Concrete Structures Subjected to Strong Earthquake Motions," Civil Engineering Studies, Structural Research Series No. 460, University of Illinois, Urbana, May 1979.

[2] ACI-ASCE Committee 352, "Recommendation for Design of Beam-Column Joints in Monolithic Reinforced Concrete Structures," *ACI Journal* , Vol. 82, No. 3, May-June 1985, pp. 266-284.

[3] Algan, B. B., "Drift and Damage Considerations in Earthquake-Resistant Design of Reinforced Concrete Buildings," Ph.D. dissertation submitted to the Graduate College, University of Illinois, Urbana, March 1983.

[4] Aranda H., G. R., "Ductility Demands for R/C Frames Irregular in Elevation," *Proceedings* , Eighth World Conference on Earthquake Engineering, Vol. IV, San Francisco, California, 1984, pp. 559-566.

[5] Aristizabal-Ochoa, J. D. and Sozen, M. A., "Behavior of Ten-Story Reinforced Concrete Walls Subjected to Earthquake Motions," Civil Engineering Studies, Structural Research Series No. 431, University of Illinois, Urbana, October 1976.

[6] Arnold, C., "Building Configuration: Characteristics for Seismic Design," *Proceedings* , Seventh World Conference on Earthquake Engineering, Vol. 4, Istanbul, Turkey, 1980, pp. 589-592.

[7] Arnold, C. and Elsesser, E., "Building Configuration: Problems and Solutions," *Proceedings* , Seventh World Conference on Earthquake Engineering, Vol. 4, Istanbul, Turkey, 1980, pp. 153-160.

[8] Becker, R. A., and Chambers, J. M., *S- An Interactive Environment for Data Analysis and Graphics,* The Wadsworth Statistics/Probability Series, 1984.

[9] Bertero, V. V., Aktan, A. E., Charney, F. A., and Sauce, R., "Earthquake Simulation Tests and Associated Studies of a 1/5th-Scale Model of a 7-Story R/C Frame-Wall Test Structure," *Report No. UCB/EERC-84/05* , Earthquake Engineering Research Center, University of California, Berkeley, June 1984.

[10] Blume, J. A. and Jhaveri, D. P., "Time-History Response of Buildings with Unusual Configurations," *Proceedings* , Fourth World Conference on Earthquake Engineering, Vol. III, Session A3, Santiago, Chile, January 1969, pp. 155-170.

[11] "Building Code Requirements for Reinforced Concrete (ACI 318-83)," ACI Committee 318, American Concrete Institute, Detroit, 1983.

[12] Charney, F. A. and Bertero, V. V., "An Evaluation of the Design and Analytical Seismic Response of a Seven-Story Reinforced Concrete Frame-Wall Structure," *Report No. UCB/EERC-82/08* , Earthquake Engineering Research Center, University of California, Berkeley, August 1982.

[13] Christensen, K. A. and Williamson, R. B., "Solving the Galvanic Cell in Ferro-Cement," *Report No. UC SESM 71-14* , Structural Engineering Laboratory, University of California, Berkeley, July 1971.

[14] Clough, R. W. and Gidwani, J., "Reinforced Concrete Frame 2: Seismic Testing and Analytical Correlation," *Report No. UCB/EERC-76/15* , Earthquake Engineering Research Center, University of California, Berkeley, June 1976.

[15] Clough, R. W. and Penzien, J., *Dynamics of Structures* , McGraw Hill, New York, N. Y., 1975.

[16] "Commentary on Building Code Requirements for Reinforced Concrete (ACI 318-83)," ACI Committee 318, American Concrete Institute, Detroit, 1983.

[17] Dalley, J. W. and Riley, W. F., *Experimental Stress Analysis* , McGraw Hill, New York, N. Y., 1965.

[18] Durrani, A. J. and Wight, J. K., " Experimental and Analytical Study of Internal Beam to Column Connections Subjected to Reversed Cyclic Loading, " *Report No. UMEE 82R3* , Department of Civil Engineering, University of Michigan, Ann Arbor, 1982.

[19] Ehsani, M. R. and Wight, J. K., "Behavior of Exterior Reinforced Concrete Beam to Column Connections Subjected to Earthquake Type Loading," *Report No. UMEE 82R5* , Department of Civil Engineering, University of Michigan, Ann Arbor, July 1982.

[20] Freeman, S. A., "Drift Limits: Are They Realistic," *Structural Moments* , No. 4, Structural Enginners Association of California, May 1980.

[21] "General Report on the Takachi-Oki Earthquake of 1968," Suzuki, Z., Chief Editor, Keigsku Publishing Co., Ltd., Tokyo, Japan, 1971.

[22] Gulkan, P. and Sozen, M. A., "Inelastic Responses of Reinforced Concrete Structures to Earthquake Motions," *ACI Journal* , Vol. 71, No. 12, December 1974, pp. 604-610.

[23] Healey, T. J. and Sozen, M. A., "Experimental Study of the Dynamic Response of a Ten-Story Reinforced Concrete Frame with a Tall First Story," Civil Engineering Studies, Structural Research Series No. 450, University of Illinois, Urbana, August 1978.

[24] Housner, G. W., "Behavior of Structures During Earthquakes," *Journal of the Engineering Mechanics Division* , ASCE, Vol. 85, No. EM4, October 1959, pp. 108-129.

[25] Humar, J. L. and Wright, E. W., "Earthquake Response of Steel-Framed Multistory Buildings with Setbacks," *Earthquake Engineering and Structural Dynamics* , Vol. 5, 1977, pp. 15-39.

[26] Jhaveri, D. P., "Earthquake Forces in Tall Buildings with Setbacks," Ph.D. dissertation presented to the University of Michigan, 1967.

[27] Kaba, S. A. and Mahin, S. A., "Interactive Computer Analysis Methods for Predicting the Inelastic Cyclic Behavior of Structural Sections," *Report No. UCB/EERC-83/18* , Earthquake Engineering Research Center, University of California, Berkeley, July 1983.

[28] Kabaila, A., Saenz, L. P., Tulin, L. G., Gerstle, K. H., and Authors, "Equation for the Stress-Strain Curve of Concrete," *ACI Journal* , Disc. 61-22, September 1964, pp. 1227-1239.

[29] Kannan, A. E. and Powell, G. H., "DRAIN-2D: A General Purpose Computer Program for Dynamic Analysis of Inelastic Plane Structures," *Report No. UCB/EERC-73/6* , Earthquake Engineering Research Center, University of California, Berkeley, April 1973.

[30] Korkut, K., "Research on the Seismic Behavior of Structures with Mass Concentrations or with Variable Width," *Bauingenieur* , Vol. 59, Springer-Verlag 1984, pp. 235-241.

[31] Kreger, M. E. and Abrams, D. P., "Measured Hysteresis Relationships for Small-Scale Beam-Column Joints," Civil Engineering Studies, Structural Research Series No. 453, University of Illinois, Urbana, August 1978.

[32] Lybas, J. M. and Sozen, M. A., "Effect of Beam Strength on Dynamic Behavior of Reinforced Concrete Coupled Walls," Civil Engineering Studies, Structural Research Series No. 444, University of Illinois, Urbana, July 1972.

[33] Meinheit, D. F. and Jirsa, J. O., "Shear Strength of R/C Beam-Column Connections," *Journal of the Structural Division* , ASCE, Vol. 107, No. ST11, November 1981, pp. 2227-2244.

[34] Merchant, H. C. and Hudson, D. E., "Mode Superposition in Multi-Degree of Freedom Systems Using Earthquake Response Spectrum Data," *Bulletin of the Seismological Society of America* , Vol. 52, No. 2, April 1962, pp. 405-416.

[35] Moehle, J. P., " Reinforced Concrete Structures," A Short Course on Recent Advances in Earthquake-Resistant Design, University of California, Berkeley, July 20-24 1987.

[36] Moehle, J. P., "MOMCUR Program, " Version 1.06, University of California, Berkeley, July 1982.

[37] Moehle, J. P. and Cavanagh, T., " Confinement Effectiveness of Crossties in R/C", *Journal of the Structural Division* , ASCE, Vol. 111, No. ST10, October, 1985 pp. 2105-2120.

[38] Moehle, J. P. and Diebold, J. W., "Experimental Study of the Seismic Response of a Two-Story Flat-Plate Structure," *Report No. UCB/EERC-84/08* , Earthquake Engineering Research Center, University of California, Berkeley, August 1984.

[39] Moehle, J. P. and Sozen, M. A., "Earthquake-Simulation Tests of a Ten-Story Reinforced Concrete Frame with a Discontinued First-Level Beam," Civil Engineering Studies, Structural Research Series No. 451, University of Illinois, Urbana, August 1978.

[40] Moehle, J. P. and Sozen, M. A., "Experiments to Study Earthquake Response of R/C Structures with Stiffness Interruptions," Civil Engineering Studies, Structural Research Series No. 483, University of Illinois, Urbana, August 1980.

[41] Mondkar, D. P. and Powell, G. H., "ANSR-1, General Purpose Computer Program for Analysis of Nonlinear Structure Response," *Report No. UCB/EERC-75/17* , Earthquake Engineering Research Center, University of California, Berkeley, December 1975.

[42] Newmark, N. M. and Roenblueth, E., *Fundamental of Earthquake Engineering* , Prentice-Hall, Inc., Englewood Cliffs, NJ, 1971.

[43] Nigam, N. C. and Jennings, P. C., "Digital Calculation of Response Spectra from Strong-Motion Earthquake Record," Earthquake Enginnering Research Laboratory, California Institute of Technology, Pasadena, June 1968.

[44] Oliva, M. G., "Shaking Table Testing of a Reinforced Concrete Frame With Biaxial Response," *Report No. UCB/EERC-80/28* , Earthquake Engineering Research Center, University of California, Berkeley, October 1980.

[45] Pantazopoulou, S. J., "Modeling Aspects of the Three Dimensional Behavior of Building Structures Subjected to Earthquakes," Ph.D. dissertation submitted to the University of California, Berkeley, 1987.

[46] Park, R. and Gamble, W. L., *Reinforced Concrete Slabs* , John Wiley and Sons, Inc., New York, N. Y., 1980.

[47] Park, R. and Pauley, T., *Reinforced Concrete Structures* , John Wiley and Sons, Inc., New York, N. Y., 1975.

[48] Park, R., Priestly, M. J. N., and Gill, W. D., "Ductility of Square-Confined Concrete Columns," *Journal of the Structural Division* , ASCE, Vol. 108, No. ST4, April 1982, pp. 929-950.

[49] Pauley, T., "Capacity Design of Reinforced Concrete Ductile Frames," *Proceedings of a Workshop on Earthquake-Resistant Reinforced concrete Building Construction* , University of California, Berkeley, July 11-15, 1977, pp. 1043-1075.

[50] Pauley, T., "A Critique of the Special Provisions for Seismic Design of the Building Code Requirements for Reinforced Concrete (ACI 318-83)," *ACI Journal* , Vol. 83, No. 2, March-April 1986, pp. 274-283.

[51] Pekau, O. A. and Green, R., "Inelastic Structures with Setbacks," *Proceedings* , Fifth World Conference on Earthquake Engineering, Vol. 2, Rome, Italy, 1974, pp.

1744-1747.

[52] Penzien, J., "Earthquake Response of Irregularly Shaped Buildings," *Proceedings* , Fourth World Conference on Earthquake Engineering, Vol. II, Session A3, Santiago, Chile, January 1969, pp. 75-89.

[53] Penzien, J. and Chopra, A. K., "Earthquake Response of Appendage on a Multi-Story Building," *Proceedings* , Third World Conference on Earthquake Engineering, Vol. II, New Zealand, 1965, pp. 476-486.

[54] Popov, E. P., "Mechanical Characteristics and Bond of Reinforcing Steel Under Seismic Conditions," *Proceedings of a Workshop on Earthquake-Resistant Reinforced Concrete Building Construction* , University of California, Berkeley, July 11-15, 1977, pp. 658-682.

[55] Popov, E. P., "Seismic Behavior of Structural Subassemblages," *Journal of the Structural Division* , ASCE, Vol. 106, No. ST7, July 1980, pp. 1451-1474.

[56] Qi, X. "The Behavior of A R/C Slab-Beam-Column Subassemblage Under Lateral Load Reversals," CE 299 Report, Division of Structural Engineering and Structural Mechanics, Department of Civil Engineering, University of California, Berkeley, November 1986.

[57] Rea, D. and Penzien, J., "Dynamic Response of a 20 ft x 20 ft Shaking Table," *Proceedings* , Fifth World Conference on Earthquake Engineering, Vol. 2, Rome, Italy, 1974, pp. 1447-1456.

[58] "Recommended Lateral Force Requirements and Commentary," Seismology Committee, Structural Engineers Association of California, San Francisco, 1980.

[59] Saidi, M. and Sozen, M. A., "Simple and Complex Models for Nonlinear Seismic Response of Reinforced Concrete Structures," Civil Engineering Studies, Structural Research Series No. 465, University of Illinois, Urbana, August 1978.

[60] Schultz, A. E., "An Experimental and Analytical Study of the Earthquake Response of R/C Frames with Yielding Columns," Ph.D. dissertation submitted to the Graduate College of the University of Illinois, Urbana, August 1985.

[61] Sheikh, S. A. and Uzumeri, S. M., "Strength and Ductility of Tied Concrete Columns," *Journal of the Structural Division* , ASCE, Vol. 106, No. ST5, May 1980, pp. 1079-1102.

[62] Shibata, A. and Sozen, M. A., "Substitute-Structure Method for Seismic Design in R/C," *Journal of the Structural Division* , ASCE, Vol. 102, No. ST1, January 1976, pp. 1-18.

[63] Shimazaki, K. and Sozen, M. A., "Seismic Drift of Reinforced Concrete Structures," Research Reports, Hazami-Gumi, Tokyo, 1984, pp. 145-166.

[64] Sivakumar, B., Gergely, P., and White, R. N., "Suggestions for the Design of R/C Lapped Splices for Seismic Loading," *Concrete International* , American Concrete Institute, February 1983, pp. 46-50.

[65] Skinner, R. I., Skitton, D. W. C., and Laws, D. A., "Unbalanced Buildings and Buildings with Light Towers under Earthquake Forces," *Proceedings* , Third World Conference on Earthquake Engineering, Vol. II, New Zealand, 1965, pp. 586-602.

[66] Sozen, M. A., "A Frame of Reference," Peck Symposium, University of Illinois, Urbana, June 1987.

[67] Takeda, T., Sozen, M. A., and Nielsen, N. N., "Reinforced Concrete Response to Simulated Earthquakes," *Journal of the Structural Division* , ASCE, Vol. 96, No. ST12, December 1970, pp. 2557-2573.

[68] "Tentative provisions for the Development of Seismic Regulations for Buildings," Applied Technology Council (ATC 3-06), NBS Special Publication 510, NSF Publication 78-08, June 1978.

[69] "The Central Greece Earthquakes of Feb.-March 1981," A Reconnaissance and Engineering Report by Gardis, P. G., et al, National Academy Press, Washington, D. C., 1982.

[70] Timoshenko, S. P. and Goodier, J. N., *Theory of Elasticity* , McGraw-Hill, New York, N. Y., 1970.

[71] Uang, C. M. and Bertero, V. V., "Earthquake Simulation Tests and Associated Studies of a 0.3-Scale Model of a Six-Story Concentrically Braced Steel Structure," *Report No. UCB/EERC-86/10* , Earthquake Engineering Research Center, University of California, Berkeley, December 1986.

[72] *Uniform Building Code* , International Conference of Building Officials, Whittier, California, 1982.

[73] Wilson, E. L., "The SAP-80 Series of Structural Analysis Programs," Version 84.00, SAP Incorporated, EL Cerrito, California, January 1983.

[74] Wilson, E. L., Der Kiureghian, A., and Bayo, E. P., "A Replacement for the SRSS Method in Seismic Analysis," *Earthquake Engineering and Structural Dynamics* , Vol. 9, 1981, pp. 187-194.

[75] Wilson, E. L. and Dovey, H. H., "Three-Dimensional Analysis of Building Systems-TABS," *Report No. UCB/EERC-72/8* , Earthquake Engineering Research Center, University of California, Berkeley, April 1972.

[76] Wolfgram, C. E. "Experimental Modeling and Analysis of Three One-Tenth-Scale Reinforced Concrete Frame-Wall Structures," Ph.D. dissertation submitted to the Graduate College of the University of Illinois, Urbana, December 1983.

[77] Wood, S. L. "Experiments to Study the Earthquake Response of Reinforced Concrete Frames with Setbacks," Thesis submitted to the Graduate College of the University of Illinois, Urbana, January 1986.

[78] Zee, H. L. and Moehle, J. P., "Behavior of Interior and Exterior Flat-Plate Connections Subjected to Inelastic Load Reversals," *Report No. UCB/EERC-84/07* , Earthquake Engineering Research Center, University of California, Berkeley, August 1984.

Table 2.1(a) Computed Vibration Periods for Prototype Structure.

Translational (Long Direction)		Translational (Short Direction)		Torsional	
1st	2nd	1st	2nd	1st	2nd
0.57	0.23	0.45	0.16	0.26	0.13

Note: All the vibration periods are in sec.

Table 2.1 (b) Computed Mode Shapes for Prototype Structure.

Long-Direction Tanslational

Floor	1st Mode	2nd Mode
	Y	Y
6	-0.88	-0.88
5	-0.79	-0.44
4	-0.64	0.15
3	-0.47	0.59
2	-0.32	0.60
1	-0.14	0.32

Short-Direction Translational

Floor	1st Mode		2nd Mode	
	X	R	X	R
6	0.88	0.0012	-0.73	0.0045
5	0.80	0.0011	-0.39	0.0032
4	0.65	0.00097	-0.081	0.0013
3	0.40	0.00081	0.51	-0.00031
2	0.26	0.00052	0.54	-0.00025
1	0.12	0.00023	0.30	-0.00012

Torsional

Floor	1st Mode		2nd Mode	
	X	R	X	R
6	-0.030	0.0056	0.47	0.0055
5	-0.025	0.0049	0.15	0.0032
4	-0.016	0.0037	-0.25	-0.00014
3	-0.38	0.0025	-0.098	-0.0028
2	-0.28	0.0017	-0.18	-0.0027
1	-0.14	0.00078	-0.12	-0.0015

Notes:
1. X: Translation in the short direction, Y: Translation in the long direction, and R: Rotation.
2. The values given in this table represent the translation and rotation of each floor for each mode.

Table 3.1 Variation of Measured Dimensions.

Floor	Long-Direction Beam				Short-Direction Beam				Column				Slab	
	Width		Depth		Width		Depth		Width		Depth		Thickness	
	$\overline{X}$	σ	$\overline{X}$	σ	$\overline{X}$	σ	$\overline{X}$	σ	$\overline{X}$	σ	$\overline{X}$	σ	$\overline{X}$	σ
1	5.07	0.12	7.12	0.060	4.08	0.068	7.60	0.025	5.03	0.038	6.60	0.060	1.94	0.078
2	4.98	0.045	7.10	0.077	4.06	0.079	7.60	0.019	5.08	0.093	6.55	0.060	1.99	0.061
3	5.02	0.096	7.09	0.069	4.09	0.11	7.64	0.020	5.13	0.11	6.59	0.14	2.10	0.072
4	4.98	0.059	7.13	0.058	4.10	0.11	7.55	0.032	5.10	0.10	6.60	0.047	2.08	0.066
5	4.96	0.030	7.10	0.066	4.09	0.087	7.64	0.020	5.07	0.083	6.52	0.11	2.00	0.11
6	4.98	0.035	7.10	0.051	4.08	0.026	7.62	0.032	5.08	0.075	6.59	0.039	2.00	0.093

Notes:

All the dimensions are in in.

$\overline{X}$:Mean Value

σ :Standard Deviation.

Table 3.2 Test Sequence.

Designation	Description
FVO.A	Free vibration at construction location, w/o lead pigs (type 1)
FVO.B	Free vibration at construction location, w/o lead pigs (type 1)
FVO.C	Free vibration at construction location, w/o lead pigs (type 2)
FVO.D	Free vibration at construction location, w/o lead pigs (type 2)
FVO.E	Free vibration at construction location, w/o lead pigs (type 3)
FVO.F	Free vibration at construction location, w/o lead pigs (type 3)
FVO.G	Free vibration on shaking table, w/o lead pigs (type 1)
FVO.H	Free vibration on shaking table, w/o lead pigs (type 1)
FVO.I	Free vibration on shaking table, w/o lead pigs (type 2)
FVO.J	Free vibration on shaking table, w/o lead pigs (type 2)
FVO.K	Free vibration on shaking table, w/o lead pigs (type 3)
FVO.L	Free vibration on shaking table, w/o lead pigs (type 3)
FVO.M	Free vibration on shaking table, with lead pigs (type 1)
FVO.N	Free vibration on shaking table, with lead pigs (type 1)
FVO.O	Free vibration on shaking table, with lead pigs (type 2)
FVO.P	Free vibration on shaking table, with lead pigs (type 2)
FVO.Q	Free vibration on shaking table, with lead pigs (type 3)
FVO.R	Free vibration on shaking table, with lead pigs (type 3)
	PHASE 1
EC6.2L	Earthquake simulation, El Centro NS 1940
FV1	Free vibration
EC7.7L	Earthquake simulation, El Centro NS 1940
FV2	Free vibration
EC16.6L	Earthquake simulation, El Centro NS 1940
FV3	Free vibration
EC49.3L	Earthquake simulation, El Centro NS 1940
FV4	Free vibration
	PHASE 2
FV5	Free vibration
EC8.1B	Earthquake simulation, El Centro NS 1940
FV6	Free vibration
EC47.7B	Earthquake simulation, El Centro NS 1940
FV7	Free vibration
MO63.4B	Earthquake simulation, Miyagi-Ken-Oki S00E 1978
FV8	Free vibration
MX10.3B	Earthquake simulation, Mexico City S60E 1985
MX19.7B	Earthquake simulation, Mexico City S60E 1985
MX34.6B	Earthquake simulation, Mexico City S60E 1985
FV9	Free vibration

Notes:

1. Phase 1: Horizontal base motions were parallel to long-direction frames.

2. Phase 2: Unidirectional horizontal motions were at 45 degrees relative to principal axes of frames.

3. All free-vibration tests on shaking table were performed with shaking table platform blocked (wooden blocks wedged against the test platform).

4. All free-vibration tests following earthquake simulations were on shaking table platform (blocked) and with lead pigs.

5. Number following earthquake simulations is percent of maximum input acceleration in g.

Table 4.1 Peak Acceleration and Spectrum Intensity.

Test	Peak acceleration (g)	Spectrum intensity (in.)
EC7.7L	0.077	1.96 (0.24)
EC16.6L	0.166	4.85 (0.60)
EC49.3L	0.493	14.2 (1.75)
EC47.7B	0.477	14.1 (1.73)
MO63.4B	0.634	18.0 (2.22)
MX34.6B	0.346	9.26 (1.14)

Note:

Numbers in the parenthesis are the ratio between calculated spectrum intensity and 20% damped intensity of scaled El Centro NS 1940.

Table 4.2 Extreme Values.

Test	V_x	M_x	V_y	M_y	T
EC7.7L	12.9	1650.	-	-	-
EC16.6L	25.0	3306.	-	-	-
EC49.3L	49.0	6092.	-	-	-
EC47.7B	28.4	4170.	31.8	4390.	687.
MO63.4B	43.0	6115.	36.1	5050.	776.
MX34.6B	46.6	6458.	28.4	3512.	587.

Notations:

1. V_x : Base shear (kips) in long direction; V_y : Base shear (kips) in short direction.

2. M_x : Base overturning moment (kips-in.) in long direction; M_y : Base overturning moment (kips-in.) in short direction.

3. T : Torque (kips-in.) at the base computed with respect to the central column.

Table 4.2 Extreme Values (cont.).

Test	Floor	X	D_x	A_x	Y	D_y	A_y	Θ
EC7.7L	1	0.073	0.073	0.14	-	-	-	-
	2	0.11	0.043	0.18	-	-	-	-
	3	0.15	0.037	0.23	-	-	-	-
	4	0.19	0.041	0.23	-	-	-	-
	5	0.23	0.045	0.26	-	-	-	-
	6	0.27	0.037	0.27	-	-	-	-
EC16.6L	1	0.16	0.16	0.23	-	-	-	-
	2	0.30	0.13	0.34	-	-	-	-
	3	0.40	0.11	0.47	-	-	-	-
	4	0.50	0.10	0.45	-	-	-	-
	5	0.59	0.096	0.54	-	-	-	-
	6	0.62	0.032	0.54	-	-	-	-
EC49.3L	1	0.51	0.51	0.49	-	-	-	-
	2	1.06	0.56	0.63	-	-	-	-
	3	1.59	0.54	0.88	-	-	-	-
	4	2.02	0.42	0.81	-	-	-	-
	5	2.35	0.36	1.05	-	-	-	-
	6	2.48	0.18	1.31	-	-	-	-
EC47.7B	1	0.30	0.30	0.33	0.45	0.45	0.33	0.0039
	2	0.72	0.41	0.43	0.99	0.54	0.40	0.0097
	3	0.99	0.28	0.68	1.45	0.46	0.45	0.014
	4	1.33	0.37	0.62	1.88	0.44	0.57	0.018
	5	1.69	0.37	0.73	2.19	0.33	0.73	0.022
	6	1.89	0.20	0.98	2.26	0.084	0.84	0.022
MO63.4B	1	0.63	0.63	0.38	0.98	0.98	0.41	0.0081
	2	1.31	0.72	0.50	2.07	1.09	0.50	0.019
	3	1.82	0.51	0.80	3.02	0.96	0.62	0.029
	4	2.39	0.58	0.82	3.91	0.88	0.72	0.038
	5	2.79	0.53	0.98	4.54	0.69	1.01	0.045
	6	3.23	0.35	1.24	4.68	0.18	1.15	0.045
MX34.6B	1	0.77	0.77	0.41	0.71	0.71	0.29	0.0
	2	1.82	1.19	0.52	1.69	1.01	0.37	0.011
	3	2.44	0.62	0.76	2.53	0.84	0.42	0.020
	4	3.30	0.91	0.83	3.26	0.74	0.50	0.028
	5	4.01	0.73	1.06	3.77	0.53	0.61	0.034
	6	4.35	0.32	1.21	4.36	0.27	0.68	0.038

Notations:

1. X : Lateral displacement (in.) in long direction; Y : Lateral displacement (in.) in short direction.

2. D_x : Inter-story drift (in.) in long direction; D_y : Inter-story drift (in.) in short direction.

3. A_x : Floor acceleration(g) in long direction; A_y : Floor acceleration (g) in short direction.

7. Θ : Floor rotation (rad.).

Notes:

1. For tests EC47.7B and MO63.4B, the sixth floor incremental rotation was set equal to zero (Appendix C).

2. For test MX36.4B, the first floor rotation was set equal to zero (Appendix C).

Table 4.3 Story Weight and Height.

Floor	Weight (lbs)	Height above footing (in)
1	15566	36
2	15615	72
3	15685	108
4	8896	144
5	8846	180
6	8716	216

Weights are based on measured dimensions.

Table 4.4 Gravity Load Strains.

Gauge	Strain (Micro strain)
sg1	-430.
sg2	-320
sg3	80
sg4	80
sg5	190
sg6	480
sg7	180
sg8	-610
sg9	-200
sg10	-210
sg11	-330
sg12	-350
sg13	-550
sg14	-390
sg15	-730
sg16	-390
sg17	-520
sg18	-440
sg19	-380
sg20	-315
sg21	-820
sg22	-460
sg23	-335
sg24	-450
sg25	-270
sg26	-830
sg27	-355
sg28	-350
sg29	-540
sg30	-460
sg31	-200
sg32	-821
sg33	-240
sg34	-20
sg35	-315
sg36	-550
sg37	-490
sg38	-110
sg39	-880
sg40	-300
sg41	-120
sg42	-80
sg43	-560
sg44	-350
sg45	-910
sg46	-200
sg47	-420
sg48	-540
sg49	-445
sg50	-450
sg51	-70
sg52	-775
sg53	-540
sg54	-150
sg55	-550
sg56	-145

Table 4.5 Maximum Strains (Micro strain).

Gauge	EC7.7L	EC16.6L	EC49.3L	EC47.7B	MO63.4B	MX34.6B
sg1	-434.	-444.	-488.	-632.	-607.	300.
sg2	-334.	-341.	415.	584.	1055.	773.
sg3	270.	565.	1136.	958.	1250.	1443.
sg4	290.	624.	1600.	1232.	1590.	1840.
sg5	274.	494.	1055.	1292.	1456.	-830.
sg6	859.	1758.	12367.	10749.	20420.	20562.
sg7	277.	546.	1173.	973.	1434.	2058.
sg8	-866.	-1095.	-1521.	3294.	7457.	12041.
sg9	-515.	1300.	3033.	1787.	13436.	15211.
sg10	-344.	701.	2416.	1264.	3331.	6950.
sg11	-425.	-487.	1924.	1094.	1872.	-
sg12	-595.	824.	1846.	887.	2656.	5820.
sg13	-716.	-888.	1277.	-783.	1377.	2134.
sg14	-413.	-415.	-396.	739.	1056.	1355.
sg15	-734.	-727.	-689.	-663.	628.	886.
sg16	-542.	-653.	2078.	1083.	1865.	2675.
sg17	-667.	-825.	1934.	944.	3565.	12395.
sg18	-510.	-573.	1110.	714.	1295.	1569.
sg19	-491.	-630.	1698.	971.	2238.	2717.
sg20	-346.	-351.	439.	990.	1197.	1484.
sg21	-832.	-845.	-832.	-763.	-600.	-614.
sg22	-558.	-595.	1368.	752.	1347.	1726.
sg23	-437.	564.	-650.	1491.	2708.	5657.
sg24	-596.	-788.	1910.	973.	2584.	6081.
sg25	-373.	-471.	1955.	1596.	2527.	3358.
sg26	-836.	-833.	-806.	-698.	-650.	-664.
sg27	-366.	-372.	467.	805.	1308.	1800.
sg28	-424.	-477.	1348.	971.	1634.	1727.
sg29	-650.	-768.	883.	-750.	1348.	1282.
sg30	-532.	-640.	-582.	508.	1043.	640.
sg31	-261.	-287.	1107.	971.	1448.	1223.
sg32	-825.	-825.	-812.	-681.	735.	-781.
sg33	-280.	-272.	413.	1286.	2060.	1438.
sg34	-204.	638.	2306.	2310.	10746.	-
sg35	-383.	-445.	1326.	1188.	1673.	1881.
sg36	-615.	-675.	995.	720.	1204.	1525.
sg37	-522.	-575.	-590.	-363.	458.	-562.
sg38	-170.	-210.	484.	400.	760.	437.
sg39	-876.	-886.	-886.	-864.	-675.	-770.
sg40	-330.	-356.	-330.	812.	1165.	503.
sg41	-185.	-280.	1570.	1770.	2290.	3410.
sg42	-164.	-282.	852.	830.	1034.	1235.
sg43	-603.	-651.	803.	-796.	844.	3084.
sg44	-357.	-351.	-343.	-419.	-410.	-384.
sg45	-913.	-916.	-923.	-952.	-985.	-909.
sg46	-220.	-242.	-301.	-252.	-266.	443.
sg47	-515.	-627.	-828.	-875.	-867.	874.
sg48	-658.	-806.	1100.	-955.	1261.	2003.
sg49	-504.	-546.	864.	837.	1018.	1106.
sg50	-526.	-617.	1769.	1098.	1992.	2077.
sg51	-150.	-255.	1522.	1081.	1755.	-
sg52	-986.	-1203.	8428.	3802.	9337.	14150.
sg53	-828.	-1112.	3430.	1858.	5360.	10581.
sg54	-219.	306.	1626.	1198.	1900.	1635.
sg55	-688.	-846.	2247.	1267.	3726.	6275.
sg56	-233.	-336.	1327.	1133.	1786.	2000.

Table 5.1 Acceleration Amplification Factor.

Test	Long direction	Short direction
EC7.7L	3.50	-
EC16.6L	3.25	-
EC49.3L	2.66	-
EC47.7B	2.90	2.49
MO63.4B	2.77	2.57
MX34.6B	4.95	2.78

Table 5.2 Variation of Lateral Stiffness (kips/in.).

Stage	Long direction	Short direction
At construction site (without lead pigs)	25.4	27.0
On shaking table (without lead pigs)	28.6	35.8
On shaking table (with lead pigs)	30.6	40.8

Lateral stiffness is defined as slope of roof lateral displacement-force relation.

Table 5.3 Variation of Vibration Period (Sec.).

Stage	Free-vibration test						EQ Simulation[1]	
	X*		Y+		θ++		X*	Y+
	Mode 1	Mode 2	Mode 1	Mode 2	Mode 1	Mode 2	Mode 1	Mode 1
Phase 1	0.17	0.062	0.16	0.049	0.094	0.044	-	-
Phase 2	0.15	0.060	0.14	0.047	0.090	0.043	-	-
Phase 3	0.27	0.10	0.25	0.087	0.15	0.070	-	-
After/during EC7.7L	0.29	0.11	-	-	-	-	0.34	-
After/during EC16.6L	0.32	0.13	-	-	-	-	0.38	-
After/during EC49.3L	0.48	0.19	0.33	-	0.23	-	0.53	-
After/during EC47.7B	0.56	0.22	0.39	-	0.29	-	0.62	0.43
After/during MO63.4B	0.67	0.24	0.48	-	0.33	-	0.71	0.54
After/during MX34.6B	0.77	0.27	0.63	-	0.36	-	0.80	0.68

Notation:

1. From the displacement history during earthquake simulations.

* X : Long-direction translational mode.

+ Y : Short-direction translational mode.

++ θ : Torsional mode.

Notes:

1. Phase 1: Structure was at the construction site, without lead pigs.

2. Phase 2: Structure was on the shaking table platform, without lead pigs.

3. Phase 3: Structure was on the shaking table platform, with lead pigs.

Table 5.4 Variation of Viscous Damping Ratio.

Stage	Damping ratio (%)
"Uncracked"	2.3
After EC7.7L	2.7
After EC16.6L	3.6
After EC49.3L	5.0
After EC47.7B	6.4
After MO63.4B	9.6
After MX34.6B	11.0

Table 6.1 Calculated and Measured Lateral Stiffness (kips/in.).

Direction	Measured	Calculated (No Flange)	Calculated (With Flange)
Long	30.6	34.0	44.0
Short	40.8	49.0	63.0

Table 6.2 Measured and Computed Vibration Periods (Sec.).

Mode	Measured	Calculated
1st (1st Long-Direction Translational)	0.27	0.26
2nd (1st Short-Direction Translational)	0.25	0.23
3rd (1st Torsional)	0.15	0.12
4th (2nd Long-Direction Translational)	0.10	0.11
5th (2nd Short-Direction Translational)	0.087	0.078
6th (2nd Torsional)	0.070	0.061

Table 6.3 Comparison of Measured and Calculated Responses.

(a) Extreme Values-Test EC7.7L

Response	Experimental	Model A	Model B
1st-floor displacement	0.073	0.049	0.060
2nd-floor displacement	0.11	0.097	0.12
3rd-floor displacement	0.15	0.14	0.16
4th-floor displacement	0.19	0.17	0.20
5th-floor displacement	0.23	0.20	0.23
6th-floor displacement	0.27	0.22	0.26
Base shear	12.9	12.9	12.8
Inter-story drift	0.20	0.14	0.17

(b) Extreme Values-Test EC16.6L

Response	Experimental	Model A	Model B	Model C
1st-floor displacement	0.16	0.11	0.13	0.13
2nd-floor displacement	0.30	0.23	0.26	0.27
3rd-floor displacement	0.40	0.32	0.36	0.38
4th-floor displacement	0.50	0.43	0.46	0.50
5th-floor displacement	0.59	0.52	0.55	0.63
6th-floor displacement	0.62	0.57	0.62	0.70
Base shear	25.0	27.4	27.1	24.8
Inter-story drift	0.45	0.32	0.37	0.39

(c) Extreme Values-Test EC49.3L

Response	Experimental	Model A	Model B	Model C	Model D
1st-floor displacement	0.51	0.27	0.28	0.25	0.41
2nd-floor displacement	1.06	0.57	0.57	0.78	0.85
3rd-floor displacement	1.59	0.79	0.82	1.09	1.20
4th-floor displacement	2.02	1.01	1.11	1.42	1.61
5th-floor displacement	2.35	1.12	1.36	1.69	1.97
6th-floor displacement	2.48	1.26	1.47	1.84	2.14
Base shear	49.0	35.8	35.9	36.9	39.7
Inter-story drift	1.55	0.82	0.86	1.11	1.24

(d) Extreme Values-Test MO63.4B

Response	Experimental	Model C	Model D
1st-floor displacement	0.63	0.28	0.42
2nd-floor displacement	1.31	0.56	0.92
3rd-floor displacement	1.82	0.82	1.32
4th-floor displacement	2.39	1.11	1.77
5th-floor displacement	2.79	1.36	2.15
6th-floor displacement	3.23	1.47	2.33
Base shear	43.0	35.9	36.9
Inter-story drift	2.0	0.86	1.38

Note:
(1) Displacements are in inches.
(2) Base shear is in kips.
(3) Inter-story drift is in percent story height.

Table 7.1 Development of Overstrength.

Analysis	Base shear (kips)	
	Rectangular	UBC
A1	8.70	6.67
A2	10.1	7.77
B	14.2	10.7
C	23.3	17.6
D	26.2	19.8
E	29.1	22.0
F	41.0	31.0
G	68.0	51.0

Table 8.1 UBC Lateral-Force Distribution for Generic Structures.

Floor	2C	3C	4C	5C	4D	5D
10	52.8	60.6	61.4	63.0	36.7	35.0
9	31.0	34.9	35.1	34.7	18.0	15.3
8	27.6	31.0	31.2	30.8	16.0	13.6
7	24.1	27.1	27.3	27.0	14.0	11.9
6	20.7	23.3	23.4	23.1	12.0	11.2
5	17.2	19.4	19.5	57.8	10.0	76.5
4	13.8	15.5	46.8	46.2	71.8	61.2
3	10.3	34.9	35.1	34.7	53.8	45.9
2	20.7	23.3	23.4	23.1	35.9	30.6
1	10.3	11.6	11.7	11.6	18.0	15.3

Table 8.2 New Lateral-Force Distributions.

Floor	2C	4D
10	61.6	45.1
9	38.2	24.7
8	33.0	21.1
7	28.0	17.6
6	22.7	14.0
5	18.2	10.8
4	12.4	60.8
3	5.25	48.1
2	6.05	30.7
1	3.03	15.4

Note: Forces are in kips.

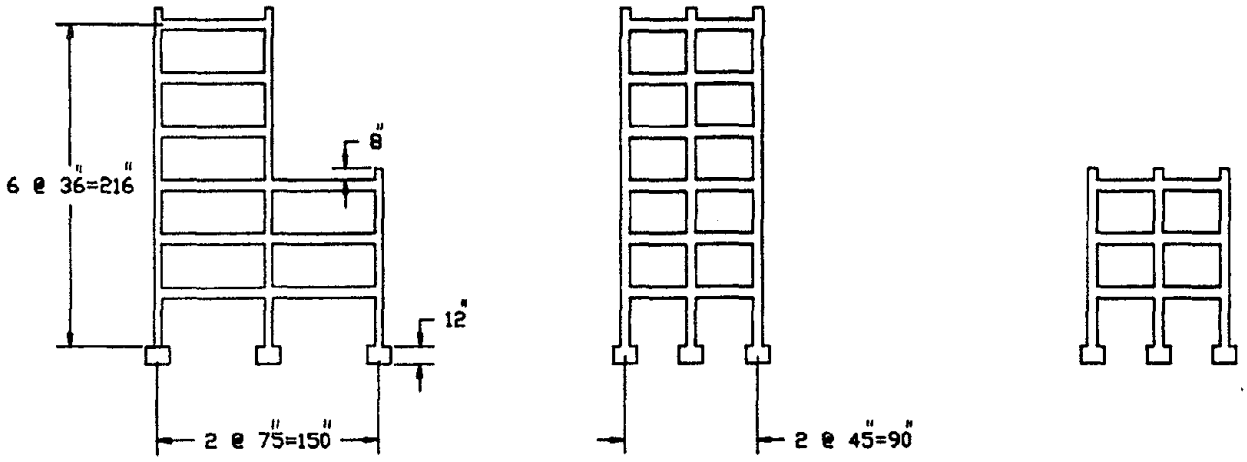

Elevation views

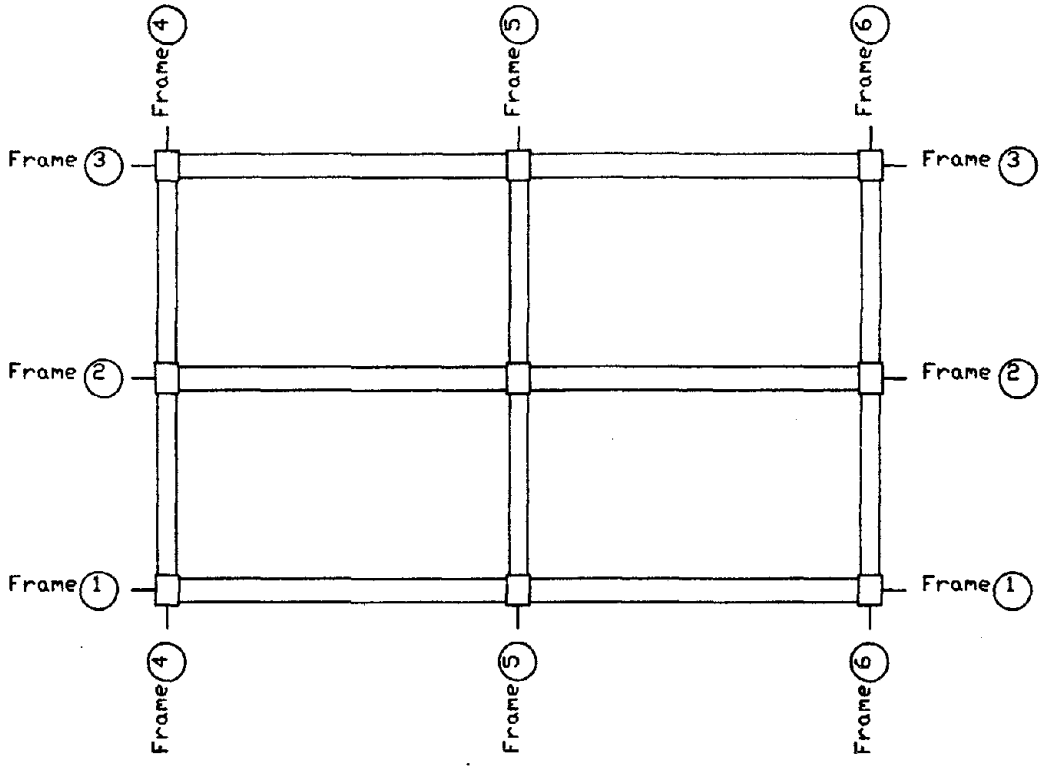

Plan view

Figure 2.1 Test Structure.

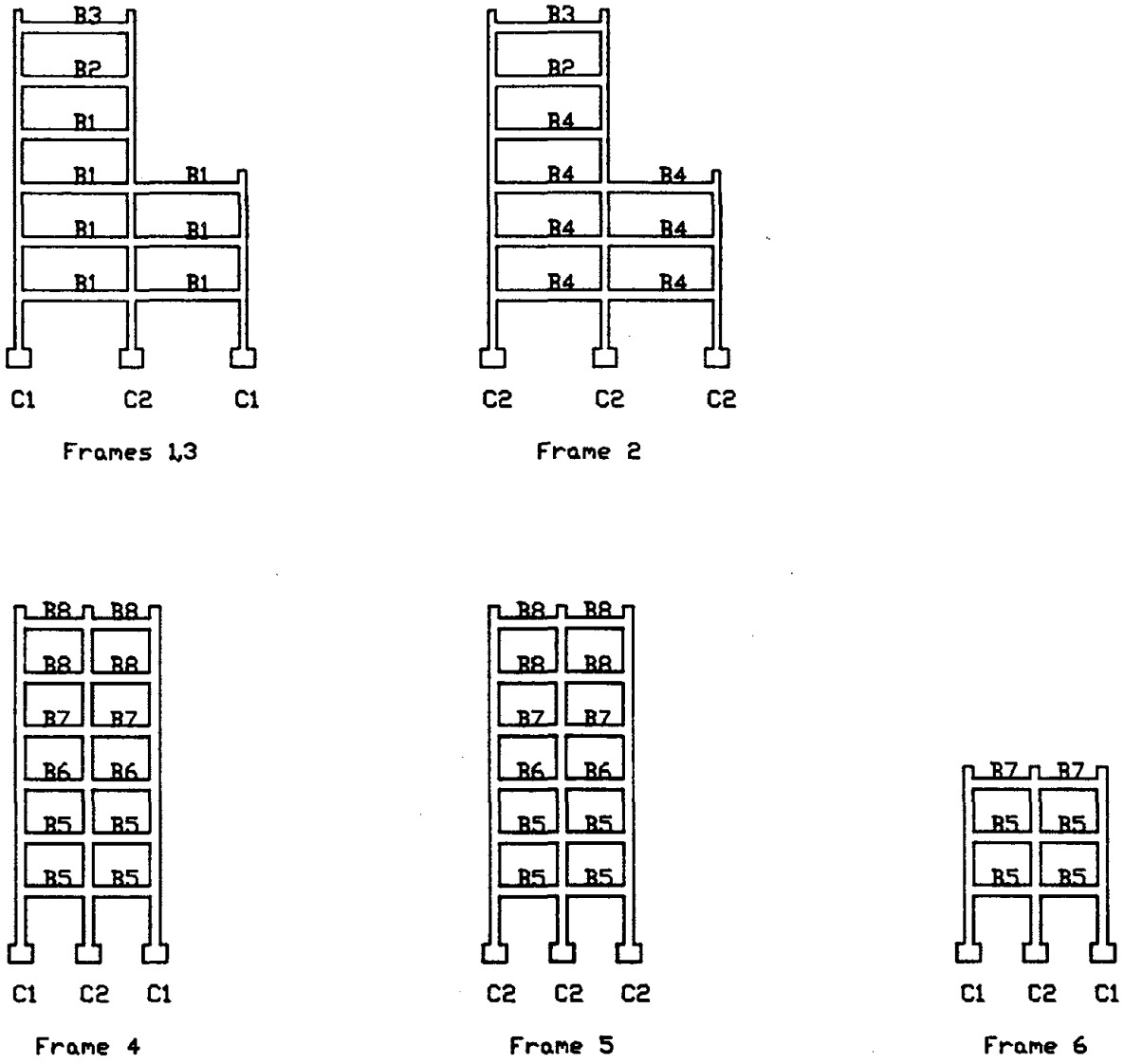

Figure 2.2 Location of Beams and Columns.

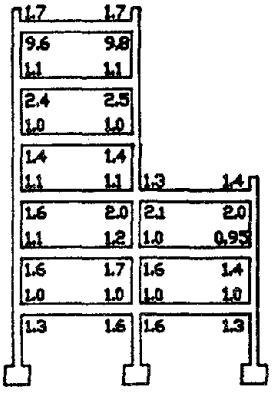

Frames 1,3

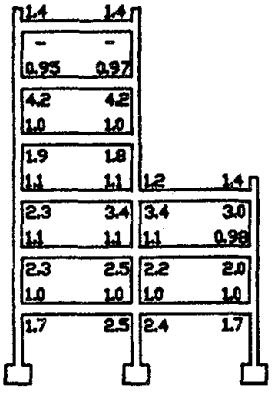

Frame 2

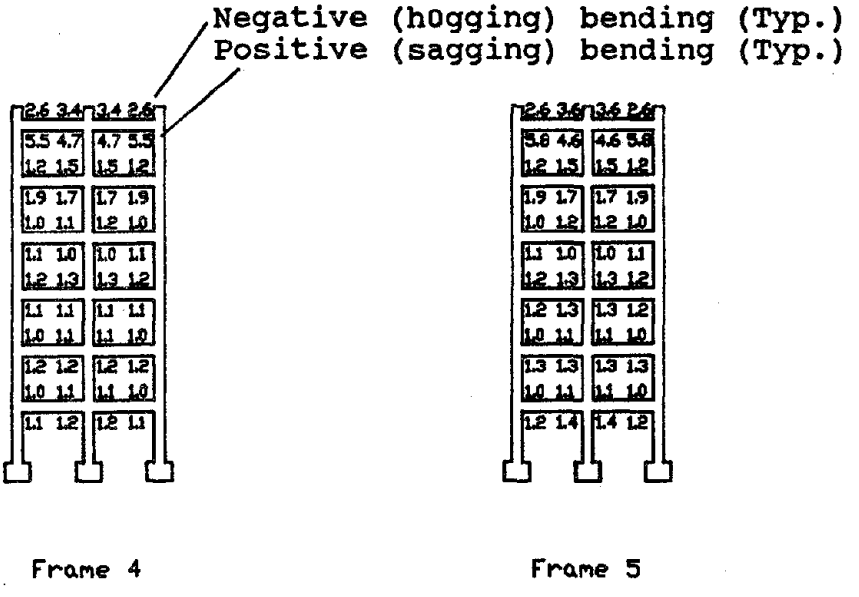

Frame 4 Frame 5 Frame 6

Figure 2.3 Beam Overstrength Ratios.

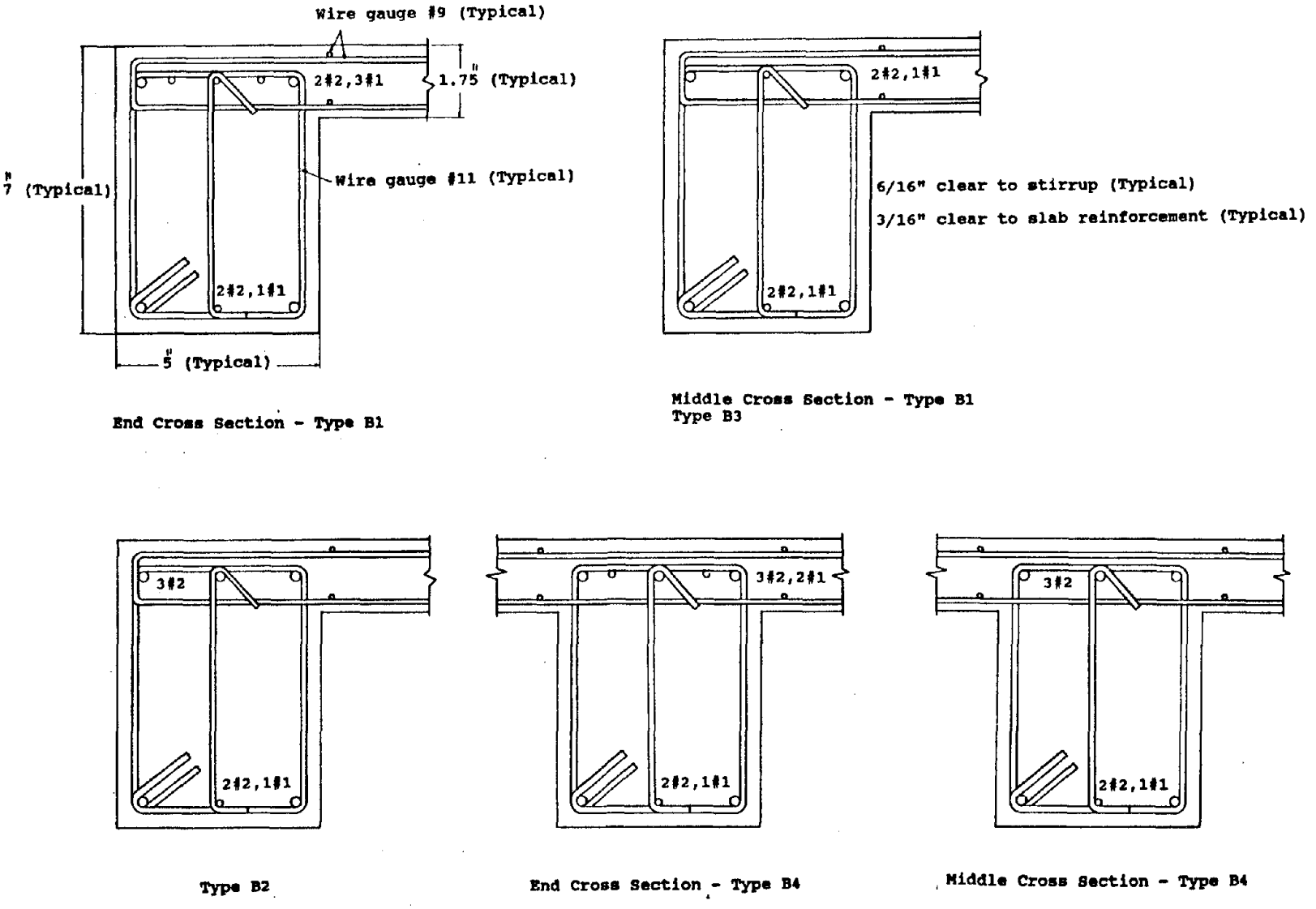

Figure 2.4(a) Beam Cross Sections (Long Direction).

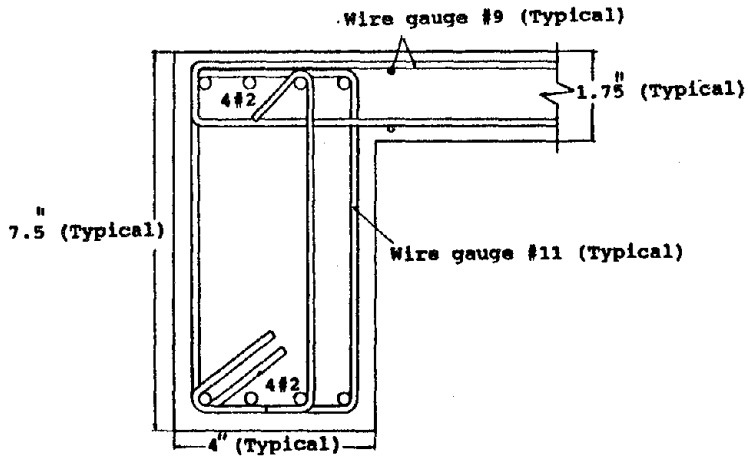

End Cross Section - Type B5

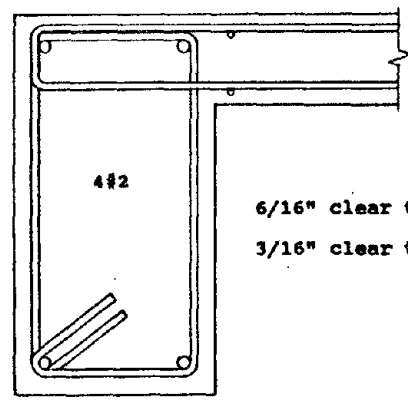

6/16" clear to stirrup (Typical)

3/16" clear to slab reinforcement (Typical)

Middle Cross Section - Types B5,B6,B7

Type B8

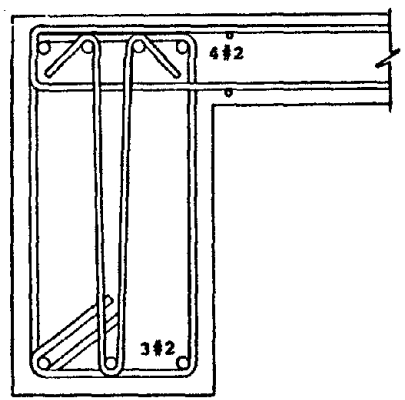

End Cross Section - Type B6

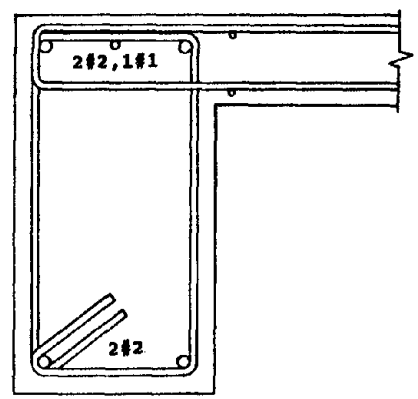

End Cross Section - Type B7

Figure 2.4(b) Beam Cross Sections (Short Direction).

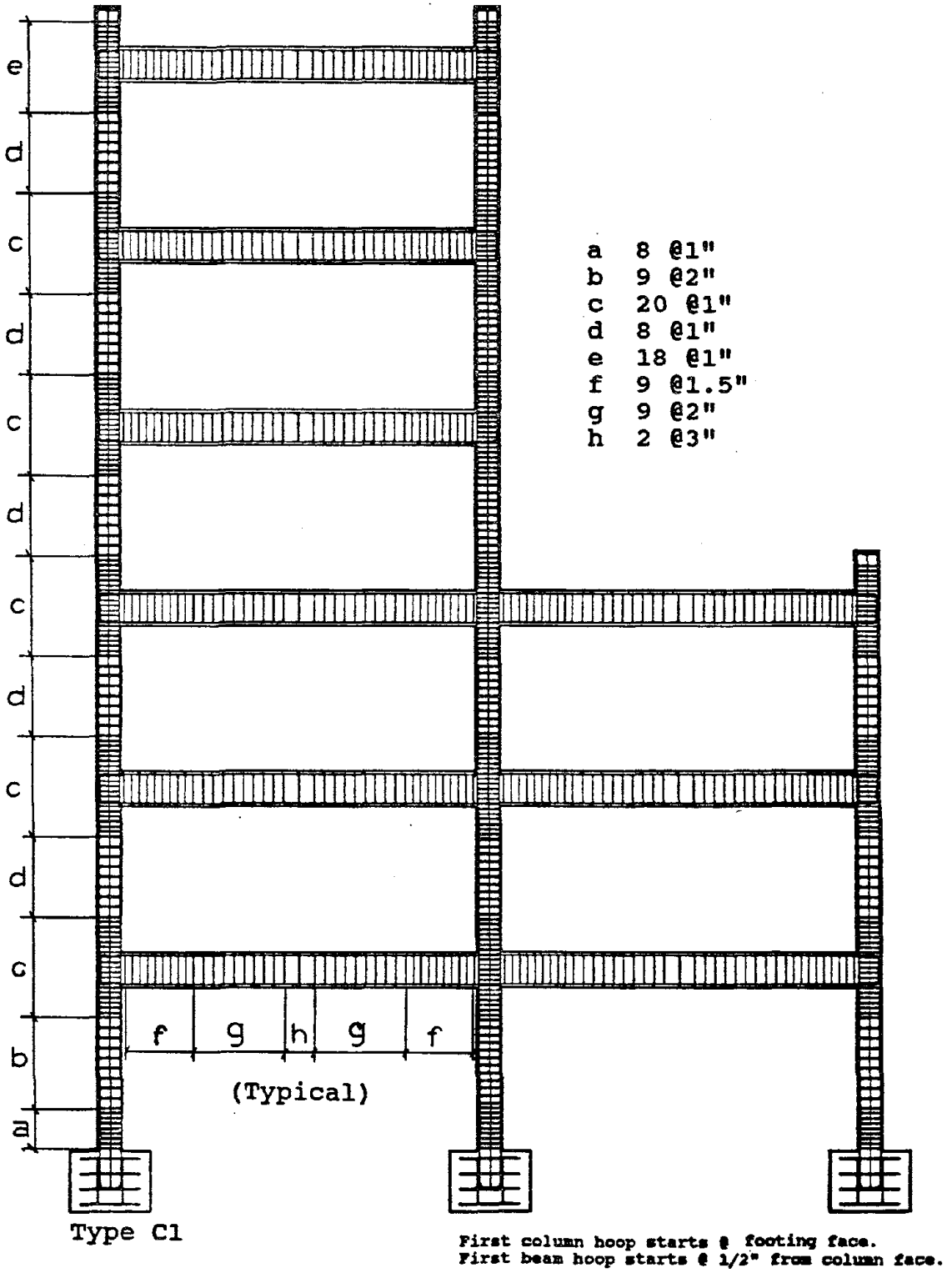

Figure 2.5(a) Transverse Reinforcement (Long Direction).

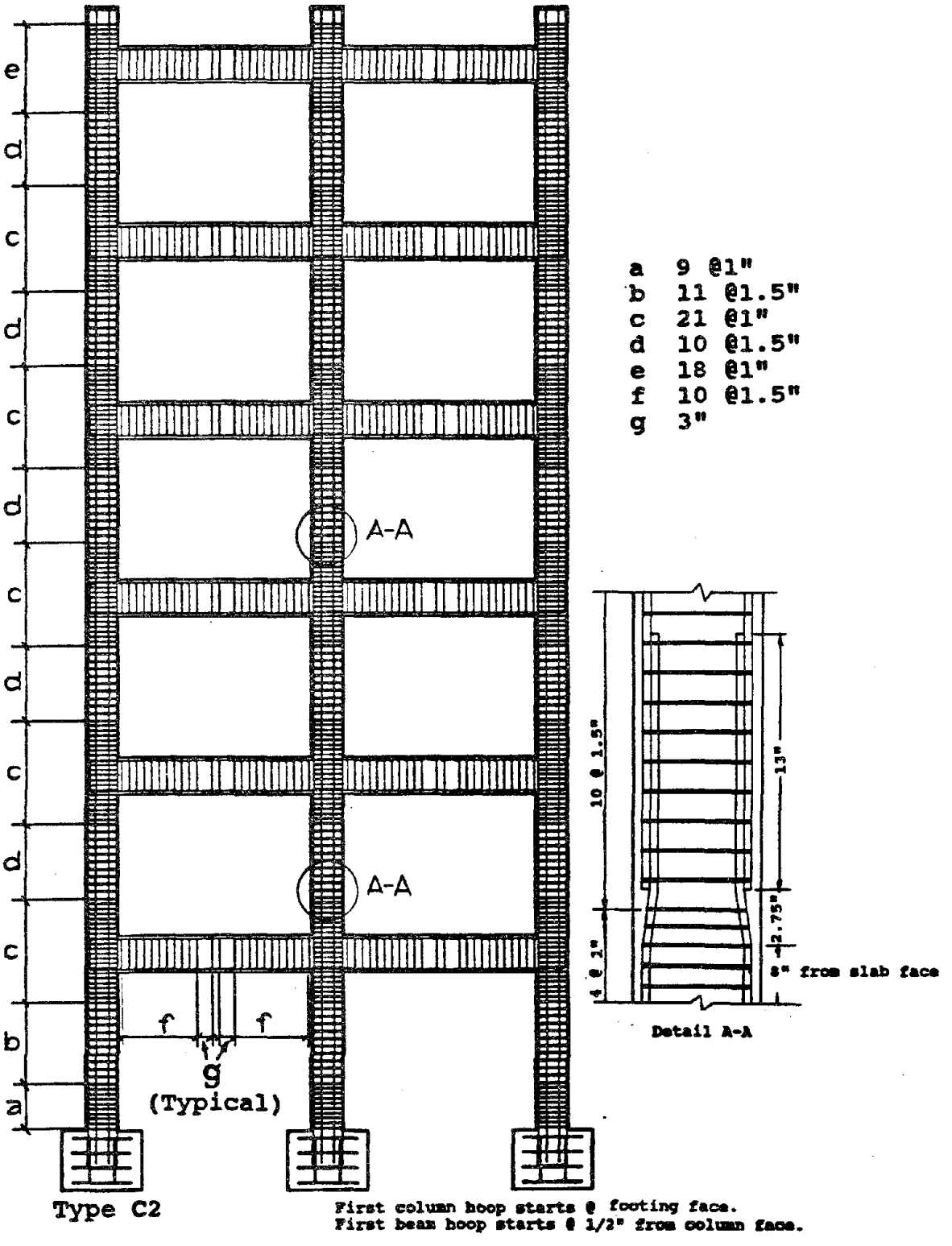

Figure 2.5(b) Transverse Reinforcement (Short Direction).

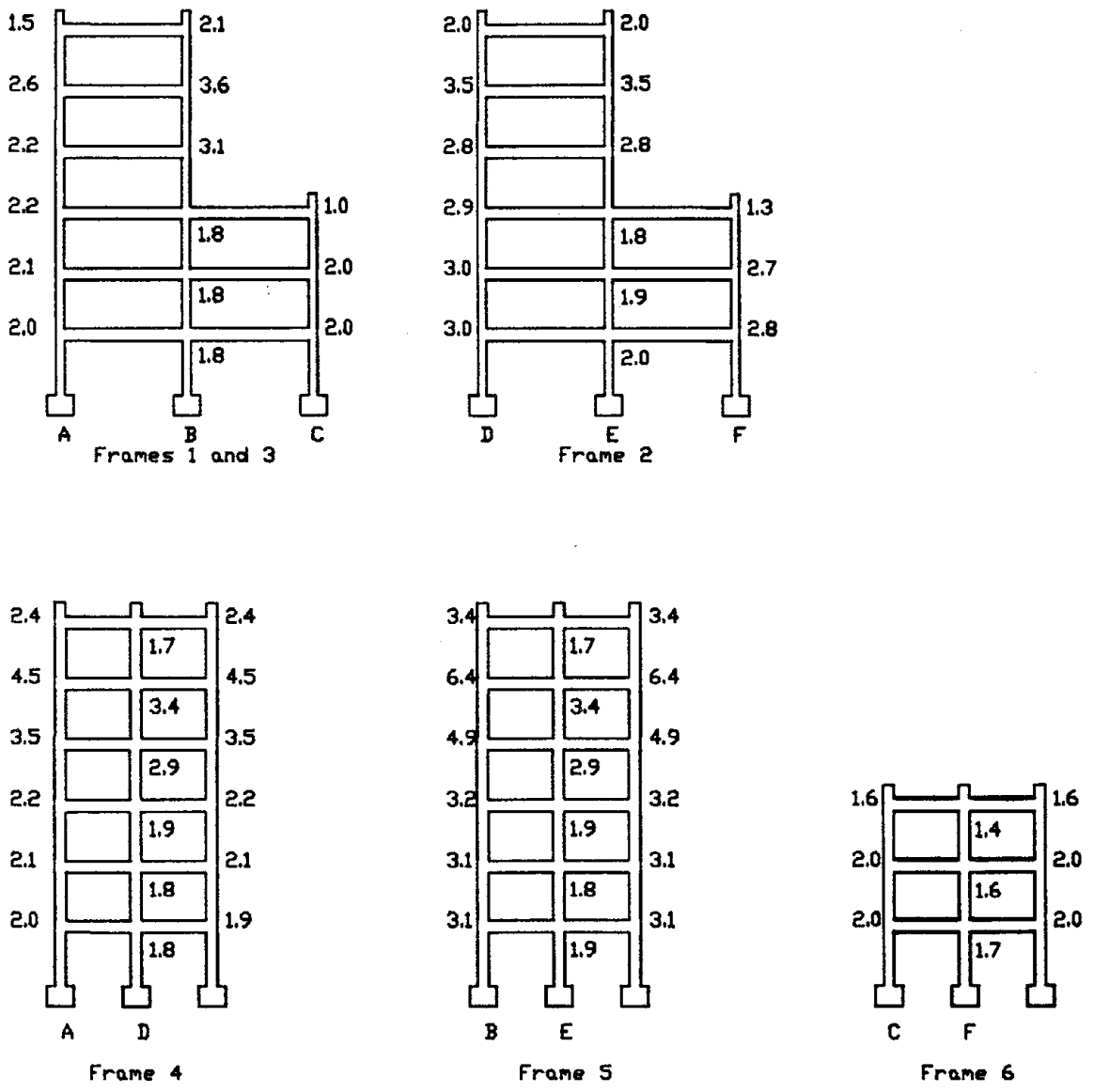

Figure 2.6 Column Overstrength Ratios.

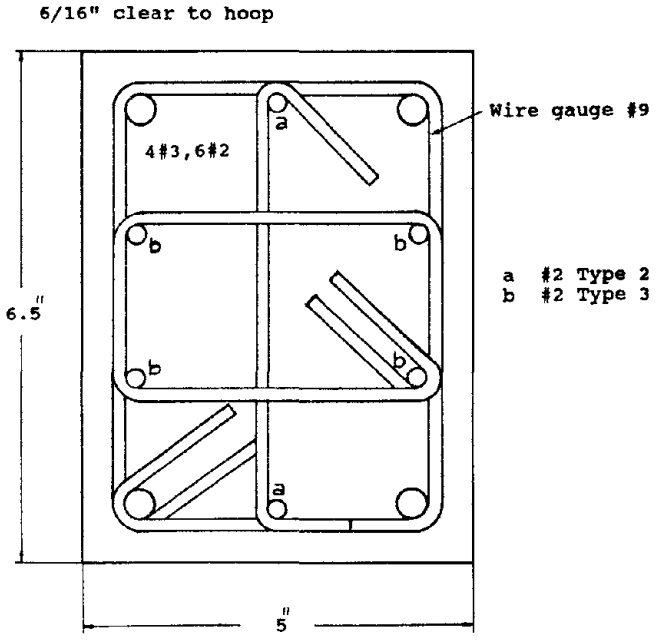

Type C2

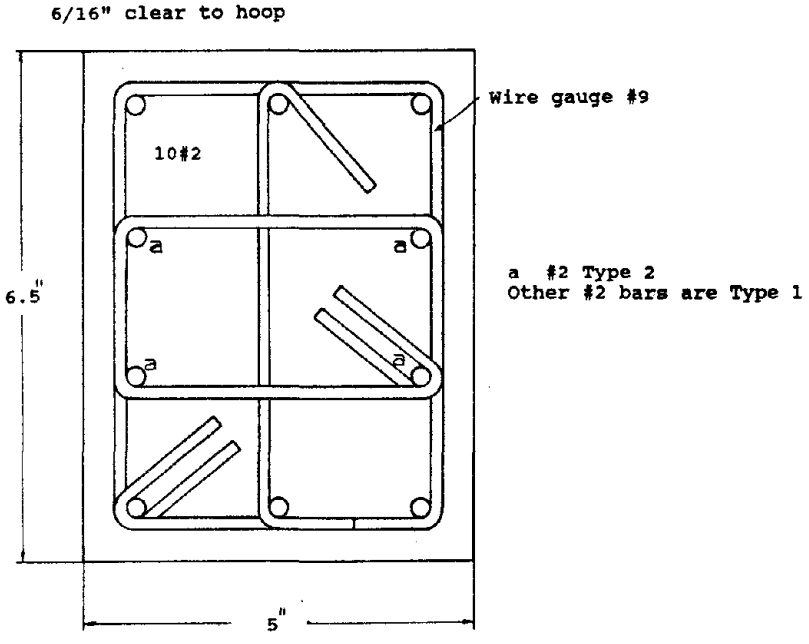

Type C1

Figure 2.7 Column Cross Sections.

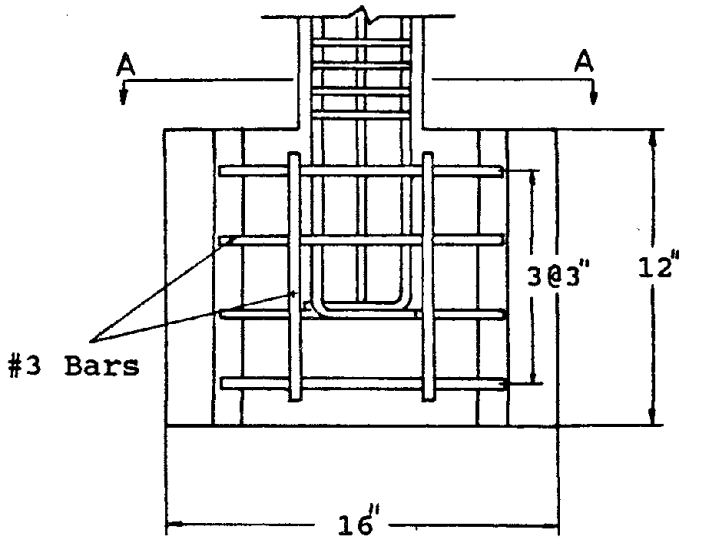

Section A-A

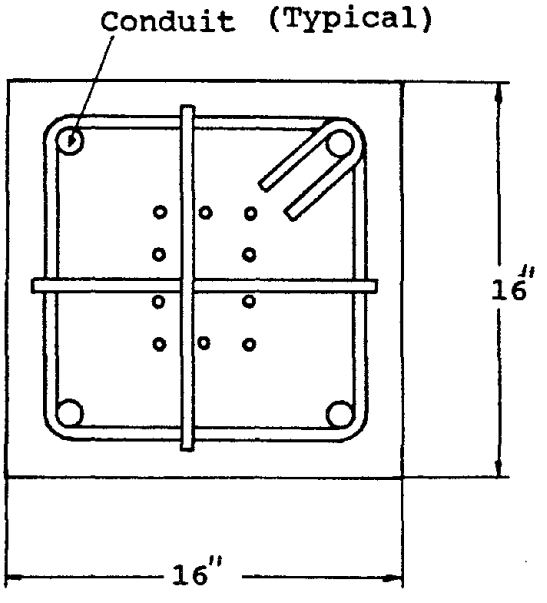

Figure 2.8 Detail of Footing.

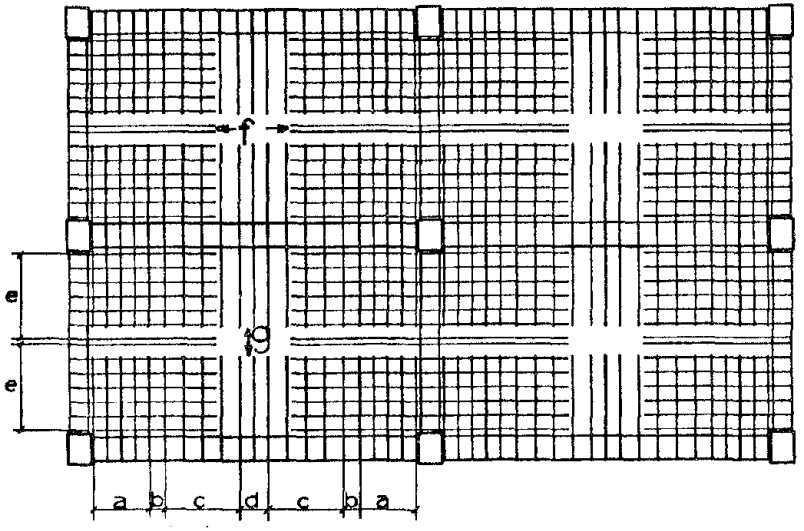

Top reinforcement

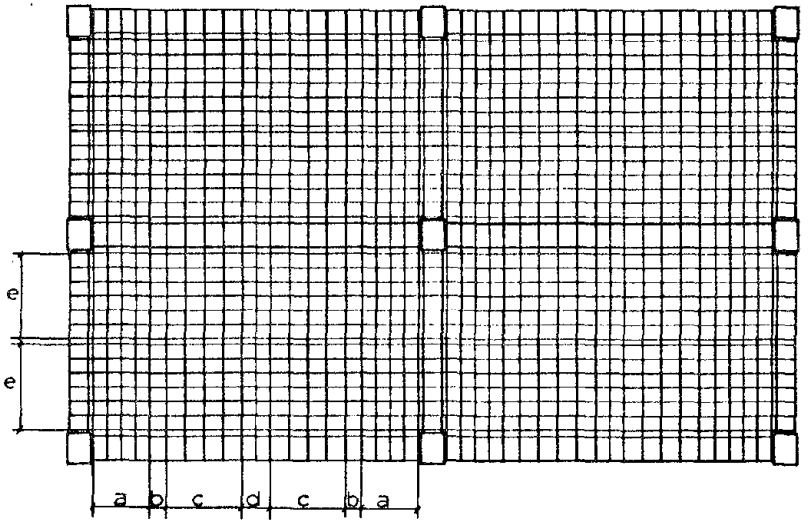

Bottom reinforcement

a	4@3"	31" long
b	3.5	31" long
c	4@4"	31" long
d	2@3"	31" long
e	6@3"	21.5" long
f	16.125"	
g	7.125"	

Figure 2.9 Slab Reinforcement.

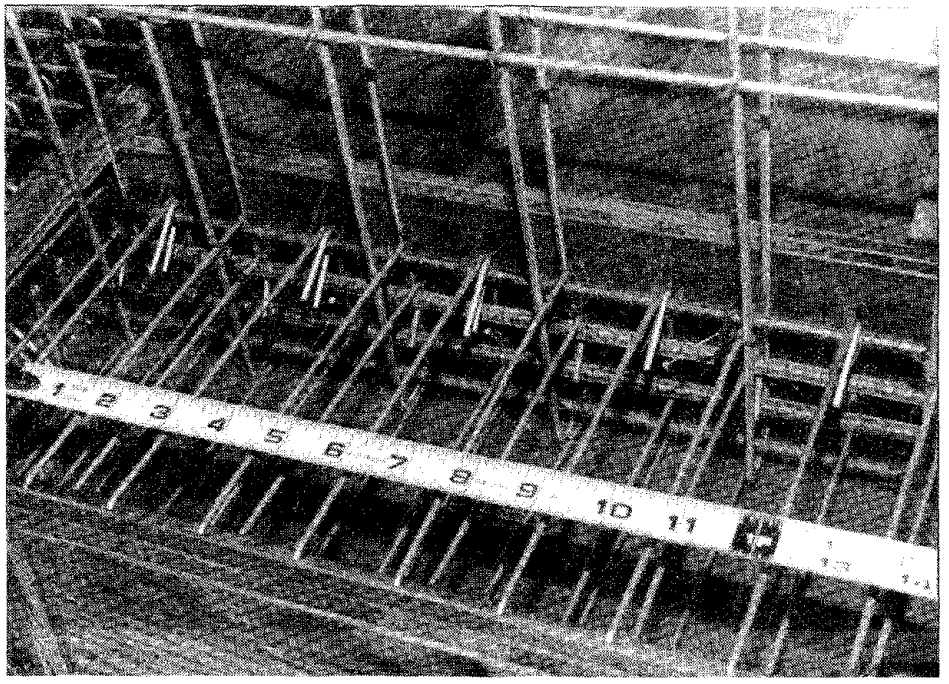

(a) Short-Direction Beam

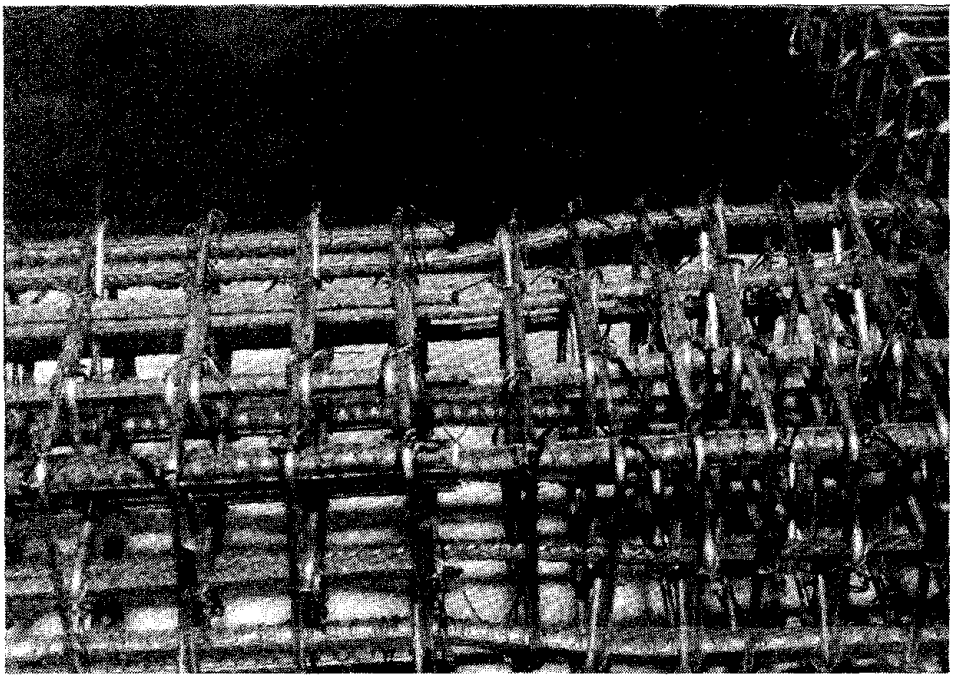

(b) Column

Figure 3.1 Detail of Reinforcement.

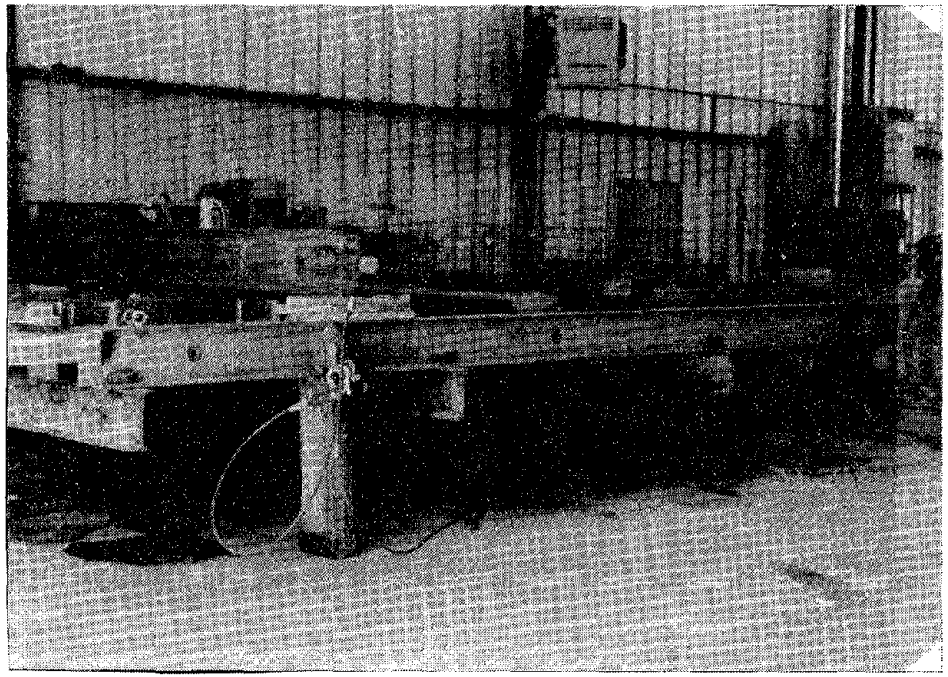

Figure 3.2 Pivoting Platform.

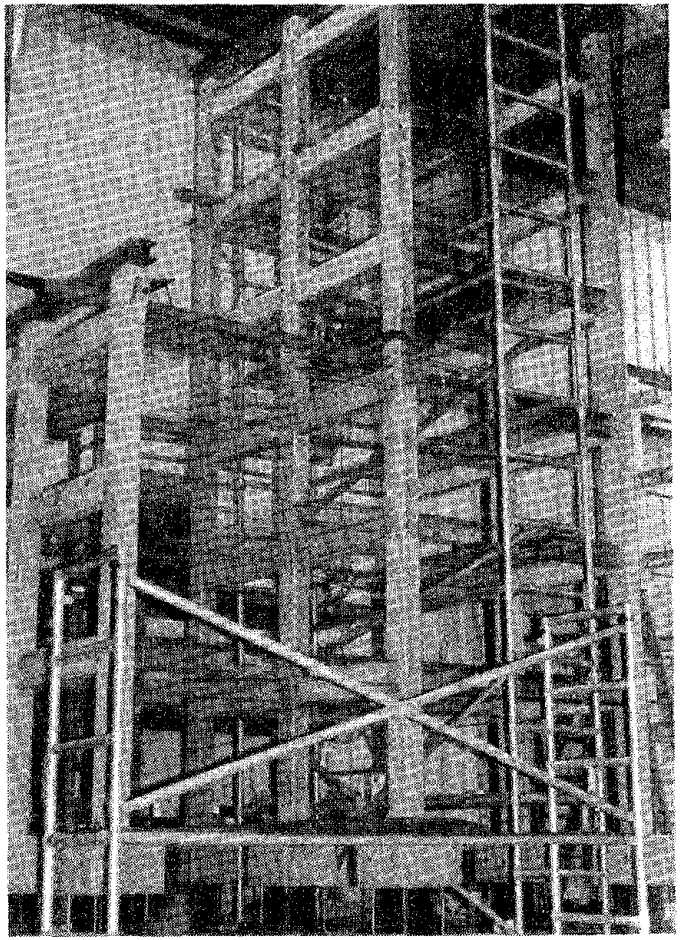

Figure 3.3 Short-Direction Frames on Steel Foundation.
(Before Casting the Long-Direction Frames).

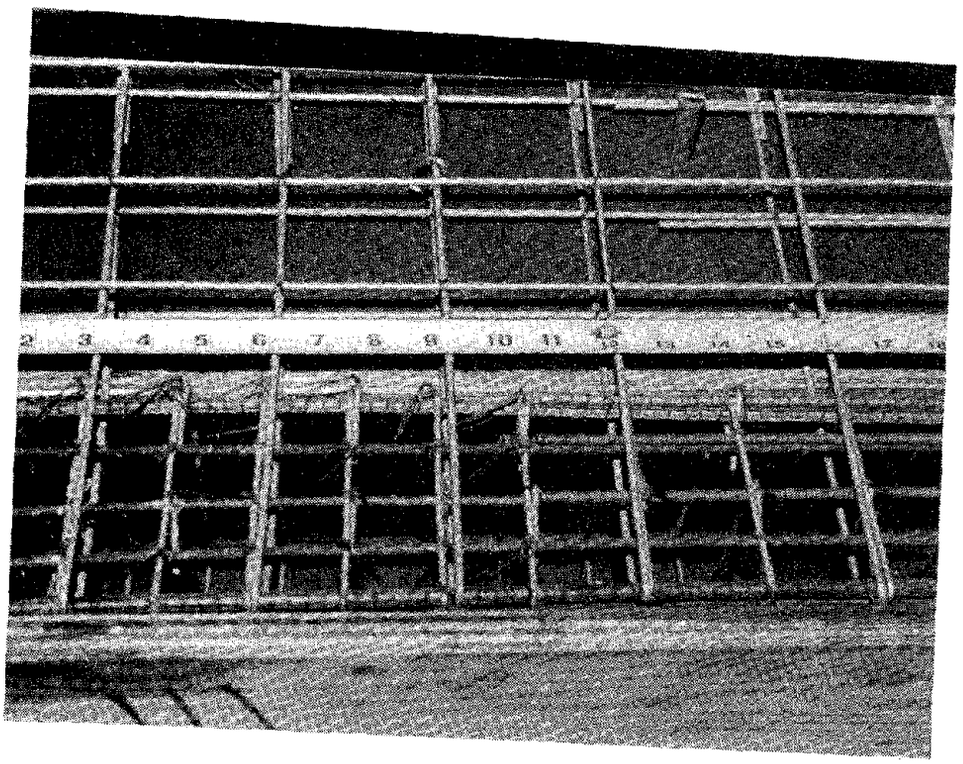

(a) Long-Direction Beam

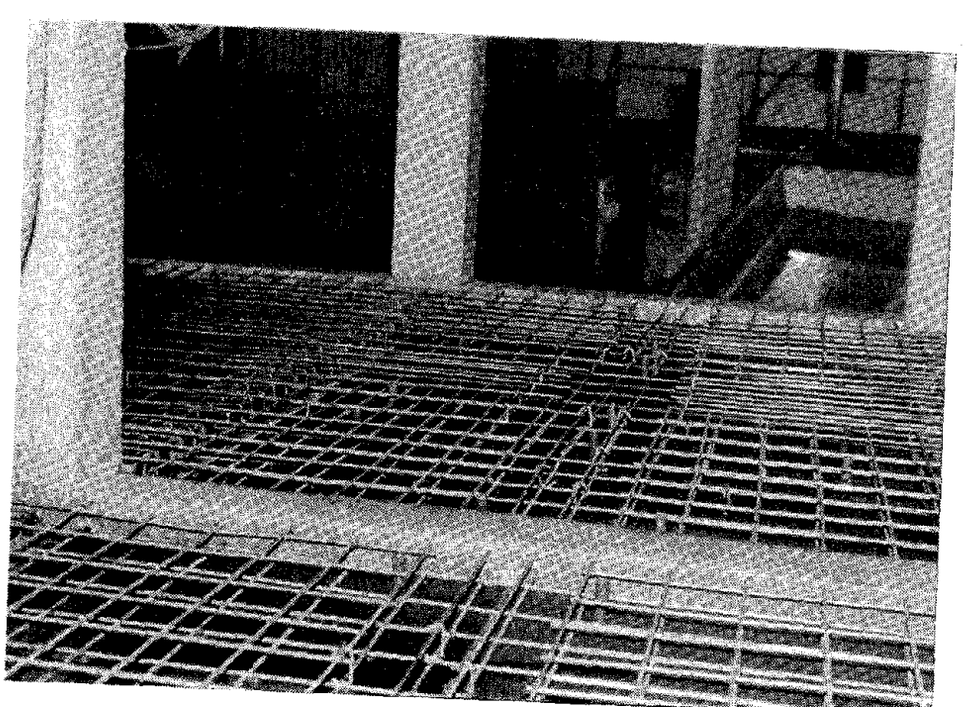

(b) Floor Slab

Figure 3.4 Detail of Reinforcement.

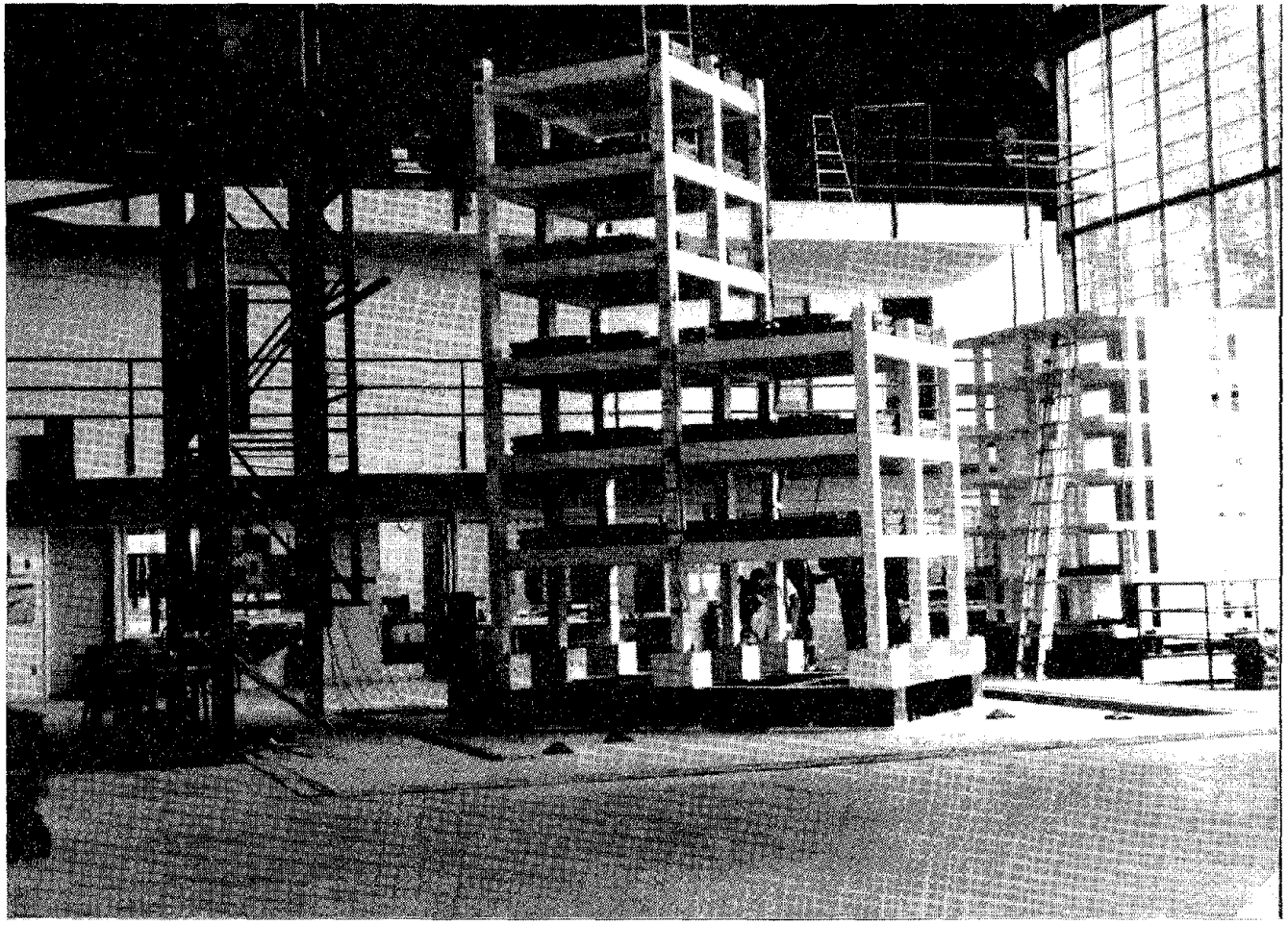

Figure 3.5 Test Structure on Shaking Table.

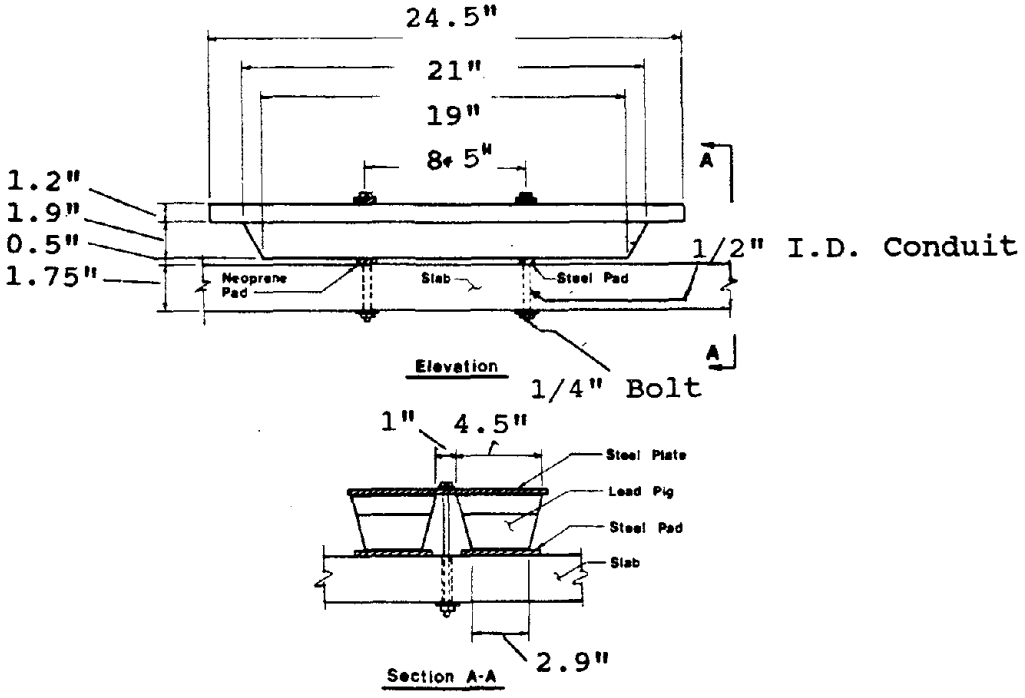

Figure 3.6(a) Lead Pigs Connection System [38].

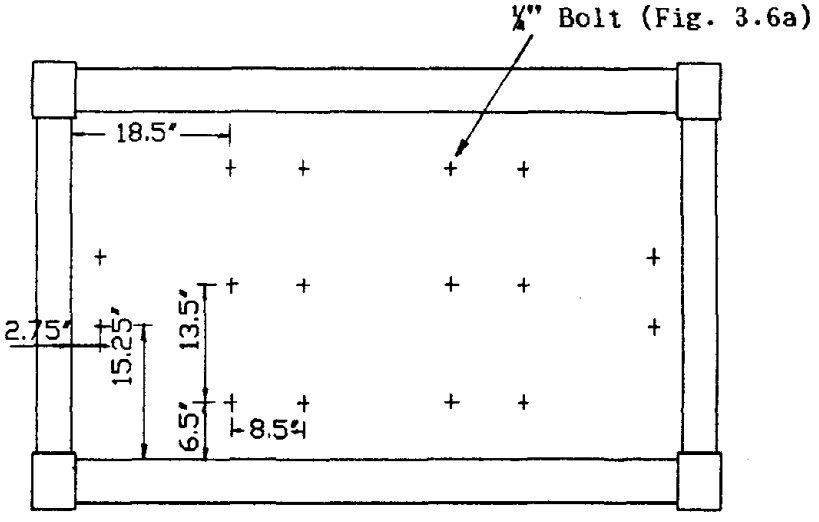

Figure 3.6 (b) Location of Lead Pigs.

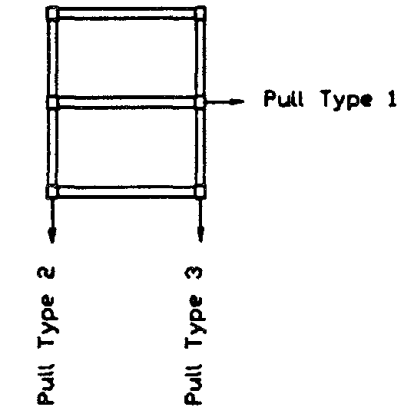

Roof Plan View

Pull Type	θ
1	36.6°
2	38.1°
3	35.3°

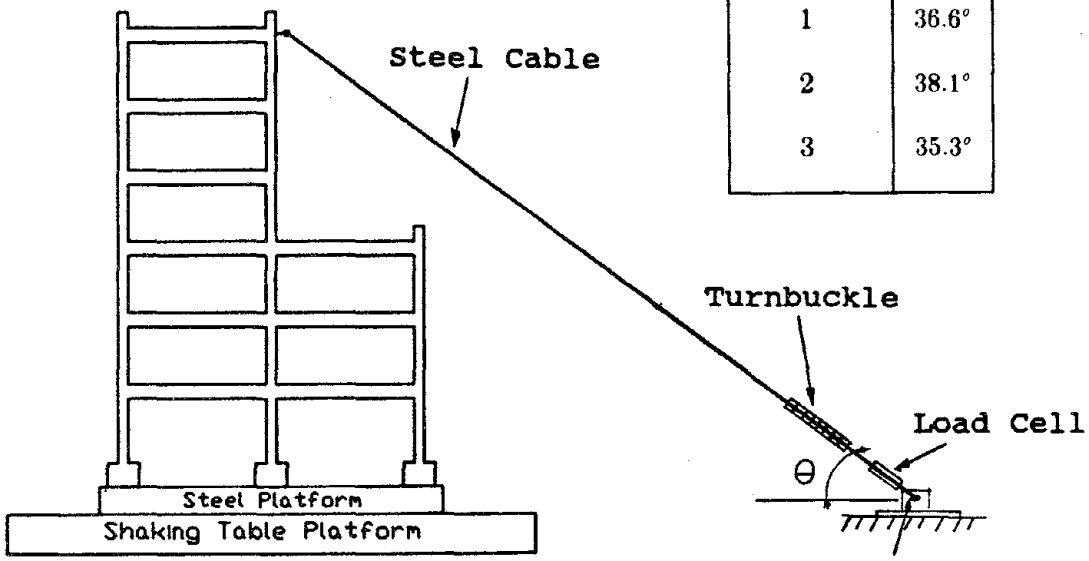

Typical Pull-back Set Up
(Pull Type 1)

Figure 3.7 Pull-Back and Free-Vibration Test Setup.

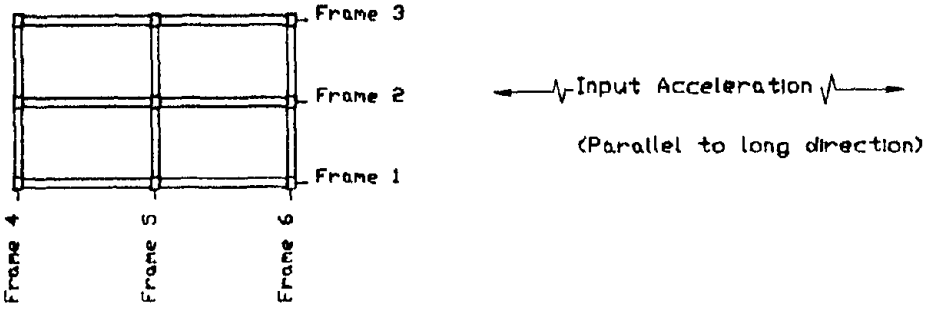

Phase 1

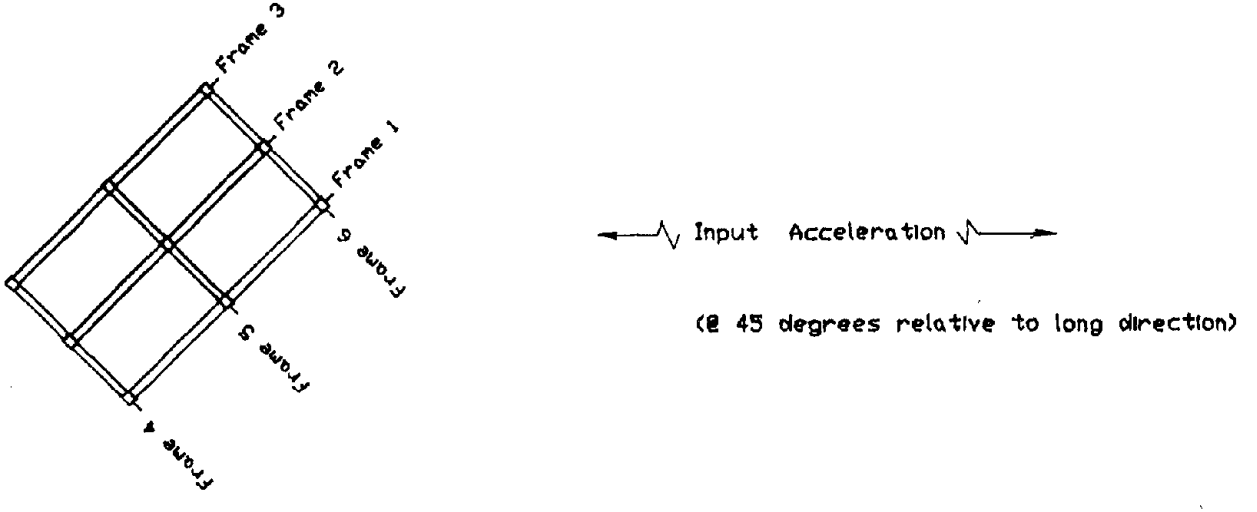

Phase 2

Figure 3.8 Orientation of Structure During Earthquake Simulations.

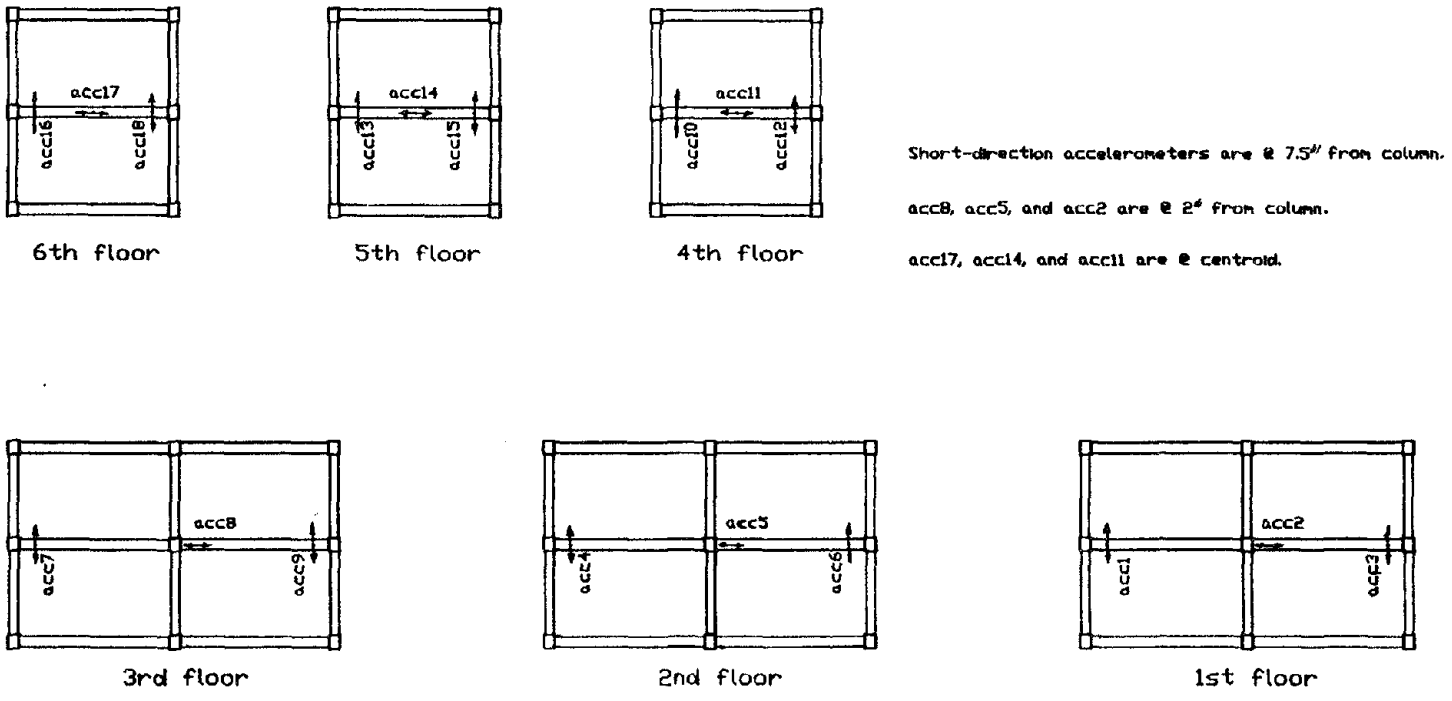

Figure 3.9 Location of Accelerometers.

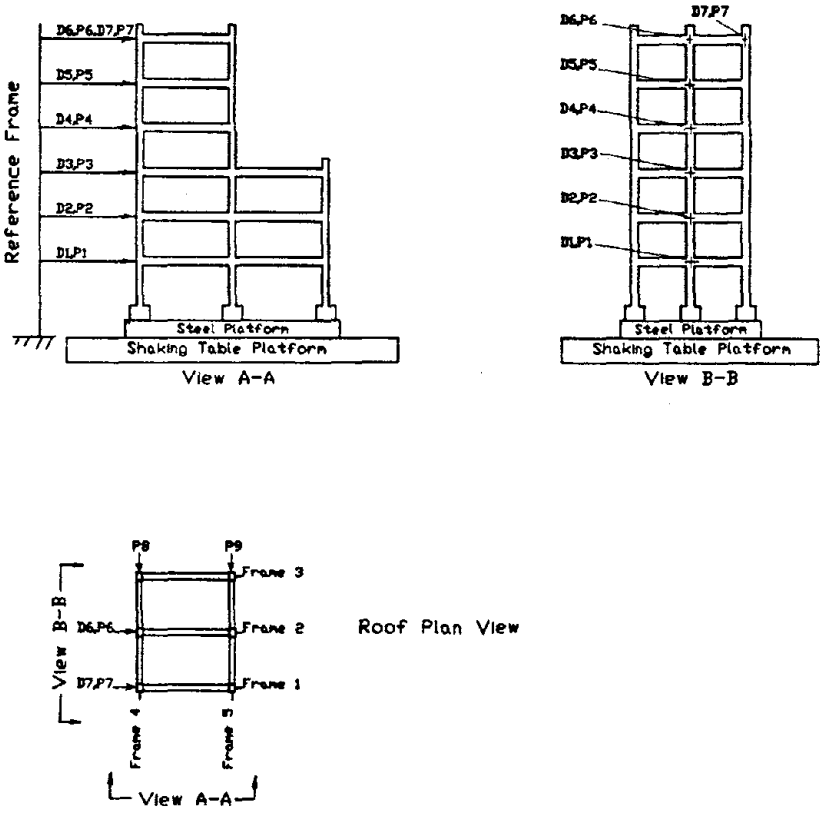

Figure 3.10(a) Instruments to Measure Lateral Displacements.

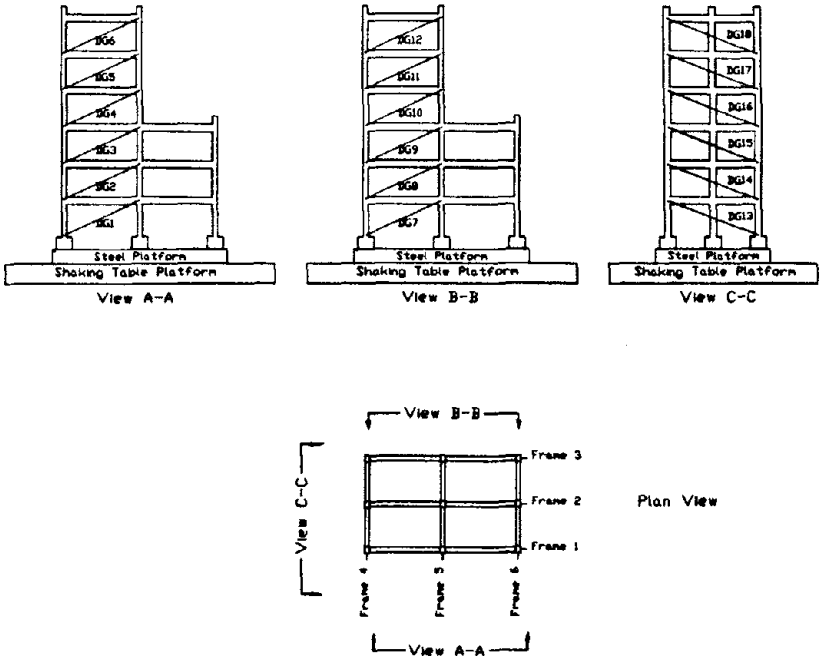

Figure 3.10(b) Instruments to Measure Diagonal Displacements.

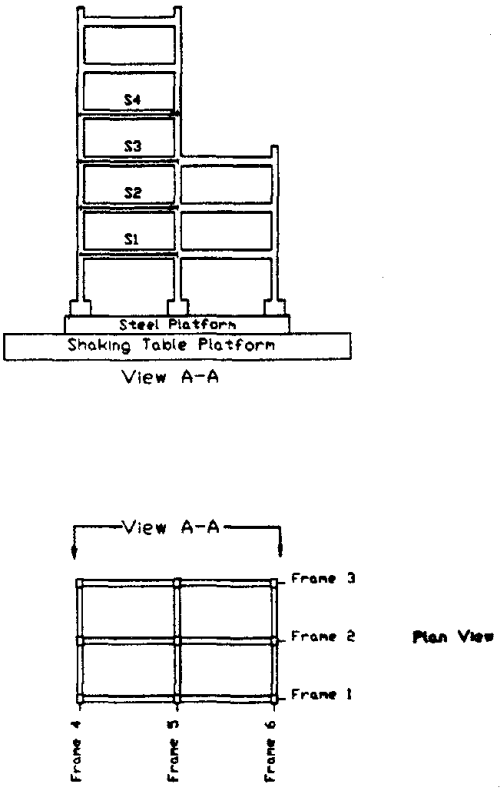

Figure 3.11(a) Instruments to Measure Slab Growth.

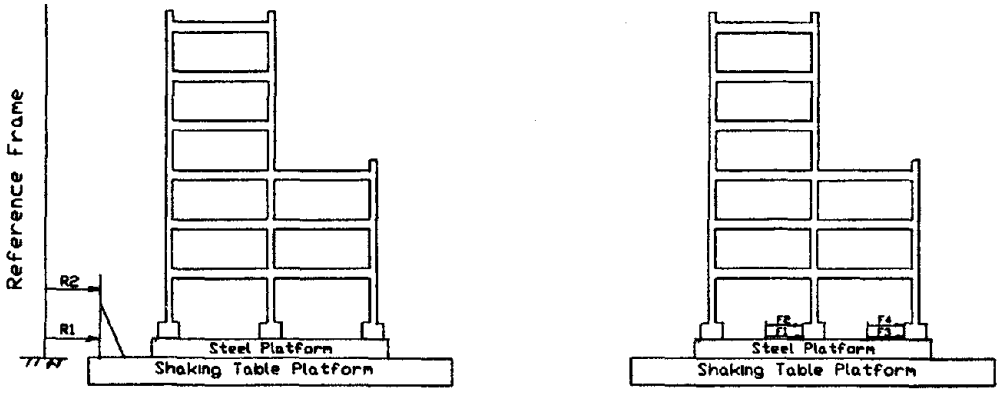

Figure 3.11(b) Instruments to Measure Shaking Table Rocking and Footing Displacements.

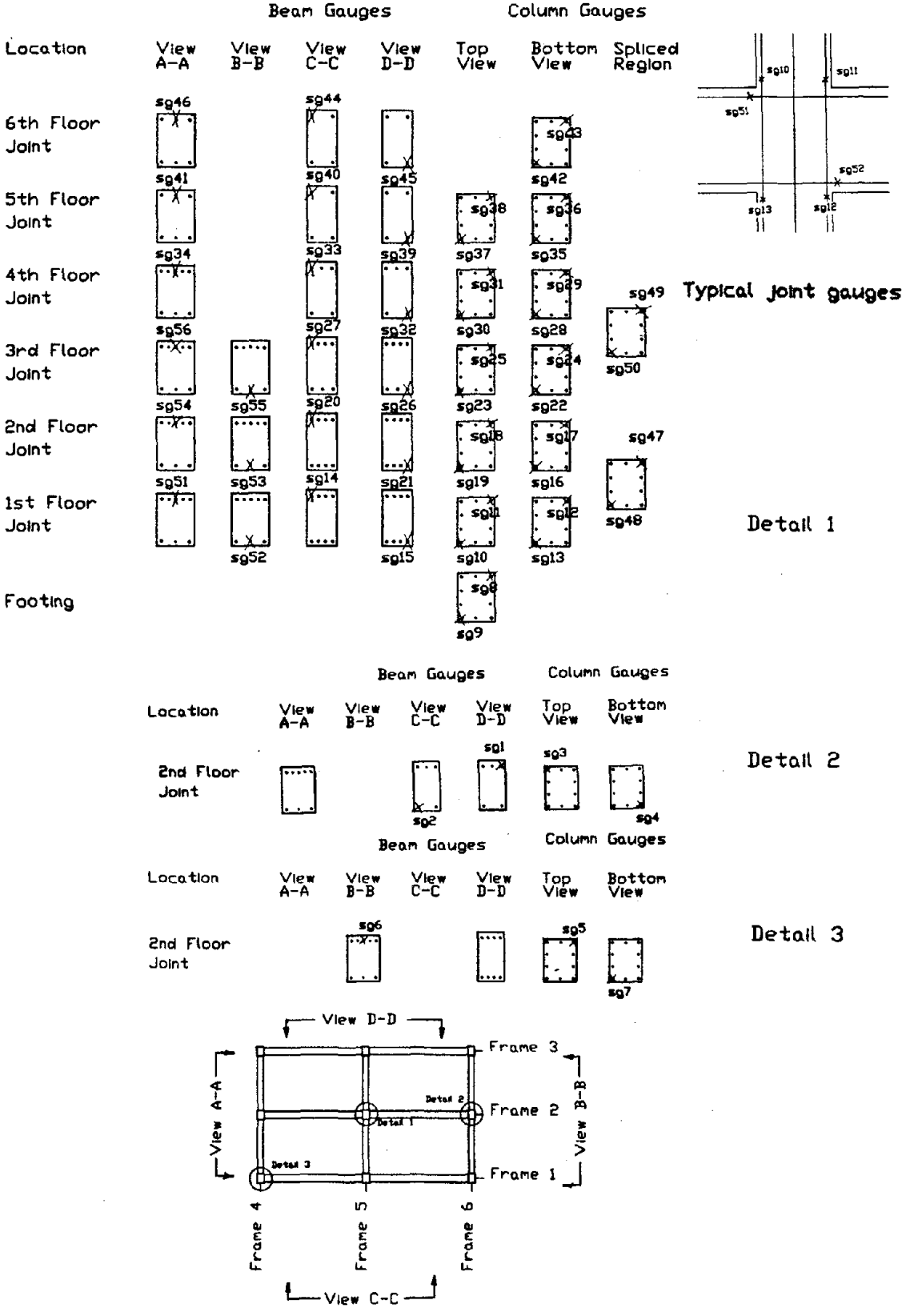

Figure 3.12 Location of Stain Gauges.

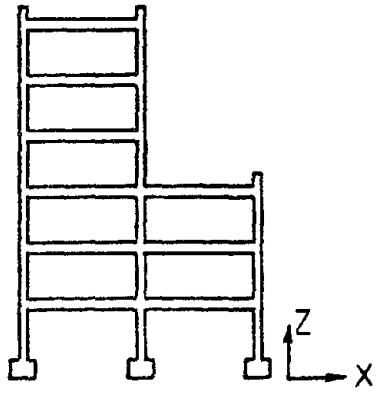

Elevation view

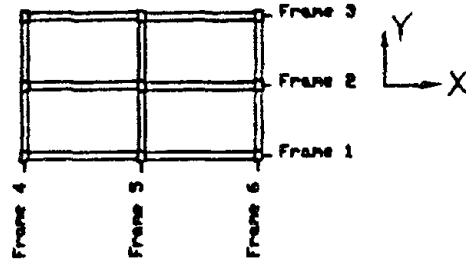

Plan view

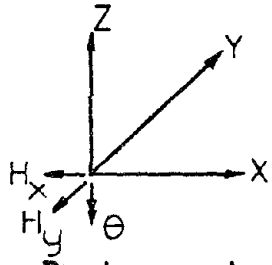

Displacements

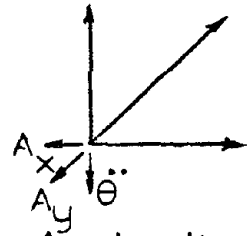

Accelerations

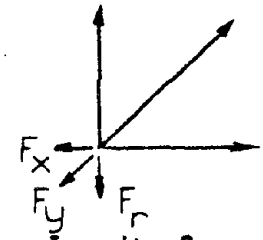

Inertia forces

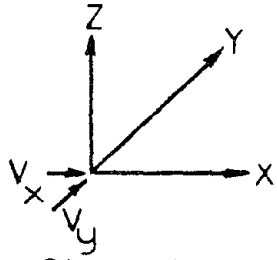

Story shears

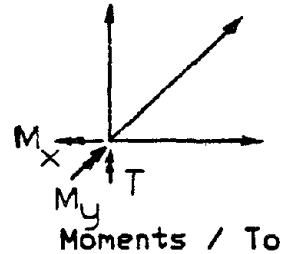

Moments / Torques

Figure 4.1 Sign Convention.

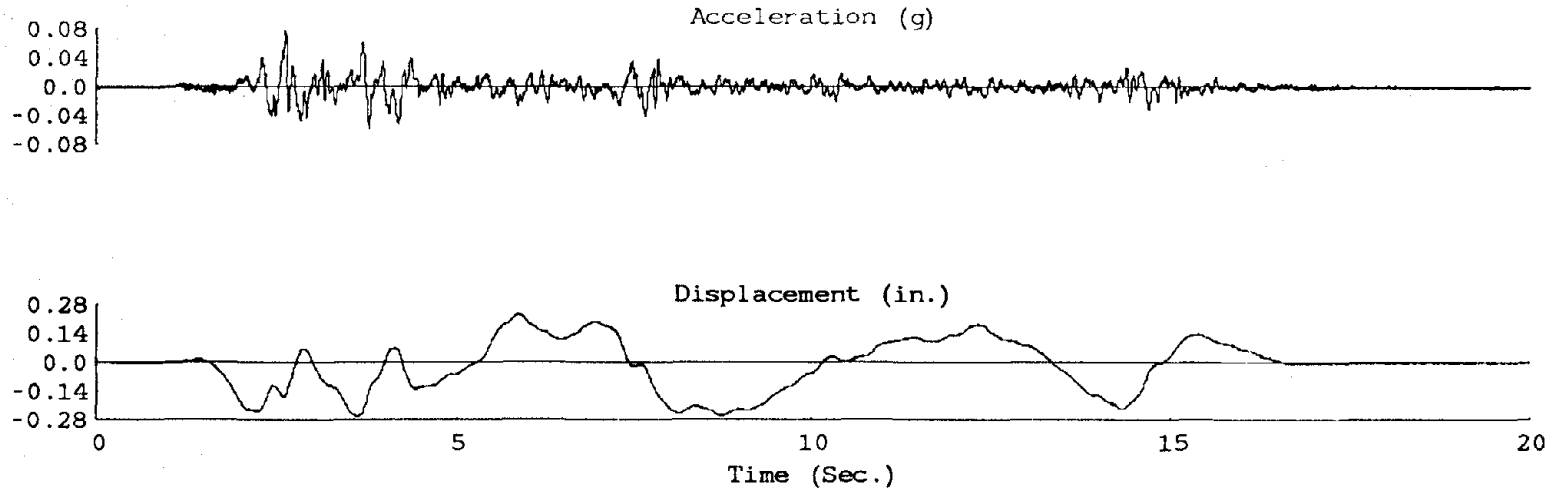

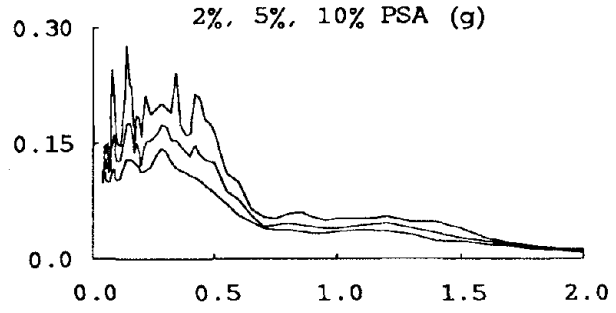

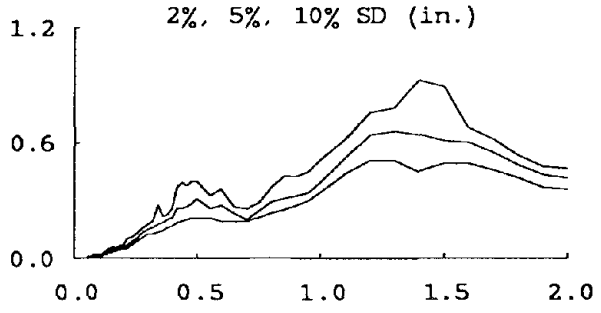

Figure 4.2(a) Input Motion Acceleration, Displacement, and Linear Elastic Spectra. (EC7.7L)

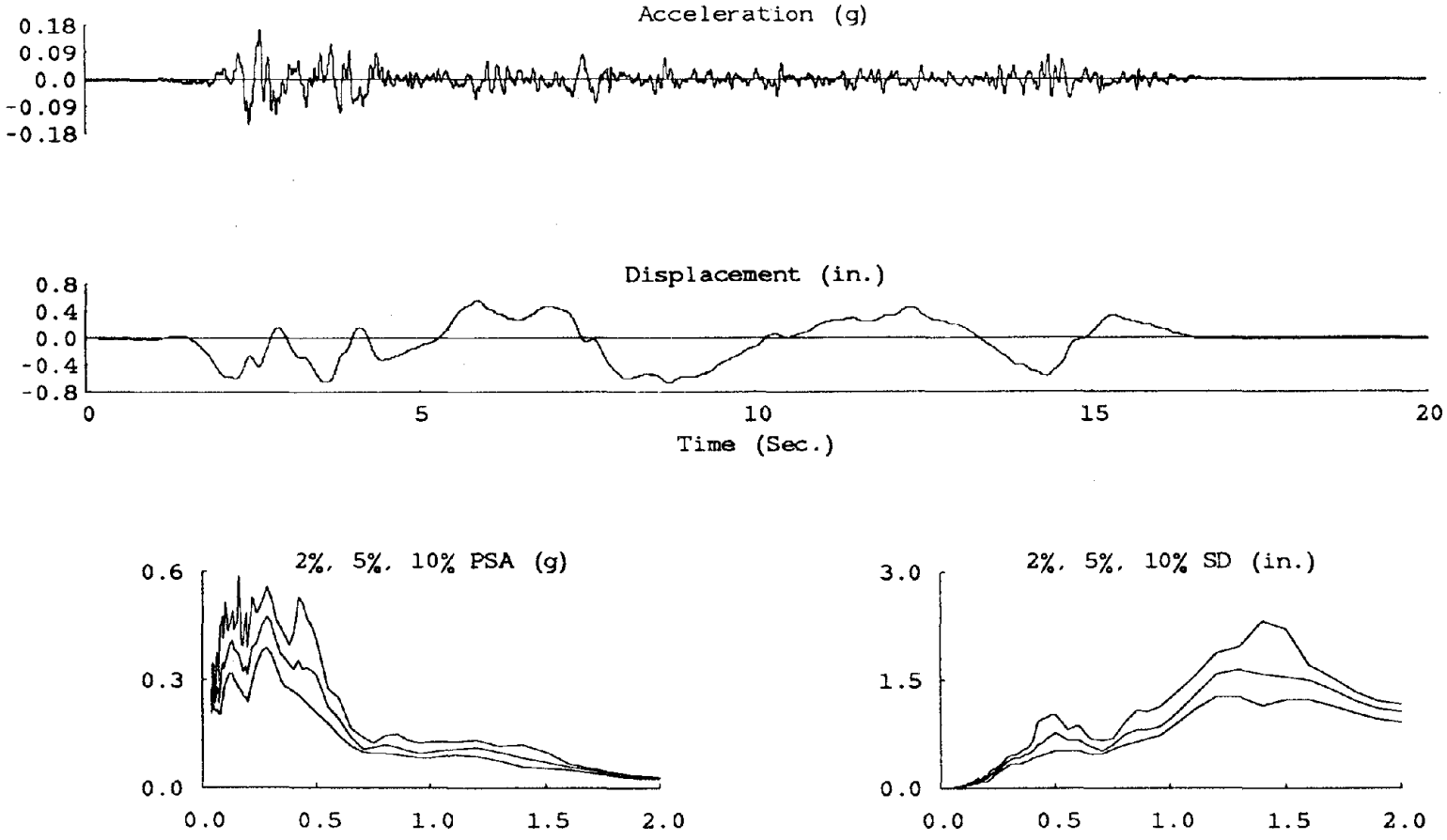

Figure 4.2(b) Input Motion Acceleration, Displacement, and Linear Elastic Spectra. (EC16.6L)

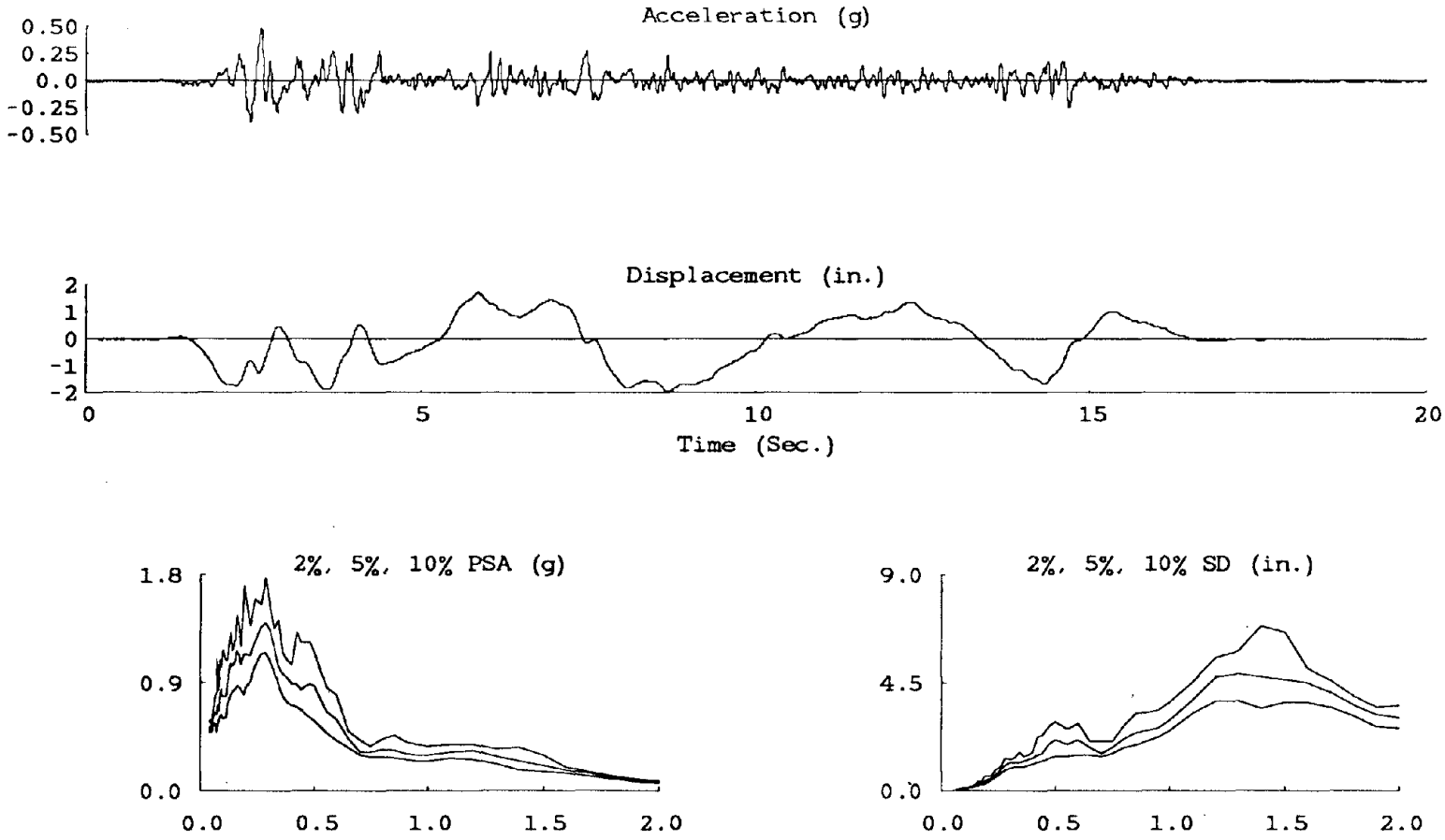

Figure 4.2(c) Input Motion Acceleration, Displacement, and Linear Elastic Spectra. (EC49.3L)

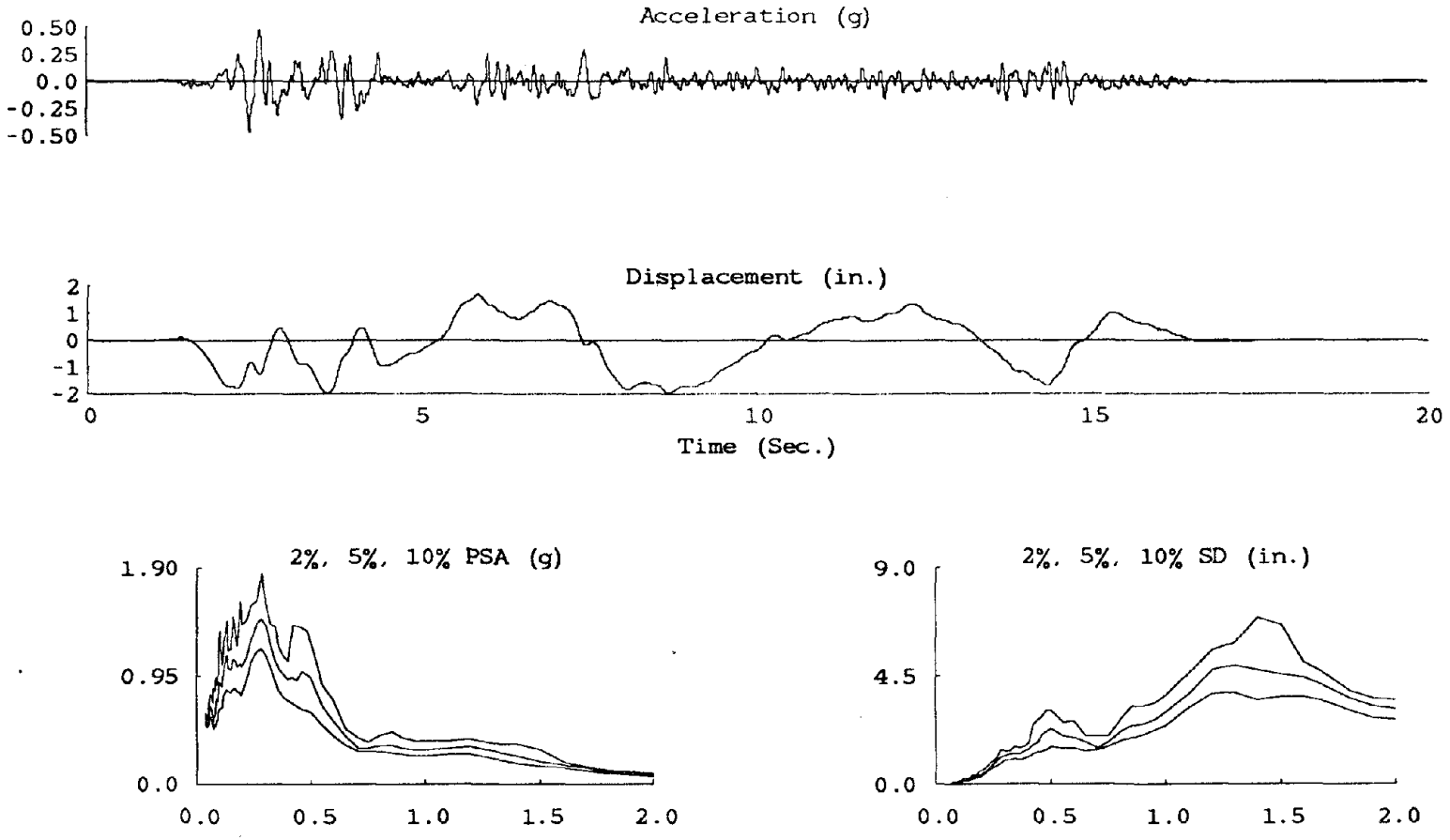

Figure 4.2(d) Input Motion Acceleration, Displacement, and Linear Elastic Spectra. (EC47.7B)

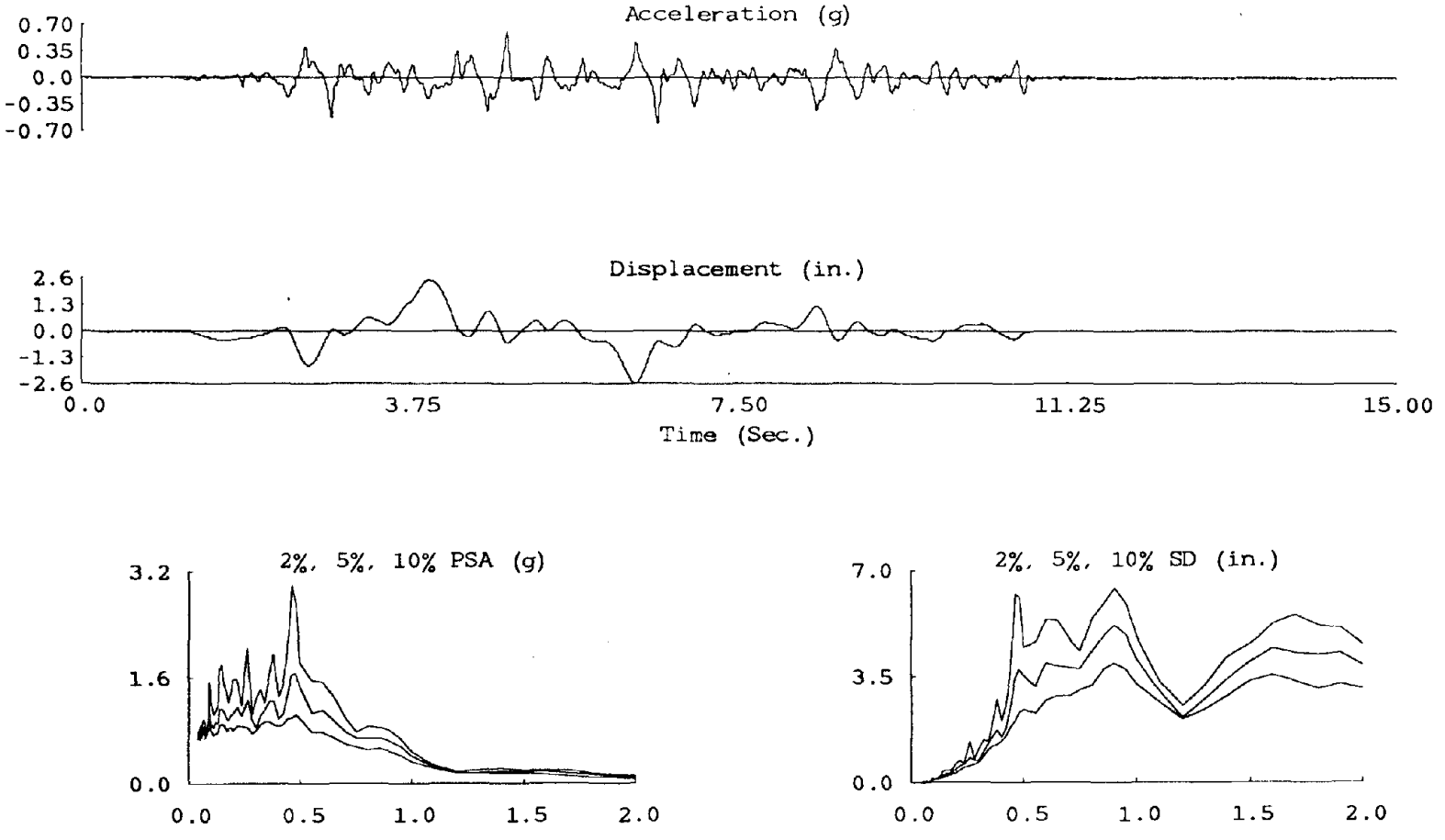

Figure 4.2(e) Input Motion Acceleration, Displacement, and Linear Elastic Spectra. (MO63.4B)

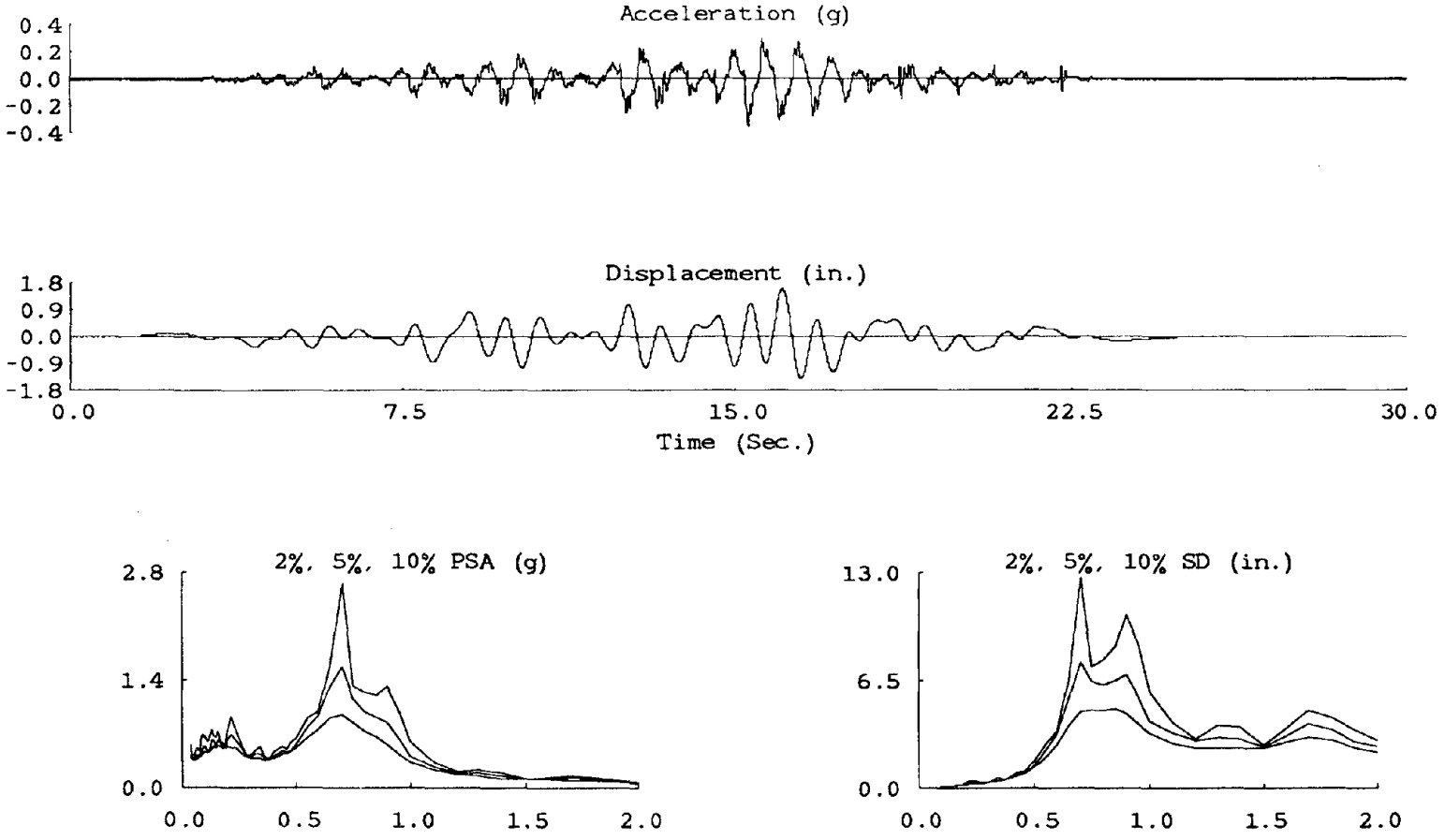

Figure 4.2(f) Input Motion Acceleration, Displacement, and Linear Elastic Spectra. (MX34.6B)

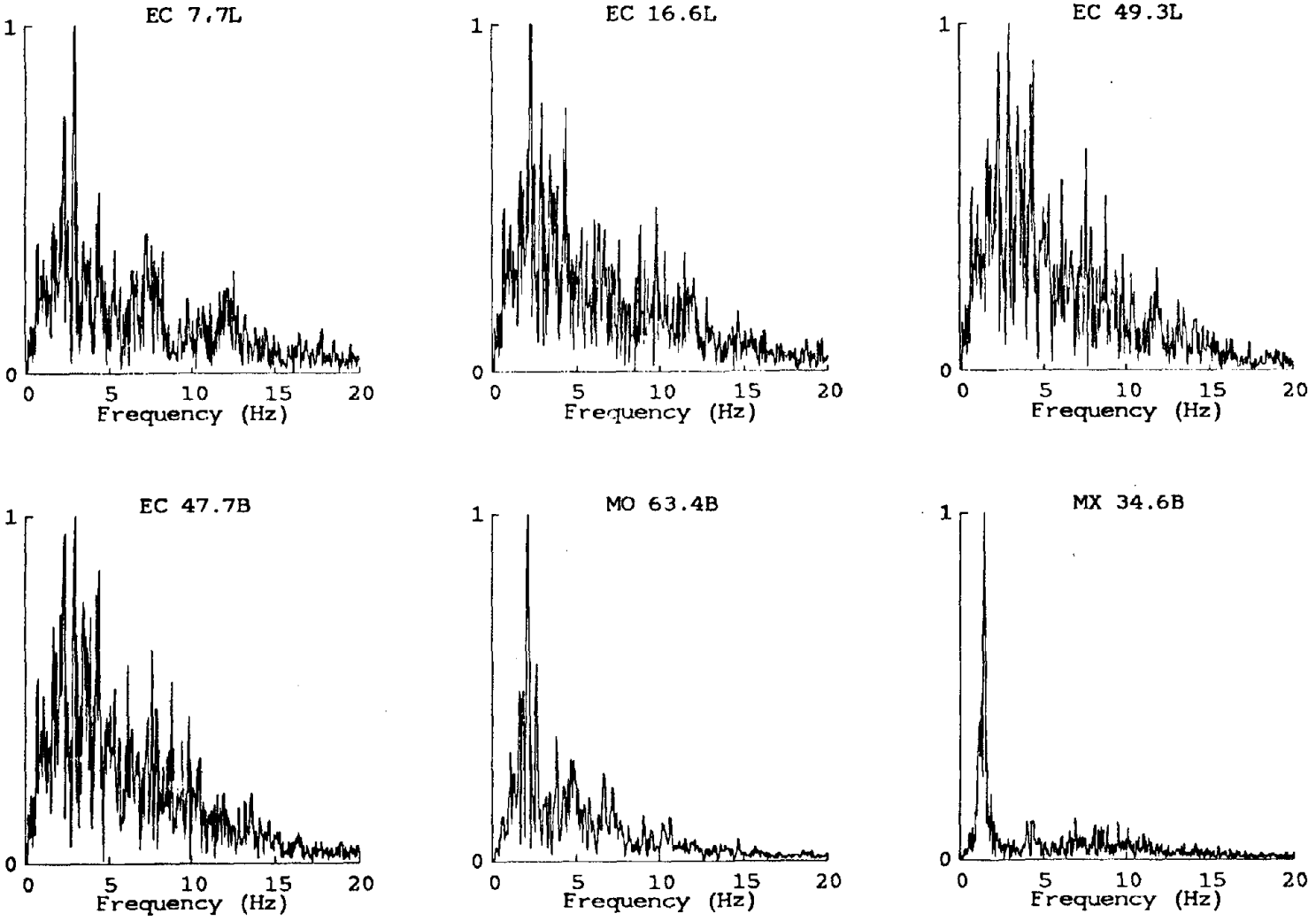

Figure 4.3 Normalized Fourier Amplitude Spectra.

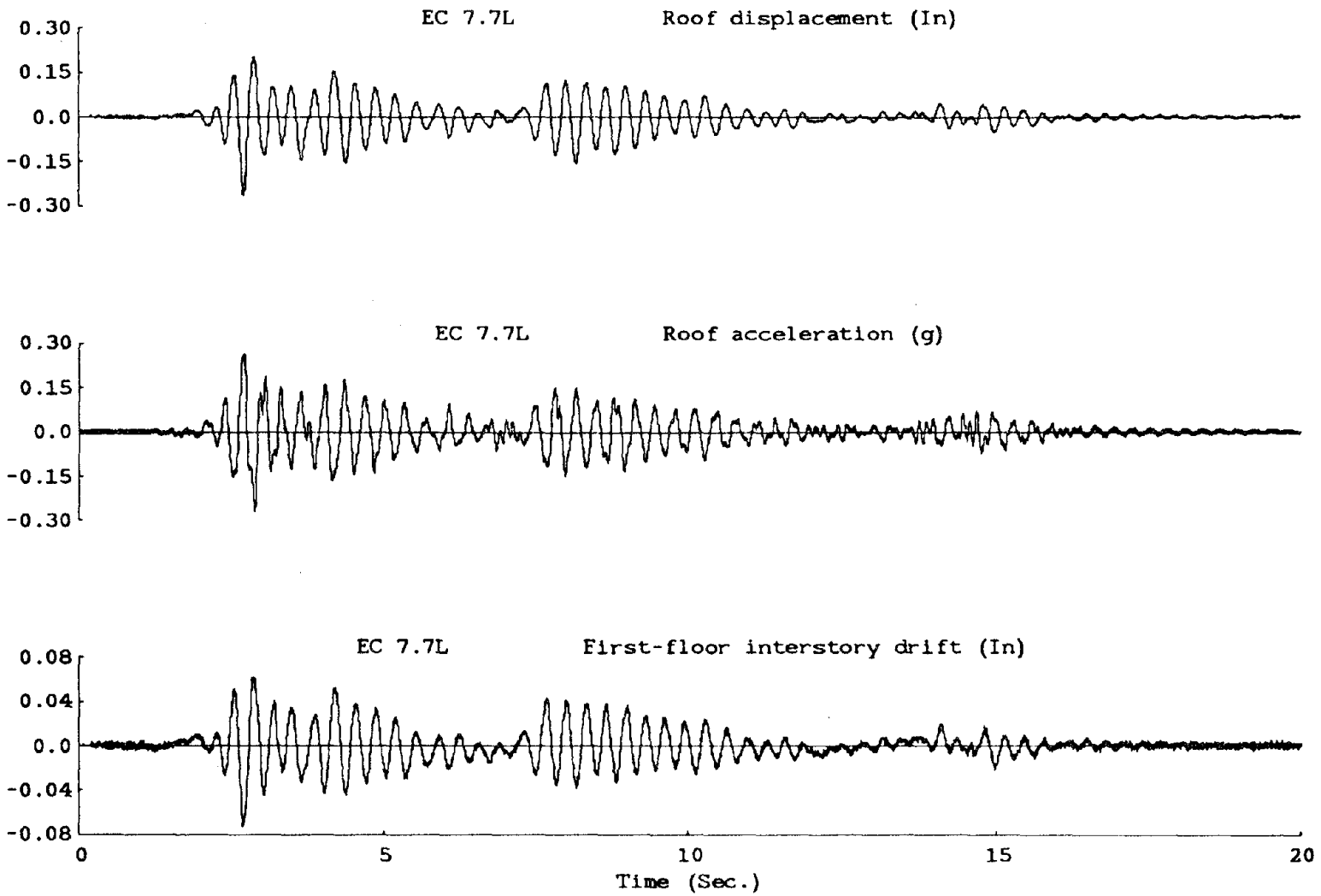

Figure 4.4(a) Response Histories (EC7.7L).

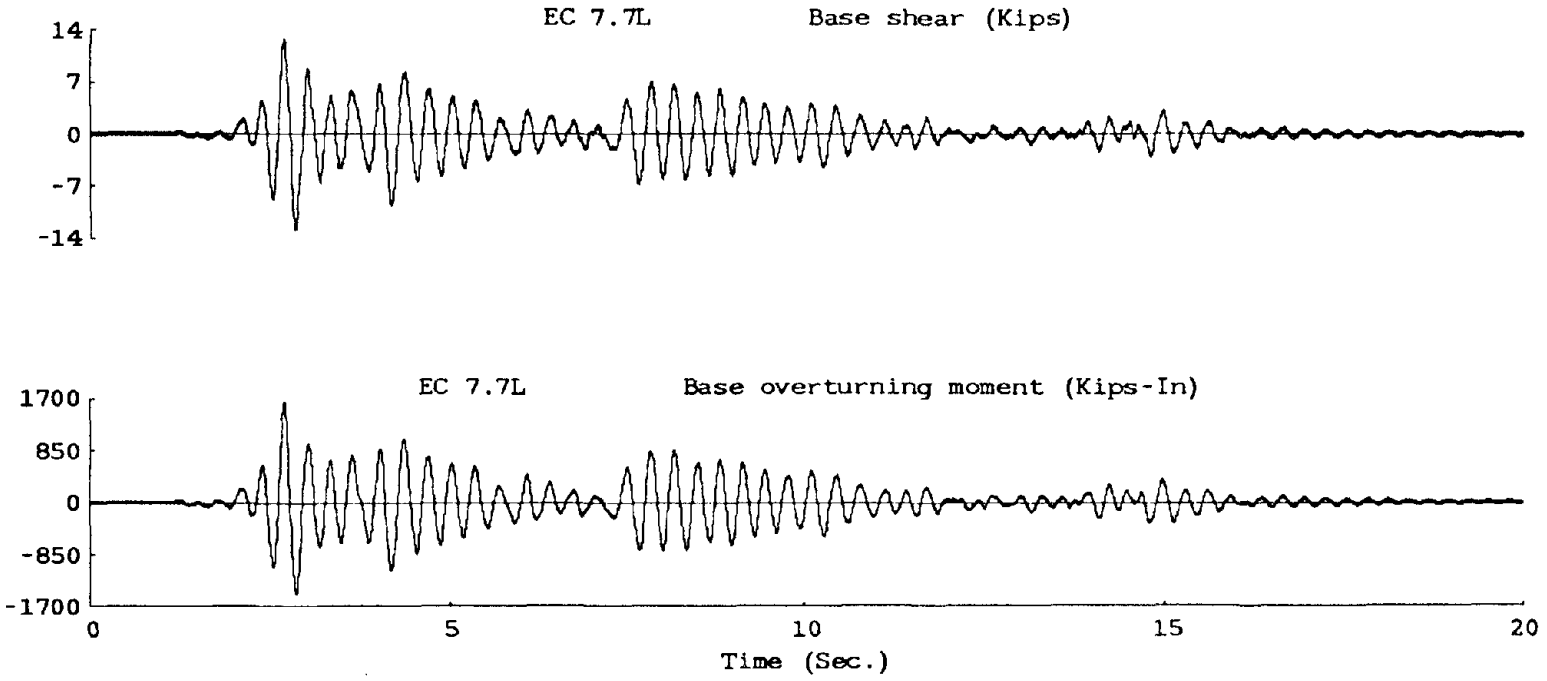

Figure 4.4a (Cont.) Response Histories (EC7.7L).

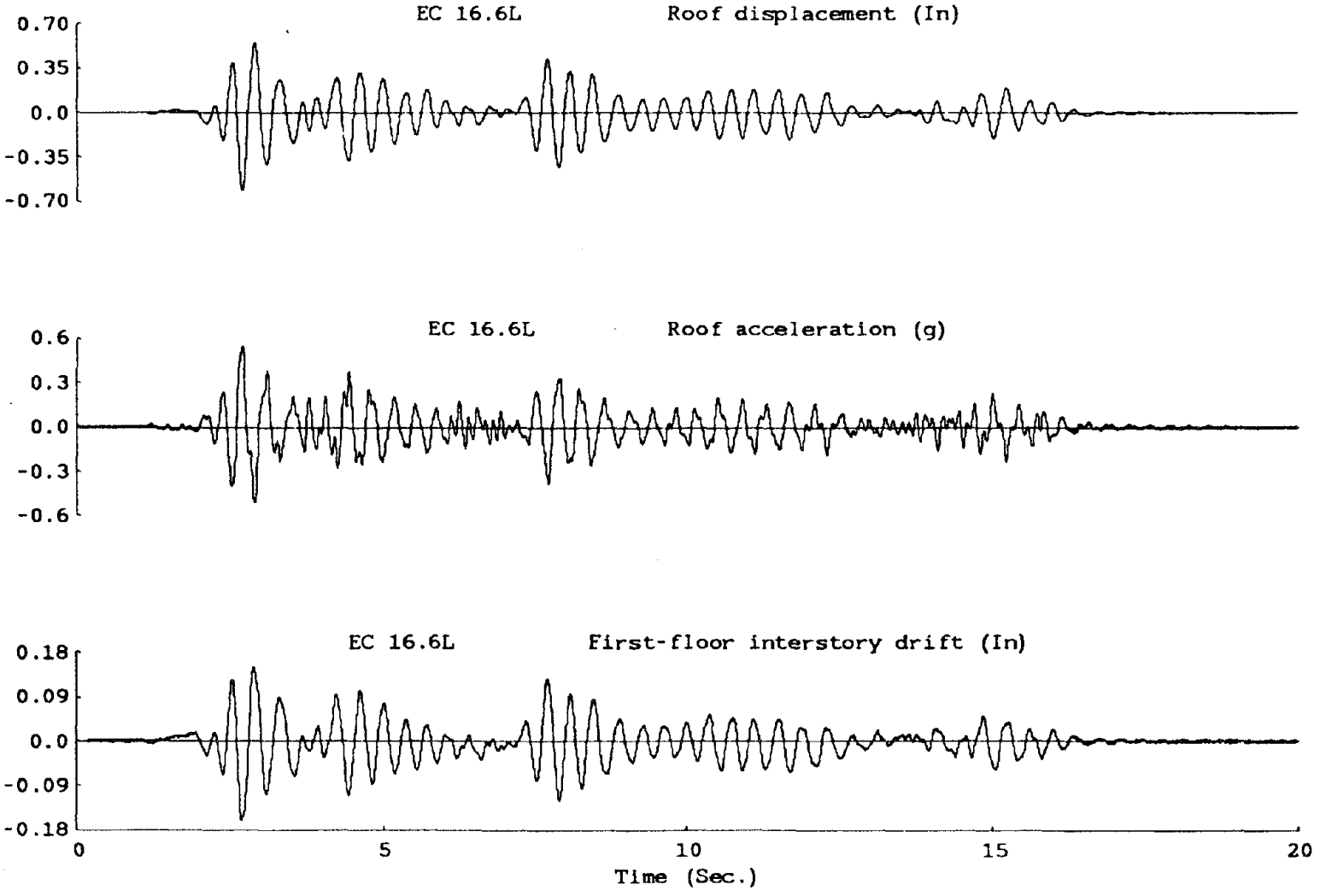

Figure 4.4(b) Response Histories (EC16.6L).

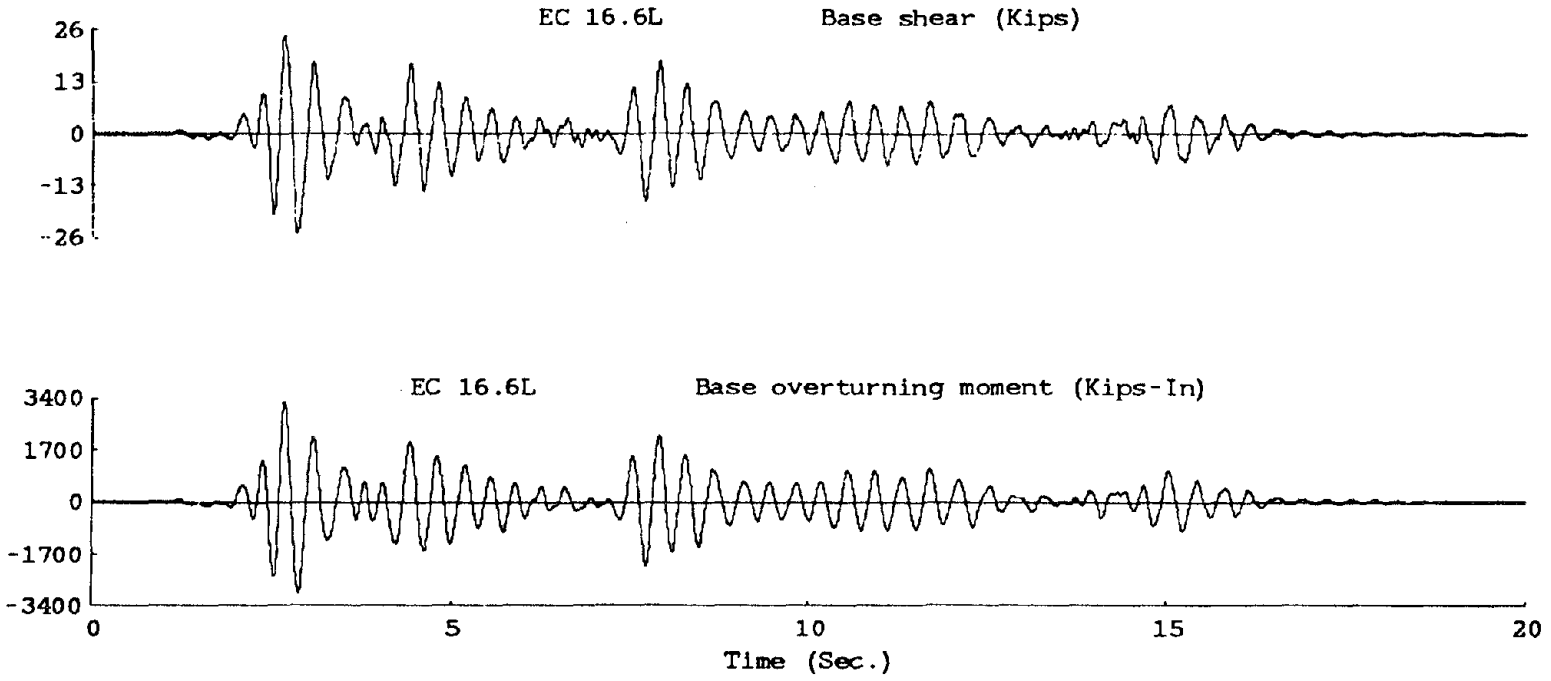

Figure 4.4b (Cont.) Response Histories (EC16.6L).

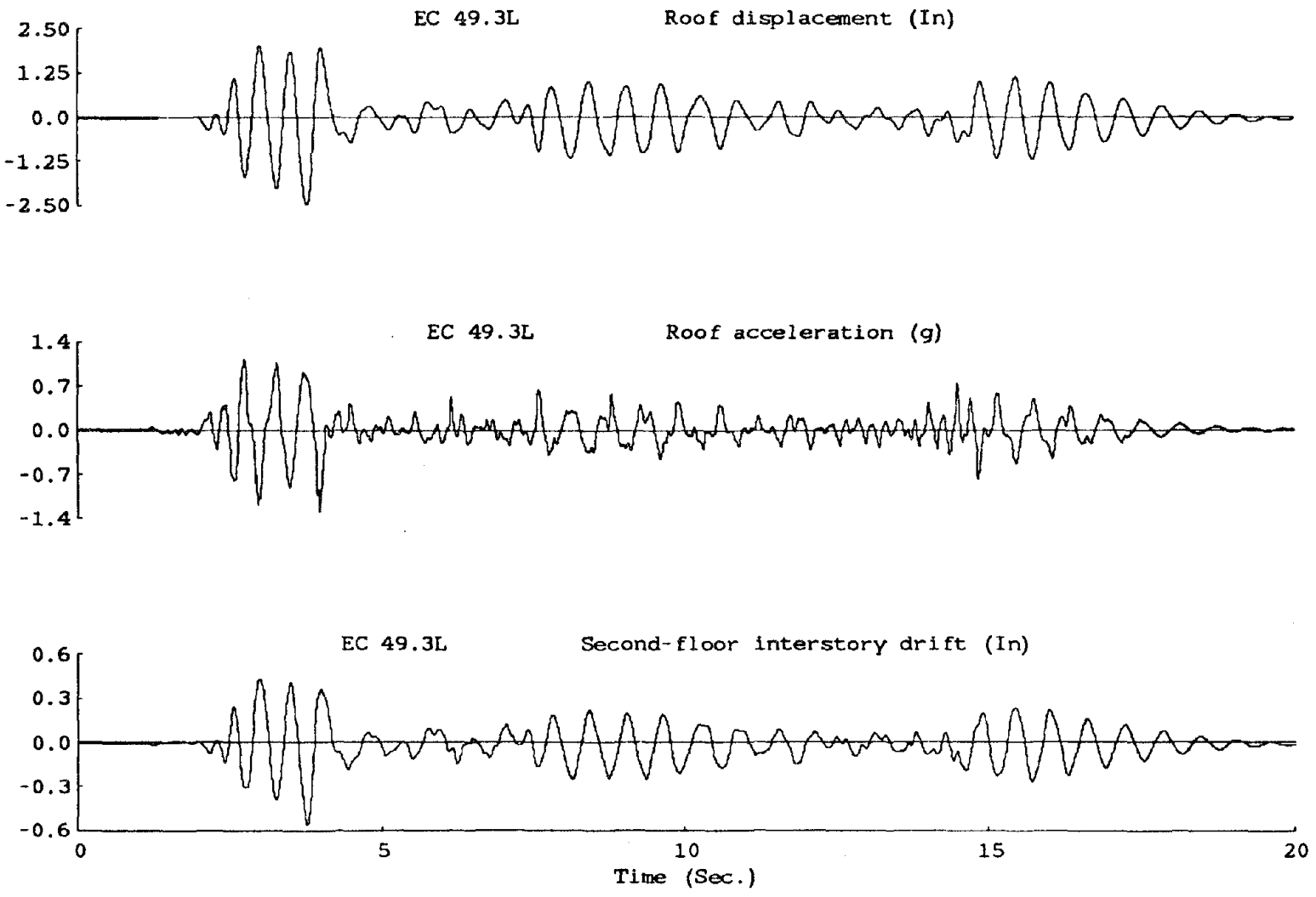

Figure 4.4(c) Response Histories (EC49.3L).

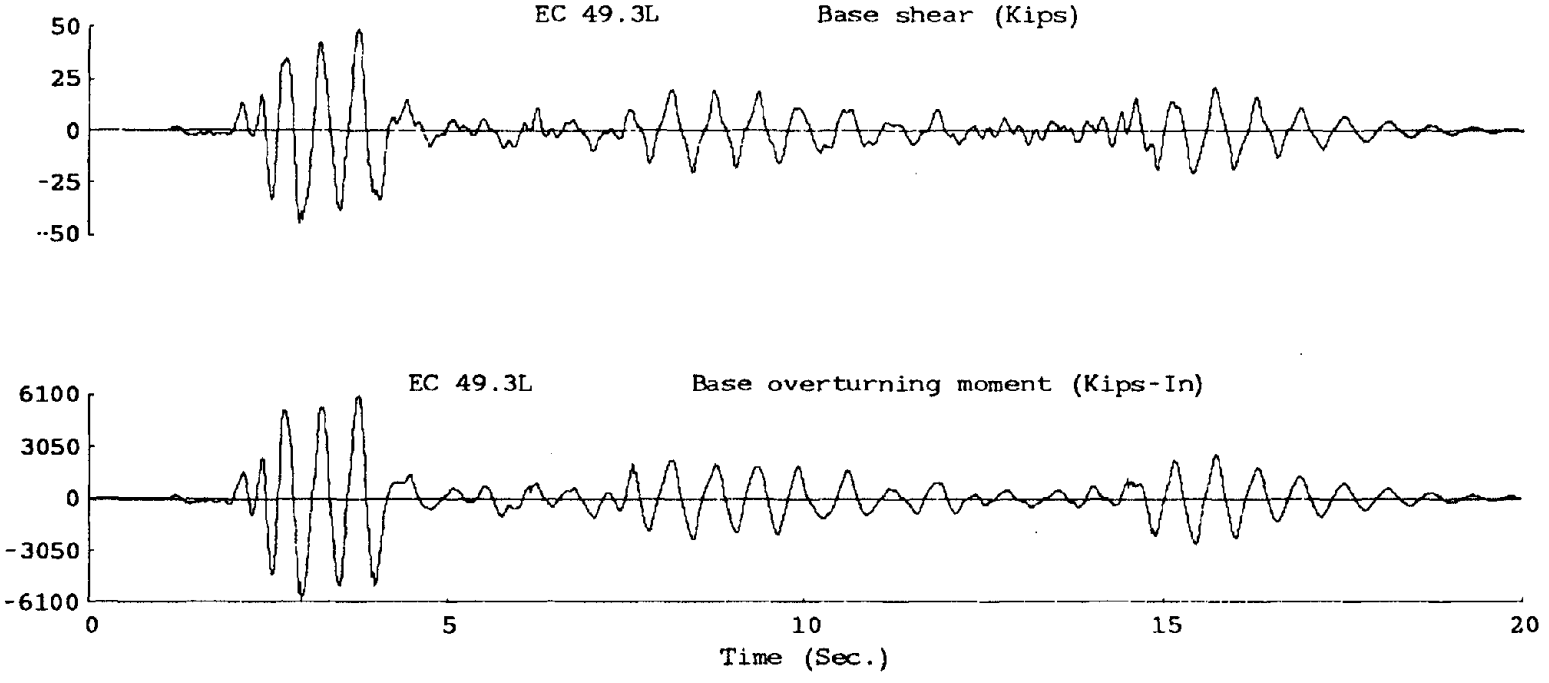

Figure 4.4c (Cont.) Response Histories (EC49.3L).

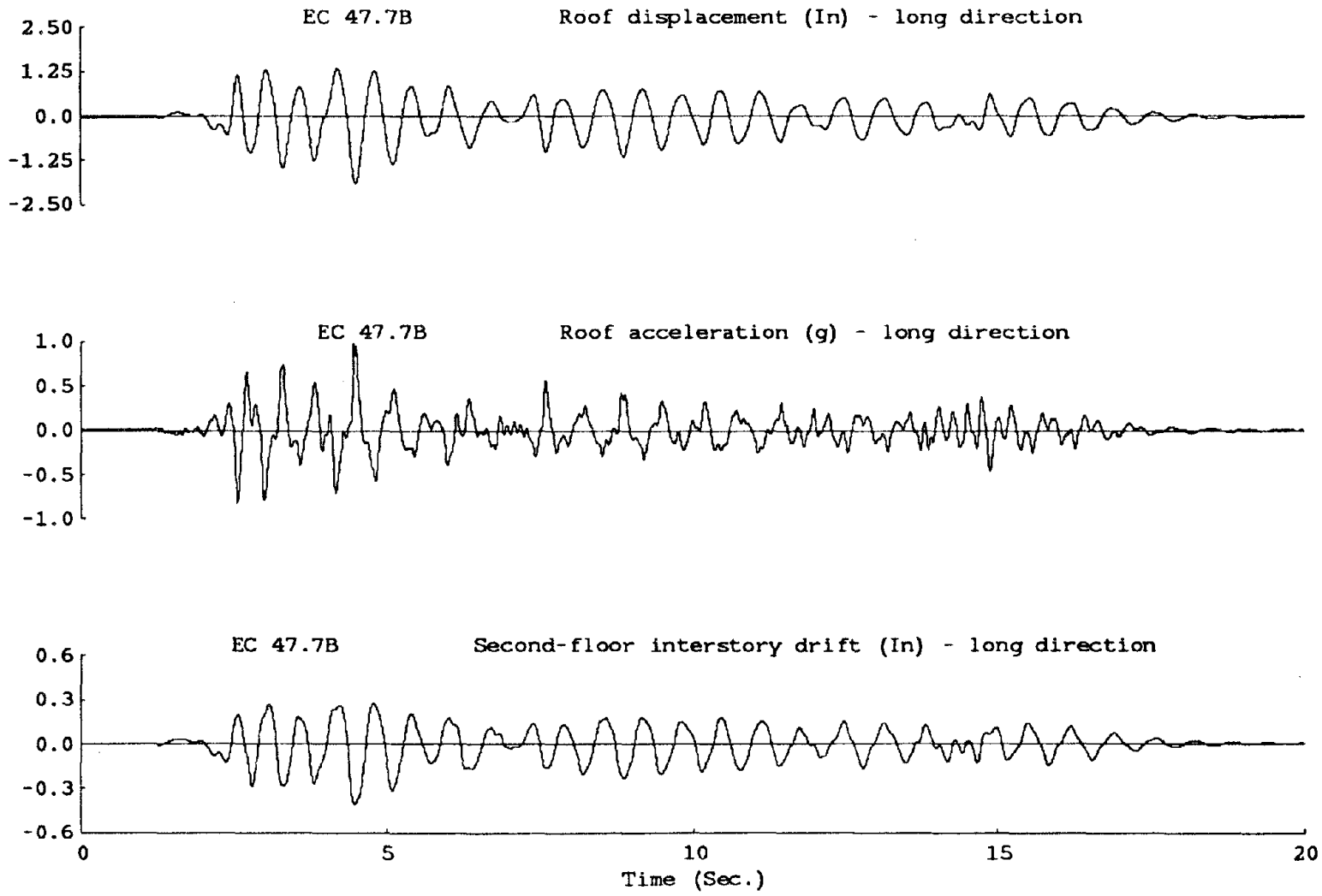

Figure 4.4(d) Response Histories (EC47.7B, Long Direction).

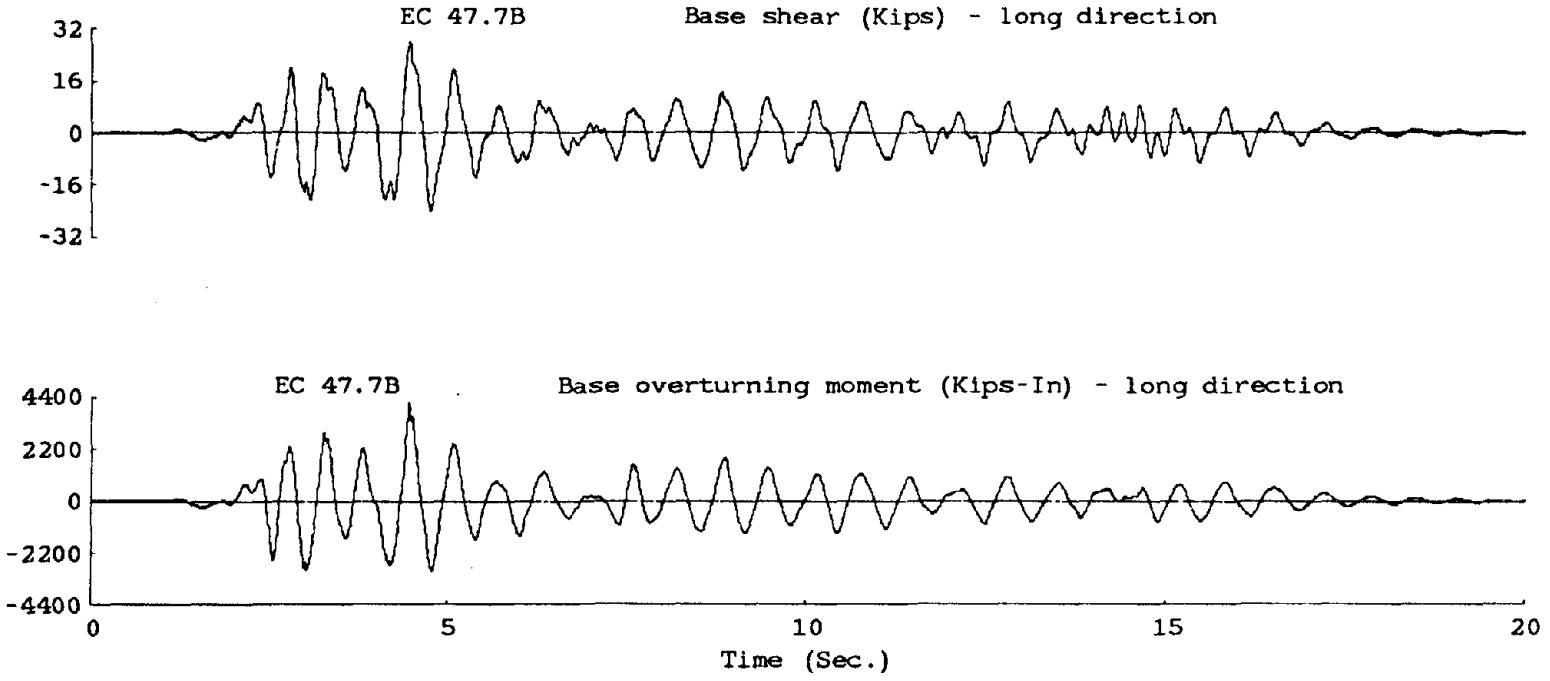

Figure 4.4d (Cont.) Response Histories (EC47.7B, Long Direction).

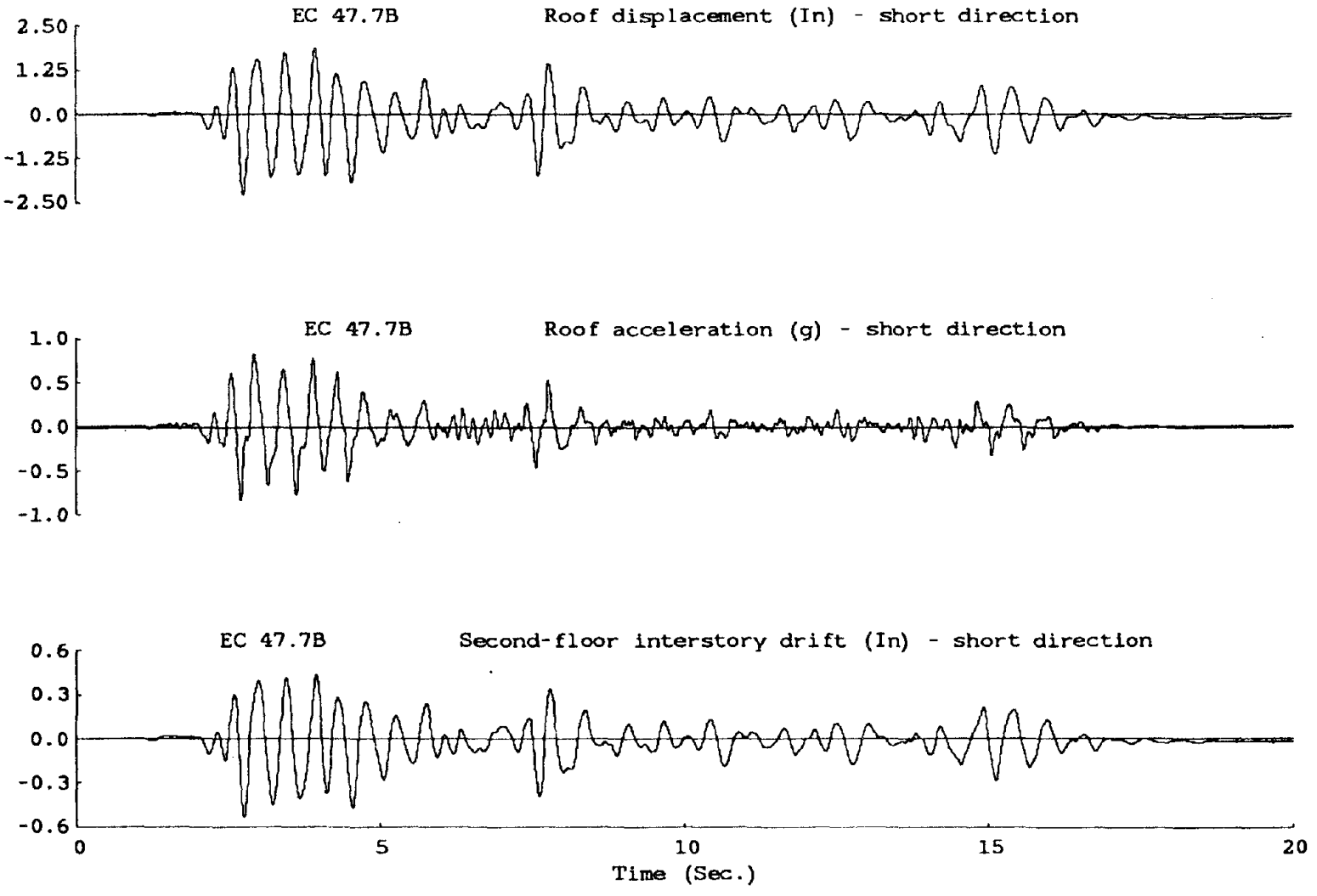

Figure 4.4(e) Response Histories (EC47.7B, Short Direction).

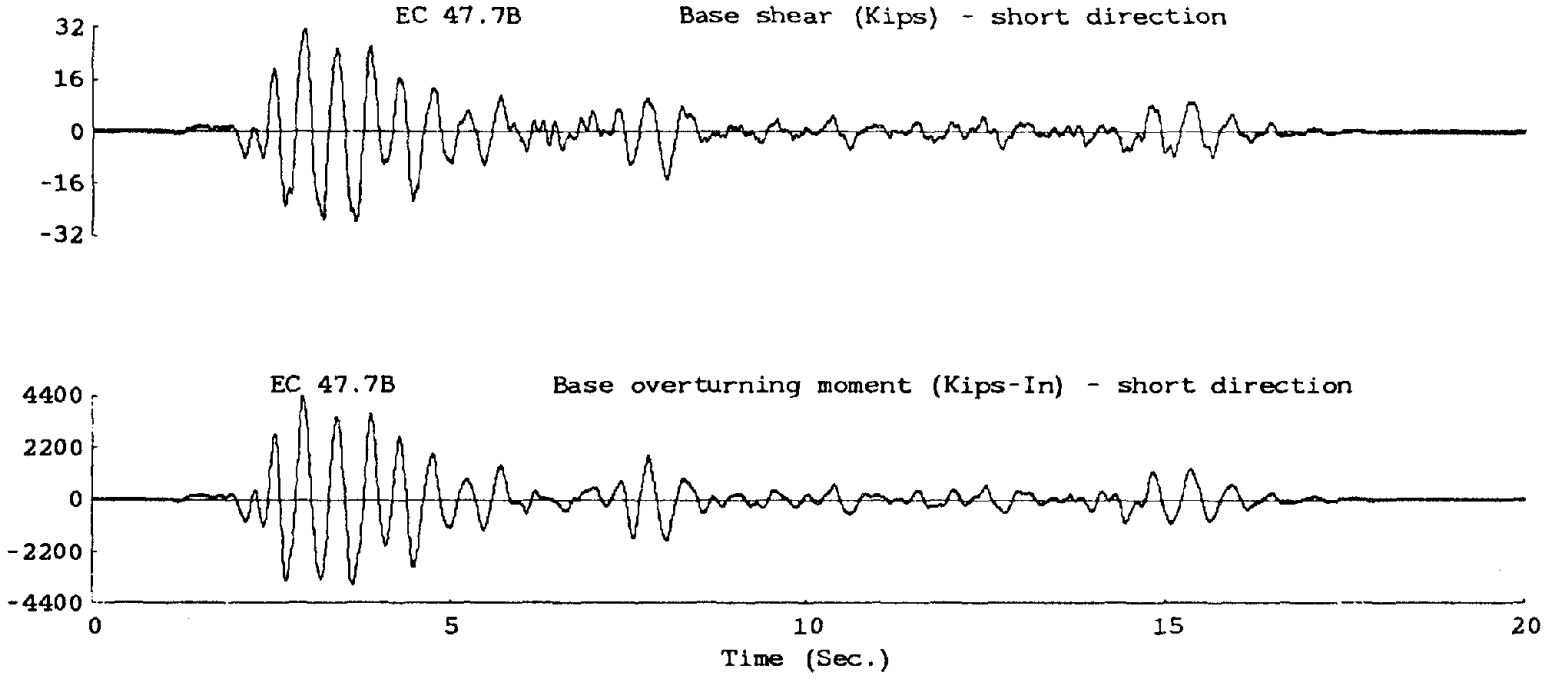

Figure 4.4e (Cont.) Response Histories (EC47.7B, Short Direction).

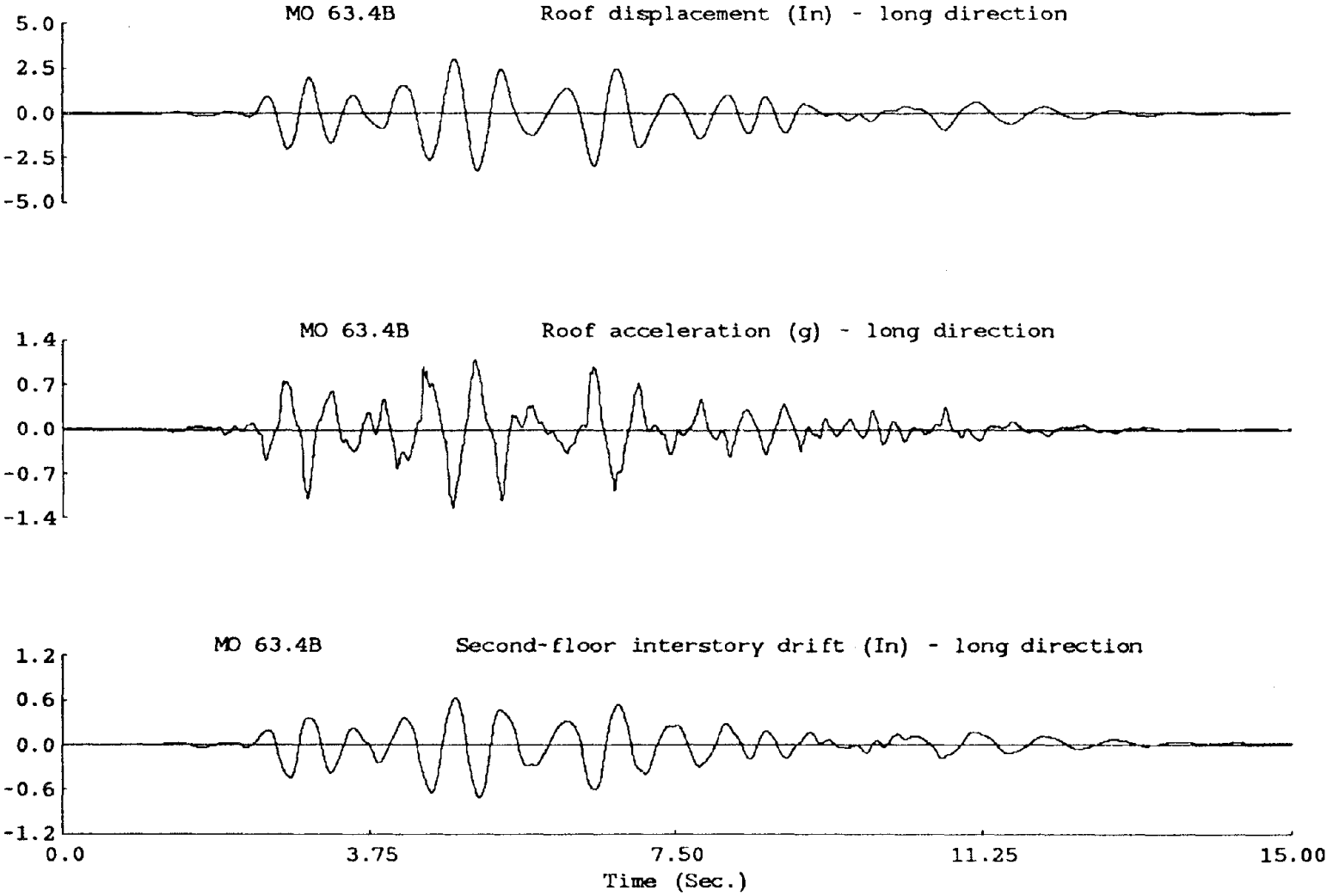

Figure 4.4(f) Response Histories (MO63.4B, Long Direction).

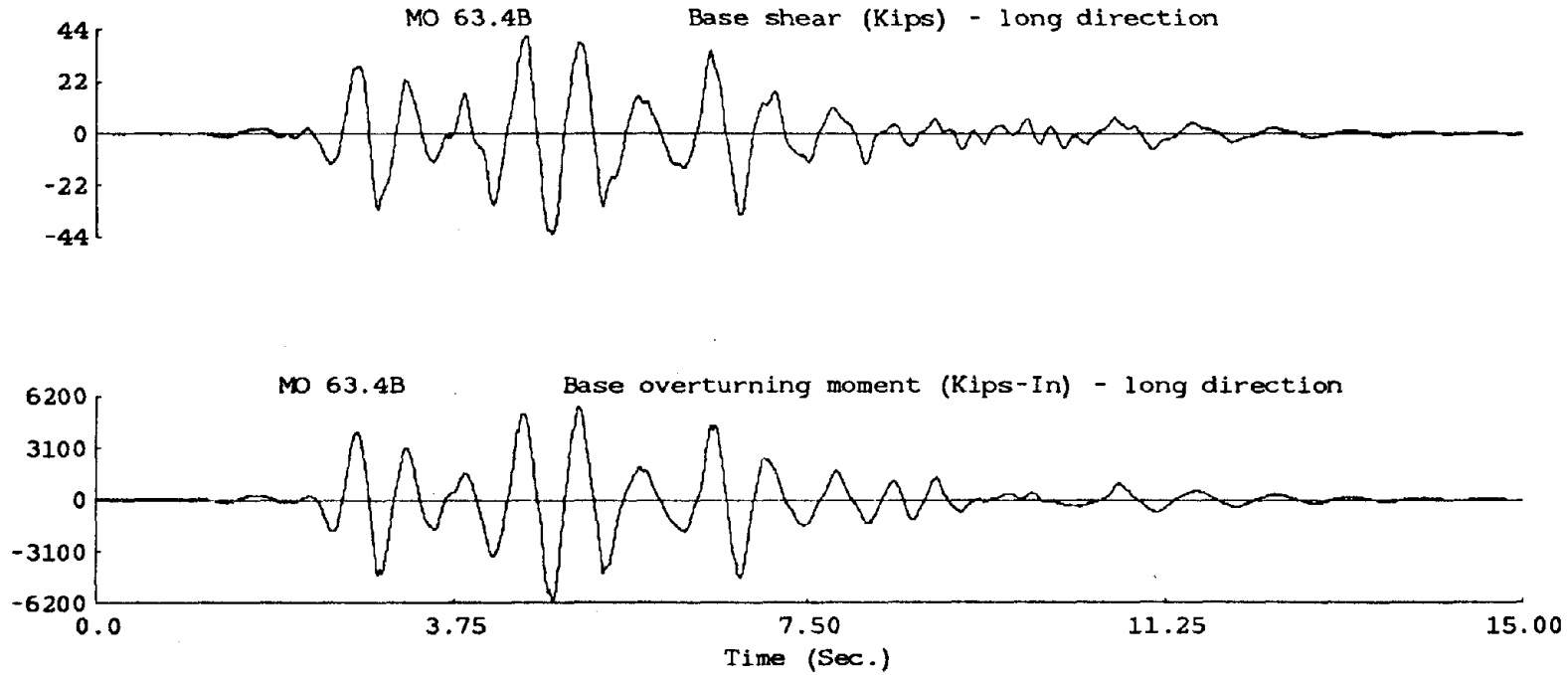

Figure 4.4f (Cont.) Response Histories (MO63.4B, Long Direction).

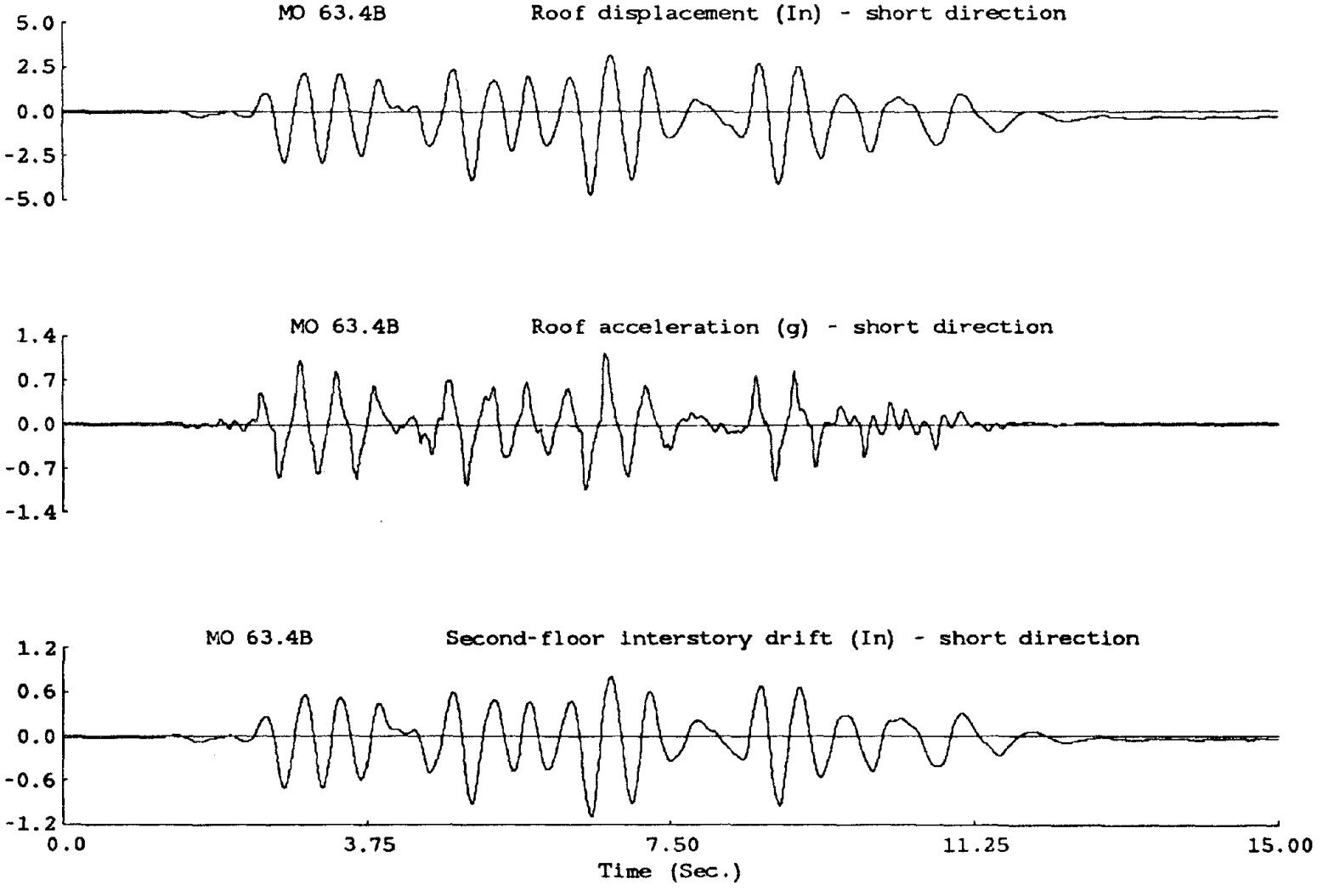

Figure 4.4(g) Response Histories (MO63.4B, Short Direction).

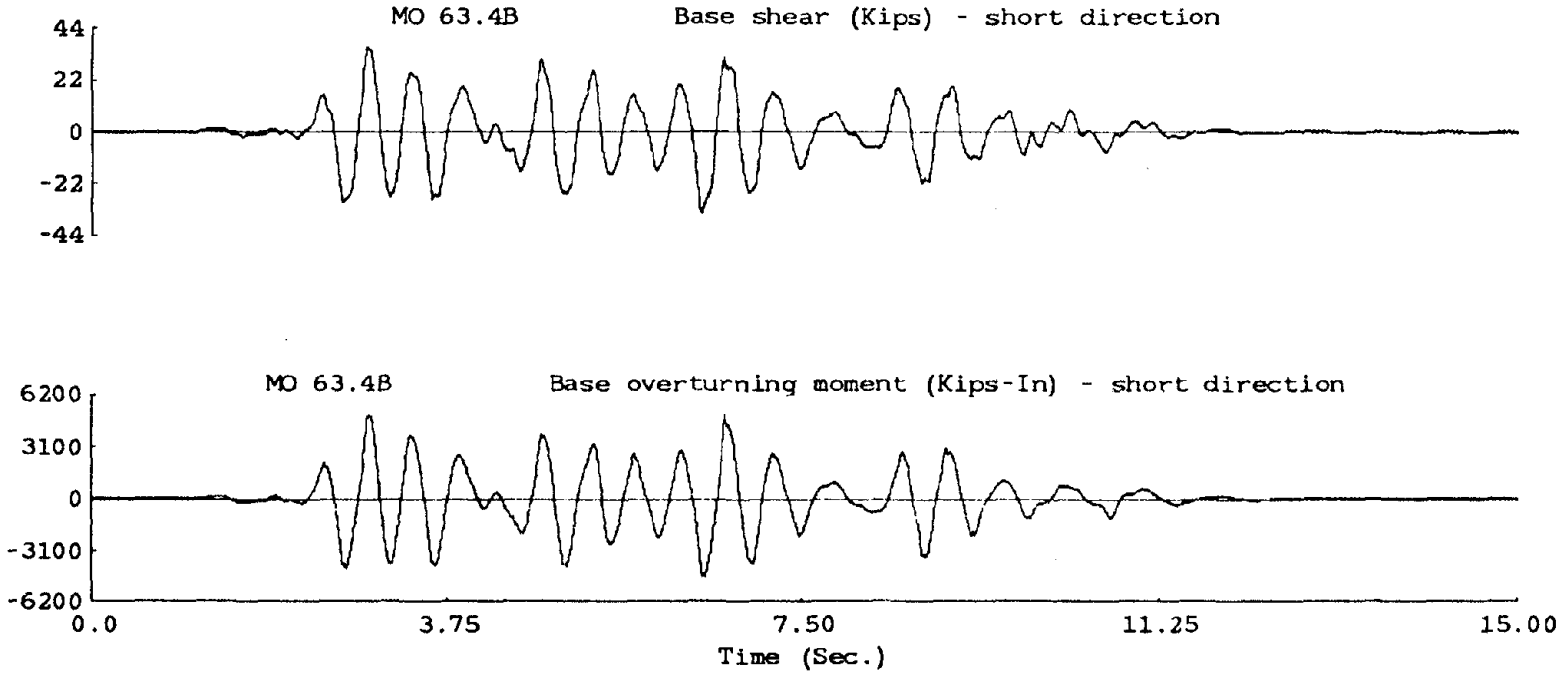

Figure 4.4g (Cont.) Response Histories (MO63.4B, Short Direction).

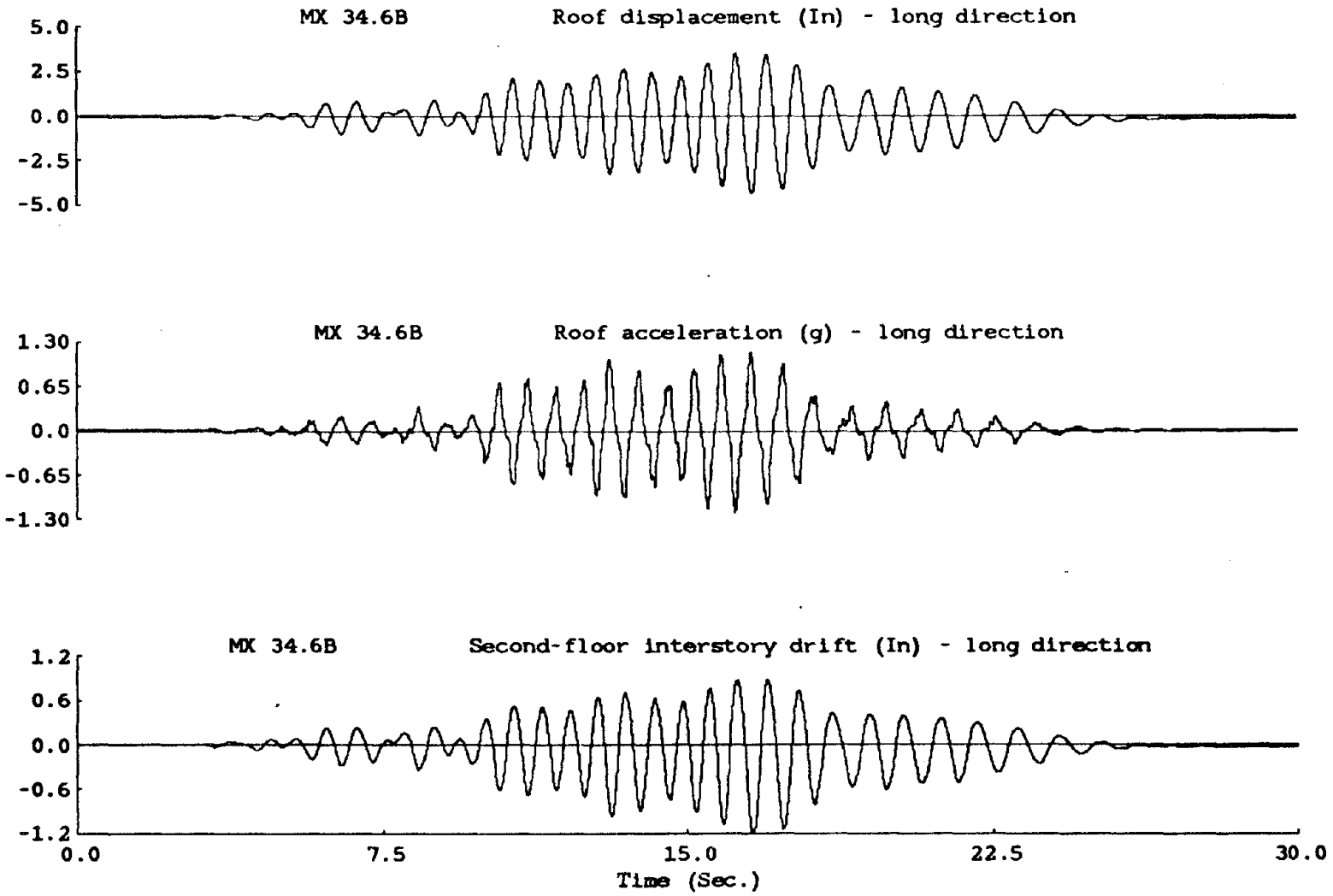

Figure 4.4(h) Response Histories (MX34.6B, Long Direction).

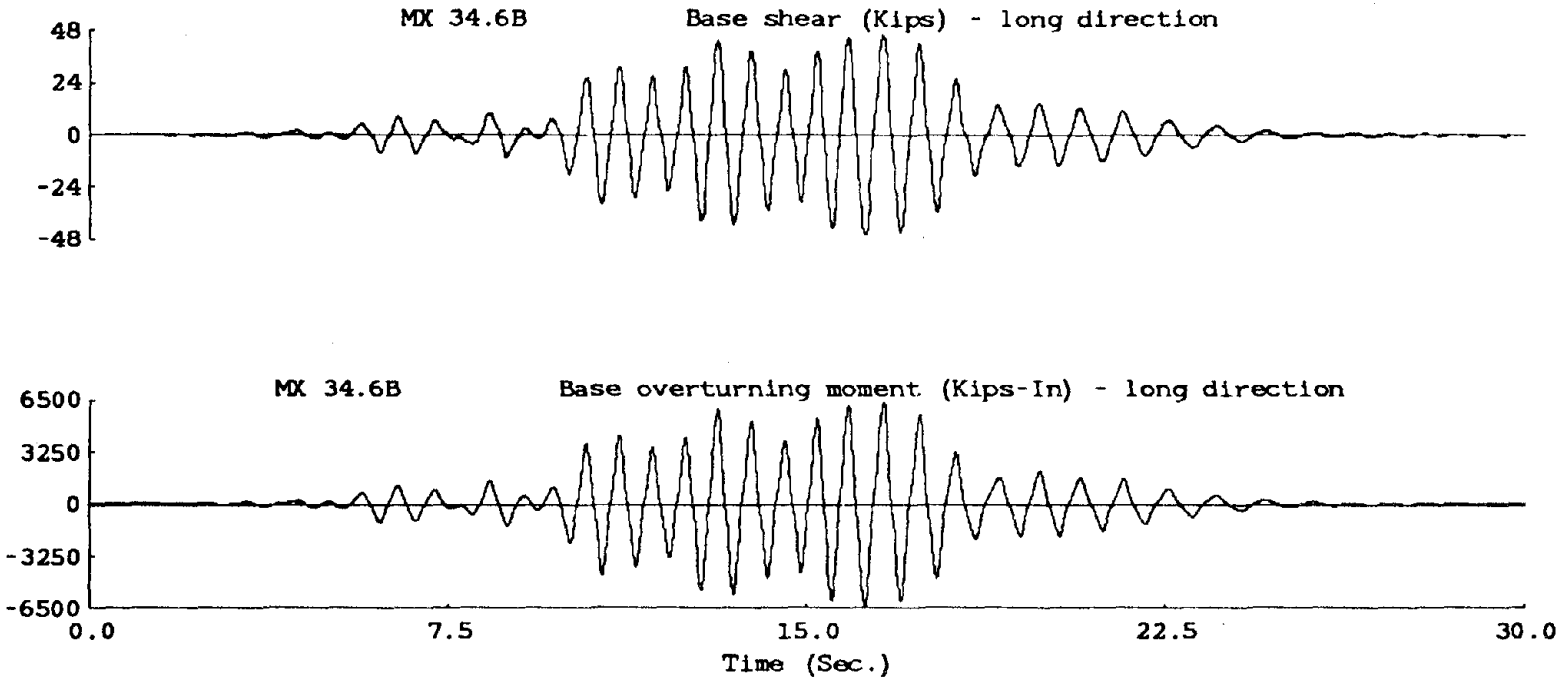

Figure 4.4h (Cont.) Response Histories (MX63.4B, Long Direction).

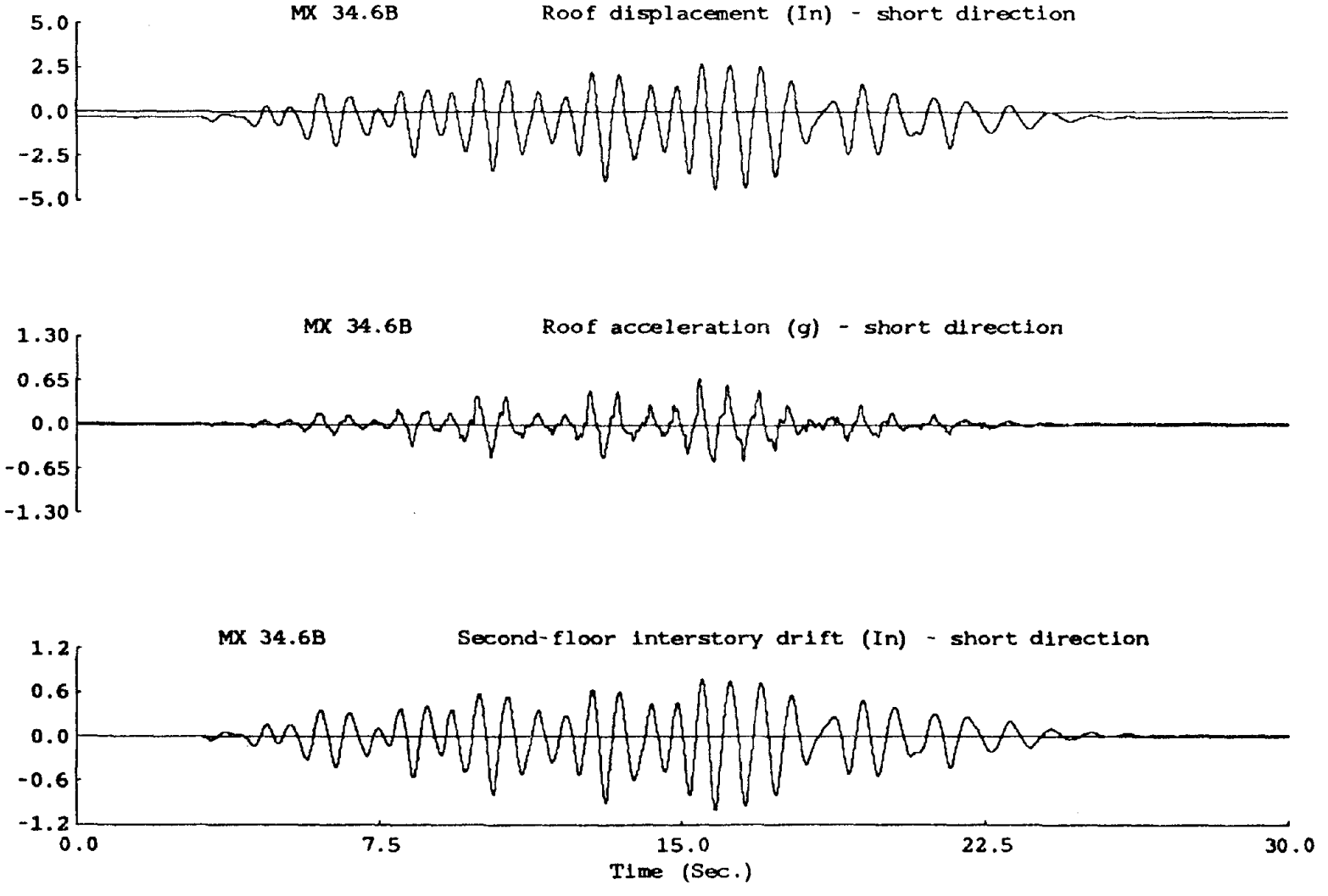

Figure 4.4(i) Response Histories (MX63.4B, Short Direction).

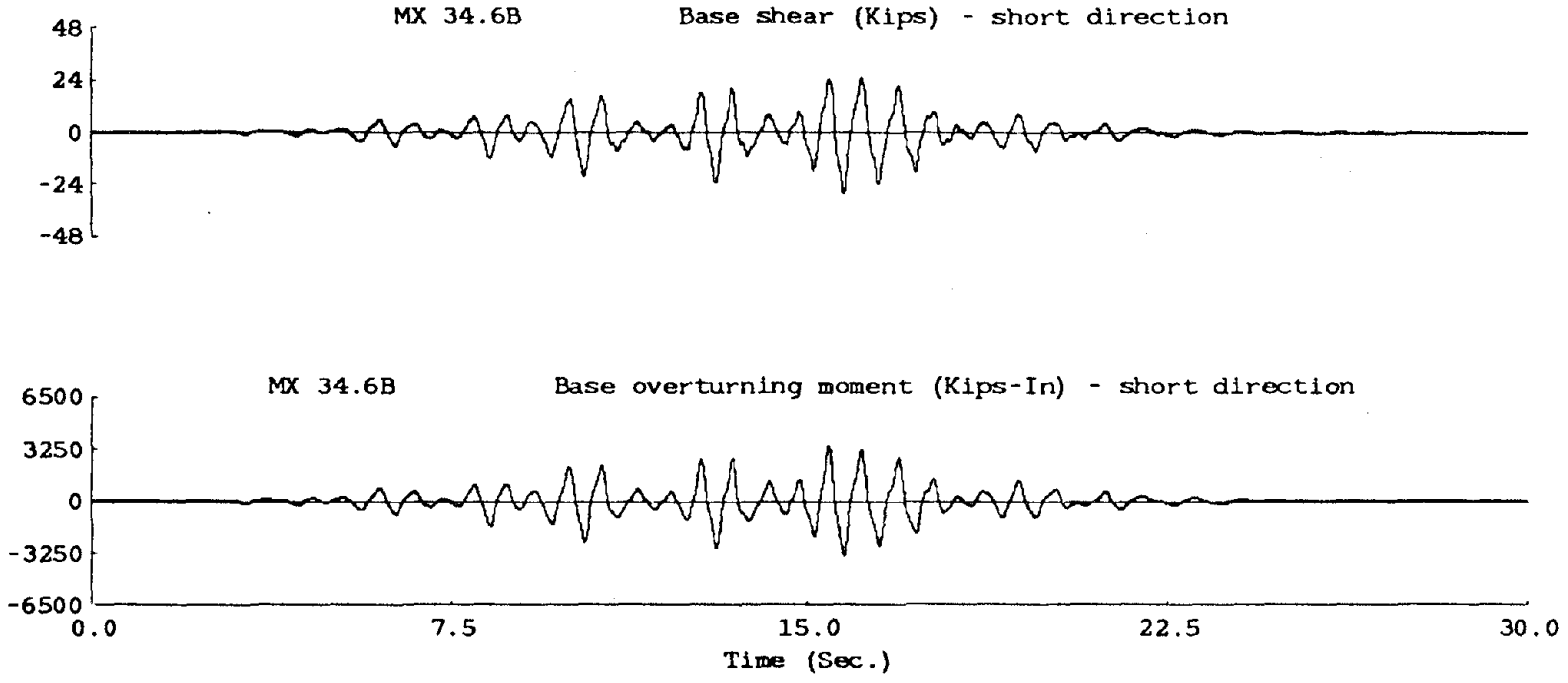

Figure 4.4i (Cont.) Response Histories (MX63.4B, Short Direction).

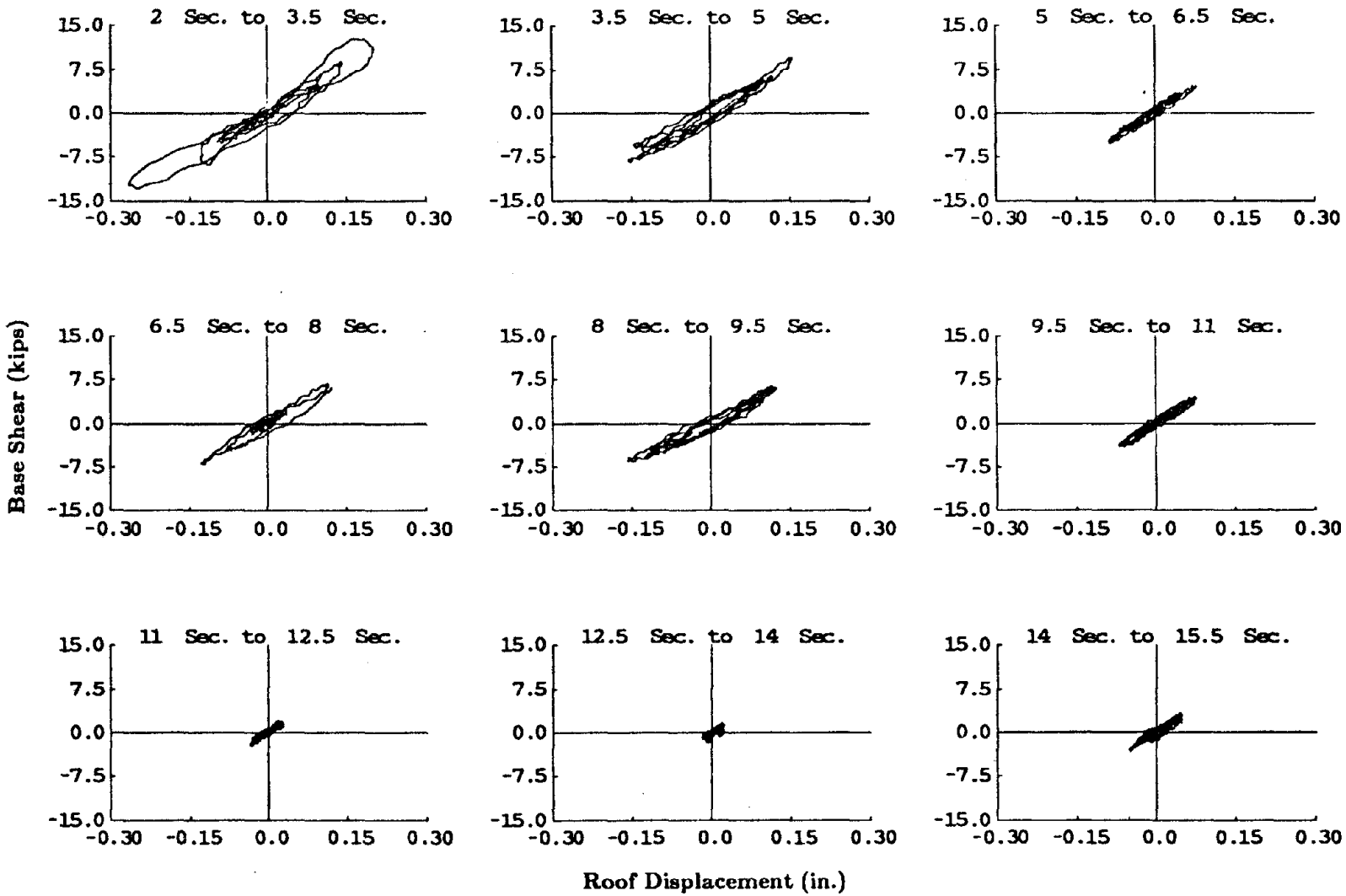

Figure 4.5(a) Relation Between Base Shear and Roof Displacement (EC7.7L).

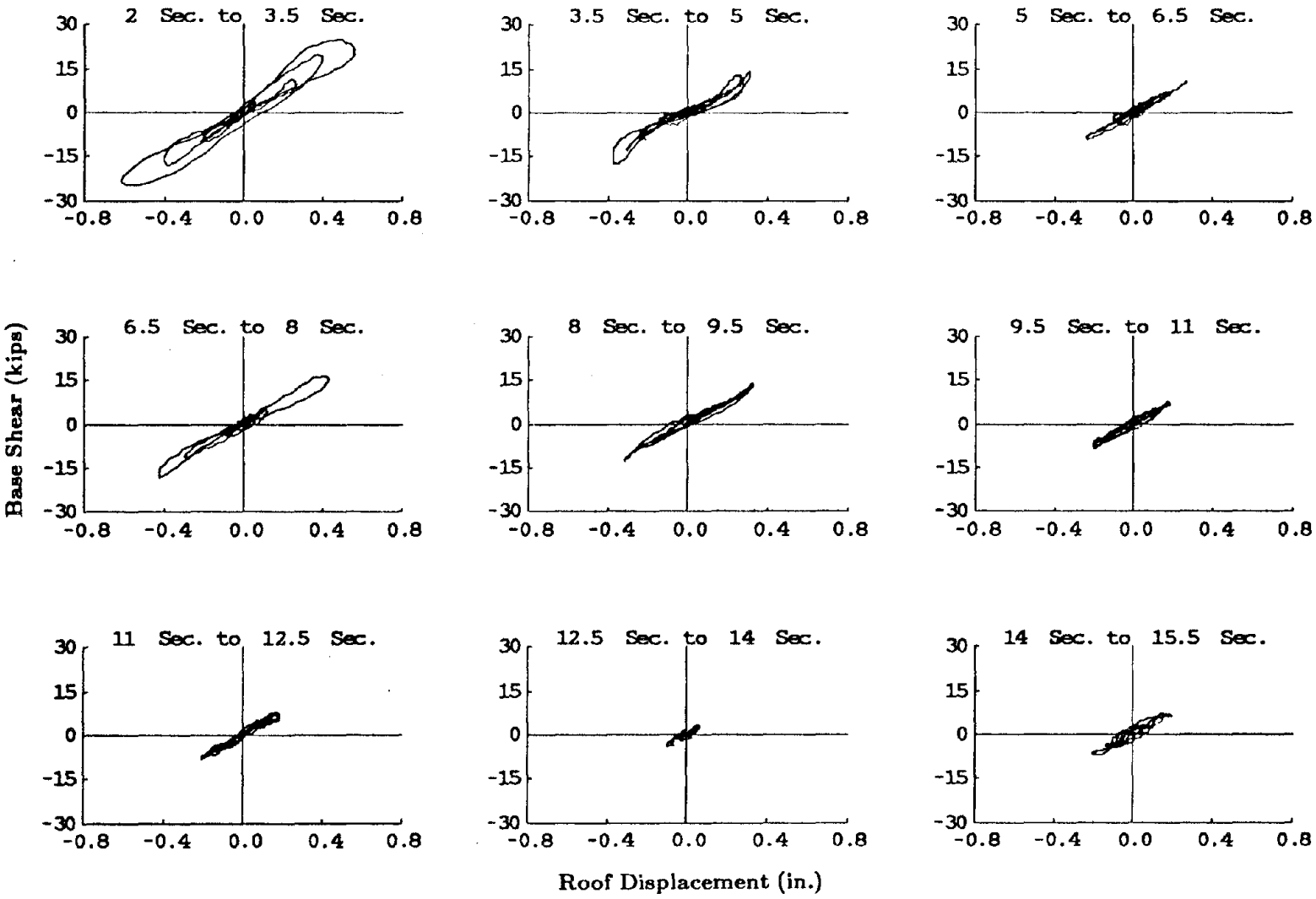

Figure 4.5(b) Relation Between Base Shear and Roof Displacement (EC16.6L).

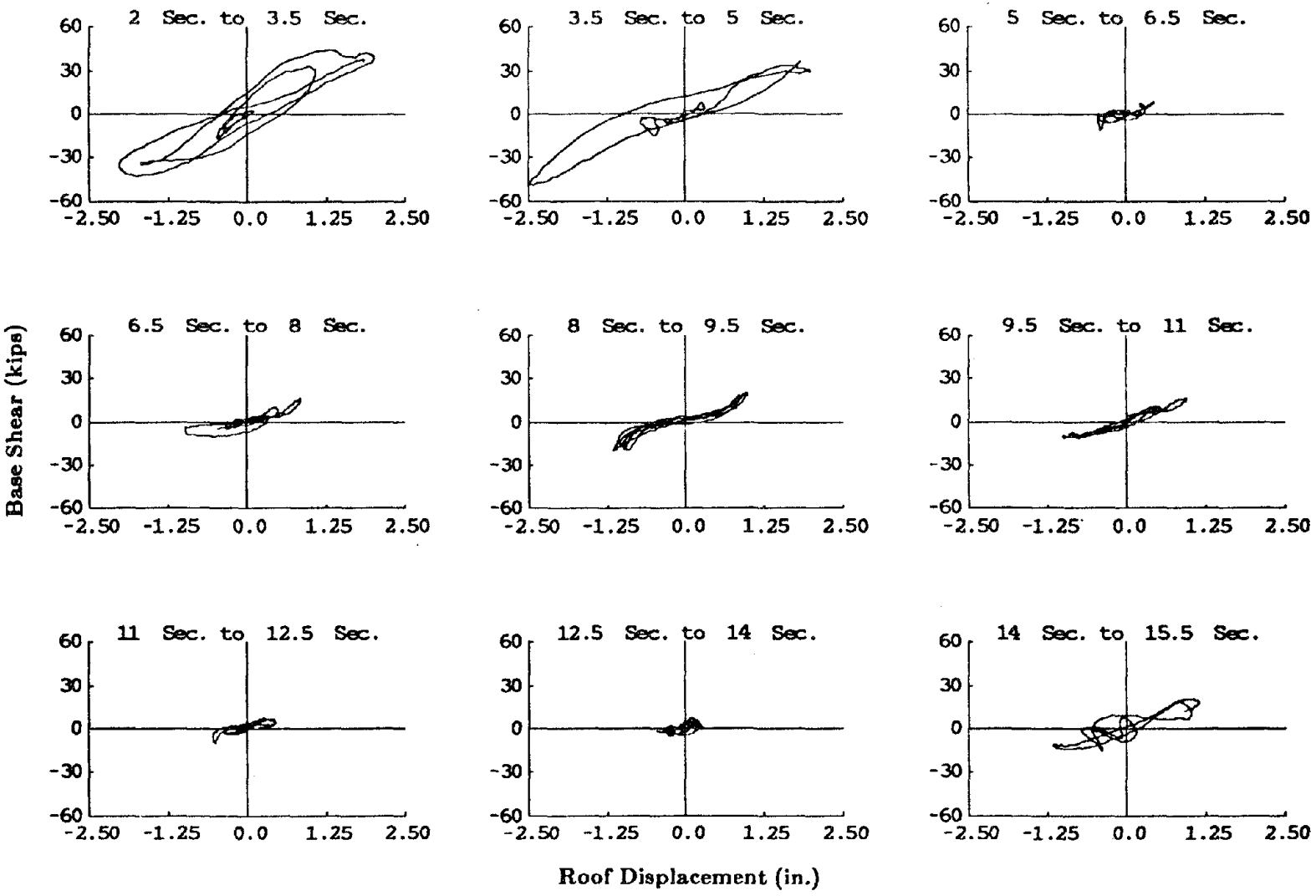

Figure 4.5(c) Relation Between Base Shear and Roof Displacement (EC49.3L).

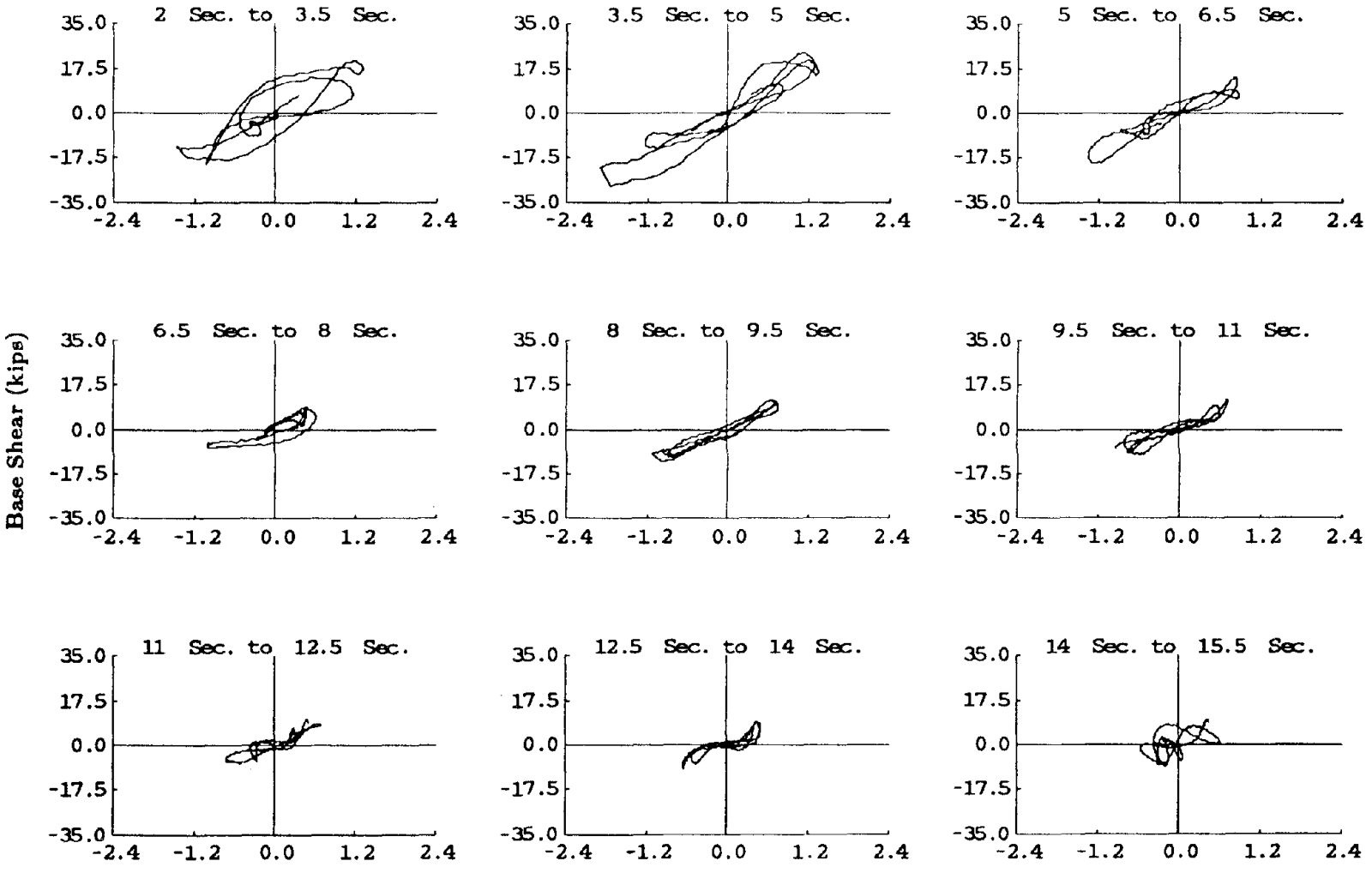

Figure 4.5(d) Relation Between Base Shear and Roof Displacement.
(EC47.7B, Long Direction)

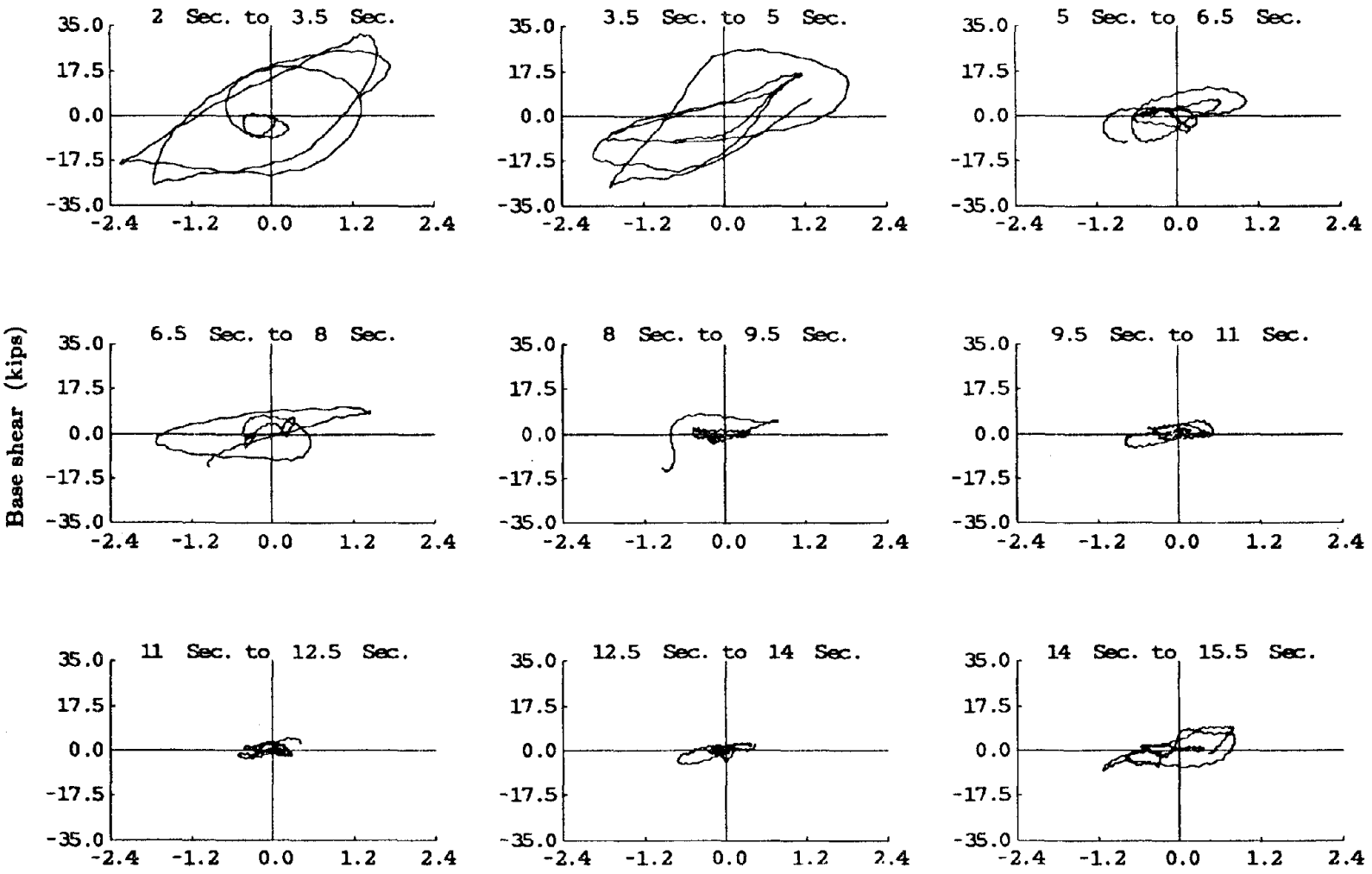

Figure 4.5(e) Relation Between Base Shear and Roof Displacement.
(EC47.7B, Short Direction)

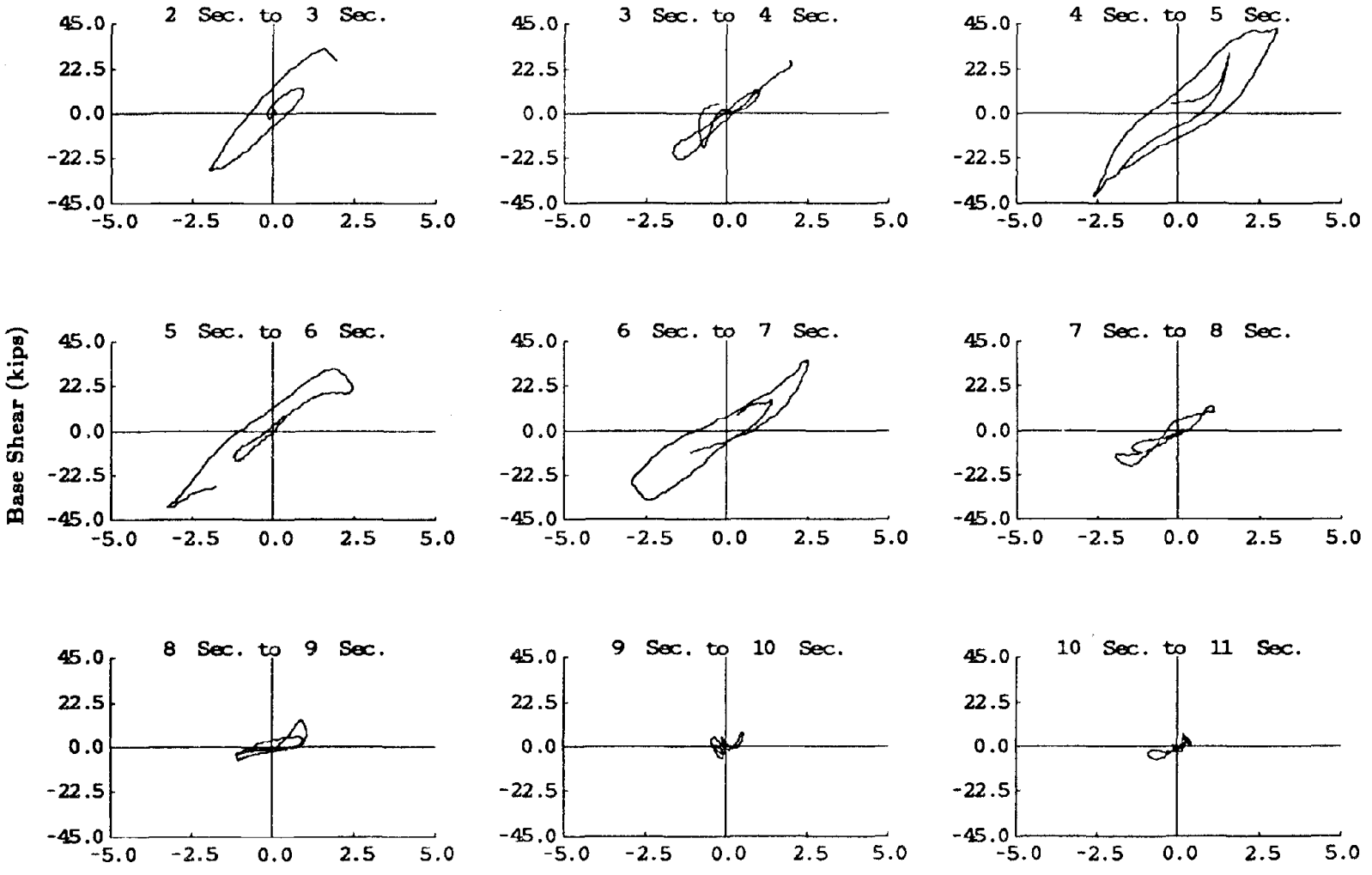

Figure 4.5(f) Relation Between Base Shear and Roof Displacement. (MO63.4B, Long Direction)

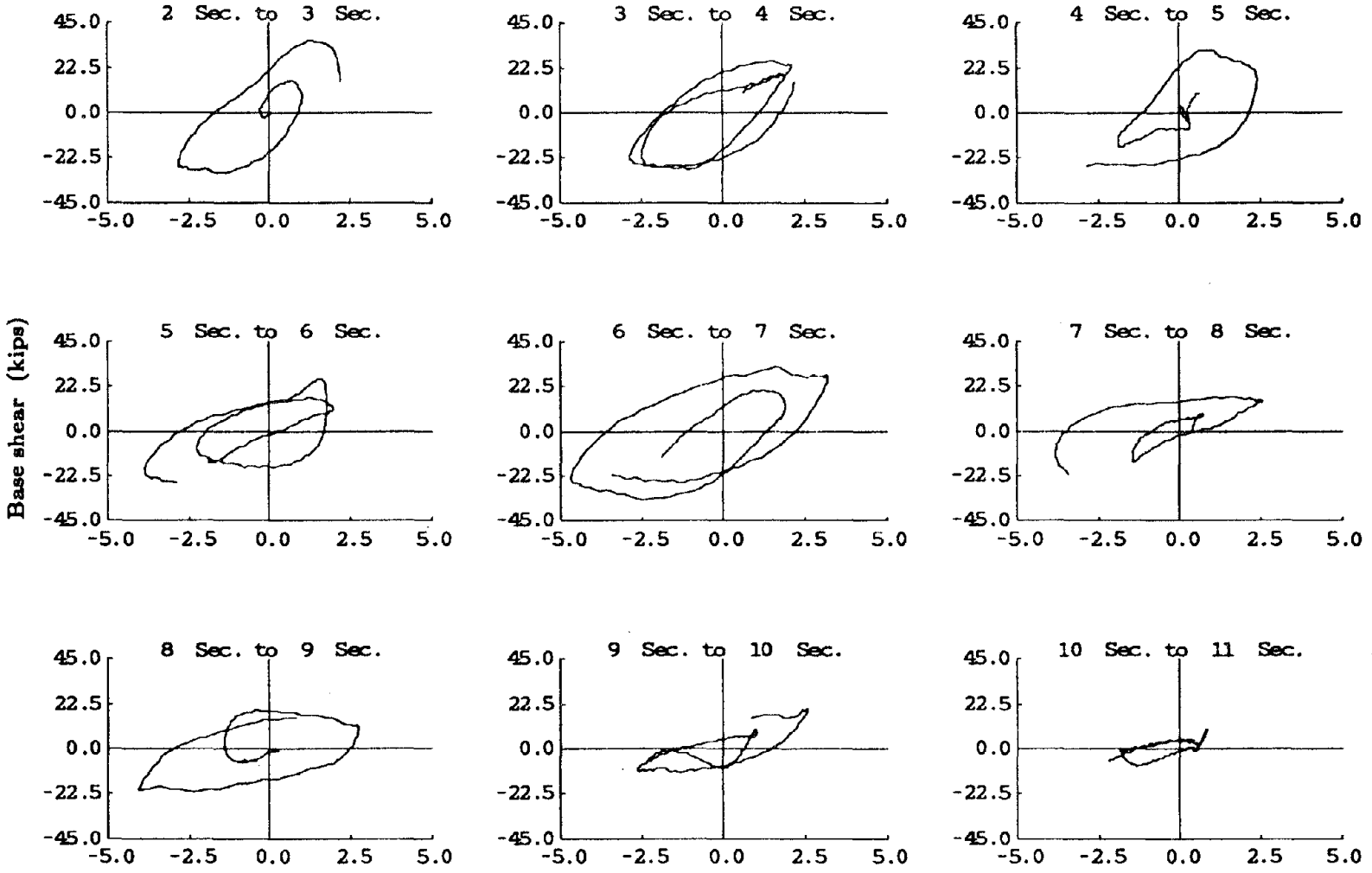

Figure 4.5(g) Relation Between Base Shear and Roof Displacement.
(MO63.4B, Short Direction)

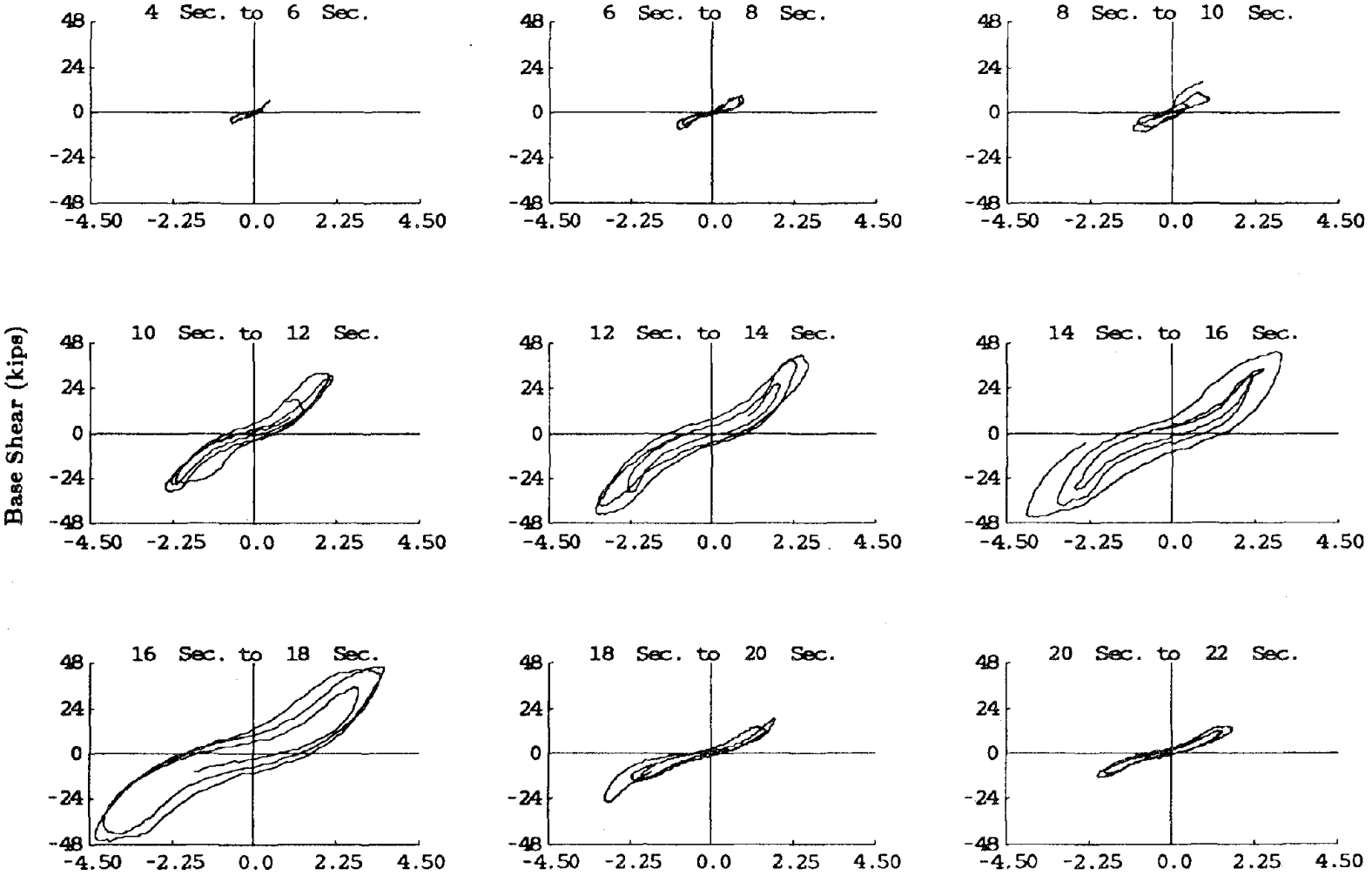

Figure 4.5(h) Relation Between Base Shear and Roof Displacement. (MX34.6B, Long Direction)

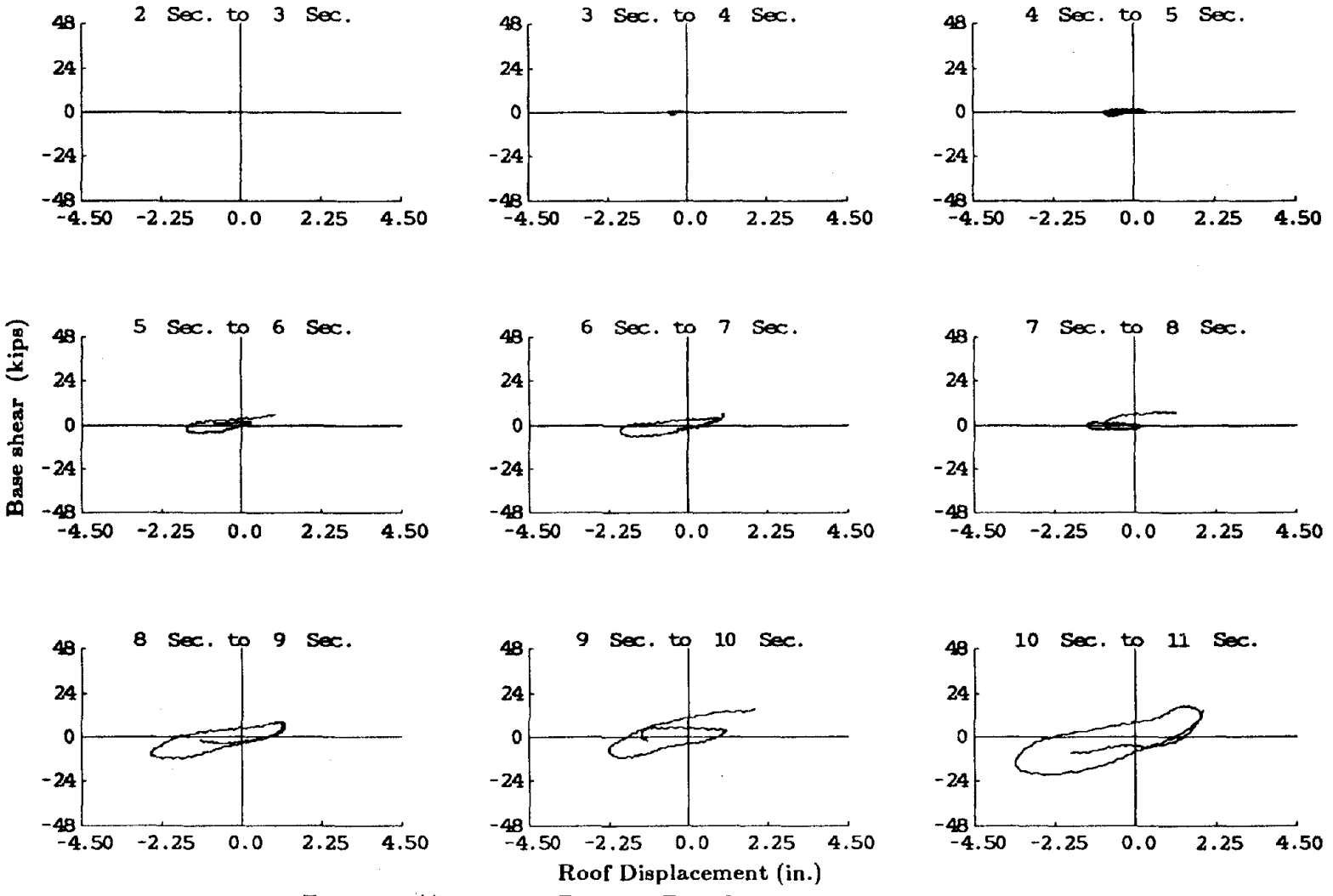

Figure 4.5(i) Relation Between Base Shear and Roof Displacement.
(MX34.6B, Short Direction)

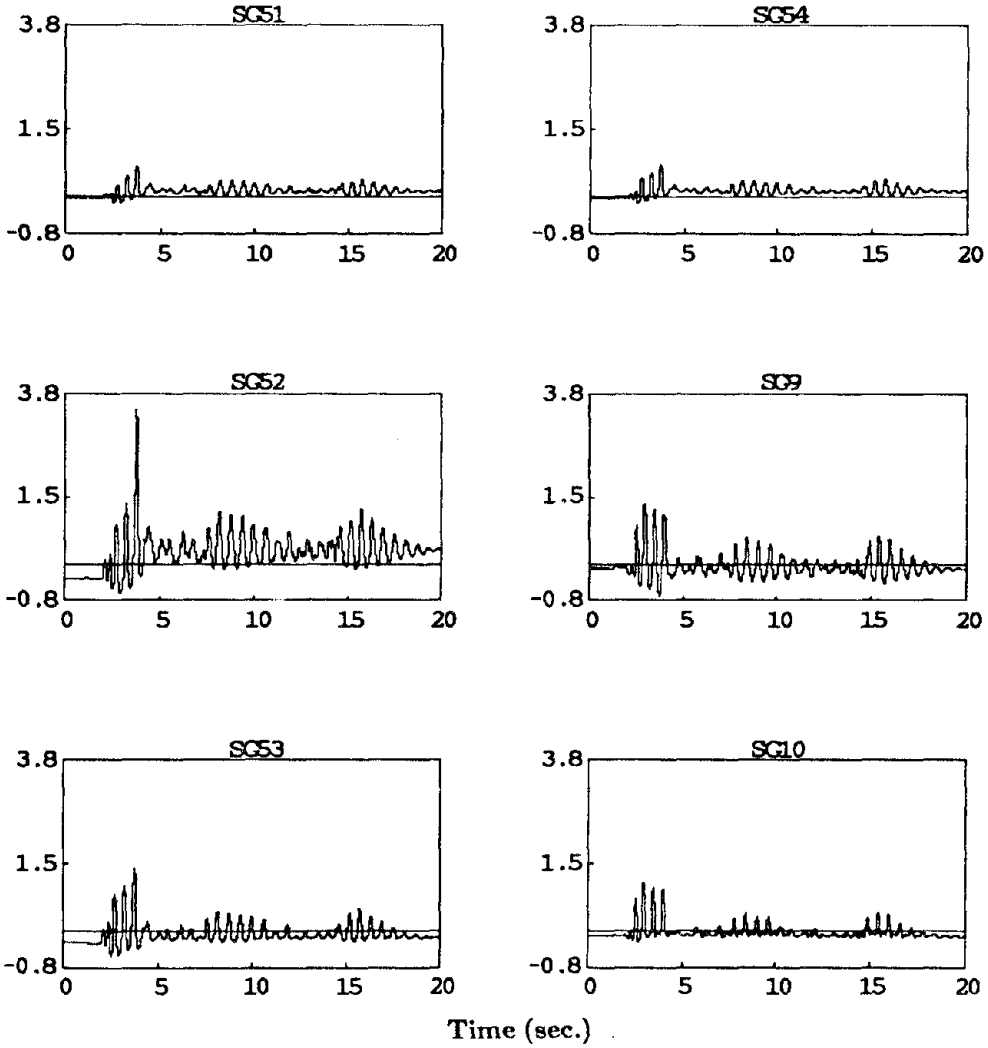

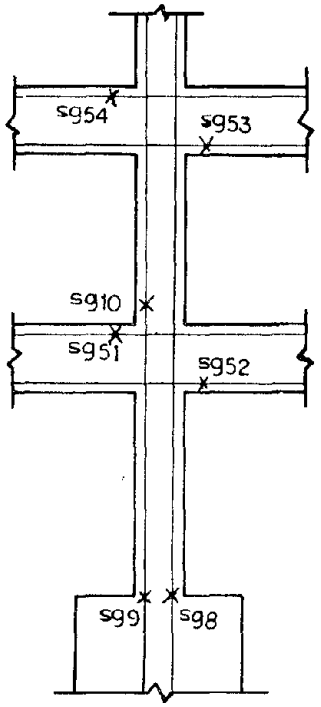

ϵ =Strain ϵ_y =Yield Strain

Figure 4.6(a) Normalized Strain Histories (EC49.3L).

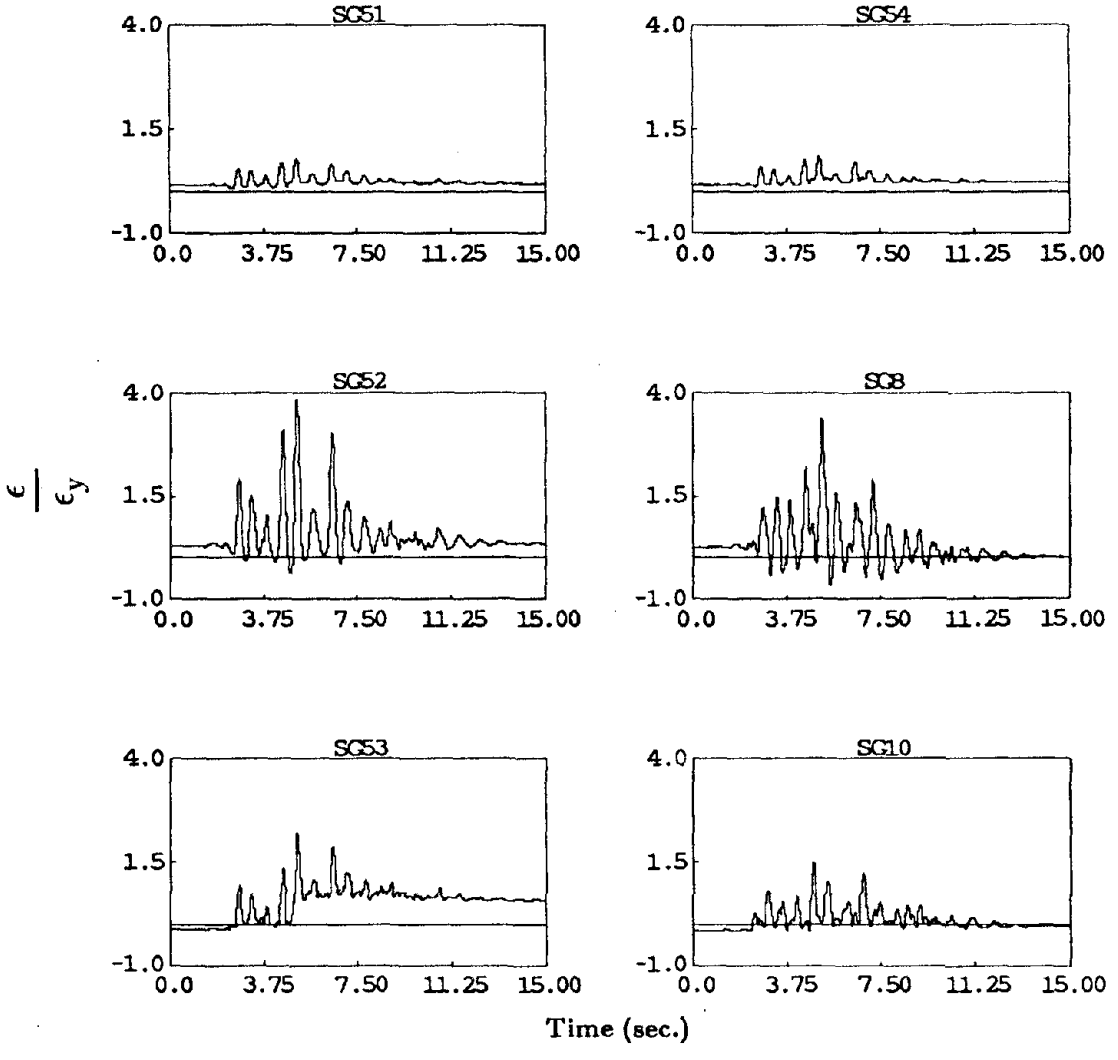

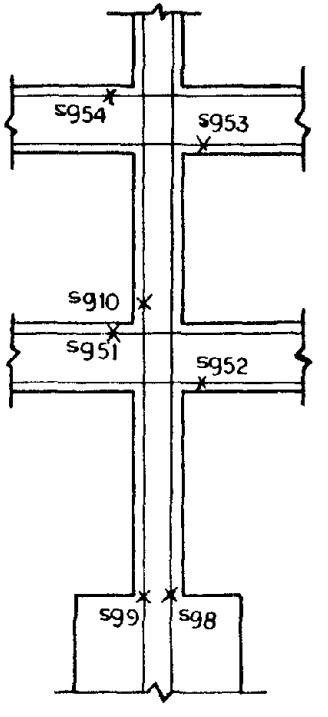

ϵ =Strain ϵ_y =Yield Strain

Figure 4.6(b) Normalized Strain Histories (MO83.4B).

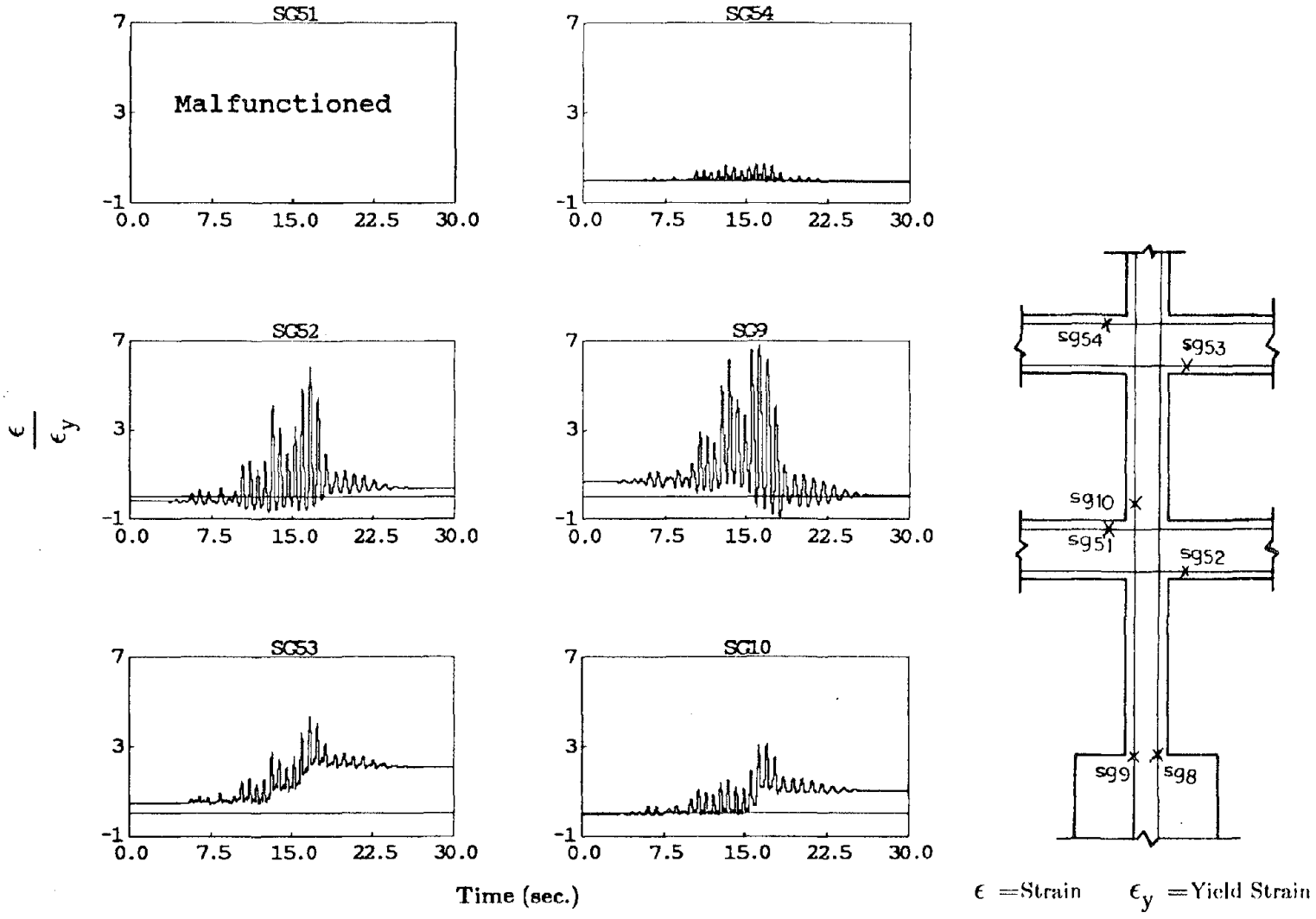

Figure 4.6(c) Normalized Strain Histories (MX34.6B).

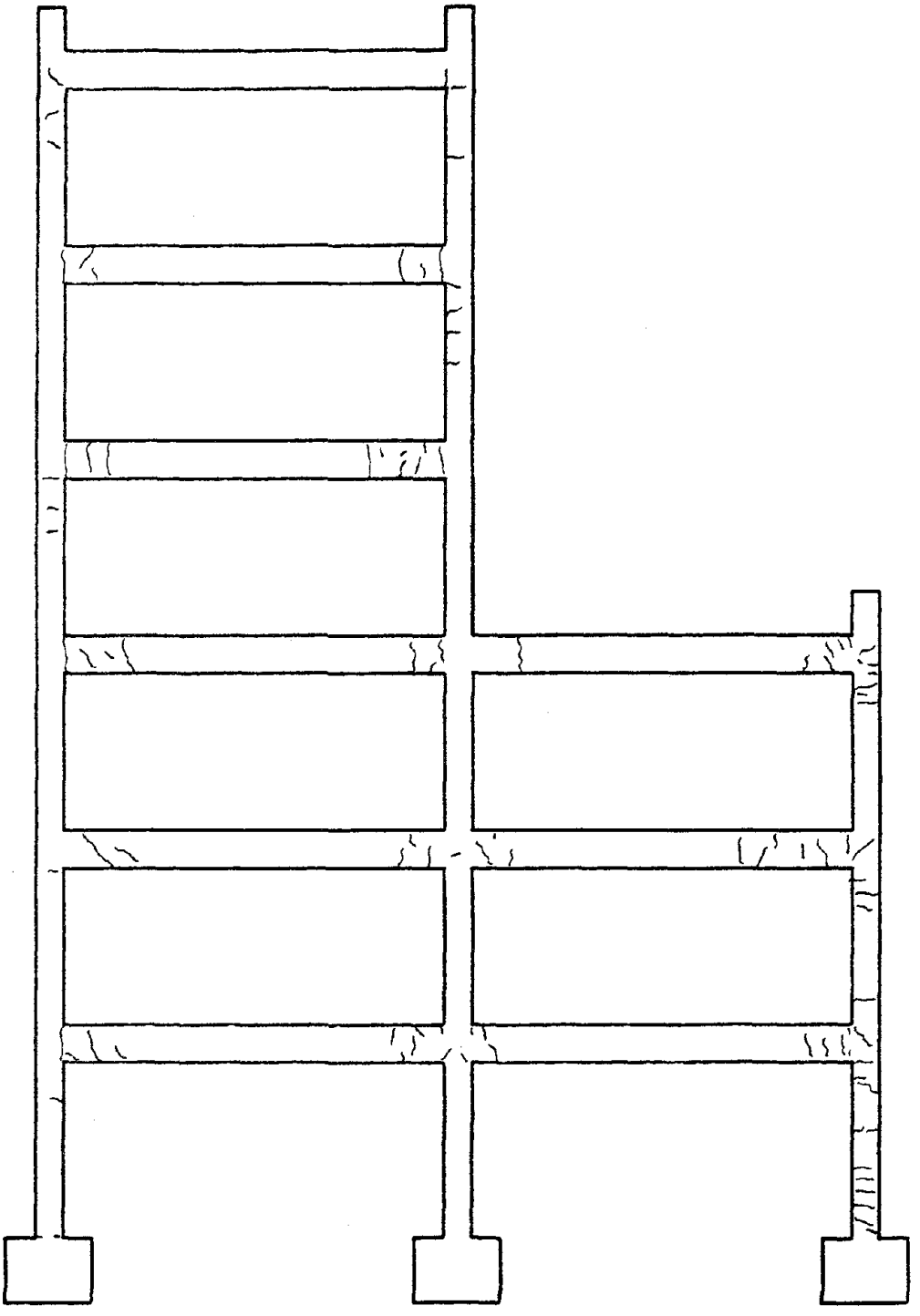

Figure 4.7(a) Crack Patterns after EC49.3L (Frame 3, Outside View).

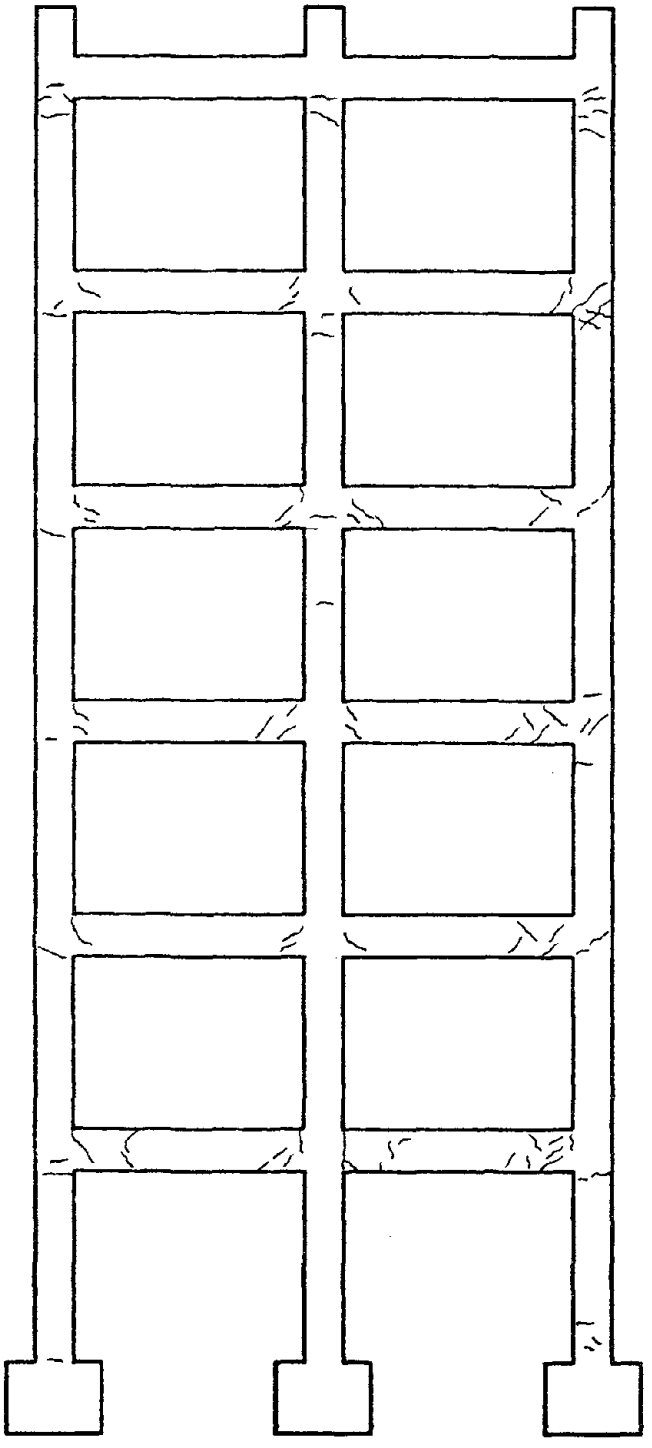

Figure 4.7(b) Crack Patterns after EC49.3L (Frame 4, Outside View).

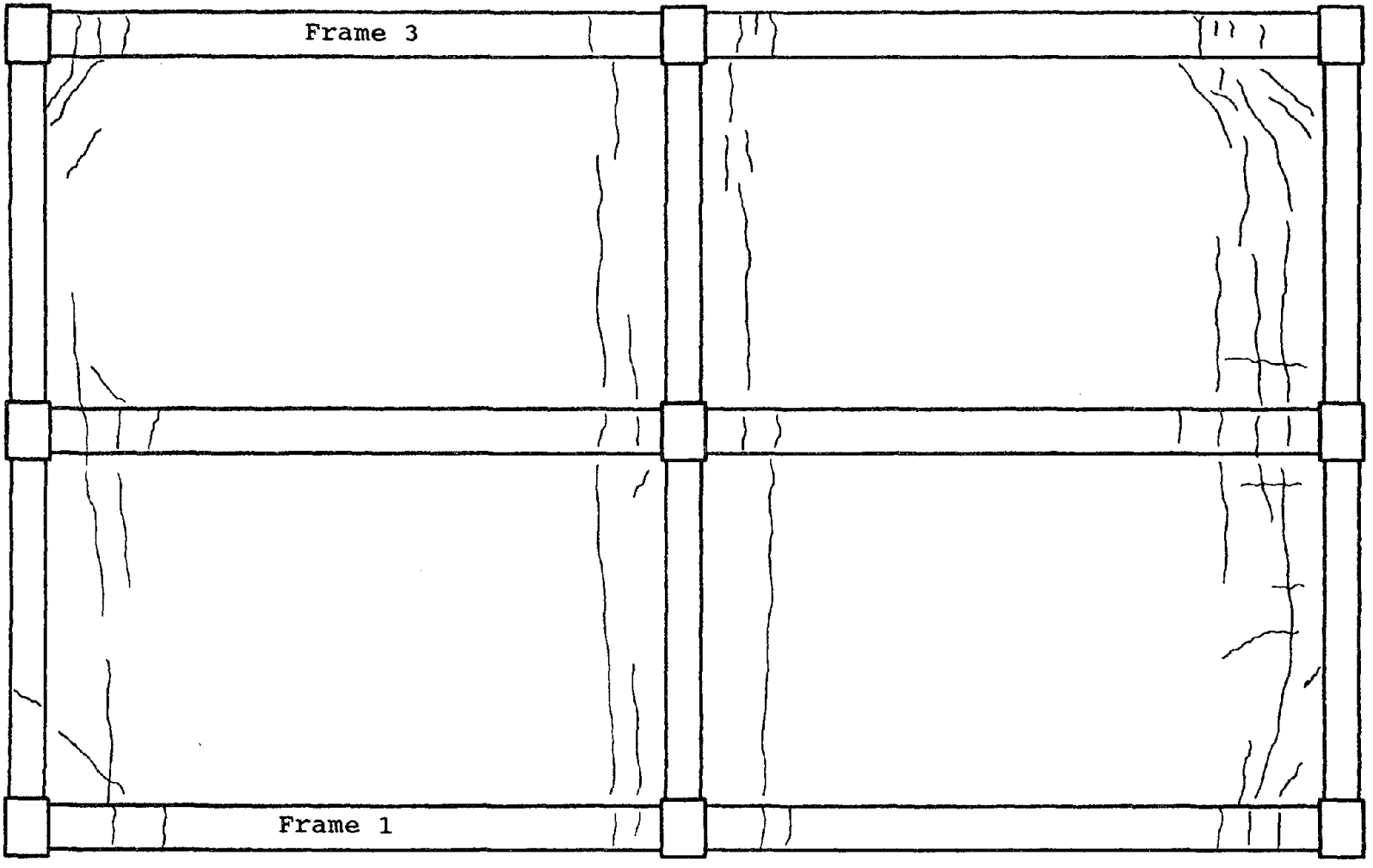

Bottom View

Figure 4.7(c) Crack Patterns after EC49.3L (First-Floor Slab).

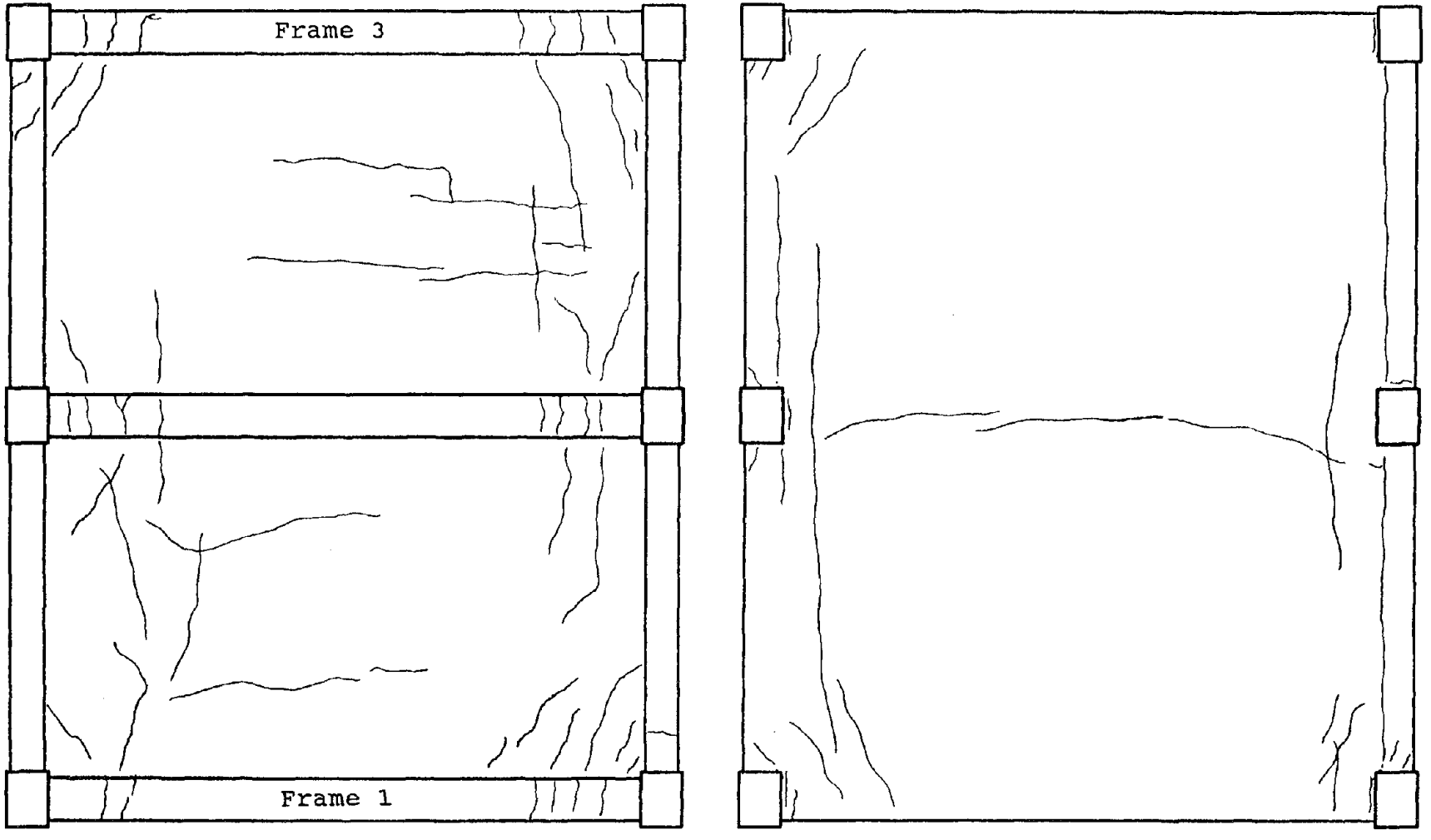

Figure 4.7(d) Crack Patterns after EC49.3L (Fourth-Floor Slab).

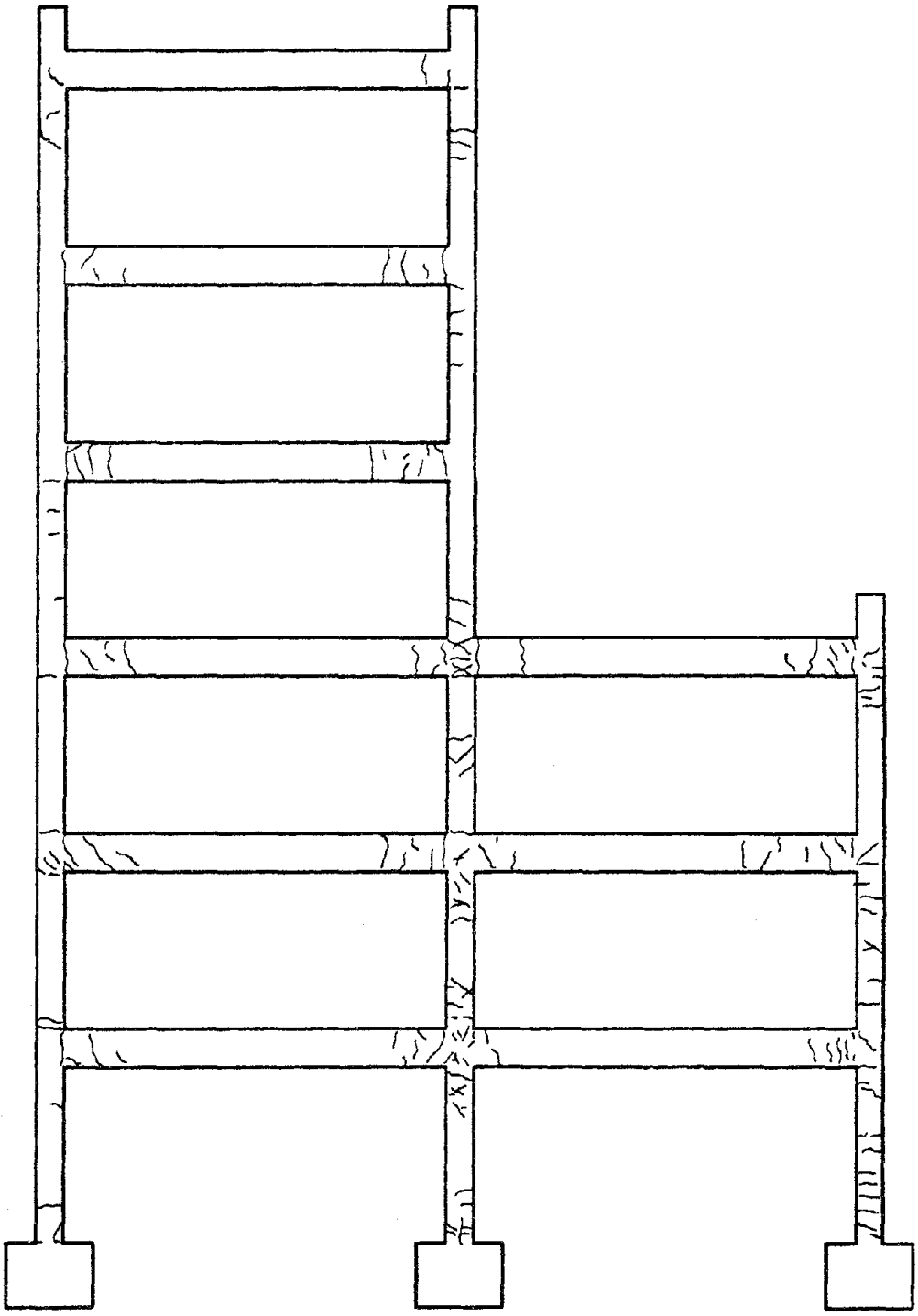

Figure 4.7(e) Crack Patterns after MO63.4B (Frame 3, Outside View).

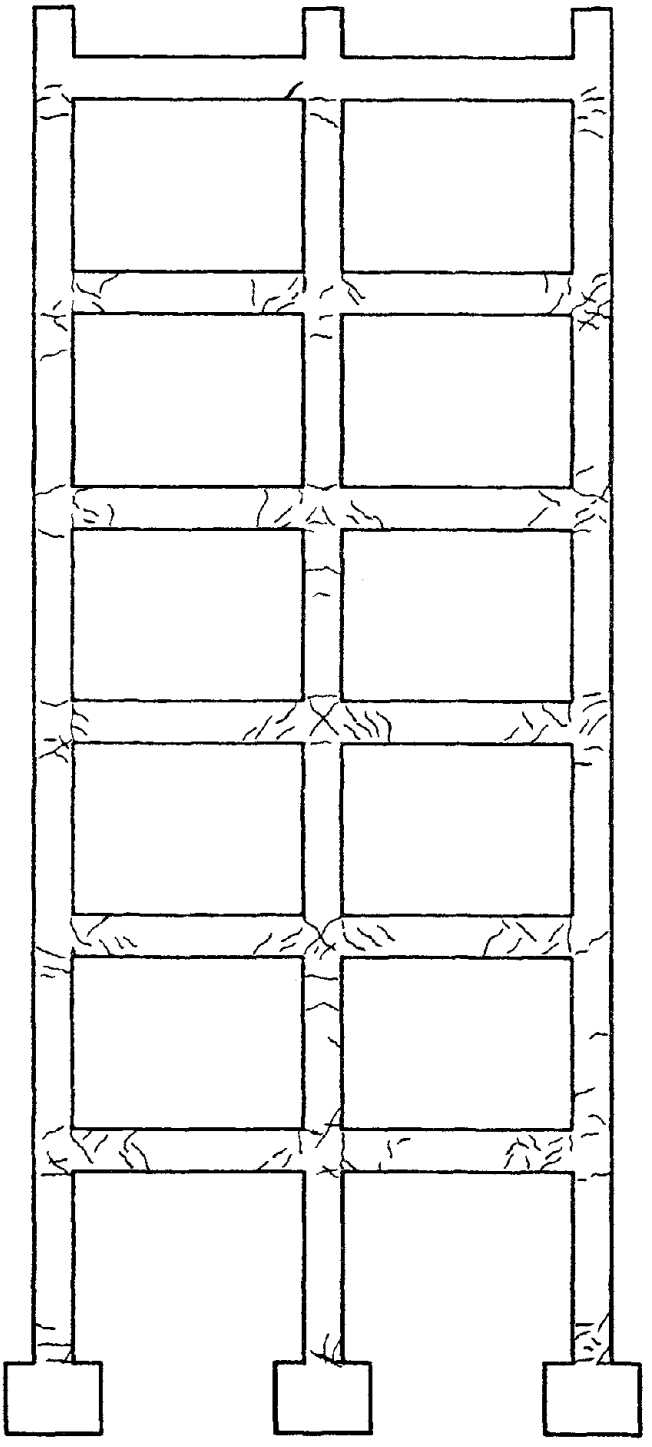

Figure 4.7(f) Crack Patterns after MO63.4B (Frame 4, Outside View).

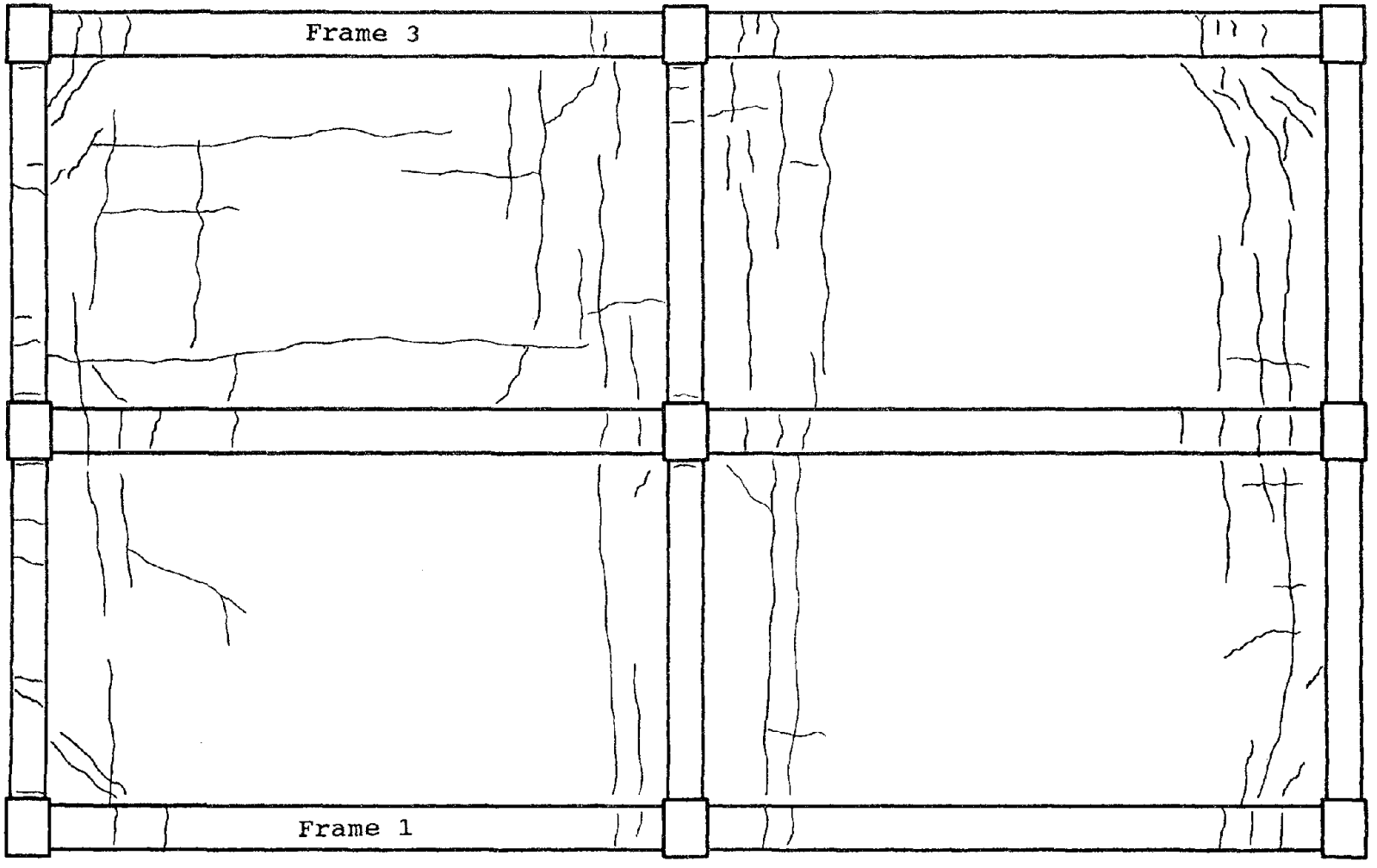

Bottom View

Figure 4.7(g) Crack Patterns after MO63.4B (First-Floor Slab).

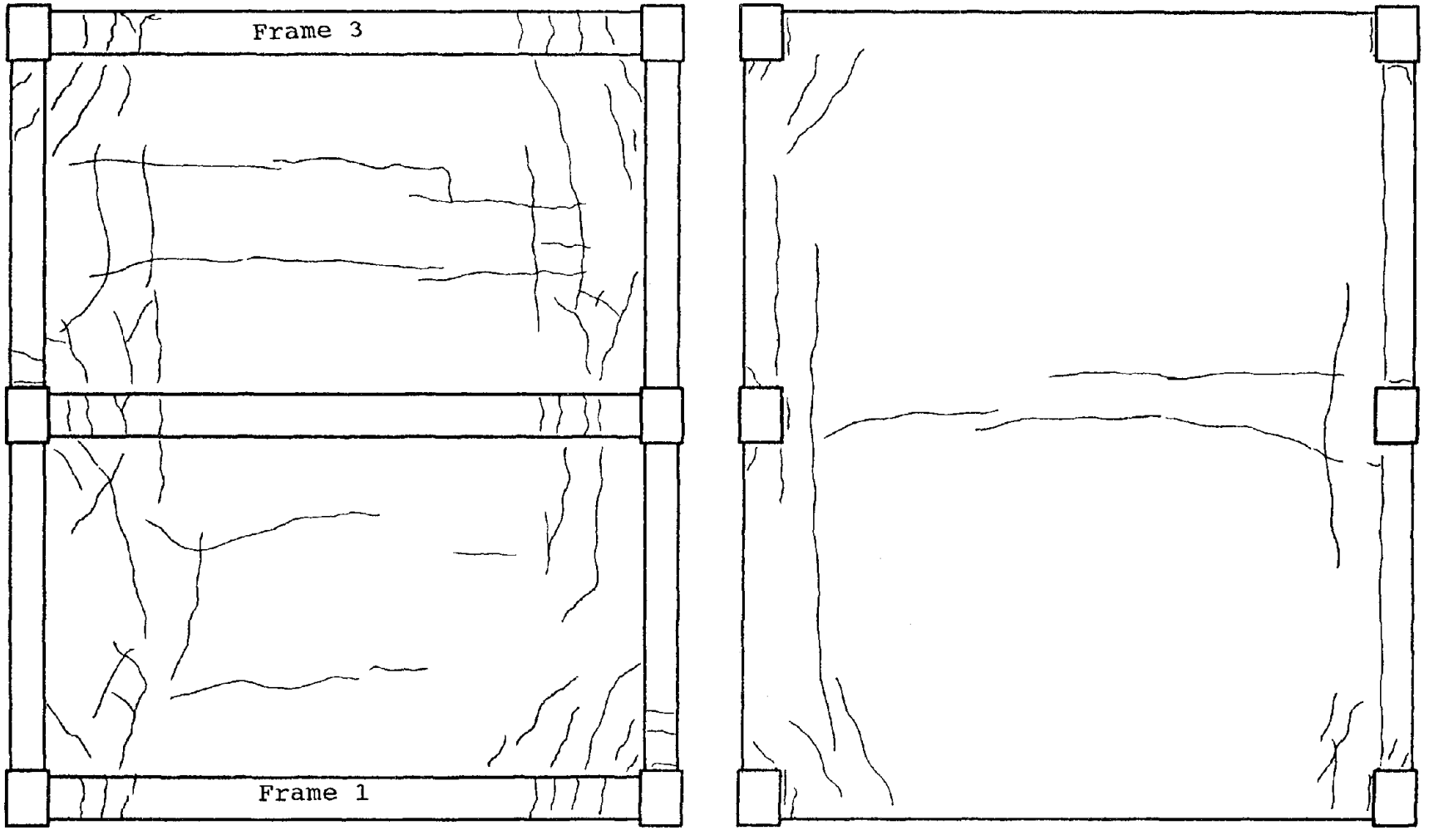

Figure 4.7(h) Crack Patterns after MO63.4B (Fourth-Floor Slab).

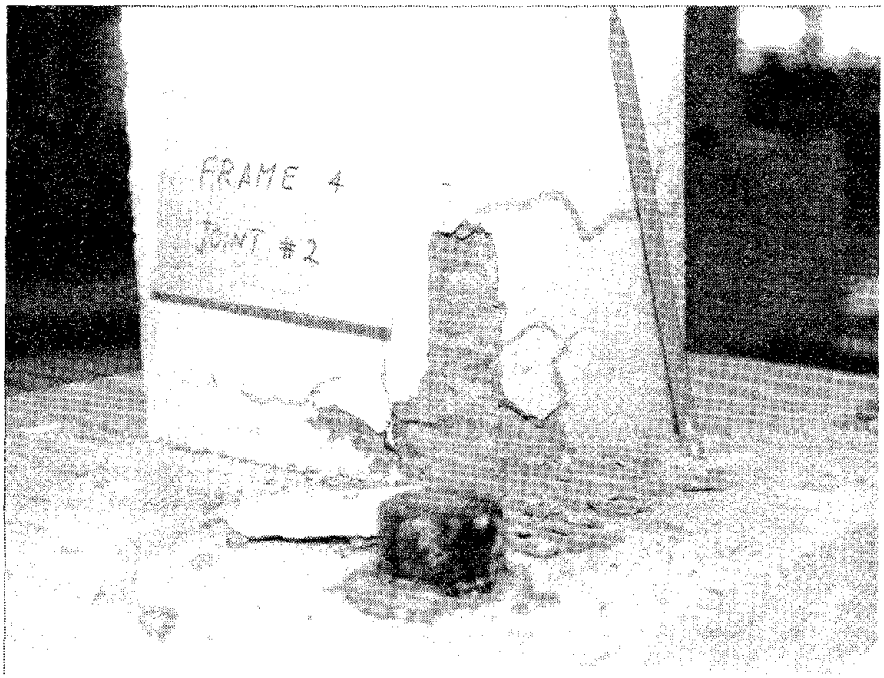

Interior Column at Footing

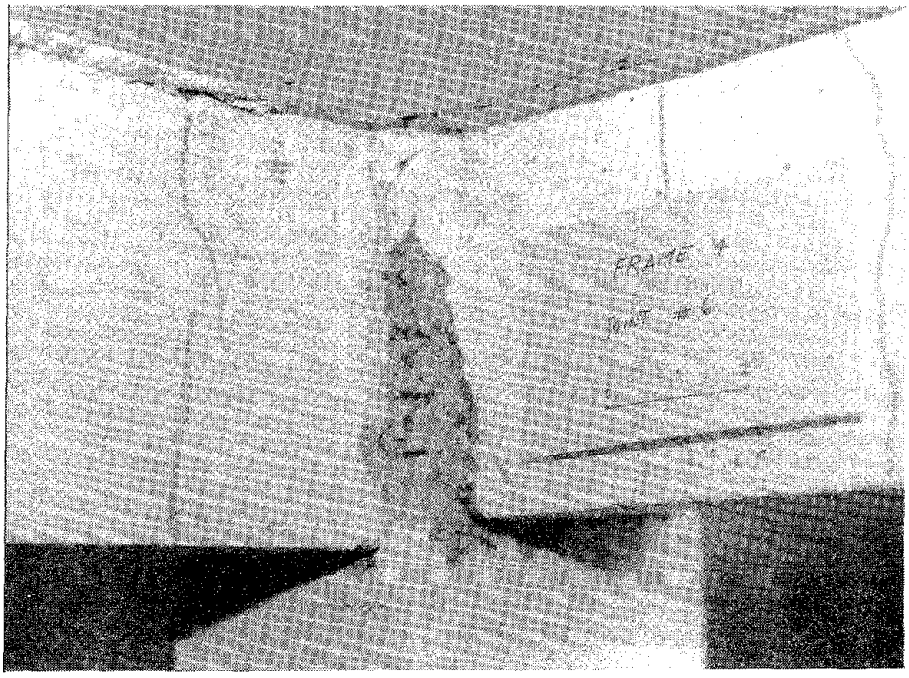

Second-Floor Corner Joint

Figure 4.8 Photographs of Typical Damage after MX34.6B.

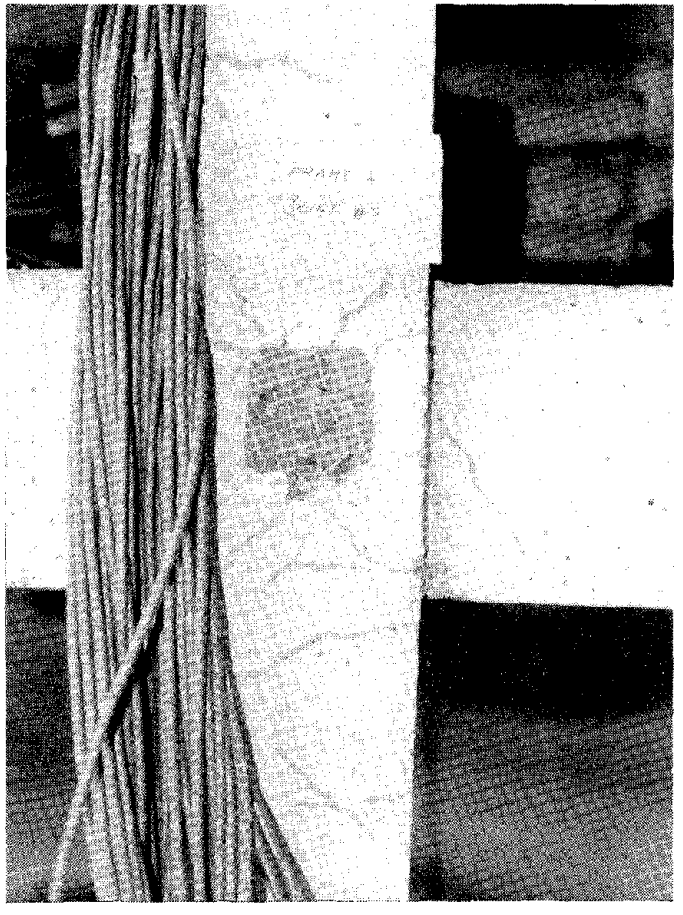

First-Floor Exterior Joint

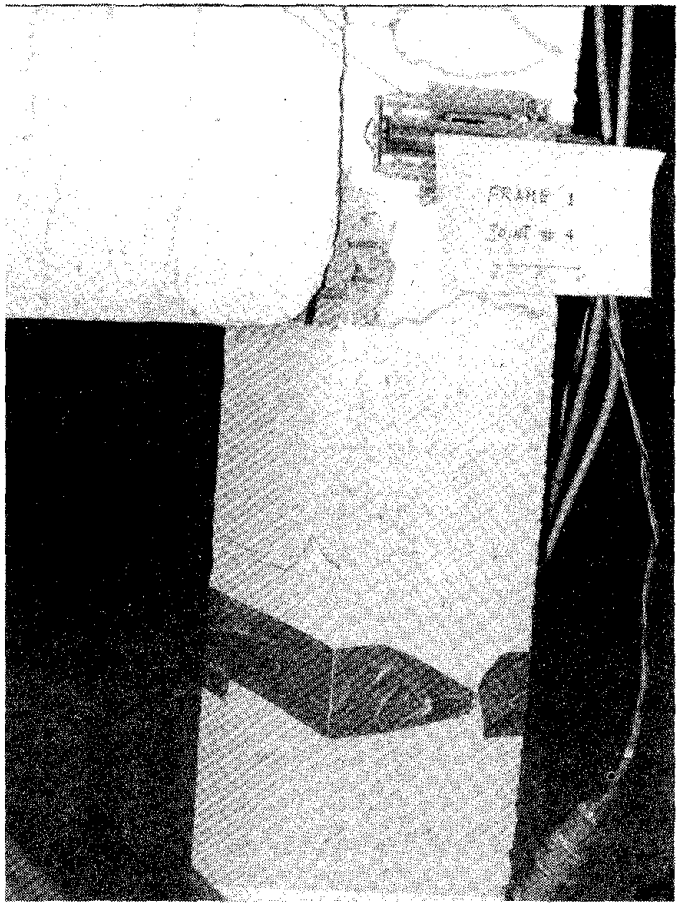

First-Floor Corner Joint

Figure 4.8 (Cont.) Photographs of Typical Damage after MX34.6B.

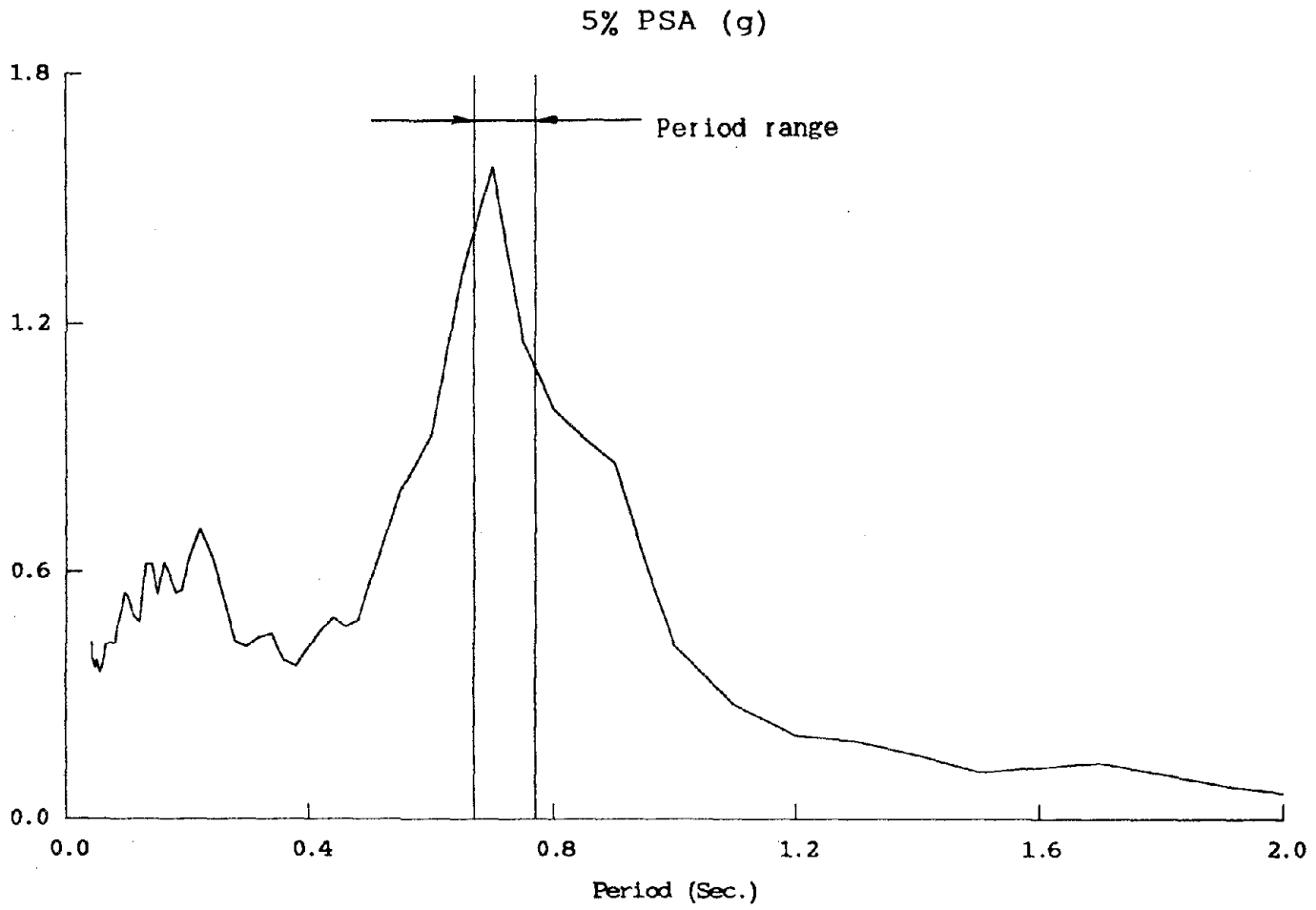

Figure 5.1 Mexico City Pseudo Acceleration Response Spectrum.

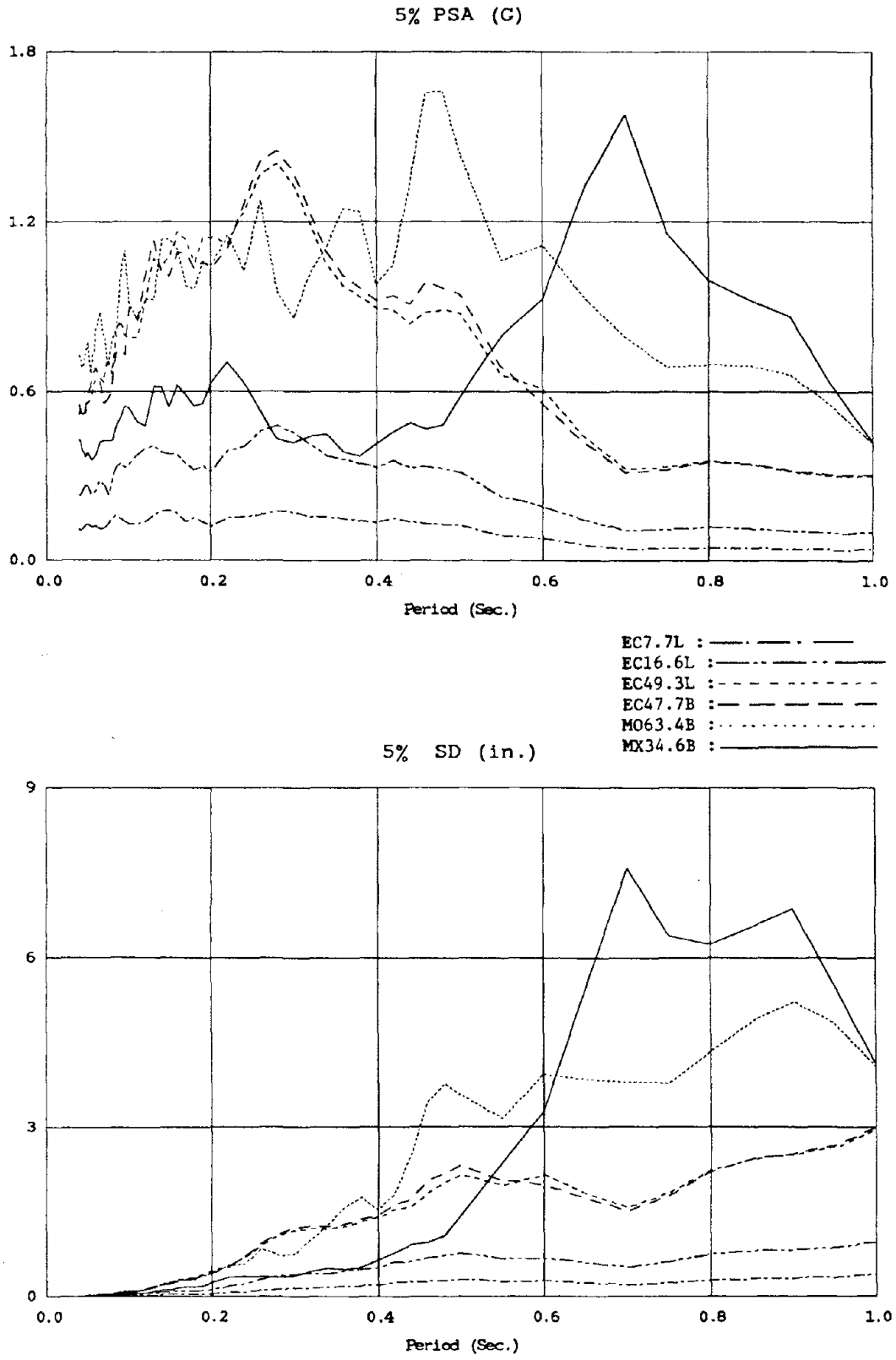

Figure 5.2 Acceleration and Displacement Response Spectra (5% Damping).

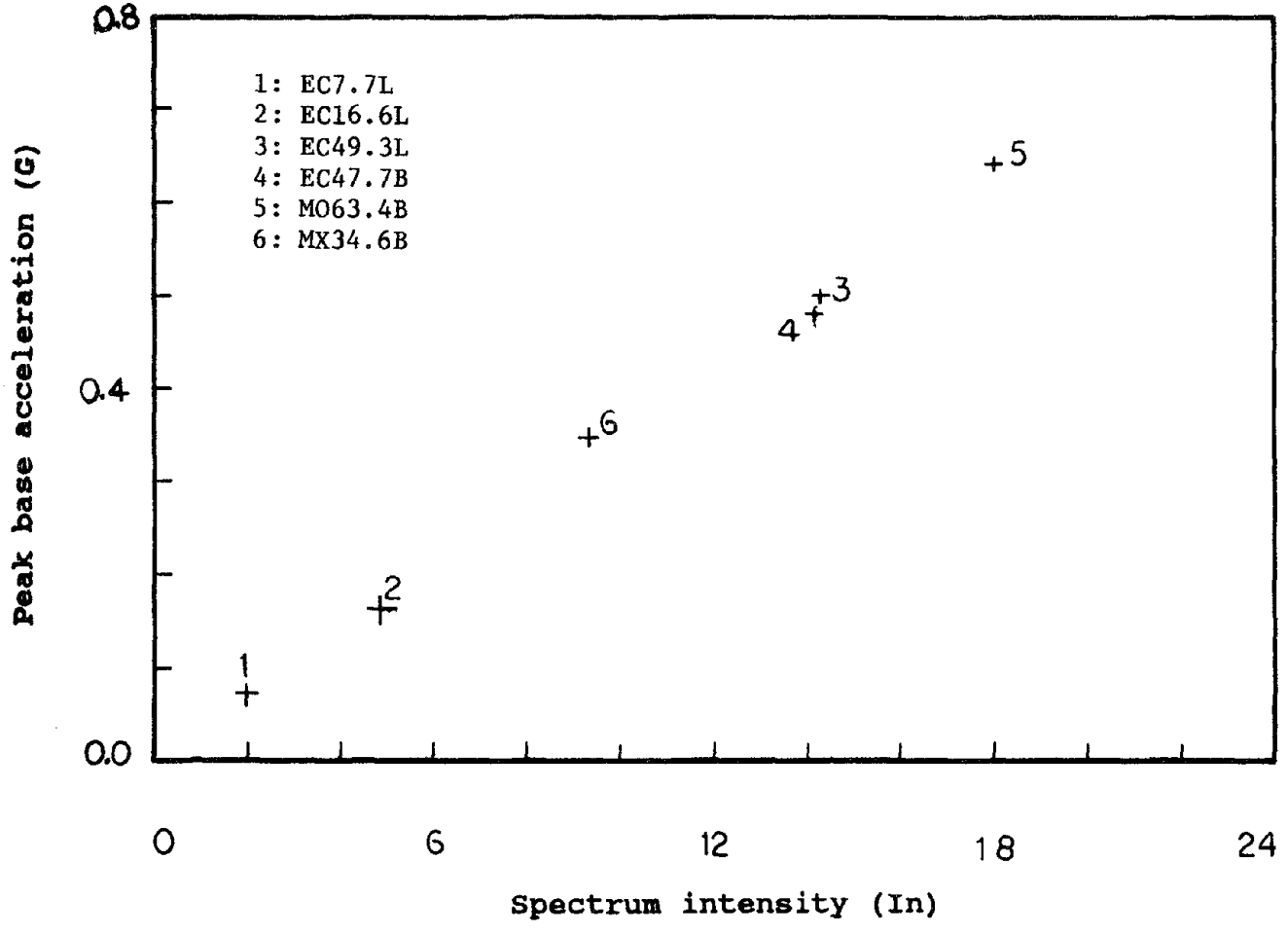

Figure 5.3 Variation of Spectrum Intensity Ratio with Peak Input Acceleration.

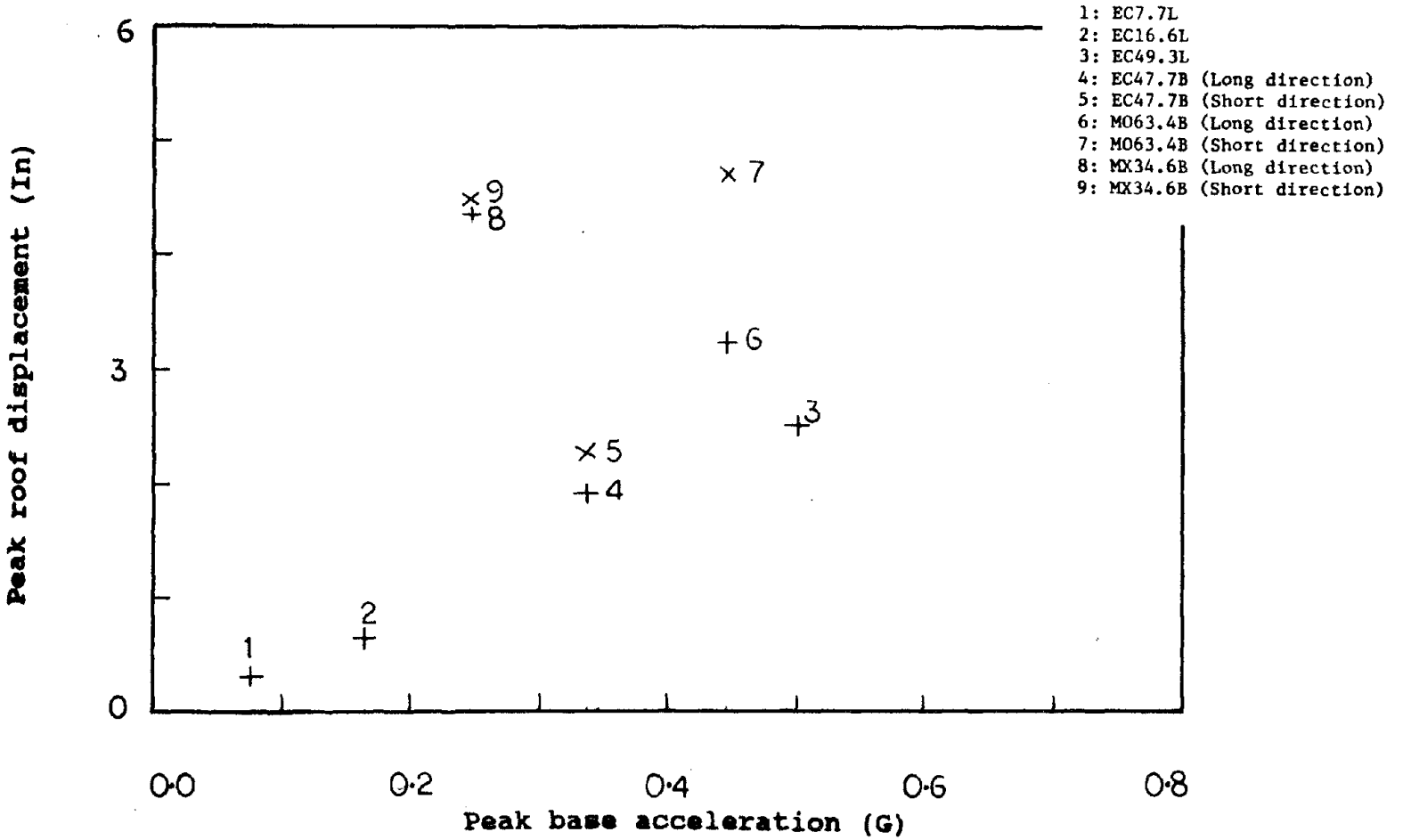

Figure 5.4 Variation of Peak Roof Displacement with Peak Input Acceleration.

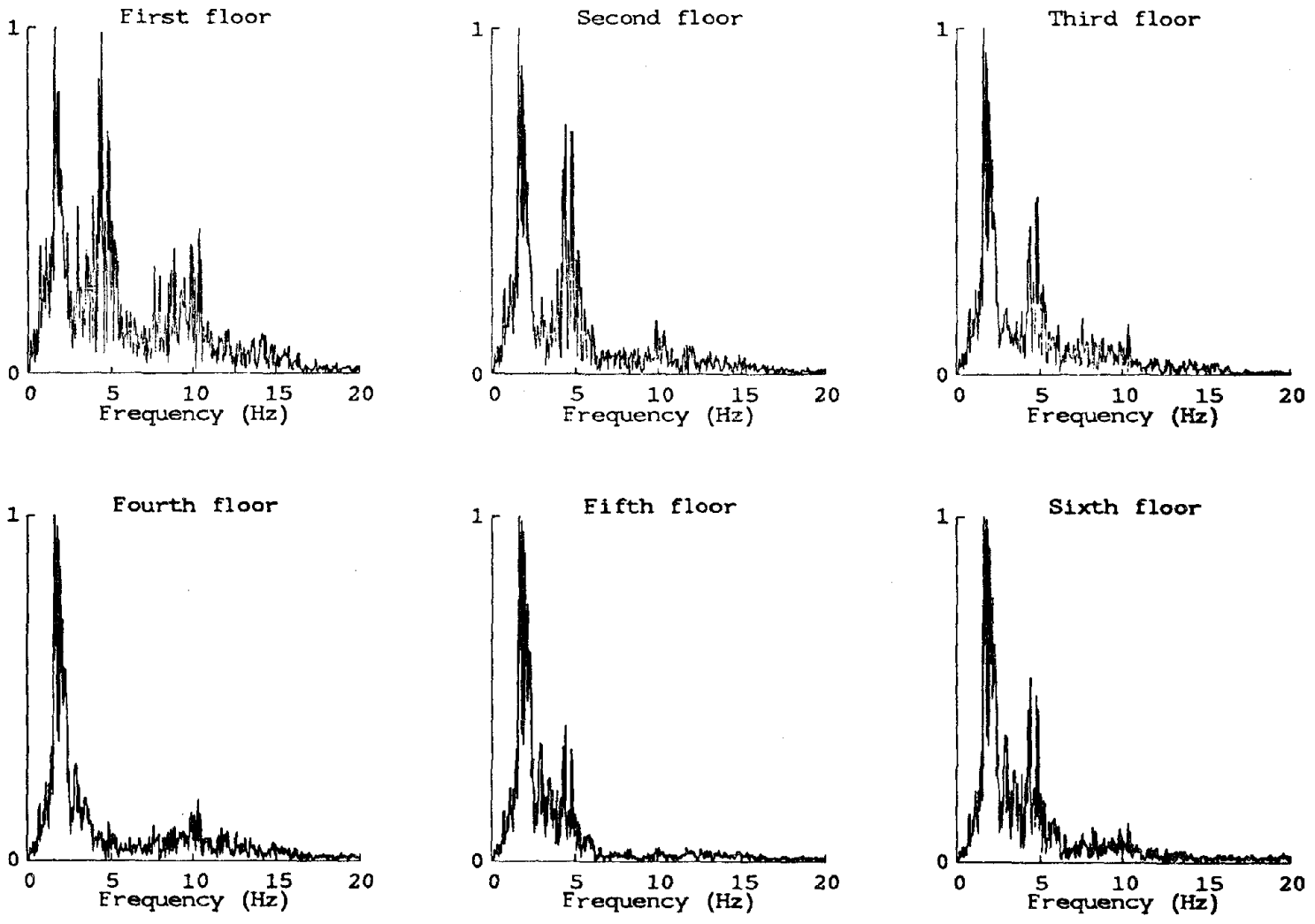

Figure 5.5(a) Fourier Amplitude Spectra (EC49.3L).

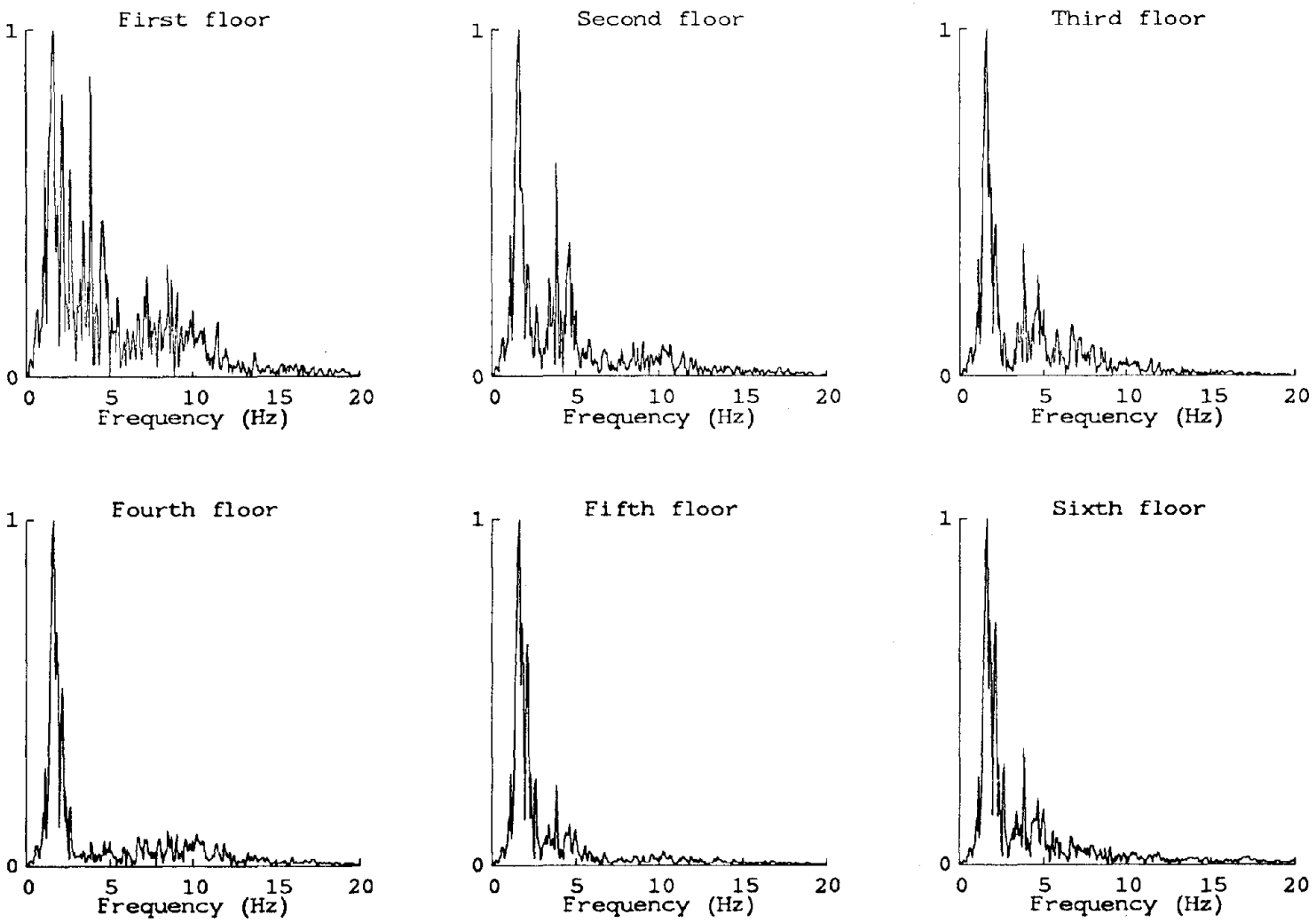

Figure 5.5(b) Fourier Amplitude Spectra (MO63.4B).

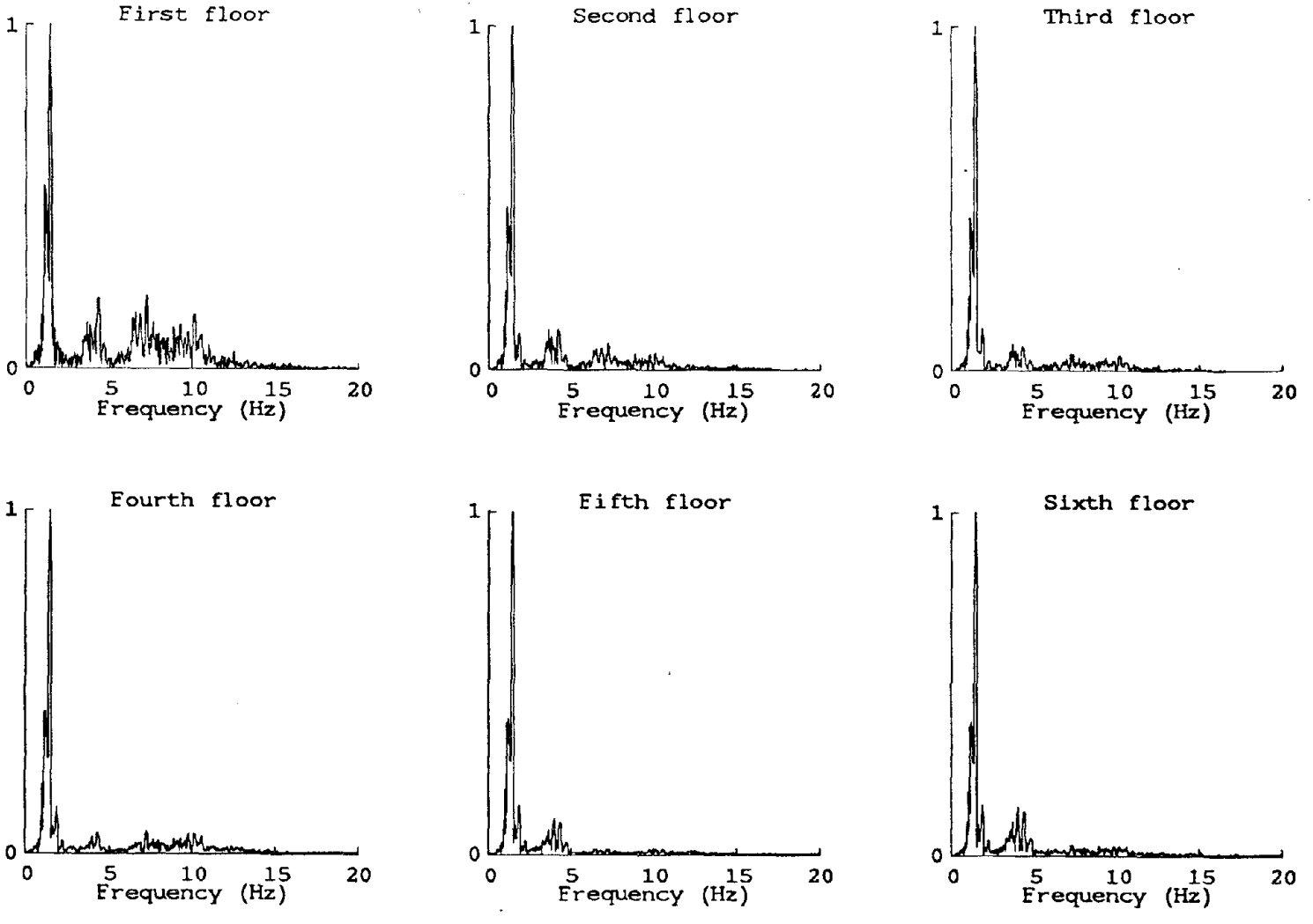

Figure 5.5(c) Fourier Amplitude Spectra (MX34.6B).

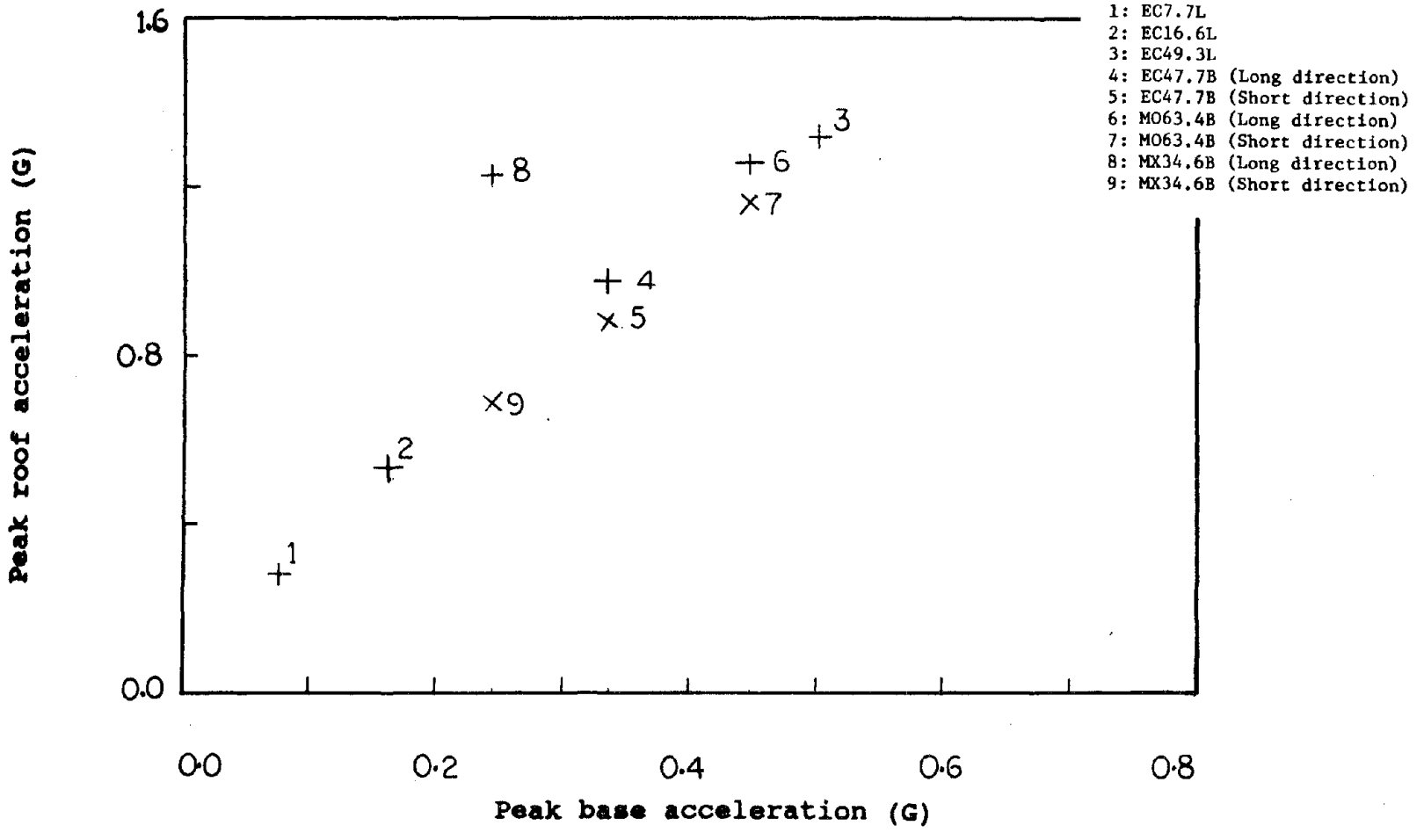

Figure 5.6 Variation of Peak Roof Acceleration with Peak Input Acceleration.

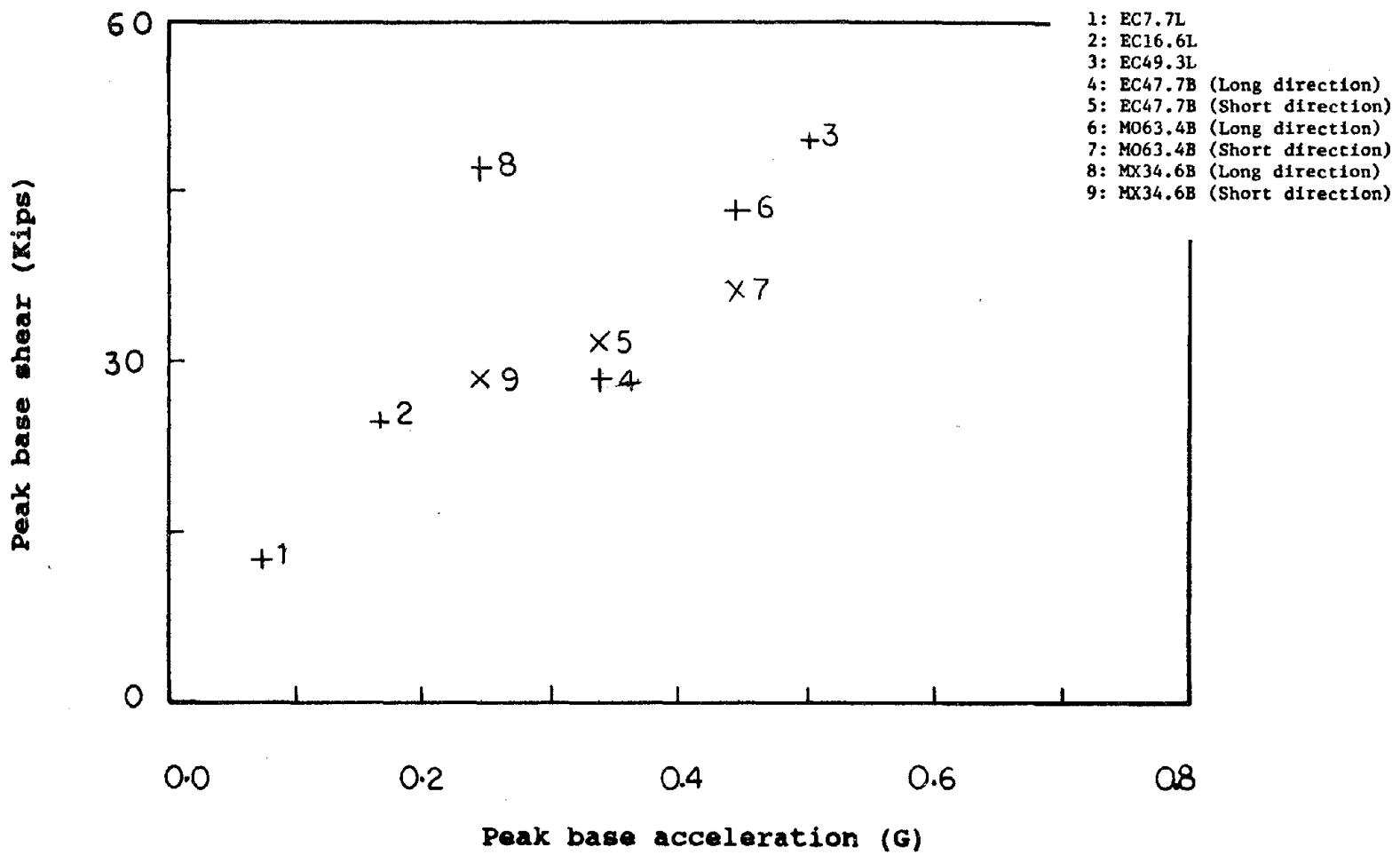

Figure 5.7 Variation of Peak Base Shear with Peak Input Acceleration.

f6=0.22V
f5=0.19V
f4=0.15V
f3=0.22V
f2=0.15V
f1=0.07V

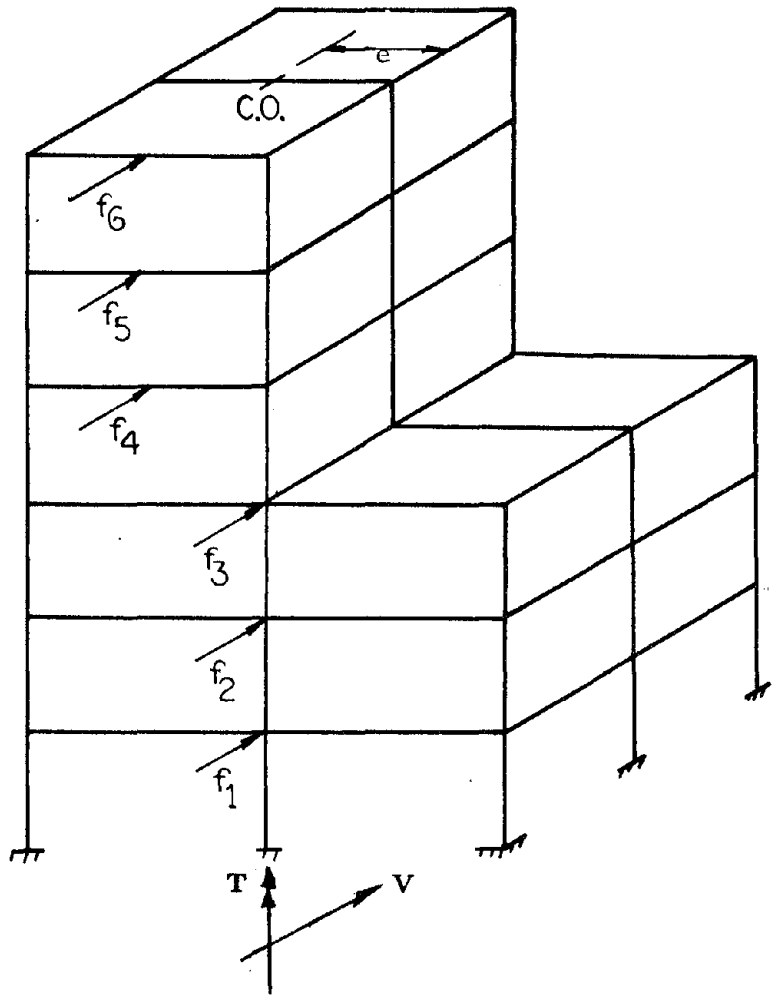

Figure 5.8 Distribution of Lateral Forces from UBC.

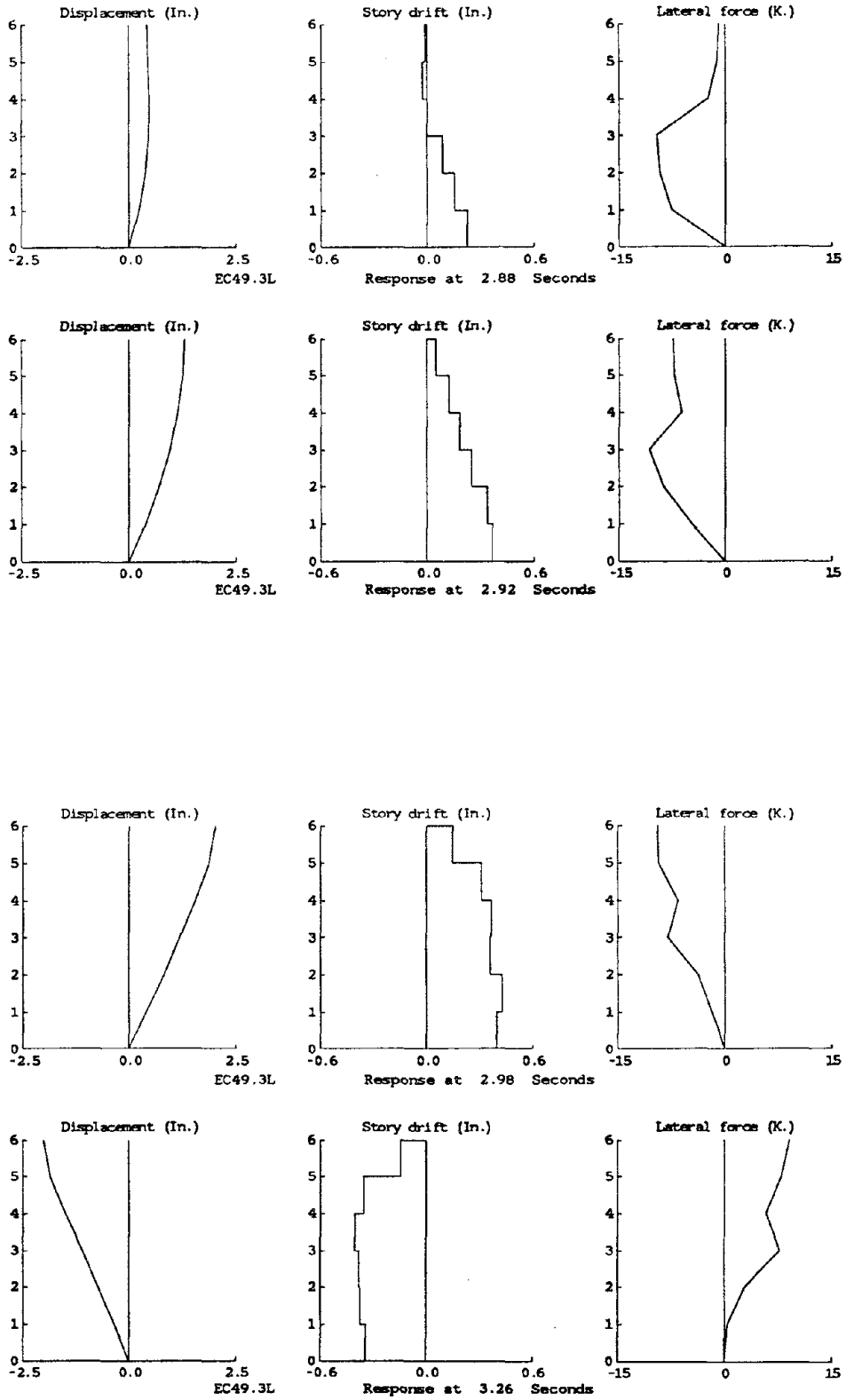

Figure 5.9 Response Profile.

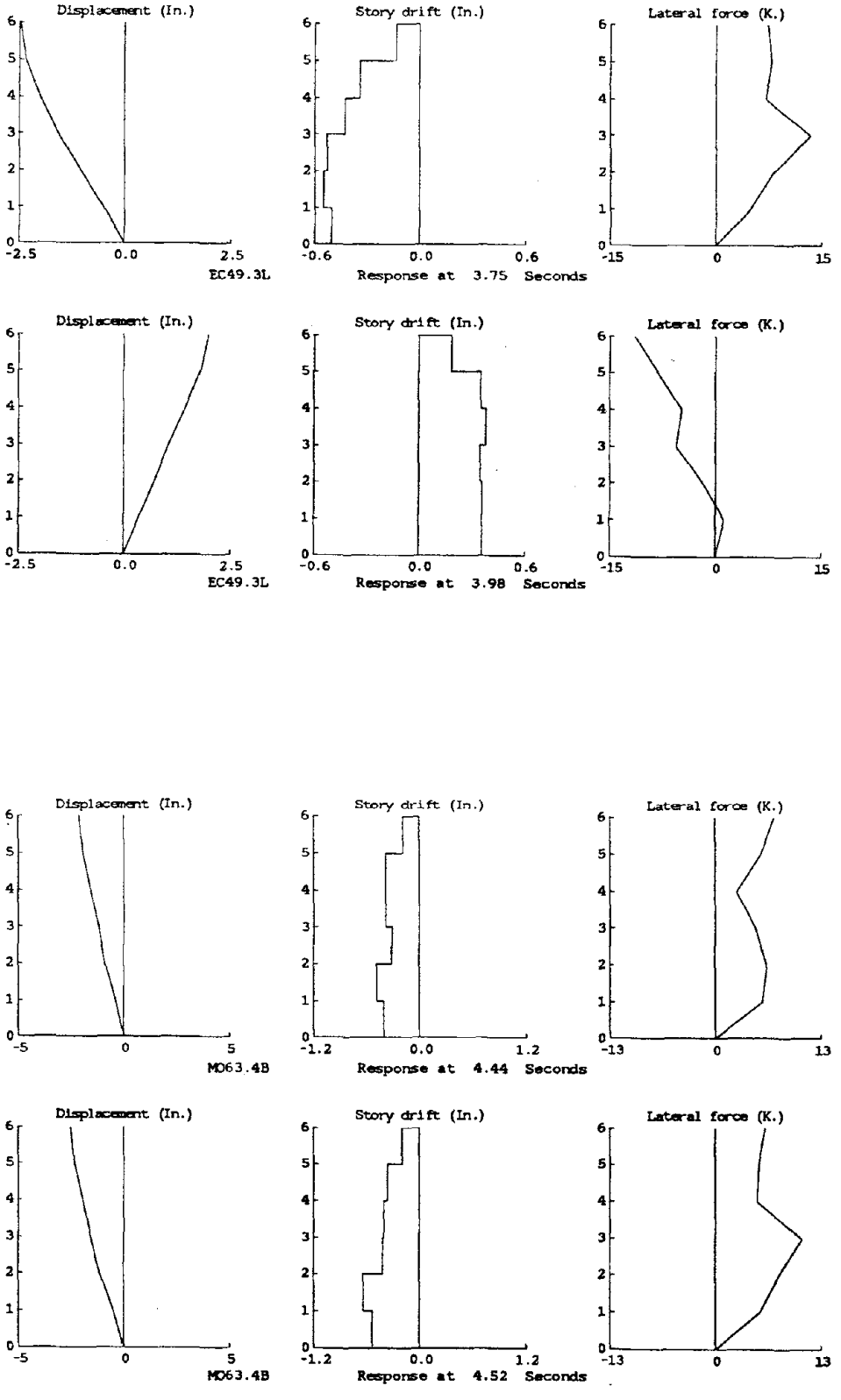

Figure 5.9 (Cont.) Response Profile.

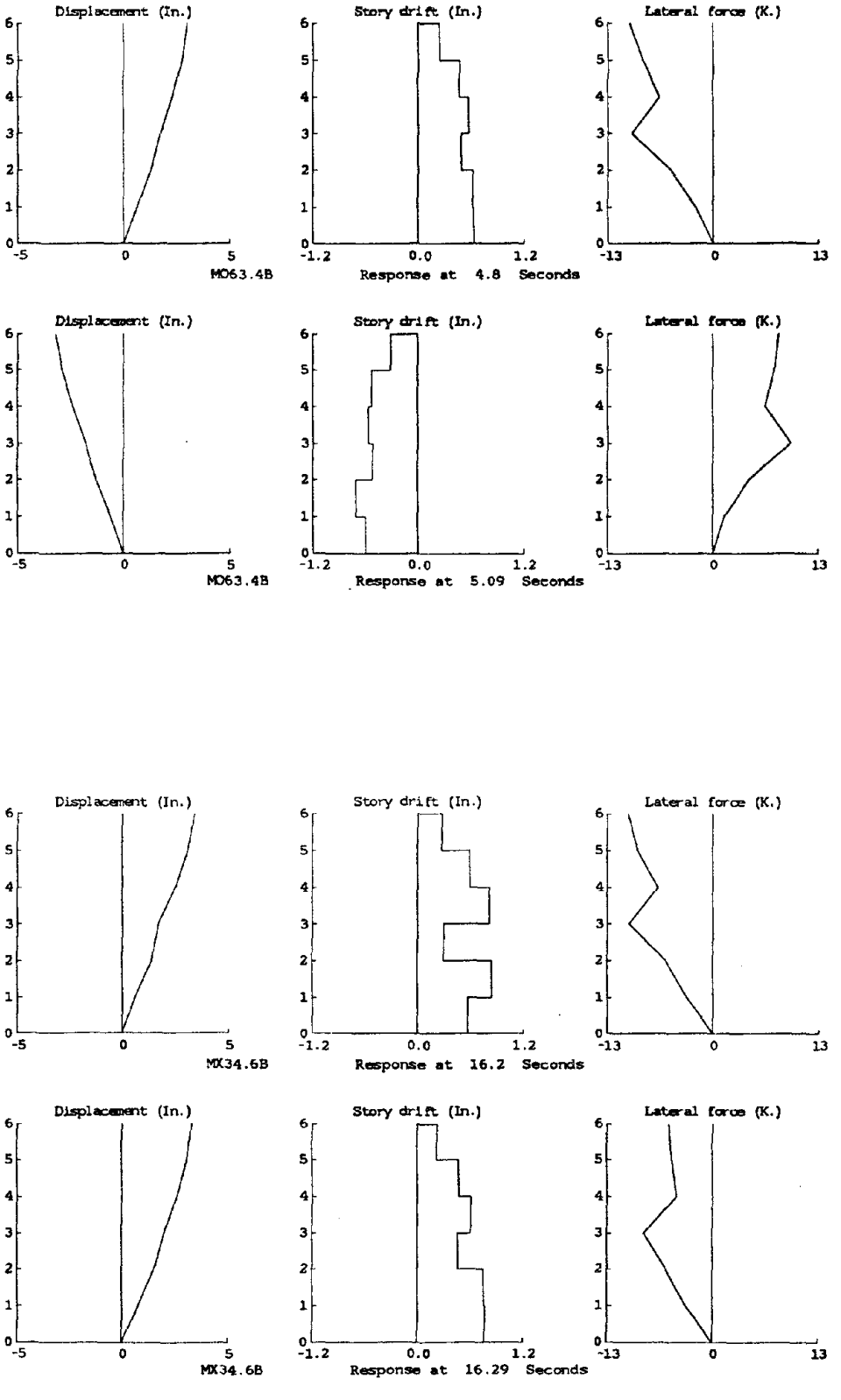

Figure 5.9 (Cont.) Response Profile.

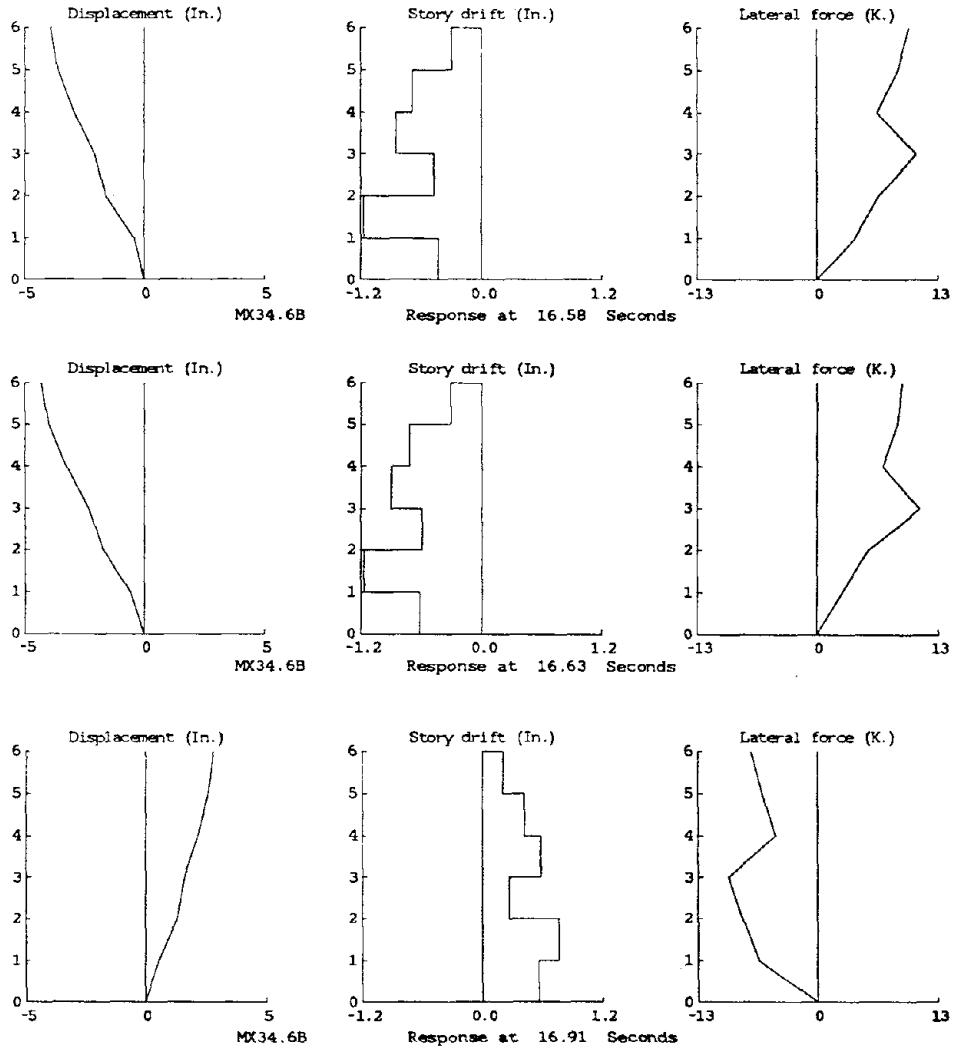

Figure 5.9 (Cont.) Response Profile.

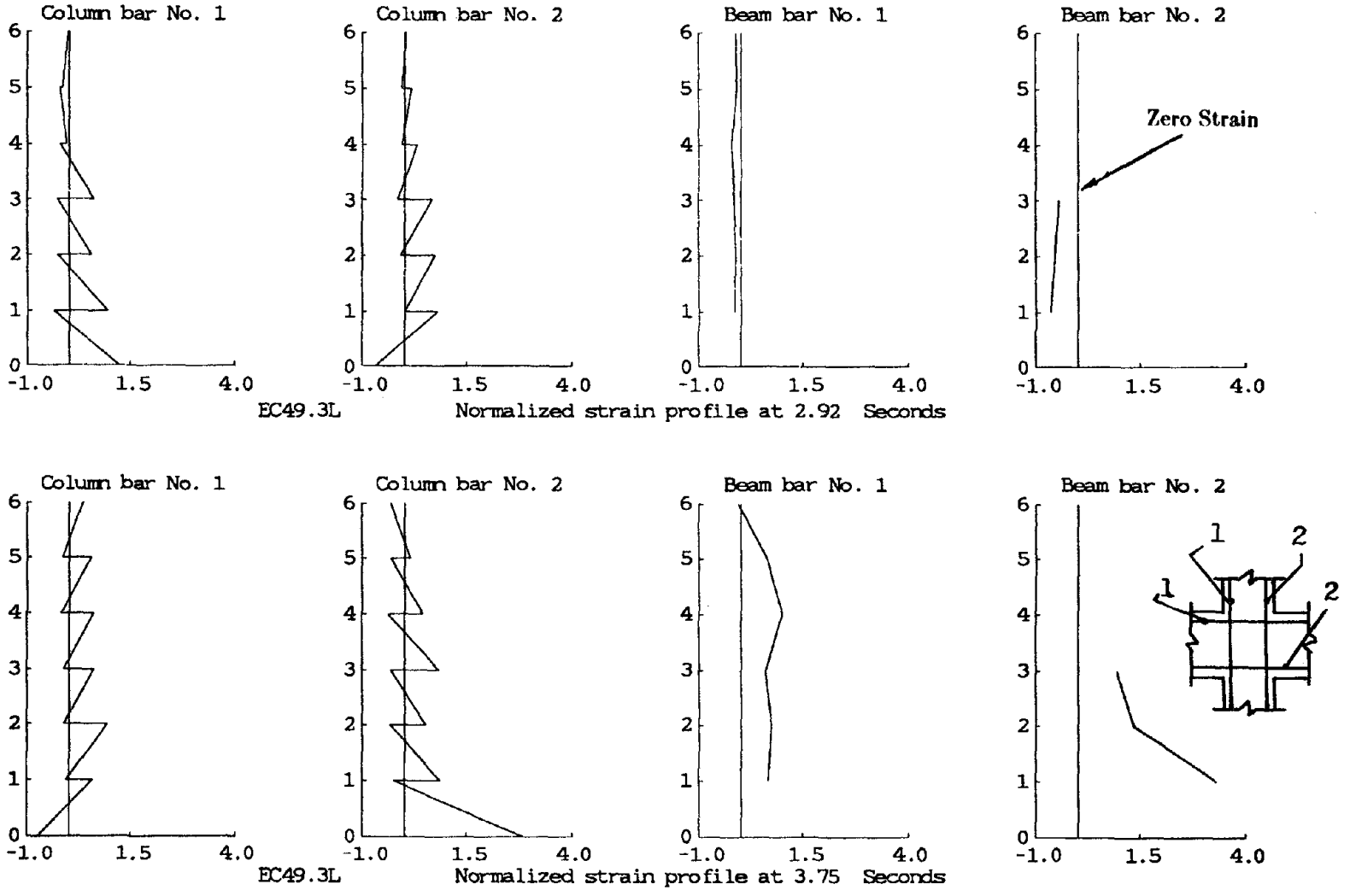

Figure 5.10(a) Variation of Reinforcement Strain over Height.

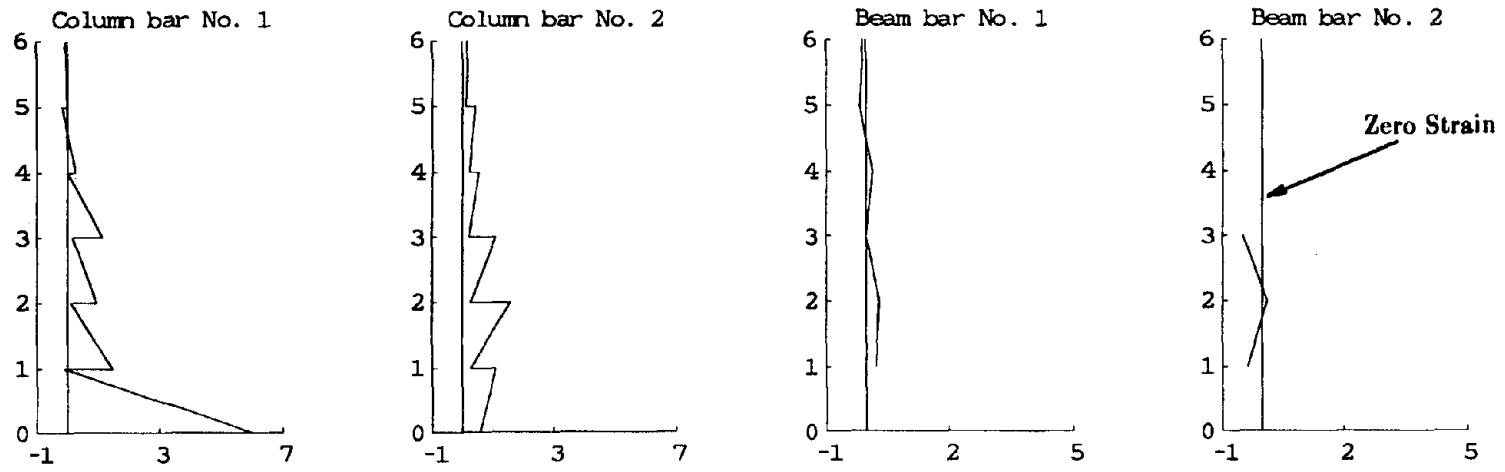

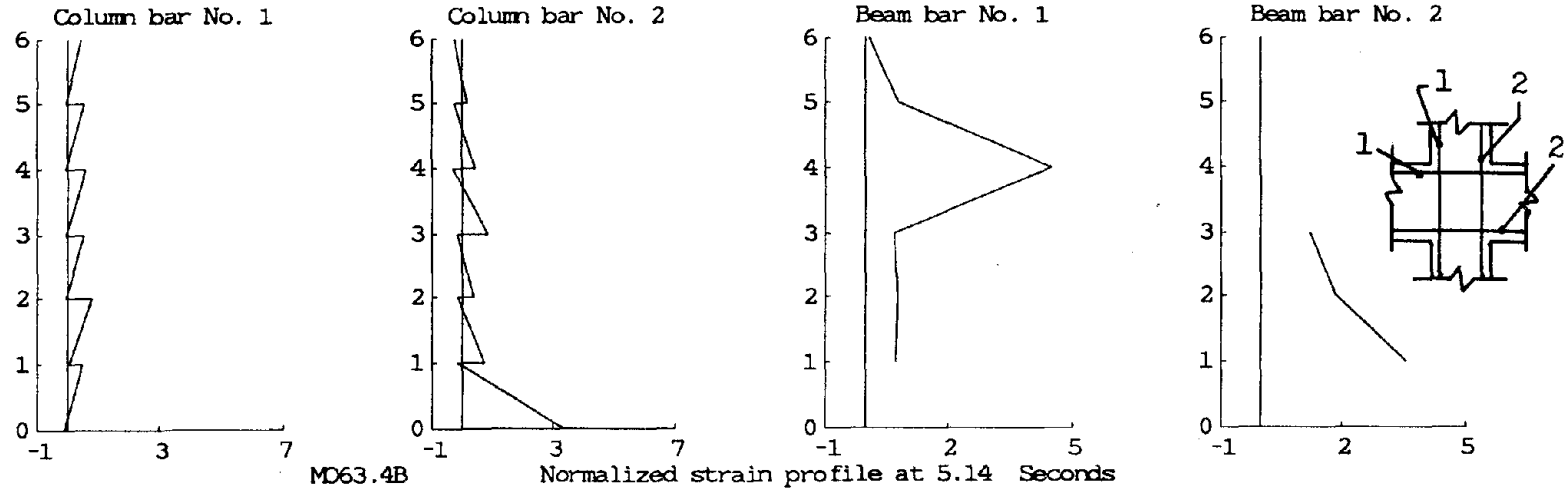

Figure 5.10(b) Variation of Reinforcement Strain over Height.

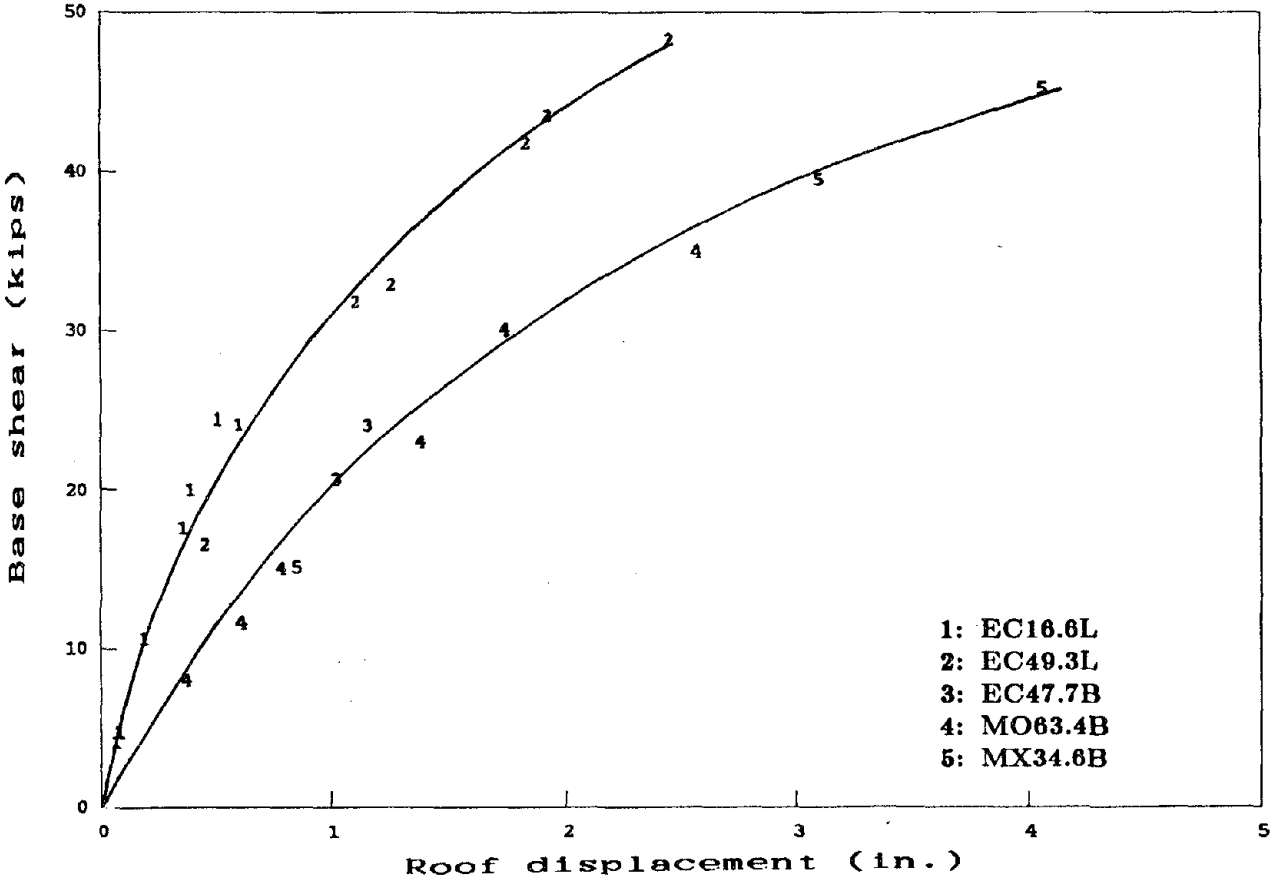

Figure 5.11 Envelope Relation Between Base Shear and Roof Displacement.

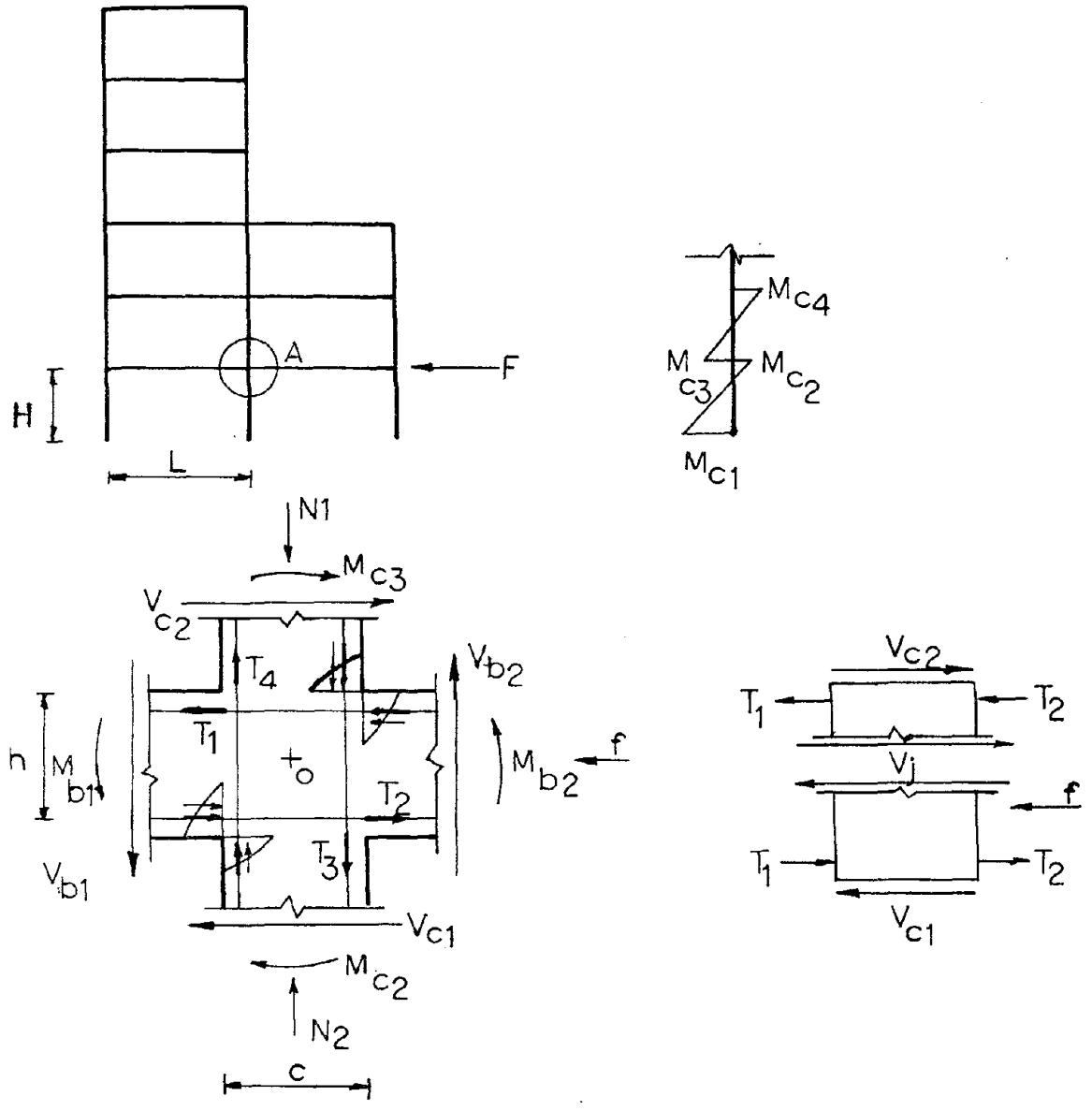

Actions and stress resultants (Detail A)

Joint shear

Figure 5.12 Free-Body Diagram of First-Floor Interior Joint.

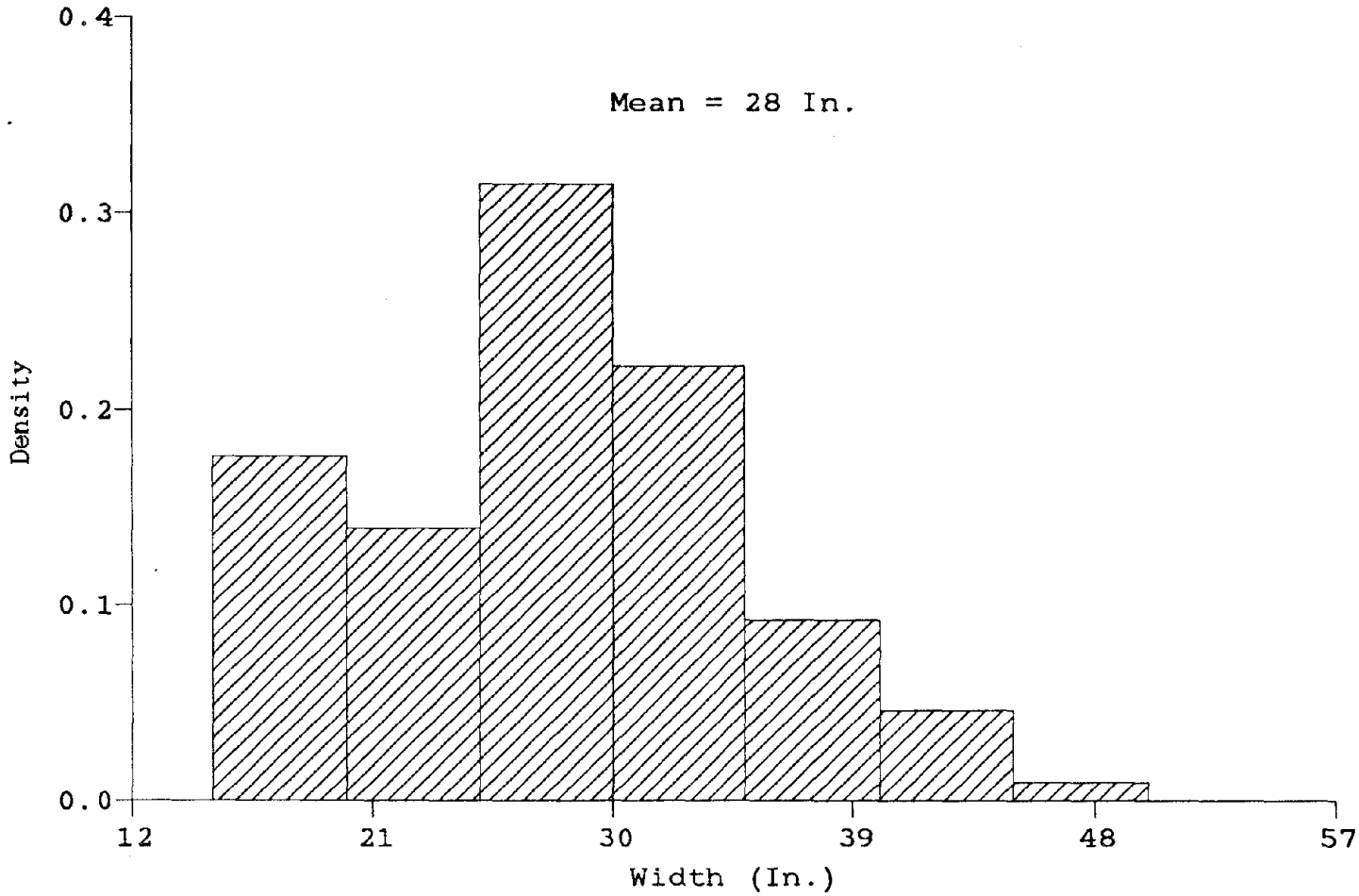

Figure 5.13 Histogram of Estimated Effective Flange Width.

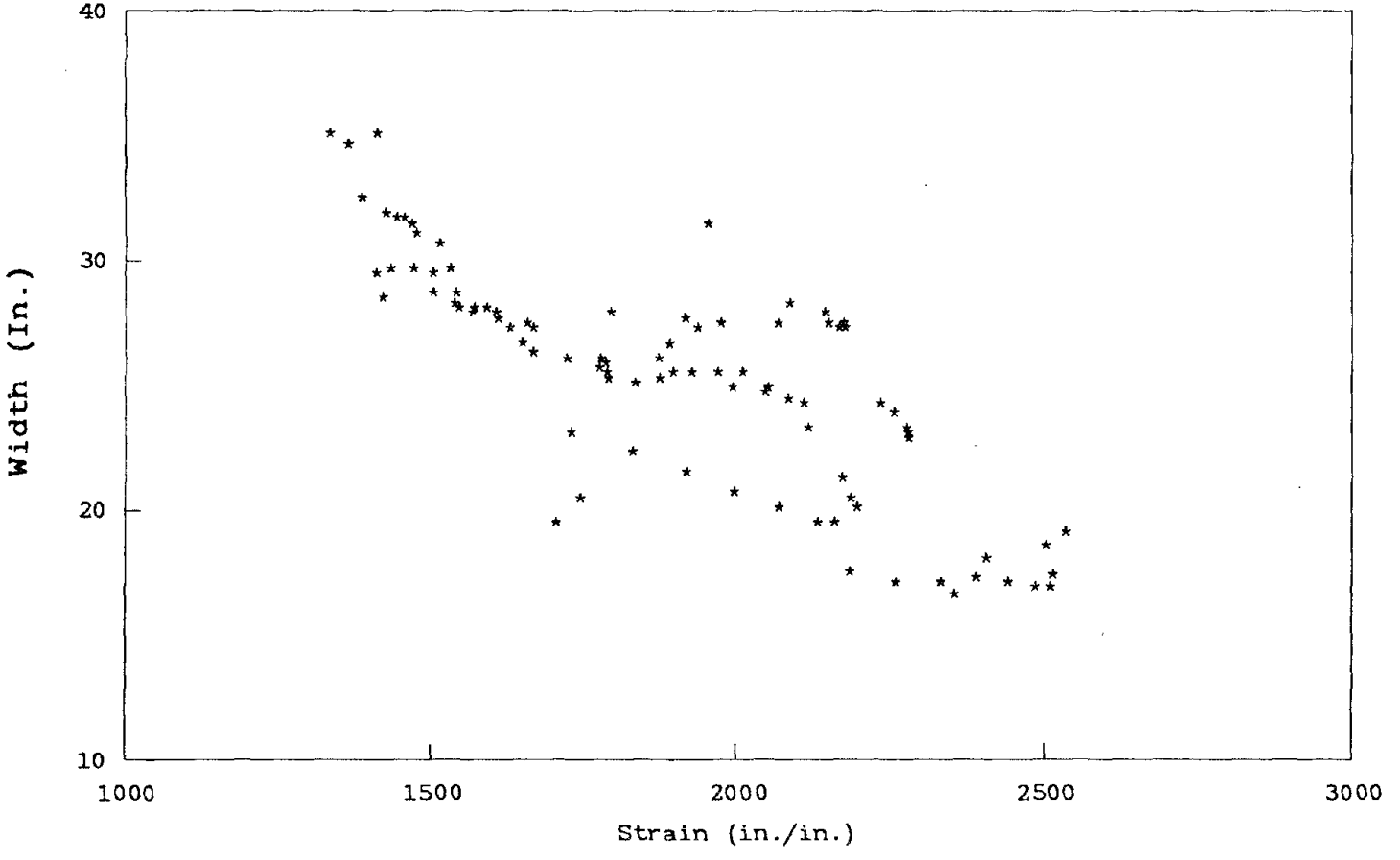

Figure 5.14 Variation of Effective Flange Width with Beam Strain.

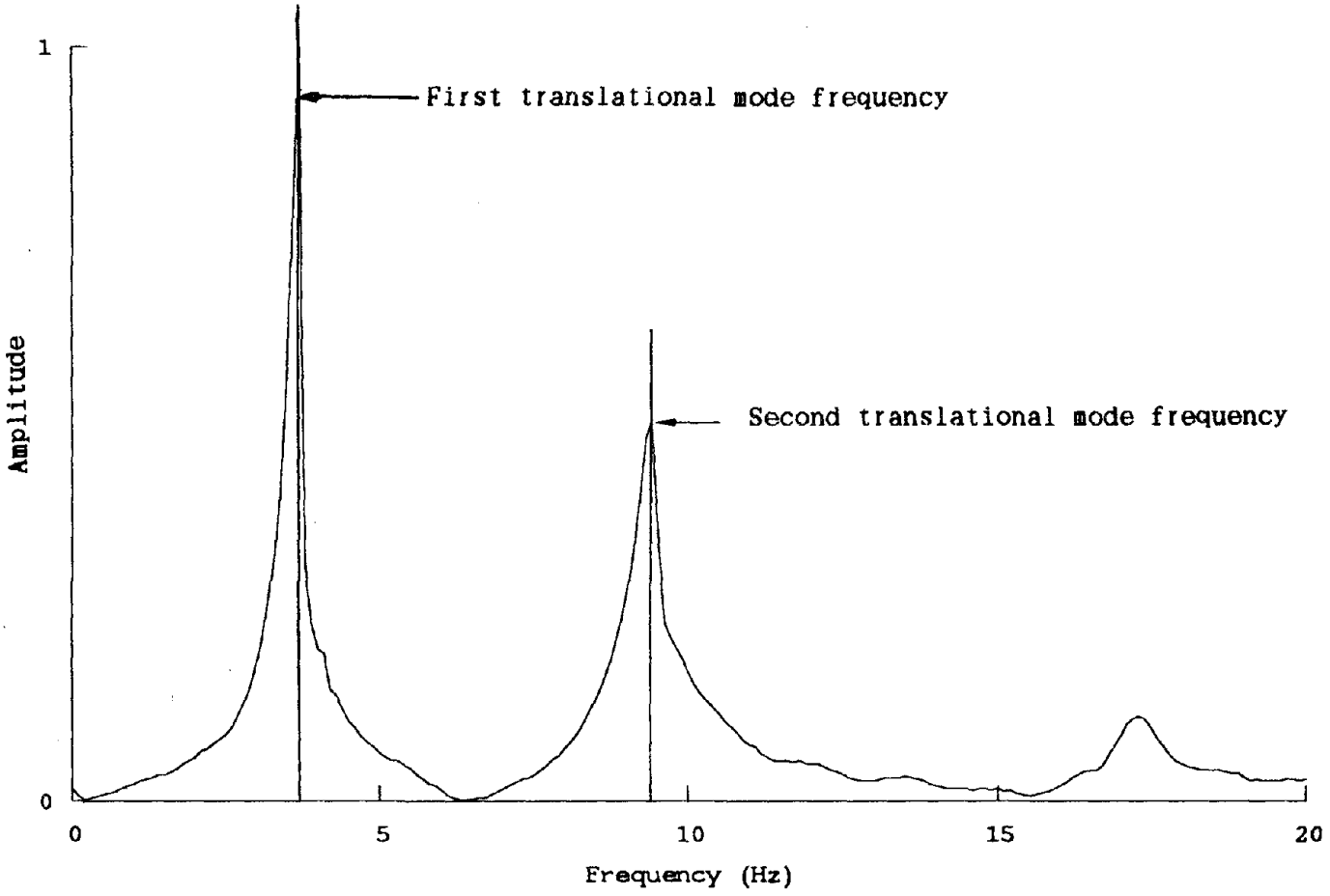

Figure 5.15 Typical Fourier Amplitude Spectrum (Long Direction).

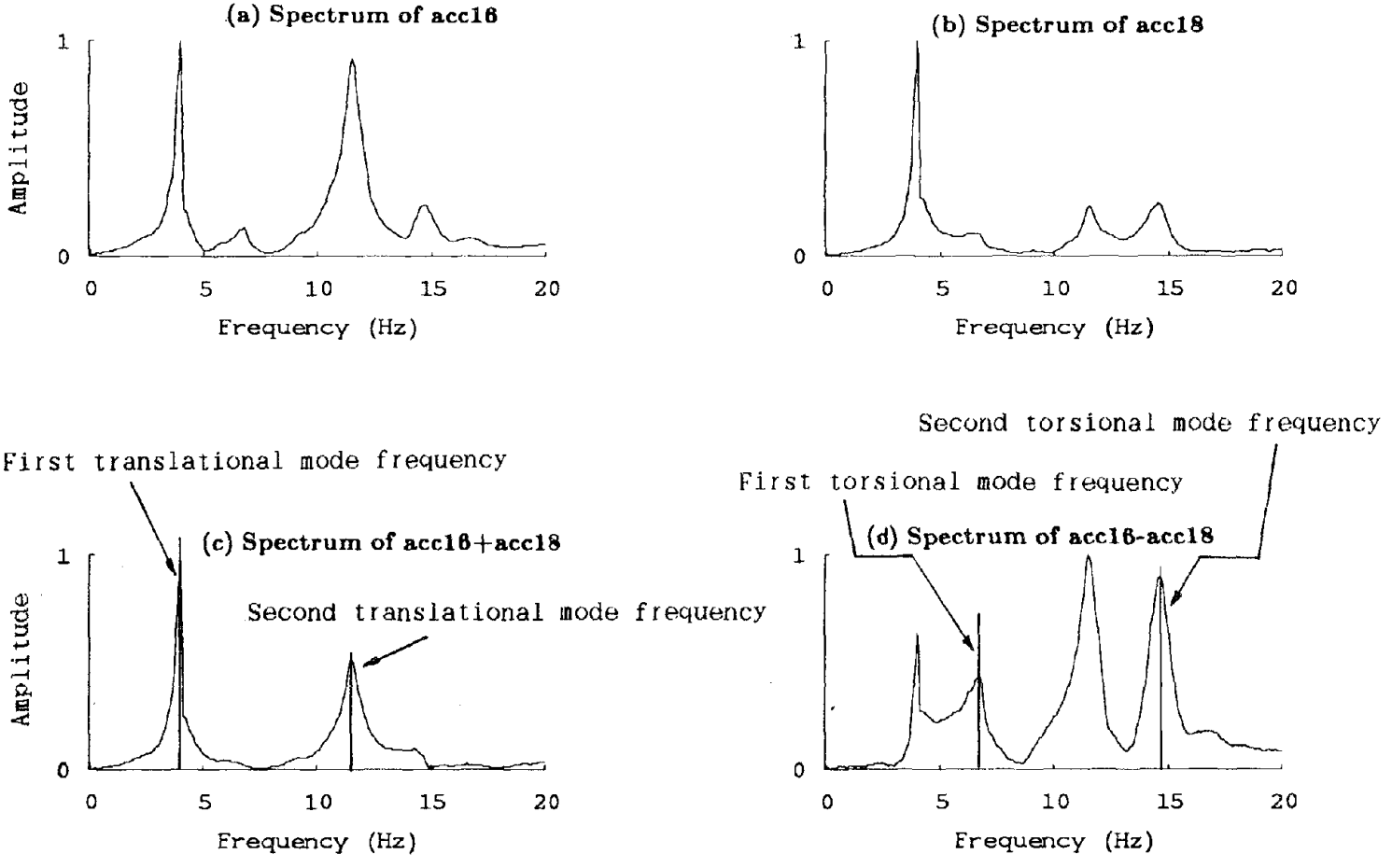

Figure 5.16 Method to Obtain Torsional and Short-Direction Translational Frequencies.

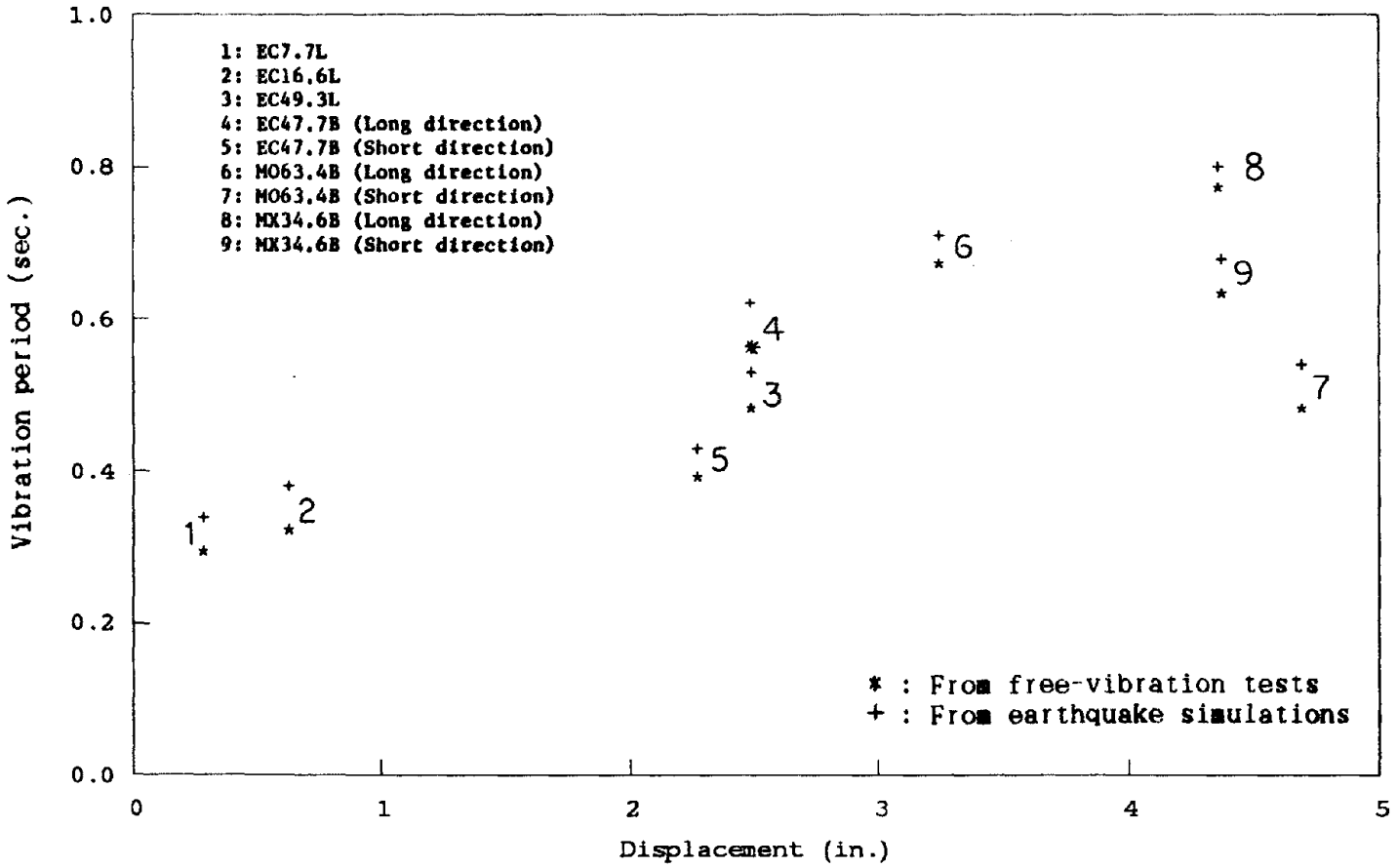

Figure 5.17 Variation of Translational Vibration Period with Peak Displacement.

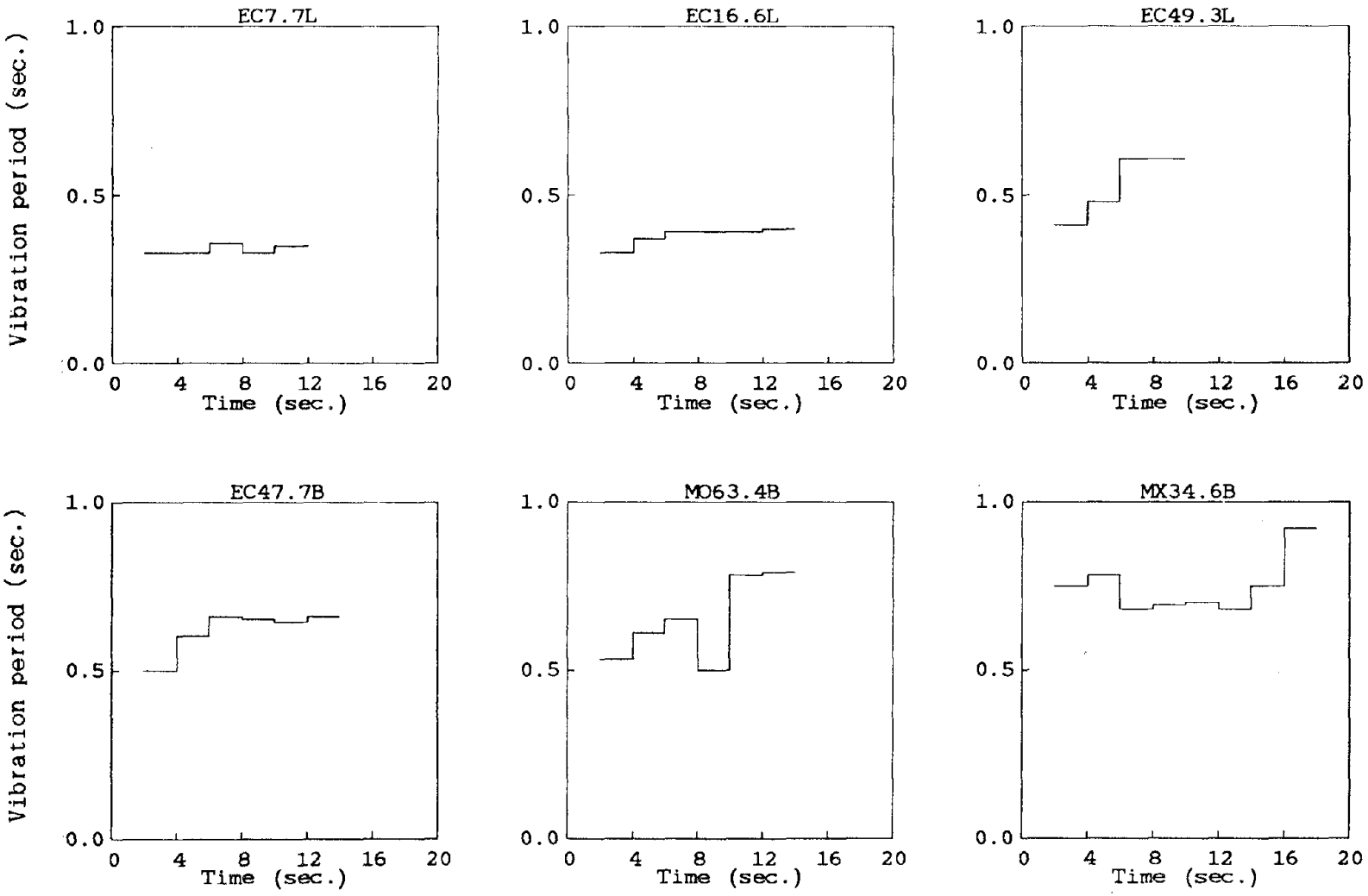

Figure 5.18 Variation of Apparent Long Direction Translational Period with Time.

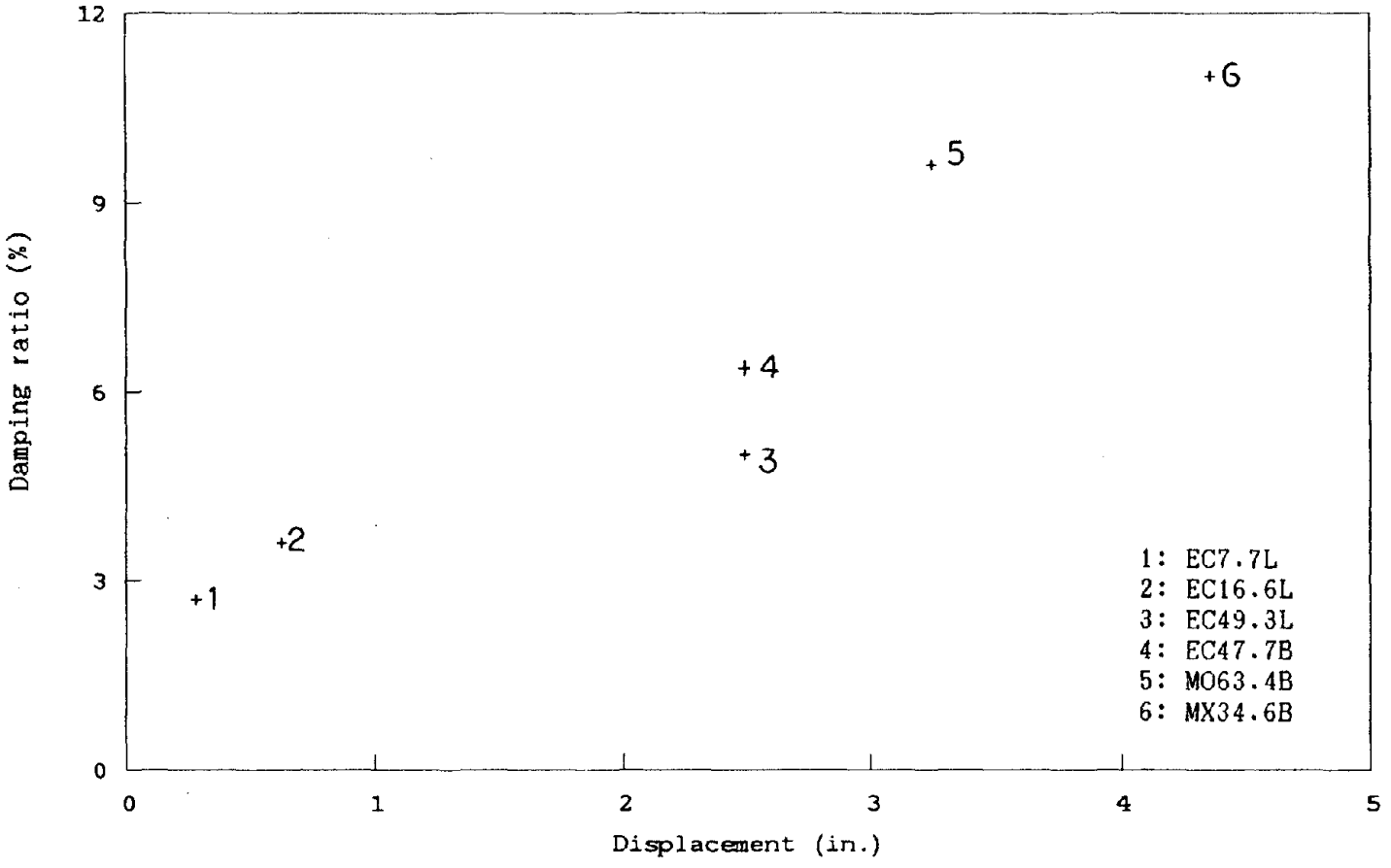

Figure 5.19 Variation of Viscous Damping Ratio with Peak Displacement.

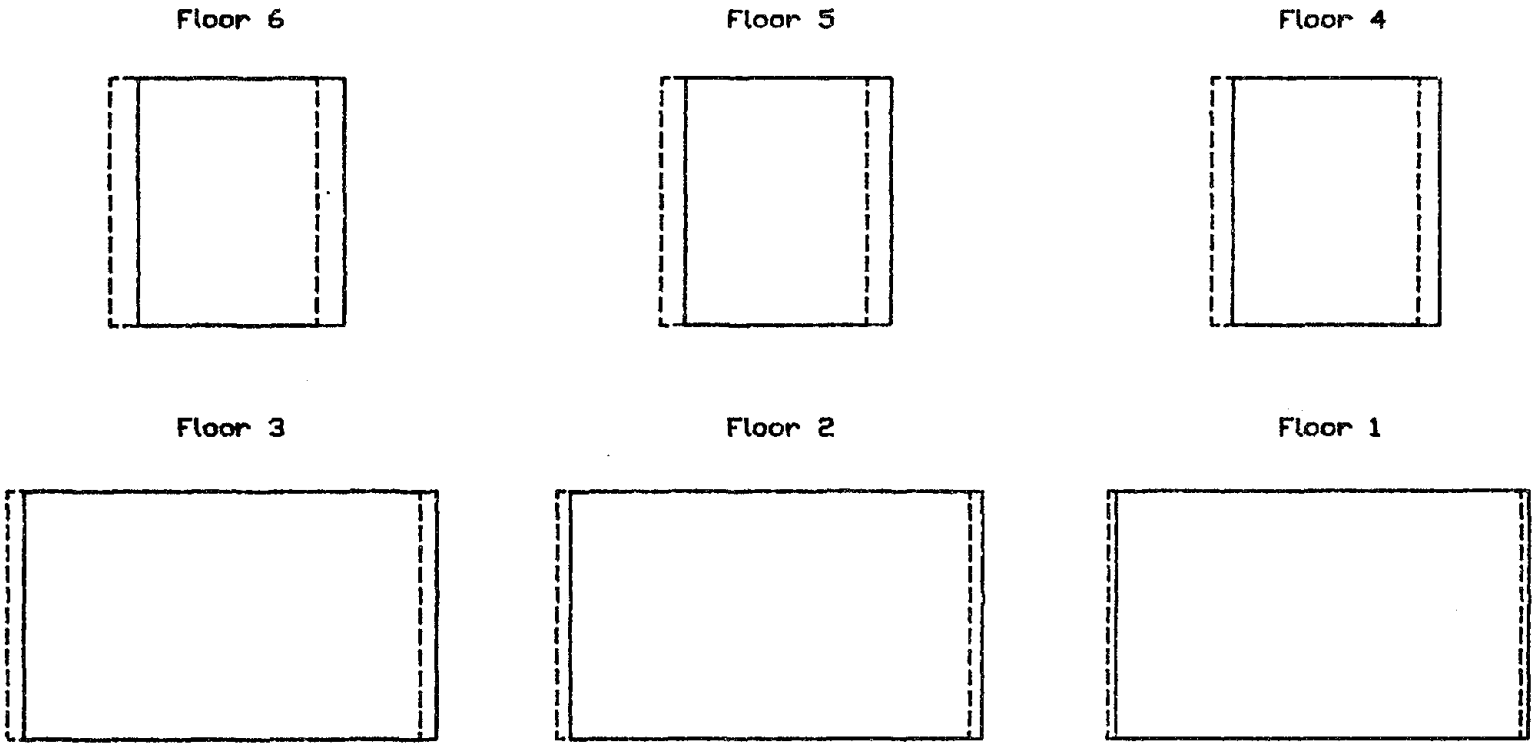

Figure 5.20(a) First Mode (1st Translational in Long Direction).

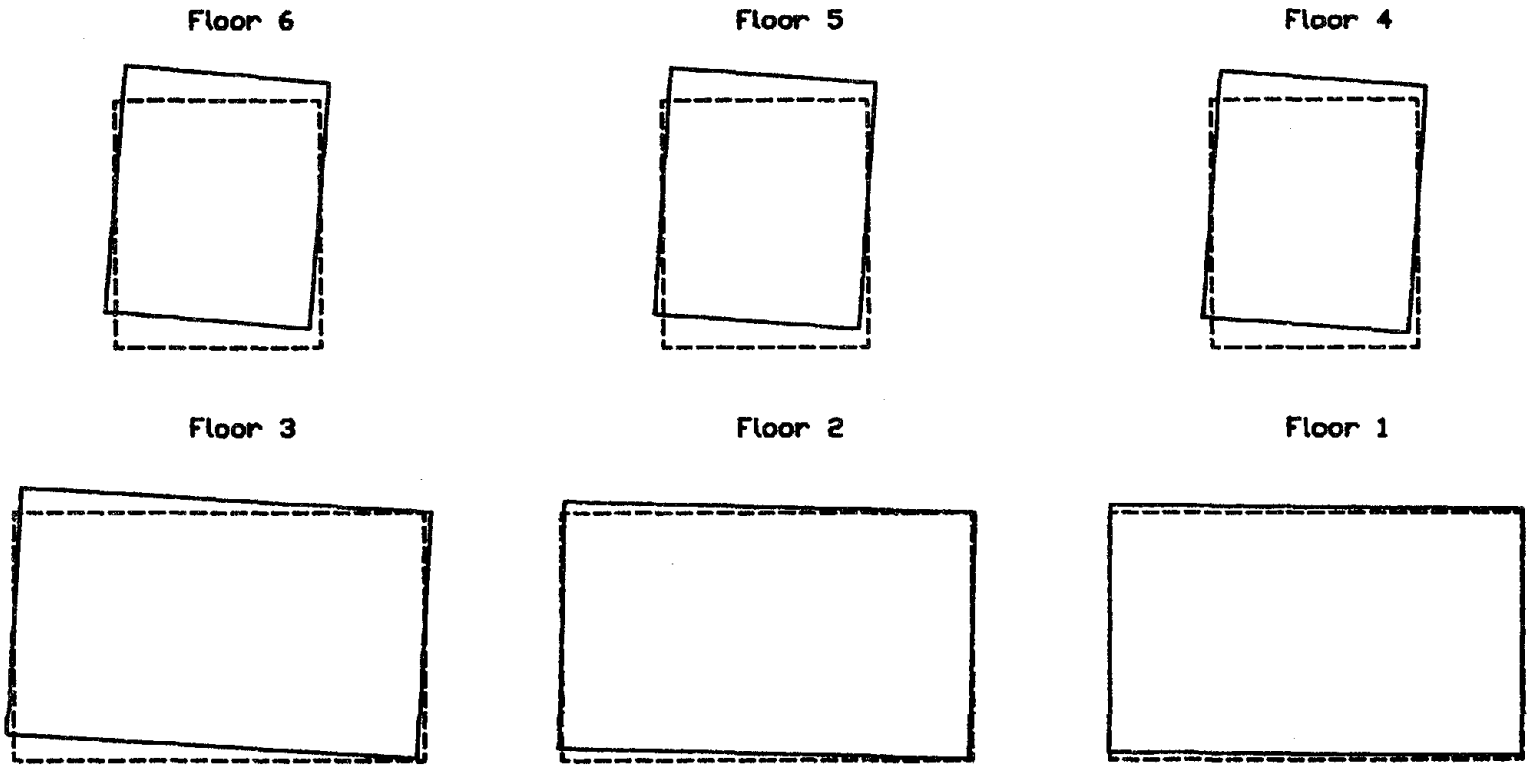

Figure 5.20(b) Second Mode Shape (1st Translational in Short Direction).

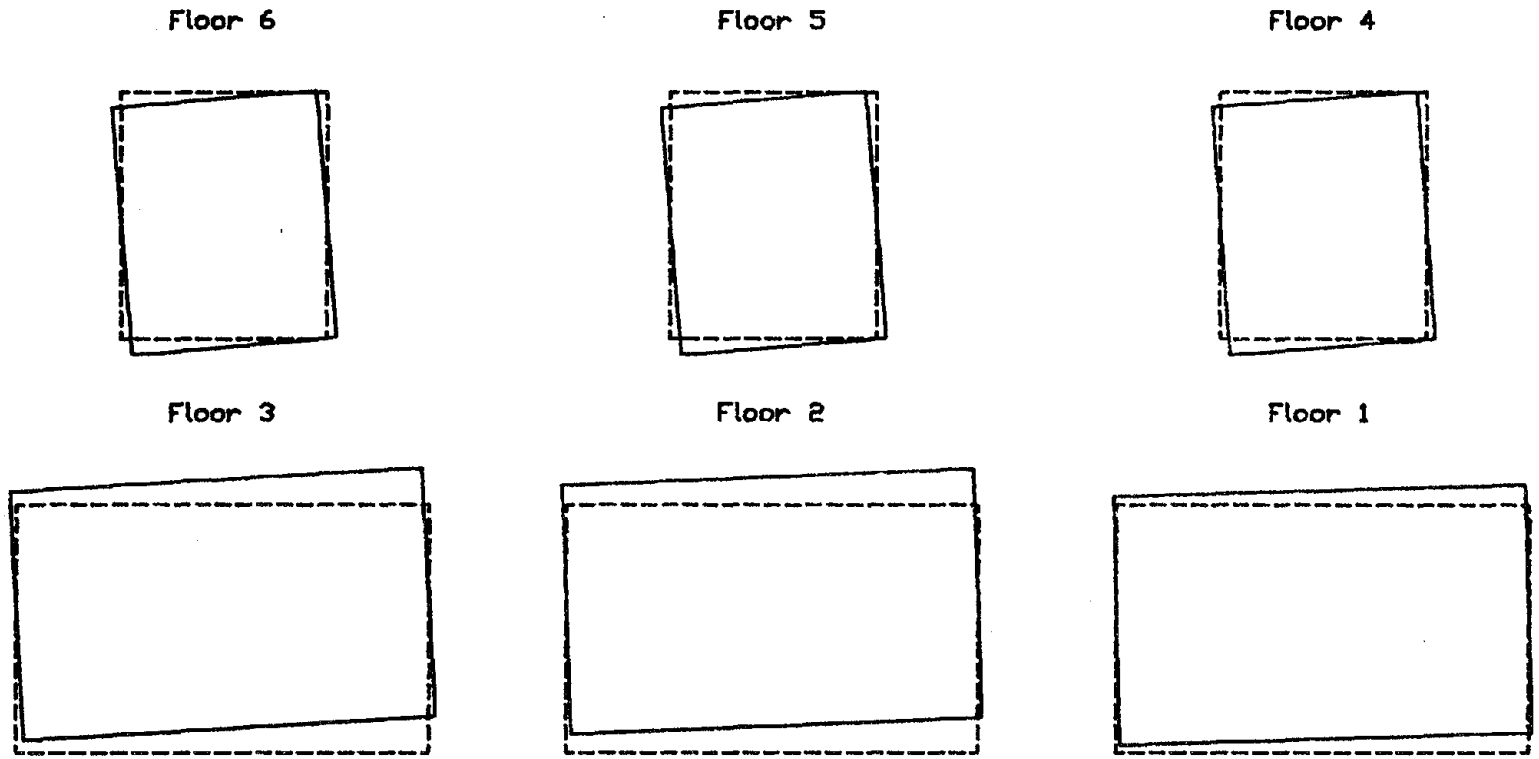

Figure 5.20(c) Third Mode Shape (1st Torsional).

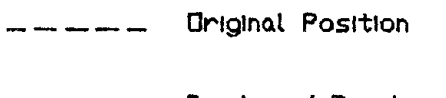

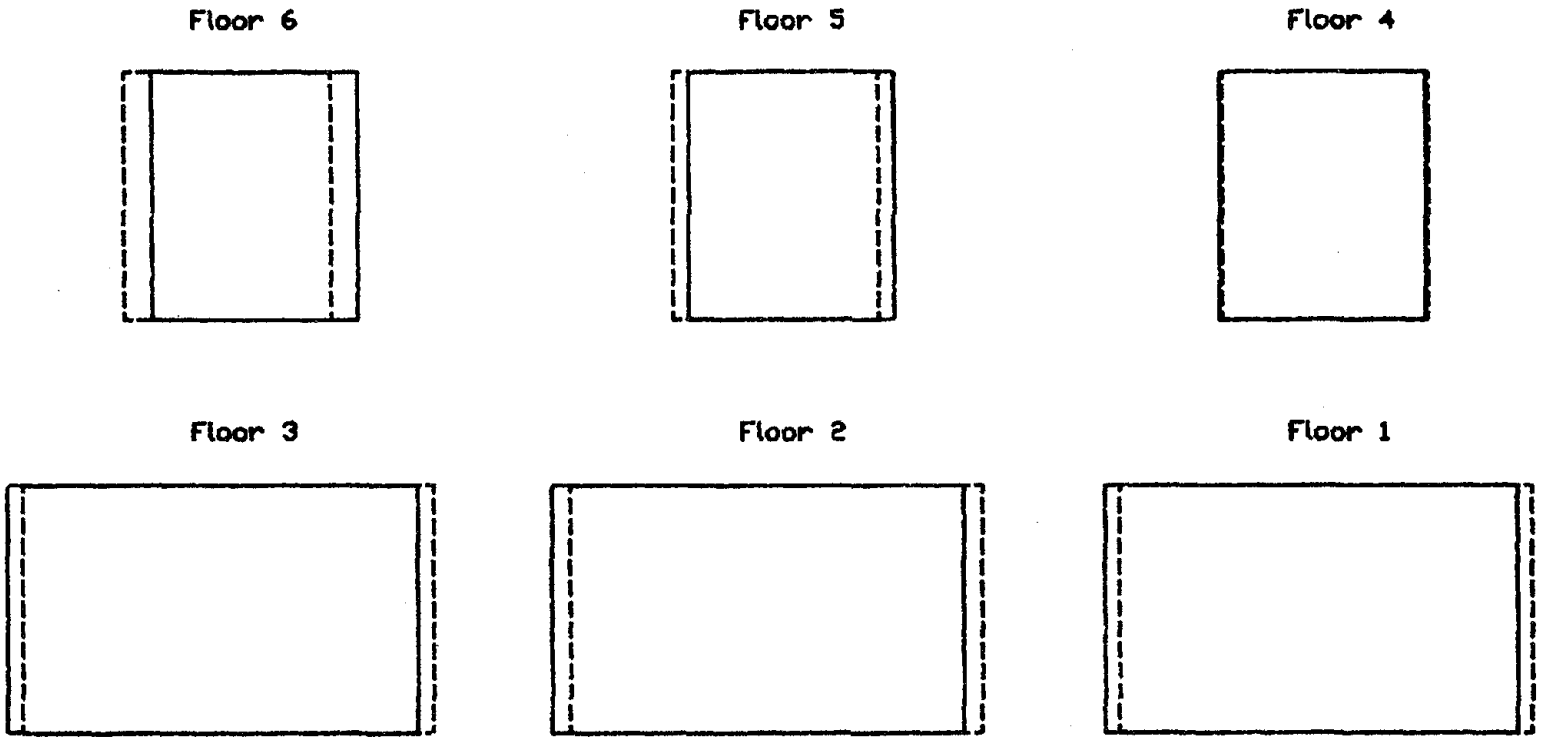

Figure 5.20(d) Fourth Mode Shape (2nd Translational in Long Direction).

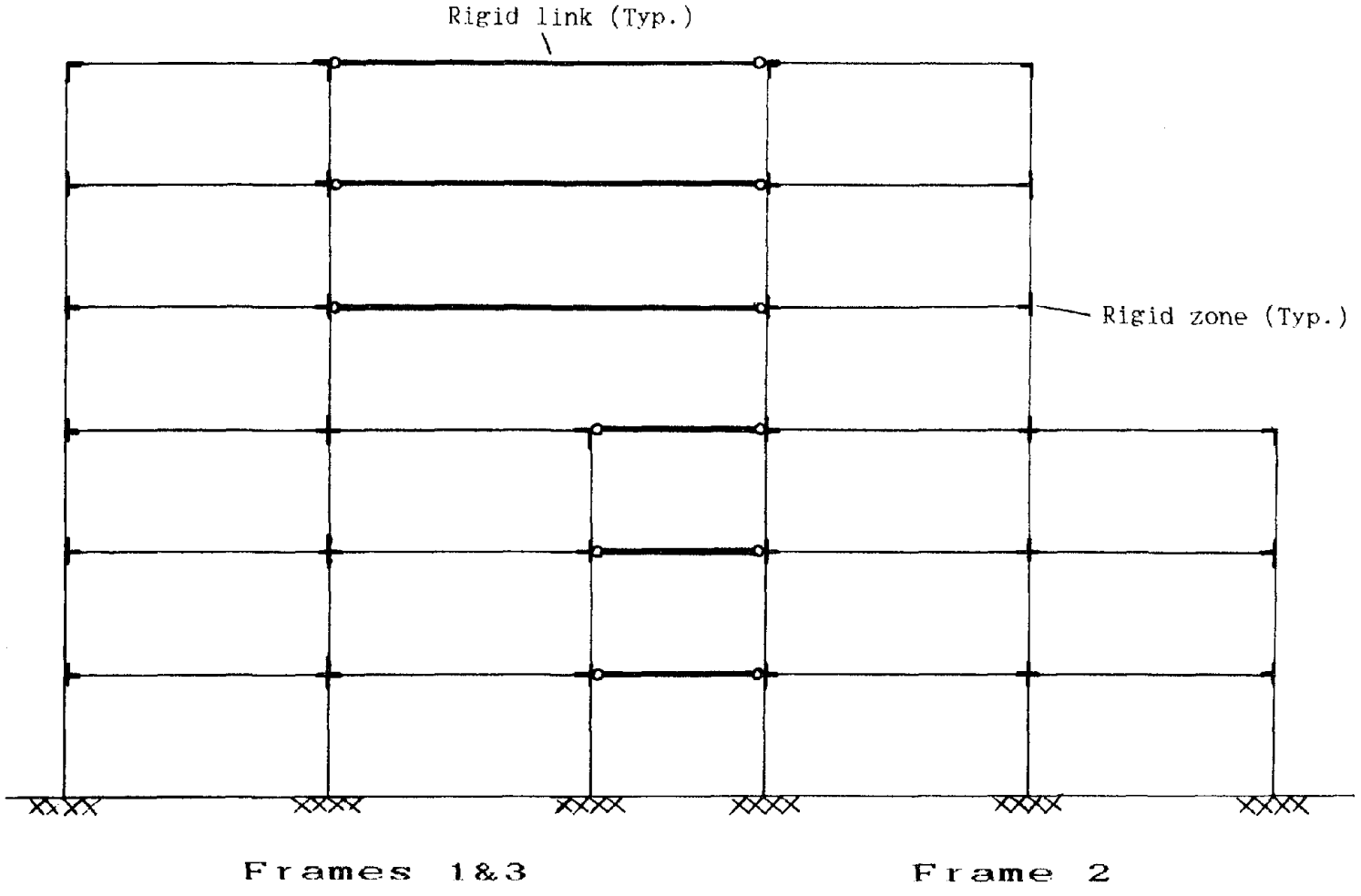

Figure 6.1 Mathematical Model Used for Correlation Studies.

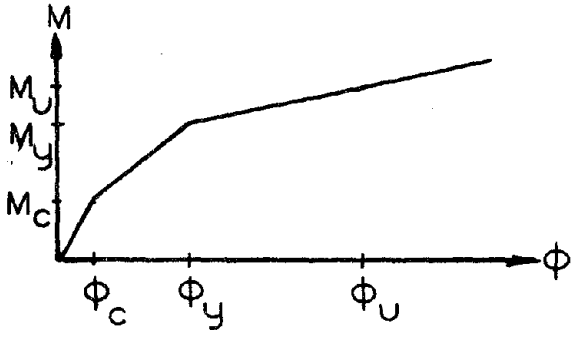

Figure 6.2 Idealized Moment-Curvature Relation.

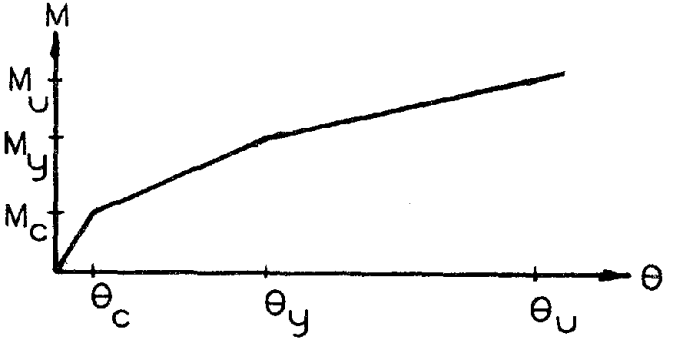

Figure 6.3 Idealized Moment-Rotation Relation.

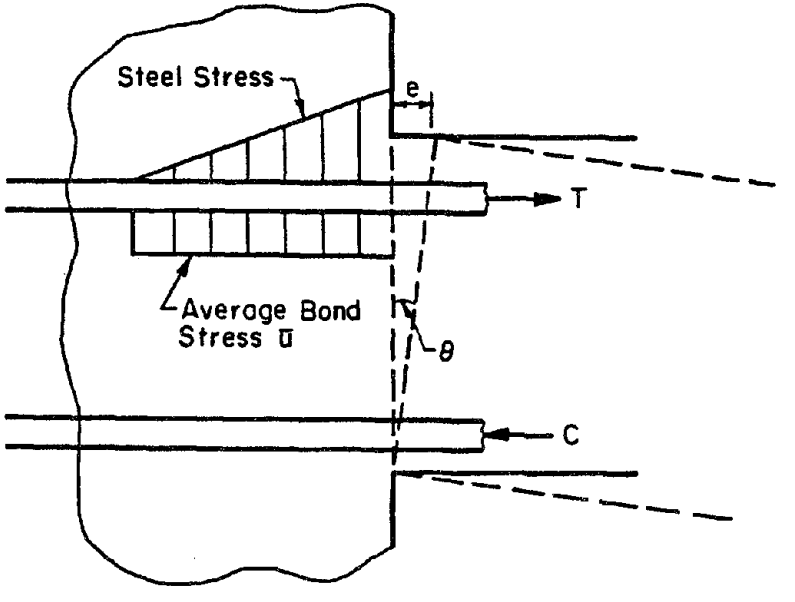

Figure 6.4 Mathematical Model to Account for Reinforcement Slip.

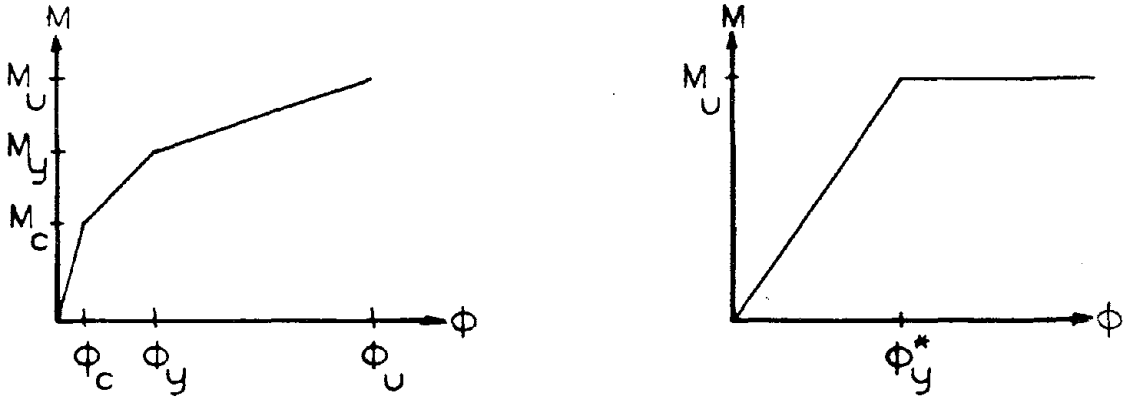

Figure 6.5 Trilinear and Equivalent Bilinear Moment-Curvature Relations.

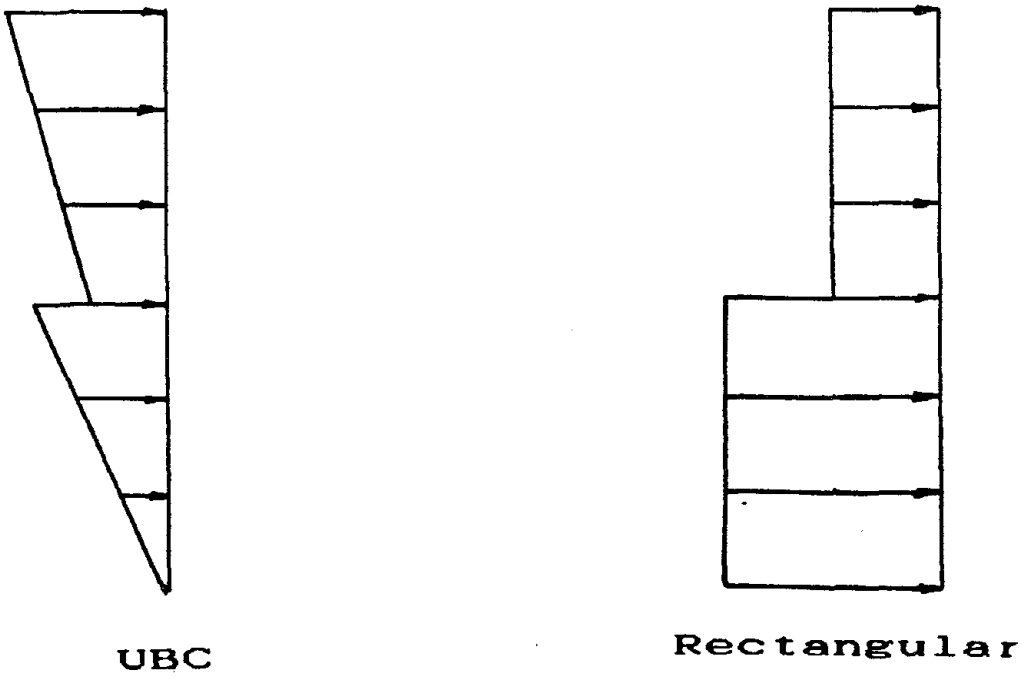

Figure 6.6 Lateral-Load Distributions.

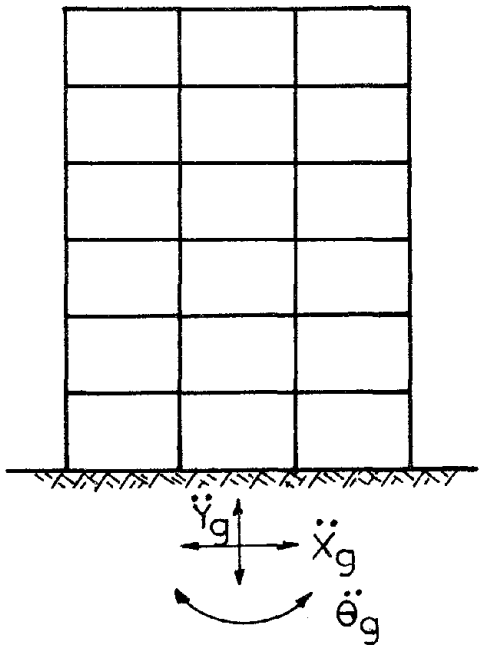

Figure 6.7 Independent Ground Accelerations.

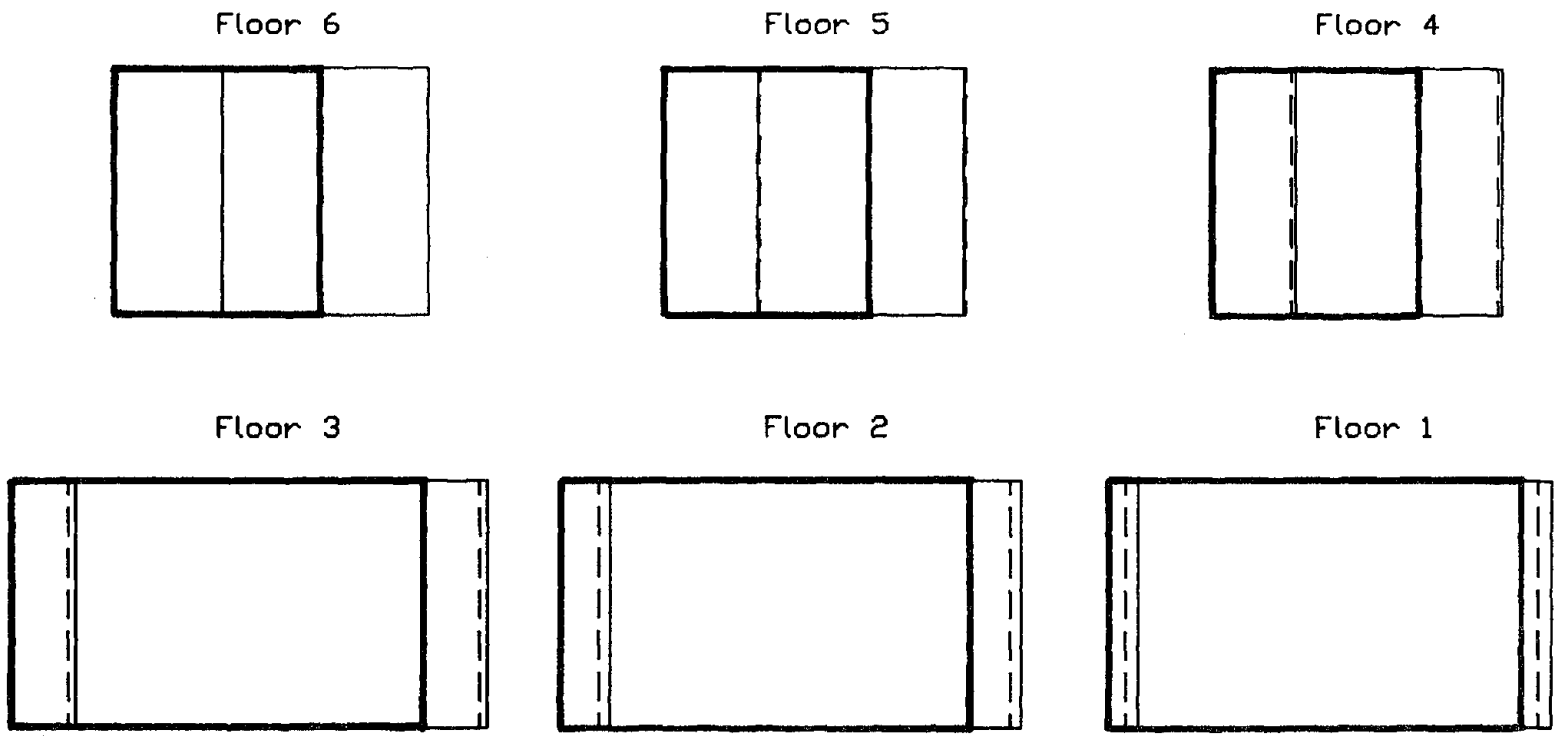

Figure 6.8(a) Computed and Measured Mode Shapes.
(1st Translational in Long Direction)

Original Position: ——
Measured : ——
Computed : - - - -

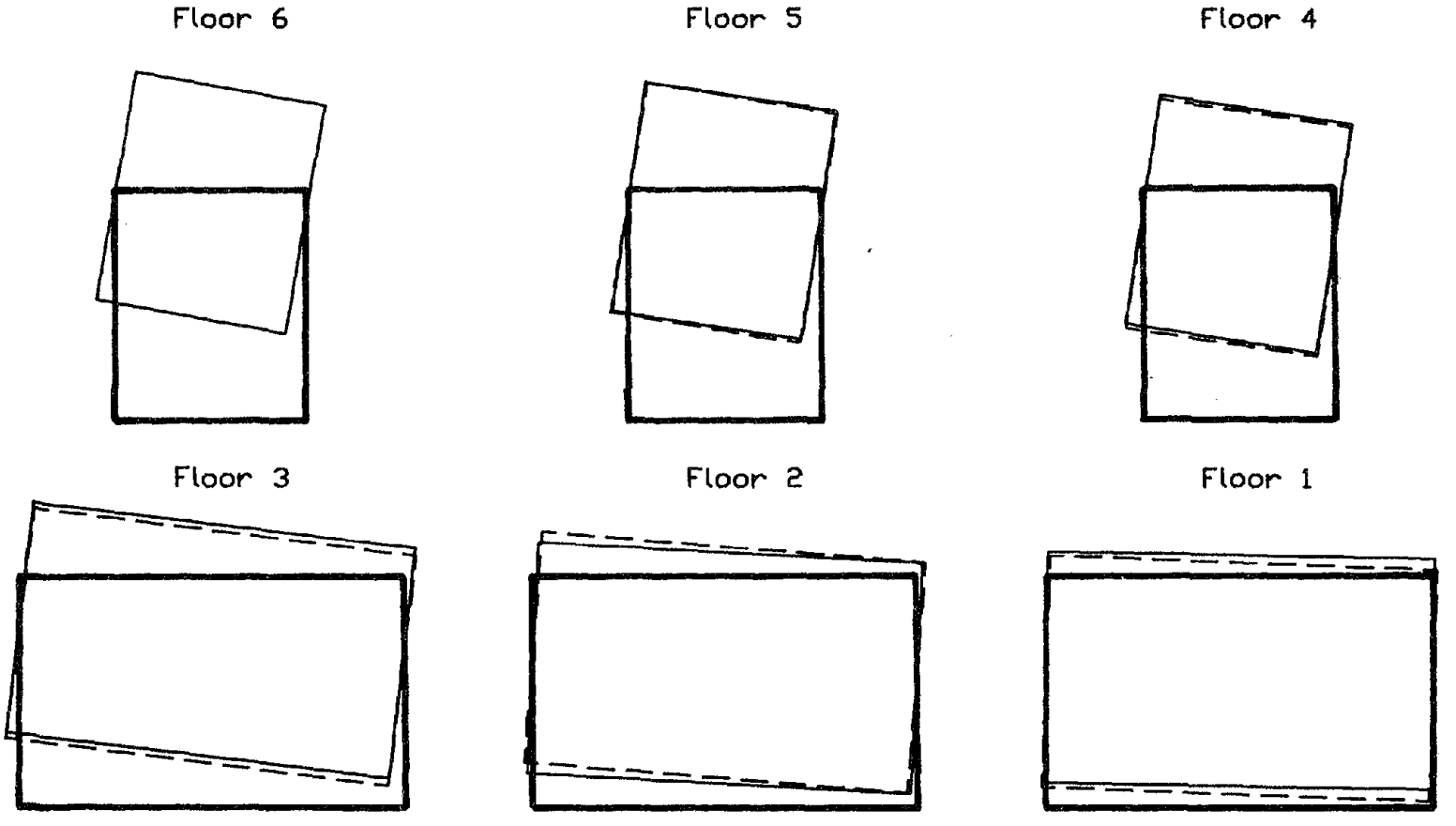

Figure 6.8(b) Computed and Measured Mode Shapes.
(1st Translational in Short Direction)

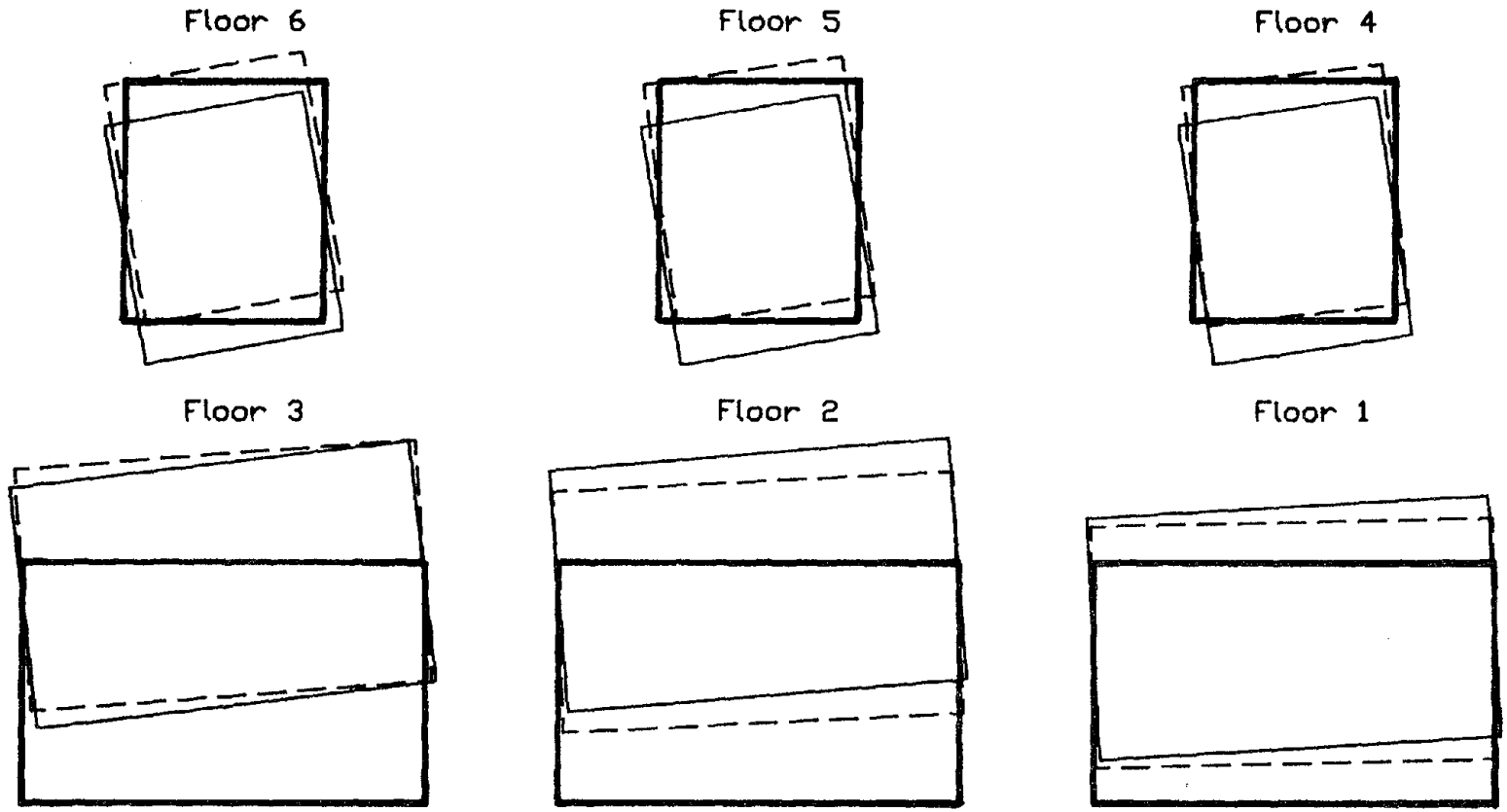

Figure 6.8(c) Computed and Measured Mode Shapes (1st Torsional).

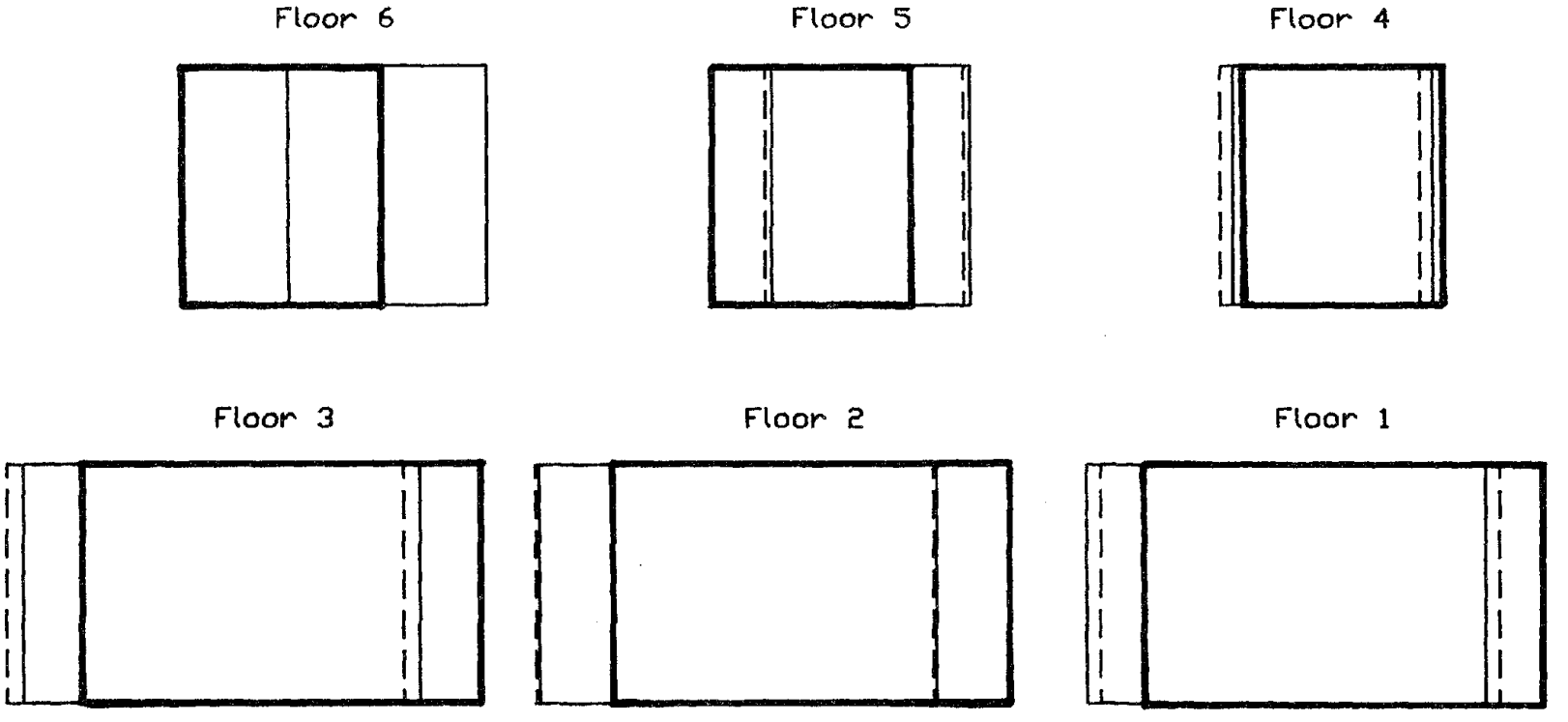

Figure 6.8(d) Computed and Measured Mode Shapes.
(2nd Translational in Short Direction)

Original Position: ——
Measured : ——
Computed : – – –

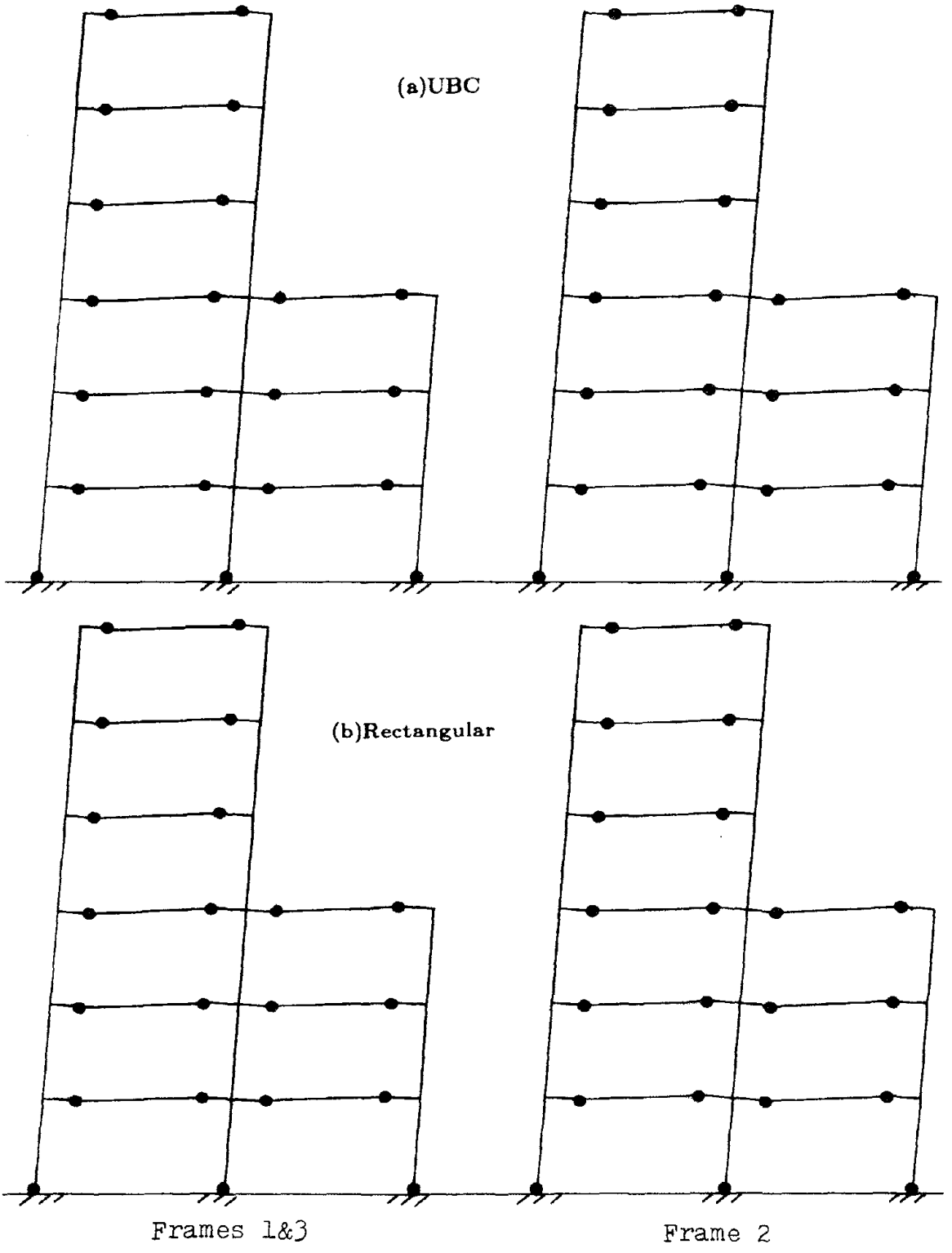

Figure 6.9(a) Computed Collapse Mechanisms (No Slab Contribution).

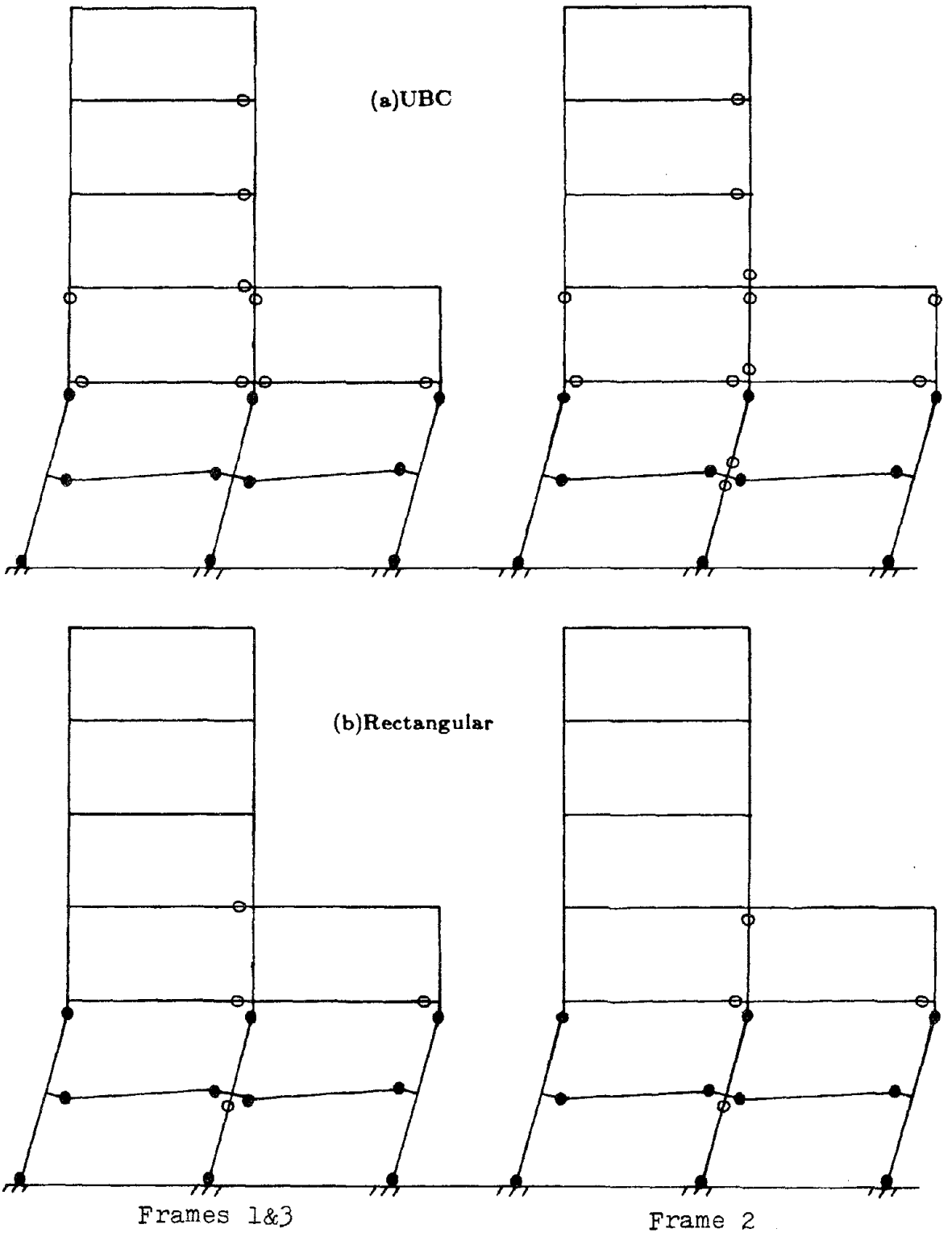

Figure 6.9(b) Computed Collapse Mechanisms (Calculated Effective Flange Width).

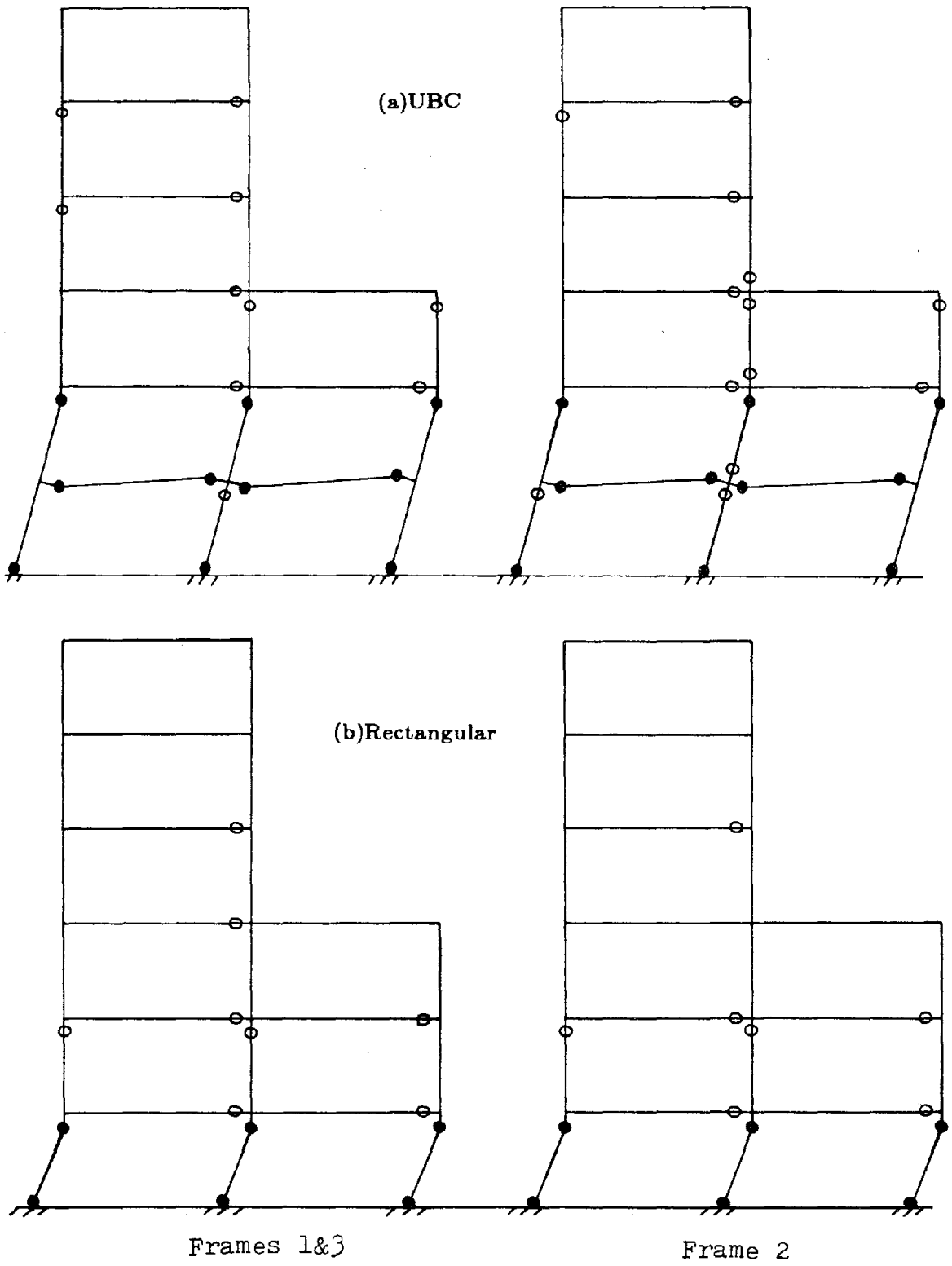

Figure 6.9(c) Computed Collapse Mechanisms (Entire Span).

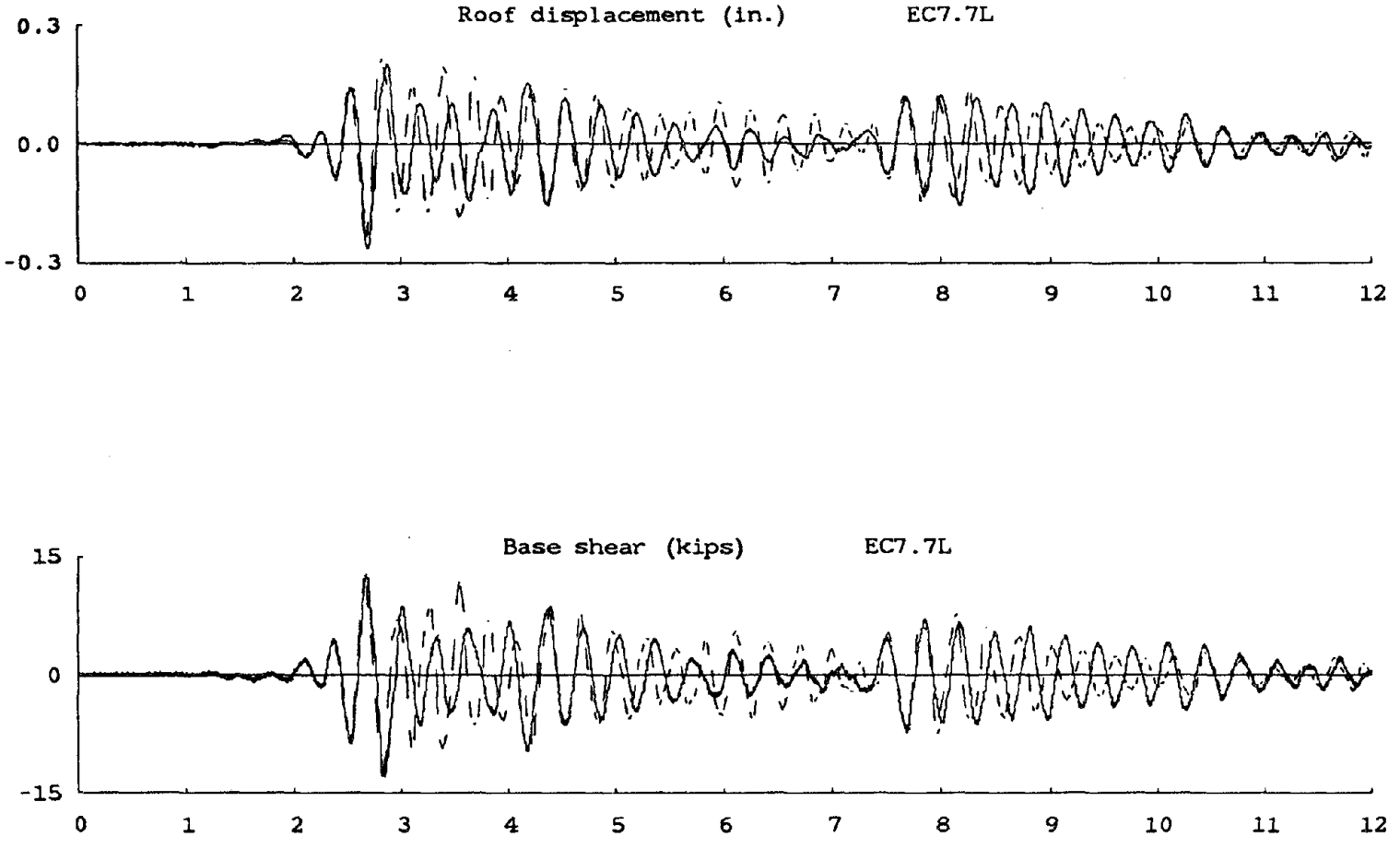

Figure 6.10(a) Comparison of Measured (Solid) and Computed (Dashed) Responses. (Test EC7.7L, Model A)

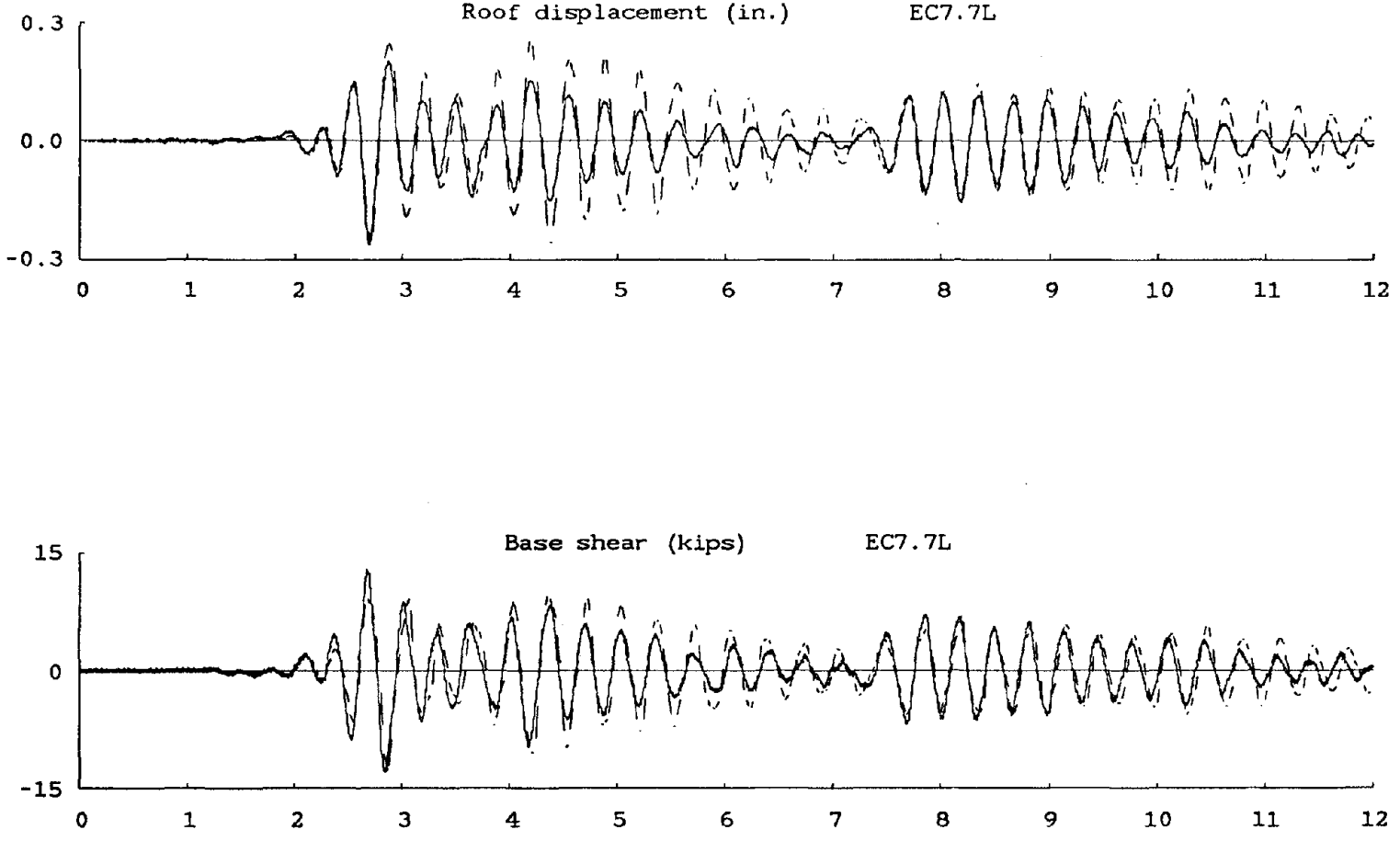

Figure 6.10(b) Comparison of Measured (Solid) and Computed (Dashed) Responses. (Test EC7.7L, Model B)

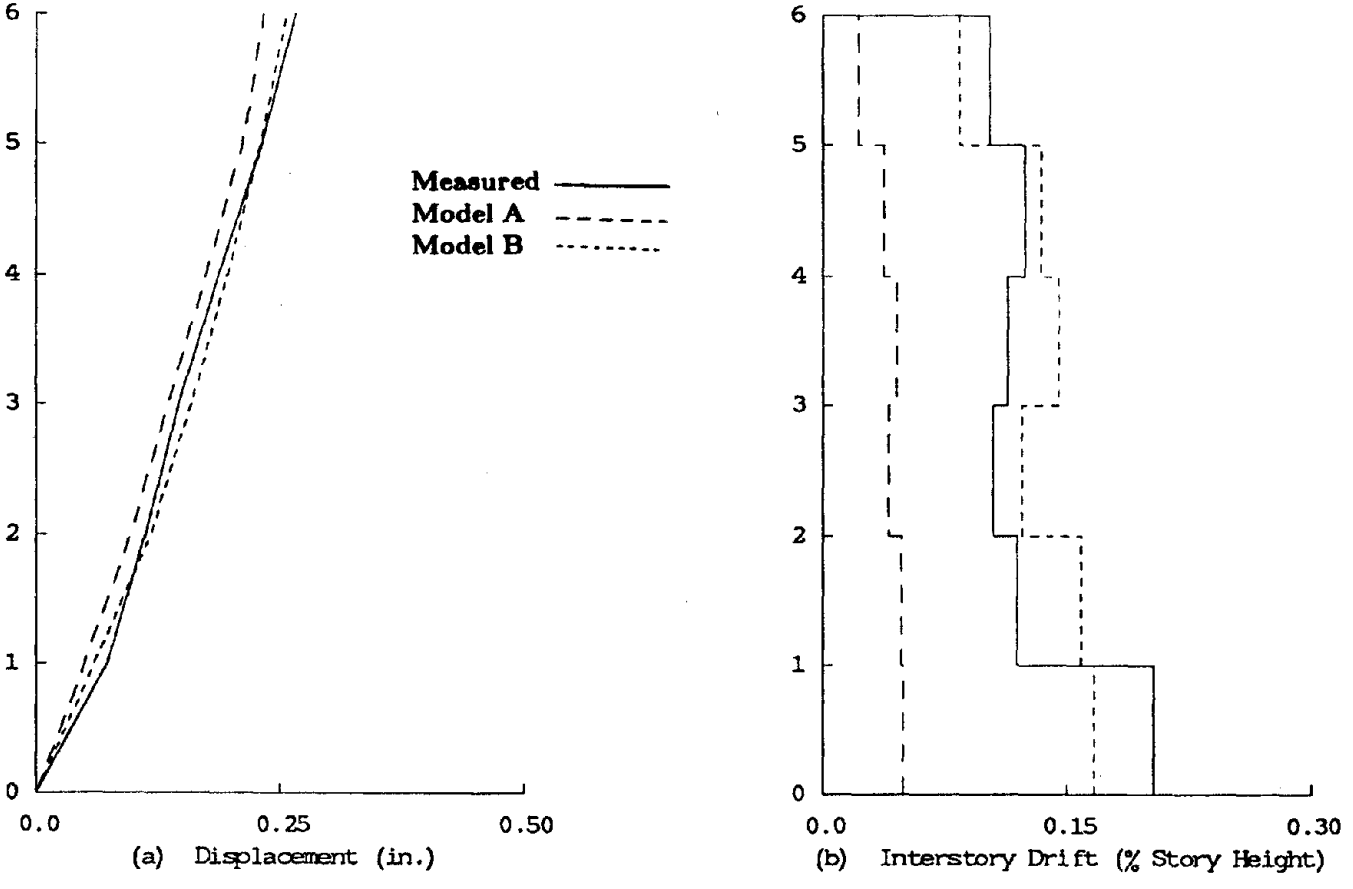

Figure 6.11 Comparison of Measured and Computed Envelopes. (Test EC7.7L)

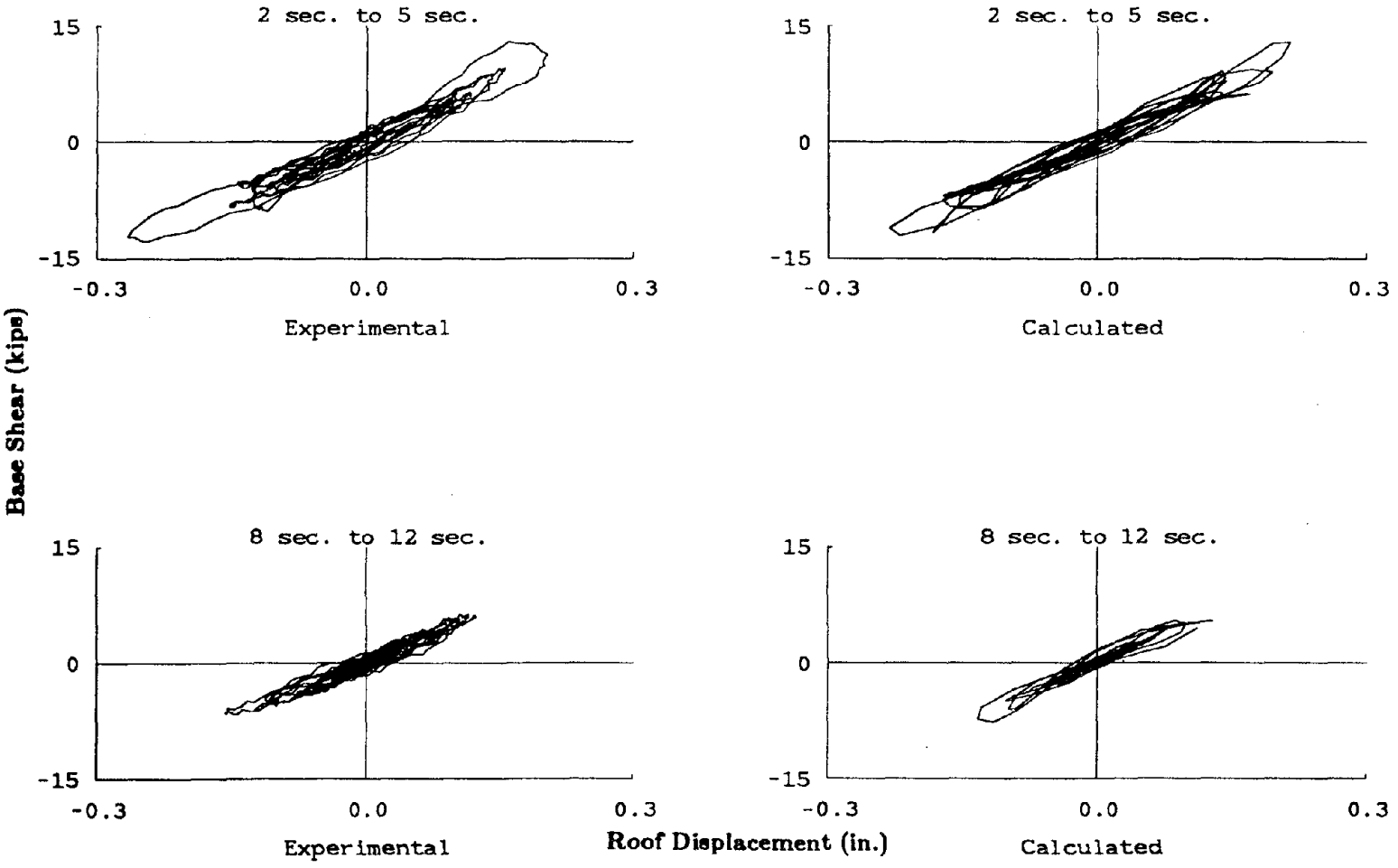

Figure 6.12(a) Comparison of Measured and Computed Hysteresis Loops. (Test EC7.7L, Model A)

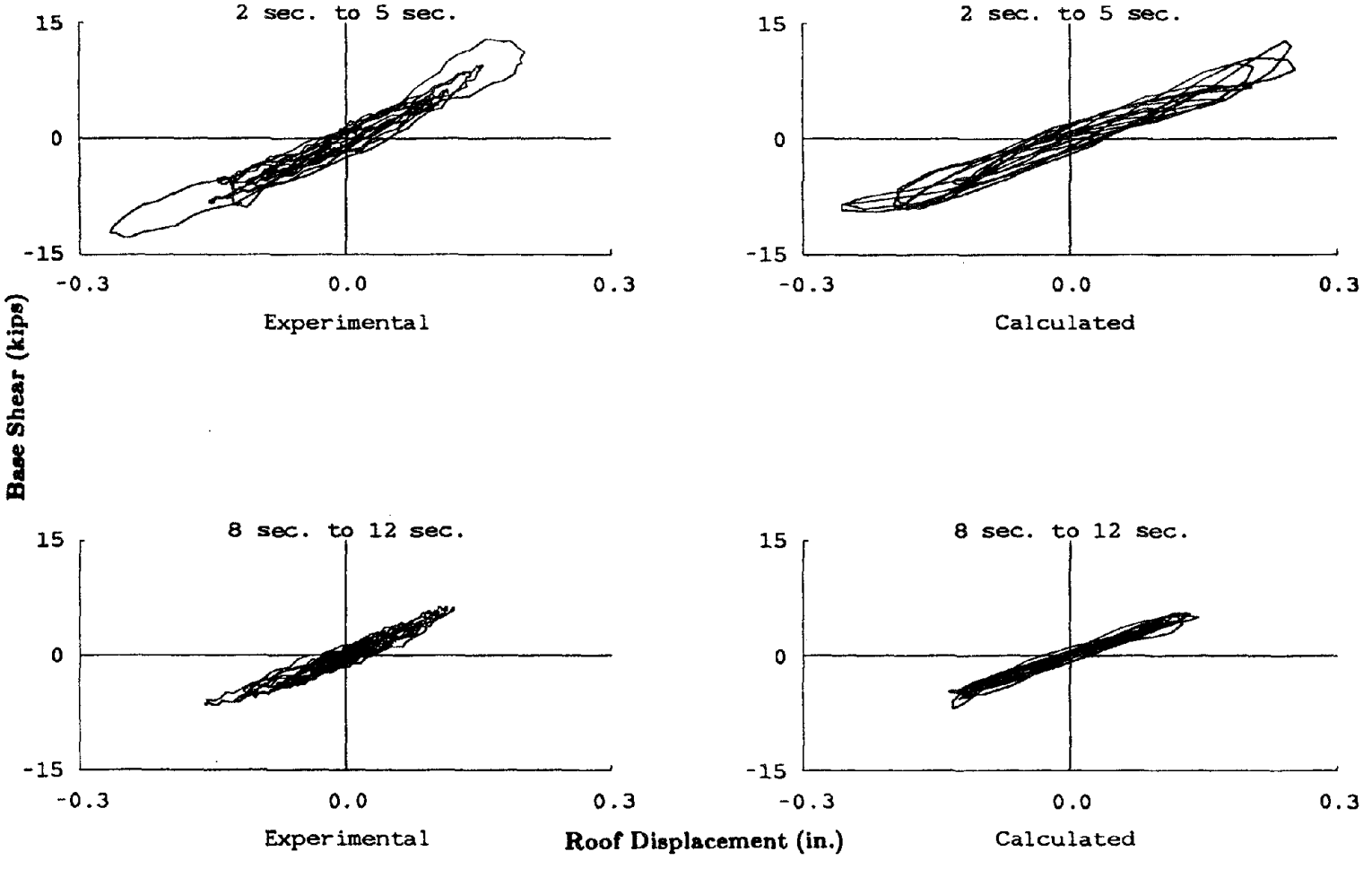

Figure 6.12(b) Comparison of Measured and Computed Hysteresis Loops. (Test EC7.7L, Model B)

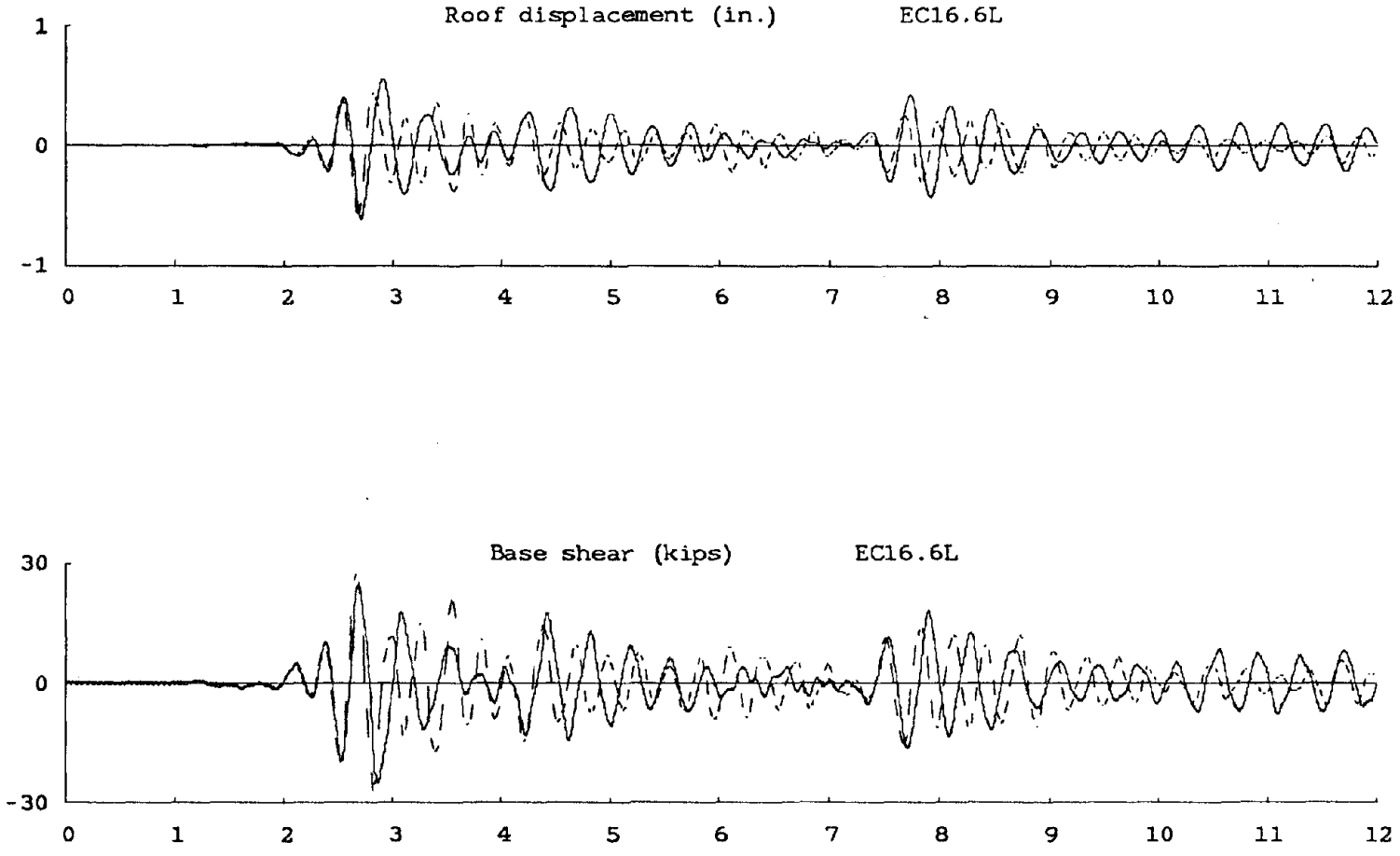

Figure 6.13(a) Comparison of Measured (Solid) and Computed (Dashed) Responses. (Test EC16.6L, Model A)

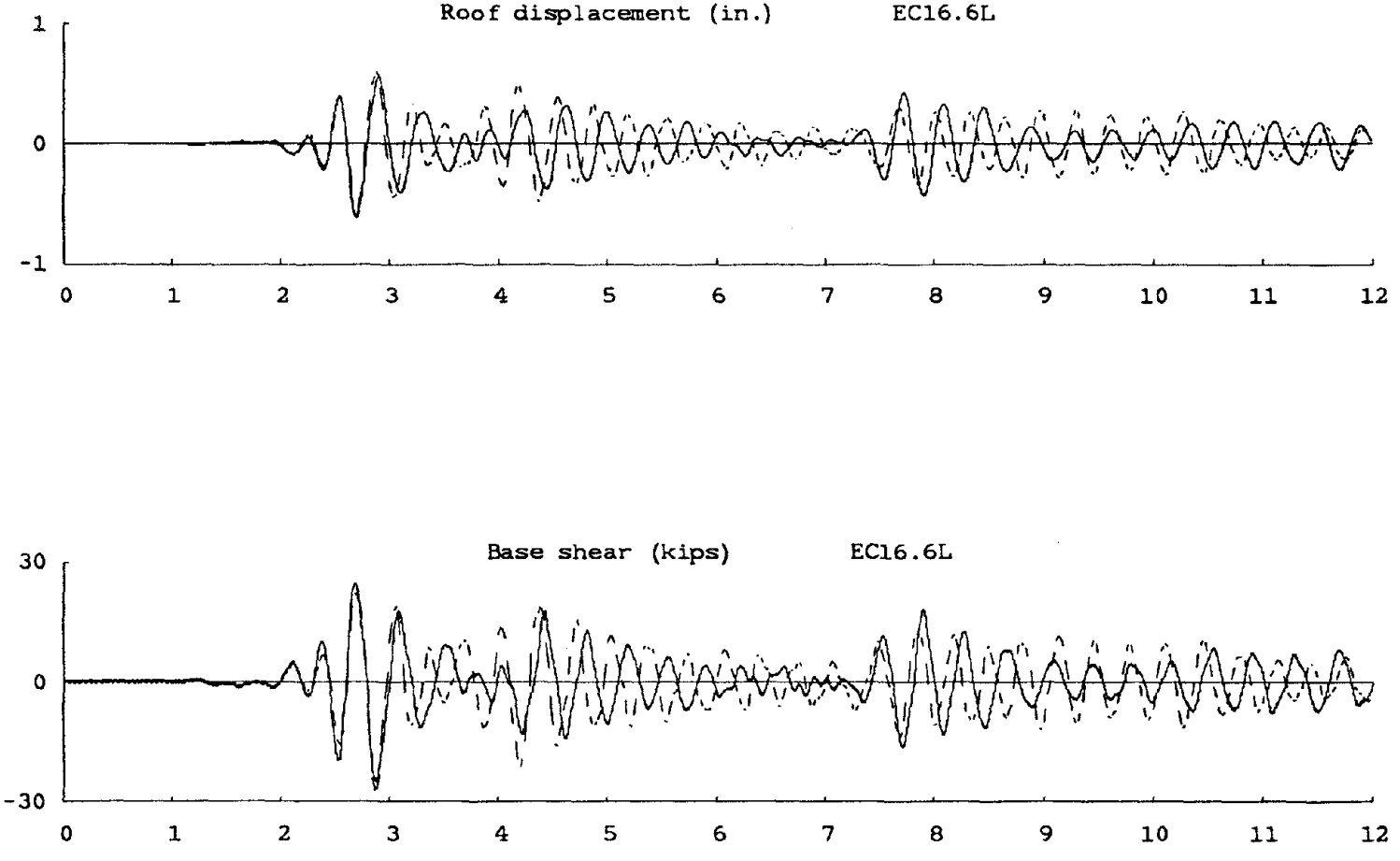

Figure 6.13(b) Comparison of Measured (Solid) and Computed (Dashed) Responses. (Test EC16.6L, Model B)

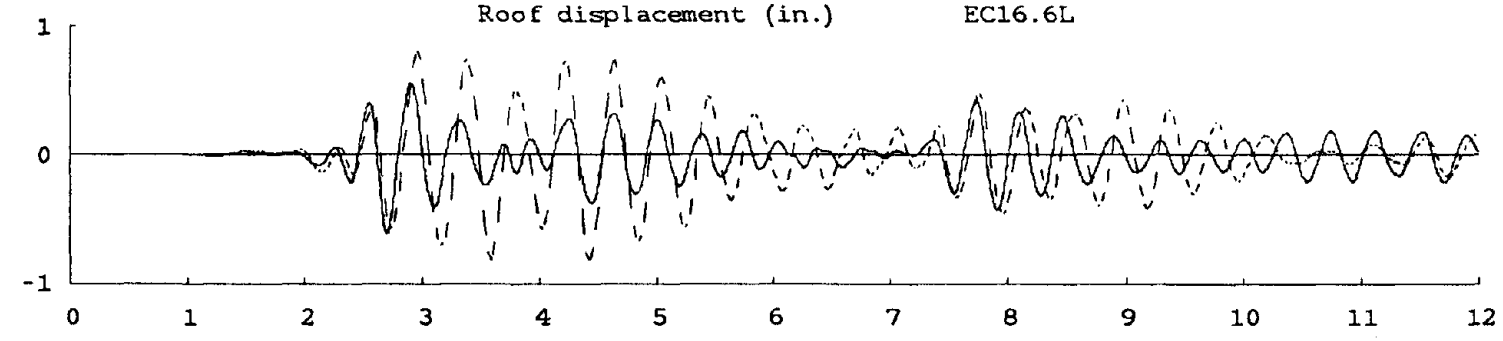

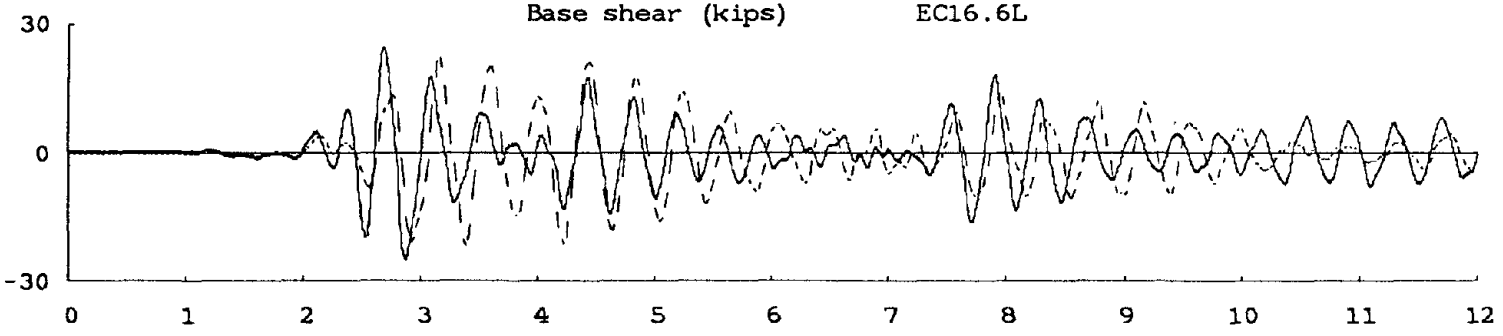

Figure 6.13(c) Comparison of Measured (Solid) and Computed (Dashed) Responses. (Test EC16.6L, Model C)

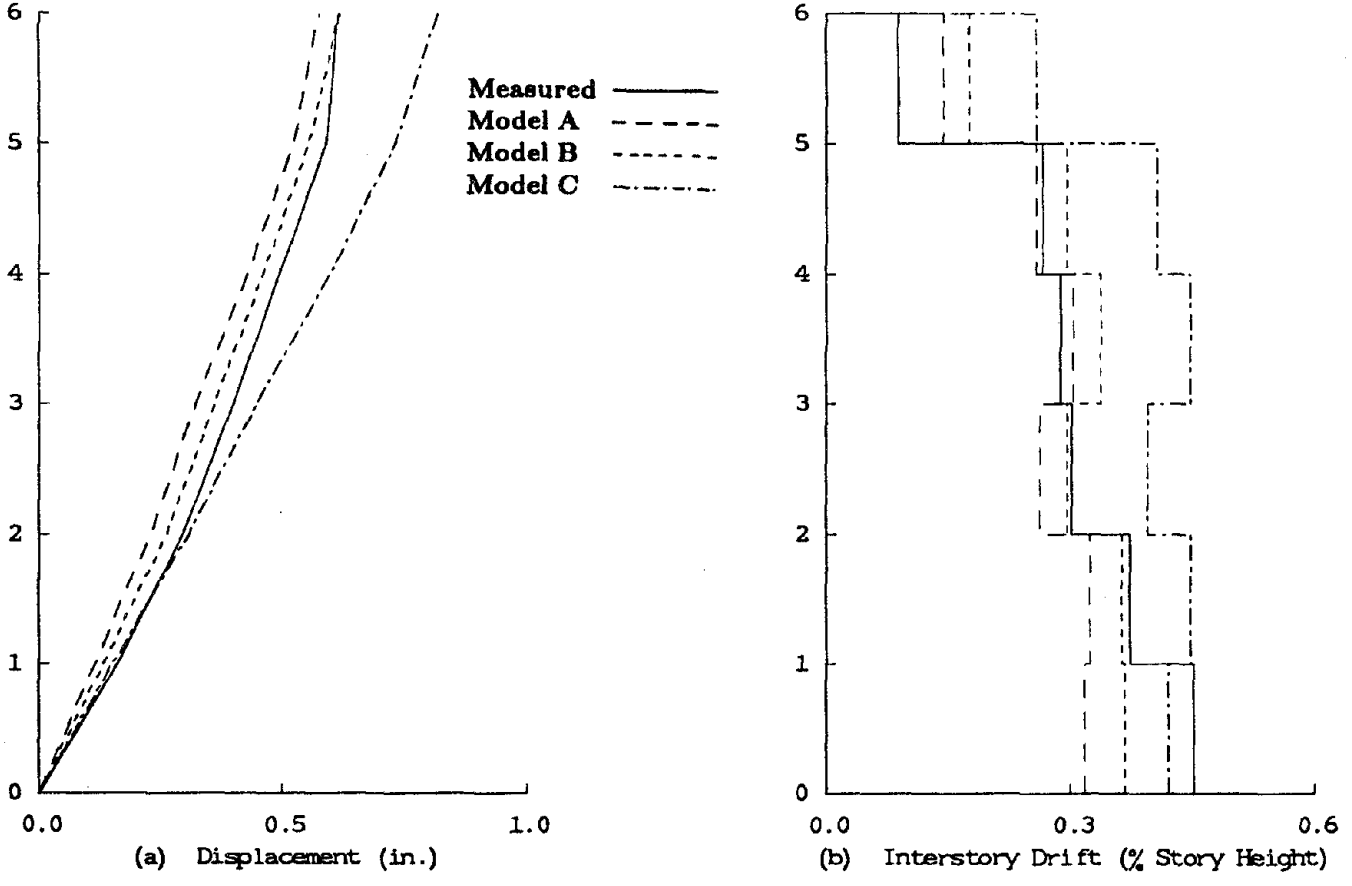

Figure 6.14 Comparison of Measured and Computed Envelopes. (Test EC16.6L)

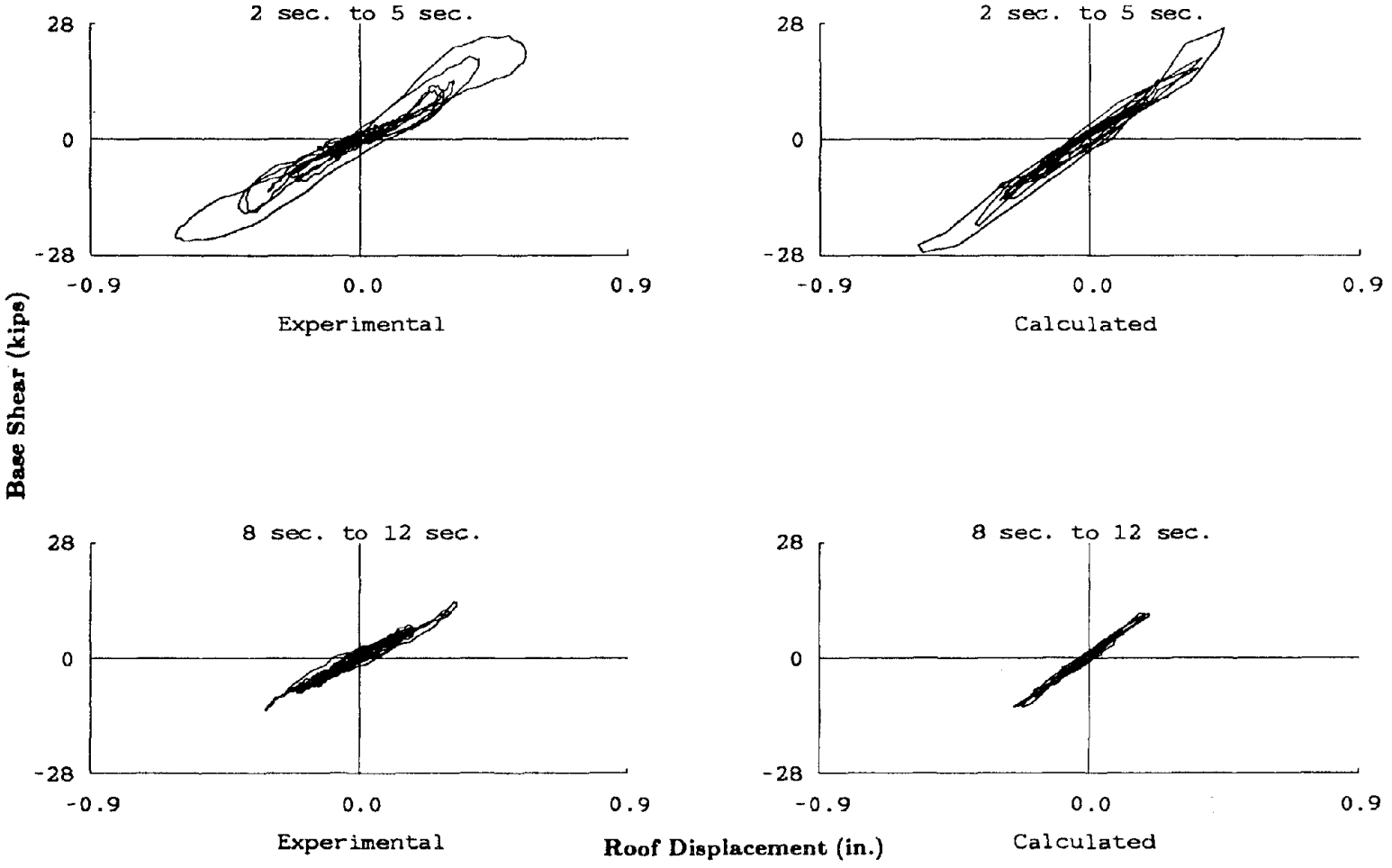

Figure 6.15(a) Comparison of Measured and Computed Hysteresis Loops. (Test EC16.6L, Model A)

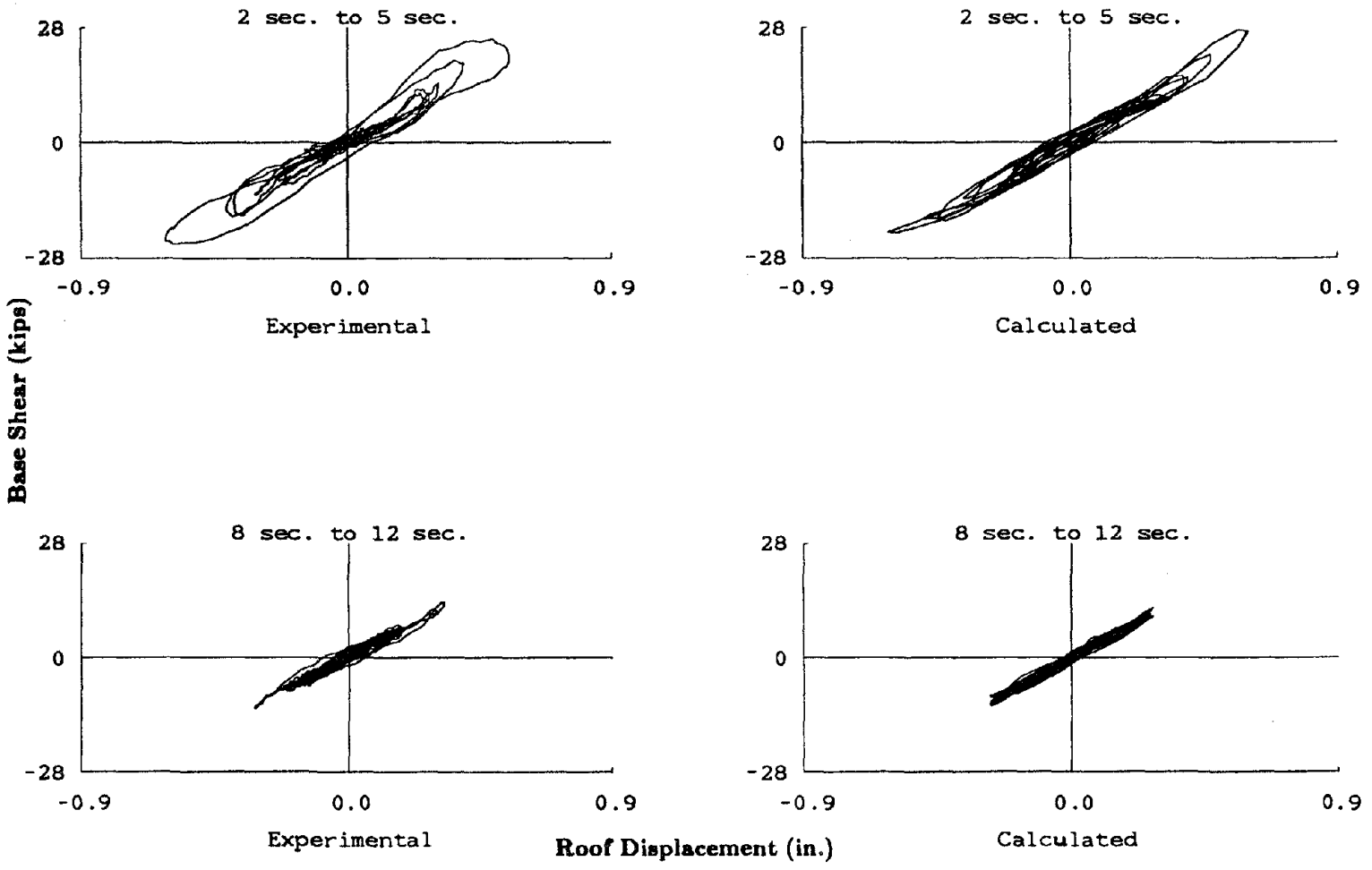

Figure 6.15(b) Comparison of Measured and Computed Hysteresis Loops. (Test EC16.6L, Model B)

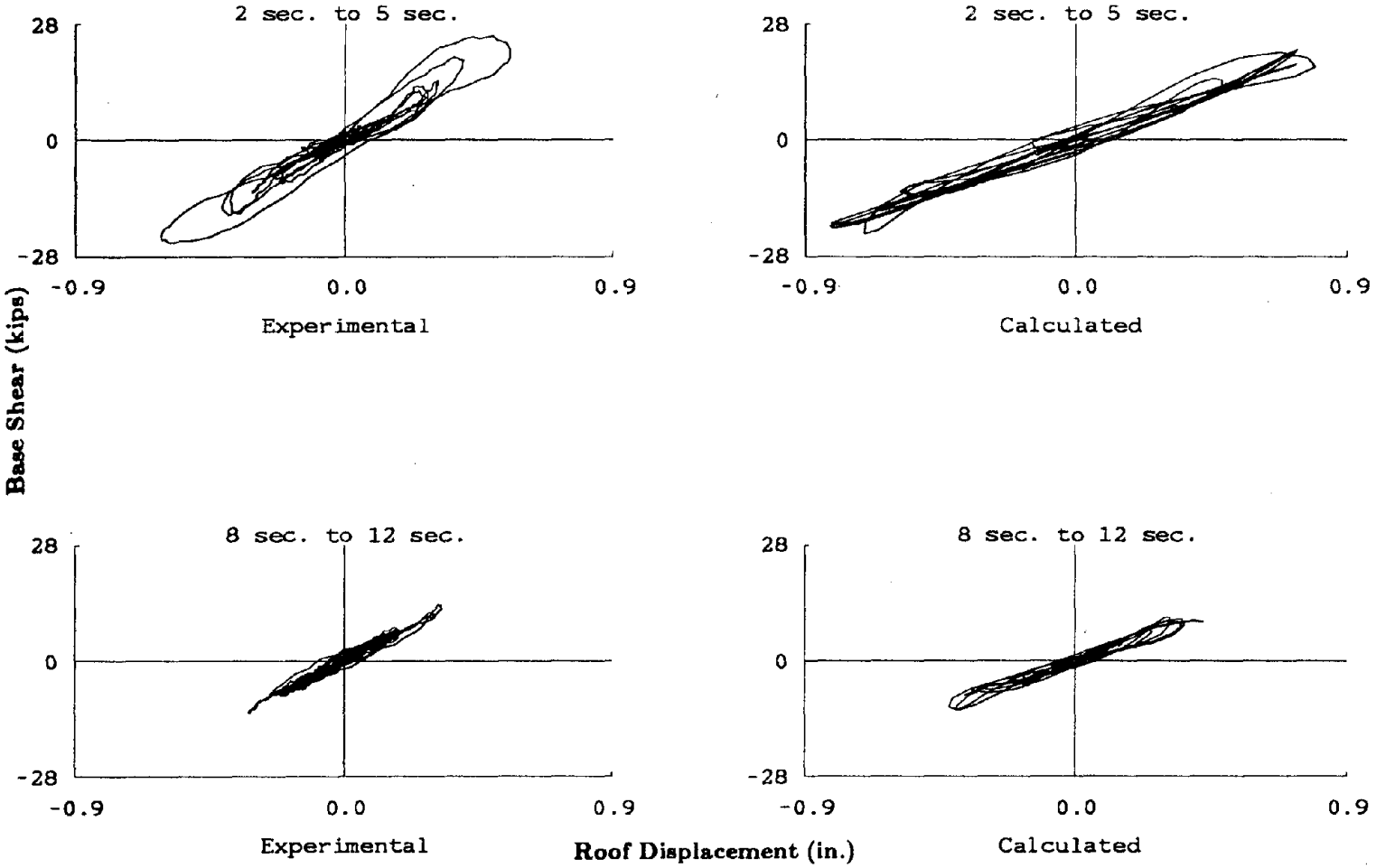

Figure 6.15(c) Comparison of Measured and Computed Hysteresis Loops. (Test EC16.6L, Model C)

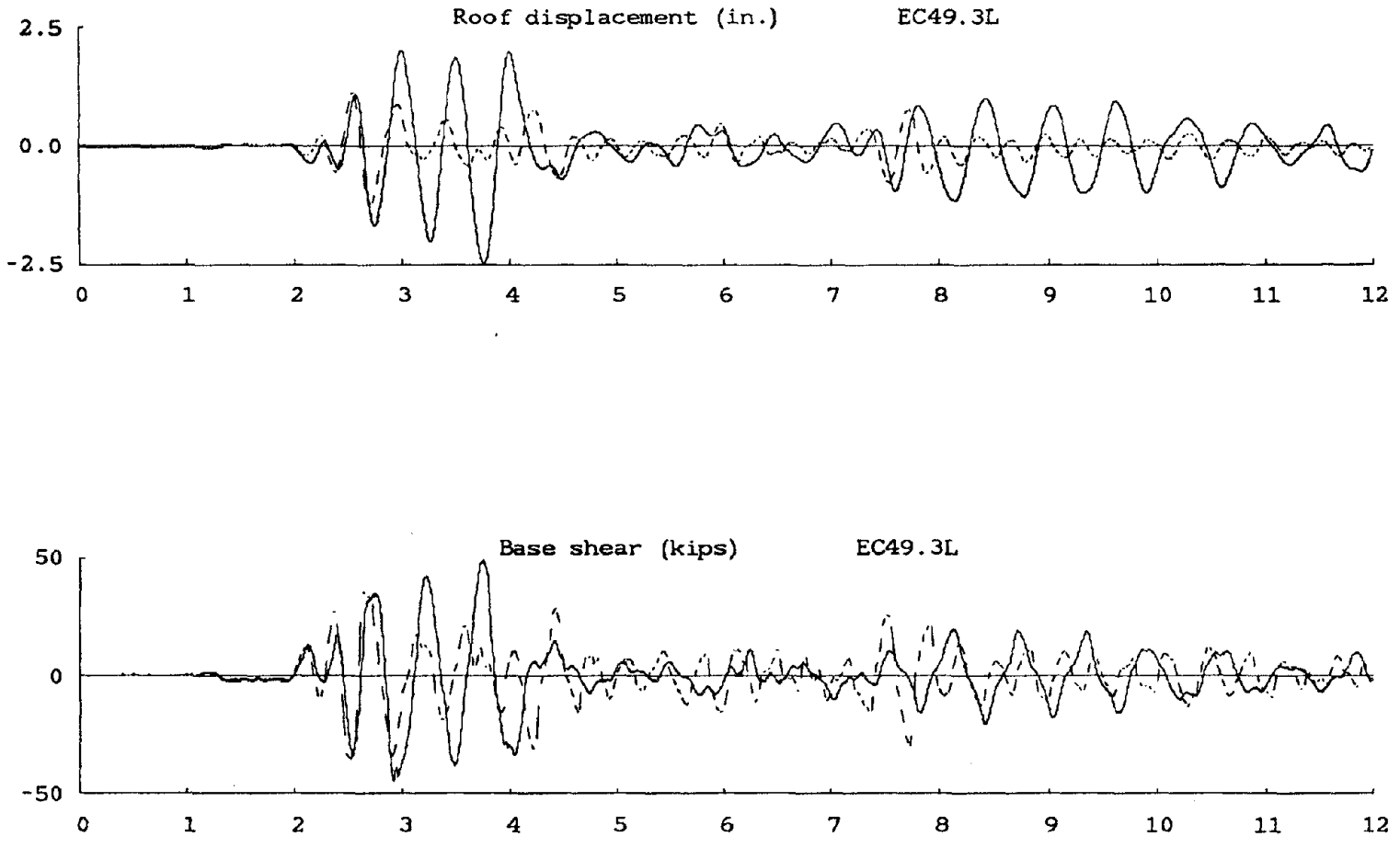

Figure 6.16(a) Comparison of Measured (Solid) and Computed (Dashed) Responses. (Test EC49.3L, Model A)

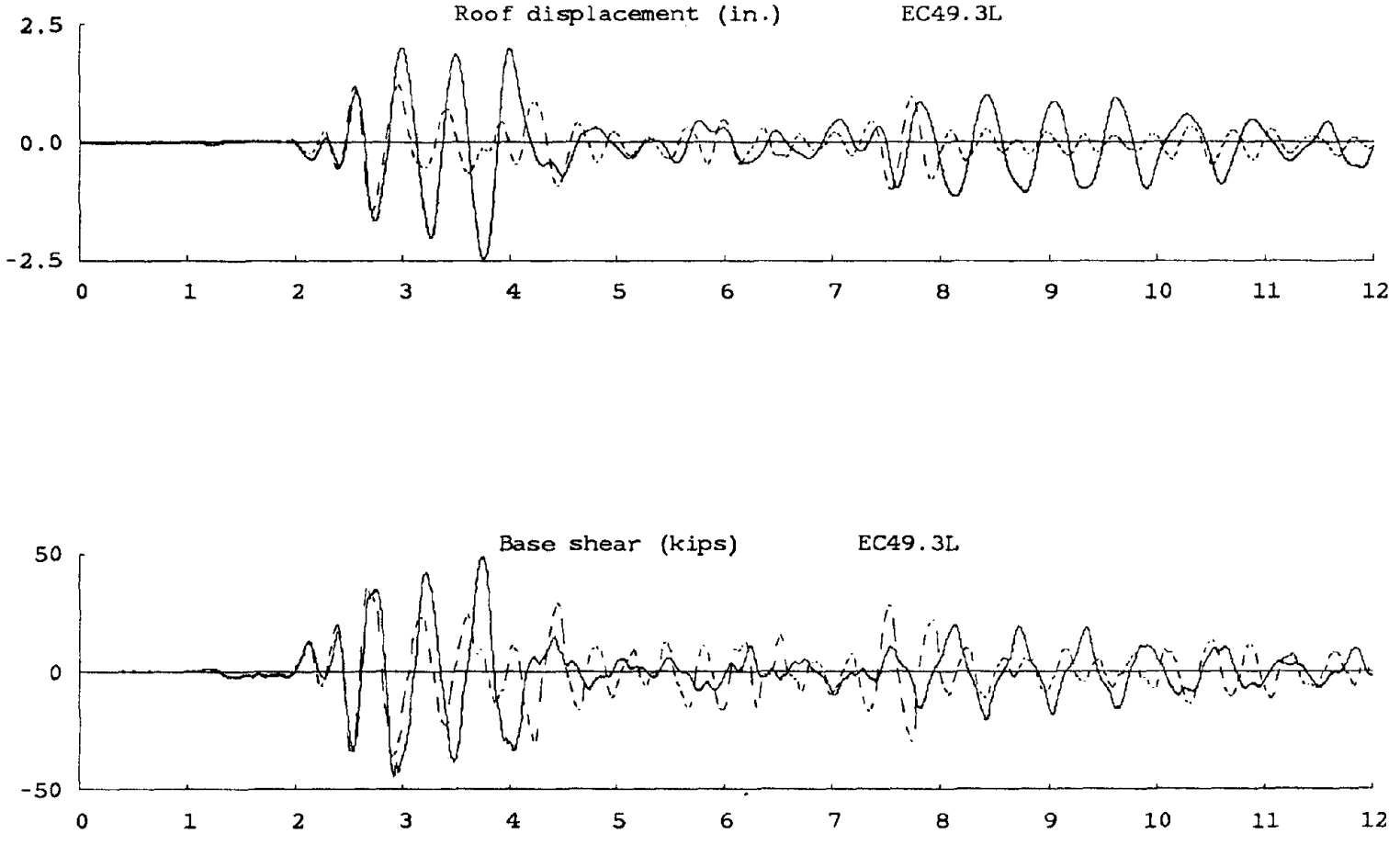

Figure 6.16(b) Comparison of Measured (Solid) and Computed (Dashed) Responses. (Test EC49.3L, Model B)

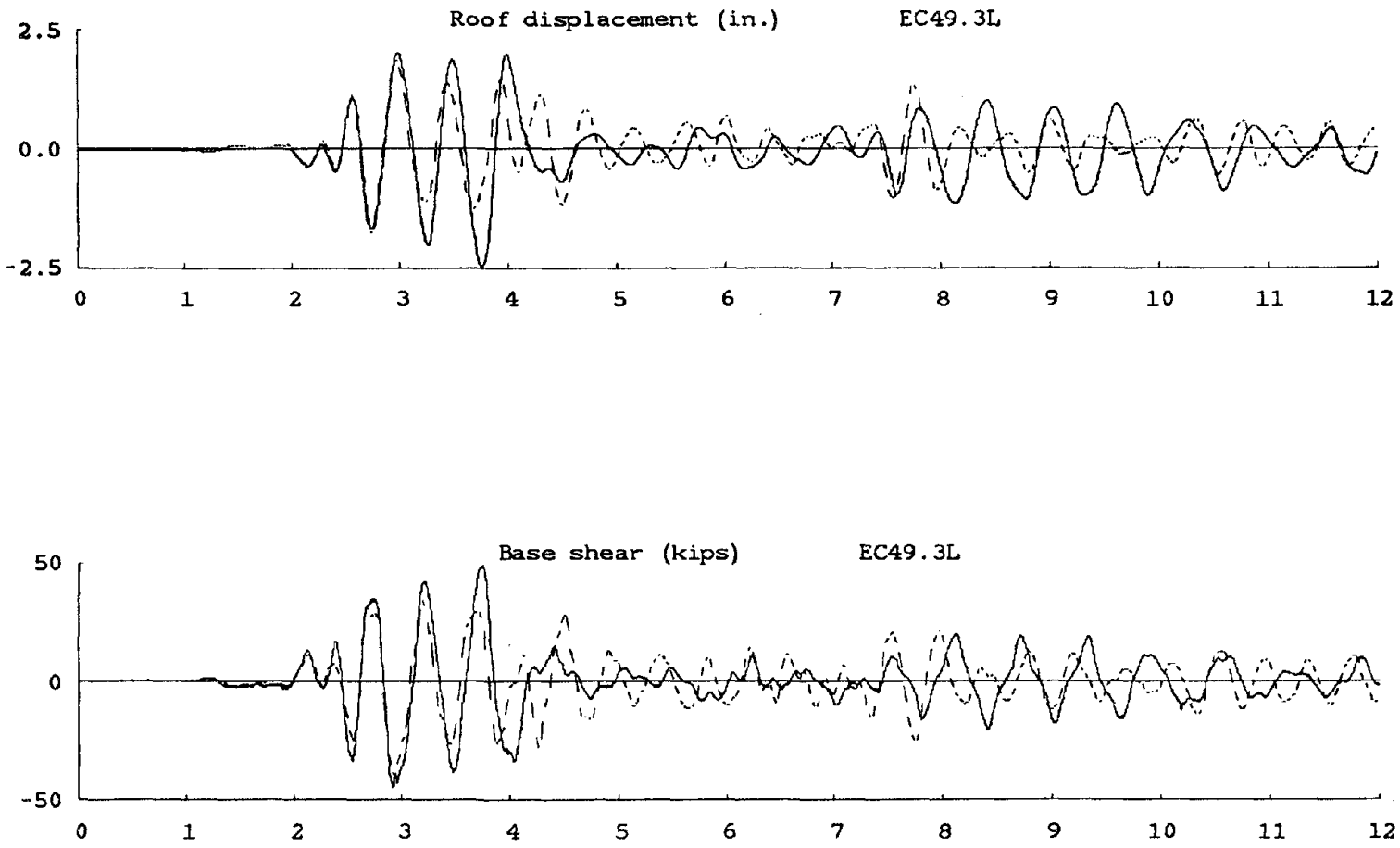

Figure 6.16(c) Comparison of Measured (Solid) and Computed (Dashed) Responses. (Test EC49.3L, Model C)

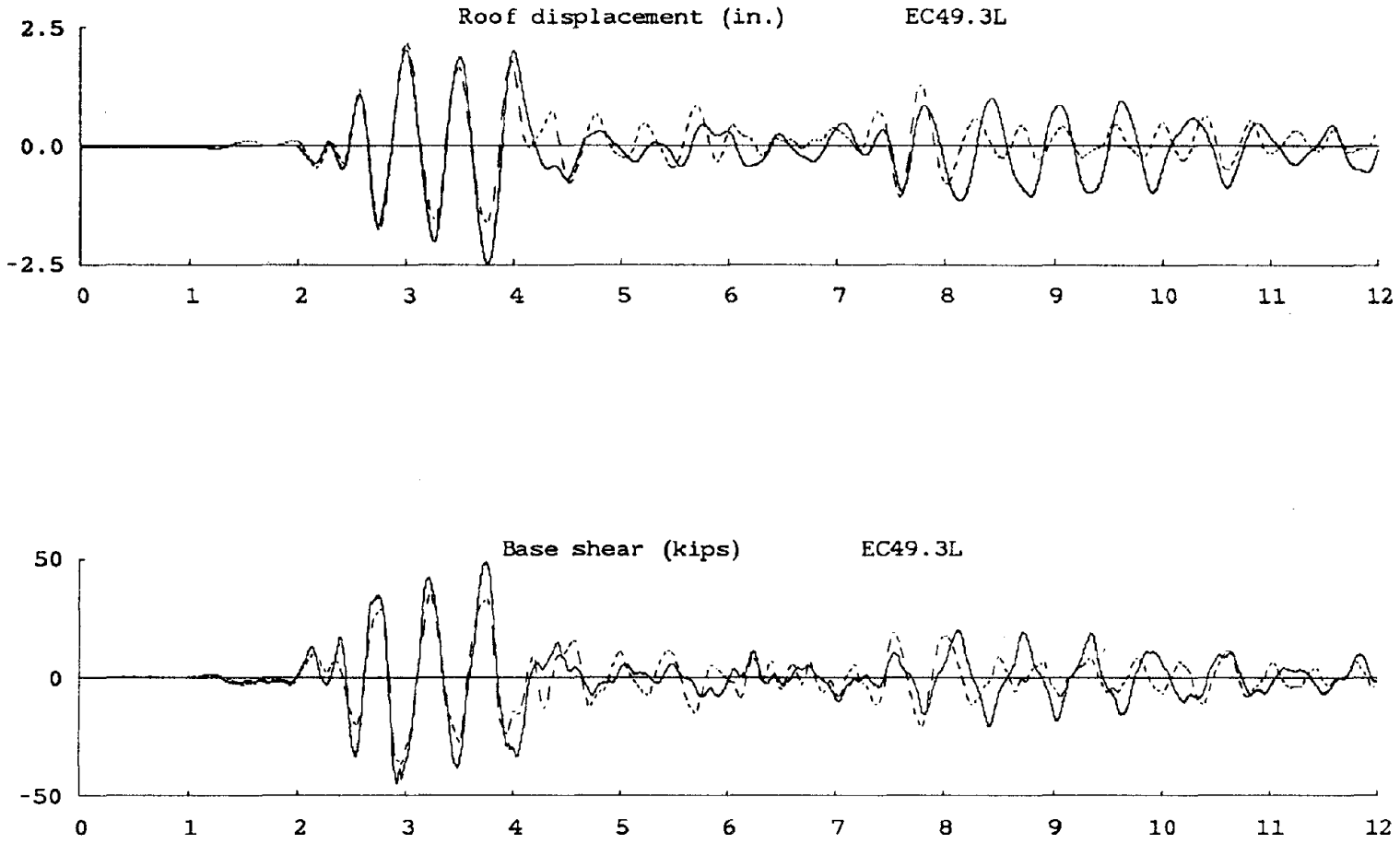

Figure 6.16(d) Comparison of Measured (Solid) and Computed (Dashed) Responses. (Test EC49.3L, Model D)

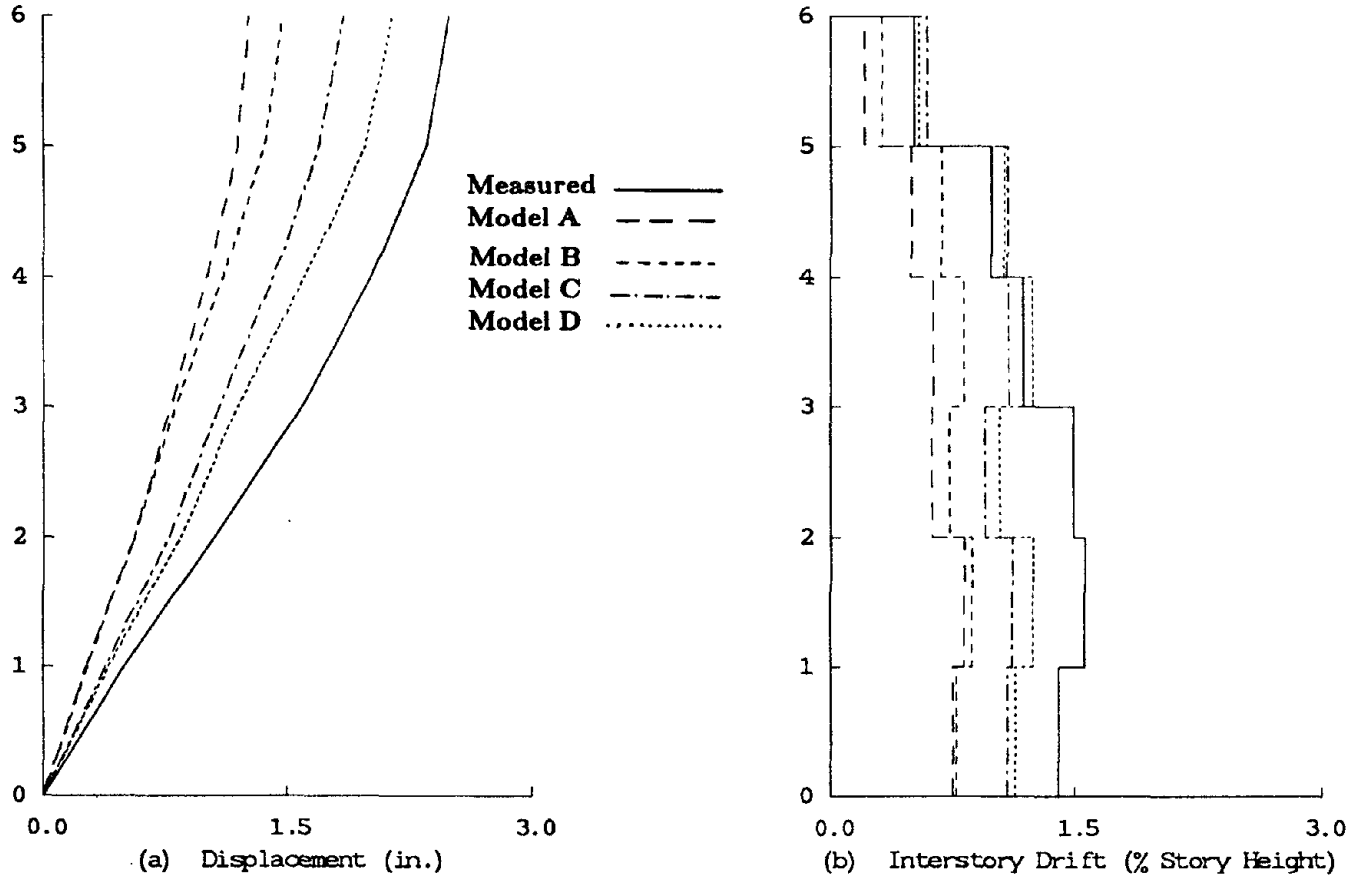

Figure 6.17 Comparison of Measured and Computed Envelopes. (Test EC49.3L)

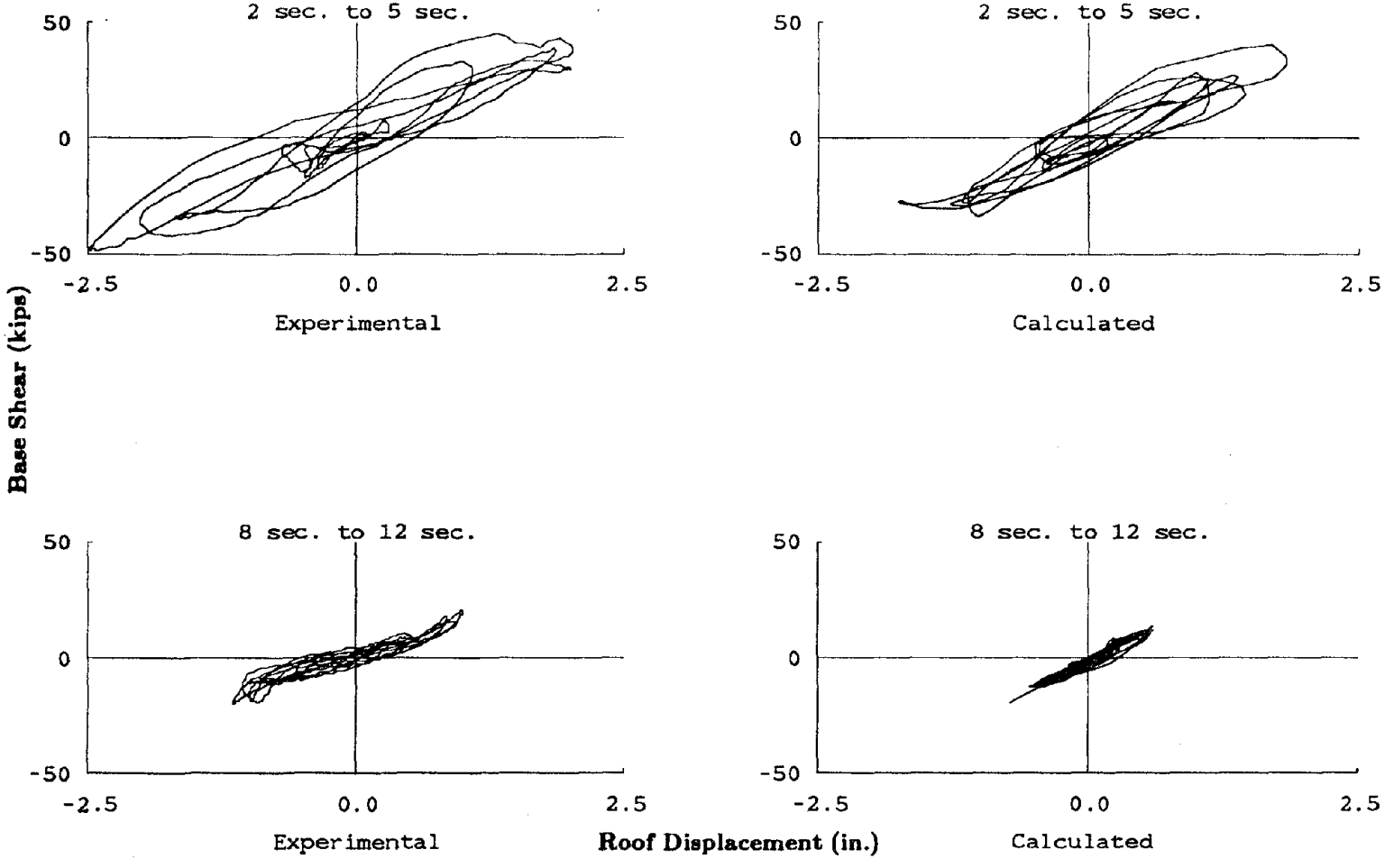

Figure 6.18(a) Comparison of Measured and Computed Hysteresis Loops. (Test EC49.3L, Model C)

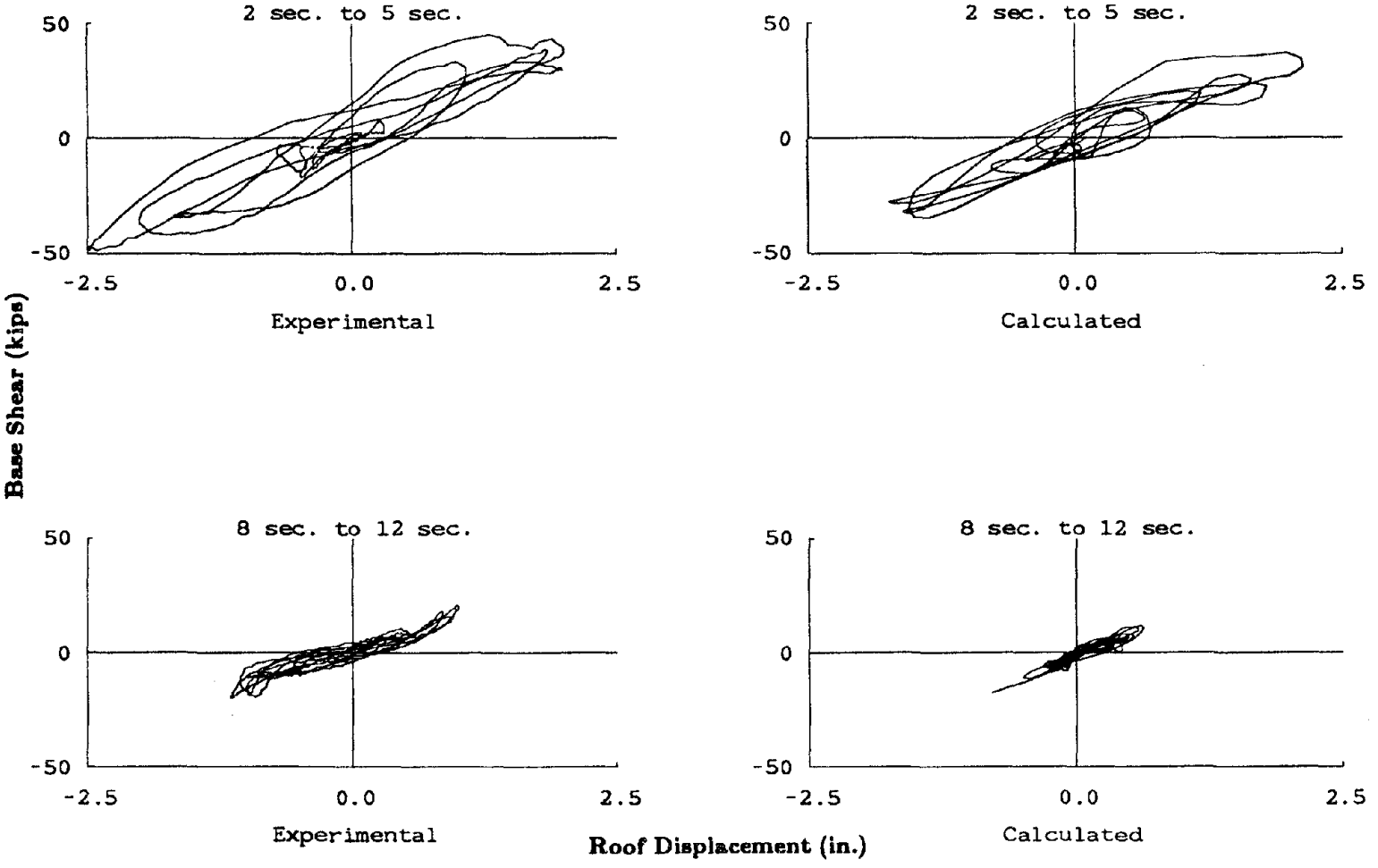

Figure 6.18(b) Comparison of Measured and Computed Hysteresis Loops. (Test EC49.3L, Model D)

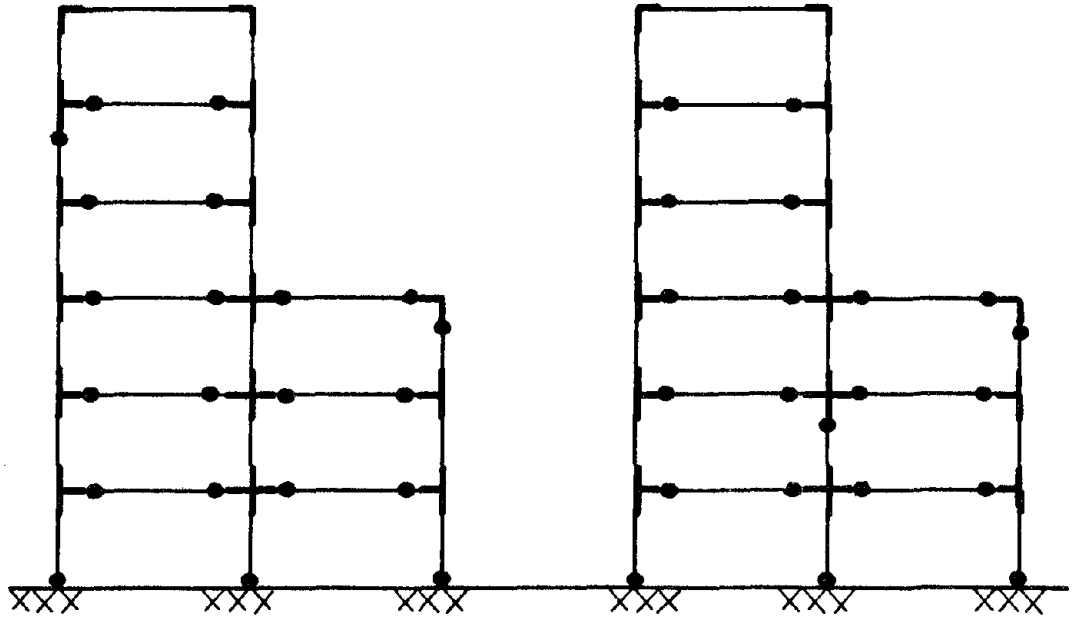

Figure 6.19 Computed Locations of Plastic Hinges.
(Test EC49.3L, Models A, B, C, and D)

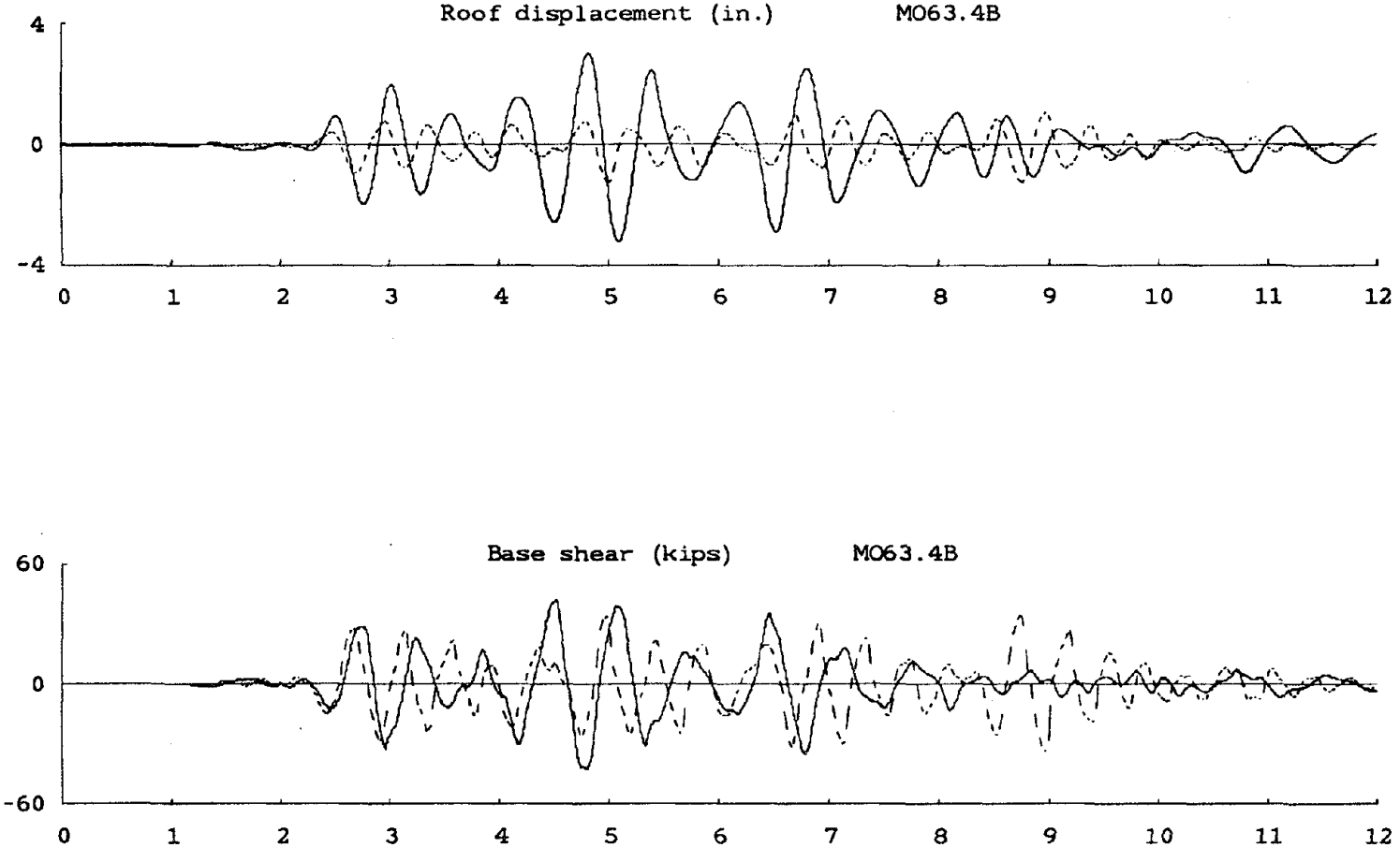

Figure 6.20(a) Comparison of Measured (Solid) and Computed (Dashed) Responses. (Test MO63.4B, Model C)

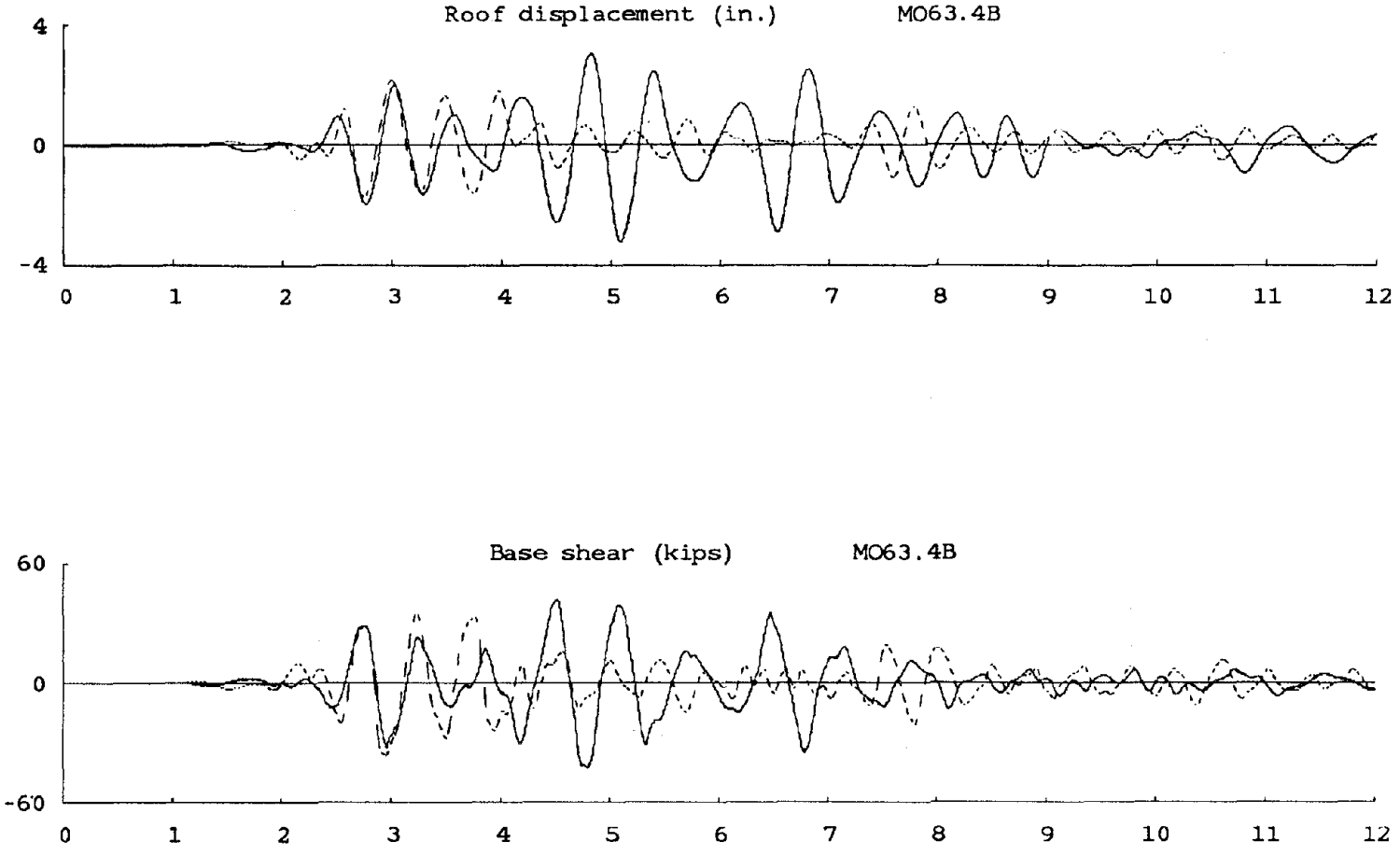

Figure 6.20(b) Comparison of Measured (Solid) and Computed (Dashed) Responses. (Test MO63.4B, Model D)

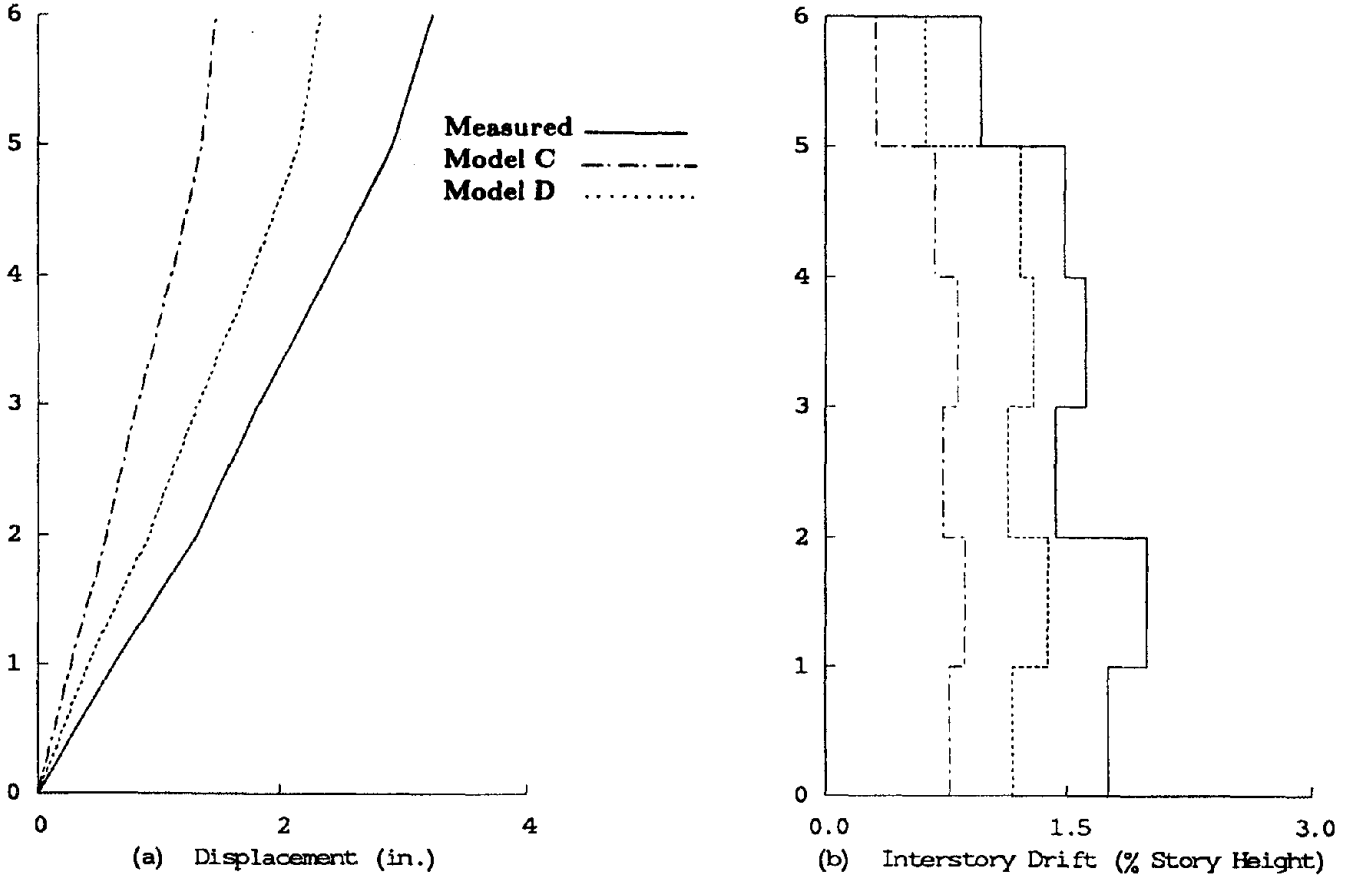

Figure 6.21 Comparison of Measured and Computed Envelopes. (Test MO63.4B)

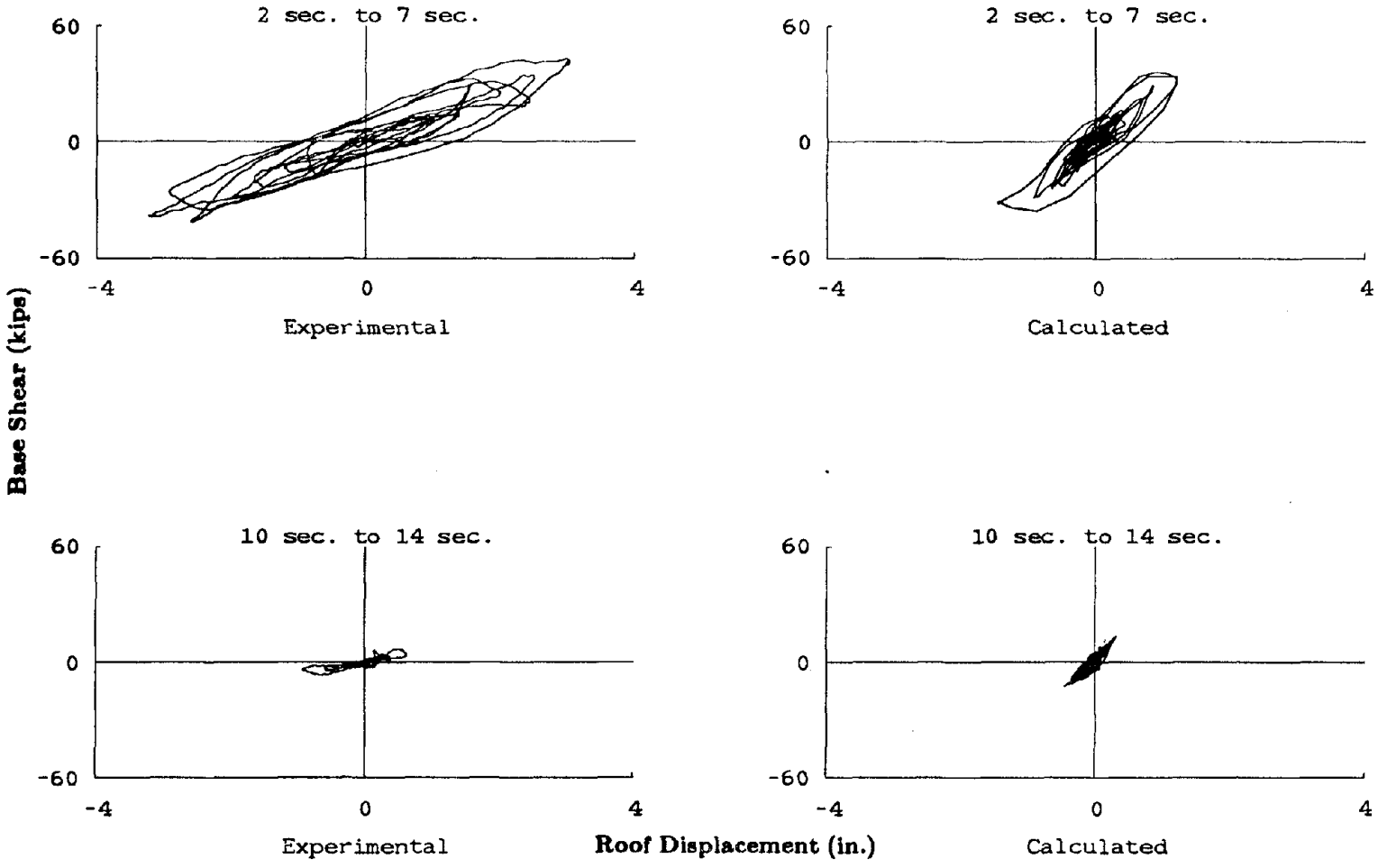

Figure 6.22(a) Comparison of Measured and Computed Hysteresis Loops. (Test MO63.4B, Model C)

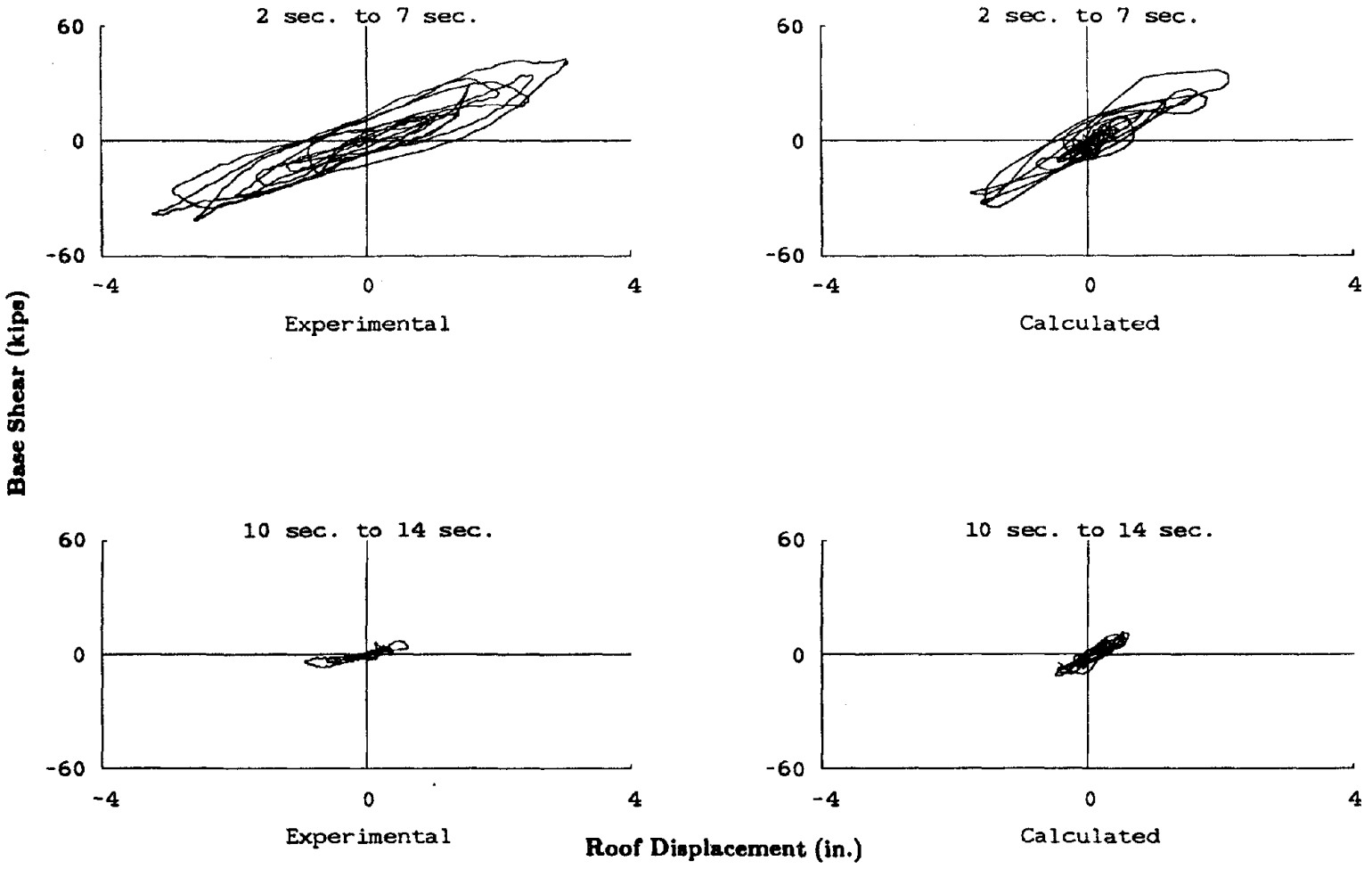

Figure 6.22(b) Comparison of Measured and Computed Hysteresis Loops. (Test MO63.4B, Model D)

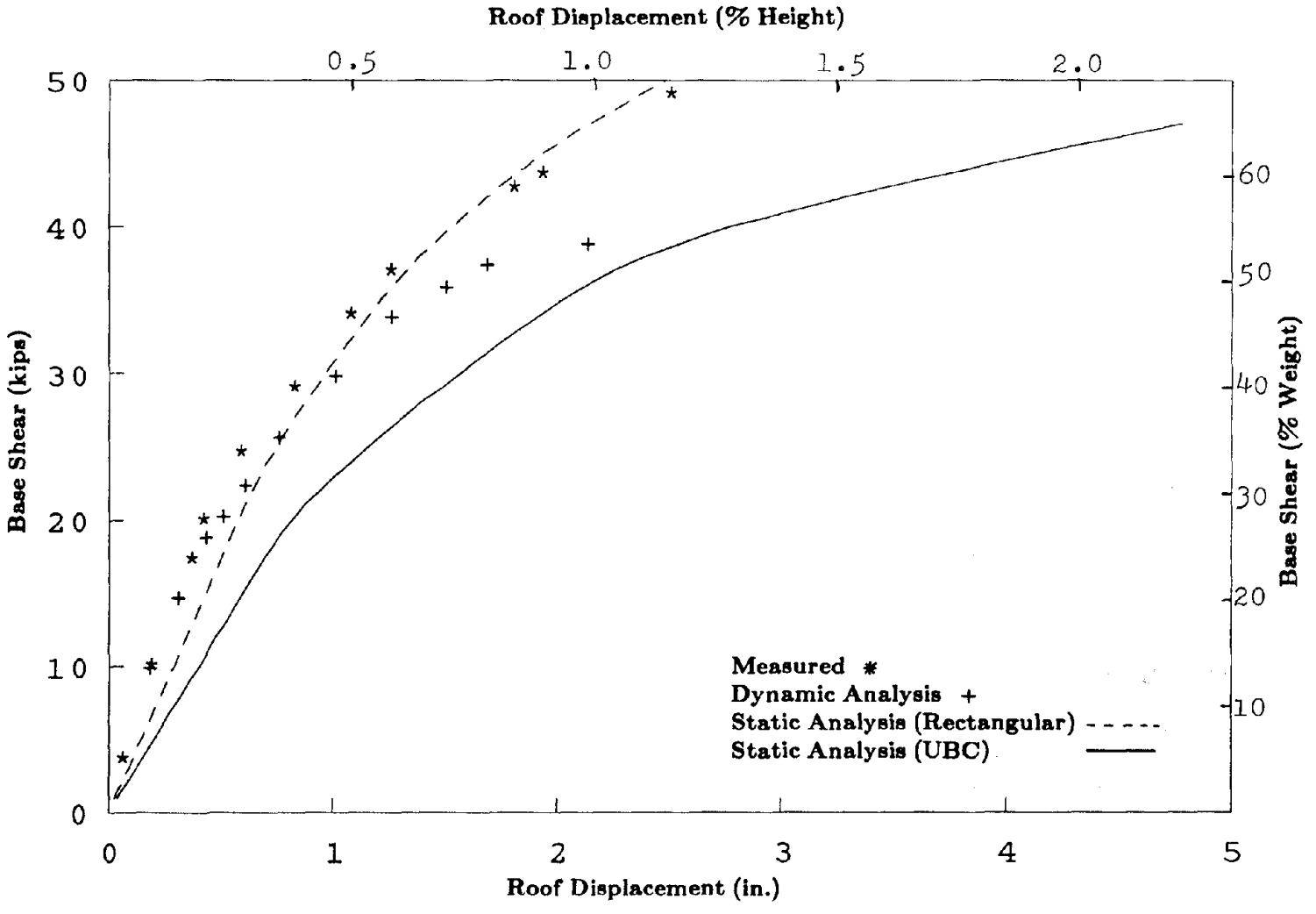

Figure 6.23 Comparison of Base Shear-Roof Displacement Relations.

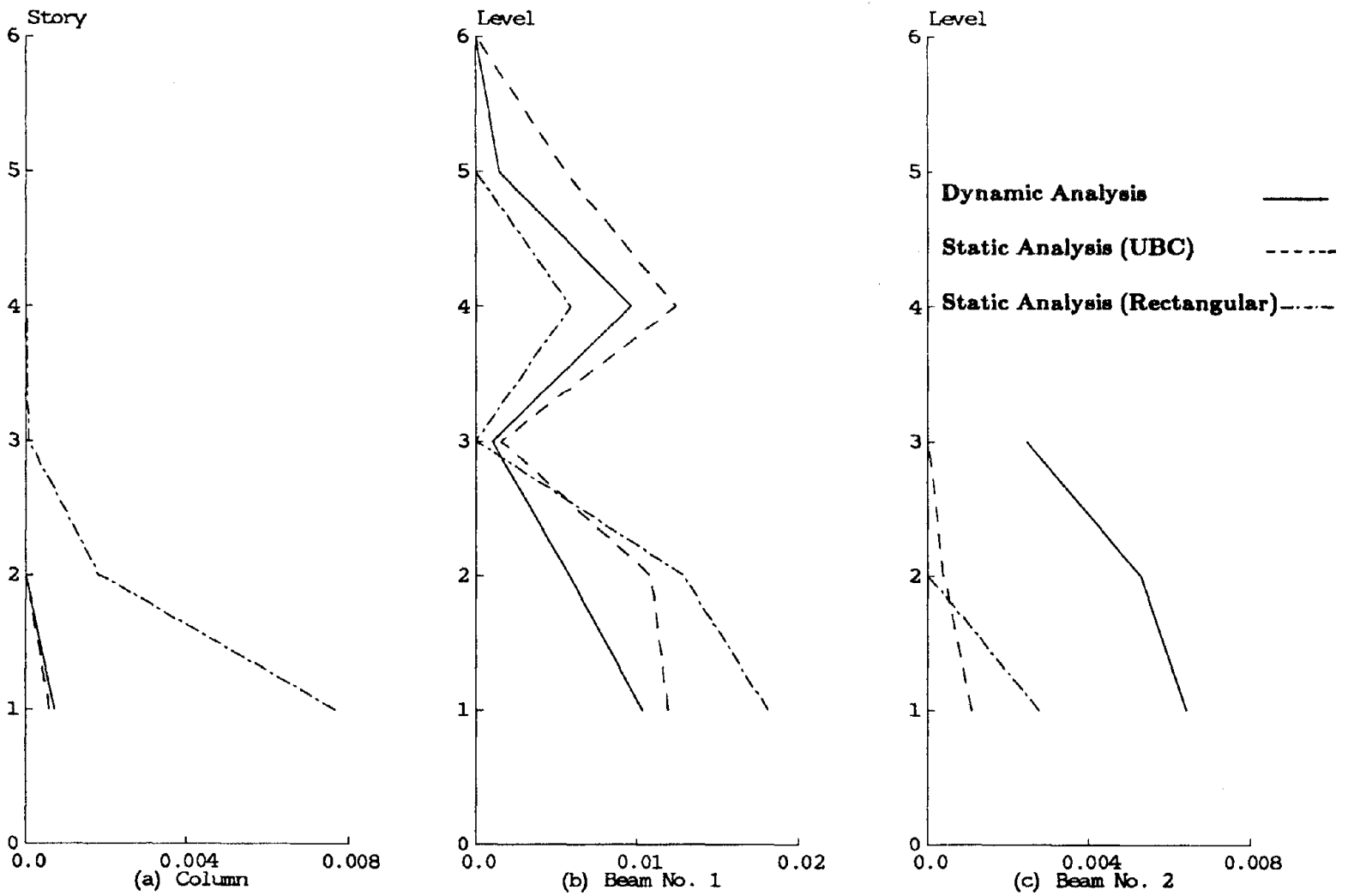

Figure 8.24 Comparison of Plastic Hinge Rotations.

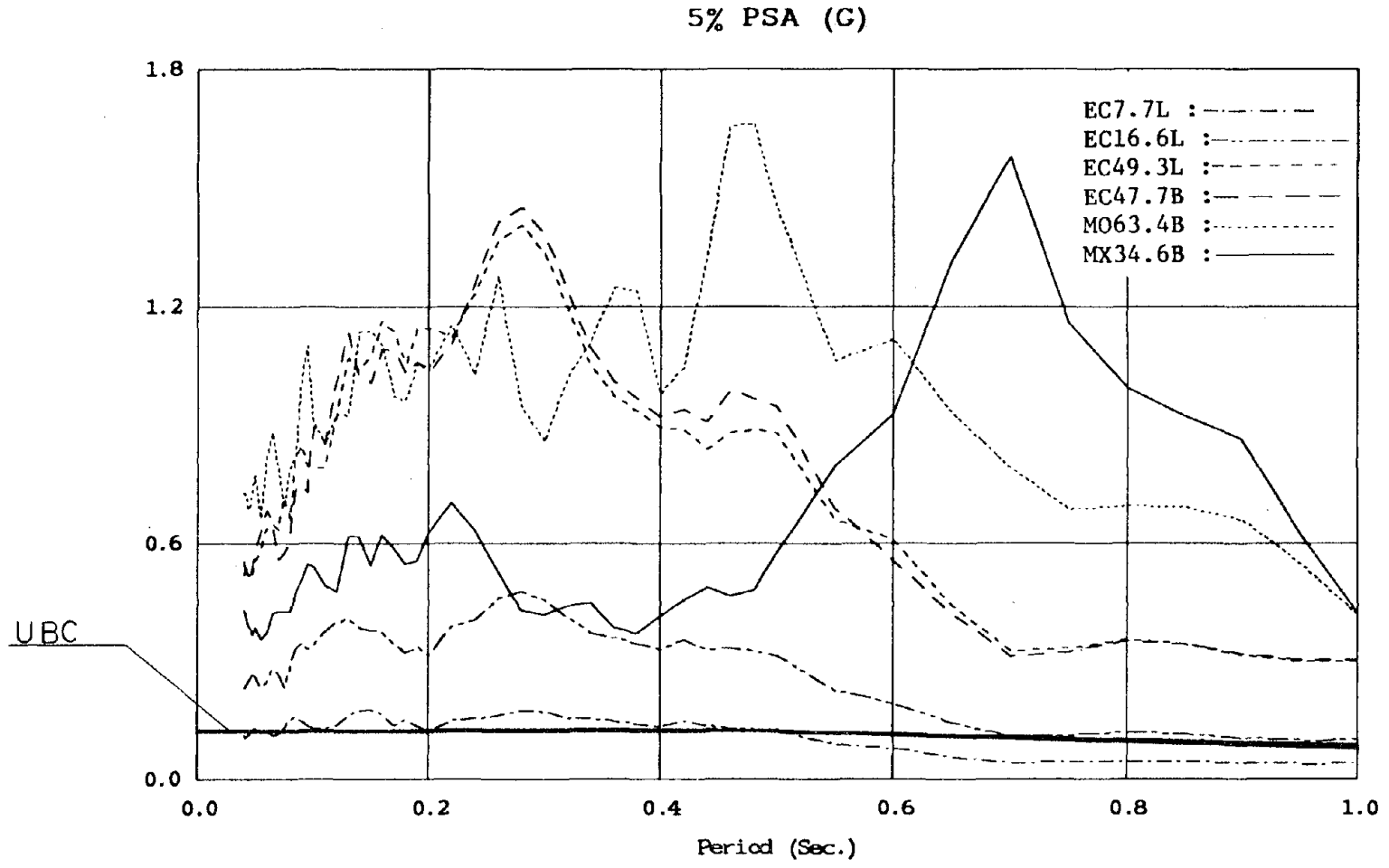

Figure 7.1 UBC Design Spectrum and 5-percent Damped Pseudo Acceleration Spectra.

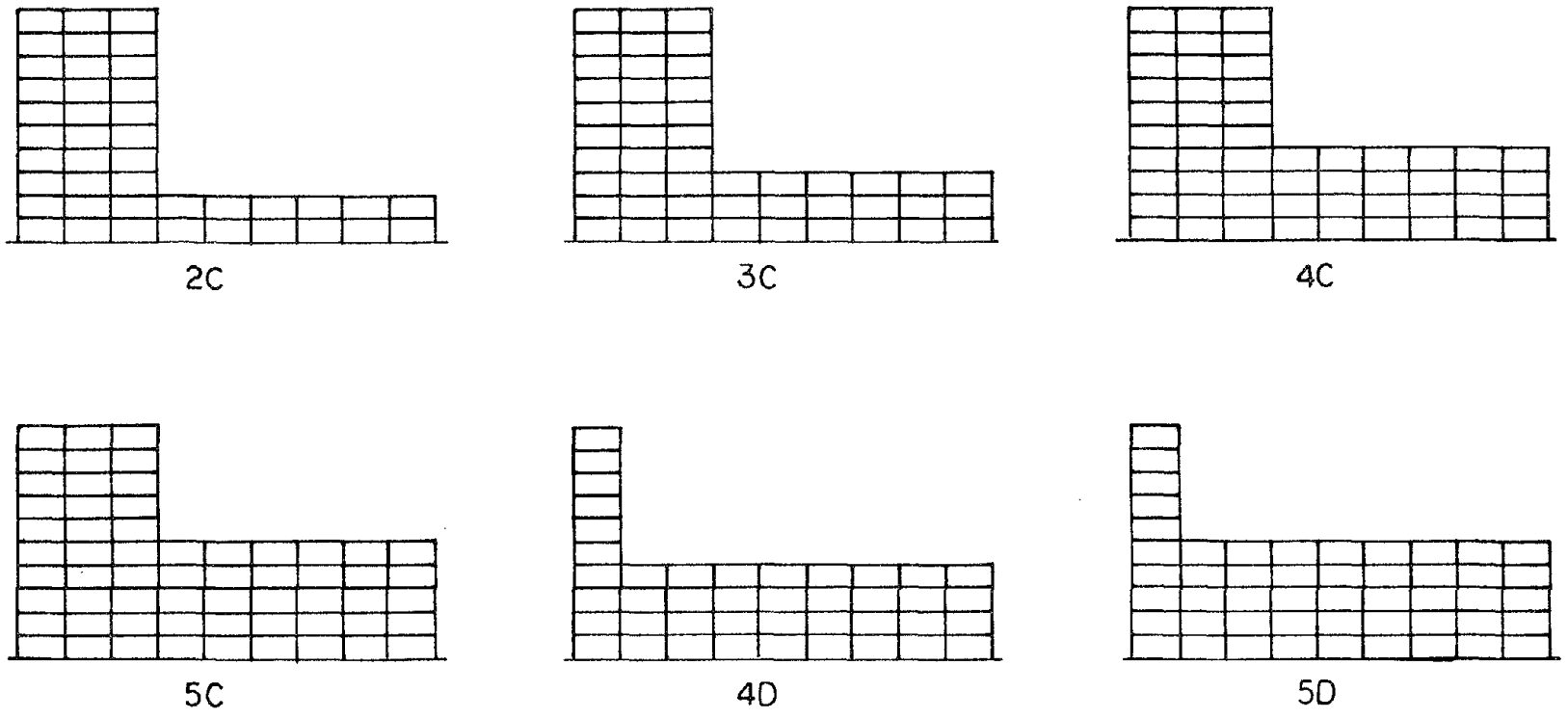

Figure 8.1 Elevation View of Generic Structures.

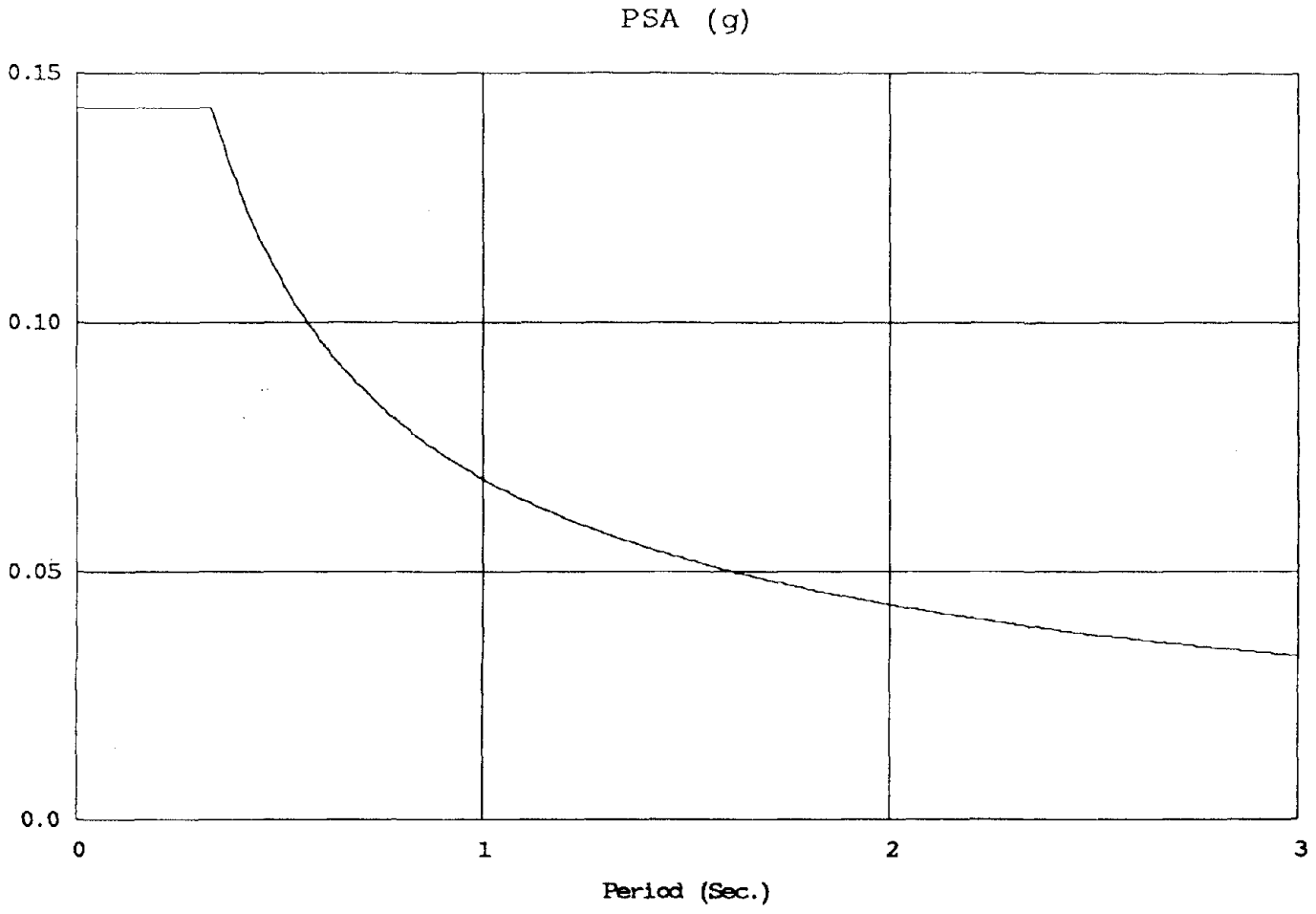

Figure 8.2 Design Acceleration Response Spectrum.

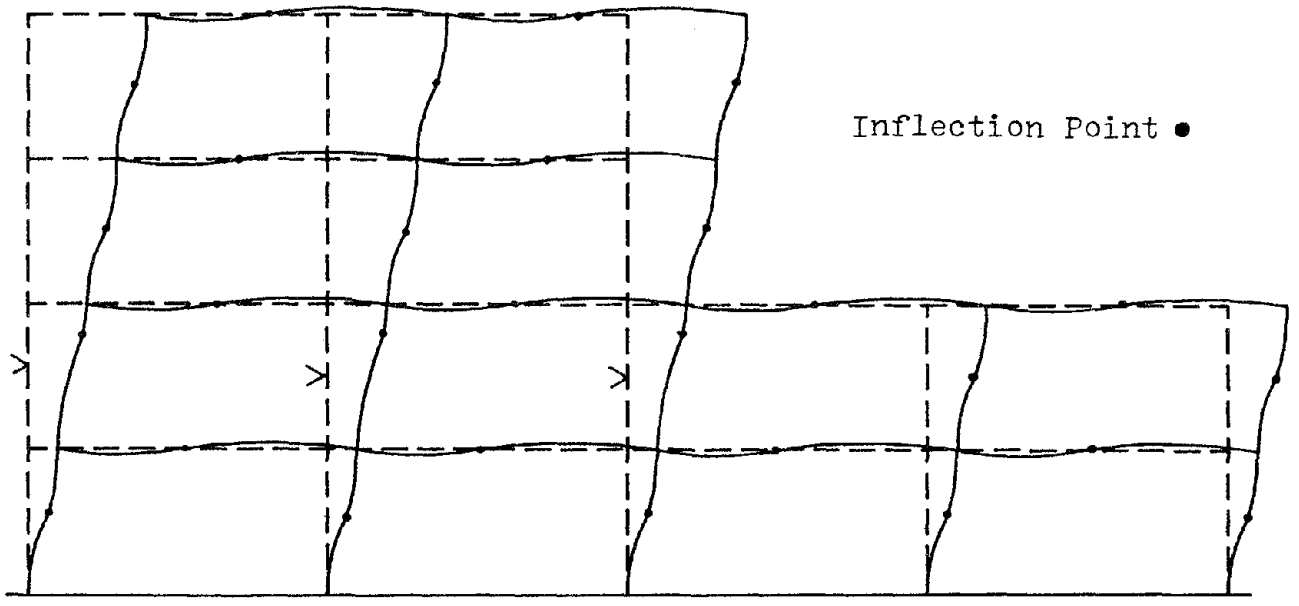

Figure 8.3 Deflected Shape of a Typical Setback Structure.

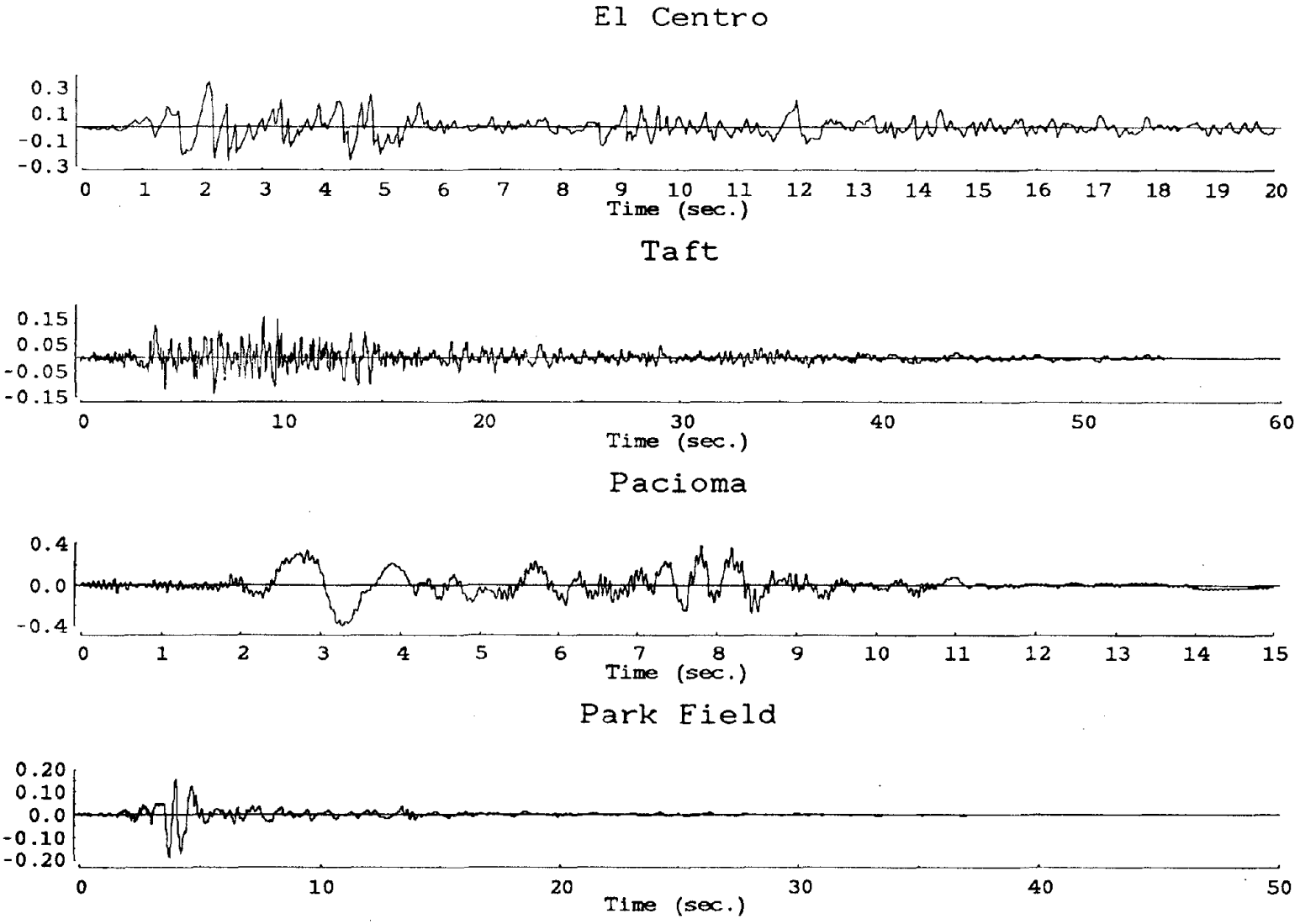

Figure 8.4(a) Input Acceleration Records.

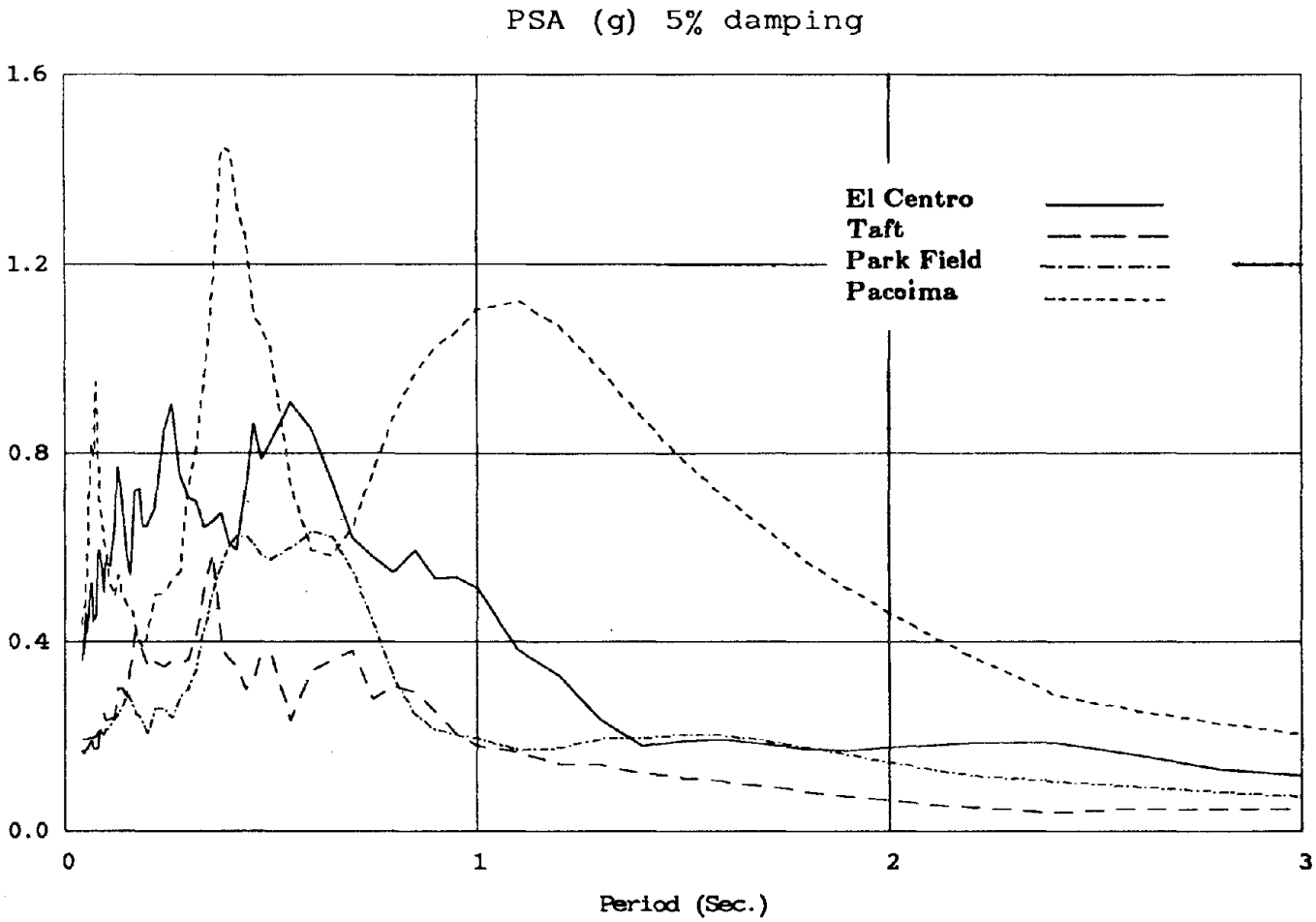

Figure 8.4(b) 5-Percent Damped Pseudo Acceleration Response Spectra.

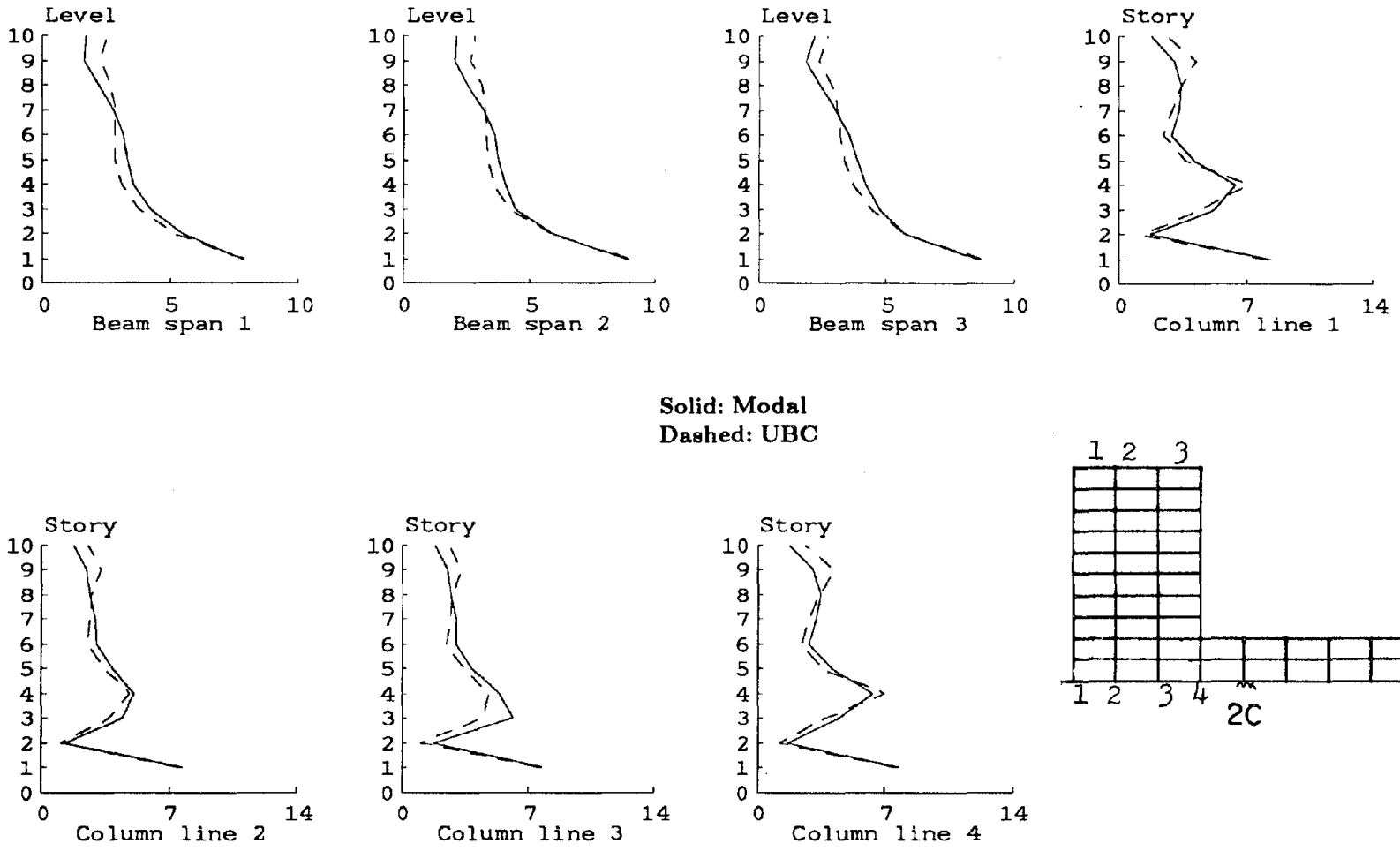

Figure 8.5(a) Variation of Positive Rotational Ductility Demand (Frame 2C).

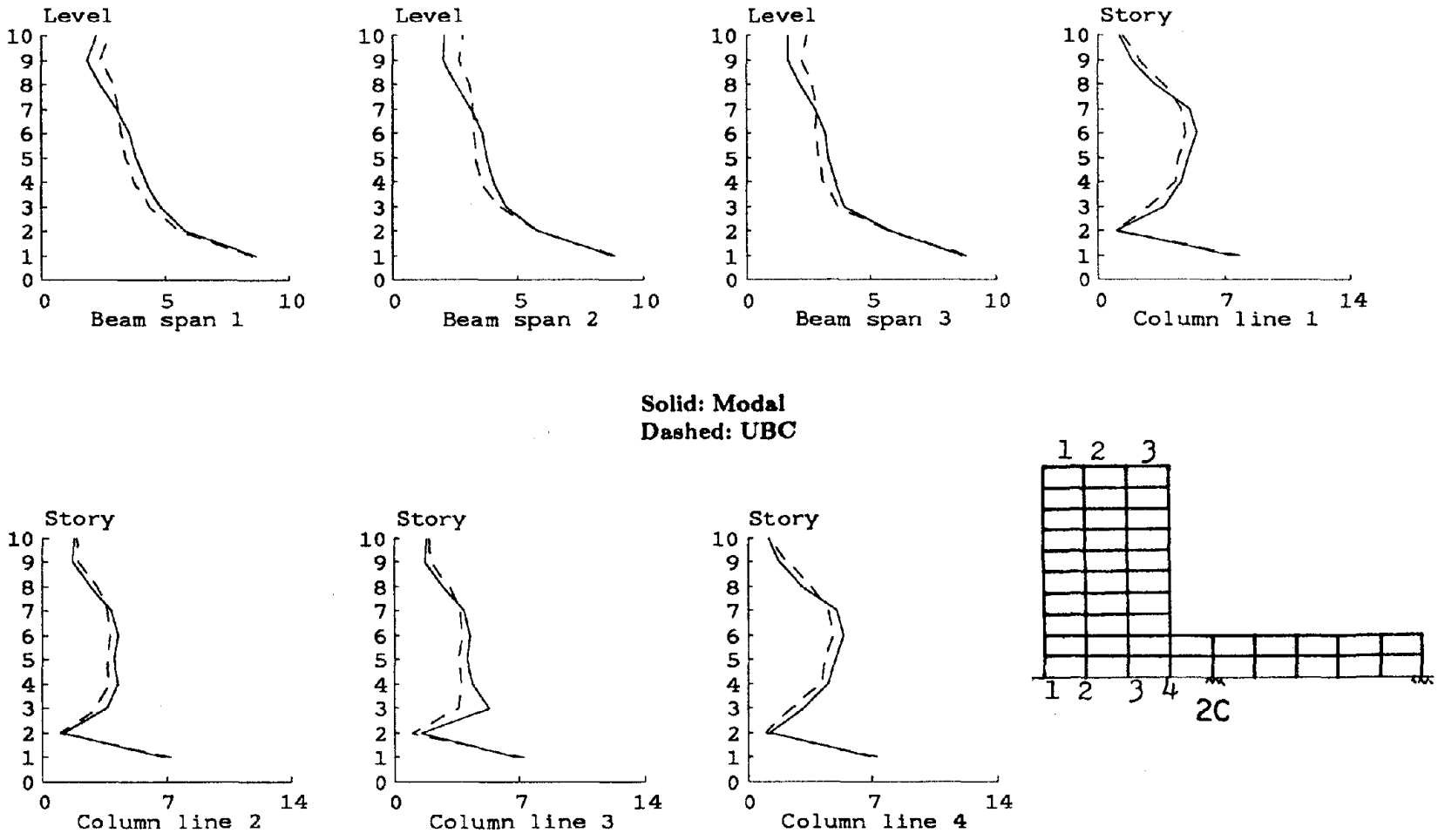

Figure 8.5a (Cont.) Variation of Negative Rotational Ductility Demand (Frame 2C).

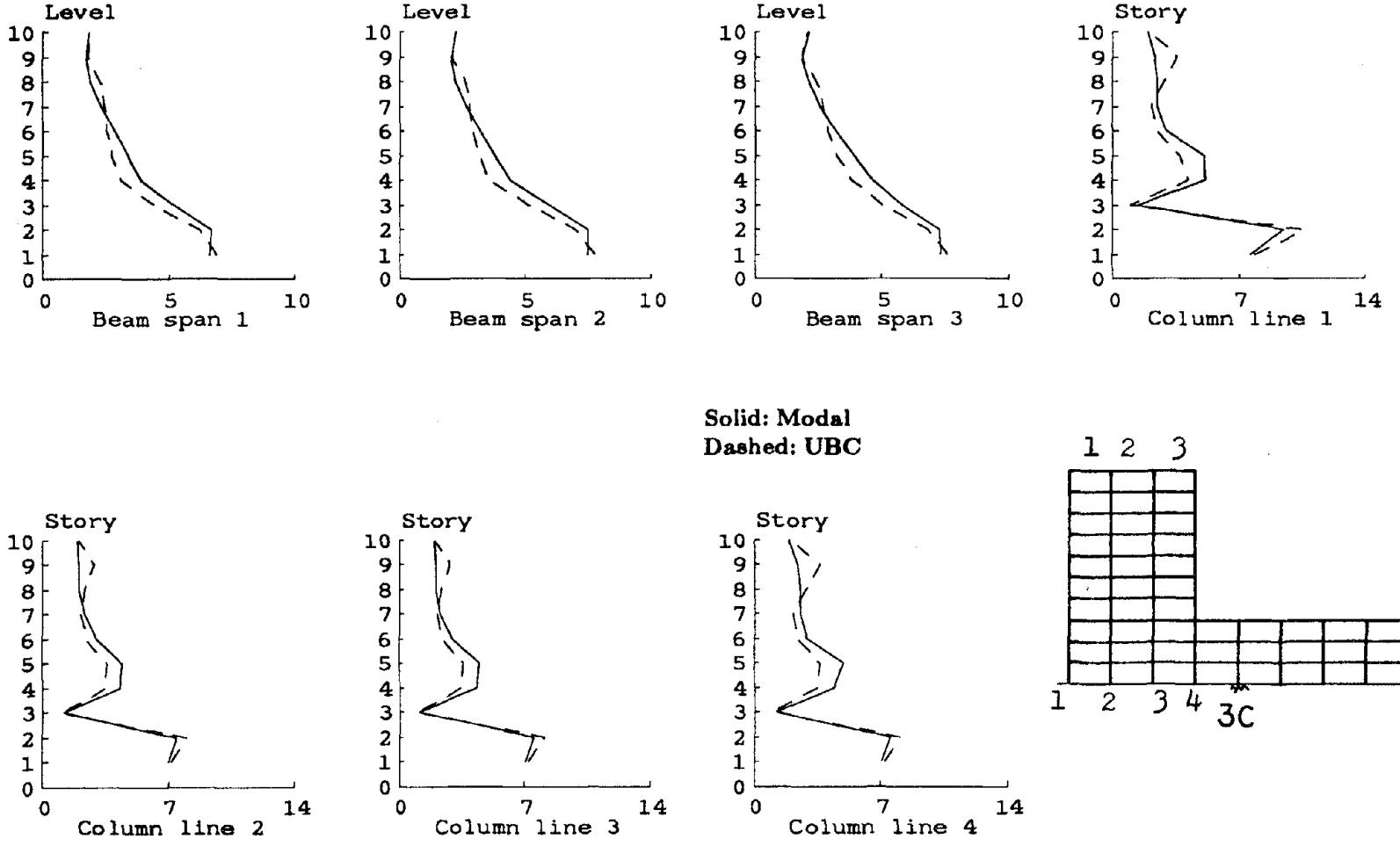

Figure 8.5(b) Variation of Positive Rotational Ductility Demand (Frame 3C).

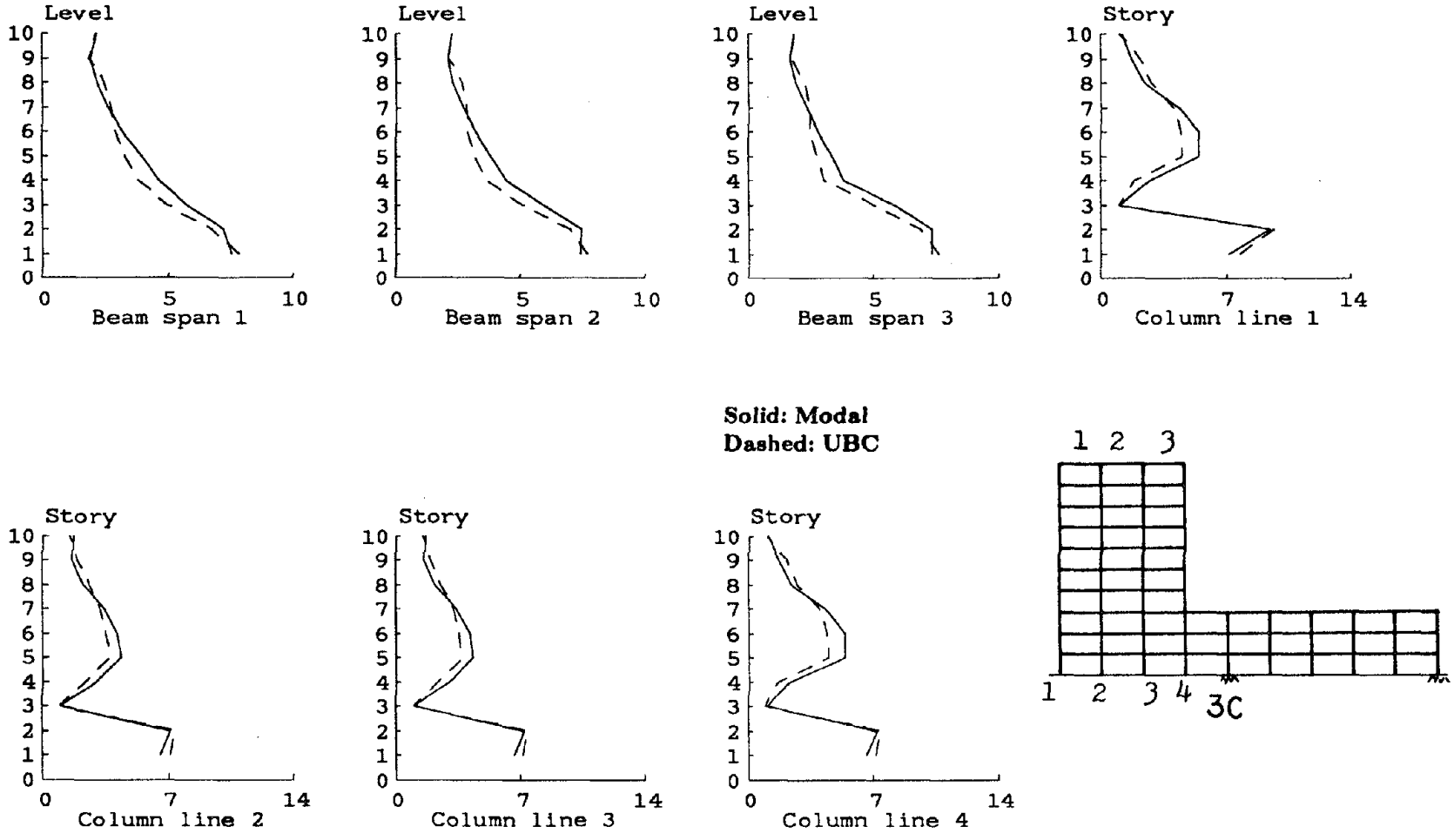

Figure 8.5b (Cont.) Variation of Negative Rotational Ductility Demand (Frame 3C).

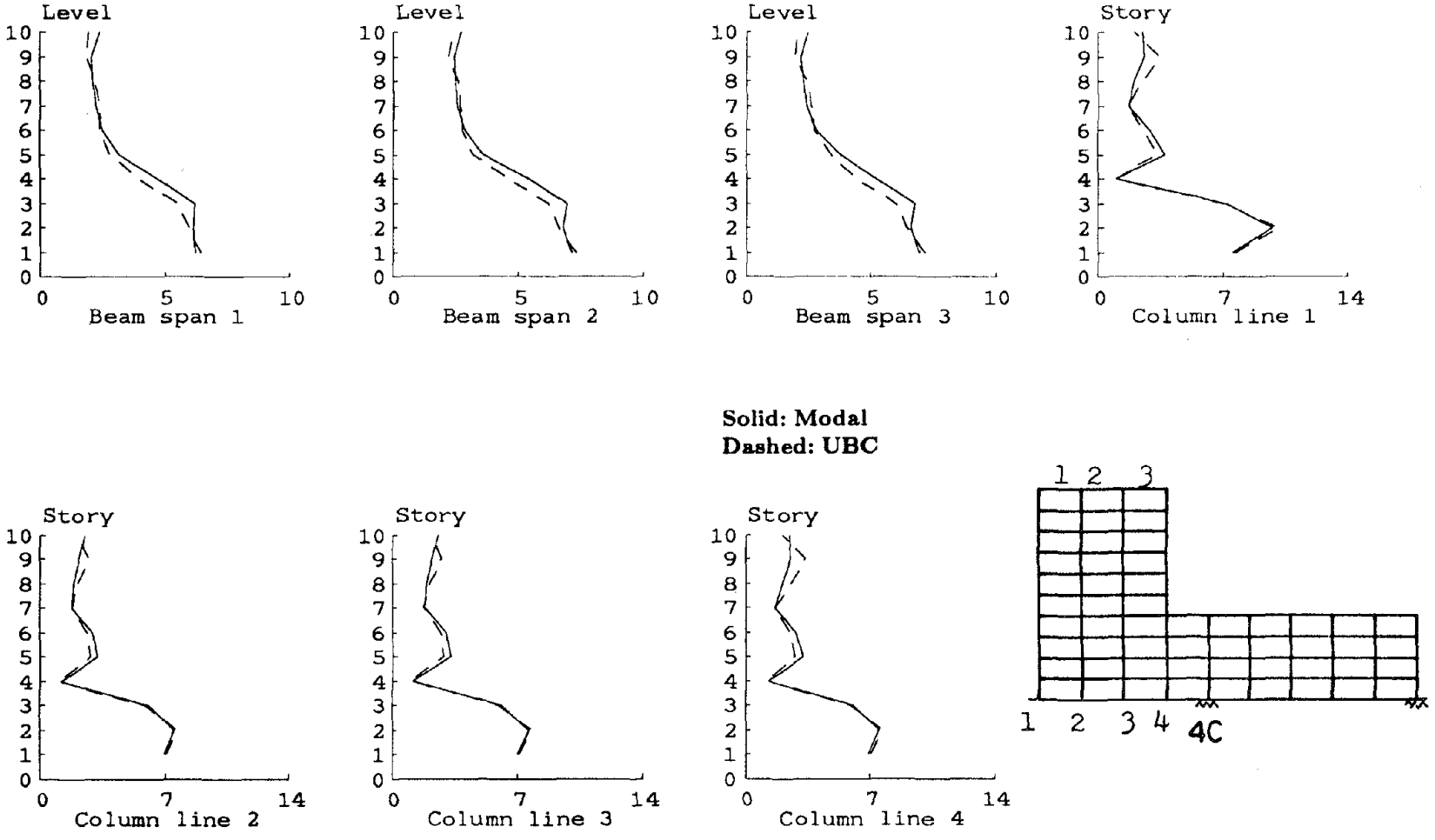

Figure 8.5(c) Variation of Positive Rotational Ductility Demand (Frame 4C).

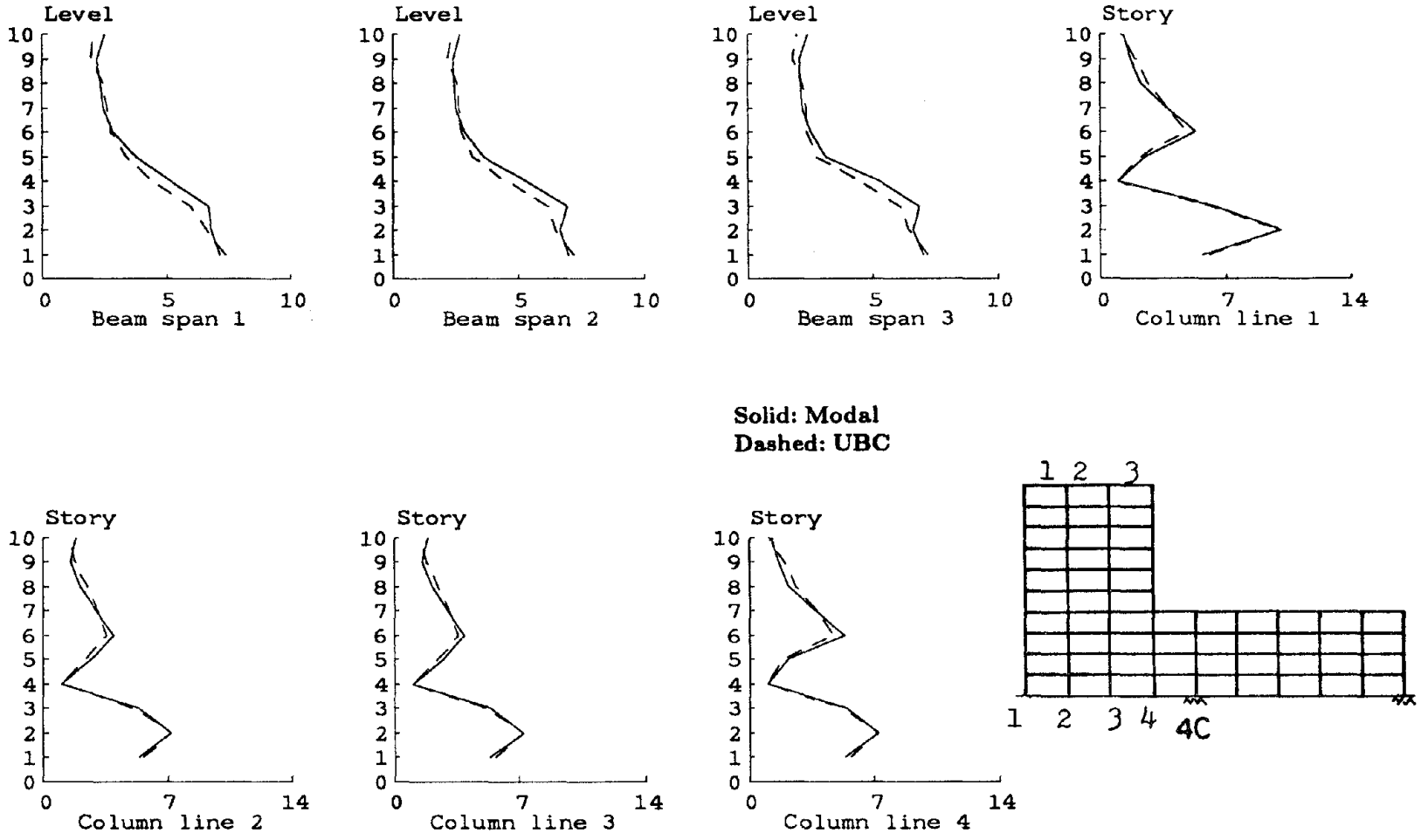

Figure 8.5c (Cont.) Variation of Negative Rotational Ductility Demand (Frame 4C).

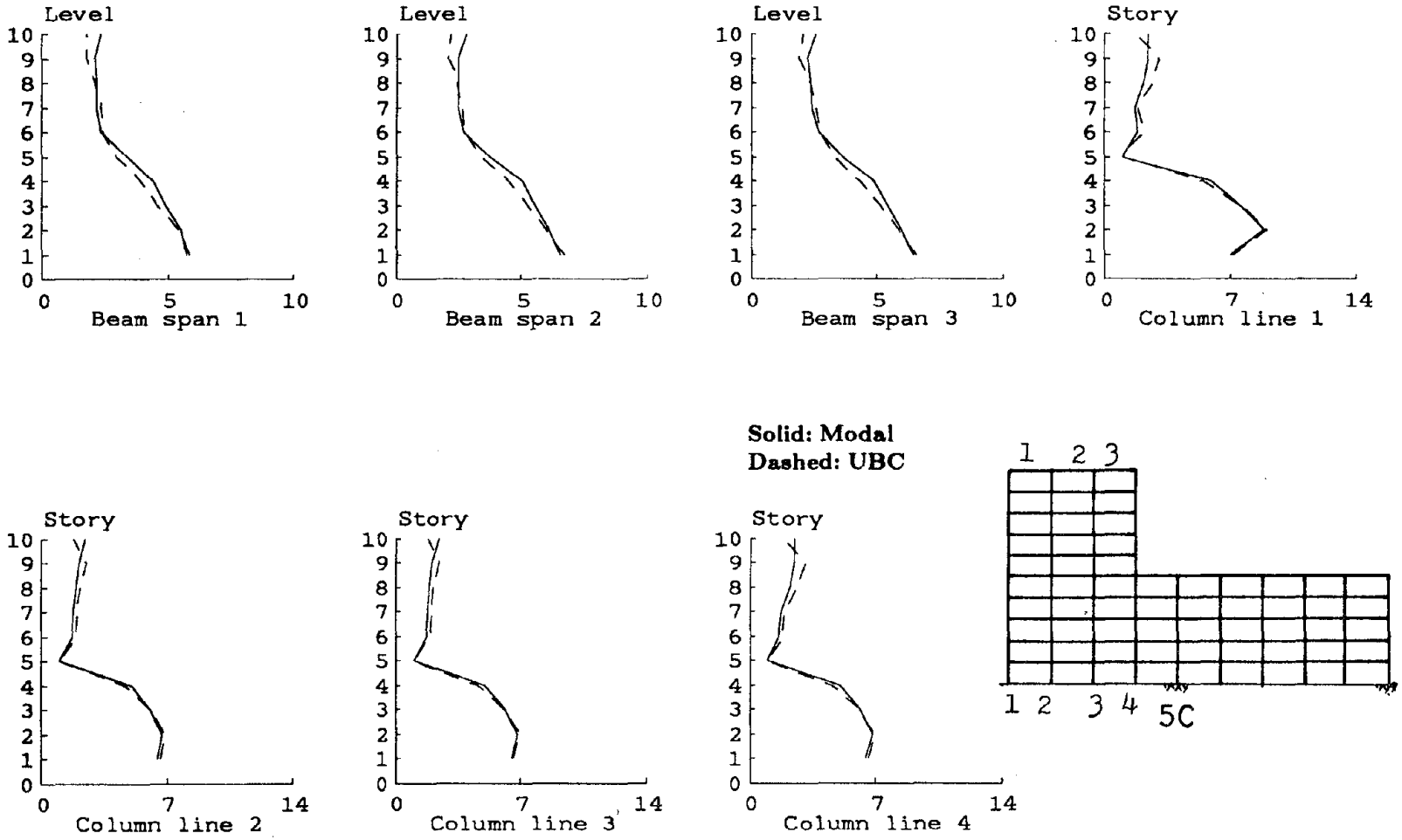

Figure 8.5(d) Variation of Positive Rotational Ductility Demand (Frame 5C).

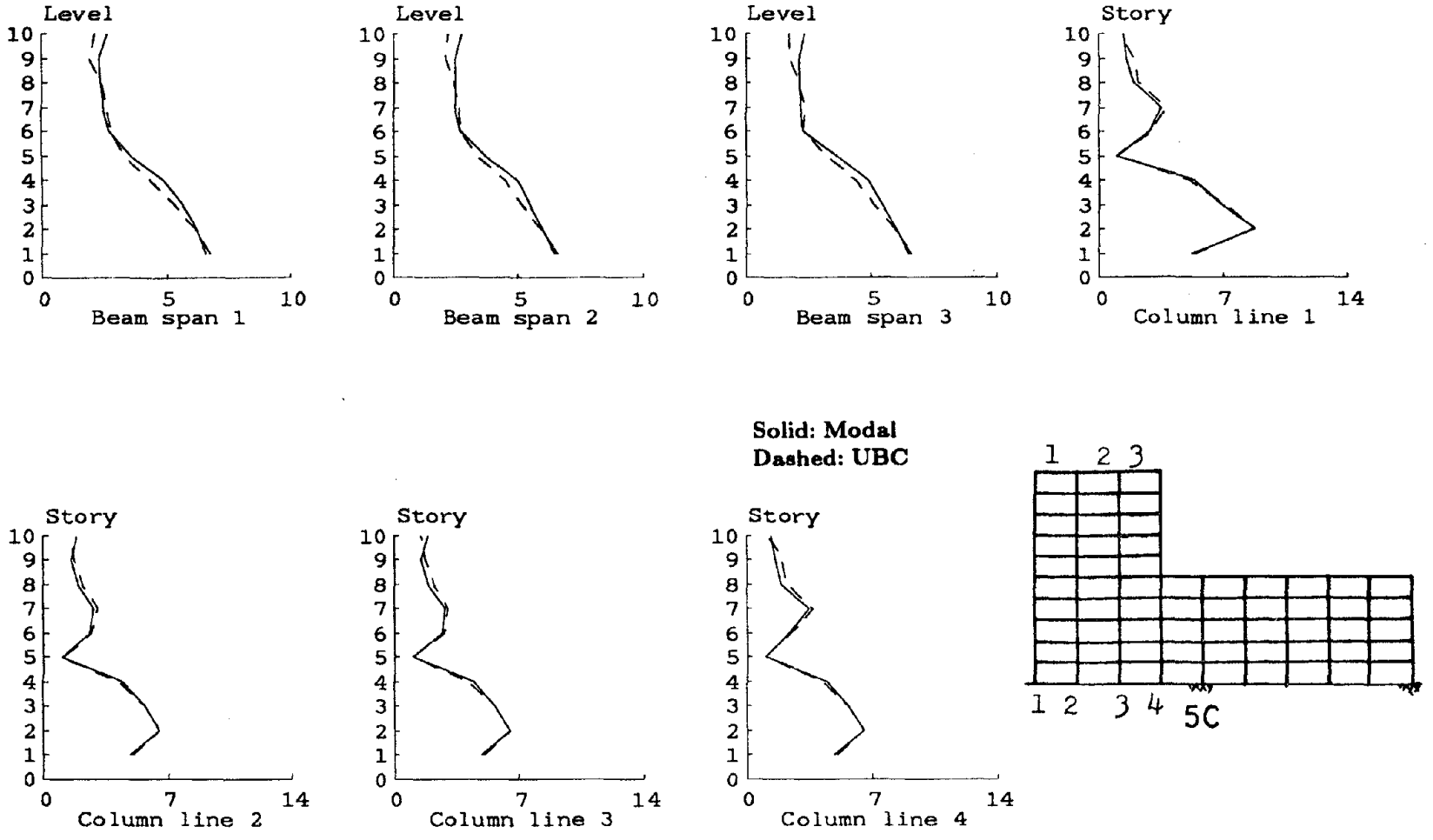

Figure 8.5d (Cont.) Variation of Negative Rotational Ductility Demand (Frame 5C).

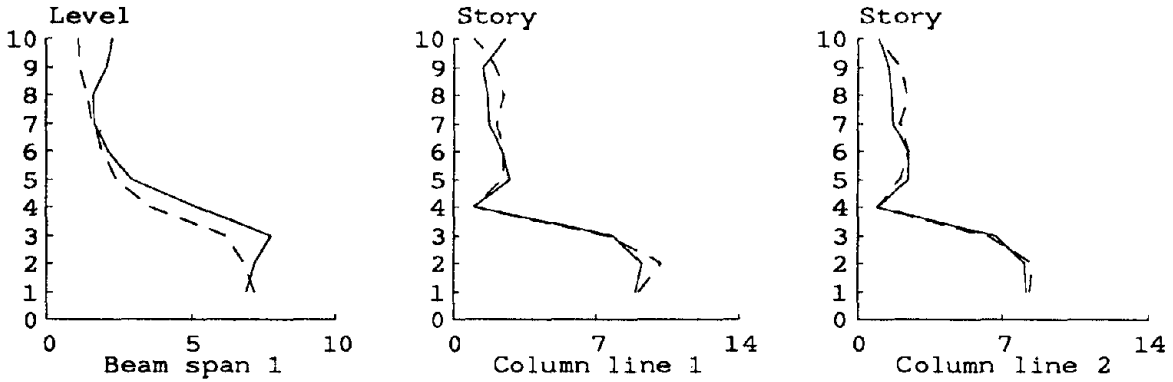

Figure 8.5(e) Variation of Positive Rotational Ductility Demand (Frame 4D).

Solid: Modal
Dashed: UBC

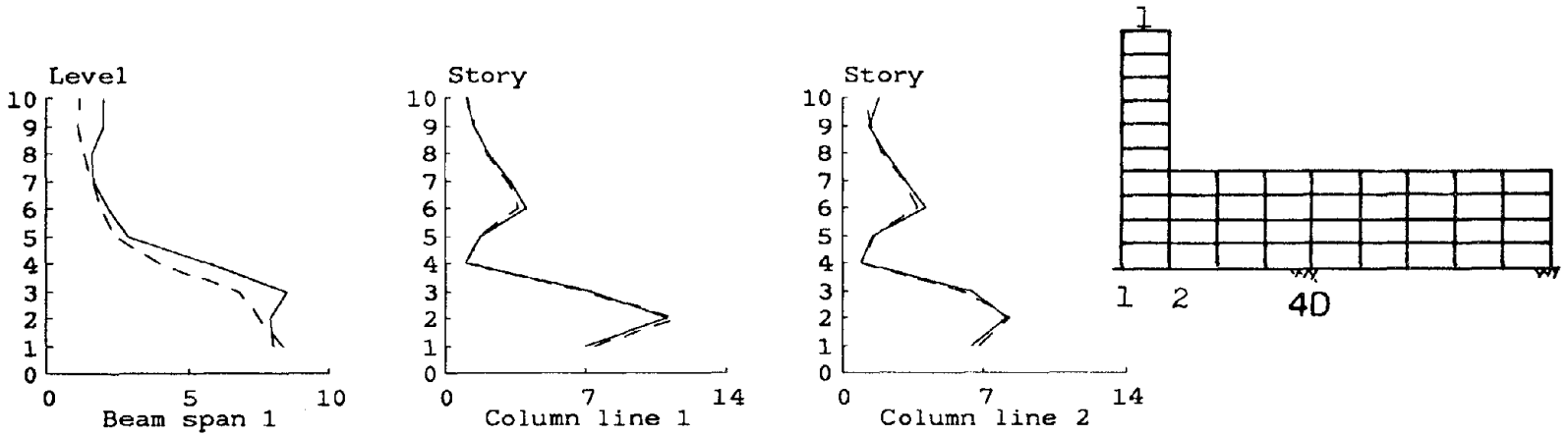

Figure 8.5e (Cont.) Variation of Negative Rotational Ductility Demand (Frame 4D).

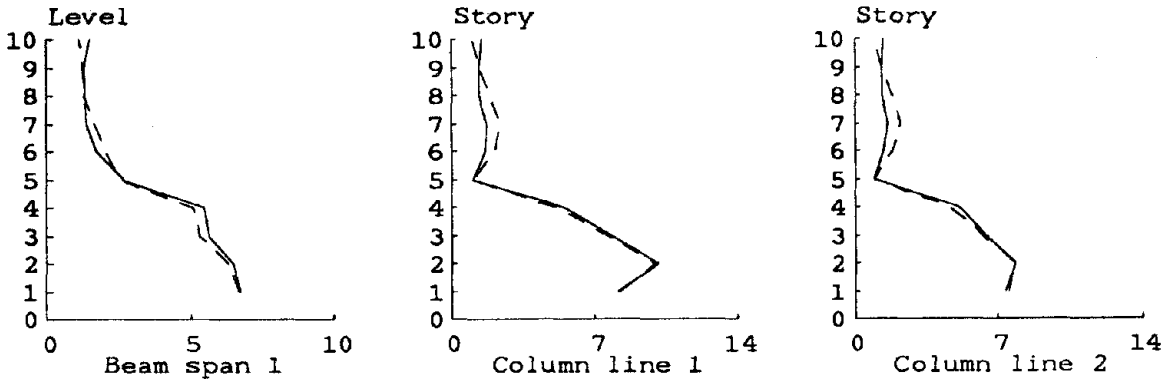

Figure 8.5(f) Variation of Positive Rotational Ductility Demand (Frame 5D).

Solid: Modal
Dashed: UBC

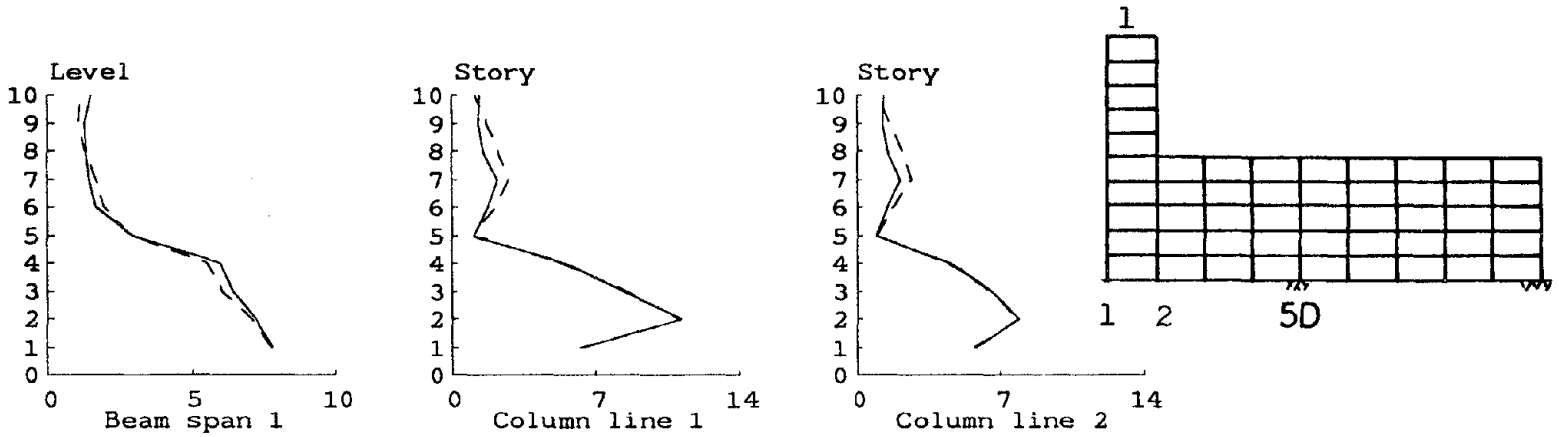

Figure 8.5f (Cont.) Variation of Negative Rotational Ductility Demand (Frame 5D).

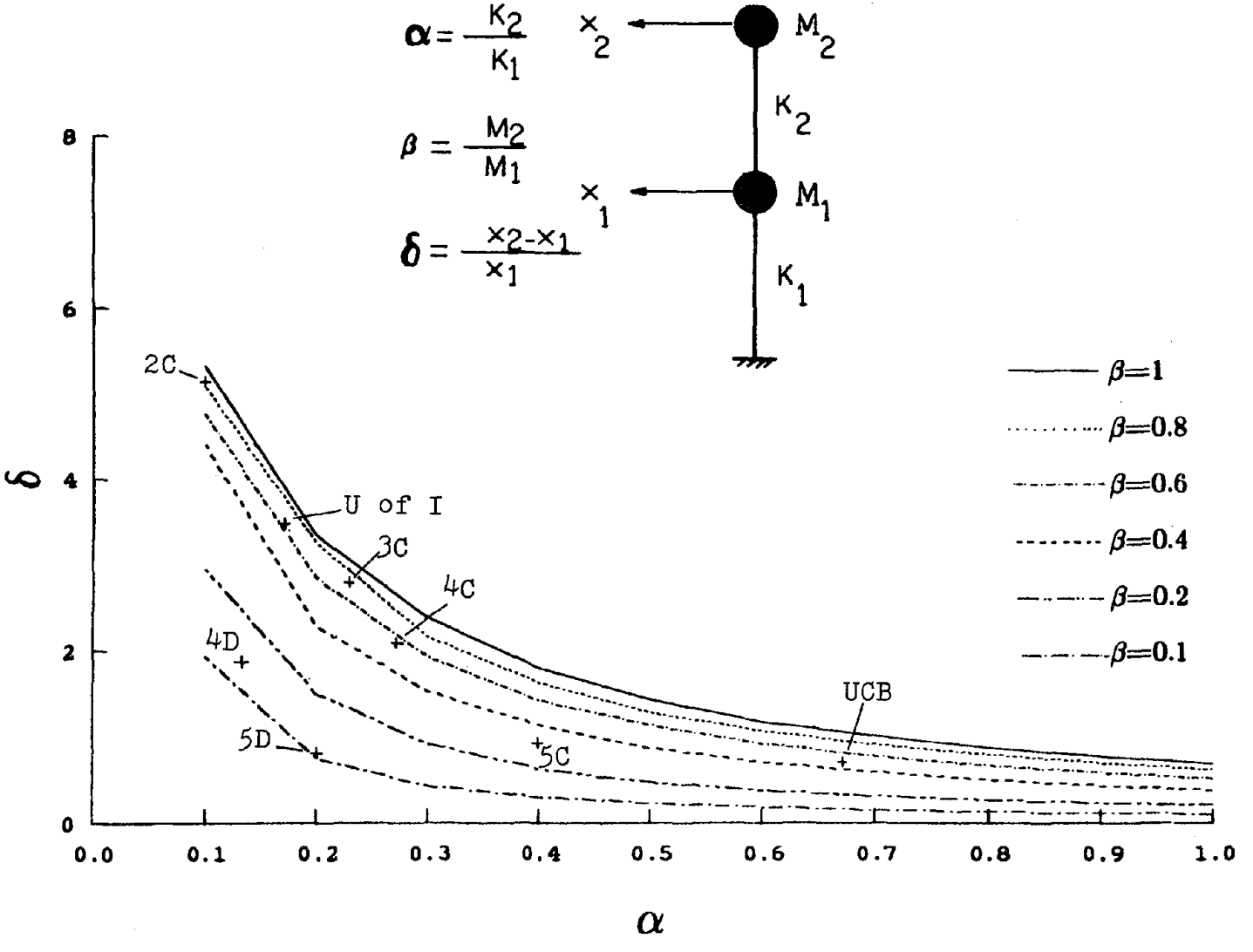

Figure 8.6 Variation of Drift Ratio with α and β.

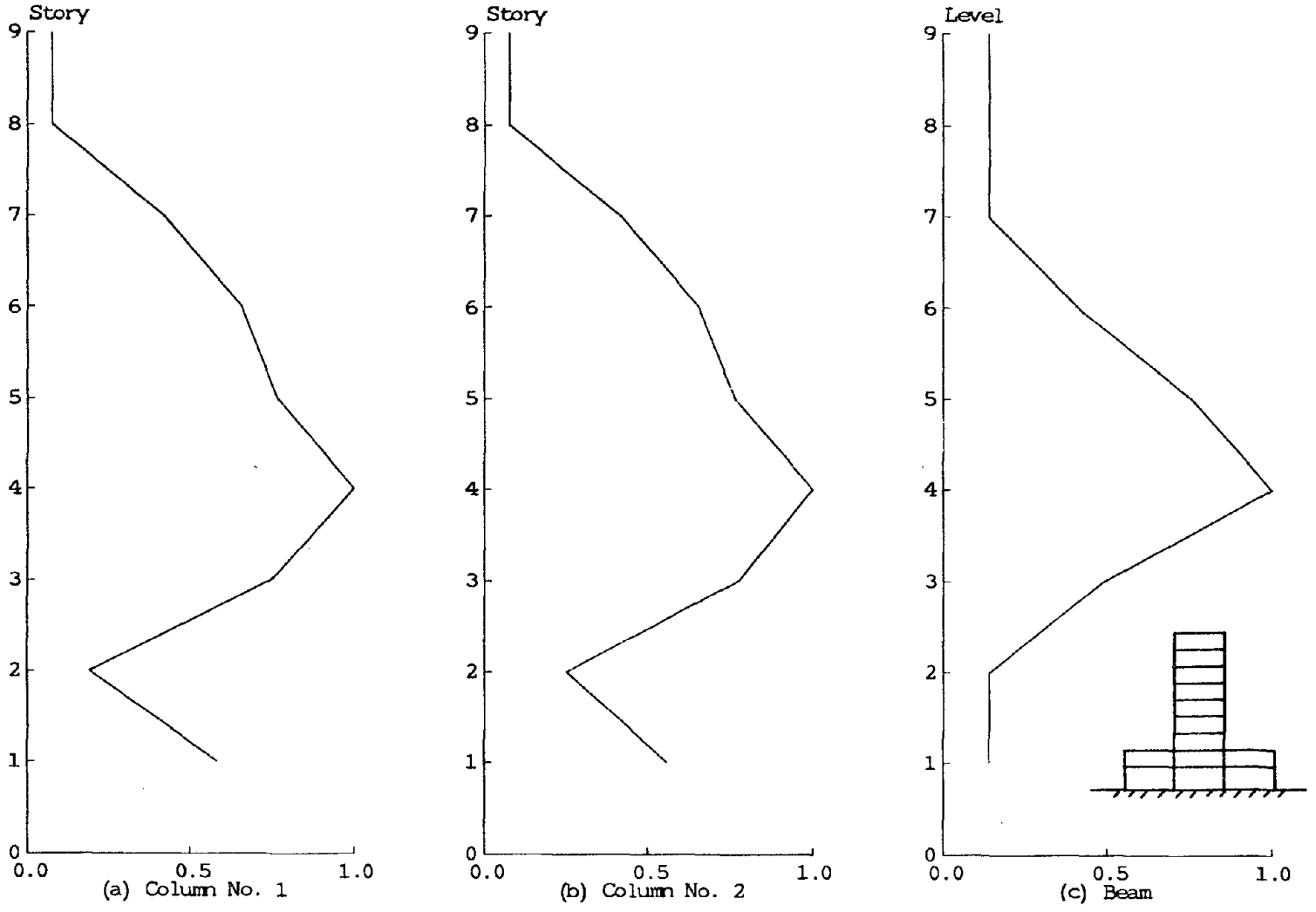

Figure 8.7 Distribution of Rotational Ductility Demand Over Height.
(Model tested at the University of Illinois)

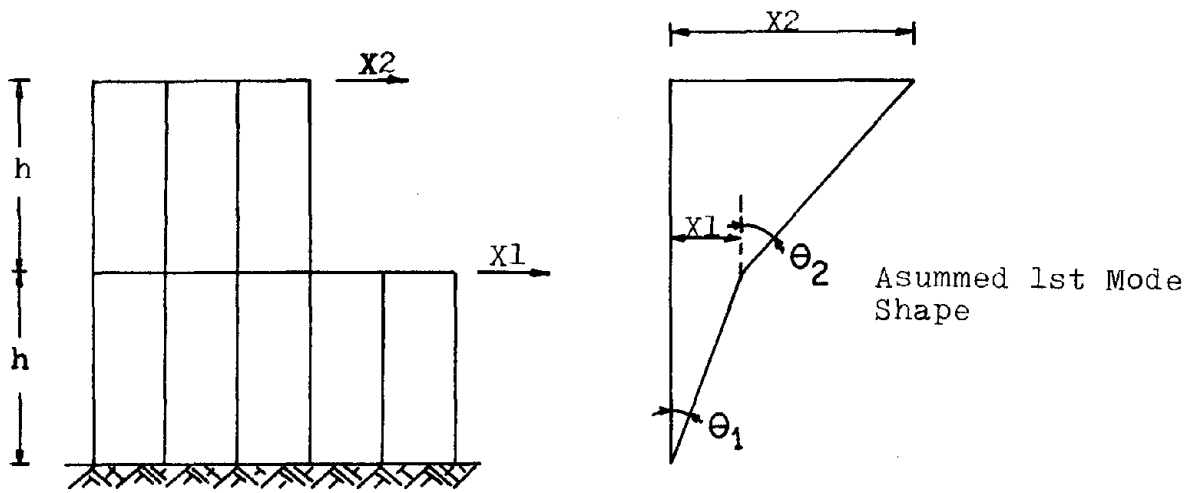

Figure 8.8 Assumed First-Mode Shape for a Typical Setback Structure.

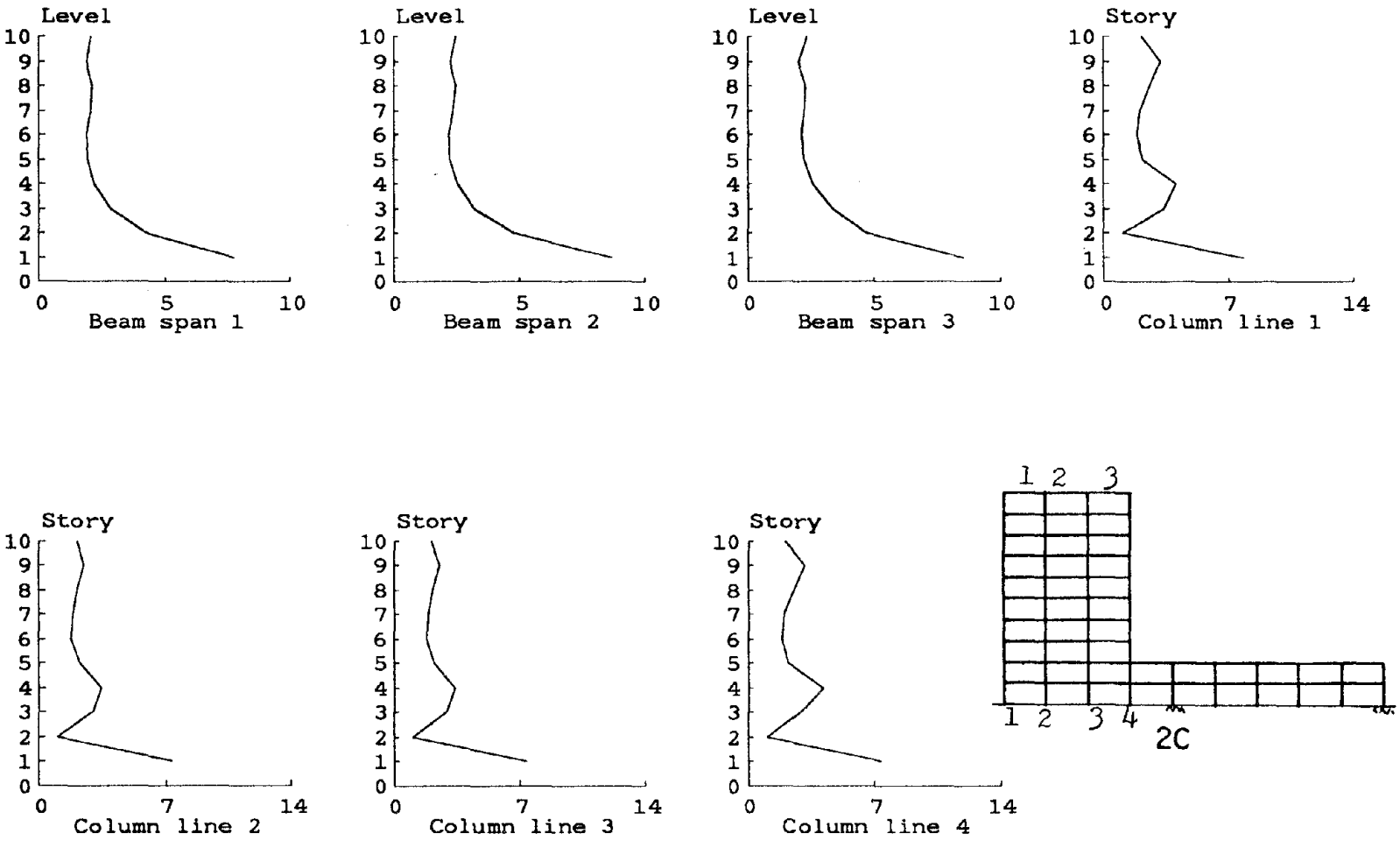

Figure 8.9(a) Variation of Positive Rotational Ductility Demand (Frame 2C). (Designed Using the Proposed Method)

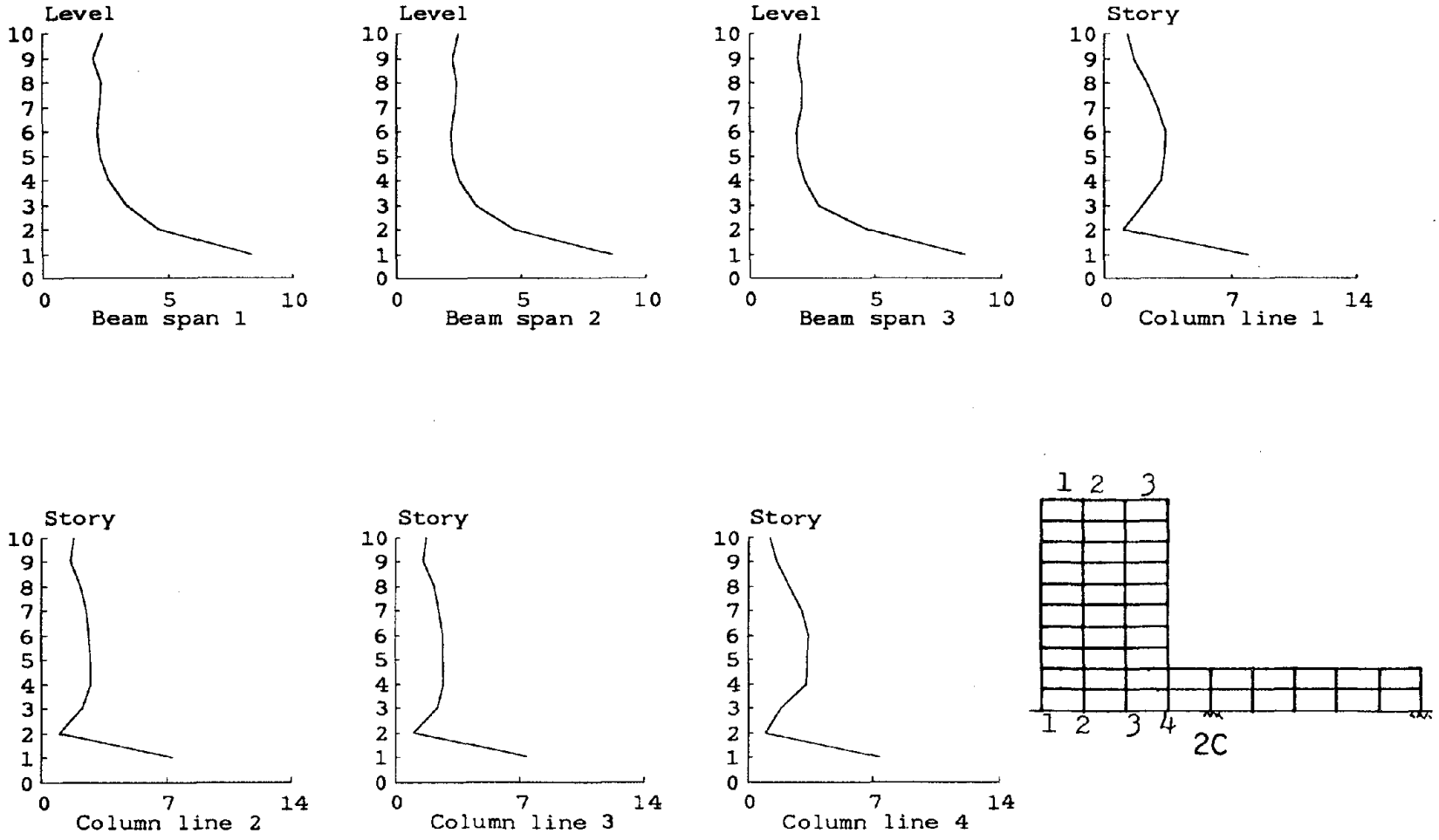

Figure 8.9a (Cont.) Variation of Negative Rotational Ductility Demand (Frame 2C). (Designed Using the Proposed Method)

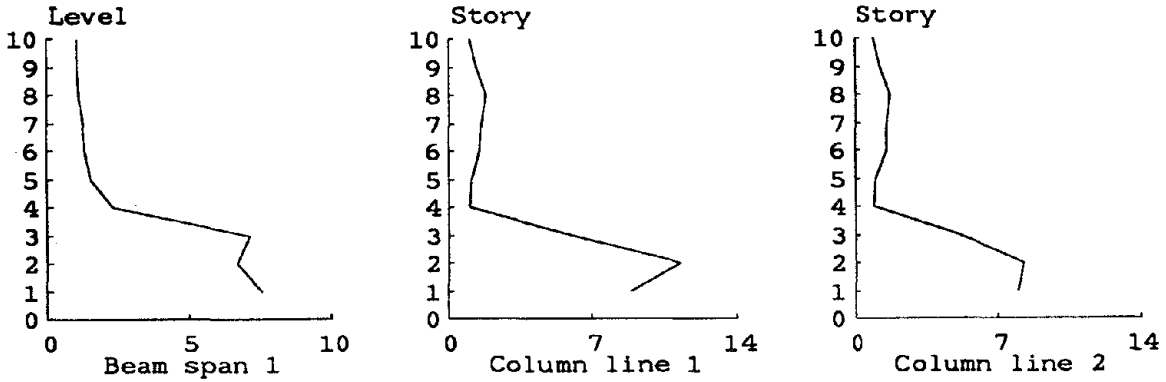

Figure 8.9(b) Variation of Positive Rotational Ductility Demand (Frame 4D). (Designed Using the Proposed Method)

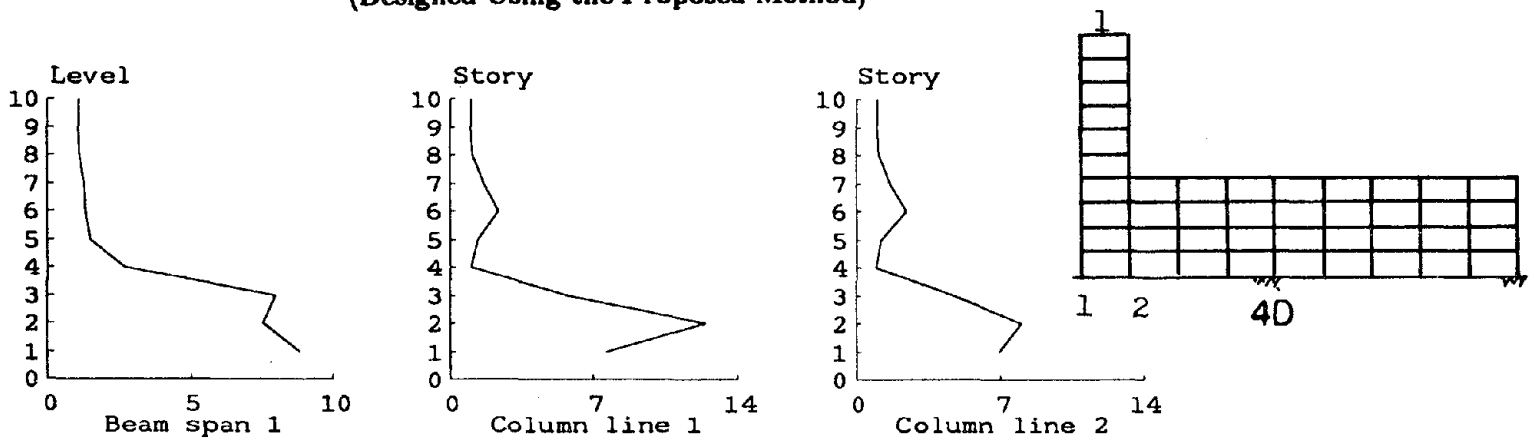

Figure 8.9b (Cont.) Variation of Negative Rotational Ductility Demand (Frame 4D). (Designed Using the Proposed Method)

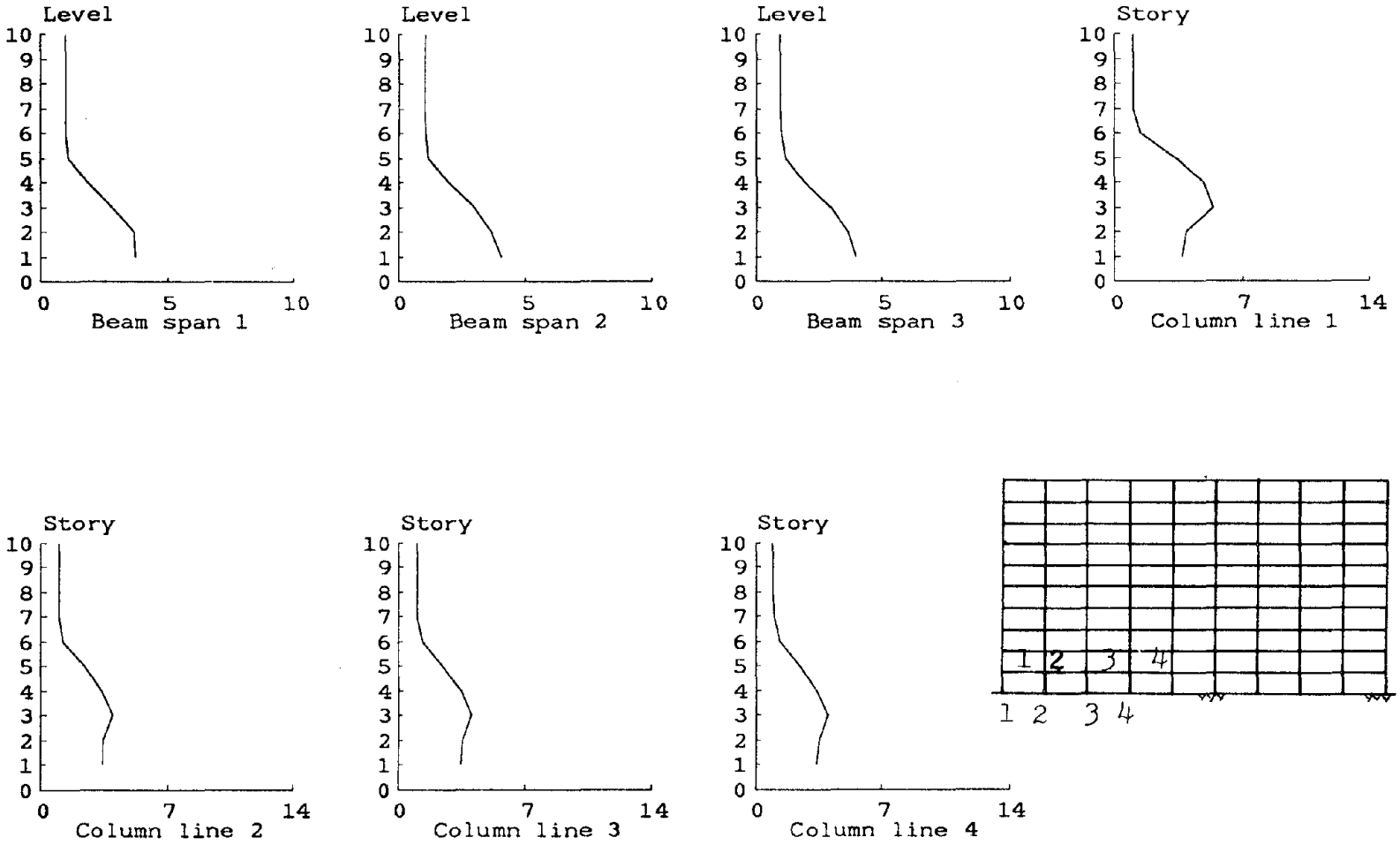

Figure 8.10(a) Variation of Positive Rotational Ductility Demand. (Uniform Frame, Pacoima)

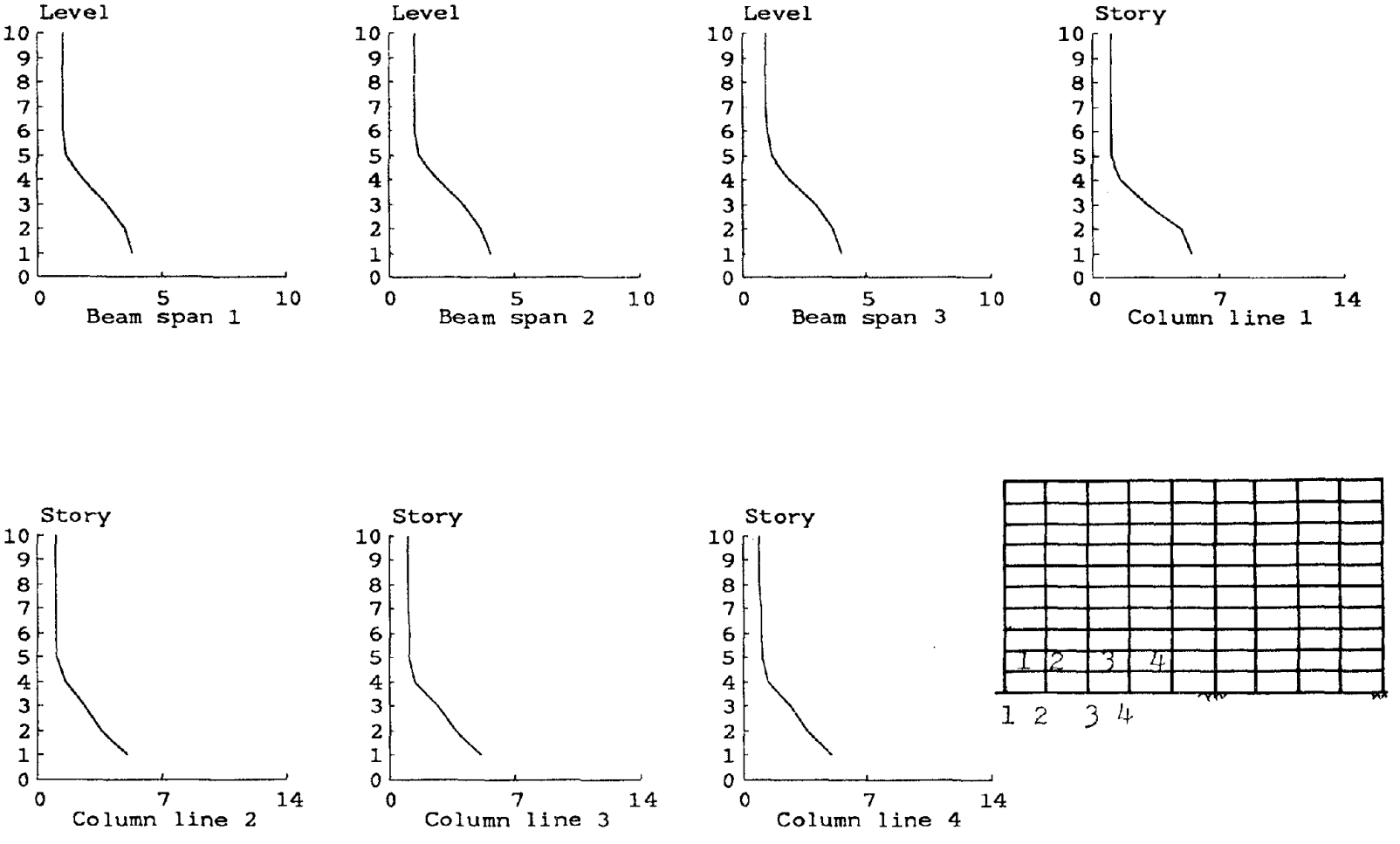

Figure 8.10a(Cont.) Variation of Negative Rotational Ductility Demand (Uniform Frame, Pacoima).

APPENDIX A
MATERIAL PROPERTIES

This appendix presents material properties of concrete and reinforcing bars that were used to construct the test structure.

A.1 Concrete

Concrete was designed to be similar to normal weight concrete used in full-scale construction. Dry weight mix proportions were 2.15:2.6:1.00 (coarse aggregate:fine aggregate:cement) with a water-cement ratio of 0.56. Cement is Type I-II Portland cement. Coarse aggregate was Radum pea gravel with maximum aggregate size of 3/8 in. Fine aggregate was a mixture of one part Tidewater blend sand and four parts Radum top sand. Concrete was ready-mixed delivered to the casting site.

Several cylinders were cast during each phase of construction (Chapter 3). These were stored with the test structure and received nominally the same treatment as the structure. Following conclusion of shaking table tests, compression tests and split cylinder tests were conducted using 3 by 6 in. and 6 by 12 in. cylinders. All the tests were in accordance with ASTM specifications. The resulting properties for 3 by 6 in. cylinders are summarized in Table A.1. Compressive strengths obtained on 6 by 12 in. cylinders averaged 92 percent of the strengths for the smaller cylinders. Mean, upper bound, and lower bound concrete stress-strain relations are plotted in Fig. A.1. The relations were obtained from the direct compression tests on 3 by 6 in. cylinders.

A.2 Steel

Beam and column longitudinal reinforcement comprised deformed nominal #3 (0.375 in. diameter), #2 (0.25 in. diameter), and #1 (0.178 in. diameter). The latter was

fabricated in the laboratory [38]. Stress-strain properties were determined along a 2.0 in. gauge length on nonmachined bars, using nominal areas to convert load to stress. Stress-strain relations for bar #1 are plotted in Fig. A.2. Mean stress-strain relations for bars #3 and #2 are plotted in Fig. A.3., and the properties are summarized in Table A.2.

Transverse reinforcement for beams and columns was gauge #11 (0.120 in. diameter) and gauge #9 (0.148 in. diameter) galvanized plain wire, respectively. Mean stress-strain relations, determined along an 8 in. gauge length, are illustrated in Fig. A.4., and the properties are summarized in Table A.2.

Slab reinforcement was gauge #9 galvanized wire. The possibility of galvanic action between bars and concrete [13] was investigated and found not to occur. The plain wire was lightly deformed to improve its bond strength. The deformations did not change the mean material properties discussed previously (Fig. A.4).

A.3 Confined Concrete

The effects of confinement on concrete properties were investigated using two specimens. Two 20-inch columns having an identical cross section as the end regions of column type "C1" (Fig. 2.7) were cast. The longitudinal spacing of the transverse reinforcement was 1 inch. Reinforcing bars had the same properties as those used to construct the test structure. The specimens were cast separately from the test structure, and the concrete properties were slightly different. The average compression strength at 37 days was 4.2 ksi.

Specimens were tested under monotonically increasing axial compression. The specimens were centered and plumbed beneath the spherical loading head of a universal testing machine. A steel plate was placed beneath and above the specimen to ensure uniform contact at the ends. Tests were conducted in load control mode, and testing was discontinued after load-carrying capacity had dropped significantly at relatively

large strains.

The average load-deflection response of the two specimens is plotted in Fig. A.5(a). Stress-strain relations for the confined concrete could not be measured directly using the experiments. However, the stress-strain relation can be inferred from measured relations between axial load and deflection. Average strain is approximated as the ratio between total measured deformation between the two ends of the specimens and an appropriate assumed gauge length. The gauge length was taken equal to the total specimen height (20") until peak load was reached. Beyond peak load, failure was assumed to occur only in the central region (assumed equal to 10 in.). This approach corresponds to the observed behavior during the tests, and extensive damage was found in this critical region which was approximately equal to 10 in. Thus, this height was used to compute strains beyond peak load. Load carried by concrete at any given strain is the difference between total load on the specimen and that carried by longitudinal reinforcement at the same strain. Previous experiments [61] have indicated that longitudinal bar strains in the critical region will be approximately equal to concrete strains in the same region. The relation between load and strain for longitudinal bars in compression was assumed to be identical to the relation measured during coupon tension tests (Fig. A.3) until the onset of buckling, which was not critical as the applied stresses were below the critical buckling stress (89 ksi as computed following the standard methods [35]). Concrete stress was obtained assuming that shell and core concrete share the concrete load up to strain of 0.0025, and that the core concrete (measured to the outside of the perimeter hoops) carries the concrete load at stains beyond 0.004. A linear transition was assumed between these strains [35].

The mean derived stress-strain relation is plotted in Fig. A.5(b). Enhanced compression strength and more importantly increased ductility are noticeable. The compression strength was increased by 49 percent. The load-carrying behavior beyond peak load was significantly improved, as easily seen by comparing unconfined and

confined concrete stress-strain relations (Fig. A.1 and Fig. A.5).

Table A.1 Summary of Concrete Properties.

Location	Age (days)	Compressive strength (ksi)		Tensile strength (ksi)		E (ksi)
		No. of tests	Mean	No. of tests	Mean	
Frame 6	365	2	4.1	2	0.43	3010
Frame 5	350	2	4.2	2	0.49	3190
Frame 4	246	2	3.9	2	0.43	2855
Floors 1,2	173	3	4.6	2	0.50	3300
Floors 3,4,5,6	127	2	4.2	2	0.45	3072

Notes:

1. Compressive strengths are from 3 by 6 in. cylinders.

2. Tensile strengths are from split tests.

3. E (mean modulus of elasticity) was obtained from secant modulus of elasticity to 45 percent of compressive strength.

Table A.2 Summary of Steel Properties.

Bar	f_y (ksi)	f_u (ksi)	ϵ_y	ϵ_{sh}	ϵ_u
#3	64.9	95.7	0.0022	0.012	0.13
#2 (Type 1)	64.4	86.0	0.0022	0.030	0.17
#2 (Type 2)	66.2	100.	0.0023	-	0.08
#2 (Type 3)	73.1	96.5	0.0025	0.025	0.13
Wire Gauge #11	56.0	94.0	0.0019	-	0.11
Wire Gauge #9	55.0	90.0	0.0019	-	0.11

Notations:

f_y : Yield Stress

f_u : Ultimate Stress

ϵ_y : Yield Strain

ϵ_{sh} : Strain-hardening Strain

ϵ_u : Ultimate Strain

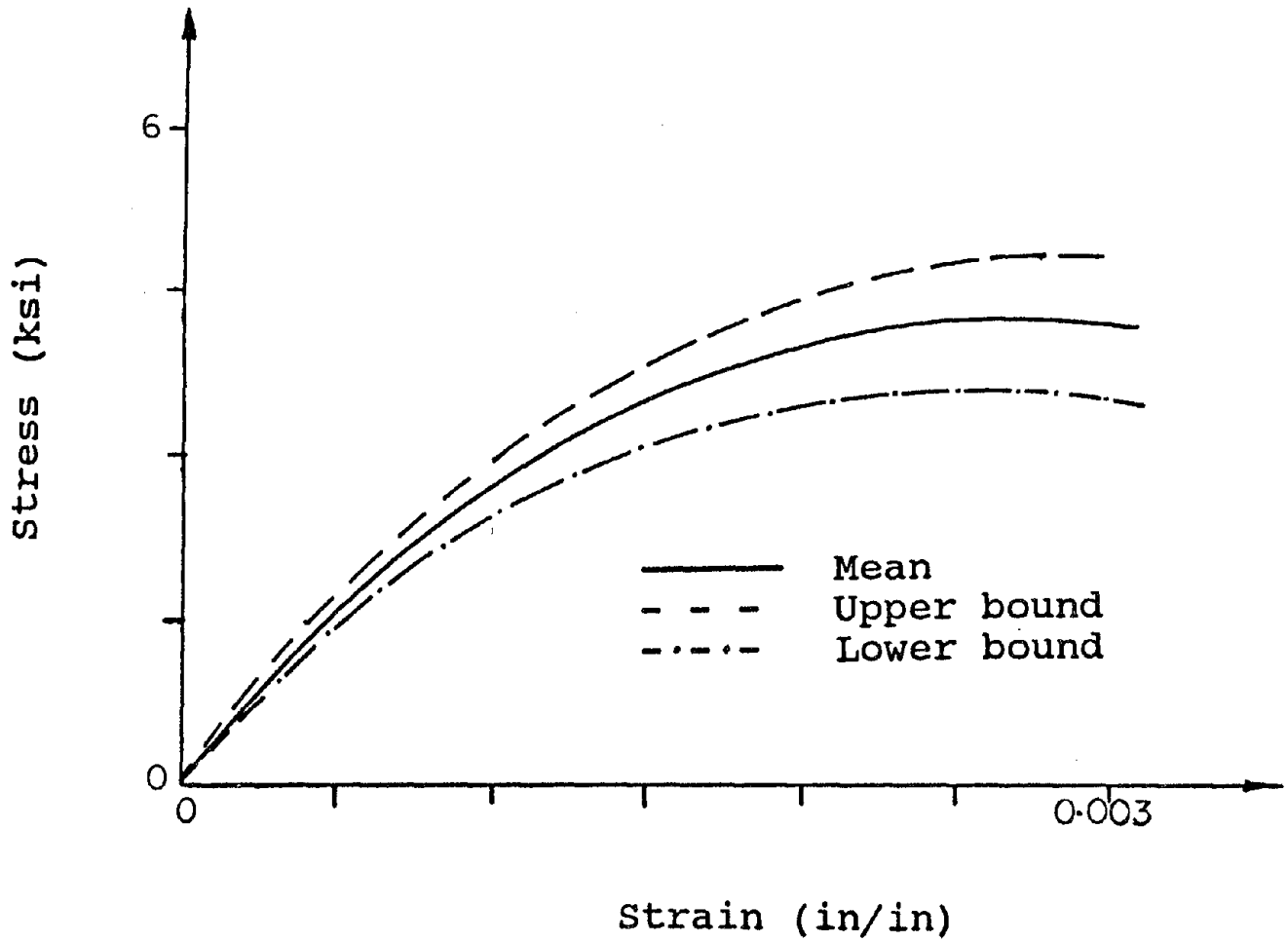

Figure A.1 Concrete Stress-Strain Curve.

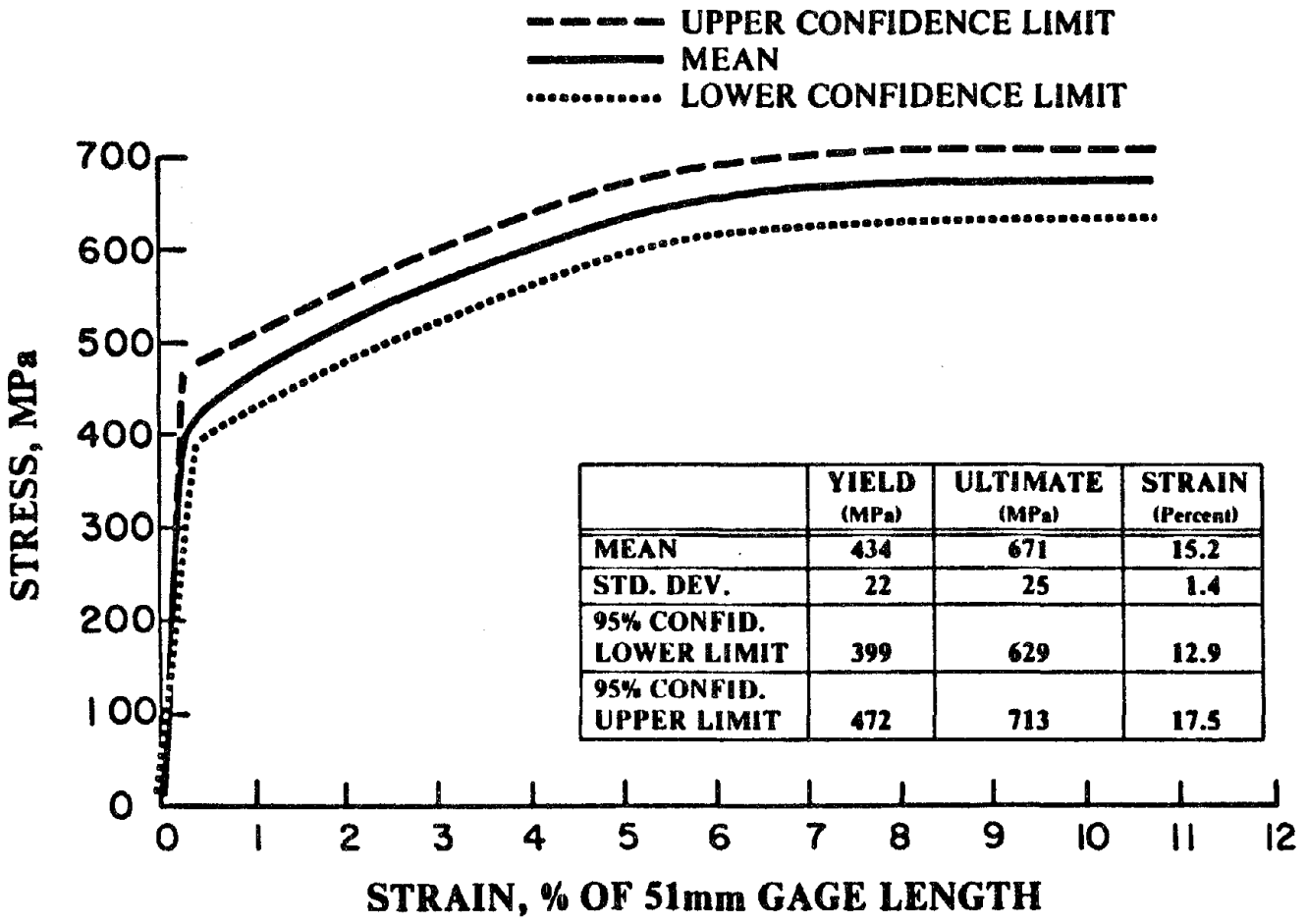

	YIELD (MPa)	ULTIMATE (MPa)	STRAIN (Percent)
MEAN	434	671	15.2
STD. DEV.	22	25	1.4
95% CONFID. LOWER LIMIT	399	629	12.9
95% CONFID. UPPER LIMIT	472	713	17.5

Figure A.2 Stress-Strain Curve (Bar #1) [78].

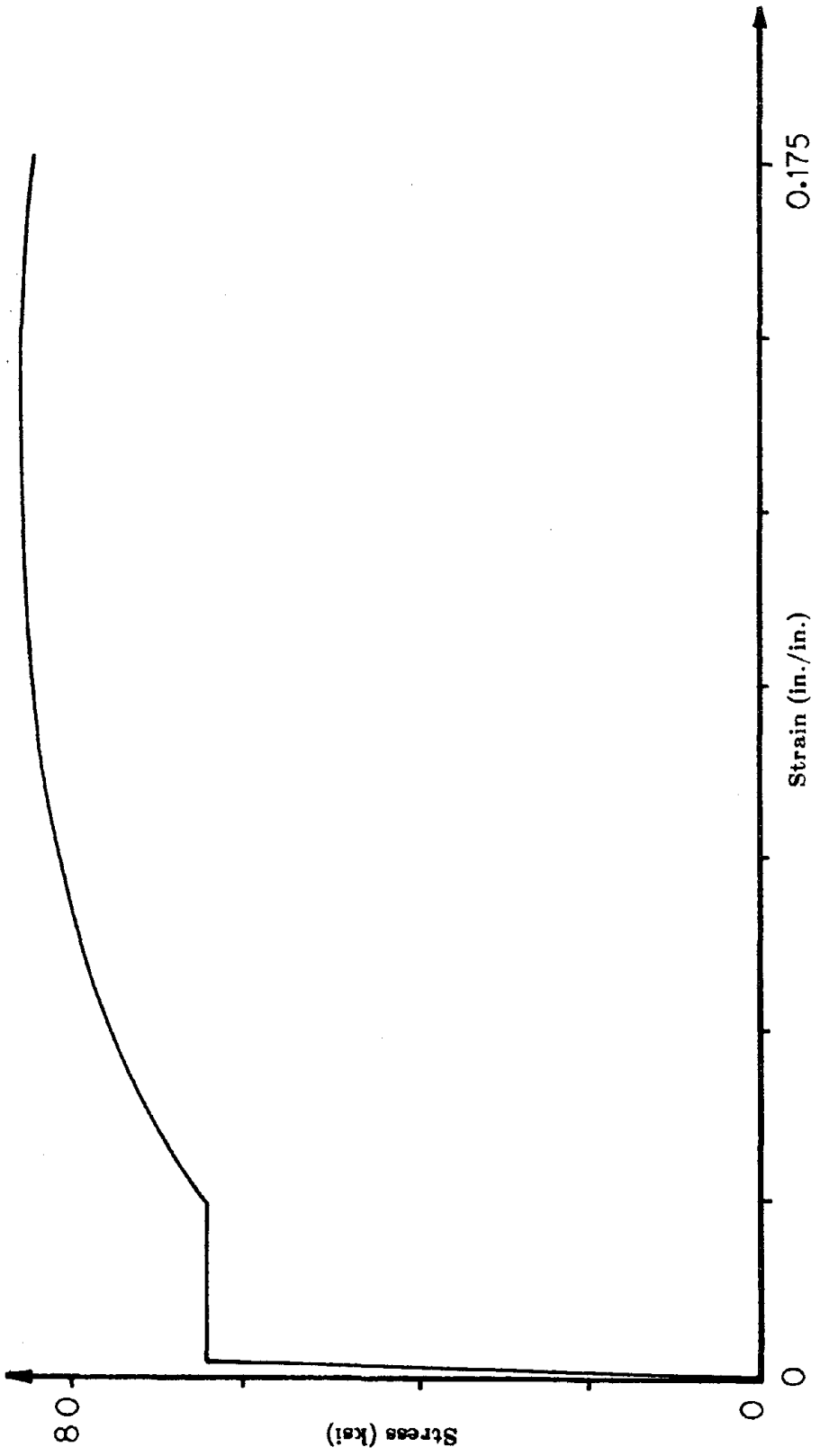

Figure A.3(a) Stress-Strain Curve (Bar #2 Type 1).

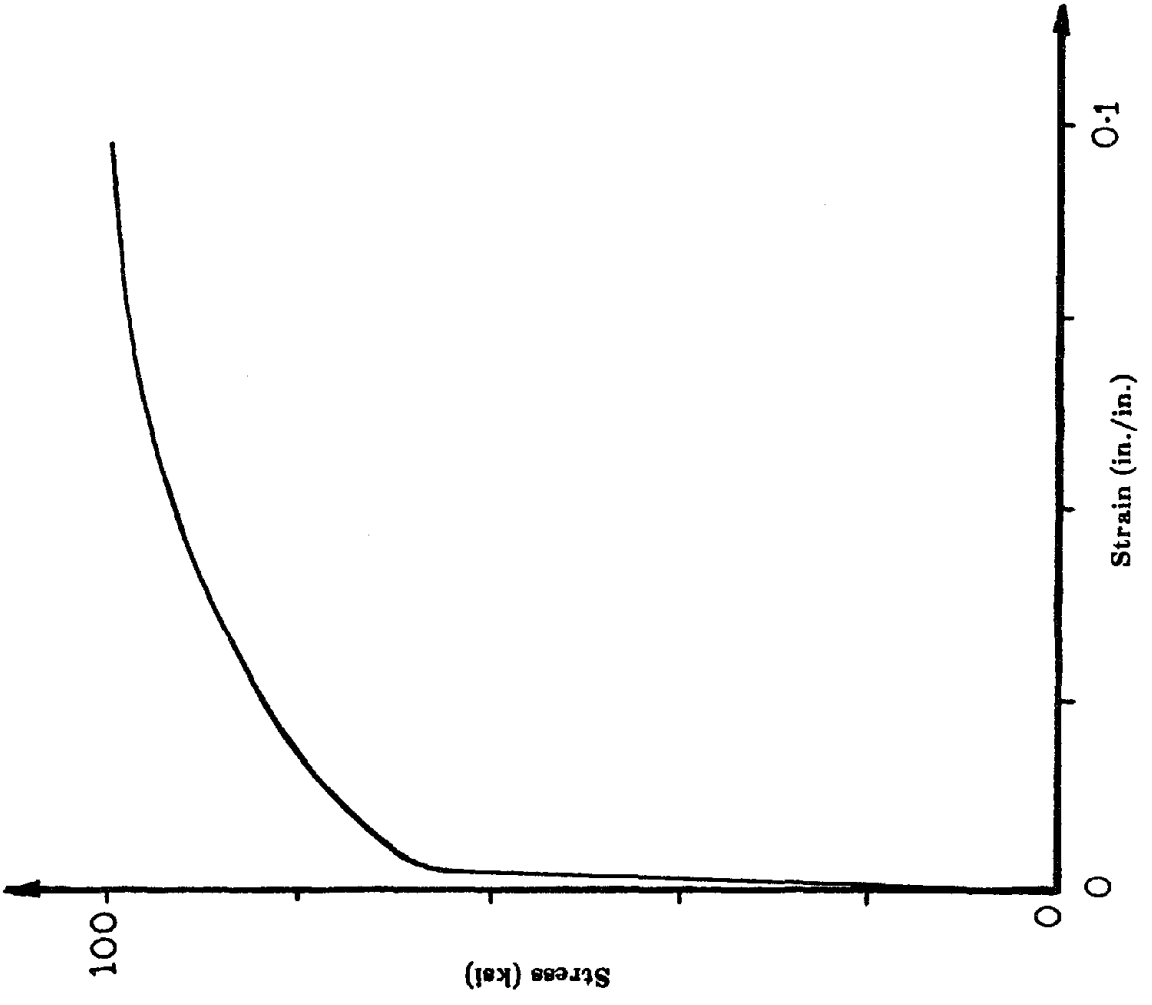

Figure A.3(b) Stress-Strain Curve (Bar #2 Type 2).

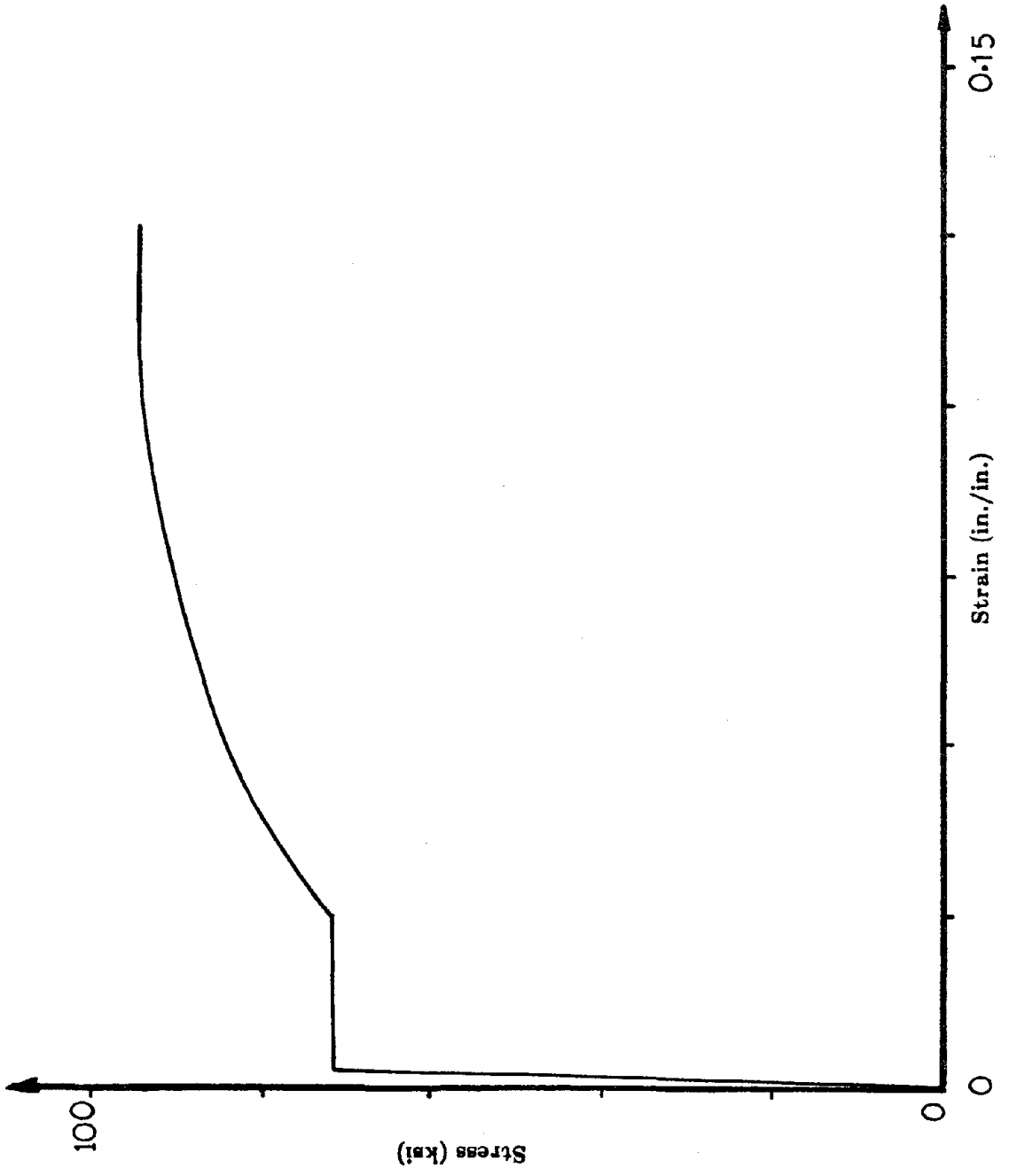

Figure A.3(c) Stress-Strain Curve (Bar #2 Type 3).

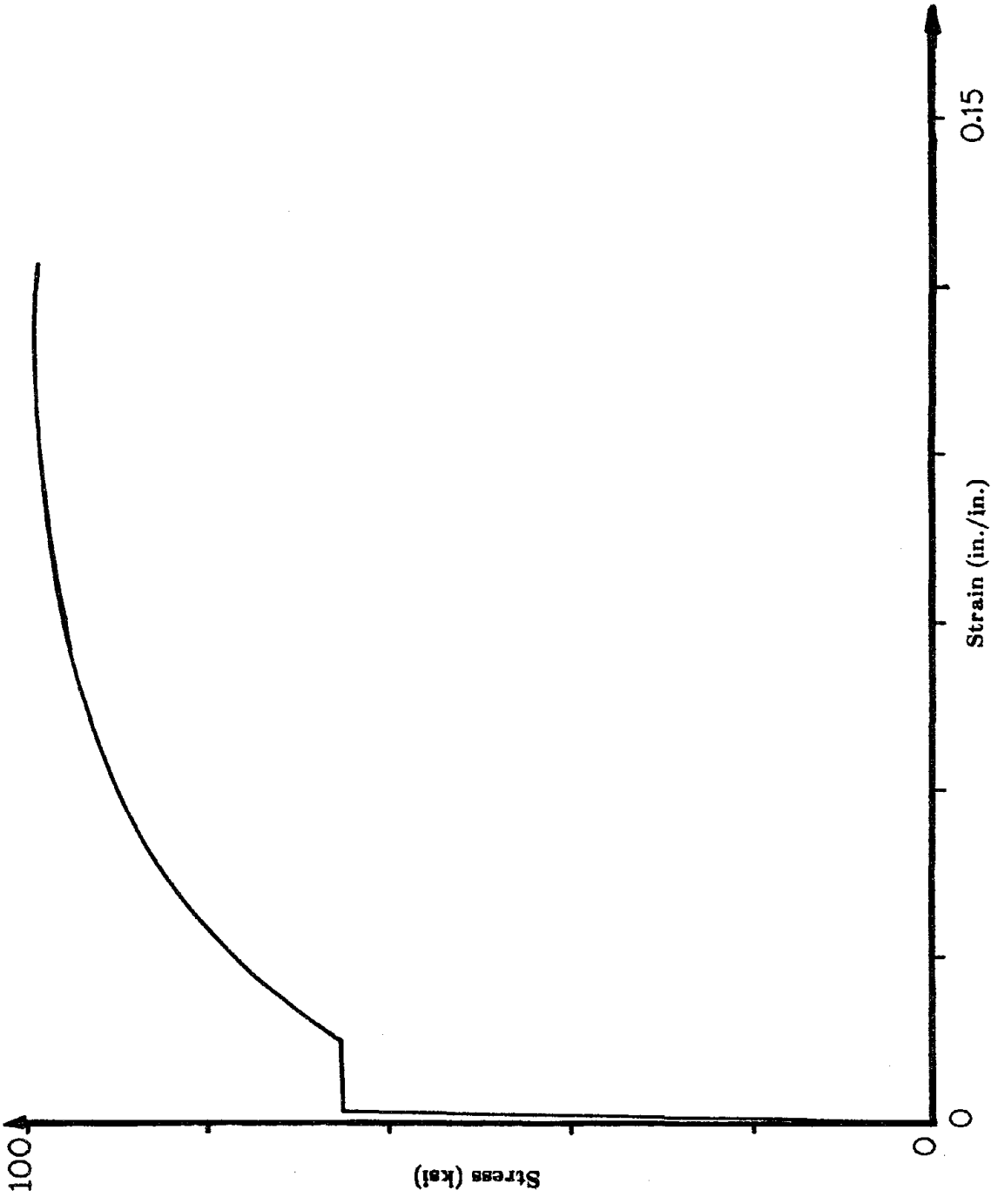

Figure A.3(d) Stress-Strain Curve (Bar #3).

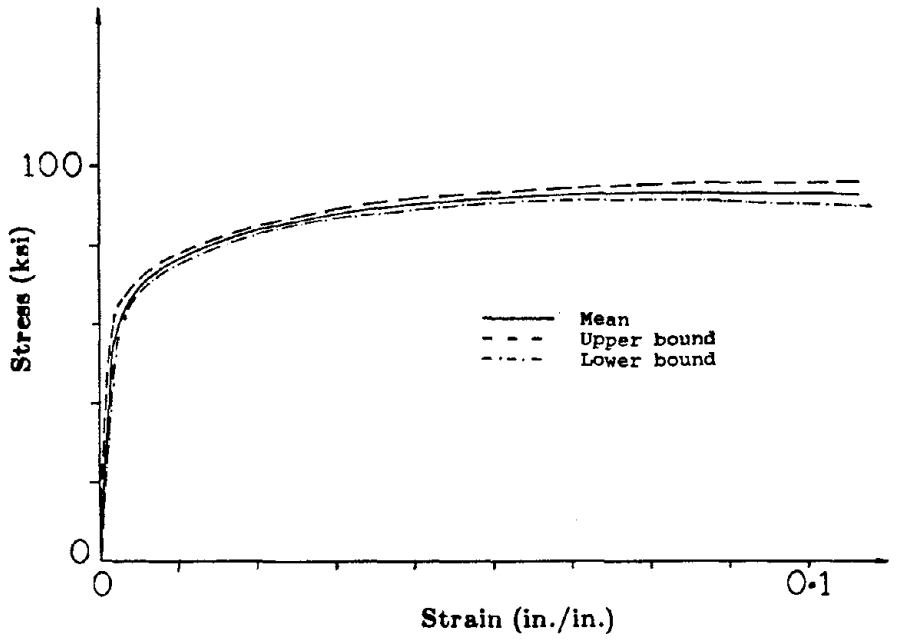

Figure A.4(a) Stress-Strain Curve (Wire Gauge #11).

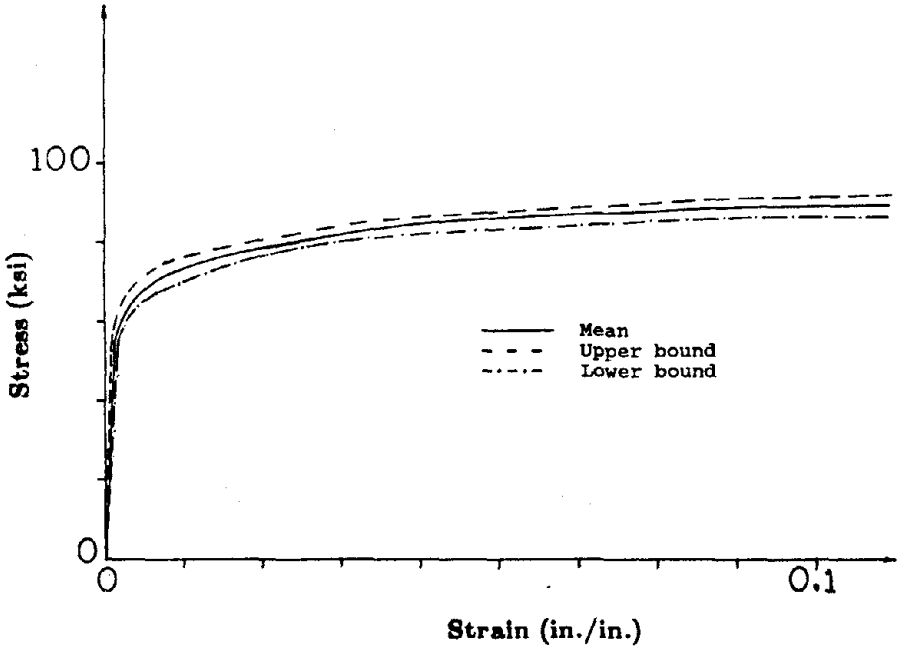

Figure A.4(b) Stress-Strain Curve (Wire Gauge #9).

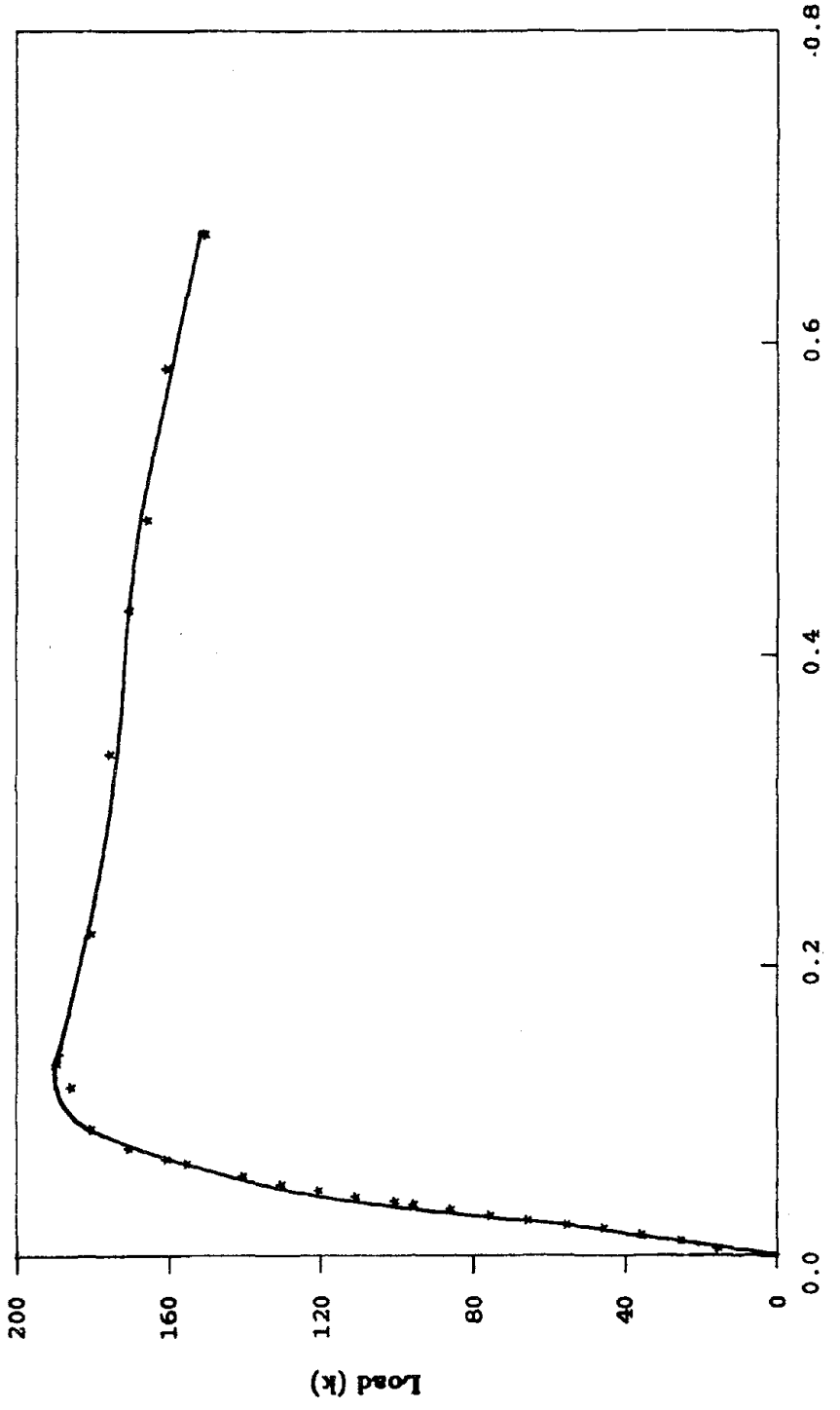

Figure A.5(a) Load-Deflection Curve for Confined Concrete.

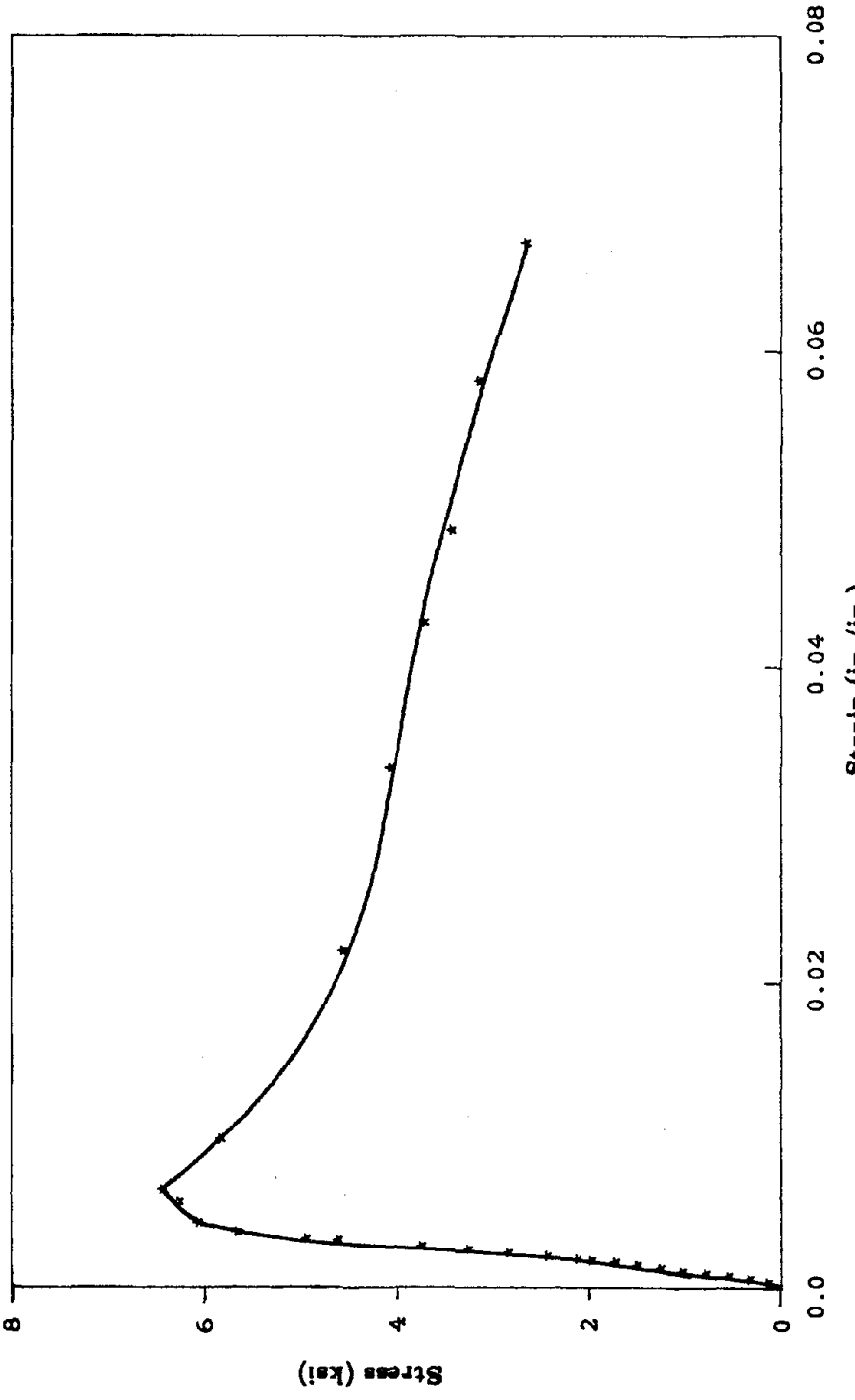

Figure A.5(b) Stress-Strain Curve for Confined Concrete.

APPENDIX B
INSTRUMENTATION

A total of 126 data channels of electronic instrumentation monitored motion of the shaking table, horizontal accelerations and relative displacements of "floors", and strains on selected beam and column reinforcing bars. The data channels were organized as indicated in Table B.1, B.2, B.3, B.4, and B.5.

The data were recorded digitally by a data acquisition system. The data collection is as follows. Any individual transducer output is first passed through a Pacific Signal Conditioner which provides the excitation voltage for the transducer, amplifies the output, and filters the output frequencies above 100 hz. A Preston Multiplier scans the signal conditioner, and reads each channel at a burst of 0.5 hz. The analog signal from the multiplier is passed through a Preston A/D Converter which converts the signal to a digital form, and the digital record is stored on the hard disk of a VAX11-750 computer. The data analysis and graphics package S [8] was utilized to process the measured test data.

DCDTs (Direct Current Displacement Transducers) D1-D7 and POTs (cable actuated potentiometers) P1-P7 (Fig. 3.10a) were fixed on a reference frame (braced against the exterior walls of the laboratory building) and targeted to the test structure at mid-depth of the short-direction beams. These DCDTs and POTs were placed to monitor the lateral displacements of the test structure at different levels. Targets were paper clips that had been bent and epoxied to the test structure surface, and "piano wire" was used to attach the DCDTs to the targets. POTs P8 and P9 (Fig. 3.10a), measuring the roof lateral displacement in the short direction, were screwed on steel plates which had been epoxied to the column stubs at the roof such that the potentiometer cable will be centered at mid-depth of the stub. POTs P8 and P9 were targeted to an interior balcony in the test laboratory at a distance of approximately 15

ft. DCDTs DG1-DG18 (Fig. 3.10b), measuring inter-story drifts in different levels, were attached to steel plates which had been epoxied to the column surface at mid-depth of the long-direction beams, and targeted to the column surface in the upper floors. DCDTs S1-S4 (Fig. 3.11a) were mounted on steel plates, epoxied to the column surface at mid-depth of the long-direction beams, and targeted to the adjacent column. These DCDTs were placed to monitor the floor member growth. DCDTs F1-F4 (Fig. 3.11b), monitoring footing rotation and translation, were mounted on steel angles that had been welded to the steel platform supporting the test structure, and targeted to the footing surface at 2.5 in. from bottom and top of the footing. DCDTs R1 and R2 (Fig. 3.11b), monitoring rocking of the shake table platform, were mounted on a reference frame outside the test site (shaking table), and targeted to a steel column prestressed to the shake table platform (the distance between the two DCDTs is 29.56 in.). The accelerometers were mounted on pieces of steel angle that had been epoxied to the top surface of slab (Fig. 3.9). Weldable stain gauges were attached to beam and column longitudinal bars near beam-column joints (Fig. 3.12) at approximately 1" form the joint face. Bar deformations were removed prior to welding of the gauges, and then the gauges were covered by "M-Coat G".

Hewlett Packard and Trans-tek 0.5", 1", and 3" DCDTs were used. The range of potentiometers used (manufactured by Celesco) was 7" and 15". Setra accelerometers with 4g and 8g range were utilized. Stain gauges were Model SG129-6S (manufactured by Ailtech Instruments) with a one-inch gauge length and a maximum strain capacity equal to 0.02 in./in.

The DCDTs were calibrated using 0.5", 1", and 2" gauge blocks, and the POTs were calibrated by displacing the potentiometer cable a known distance. Accelerometers were calibrated statically by pivoting them toward and away from the floor for negative and positive one-g accelerations. The strain gauges were calibrated by placing a "shunt" resistor across the gauge and measuring change in the gauge resistance. The gauge

factor had been specified by the manufacturer, and the standard procedures [17] were followed to calibrate the gauge.

Table B.1 List of Instrumentation (EC6.2L, EC7.7L, and EC16.6L).

Channel	Label	Description	Units
1	h1disp	Displacement of table actuator	in.
2	h2disp	Displacement of table actuator	in.
3	avghacc	Average horizontal table acceleration	g
4	avgvacc	Average vertical table acceleration	g
5	pitchacc	Table pitch acceleration	rad/s/s
6	rollacc	Table roll acceleration	rad/s/s
7	twistacc	Table twist acceleration	rad/s/s
8	v1disp	Vertical table displacement	in.
9	v2disp	Vertical table displacement	in.
10	v3disp	Vertical table displacement	in.
11	hspan	Command signal (table displacement)	in.
12	hvel	Horizontal table velocity	in./sec.
13	acc1	First-floor acceleration (short direction)	g
14	acc2	First-floor acceleration (long direction)	g
15	acc3	First-floor acceleration (short direction)	g
16	acc4	Second-floor acceleration (short direction)	g
17	acc5	Second-floor acceleration (long direction)	g
18	acc6	Second-floor acceleration (short direction)	g
19	acc7	Third-floor acceleration (short direction)	g
20	acc8	Third-floor acceleration (long direction)	g
21	acc9	Third-floor acceleration (short direction)	g
22	acc10	Fourth-floor acceleration (short direction)	g
23	acc11	Fourth-floor acceleration (long direction)	g
24	acc12	Fourth-floor acceleration (short direction)	g
25	acc13	Fifth-floor acceleration (short direction)	g
26	acc14	Fifth-floor acceleration (long direction)	g
27	acc15	Fifth-floor acceleration (short direction)	g
28	acc16	Sixth-floor acceleration (short direction)	g
29	acc17	Sixth-floor acceleration (long direction)	g
30	acc18	Sixth-floor acceleration (short direction)	g
31	D1	First-floor lateral displacement	in.
32	D2	Second-floor lateral displacement	in.
33	D3	Third-floor lateral displacement	in.
34	D4	Fourth-floor lateral displacement	in.
35	D5	Fifth-floor lateral displacement	in.
36	D6	Sixth-floor lateral displacement	in.
37	D7	Sixth-floor lateral displacement	in.
38	DG1	First-floor diagonal measurement	in.
39	DG2	Second-floor diagonal measurement	in.
40	DG3	Third-floor diagonal measurement	in.
41	DG4	Fourth-floor diagonal measurement	in.
42	DG5	Fifth-floor diagonal measurement	in.
43	DG6	Sixth-floor diagonal measurement	in.
44	DG7	First-floor diagonal measurement	in.
45	DG8	Second-floor diagonal measurement	in.
46	DG9	Third-floor diagonal measurement	in.
47	DG10	Fourth-floor diagonal measurement	in.
48	DG11	Fifth-floor diagonal measurement	in.
49	DG12	Sixth-floor diagonal measurement	in.
50	F4	Footing rocking and slip	in.
51	F3	Footing rocking and slip	in.
52	F2	Footing rocking and slip	in.
53	F1	Footing rocking and slip	in.
54	R2	Shaking table rocking	in.
55	R1	Shaking table rocking	in.
56	P1	First-floor lateral displacement	in.
57	P2	Second-floor lateral displacement	in.
58	P3	Third-floor lateral displacement	in.
59	P4	Fourth-floor lateral displacement	in.
60	P5	Fifth-floor lateral displacement	in.
61	P6	Sixth-floor lateral displacement	in.
62	P7	Sixth-floor lateral displacement	in.
63	P8	Sixth-floor lateral displacement	in.
64	P9	Sixth-floor lateral displacement	in.

Channel	Label	Description	Units
65	sg1	Short-direction beam strain gauge (2nd floor)	milli-strain
66	sg2	short-direction beam strain gauge (2nd floor)	milli-strain
67	sg3	Column strain gague (3rd floor)	milli-strain
68	sg4	Column strain gauge (2nd floor)	milli-strain
69	sg5	Column strain gague (3rd floor)	milli-strain
70	sg6	Long-direction beam strain gague (2nd floor)	milli-strain
71	sg7	Column strain gague (2nd floor)	milli-strain
72	sg8	Column strain gague (foundation)	milli-strain
73	sg9	Column strain gague (foundation)	milli-strain
74	sg10	Column strain gague (2nd floor)	milli-strain
75	sg11	Column strain gague (2nd floor)	milli-strain
76	sg12	Column strain gauge (1st floor)	milli-strain
77	sg13	Column strain gauge (1st floor)	milli-strain
78	sg14	Short-direction beam strain gauge (1st floor)	milli-strain
79	sg15	Short-direction beam strain gauge (1st floor)	milli-strain
80	sg16	Column strain gauge (2nd floor)	milli-strain
81	sg17	Column strain gauge (2nd floor)	milli-strain
82	sg18	Column strain gauge (3rd floor)	milli-strain
83	sg19	Column strain gauge (3rd floor)	milli-strain
84	sg20	Short-direction beam strain gauge (2nd floor)	milli-strain
85	sg21	Short-direction beam strain gauge (2nd floor)	milli-strain
86	sg22	Column strain gauge (3rd floor)	milli-strain
87	sg23	Column strain gauge (4th floor)	milli-strain
88	sg24	Column strain gauge (3rd floor)	milli-strain
89	sg25	Column strain gague (4th floor)	milli-strain
90	sg26	Short-direction beam strain gauge (3rd floor)	milli-strain
91	sg27	Short-direction beam strain gauge (3rd floor)	milli-strain
92	sg28	Column strain gauge (4th floor)	milli-strain
93	sg29	Column strain gauge (4th floor)	milli-strain
94	sg30	Column strain gauge (5th floor)	milli-strain
95	sg31	Column strain gauge (5th floor)	milli-strain
96	sg32	Short-direction beam strain gauge (5th floor)	milli-strain
97	sg33	Short-direction beam strain gauge (5th floor)	milli-strain
98	sg34	Long-direction beam strain gauge (5th floor)	milli-strain
99	sg35	Column strain gauge (5th floor)	milli-strain
100	sg36	Column strain gauge (5th floor)	milli-strain
101	sg37	Column strain gauge (6th floor)	milli-strain
102	sg38	Column strain gauge (6th floor)	milli-strain
103	sg39	Short-direction beam strain gauge (5th floor)	milli-strain
104	sg40	Short-direction beam strain gauge (5th floor)	milli-strain
105	sg41	Long-direction beam strain gauge (5th floor)	milli-strain
106	sg42	Column strain gauge (6th floor)	milli-strain
107	sg43	Column strain gauge (6th floor)	milli-strain
108	sg44	Short-direction beam strain gauge (6th floor)	milli-strain
109	sg45	Short-direction beam strain gauge (6th floor)	milli-strain
110	sg46	Long-direction beam strain gauge (6th floor)	milli-strain
111	sg47	Column strain gauge (spliced bar between 1st & 2nd floors)	milli-strain
112	sg48	Column strain gauge (spliced bar between 1st & 2nd floors)	milli-strain
113	sg49	Column strain gauge (spliced bar between 3rd & 4th floors)	milli-strain
114	sg50	Column strain gauge (spliced bar between 3rd & 4th floors)	milli-strain
115	sg51	Long-direction strain gauge (1st floor)	milli-strain
116	sg52	Long-direction strain gauge (1st floor)	milli-strain
117	sg53	Long-direction strain gauge (2nd floor)	milli-strain
118	sg54	Long-direction strain gauge (2nd floor)	milli-strain
119	sg55	Long-direction strain gauge (3rd floor)	milli-strain
120	sg56	Long-direction strain gauge (3rd floor)	milli-strain
121	-	-	-
122	-	-	-
123	-	-	-
124	-	-	-
125	-	-	-
126	-	-	-

Table B.2 List of Instrumentation (EC49.3L).

Channel	Label	Description	Units
1	h1disp	Displacement of table actuator	in.
2	h2disp	Displacement of table actuator	in.
3	avghacc	Average horizontal table acceleration	g
4	avgvacc	Average vertical table acceleration	g
5	pitchacc	Table pitch acceleration	rad/s/s
6	rollacc	Table roll acceleration	rad/s/s
7	twistacc	Table twist acceleration	rad/s/s
8	v1disp	Vertical table displacement	in.
9	v2disp	Vertical table displacement	in.
10	v3disp	Vertical table displacement	in.
11	hspan	Command signal (table displacement)	in.
12	hvel	Horizontal table velocity	in./sec.
13	acc1	First-floor acceleration (short direction)	g
14	acc2	First-floor acceleration (long direction)	g
15	acc3	First-floor acceleration (short direction)	g
16	acc4	Second-floor acceleration (short direction)	g
17	acc5	Second-floor acceleration (long direction)	g
18	acc6	Second-floor acceleration (short direction)	g
19	acc7	Third-floor acceleration (short direction)	g
20	acc8	Third-floor acceleration (long direction)	g
21	acc9	Third-floor acceleration (short direction)	g
22	acc10	Fourth-floor acceleration (short direction)	g
23	acc11	Fourth-floor acceleration (long direction)	g
24	acc12	Fourth-floor acceleration (short direction)	g
25	acc13	Fifth-floor acceleration (short direction)	g
26	acc14	Fifth-floor acceleration (long direction)	g
27	acc15	Fifth-floor acceleration (short direction)	g
28	acc16	Sixth-floor acceleration (short direction)	g
29	acc17	Sixth-floor acceleration (long direction)	g
30	acc18	Sixth-floor acceleration (short direction)	g
31	S1	First-floor slab growth	in.
32	S2	Second-floor slab growth	in.
33	D3	Third-floor lateral displacement	in.
34	D4	Fourth-floor lateral displacement	in.
35	D5	Fifth-floor lateral displacement	in.
36	-	-	-
37	D6	Sixth-floor lateral displacement	in.
38	DG1	First-floor diagonal measurement	in.
39	DG2	Second-floor diagonal measurement	in.
40	DG3	Third-floor diagonal measurement	in.
41	DG4	Fourth-floor diagonal measurement	in.
42	DG5	Fifth-floor diagonal measurement	in.
43	DG6	Sixth-floor diagonal measurement	in.
44	DG7	First-floor diagonal measurement	in.
45	DG8	Second-floor diagonal measurement	in.
46	DG9	Third-floor diagonal measurement	in.
47	DG10	Fourth-floor diagonal measurement	in.
48	DG11	Fifth-floor diagonal measurement	in.
49	DG12	Sixth-floor diagonal measurement	in.
50	F4	Footing rocking and slip	in.
51	F3	Footing rocking and slip	in.
52	F2	Footing rocking and slip	in.
53	F1	Footing rocking and slip	in.
54	S3	Third-floor slab growth	in.
55	S4	Fourth-floor slab growth	in.
56	P1	First-floor lateral displacement	in.
57	P2	Second-floor lateral displacement	in.
58	P3	Third-floor lateral displacement	in.
59	P4	Fourth-floor lateral displacement	in.
60	P5	Fifth-floor lateral displacement	in.
61	P6	Sixth-floor lateral displacement	in.
62	P7	Sixth-floor lateral displacement	in.
63	P8	Sixth-floor lateral displacement	in.
64	P9	Sixth-floor lateral displacement	in.

Channel	Label	Description	Units
65	sg1	Short-direction beam strain gauge (2nd floor)	milli-strain
66	sg2	short-direction beam strain gauge (2nd floor)	milli-strain
67	sg3	Column strain gague (3rd floor)	milli-strain
68	sg4	Column strain gauge (2nd floor)	milli-strain
69	sg5	Column strain gague (3rd floor)	milli-strain
70	sg6	Long-direction beam strain gague (2nd floor)	milli-strain
71	sg7	Column strain gague (2nd floor)	milli-strain
72	sg8	Column strain gague (foundation)	milli-strain
73	sg9	Column strain gague (foundation)	milli-strain
74	sg10	Column strain gague (2nd floor)	milli-strain
75	sg11	Column strain gague (2nd floor)	milli-strain
76	sg12	Column strain gauge (1st floor)	milli-strain
77	sg13	Column strain gauge (1st floor)	milli-strain
78	sg14	Short-direction beam strain gauge (1st floor)	milli-strain
79	sg15	Short-direction beam strain gauge (1st floor)	milli-strain
80	sg16	Column strain gauge (2nd floor)	milli-strain
81	sg17	Column strain gauge (2nd floor)	milli-strain
82	sg18	Column strain gauge (3rd floor)	milli-strain
83	sg19	Column strain gauge (3rd floor)	milli-strain
84	sg20	Short-direction beam strain gauge (2nd floor)	milli-strain
85	sg21	Short-direction beam strain gauge (2nd floor)	milli-strain
86	sg22	Column strain gauge (3rd floor)	milli-strain
87	sg23	Column strain gauge (4th floor)	milli-strain
88	sg24	Column strain gauge (3rd floor)	milli-strain
89	sg25	Column strain gague (4th floor)	milli-strain
90	sg26	Short-direction beam strain gauge (3rd floor)	milli-strain
91	sg27	Short-direction beam strain gauge (3rd floor)	milli-strain
92	sg28	Column strain gauge (4th floor)	milli-strain
93	sg29	Column strain gauge (4th floor)	milli-strain
94	sg30	Column strain gauge (5th floor)	milli-strain
95	sg31	Column strain gauge (5th floor)	milli-strain
96	sg32	Short-direction beam strain gauge (5th floor)	milli-strain
97	sg33	Short-direction beam strain gauge (5th floor)	milli-strain
98	sg34	Long-direction beam strain gauge (5th floor)	milli-strain
99	sg35	Column strain gauge (5th floor)	milli-strain
100	sg36	Column strain gauge (5th floor)	milli-strain
101	sg37	Column strain gauge (6th floor)	milli-strain
102	sg38	Column strain gauge (6th floor)	milli-strain
103	sg39	Short-direction beam strain gauge (5th floor)	milli-strain
104	sg40	Short-direction beam strain gauge (5th floor)	milli-strain
105	sg41	Long-direction beam strain gauge (5th floor)	milli-strain
106	sg42	Column strain gauge (6th floor)	milli-strain
107	sg43	Column strain gauge (6th floor)	milli-strain
108	sg44	Short-direction beam strain gauge (6th floor)	milli-strain
109	sg45	Short-direction beam strain gauge (6th floor)	milli-strain
110	sg46	Long-direction beam strain gauge (6th floor)	milli-strain
111	sg47	Column strain gauge (spliced bar between 1st & 2nd floors)	milli-strain
112	sg48	Column strain gauge (spliced bar between 1st & 2nd floors)	milli-strain
113	sg49	Column strain gauge (spliced bar between 3rd & 4th floors)	milli-strain
114	sg50	Column strain gauge (spliced bar between 3rd & 4th floors)	milli-strain
115	sg51	Long-direction strain gauge (1st floor)	milli-strain
116	sg52	Long-direction strain gauge (1st floor)	milli-strain
117	sg53	Long-direction strain gauge (2nd floor)	milli-strain
118	sg54	Long-direction strain gauge (2nd floor)	milli-strain
119	sg55	Long-direction strain gauge (3rd floor)	milli-strain
120	sg56	Long-direction strain gauge (3rd floor)	milli-strain
121	-	-	-
122	-	-	-
123	-	-	-
124	-	-	-
125	-	-	-
126	-	-	-

Table B.3 List of Instrumentation (EC8.1B and EC47.7B).

Channel	Label	Description	Units
1	h1disp	Displacement of table actuator	in.
2	h2disp	Displacement of table actuator	in.
3	avghacc	Average horizontal table acceleration	g
4	avgvacc	Average vertical table acceleration	g
5	pitchacc	Table pitch acceleration	rad/s/s
6	rollacc	Table roll acceleration	rad/s/s
7	twistacc	Table twist acceleration	rad/s/s
8	v1disp	Vertical table displacement	in.
9	v2disp	Vertical table displacement	in.
10	v3disp	Vertical table displacement	in.
11	hspan	Command signal (table displacement)	in.
12	hvel	Horizontal table velocity	in./sec.
13	acc1	First-floor acceleration (short direction)	g
14	acc2	First-floor acceleration (long direction)	g
15	acc3	First-floor acceleration (short direction)	g
16	acc4	Second-floor acceleration (short direction)	g
17	acc5	Second-floor acceleration (long direction)	g
18	acc6	Second-floor acceleration (short direction)	g
19	acc7	Third-floor acceleration (short direction)	g
20	acc8	Third-floor acceleration (long direction)	g
21	acc9	Third-floor acceleration (short direction)	g
22	acc10	Fourth-floor acceleration (short direction)	g
23	acc11	Fourth-floor acceleration (long direction)	g
24	acc12	Fourth-floor acceleration (short direction)	g
25	acc13	Fifth-floor acceleration (short direction)	g
26	acc14	Fifth-floor acceleration (long direction)	g
27	acc15	Fifth-floor acceleration (short direction)	g
28	acc16	Sixth-floor acceleration (short direction)	g
29	acc17	Sixth-floor acceleration (long direction)	g
30	acc18	Sixth-floor acceleration (short direction)	g
31	S1	First-floor slab growth	in.
32	S2	Second-floor slab growth	in.
33	D3	Third-floor lateral displacement	in.
34	D4	Fourth-floor lateral displacement	in.
35	D5	Fifth-floor lateral displacement	in.
36	D6	Sixth-floor lateral displacement	in.
37	D7	Sixth-floor lateral displacement	in.
38	DG1	First-floor diagonal measurement	in.
39	DG2	Second-floor diagonal measurement	in.
40	DG3	Third-floor diagonal measurement	in.
41	DG4	Fourth-floor diagonal measurement	in.
42	DG5	Fifth-floor diagonal measurement	in.
43	DG6	Sixth-floor diagonal measurement	in.
44	DG7	First-floor diagonal measurement	in.
45	DG8	Second-floor diagonal measurement	in.
46	DG9	Third-floor diagonal measurement	in.
47	DG10	Fourth-floor diagonal measurement	in.
48	DG11	Fifth-floor diagonal measurement	in.
49	DG12	Sixth-floor diagonal measurement	in.
50	F4	Footing rocking and slip	in.
51	F3	Footing rocking and slip	in.
52	F2	Footing rocking and slip	in.
53	F1	Footing rocking and slip	in.
54	S3	Third-floor slab growth	in.
55	S4	Fourth-floor slab growth	in.
56	P1	First-floor lateral displacement	in.
57	P2	Second-floor lateral displacement	in.
58	P3	Third-floor lateral displacement	in.
59	P4	Fourth-floor lateral displacement	in.
60	P5	Fifth-floor lateral displacement	in.
61	P6	Sixth-floor lateral displacement	in.
62	P7	Sixth-floor lateral displacement	in.
63	P8	Sixth-floor lateral displacement	in.
64	P9	Sixth-floor lateral displacement	in.

Channel	Label	Description	Units
65	sg1	Short-direction beam strain gauge (2nd floor)	milli-strain
66	sg2	short-direction beam strain gauge (2nd floor)	milli-strain
67	sg3	Column strain gague (3rd floor)	milli-strain
68	sg4	Column strain gague (2nd floor)	milli-strain
69	sg5	Column strain gague (3rd floor)	milli-strain
70	sg6	Long-direction beam strain gague (2nd floor)	milli-strain
71	sg7	Column strain gague (2nd floor)	milli-strain
72	sg8	Column strain gague (foundation)	milli-strain
73	sg9	Column strain gague (foundation)	milli-strain
74	sg10	Column strain gague (2nd floor)	milli-strain
75	sg11	Column strain gague (2nd floor)	milli-strain
76	sg12	Column strain gauge (1st floor)	milli-strain
77	sg13	Column strain gauge (1st floor)	milli-strain
78	sg14	Short-direction beam strain gauge (1st floor)	milli-strain
79	sg15	Short-direction beam strain gauge (1st floor)	milli-strain
80	sg16	Column strain gauge (2nd floor)	milli-strain
81	sg17	Column strain gauge (2nd floor)	milli-strain
82	sg18	Column strain gauge (3rd floor)	milli-strain
83	sg19	Column strain gauge (3rd floor)	milli-strain
84	sg20	Short-direction beam strain gauge (2nd floor)	milli-strain
85	sg21	Short-direction beam strain gauge (2nd floor)	milli-strain
86	sg22	Column strain gauge (3rd floor)	milli-strain
87	sg23	Column strain gauge (4th floor)	milli-strain
88	sg24	Column strain gauge (3rd floor)	milli-strain
89	sg25	Column strain gague (4th floor)	milli-strain
90	sg26	Short-direction beam strain gauge (3rd floor)	milli-strain
91	sg27	Short-direction beam strain gauge (3rd floor)	milli-strain
92	sg28	Column strain gauge (4th floor)	milli-strain
93	sg29	Column strain gauge (4th floor)	milli-strain
94	sg30	Column strain gauge (5th floor)	milli-strain
95	sg31	Column strain gauge (5th floor)	milli-strain
96	sg32	Short-direction beam strain gauge (5th floor)	milli-strain
97	sg33	Short-direction beam strain gauge (5th floor)	milli-strain
98	sg34	Long-direction beam strain gauge (5th floor)	milli-strain
99	sg35	Column strain gauge (5th floor)	milli-strain
100	sg36	Column strain gauge (5th floor)	milli-strain
101	sg37	Column strain gauge (6th floor)	milli-strain
102	sg38	Column strain gauge (6th floor)	milli-strain
103	sg39	Short-direction beam strain gauge (5th floor)	milli-strain
104	sg40	Short-direction beam strain gauge (5th floor)	milli-strain
105	sg41	Long-direction beam strain gauge (5th floor)	milli-strain
106	sg42	Column strain gauge (6th floor)	milli-strain
107	sg43	Column strain gauge (6th floor)	milli-strain
108	sg44	Short-direction beam strain gauge (6th floor)	milli-strain
109	sg45	Short-direction beam strain gauge (6th floor)	milli-strain
110	sg46	Long-direction beam strain gauge (6th floor)	milli-strain
111	sg47	Column strain gauge (spliced bar between 1st & 2nd floors)	milli-strain
112	sg48	Column strain gauge (spliced bar between 1st & 2nd floors)	milli-strain
113	sg49	Column strain gauge (spliced bar between 3rd & 4th floors)	milli-strain
114	sg50	Column strain gauge (spliced bar between 3rd & 4th floors)	milli-strain
115	sg51	Long-direction strain gauge (1st floor)	milli-strain
116	sg52	Long-direction strain gauge (1st floor)	milli-strain
117	sg53	Long-direction strain gauge (2nd floor)	milli-strain
118	sg54	Long-direction strain gauge (2nd floor)	milli-strain
119	sg55	Long-direction strain gauge (3rd floor)	milli-strain
120	sg56	Long-direction strain gauge (3rd floor)	milli-strain
121	DG13	First-floor diagonal measurement	in.
122	DG14	Second-floor diagonal measurement	in.
123	DG15	Third-floor diagonal measurement	in.
124	DG16	Fourth-floor diagonal measurement	in.
125	DG17	Fifth-floor diagonal measurement	in.
126	DG18	Sixth-floor diagonal measurement	in.

Table B.4 List of Instrumentation (MO63.4B).

Channel	Label	Description	Units
1	h1disp	Displacement of table actuator	in.
2	h2disp	Displacement of table actuator	in.
3	avghacc	Average horizontal table acceleration	g
4	avgvacc	Average vertical table acceleration	g
5	pitchacc	Table pitch acceleration	rad/s/s
6	rollacc	Table roll acceleration	rad/s/s
7	twistacc	Table twist acceleration	rad/s/s
8	v1disp	Vertical table displacement	in.
9	v2disp	Vertical table displacement	in.
10	v3disp	Vertical table displacement	in.
11	hspan	Command signal (table displacement)	in.
12	transacc	Transverse table acceleration	g
13	acc1	First-floor acceleration (short direction)	g
14	acc2	First-floor acceleration (long direction)	g
15	acc3	First-floor acceleration (short direction)	g
16	acc4	Second-floor acceleration (short direction)	g
17	acc5	Second-floor acceleration (long direction)	g
18	acc6	Second-floor acceleration (short direction)	g
19	acc7	Third-floor acceleration (short direction)	g
20	acc8	Third-floor acceleration (long direction)	g
21	acc9	Third-floor acceleration (short direction)	g
22	acc10	Fourth-floor acceleration (short direction)	g
23	acc11	Fourth-floor acceleration (long direction)	g
24	acc12	Fourth-floor acceleration (short direction)	g
25	acc13	Fifth-floor acceleration (short direction)	g
26	acc14	Fifth-floor acceleration (long direction)	g
27	acc15	Fifth-floor acceleration (short direction)	g
28	acc16	Sixth-floor acceleration (short direction)	g
29	acc17	Sixth-floor acceleration (long direction)	g
30	acc18	Sixth-floor acceleration (short direction)	g
31	S1	First-floor slab growth	in.
32	S2	Second-floor slab growth	in.
33	D3	Third-floor lateral displacement	in.
34	D4	Fourth-floor lateral displacement	in.
35	D5	Fifth-floor lateral displacement	in.
36	D6	Sixth-floor lateral displacement	in.
37	D7	Sixth-floor lateral displacement	in.
38	DG1	First-floor diagonal measurement	in.
39	DG2	Second-floor diagonal measurement	in.
40	DG3	Third-floor diagonal measurement	in.
41	DG4	Fourth-floor diagonal measurement	in.
42	DG5	Fifth-floor diagonal measurement	in.
43	DG6	Sixth-floor diagonal measurement	in.
44	DG7	First-floor diagonal measurement	in.
45	DG8	Second-floor diagonal measurement	in.
46	DG9	Third-floor diagonal measurement	in.
47	DG10	Fourth-floor diagonal measurement	in.
48	DG11	Fifth-floor diagonal measurement	in.
49	DG12	Sixth-floor diagonal measurement	in.
50	F4	Footing rocking and slip	in.
51	F3	Footing rocking and slip	in.
52	F2	Footing rocking and slip	in.
53	F1	Footing rocking and slip	in.
54	S3	Third-floor slab growth	in.
55	S4	Fourth-floor slab growth	in.
56	P1	First-floor lateral displacement	in.
57	P2	Second-floor lateral displacement	in.
58	P3	Third-floor lateral displacement	in.
59	P4	Fourth-floor lateral displacement	in.
60	P5	Fifth-floor lateral displacement	in.
61	P6	Sixth-floor lateral displacement	in.
62	P7	Sixth-floor lateral displacement	in.
63	P8	Sixth-floor lateral displacement	in.
64	P9	Sixth-floor lateral displacement	in.

Channel	Label	Description	Units
65	sg1	Short-direction beam strain gauge (2nd floor)	milli-strain
66	sg2	short-direction beam strain gauge (2nd floor)	milli-strain
67	sg3	Column strain gague (3rd floor)	milli-strain
68	sg4	Column strain gague (2nd floor)	milli-strain
69	sg5	Column strain gague (3rd floor)	milli-strain
70	sg6	Long-direction beam strain gague (2nd floor)	milli-strain
71	sg7	Column strain gague (2nd floor)	milli-strain
72	sg8	Column strain gague (foundation)	milli-strain
73	sg9	Column strain gague (foundation)	milli-strain
74	sg10	Column strain gague (2nd floor)	milli-strain
75	sg11	Column strain gague (2nd floor)	milli-strain
76	sg12	Column strain gauge (1st floor)	milli-strain
77	sg13	Column strain gauge (1st floor)	milli-strain
78	sg14	Short-direction beam strain gauge (1st floor)	milli-strain
79	sg15	Short-direction beam strain gauge (1st floor)	milli-strain
80	sg16	Column strain gauge (2nd floor)	milli-strain
81	sg17	Column strain gauge (2nd floor)	milli-strain
82	sg18	Column strain gauge (3rd floor)	milli-strain
83	sg19	Column strain gauge (3rd floor)	milli-strain
84	sg20	Short-direction beam strain gauge (2nd floor)	milli-strain
85	sg21	Short-direction beam strain gauge (2nd floor)	milli-strain
86	sg22	Column strain gauge (3rd floor)	milli-strain
87	sg23	Column strain gauge (4th floor)	milli-strain
88	sg24	Column strain gauge (3rd floor)	milli-strain
89	sg25	Column strain gague (4th floor)	milli-strain
90	sg26	Short-direction beam strain gauge (3rd floor)	milli-strain
91	sg27	Short-direction beam strain gauge (3rd floor)	milli-strain
92	sg28	Column strain gauge (4th floor)	milli-strain
93	sg29	Column strain gauge (4th floor)	milli-strain
94	sg30	Column strain gauge (5th floor)	milli-strain
95	sg31	Column strain gauge (5th floor)	milli-strain
96	sg32	Short-direction beam strain gauge (5th floor)	milli-strain
97	sg33	Short-direction beam strain gauge (5th floor)	milli-strain
98	sg34	Long-direction beam strain gauge (5th floor)	milli-strain
99	sg35	Column strain gauge (5th floor)	milli-strain
100	sg36	Column strain gauge (5th floor)	milli-strain
101	sg37	Column strain gauge (6th floor)	milli-strain
102	sg38	Column strain gauge (6th floor)	milli-strain
103	sg39	Short-direction beam strain gauge (5th floor)	milli-strain
104	sg40	Short-direction beam strain gauge (5th floor)	milli-strain
105	sg41	Long-direction beam strain gauge (5th floor)	milli-strain
106	sg42	Column strain gauge (6th floor)	milli-strain
107	sg43	Column strain gauge (6th floor)	milli-strain
108	sg44	Short-direction beam strain gauge (6th floor)	milli-strain
109	sg45	Short-direction beam strain gauge (6th floor)	milli-strain
110	sg46	Long-direction beam strain gauge (6th floor)	milli-strain
111	sg47	Column strain gauge (spliced bar between 1st & 2nd floors)	milli-strain
112	sg48	Column strain gauge (spliced bar between 1st & 2nd floors)	milli-strain
113	sg49	Column strain gauge (spliced bar between 3rd & 4th floors)	milli-strain
114	sg50	Column strain gauge (spliced bar between 3rd & 4th floors)	milli-strain
115	sg51	Long-direction strain gauge (1st floor)	milli-strain
116	sg52	Long-direction strain gauge (1st floor)	milli-strain
117	sg53	Long-direction strain gauge (2nd floor)	milli-strain
118	sg54	Long-direction strain gauge (2nd floor)	milli-strain
119	sg55	Long-direction strain gauge (3rd floor)	milli-strain
120	sg56	Long-direction strain gauge (3rd floor)	milli-strain
121	DG13	First-floor diagonal measurement	in.
122	DG14	Second-floor diagonal measurement	in.
123	DG15	Third-floor diagonal measurement	in.
124	DG16	Fourth-floor diagonal measurement	in.
125	DG17	Fifth-floor diagonal measurement	in.
126	DG18	Sixth-floor diagonal measurement	in.

Table B.5 List of Instrumentation (MX10.3B, MX19.7B, and MX34.6B).

Channel	Label	Description	Units
1	h1disp	Displacement of table actuator	in.
2	h2disp	Displacement of table actuator	in.
3	avghacc	Average horizontal table acceleration	g
4	avgvacc	Average vertical table acceleration	g
5	pitchacc	Table pitch acceleration	rad/s/s
6	rollacc	Table roll acceleration	rad/s/s
7	twistacc	Table twist acceleration	rad/s/s
8	v1disp	Vertical table displacement	in.
9	v2disp	Vertical table displacement	in.
10	v3disp	Vertical table displacement	in.
11	hspan	Command signal (table displacement)	in.
12	tranacc	Transverse table acceleration	g
13	acc1	First-floor acceleration (short direction)	g
14	acc2	First-floor acceleration (long direction)	g
15	acc3	First-floor acceleration (short direction)	g
16	acc4	Second-floor acceleration (short direction)	g
17	acc5	Second-floor acceleration (long direction)	g
18	acc6	Second-floor acceleration (short direction)	g
19	acc7	Third-floor acceleration (short direction)	g
20	acc8	Third-floor acceleration (long direction)	g
21	acc9	Third-floor acceleration (short direction)	g
22	acc10	Fourth-floor acceleration (short direction)	g
23	acc11	Fourth-floor acceleration (long direction)	g
24	acc12	Fourth-floor acceleration (short direction)	g
25	acc13	Fifth-floor acceleration (short direction)	g
26	acc14	Fifth-floor acceleration (long direction)	g
27	acc15	Fifth-floor acceleration (short direction)	g
28	acc16	Sixth-floor acceleration (short direction)	g
29	acc17	Sixth-floor acceleration (long direction)	g
30	acc18	Sixth-floor acceleration (short direction)	g
31	-	-	-
32	-	-	-
33	-	-	-
34	-	-	-
35	-	-	-
36	-	-	-
37	-	-	-
38	DG1	First-floor diagonal measurement	in.
39	DG2	Second-floor diagonal measurement	in.
40	DG3	Third-floor diagonal measurement	in.
41	DG4	Fourth-floor diagonal measurement	in.
42	DG5	Fifth-floor diagonal measurement	in.
43	DG6	Sixth-floor diagonal measurement	in.
44	DG7	First-floor diagonal measurement	in.
45	DG8	Second-floor diagonal measurement	in.
46	DG9	Third-floor diagonal measurement	in.
47	DG10	Fourth-floor diagonal measurement	in.
48	DG11	Fifth-floor diagonal measurement	in.
49	DG12	Sixth-floor diagonal measurement	in.
50	-	-	-
51	-	-	-
52	-	-	-
53	-	-	-
54	-	-	-
55	-	-	-
56	P1	First-floor lateral displacement	in.
57	P2	Second-floor lateral displacement	in.
58	P3	Third-floor lateral displacement	in.
59	P4	Fourth-floor lateral displacement	in.
60	P5	Fifth-floor lateral displacement	in.
61	P6	Sixth-floor lateral displacement	in.
62	P7	Sixth-floor lateral displacement	in.
63	P8	Sixth-floor lateral displacement	in.
64	P9	Sixth-floor lateral displacement	in.

Channel	Label	Description	Units
65	sg1	Short-direction beam strain gauge (2nd floor)	milli-strain
66	sg2	short-direction beam strain gauge (2nd floor)	milli-strain
67	sg3	Column strain gague (3rd floor)	milli-strain
68	sg4	Column strain gauge (2nd floor)	milli-strain
69	sg5	Column strain gague (3rd floor)	milli-strain
70	sg6	Long-direction beam strain gague (2nd floor)	milli-strain
71	sg7	Column strain gague (2nd floor)	milli-strain
72	sg8	Column strain gague (foundation)	milli-strain
73	sg9	Column strain gague (foundation)	milli-strain
74	sg10	Column strain gague (2nd floor)	milli-strain
75	sg11	Column strain gague (2nd floor)	milli-strain
76	sg12	Column strain gauge (1st floor)	milli-strain
77	sg13	Column strain gauge (1st floor)	milli-strain
78	sg14	Short-direction beam strain gauge (1st floor)	milli-strain
79	sg15	Short-direction beam strain gauge (1st floor)	milli-strain
80	sg16	Column strain gauge (2nd floor)	milli-strain
81	sg17	Column strain gauge (2nd floor)	milli-strain
82	sg18	Column strain gauge (3rd floor)	milli-strain
83	sg19	Column strain gauge (3rd floor)	milli-strain
84	sg20	Short-direction beam strain gauge (2nd floor)	milli-strain
85	sg21	Short-direction beam strain gauge (2nd floor)	milli-strain
86	sg22	Column strain gauge (3rd floor)	milli-strain
87	sg23	Column strain gauge (4th floor)	milli-strain
88	sg24	Column strain gauge (3rd floor)	milli-strain
89	sg25	Column strain gague (4th floor)	milli-strain
90	sg26	Short-direction beam strain gauge (3rd floor)	milli-strain
91	sg27	Short-direction beam strain gauge (3rd floor)	milli-strain
92	sg28	Column strain gauge (4th floor)	milli-strain
93	sg29	Column strain gauge (4th floor)	milli-strain
94	sg30	Column strain gauge (5th floor)	milli-strain
95	sg31	Column strain gauge (5th floor)	milli-strain
96	sg32	Short-direction beam strain gauge (5th floor)	milli-strain
97	sg33	Short-direction beam strain gauge (5th floor)	milli-strain
98	sg34	Long-direction beam strain gauge (5th floor)	milli-strain
99	sg35	Column strain gauge (5th floor)	milli-strain
100	sg36	Column strain gauge (5th floor)	milli-strain
101	sg37	Column strain gauge (6th floor)	milli-strain
102	sg38	Column strain gauge (6th floor)	milli-strain
103	sg39	Short-direction beam strain gauge (5th floor)	milli-strain
104	sg40	Short-direction beam strain gauge (5th floor)	milli-strain
105	sg41	Long-direction beam strain gauge (5th floor)	milli-strain
106	sg42	Column strain gauge (6th floor)	milli-strain
107	sg43	Column strain gauge (6th floor)	milli-strain
108	sg44	Short-direction beam strain gauge (6th floor)	milli-strain
109	sg45	Short-direction beam strain gauge (6th floor)	milli-strain
110	sg46	Long-direction beam strain gauge (6th floor)	milli-strain
111	sg47	Column strain gauge (spliced bar between 1st & 2nd floors)	milli-strain
112	sg48	Column strain gauge (spliced bar between 1st & 2nd floors)	milli-strain
113	sg49	Column strain gauge (spliced bar between 3rd & 4th floors)	milli-strain
114	sg50	Column strain gauge (spliced bar between 3rd & 4th floors)	milli-strain
115	sg51	Long-direction strain gauge (1st floor)	milli-strain
116	sg52	Long-direction strain gauge (1st floor)	milli-strain
117	sg53	Long-direction strain gauge (2nd floor)	milli-strain
118	sg54	Long-direction strain gauge (2nd floor)	milli-strain
119	sg55	Long-direction strain gauge (3rd floor)	milli-strain
120	sg56	Long-direction strain gauge (3rd floor)	milli-strain
121	DG13	First-floor diagonal measurement	in.
122	DG14	Second-floor diagonal measurement	in.
123	DG15	Third-floor diagonal measurement	in.
124	DG16	Fourth-floor diagonal measurement	in.
125	DG17	Fifth-floor diagonal measurement	in.
126	DG18	Sixth-floor diagonal measurement	in.

APPENDIX C
DISPLACEMENTS

The lateral displacements were measured by two different procedures. In the first procedure, DCDTs and POTs directly measured absolute displacement at the mid-depth of the short-direction beams in each floor (Fig. 3.10a). Lateral displacements relative to the base were obtained by subtracting rigid-body movements due to shake table translation and pitch. In the second procedure, inter-story lateral drifts were derived from diagonal DCDT measurements (Fig. 3.10b). Individual inter-story drift measurements were added to obtain the total floor relative displacements. Additional displacements due to "slab growth" were added to the displacements at the first, second, third, and fourth levels (Fig. 3.11a).

Due to occasional instrument malfunctions, it was necessary to use either one method or a combination of both to derive the lateral displacements. For each test, the method used to derive the lateral displacements is summarized as follows.

(a) Test EC7.7L

X1=D1

X2=D2

X3=D3

X4=D4

X5=D5

X6=D6

Notes:

(1) D1, D2, ..., and D6 refer to DCDT readings minus the lateral displacement due to rigid-body movements of the shake table platform.

(2) X1, X2, ..., and X6 are the reported first, second, ..., and sixth-floor relative lateral

displacements.

(b) Test EC16.6L

X1=D1

X2=P2

X3=D3

X4=D4

X5=D5

X6=X5+0.555(DG6+DG12)

Notes:

(1) P2 refers to potentiometer reading at the second floor minus the lateral displacement due to rigid-body movements of the shake table platform.

(2) The second-floor DCDT D2 malfunctioned during this test. Thus, POT P2 reading was used.

(3) The sixth-floor DCDT D6 and POT P6 malfunctioned during this test. The sixth-floor displacement (X6) was taken as the sum of the fifth-floor displacement (X5) and the sixth-floor inter-story drift, as computed by the diagonal measurements (DG6 and DG12).

(4) Simple geometry was used to compute the inter-story drift from the diagonal measurements.

(c) Test EC49.3L

X1=P1+Slab growth(S1)

X2=P2+Slab growth(S2)

X3=D3+Slab growth(S3)

X4=X3+0.555(DG4+DG10)+Slab growth(S4)

X5=X4+0.555(DG5+DG11)

X6=X5+0.555(DG6+DG12)

Notes:

(1) DCDTs D1 and D2 had been shifted to other locations (Table B.2); thus, POTs P1 and P2 were used instead.

(2) P1 and P2 refer to potentiometer readings at the first and second floor minus the lateral displacement due to rigid-body movements of the shake table platform.

(3) The fourth, fifth, and sixth-floor lateral displacements were obtained by adding the inter-story drifts, measured by diagonal DCDTs (Fig. 3.10(b)).

(d) Tests EC47.7B and MO63.4B

X1=0.555(DG7+DG1)+Slab growth (S1)

Y1=-1.281DG13-0.924(DG7-DG1)

Θ1=0.0247(DG1-DG7)

X2=X1+0.555(DG8+DG2)+Slab growth (S2)

Y2=Y1-1.281DG14-0.924(DG8-DG2)

Θ2=Θ1+0.0247(DG2-DG8)

X3=X2+0.555(DG9+DG3)+Slab growth (S3)

Y3=Y2-1.281DG15-0.924(DG9-DG3)

Θ3=Θ2+0.0247(DG3-DG9)

X4=X3+0.555(DG10+DG4)+Slab growth (S4)

Y4=Y3-1.281DG16-0.924(DG10-DG4)

Θ4=Θ3+0.0247(DG4-DG10)

X5=X4+0.555(DG11+DG5)

Y5=Y4+1.281DG17-0.924(DG11-DG5)

Θ5=Θ4+0.0247(DG5-DG11)

X6=X5+1.11DG12

Y6=Y5-1.281DG18

$\theta 6=\theta 5$

Notes:

(1) The above relations were derived using simple trigonometry and assuming floor beams and columns did not elongate or compress.

(2) DG12 malfunctioned. It was assumed that the incremental rotation in the sixth floor is equal to zero, i.e., DG12=DG6.

(e) Test MX34.6B

X1=1.11DG1

Y1=-1.281DG13

$\theta 1=0$

X2=X1+0.555(DG8+DG2)

Y2=Y1-1.281DG14-0.924(DG8-DG2)

$\theta 2=\theta 1+0.0247$(DG2-DG8)

X3=X2+0.555(DG9+DG3)

Y3=Y2-1.281DG15-0.924(DG9-DG3)

$\theta 3=\theta 2+0.0247$(DG3-DG9)

X4=X3+0.555(DG10+DG4)

Y4=Y3-1.281DG16-0.924(DG10-DG4)

$\theta 4=\theta 3+0.0247$(DG4-DG10)

X5=X4+0.555(DG11+DG5)

Y5=Y4-1.281DG17-0.924(DG11-DG5)

$\theta 5=\theta 4+0.0247$(DG5-DG11)

X6=X5+0.555(DG12+DG6)

Y6=Y5-1.281DG18-0.924(DG12-DG6)

$\theta 6=\theta 5+0.0247$(DG6-DG12)

Notes:

(1) DG7 fell off during this test. It was assumed that the first-floor rotation is equal to zero, i.e., DG1=DG7.

(2) DCDTs S1-S4 had been removed prior to this test (Table 5.4); thus, the additional displacement due to slab growth could not be obtained.

APPENDIX D
NOTATIONS

This appendix summarizes the notations used in this report. If a notation is identical in all the chapters, it is defined once. The notations are described separately for each chapter.

(a) Chapter 1

c=Ratio of tower area to base plan area;

C_{an}=Appendage seismic coefficient in the nth mode;

g=Acceleration of gravity;

K_a=Appendage generalized spring constant;

l_s=Ratio of base portion to overall building height;

m_a=Appendage generalized mass;

p=Ratio of base height to tower height;

X_a=Generalized displacement of appendage;

X_n=Generalized displacement of building without appendage.

(b) Chapter 2

A_g=Column cross-sectional area;

b=Beam web width;

C=Numerical response coefficient;

D=Service dead load;

E=Code design earthquake load;

f_c' =Concrete compressive strength;

h=Beam depth minus slab thickness;

I=Occupancy importance factor;

K=Numerical coefficient depending on lateral resisting system;

L=Service live load;

N=Number of floors;

P=Column axial load;

S=Numerical coefficient for site-structure interaction;

S_a=Acceleration spectrum;

U=Ultimate design load;

V=Base shear;

W=Total dead load of structure;

W_i=ith floor weight;

X_i=Height of the ith floor above base;

Z=Numerical coefficient dependent on seismic zone.

(c) Chapter 5

c=Column width;

d=Effective beam depth;

e=Eccentricity between center of mass and central column;

f6, f5, and f4=Lateral forces at the 6th, 5th, and 4th floors, as specified by the UBC;

h=Beam depth;

H=Story height;

L=Span width;

Mb=Beam moment;

Mc=Column moment;

T=Reinforcement tensile force;

Vb=Beam shear;

Vc=Column shear;

Vj=Horizontal joint shear.

(d) Chapter 6

B=Dynamic load matrix;

C=Damping matrix;

d_b=Diameter of reinforcing bar;

E_s=Steel modulus of elasticity;

f_s=Steel stress at joint face;

jd=Distance between tension-compression couple;

K=Stiffness matrix;

M=Mass matrix;

M_c=Cracking moment;

M_u=Ultimate moment;

M_y=Yield moment;

N=Number of degrees of freedom;

r=Relative displacement vector;

$\dot{r}$=Velocity vector;

$\ddot{r}$=Acceleration vector;

r1, r2, and r3=Influence coefficient vectors;

$\overline{U}$=Average bond stress;

$\ddot{U}_g$=Input acceleration vector;

X=Vector defining x coordinate of joints;

$\overline{X}$=X coordinate of center of rotation;

$\ddot{X}_g$=Horizontal input acceleration;

Y=Vector defining y coordinate of joints;

$\overline{Y}$=Y coordinate of center of rotation;

$\ddot{Y}_g$=Vertical input acceleration;

ϕ^*=Equivalent yield curvature for an elastic-perfectly moment-curvature relation;

ϕ_c=Curvature at cracking moment;

ϕ_u=Curvature at ultimate moment;

ϕ_y=Curvature at yield moment;

θ_c=Rotation at cracking moment;

$\ddot{\theta}_g$=Rotational input acceleration;

θ_u=Rotation at ultimate moment;

θ_y=Rotation at yield moment.

(e) Chapter 7

ϕ=Reduction factor.

(f) Chapter 8

A_a=Seismic coefficient representing peak effective acceleration;

A_v=Coefficient representing peak velocity-related acceleration;

C_s=Design force coefficient;

E=Modulus of elasticity;

F_i=Lateral force at the ith floor;

F_t=Concentrated force at roof;

h=Story height;

h_i=Height of the ith floor above base;

H=Total height of tower or base;

I_c=Column moment of inertia;

I_g=Beam moment of inertia;

K1 and K2=Stiffnesses in a 2DOF system;

[K1]=Stiffness matrix for base without tower;

[K2]=Stiffness matrix for tower fixed at its base;

$K1^*$ and $K2^*$=Generalized stiffnesses for an equivalent 2DOF system;

K_c=Column stiffness;

K_{ga}=Beam stiffness of (i+1)th floor;

K_{gb}=Beam stiffness of (i-1)th floor;

K_i=ith-floor story stiffness for tower or base;

L=Member length;

M1 and M2=Masses in a 2DOF system;

[M1]=Mass matrix for base without tower;

[M2]=Mass matrix for tower fixed at its base;

$M1^*$ and $M2^*$=Generalized masses for an equivalent 2DOF system;

M_i=ith-floor mass for tower or base;

M_y=Flexural capacity;

N=Number of stories in base or tower;

R=Response modification factor;

S=Coefficient representing profile characteristics of site;

T=Fundamental vibration period;

X1 and X2=Lateral displacements of each degree of freedom in a 2DOF system;

α=Stiffness ratio;

β=Mass ratio;

δ=Inter-story drift ratio;

μ_θ=Member rotational ductility;

$\phi 1$=Assumed first-mode shape for base without tower;

$\phi 2$=Assumed first-mode shape for tower fixed at its base;

ϕ_i=Value of first-mode shape at the ith floor;

θ_p=Computed plastic hinge rotation;

θ_u=Ultimate plastic hinge rotation;

θ_y=Rotation at incipient yield condition.

EARTHQUAKE ENGINEERING RESEARCH CENTER REPORT SERIES

EERC reports are available from the National Information Service for Earthquake Engineering(NISEE) and from the National Technical Information Service(NTIS). Numbers in parentheses are Accession Numbers assigned by the National Technical Information Service; these are followed by a price code. Contact NTIS, 5285 Port Royal Road, Springfield Virginia, 22161 for more information. Reports without Accession Numbers were not available from NTIS at the time of printing. For a current complete list of EERC reports (from EERC 67-1) and availablity information, please contact University of California, EERC, NISEE, 1301 South 46th Street, Richmond, California 94804.

UCB/EERC-80/01 "Earthquake Response of Concrete Gravity Dams Including Hydrodynamic and Foundation Interaction Effects," by Chopra, A.K., Chakrabarti, P. and Gupta, S., January 1980, (AD-A087297)A10.

UCB/EERC-80/02 "Rocking Response of Rigid Blocks to Earthquakes," by Yim, C.S., Chopra, A.K. and Penzien, J., January 1980, (PB80 166 002)A04.

UCB/EERC-80/03 "Optimum Inelastic Design of Seismic-Resistant Reinforced Concrete Frame Structures," by Zagajeski, S.W. and Bertero, V.V., January 1980, (PB80 164 635)A06.

UCB/EERC-80/04 "Effects of Amount and Arrangement of Wall-Panel Reinforcement on Hysteretic Behavior of Reinforced Concrete Walls," by Iliya, R. and Bertero, V.V., February 1980, (PB81 122 525)A09.

UCB/EERC-80/05 "Shaking Table Research on Concrete Dam Models," by Niwa, A. and Clough, R.W., September 1980, (PB81 122 368)A06.

UCB/EERC-80/06 "The Design of Steel Energy-Absorbing Restrainers and their Incorporation into Nuclear Power Plants for Enhanced Safety (Vol 1a): Piping with Energy Absorbing Restrainers: Parameter Study on Small Systems," by Powell, G.H., Oughourlian, C. and Simons, J., June 1980.

UCB/EERC-80/07 "Inelastic Torsional Response of Structures Subjected to Earthquake Ground Motions," by Yamazaki, Y., April 1980, (PB81 122 327)A08.

UCB/EERC-80/08 "Study of X-Braced Steel Frame Structures under Earthquake Simulation," by Ghanaat, Y., April 1980, (PB81 122 335)A11.

UCB/EERC-80/09 "Hybrid Modelling of Soil-Structure Interaction," by Gupta, S., Lin, T.W. and Penzien, J., May 1980, (PB81 122 319)A07.

UCB/EERC-80/10 "General Applicability of a Nonlinear Model of a One Story Steel Frame," by Sveinsson, B.I. and McNiven, H.D., May 1980, (PB81 124 877)A06.

UCB/EERC-80/11 "A Green-Function Method for Wave Interaction with a Submerged Body," by Kioka, W., April 1980, (PB81 122 269)A07.

UCB/EERC-80/12 "Hydrodynamic Pressure and Added Mass for Axisymmetric Bodies.," by Nilrat, F., May 1980, (PB81 122 343)A08.

UCB/EERC-80/13 "Treatment of Non-Linear Drag Forces Acting on Offshore Platforms," by Dao, B.V. and Penzien, J., May 1980, (PB81 153 413)A07.

UCB/EERC-80/14 "2D Plane/Axisymmetric Solid Element (Type 3-Elastic or Elastic-Perfectly Plastic) for the ANSR-II Program," by Mondkar, D.P. and Powell, G.H., July 1980, (PB81 122 350)A03.

UCB/EERC-80/15 "A Response Spectrum Method for Random Vibrations," by Der Kiureghian, A., June 1981, (PB81 122 301)A03.

UCB/EERC-80/16 "Cyclic Inelastic Buckling of Tubular Steel Braces," by Zayas, V.A., Popov, E.P. and Martin, S.A., June 1981, (PB81 124 885)A10.

UCB/EERC-80/17 "Dynamic Response of Simple Arch Dams Including Hydrodynamic Interaction," by Porter, C.S. and Chopra, A.K., July 1981, (PB81 124 000)A13.

UCB/EERC-80/18 "Experimental Testing of a Friction Damped Aseismic Base Isolation System with Fail-Safe Characteristics," by Kelly, J.M., Beucke, K.E. and Skinner, M.S., July 1980, (PB81 148 595)A04.

UCB/EERC-80/19 "The Design of Steel Emergy-Absorbing Restrainers and their Incorporation into Nuclear Power Plants for Enhanced Safety (Vol.1B): Stochastic Seismic Analyses of Nuclear Power Plant Structures and Piping Systems Subjected to Multiple Supported Excitations," by Lee, M.C. and Penzien, J., June 1980, (PB82 201 872)A08.

UCB/EERC-80/20 "The Design of Steel Energy-Absorbing Restrainers and their Incorporation into Nuclear Power Plants for Enhanced Safety (Vol 1C): Numerical Method for Dynamic Substructure Analysis," by Dickens, J.M. and Wilson, E.L., June 1980.

UCB/EERC-80/21 "The Design of Steel Energy-Absorbing Restrainers and their Incorporation into Nuclear Power Plants for Enhanced Safety (Vol 2): Development and Testing of Restraints for Nuclear Piping Systems," by Kelly, J.M. and Skinner, M.S., June 1980.

UCB/EERC-80/22 "3D Solid Element (Type 4-Elastic or Elastic-Perfectly-Plastic) for the ANSR-II Program," by Mondkar, D.P. and Powell, G.H., July 1980, (PB81 123 242)A03.

UCB/EERC-80/23 "Gap-Friction Element (Type 5) for the Ansr-II Program," by Mondkar, D.P. and Powell, G.H., July 1980, (PB81 122 285)A03.

UCB/EERC-80/24 "U-Bar Restraint Element (Type 11) for the ANSR-II Program," by Oughourlian, C. and Powell, G.H., July 1980, (PB81 122 293)A03.

UCB/EERC-80/25 "Testing of a Natural Rubber Base Isolation System by an Explosively Simulated Earthquake," by Kelly, J.M., August 1980, (PB81 201 360)A04.

UCB/EERC-80/26 "Input Identification from Structural Vibrational Response," by Hu, Y., August 1980, (PB81 152 308)A05.

UCB/EERC-80/27 "Cyclic Inelastic Behavior of Steel Offshore Structures," by Zayas, V.A., Mahin, S.A. and Popov, E.P., August 1980, (PB81 196 180)A15.

UCB/EERC-80/28 "Shaking Table Testing of a Reinforced Concrete Frame with Biaxial Response," by Oliva, M.G., October 1980, (PB81 154 304)A10.

UCB/EERC-80/29 "Dynamic Properties of a Twelve-Story Prefabricated Panel Building," by Bouwkamp, J.G., Kollegger, J.P. and Stephen, R.M., October 1980, (PB82 138 777)A07.

UCB/EERC-80/30 "Dynamic Properties of an Eight-Story Prefabricated Panel Building," by Bouwkamp, J.G., Kollegger, J.P. and Stephen, R.M., October 1980, (PB81 200 313)A05.

UCB/EERC-80/31 "Predictive Dynamic Response of Panel Type Structures under Earthquakes," by Kollegger, J.P. and Bouwkamp, J.G., October 1980, (PB81 152 316)A04.

UCB/EERC-80/32 "The Design of Steel Energy-Absorbing Restrainers and their Incorporation into Nuclear Power Plants for Enhanced Safety (Vol 3): Testing of Commercial Steels in Low-Cycle Torsional Fatique," by Spanner, P., Parker, E.R., Jongewaard, E. and Dory, M., 1980.

UCB/EERC-80/33 "The Design of Steel Energy-Absorbing Restrainers and their Incorporation into Nuclear Power Plants for Enhanced Safety (Vol 4): Shaking Table Tests of Piping Systems with Energy-Absorbing Restrainers," by Stiemer, S.F. and Godden, W.G., September 1980, (PB82 201 880)A05.

UCB/EERC-80/34 "The Design of Steel Energy-Absorbing Restrainers and their Incorporation into Nuclear Power Plants for Enhanced Safety (Vol 5): Summary Report," by Spencer, P., 1980.

UCB/EERC-80/35 "Experimental Testing of an Energy-Absorbing Base Isolation System," by Kelly, J.M., Skinner, M.S. and Beucke, K.E., October 1980, (PB81 154 072)A04.

UCB/EERC-80/36 "Simulating and Analyzing Artificial Non-Stationary Earth Ground Motions," by Nau, R.F., Oliver, R.M. and Pister, K.S., October 1980, (PB81 153 397)A04.

UCB/EERC-80/37 "Earthquake Engineering at Berkeley - 1980," by , September 1980, (PB81 205 674)A09.

UCB/EERC-80/38 "Inelastic Seismic Analysis of Large Panel Buildings," by Schricker, V. and Powell, G.H., September 1980, (PB81 154 338)A13.

UCB/EERC-80/39 "Dynamic Response of Embankment, Concrete-Gavity and Arch Dams Including Hydrodynamic Interation," by Hall, J.F. and Chopra, A.K., October 1980, (PB81 152 324)A11.

UCB/EERC-80/40 "Inelastic Buckling of Steel Struts under Cyclic Load Reversal.," by Black, R.G. , Wenger, W.A. and Popov, E.P., October 1980, (PB81 154 312)A08.

UCB/EERC-80/41 "Influence of Site Characteristics on Buildings Damage during the October 3,1974 Lima Earthquake," by Repetto, P., Arango, I. and Seed, H.B., September 1980, (PB81 161 739)A05.

UCB/EERC-80/42 "Evaluation of a Shaking Table Test Program on Response Behavior of a Two Story Reinforced Concrete Frame," by Blondet, J.M., Clough, R.W. and Mahin, S.A., December 1980, (PB82 196 544)A11.

UCB/EERC-80/43 "Modelling of Soil-Structure Interaction by Finite and Infinite Elements," by Medina, F., December 1980, (PB81 229 270)A04.

UCB/EERC-81/01 "Control of Seismic Response of Piping Systems and Other Structures by Base Isolation," by Kelly, J.M., January 1981, (PB81 200 735)A05.

UCB/EERC-81/02 "OPTNSR- An Interactive Software System for Optimal Design of Statically and Dynamically Loaded Structures with Nonlinear Response," by Bhatti, M.A., Ciampi, V. and Pister, K.S., January 1981, (PB81 218 851)A09.

UCB/EERC-81/03 "Analysis of Local Variations in Free Field Seismic Ground Motions," by Chen, J.-C., Lysmer, J. and Seed, H.B., January 1981, (AD-A099508)A13.

UCB/EERC-81/04 "Inelastic Structural Modeling of Braced Offshore Platforms for Seismic Loading. ," by Zayas, V.A., Shing, P.-S.B., Mahin, S.A. and Popov, E.P., January 1981, (PB82 138 777)A07.

UCB/EERC-81/05 "Dynamic Response of Light Equipment in Structures," by Der Kiureghian, A., Sackman, J.L. and Nour-Omid, B., April 1981, (PB81 218 497)A04.

UCB/EERC-81/06 "Preliminary Experimental Investigation of a Broad Base Liquid Storage Tank," by Bouwkamp, J.G., Kollegger, J.P. and Stephen, R.M., May 1981, (PB82 140 385)A03.

UCB/EERC-81/07 "The Seismic Resistant Design of Reinforced Concrete Coupled Structural Walls," by Aktan, A.E. and Bertero, V.V., June 1981, (PB82 113 358)A11.

UCB/EERC-81/08 "Unassigned," by Unassigned, 1981.

UCB/EERC-81/09 "Experimental Behavior of a Spatial Piping System with Steel Energy Absorbers Subjected to a Simulated Differential Seismic Input," by Stiemer, S.F., Godden, W.G. and Kelly, J.M., July 1981, (PB82 201 898)A04.

UCB/EERC-81/10 "Evaluation of Seismic Design Provisions for Masonry in the United States," by Sveinsson, B.I., Mayes, R.L. and McNiven, H.D., August 1981, (PB82 166 075)A08.

UCB/EERC-81/11 "Two-Dimensional Hybrid Modelling of Soil-Structure Interaction," by Tzong, T.-J., Gupta, S. and Penzien, J., August 1981, (PB82 142 118)A04.

UCB/EERC-81/12 "Studies on Effects of Infills in Seismic Resistant R/C Construction," by Brokken, S. and Bertero, V.V., October 1981, (PB82 166 190)A09.

UCB/EERC-81/13 "Linear Models to Predict the Nonlinear Seismic Behavior of a One-Story Steel Frame," by Valdimarsson, H., Shah, A.H. and McNiven, H.D., September 1981, (PB82 138 793)A07.

UCB/EERC-81/14 "TLUSH: A Computer Program for the Three-Dimensional Dynamic Analysis of Earth Dams," by Kagawa, T., Mejia, L.H., Seed, H.B. and Lysmer, J., September 1981, (PB82 139 940)A06.

UCB/EERC-81/15 "Three Dimensional Dynamic Response Analysis of Earth Dams," by Mejia, L.H. and Seed, H.B., September 1981, (PB82 137 274)A12.

UCB/EERC-81/16 "Experimental Study of Lead and Elastomeric Dampers for Base Isolation Systems," by Kelly, J.M. and Hodder, S.B., October 1981, (PB82 166 182)A05.

UCB/EERC-81/17 "The Influence of Base Isolation on the Seismic Response of Light Secondary Equipment," by Kelly, J.M., April 1981, (PB82 255 266)A04.

UCB/EERC-81/18 "Studies on Evaluation of Shaking Table Response Analysis Procedures," by Blondet, J. Marcial, November 1981, (PB82 197 278)A10.

UCB/EERC-81/19 "DELIGHT.STRUCT: A Computer-Aided Design Environment for Structural Engineering. ," by Balling, R.J., Pister, K.S. and Polak, E., December 1981, (PB82 218 496)A07.

UCB/EERC-81/20 "Optimal Design of Seismic-Resistant Planar Steel Frames," by Balling, R.J., Ciampi, V. and Pister, K.S., December 1981, (PB82 220 179)A07.

UCB/EERC-82/01 "Dynamic Behavior of Ground for Seismic Analysis of Lifeline Systems," by Sato, T. and Der Kiureghian, A., January 1982, (PB82 218 926)A05.

UCB/EERC-82/02 "Shaking Table Tests of a Tubular Steel Frame Model," by Ghanaat, Y. and Clough, R.W., January 1982, (PB82 220 161)A07.

UCB/EERC-82/03 "Behavior of a Piping System under Seismic Excitation: Experimental Investigations of a Spatial Piping System supported by Mechanical Shock Arrestors," by Schneider, S., Lee, H.-M. and Godden, W. G., May 1982, (PB83 172 544)A09.

UCB/EERC-82/04 "New Approaches for the Dynamic Analysis of Large Structural Systems," by Wilson, E.L., June 1982, (PB83 148 080)A05.

UCB/EERC-82/05 "Model Study of Effects of Damage on the Vibration Properties of Steel Offshore Platforms," by Shahrivar, F. and Bouwkamp, J.G., June 1982, (PB83 148 742)A10.

UCB/EERC-82/06 "States of the Art and Pratice in the Optimum Seismic Design and Analytical Response Prediction of R/C Frame Wall Structures," by Aktan, A.E. and Bertero, V.V., July 1982, (PB83 147 736)A05.

UCB/EERC-82/07 "Further Study of the Earthquake Response of a Broad Cylindrical Liquid-Storage Tank Model," by Manos, G.C. and Clough, R.W., July 1982, (PB83 147 744)A11.

UCB/EERC-82/08 "An Evaluation of the Design and Analytical Seismic Response of a Seven Story Reinforced Concrete Frame," by Charney, F.A. and Bertero, V.V., July 1982, (PB83 157 628)A09.

UCB/EERC-82/09 "Fluid-Structure Interactions: Added Mass Computations for Incompressible Fluid. ," by Kuo, J.S.-H., August 1982, (PB83 156 281)A07.

UCB/EERC-82/10 "Joint-Opening Nonlinear Mechanism: Interface Smeared Crack Model," by Kuo, J.S.-H., August 1982, (PB83 149 195)A05.

UCB/EERC-82/11 "Dynamic Response Analysis of Techi Dam," by Clough, R.W., Stephen, R.M. and Kuo, J.S.-H., August 1982, (PB83 147 496)A06.

UCB/EERC-82/12 "Prediction of the Seismic Response of R/C Frame-Coupled Wall Structures," by Aktan, A.E., Bertero, V.V. and Piazzo, M., August 1982, (PB83 149 203)A09.

UCB/EERC-82/13 "Preliminary Report on the Smart 1 Strong Motion Array in Taiwan," by Bolt, B.A. , Loh, C.H., Penzien, J. and Tsai, Y.B., August 1982, (PB83 159 400)A10.

UCB/EERC-82/14 "Shaking-Table Studies of an Eccentrically X-Braced Steel Structure," by Yang, M.S., September 1982, (PB83 260 778)A12.

UCB/EERC-82/15 "The Performance of Stairways in Earthquakes," by Roha, C., Axley, J.W. and Bertero, V.V., September 1982, (PB83 157 693)A07.

UCB/EERC-82/16 "The Behavior of Submerged Multiple Bodies in Earthquakes," by Liao, W.-G., September 1982, (PB83 158 709)A07.

UCB/EERC-82/17 "Effects of Concrete Types and Loading Conditions on Local Bond-Slip Relationships," by Cowell, A.D., Popov, E.P. and Bertero, V.V., September 1982, (PB83 153 577)A04.

UCB/EERC-82/18 "Mechanical Behavior of Shear Wall Vertical Boundary Members: An Experimental Investigation," by Wagner, M.T. and Bertero, V.V., October 1982, (PB83 159 764)A05.

UCB/EERC-82/19 "Experimental Studies of Multi-support Seismic Loading on Piping Systems," by Kelly, J.M. and Cowell, A.D., November 1982.

UCB/EERC-82/20 "Generalized Plastic Hinge Concepts for 3D Beam-Column Elements," by Chen, P. F.-S. and Powell, G.H., November 1982, (PB83 247 981)A13.

UCB/EERC-82/21 "ANSR-II: General Computer Program for Nonlinear Structural Analysis," by Oughourlian, C.V. and Powell, G.H., November 1982, (PB83 251 330)A12.

UCB/EERC-82/22 "Solution Strategies for Statically Loaded Nonlinear Structures," by Simons, J.W. and Powell, G.H., November 1982, (PB83 197 970)A06.

UCB/EERC-82/23 "Analytical Model of Deformed Bar Anchorages under Generalized Excitations," by Ciampi, V., Eligehausen, R., Bertero, V.V. and Popov, E.P., November 1982, (PB83 169 532)A06.

UCB/EERC-82/24 "A Mathematical Model for the Response of Masonry Walls to Dynamic Excitations," by Sucuoglu, H., Mengi, Y. and McNiven, H.D., November 1982, (PB83 169 011)A07.

UCB/EERC-82/25 "Earthquake Response Considerations of Broad Liquid Storage Tanks," by Cambra, F.J., November 1982, (PB83 251 215)A09.

UCB/EERC-82/26 "Computational Models for Cyclic Plasticity, Rate Dependence and Creep," by Mosaddad, B. and Powell, G.H., November 1982, (PB83 245 829)A08.

UCB/EERC-82/27 "Inelastic Analysis of Piping and Tubular Structures," by Mahasuverachai, M. and Powell, G.H., November 1982, (PB83 249 987)A07.

UCB/EERC-83/01 "The Economic Feasibility of Seismic Rehabilitation of Buildings by Base Isolation," by Kelly, J.M., January 1983, (PB83 197 988)A05.

UCB/EERC-83/02 "Seismic Moment Connections for Moment-Resisting Steel Frames.," by Popov, E.P., January 1983, (PB83 195 412)A04.

UCB/EERC-83/03 "Design of Links and Beam-to-Column Connections for Eccentrically Braced Steel Frames," by Popov, E.P. and Malley, J.O., January 1983, (PB83 194 811)A04.

UCB/EERC-83/04 "Numerical Techniques for the Evaluation of Soil-Structure Interaction Effects in the Time Domain," by Bayo, E. and Wilson, E.L., February 1983, (PB83 245 605)A09.

UCB/EERC-83/05 "A Transducer for Measuring the Internal Forces in the Columns of a Frame-Wall Reinforced Concrete Structure," by Sause, R. and Bertero, V.V., May 1983, (PB84 119 494)A06.

UCB/EERC-83/06 "Dynamic Interactions Between Floating Ice and Offshore Structures," by Croteau, P., May 1983, (PB84 119 486)A16.

UCB/EERC-83/07 "Dynamic Analysis of Multiply Tuned and Arbitrarily Supported Secondary Systems. ," by Igusa, T. and Der Kiureghian, A., July 1983, (PB84 118 272)A11.

UCB/EERC-83/08 "A Laboratory Study of Submerged Multi-body Systems in Earthquakes," by Ansari, G.R., June 1983, (PB83 261 842)A17.

UCB/EERC-83/09 "Effects of Transient Foundation Uplift on Earthquake Response of Structures," by Yim, C.-S. and Chopra, A.K., June 1983, (PB83 261 396)A07.

UCB/EERC-83/10 "Optimal Design of Friction-Braced Frames under Seismic Loading," by Austin, M.A. and Pister, K.S., June 1983, (PB84 119 288)A06.

UCB/EERC-83/11 "Shaking Table Study of Single-Story Masonry Houses: Dynamic Performance under Three Component Seismic Input and Recommendations," by Manos, G.C., Clough, R.W. and Mayes, R.L., July 1983, (UCB/EERC-83/11)A08.

UCB/EERC-83/12 "Experimental Error Propagation in Pseudodynamic Testing," by Shiing, P.B. and Mahin, S.A., June 1983, (PB84 119 270)A09.

UCB/EERC-83/13 "Experimental and Analytical Predictions of the Mechanical Characteristics of a 1/5-scale Model of a 7-story R/C Frame-Wall Building Structure," by Aktan, A.E., Bertero, V.V., Chowdhury, A.A. and Nagashima, T., June 1983, (PB84 119 213)A07.

UCB/EERC-83/14 "Shaking Table Tests of Large-Panel Precast Concrete Building System Assemblages," by Oliva, M.G. and Clough, R.W., June 1983, (PB86 110 210/AS)A11.

UCB/EERC-83/15 "Seismic Behavior of Active Beam Links in Eccentrically Braced Frames," by Hjelmstad, K.D. and Popov, E.P., July 1983, (PB84 119 676)A09.

UCB/EERC-83/16 "System Identification of Structures with Joint Rotation," by Dimsdale, J.S., July 1983, (PB84 192 210)A06.

UCB/EERC-83/17 "Construction of Inelastic Response Spectra for Single-Degree-of-Freedom Systems," by Mahin, S. and Lin, J., June 1983, (PB84 208 834)A05.

UCB/EERC-83/18 "Interactive Computer Analysis Methods for Predicting the Inelastic Cyclic Behaviour of Structural Sections," by Kaba, S. and Mahin, S., July 1983, (PB84 192 012)A06.

UCB/EERC-83/19 "Effects of Bond Deterioration on Hysteretic Behavior of Reinforced Concrete Joints," by Filippou, F.C., Popov, E.P. and Bertero, V.V., August 1983, (PB84 192 020)A10.

UCB/EERC-83/20 "Analytical and Experimental Correlation of Large-Panel Precast Building System Performance," by Oliva, M.G., Clough, R.W., Velkov, M. and Gavrilovic, P., November 1983.

UCB/EERC-83/21 "Mechanical Characteristics of Materials Used in a 1/5 Scale Model of a 7-Story Reinforced Concrete Test Structure," by Bertero, V.V., Aktan, A.E., Harris, H.G. and Chowdhury, A.A., October 1983, (PB84 193 697)A05.

UCB/EERC-83/22 "Hybrid Modelling of Soil-Structure Interaction in Layered Media," by Tzong, T.-J. and Penzien, J., October 1983, (PB84 192 178)A08.

UCB/EERC-83/23 "Local Bond Stress-Slip Relationships of Deformed Bars under Generalized Excitations," by Eligehausen, R., Popov, E.P. and Bertero, V.V., October 1983, (PB84 192 848)A09.

UCB/EERC-83/24 "Design Considerations for Shear Links in Eccentrically Braced Frames," by Malley, J.O. and Popov, E.P., November 1983, (PB84 192 186)A07.

UCB/EERC-84/01 "Pseudodynamic Test Method for Seismic Performance Evaluation: Theory and Implementation," by Shing, P.-S. B. and Mahin, S.A., January 1984, (PB84 190 644)A08.

UCB/EERC-84/02 "Dynamic Response Behavior of Kiang Hong Dian Dam," by Clough, R.W., Chang, K.-T., Chen, H.-Q. and Stephen, R.M., April 1984, (PB84 209 402)A08.

UCB/EERC-84/03 "Refined Modelling of Reinforced Concrete Columns for Seismic Analysis," by Kaba, S.A. and Mahin, S.A., April 1984, (PB84 234 384)A06.

UCB/EERC-84/04 "A New Floor Response Spectrum Method for Seismic Analysis of Multiply Supported Secondary Systems," by Asfura, A. and Der Kiureghian, A., June 1984, (PB84 239 417)A06.

UCB/EERC-84/05 "Earthquake Simulation Tests and Associated Studies of a 1/5th-scale Model of a 7-Story R/C Frame-Wall Test Structure," by Bertero, V.V., Aktan, A.E., Charney, F.A. and Sause, R., June 1984, (PB84 239 409)A09.

UCB/EERC-84/06 "R/C Structural Walls: Seismic Design for Shear," by Aktan, A.E. and Bertero, V.V., 1984.

UCB/EERC-84/07 "Behavior of Interior and Exterior Flat-Plate Connections subjected to Inelastic Load Reversals," by Zee, H.L. and Moehle, J.P., August 1984, (PB86 117 629/AS)A07.

UCB/EERC-84/08 "Experimental Study of the Seismic Behavior of a Two-Story Flat-Plate Structure. ," by Moehle, J.P. and Diebold, J.W., August 1984, (PB86 122 553/AS)A12.

UCB/EERC-84/09 "Phenomenological Modeling of Steel Braces under Cyclic Loading," by Ikeda, K., Mahin, S.A. and Dermitzakis, S.N., May 1984, (PB86 132 198/AS)A08.

UCB/EERC-84/10 "Earthquake Analysis and Response of Concrete Gravity Dams," by Fenves, G. and Chopra, A.K., August 1984, (PB85 193 902/AS)A11.

UCB/EERC-84/11 "EAGD-84: A Computer Program for Earthquake Analysis of Concrete Gravity Dams," by Fenves, G. and Chopra, A.K., August 1984, (PB85 193 613/AS)A05.

UCB/EERC-84/12 "A Refined Physical Theory Model for Predicting the Seismic Behavior of Braced Steel Frames," by Ikeda, K. and Mahin, S.A., July 1984, (PB85 191 450/AS)A09.

UCB/EERC-84/13 "Earthquake Engineering Research at Berkeley - 1984," by , August 1984, (PB85 197 341/AS)A10.

UCB/EERC-84/14 "Moduli and Damping Factors for Dynamic Analyses of Cohesionless Soils," by Seed, H.B., Wong, R.T., Idriss, I.M. and Tokimatsu, K., September 1984, (PB85 191 468/AS)A04.

UCB/EERC-84/15 "The Influence of SPT Procedures in Soil Liquefaction Resistance Evaluations," by Seed, H.B., Tokimatsu, K., Harder, L.F. and Chung, R.M., October 1984, (PB85 191 732/AS)A04.

UCB/EERC-84/16 "Simplified Procedures for the Evaluation of Settlements in Sands Due to Earthquake Shaking," by Tokimatsu, K. and Seed, H.B., October 1984, (PB85 197 887/AS)A03.

UCB/EERC-84/17 "Evaluation of Energy Absorption Characteristics of Bridges under Seismic Conditions," by Imbsen, R.A. and Penzien, J., November 1984.

UCB/EERC-84/18 "Structure-Foundation Interactions under Dynamic Loads," by Liu, W.D. and Penzien, J., November 1984, (PB87 124 889/AS)A11.

UCB/EERC-84/19 "Seismic Modelling of Deep Foundations," by Chen, C.-H. and Penzien, J., November 1984, (PB87 124 798/AS)A07.

UCB/EERC-84/20 "Dynamic Response Behavior of Quan Shui Dam," by Clough, R.W., Chang, K.-T., Chen, H.-Q., Stephen, R.M., Ghanaat, Y. and Qi, J.-H., November 1984, (PB86 115177/AS)A07.

UCB/EERC-85/01 "Simplified Methods of Analysis for Earthquake Resistant Design of Buildings," by Cruz, E.F. and Chopra, A.K., February 1985, (PB86 112299/AS)A12.

UCB/EERC-85/02 "Estimation of Seismic Wave Coherency and Rupture Velocity using the SMART 1 Strong-Motion Array Recordings," by Abrahamson, N.A., March 1985, (PB86 214 343)A07.

UCB/EERC-85/03 "Dynamic Properties of a Thirty Story Condominium Tower Building," by Stephen, R.M., Wilson, E.L. and Stander, N., April 1985, (PB86 118965/AS)A06.

UCB/EERC-85/04 "Development of Substructuring Techniques for On-Line Computer Controlled Seismic Performance Testing," by Dermitzakis, S. and Mahin, S., February 1985, (PB86 132941/AS)A08.

UCB/EERC-85/05 "A Simple Model for Reinforcing Bar Anchorages under Cyclic Excitations," by Filippou, F.C., March 1985, (PB86 112 919/AS)A05.

UCB/EERC-85/06 "Racking Behavior of Wood-framed Gypsum Panels under Dynamic Load," by Oliva, M.G., June 1985.

UCB/EERC-85/07 "Earthquake Analysis and Response of Concrete Arch Dams," by Fok, K.-L. and Chopra, A.K., June 1985, (PB86 139672/AS)A10.

UCB/EERC-85/08 "Effect of Inelastic Behavior on the Analysis and Design of Earthquake Resistant Structures," by Lin, J.P. and Mahin, S.A., June 1985, (PB86 135340/AS)A08.

UCB/EERC-85/09 "Earthquake Simulator Testing of a Base-Isolated Bridge Deck," by Kelly, J.M., Buckle, I.G. and Tsai, H.-C., January 1986, (PB87 124 152/AS)A06.

UCB/EERC-85/10 "Simplified Analysis for Earthquake Resistant Design of Concrete Gravity Dams," by Fenves, G. and Chopra, A.K., June 1986, (PB87 124 160/AS)A08.

UCB/EERC-85/11 "Dynamic Interaction Effects in Arch Dams," by Clough, R.W., Chang, K.-T., Chen, H.-Q. and Ghanaat, Y., October 1985, (PB86 135027/AS)A05.

UCB/EERC-85/12 "Dynamic Response of Long Valley Dam in the Mammoth Lake Earthquake Series of May 25-27, 1980," by Lai, S. and Seed, H.B., November 1985, (PB86 142304/AS)A05.

UCB/EERC-85/13 "A Methodology for Computer-Aided Design of Earthquake-Resistant Steel Structures," by Austin, M.A., Pister, K.S. and Mahin, S.A., December 1985, (PB86 159480/AS)A10 .

UCB/EERC-85/14 "Response of Tension-Leg Platforms to Vertical Seismic Excitations," by Liou, G.-S., Penzien, J. and Yeung, R.W., December 1985, (PB87 124 871/AS)A08.

UCB/EERC-85/15 "Cyclic Loading Tests of Masonry Single Piers: Volume 4 - Additional Tests with Height to Width Ratio of 1," by Sveinsson, B., McNiven, H.D. and Sucuoglu, H., December 1985, (PB87 165 031/AS)A08.

UCB/EERC-85/16 "An Experimental Program for Studying the Dynamic Response of a Steel Frame with a Variety of Infill Partitions," by Yanev, B. and McNiven, H.D., December 1985.

UCB/EERC-86/01 "A Study of Seismically Resistant Eccentrically Braced Steel Frame Systems," by Kasai, K. and Popov, E.P., January 1986, (PB87 124 178/AS)A14.

UCB/EERC-86/02 "Design Problems in Soil Liquefaction," by Seed, H.B., February 1986, (PB87 124 186/AS)A03.

UCB/EERC-86/03 "Implications of Recent Earthquakes and Research on Earthquake-Resistant Design and Construction of Buildings," by Bertero, V.V., March 1986, (PB87 124 194/AS)A05.

UCB/EERC-86/04 "The Use of Load Dependent Vectors for Dynamic and Earthquake Analyses," by Leger, P., Wilson, E.L. and Clough, R.W., March 1986, (PB87 124 202/AS)A12.

UCB/EERC-86/05 "Two Beam-To-Column Web Connections," by Tsai, K.-C. and Popov, E.P., April 1986 , (PB87 124 301/AS)A04.

UCB/EERC-86/06 "Determination of Penetration Resistance for Coarse-Grained Soils using the Becker Hammer Drill," by Harder, L.F. and Seed, H.B., May 1986, (PB87 124 210/AS)A07.

UCB/EERC-86/07 "A Mathematical Model for Predicting the Nonlinear Response of Unreinforced Masonry Walls to In-Plane Earthquake Excitations," by Mengi, Y. and McNiven, H.D., May 1986, (PB87 124 780/AS)A06.

UCB/EERC-86/08 "The 19 September 1985 Mexico Earthquake: Building Behavior," by Bertero, V.V., July 1986.

UCB/EERC-86/09 "EACD-3D: A Computer Program for Three-Dimensional Earthquake Analysis of Concrete Dams," by Fok, K.-L., Hall, J.F. and Chopra, A.K., July 1986, (PB87 124 228/AS)A08.

UCB/EERC-86/10 "Earthquake Simulation Tests and Associated Studies of a 0.3-Scale Model of a Six-Story Concentrically Braced Steel Structure," by Uang, C.-M. and Bertero, V.V., December 1986, (PB87 163564/AS)A17.

UCB/EERC-86/11 "Mechanical Characteristics of Base Isolation Bearings for a Bridge Deck Model Test," by Kelly, J.M., Buckle, I.G. and Koh, C.-G., 1987.

UCB/EERC-86/12 "Modelling of Dynamic Response of Elastomeric Isolation Bearings," by Koh, C.-G. and Kelly, J.M., 1987.

UCB/EERC-87/01 "The FPS Earthquake Resisting System: Experimental Report," by Zayas, V.A., Low, S.S. and Mahin, S.A., June 1987.

UCB/EERC-87/02 "Earthquake Simulator Tests and Associated Studies of a 0.3-Scale Model of a Six-Story Eccentrically Braced Steel Structure," by Whittaker, A., Uang, C.-M. and Bertero, V.V., July 1987.

UCB/EERC-87/03 "A Displacement Control and Uplift Restraint Device for Base-Isolated Structures," by Kelly, J.M., Griffith, M.C. and Aiken, I.G., April 1987.

UCB/EERC-87/04 "Earthquake Simulator Testing of a Combined Sliding Bearing and Rubber Bearing Isolation System," by Kelly, J.M. and Chalhoub, M.S., 1987.

UCB/EERC-87/05 "Three-Dimensional Inelastic Analysis of Reinforced Concrete Frame-Wall Structures," by Moazzami, S. and Bertero, V.V., May 1987.

UCB/EERC-87/06 "Experiments on Eccentrically Braced Frames With Composite Floors," by Ricles, J. and Popov, E., June 1987.

UCB/EERC-87/07 "Dynamic Analysis of Seismically Resistant Eccentrically Braced Frames," by Ricles, J. and Popov, E., June 1987.

UCB/EERC-87/08 "Undrained Cyclic Triaxial Testing of Gravels - The Effect of Membrane Compliance, " by Evans, M.D. and Seed, H.B., July 1987.

UCB/EERC-87/09 "Hybrid Solution Techniques For Generalized Pseudo-Dynamic Testing," by Thewalt, C. and Mahin, S. A., July 1987.

UCB/EERC-87/10 "Investigation of Ultimate Behavior of AISC Group 4 and 5 Heavy Steel Rolled-Section Splices with Full and Partial Penetration Butt Welds," by Bruneau, M. and Mahin, S.A., July 1987.

UCB/EERC-87/11 "Residual Strength of Sand From Dam Failures in the Chilean Earthquake of March 3, 1985," by De Alba, P., Seed, H. B., Retamal, E. and Seed, R. B., September 1987.

UCB/EERC-87/12 "Inelastic Response of Structures With Mass And/Or Stiffness Eccentricities In Plan Subjected to Earthquake Excitation," by Bruneau, M., September 1987.

UCB/EERC-87/13 "CSTRUCT: An Interactive Computer Environment For the Design and Analysis of Earthquake Resistant Steel Structures," by Austin, M.A., Mahin, S.A. and Pister, K.S., September 1987.

UCB/EERC-87/14 "Experimental Study of Reinforced Concrete Columns Subjected to Multi-Axial Loading," by Low, S.S. and Moehle, J.P., September 1987.

UCB/EERC-87/15 "Relationships Between Soil Conditions and Earthquake Ground Motions in Mexico City in the Earthquake of Sept. 19, 1985," by Seed, H.B., Romo, M.P., Sun, J., and Jaime, A., October 1987.

UCB/EERC-87/16 "Experimental Study of Seismic Response of R.C. Setback Buildings," by Shahrooz, B.M. and Moehle, J.P., October 1987.